

TOWARDS IMPROVING THE PROPERTIES AND FURTHERING ACCEPTANCE  
OF ADVANCED TECHNOLOGY NUCLEAR FUELS

by

Jennifer K. Watkins



A dissertation

submitted in partial fulfillment

of the requirements for the degree of

Doctor of Philosophy in Materials Science and Engineering

Boise State University

May 2022

© 2022

Jennifer K. Watkins

ALL RIGHTS RESERVED

BOISE STATE UNIVERSITY GRADUATE COLLEGE

**DEFENSE COMMITTEE AND FINAL READING APPROVALS**

of the dissertation submitted by

Jennifer K. Watkins

Dissertation Title:   Towards Improving the Properties and Furthering Acceptance of  
Advanced Technology Nuclear Fuels

Date of Final Oral Examination:                   14 March 2022

The following individuals read and discussed the dissertation submitted by student Jennifer K. Watkins, and they evaluated their presentation and response to questions during the final oral examination. They found that the student passed the final oral examination.

Brian J. Jaques, Ph.D., P.E.	Chair, Supervisory Committee
Darryl Butt, Ph.D.	Member, Supervisory Committee
Lan Li, Ph.D.	Member, Supervisory Committee
Kathryn Metzger, Ph.D.	Member, Supervisory Committee
Adrian Wagner	Member, Supervisory Committee

The final reading approval of the dissertation was granted by Brian J. Jaques, Ph.D., P.E., Chair of the Supervisory Committee. The dissertation was approved by the Graduate College.

## DEDICATION

For my family and friends who have supported me throughout this journey.

## ACKNOWLEDGMENTS

The views and opinions of authors expressed herein do not necessarily state or reflect those of the U.S. Government or any agency thereof.

I would like to acknowledge the support from all the members of my committee. To Dr. Darryl Butt, who hired me into the AML and allowed me to participate in numerous research opportunities which propelled me to become the successful materials scientist and engineer I am today. To Dr. Brian Jaques, who was the first to teach me about nuclear materials and how to handle radiological materials safely and efficiently in a laboratory setting. He has also demonstrated and mentored me in how to perform research in a logical and methodical manner and has always pushed me to think critically and strive to be a better scientist and engineer. To Dr. Lan Li who has supported me in and out of the classroom since my undergraduate studies. To Dr. Kathryn Metzger, who has been a role model of what a confident and successful female engineer should be like. To Adrian Wagner, who has been my mentor and friend through the final years of my graduate work, always providing positivity, support, and guidance.

To my family who, despite not understanding what “all this science stuff is”, have always loved and supported me through the trials and tribulations of my college experience. To my close friends, without who I would not have made it to this point in my education and research career: Dr. Kassi Smith, Jordan Vandegrift, Kelci Lester, Kiyoo Fujimoto, Tammie Elliott, Mandi Dietz, Matthew Humphrey, and The Tierney family

(Kendall, Robert, and Gianna). To my significant other, John Paul Kammeyer, who is my biggest fan and most ardent supporter, thank you for helping me get to the finish line.

I would also like to acknowledge all the faculty, staff, and students who I met at Boise State who have provided support during my early college education and research career: Dr. Amy Moll, Dr. Megan Frary, Dr. David Estrada, Dr. Harold Ackler, Dr. Eric Jankowski, Dr. Elton Graugnard, Dr. Claire Xiong, Dr. Mike Hurley, Dr. Peter Mullner, Dr. Janet Callahan, Dr. Rick Uvic, Dr. Paul Simmonds, Dr. Nick Bullos, Dr. Karthik Chinnathambi, Dr. Janelle Wharry, Dr. Gordon Alanko, Dr. Patrick Price, Dr. Ember Sikorski, Dr. Corey Efaw, Dr. Steve Johns, Dr. Kayla Yano, Dr. Armen Kvrryan, Dr. Steve Letourneau, Joe Croteau, Allyssa Bateman, Addie Lupercio, Tim Phero, Sam Pedersen, Yai Rodriguez, Scott Riley, Kaelee Novich, and so many others who I encountered during my time at BSU. From Idaho National Laboratory and the Center for Advanced Energy Studies: Tim Hyde, Dr. Patrick Hogan, Kip Archibald, Seth Ashby, Connor Michelich, Connor Woolum, Steve Steffler, Darrel Jonak, Brooke Barker, Chris Vetsch, Zach Rowe, Jenn Landon, Mike Chapple, Cody Misseldine, Dr. Kevin Tolman, Dr. Fidelma Giulia Di Lemma, Dr. Yaqiao Wu, Dr. Jatuporn Burns, and many others. I know there are many others who I forgot to include, but please know I appreciate and thank you for your support.

I would like to acknowledge the financial support and sponsorship of my PhD work from the following sources: Idaho National Laboratory graduate fellowship program, U.S. Department of Energy under DOE Idaho Operations Office contract DE-AC07-05ID14517, and a funding opportunity through a collaboration with Westinghouse Electric Company (DE-NE0008824), U.S. Department of Energy Integrated University

Program graduate fellowship, and Boise State's Micron School of Materials Science and Engineering.

## ABSTRACT

To avoid detrimental environmental impacts from climate change, the world community needs to push for the use of clean energy technologies. Development of proposed advanced technology nuclear fuels supports efforts to ensure nuclear energy is included as a non-carbon emitting source of electricity generation. Advanced technology nuclear fuels, also referred to as accident tolerant fuels (ATFs), have received renewed interest for use in the current nuclear reactor fleet as well as in advanced reactor technologies due to their high uranium loading, desirable thermophysical properties, and performance under irradiation as compared to the benchmark oxide fuel. A limiting consideration for the implementation of these ATFs is their poor performance in oxidative and corrosion conditions, as well as challenges associated with synthesis and fabrication. As a full understanding of these ATFs has not been achieved, this work aims to advance the state of knowledge related to these fuels and their composites in corrosion conditions, their grain growth mechanisms, and includes efforts to improve thermal conductivity in the benchmark oxide fuel using these ATFs. Chapter Two presents a study of uranium mononitride (UN) and UN composites with uranium dioxide (UO<sub>2</sub>) under hydrothermal corrosion conditions to assess the mechanism of degradation at elevated temperatures, identified as secondary phase formation at the grain boundaries leading to pellet collapse. Chapter Three combines experimental and theoretical studies of composite systems, UN-Zr and UN-Y, for the purposes of improving the corrosion resistance of monolithic UN. The results indicate the formation of undesirable secondary

phases in the sintered materials and provided insight to the atomic level structural changes which occurred due to the addition of the metallic constituents. An extensive review (included as Appendices A, B, and C) of the state of the literature for oxidation performance of UN, triuranium disilicide ( $U_3Si_2$ ), uranium carbide (UC), and uranium diboride ( $UB_2$ ), was performed to identify the challenges and opportunities to alloyed and composite architectures of these ATF candidates to mitigate corrosion behavior.

In addition, an understanding of the microstructural evolution during the fabrication of various fuel forms, such as grain growth, is important in predicting its performance under irradiation (e.g., fracture, creep, fission gas release, thermal conductivity, etc.). Accordingly, it is important to understand the driving force behind grain growth and the factors which influence it. Chapter Four presents a fundamental study on grain growth in conventionally sintered UN. The study identified the most likely mechanism and proposed an activation energy for grain growth with a discussion on the factors that influenced it, as well as the lack of expected texture present in the sintered samples. Chapter Five describes work on successful incorporation of uranium diboride ( $UB_2$ , another ATF candidate) to a  $UO_2$  matrix via conventional fabrication and sintering methods, for the purposes of improving overall thermal conductivity of the bulk composite. Presented together, this work provides foundational inquiry and analysis which can be used to further research on ATF candidates and assist in acceleration of qualifying these fuels for use in the current and future nuclear reactor fleets.

## TABLE OF CONTENTS

DEDICATION .....	iv
ACKNOWLEDGMENTS .....	v
ABSTRACT .....	viii
LIST OF TABLES .....	xv
LIST OF FIGURES .....	xvii
LIST OF ABBREVIATIONS .....	xxxi
CHAPTER ONE: INTRODUCTION .....	1
1.1 Motivation.....	1
1.2 Project Objective and Scope.....	9
1.2.1 Objectives.....	10
References .....	16
CHAPTER TWO: MICROSTRUCTURAL DEGRADATION OF UN AND UN-UO <sub>2</sub> COMPOSITES IN HYDROTHERMAL OXIDATION CONDITIONS.....	18
Abstract .....	19
2.1 Introduction.....	20
2.1.1 Motivation for research.....	20
2.2 Materials and Methods .....	21
2.2.1 UN powder synthesis.....	21
2.2.2 Pellet fabrication and sintering.....	23
2.2.3 Hydrothermal oxidation.....	24

2.3 Results.....	26
2.3.1 UN powder synthesis.....	26
2.3.2 Pellet fabrication and sintering .....	27
2.3.3 Pellets post-autoclave .....	29
2.3.4 Post-autoclave XRD analysis – Pellets.....	32
2.3.5 Post-autoclave XRD analysis – Sludge .....	33
2.3.6 Post-autoclave morphology – Pellets .....	34
2.3.7 Post-autoclave morphology – Sludge.....	37
2.4 Discussion .....	38
2.4.1 Post-autoclave – Pellets .....	38
2.4.2 Post-autoclave – Sludge.....	43
2.5 Conclusions .....	44
Acknowledgements .....	46
References.....	46
CHAPTER THREE: IMPROVED HYDROTHERMAL CORROSION RESISTANCE OF UN FUEL FORMS VIA ADDITION OF METALLIC CONSTITUENTS .....	50
Abstract.....	51
3.1 Introduction .....	51
3.1.1 Motivation for research .....	51
3.1.2 Background.....	53
3.2 Materials and Methods.....	54
3.2.1 UN powder synthesis.....	54
3.2.2 Thermodynamic calculations .....	56
3.2.3 Powder mixing and characterization .....	57

3.2.4 Pellet fabrication, sintering, and characterization .....	58
3.2.5 Electronic calculations .....	60
3.3. Results and Discussion .....	60
3.3.1 Metallic element selection.....	60
3.3.2 Powder and pellet characterization.....	62
3.4. Conclusions.....	74
Acknowledgements.....	76
References .....	76
CHAPTER FOUR: INVESTIGATING GRAIN GROWTH OF CONVENTIONALLY SINTERED URANIUM MONONITRIDE.....	81
Abstract .....	83
4.1 Introduction.....	83
4.2 Materials and Methods .....	85
4.2.2 Pellet fabrication and sintering.....	85
4.2.2 X-ray Diffraction .....	86
4.2.3 Microstructural analysis.....	87
4.2.4 Calculations for kinetics and grain growth mechanisms .....	88
4.3 Results and Discussion .....	90
4.3.1 Pellet fabrication and sintering.....	90
4.3.2 X-ray Diffraction .....	92
4.3.3 Microstructural analysis.....	94
4.3.4 Determination of grain growth exponent and activation energies..	100
4.4 Summary.....	115
Acknowledgements.....	116

References.....	117
<b>CHAPTER FIVE: ENHANCING THERMAL CONDUCTIVITY OF UO<sub>2</sub> WITH THE ADDITION OF UB<sub>2</sub> VIA CONVENTIONAL SINTERING TECHNIQUES .....</b>	
Abstract.....	124
5.1 Introduction.....	124
5.2 Background .....	126
5.3 Materials and Methods.....	127
5.3.1 Powder synthesis, pellet fabrication and sintering.....	127
5.3.2 X-ray Diffraction (XRD).....	129
5.3.3 Microstructure and elemental analysis .....	130
5.3.4 Thermal diffusivity, specific heat, and thermal conductivity .....	131
5.4 Results and Discussion .....	132
5.4.1 X-ray Diffraction.....	132
5.4.2 Microstructure and elemental analysis .....	135
5.4.3 Thermal diffusivity, specific heat capacity, and thermal conductivity .....	137
5.5 Summary .....	143
Acknowledgements .....	145
References.....	146
<b>CHAPTER SIX: SUMMARY AND FUTURE WORK.....</b>	
6.1 Summary .....	152
6.1.1 Uranium mononitride .....	153
6.1.2 Uranium diboride as a secondary phase in UO <sub>2</sub> .....	155
6.2 Future Work .....	155

6.2.1 Research opportunities for ATFs.....	155
6.2.2 Research opportunities for individual fuel forms.....	156
6.2.3 Conclusions .....	160
APPENDIX A: CHALLENGES AND OPPORTUNITIES TO ALLOYED AND COMPOSITE FUEL ARCHITECTURES TO MITIGATE HIGH URANIUM DENSITY FUEL OXIDATION: URANIUM MONONITRIDE .....	162
APPENDIX B: CHALLENGES AND OPPORTUNITIES TO ALLOYED AND COMPOSITE FUEL ARCHITECTURES TO MITIGATE HIGH URANIUM DENSITY FUEL OXIDATION: URANIUM SILICIDE .....	232
APPENDIX C: CHALLENGES AND OPPORTUNITIES TO ALLOYED AND COMPOSITE FUEL ARCHITECTURES TO MITIGATE HIGH URANIUM DENSITY FUEL OXIDATION: URANIUM DIBORIDE AND URANIUM CARBIDE.....	294
APPENDIX D: SUPPLEMENTARY FILE FOR CHAPTER FOUR: INVESTIGATING GRAIN GROWTH OF CONVENTIONALLY SINTERED URANIUM MONONITRIDE.....	358
APPENDIX E: SUPPLEMENTARY FILE FOR CHAPTER FIVE: ENHANCING THERMAL CONDUCTIVITY OF UO <sub>2</sub> WITH THE ADDITION OF UB <sub>2</sub> VIA CONVENTIONAL SINTERING TECHNIQUES .....	363

## LIST OF TABLES

Table 3.1.	Properties of the candidate elements screened for use in creation of a UN-metallic composite fuel pellet. ....	55
Table 4.1	Values of the grain growth exponent, $n$ , for various mechanisms. Taken from Brook [18]. ....	102
Table 4.2	$R^2$ values for linear regression fitting from grain growth data raised to various $n$ values versus time plots for the samples sintered at various dwell temperatures. The best fit to the $R^2$ values used in obtaining the grain growth rate constant are highlighted in the table for each temperature profile. ....	104
Table 4.3	Calculated grain growth activation energies for the sintered samples used in this study and for data extracted from Metroka [11] when considering a consistent dominant grain growth mechanism ( $n = 2$ and $n = 3$ ). ....	109
Table 5.1	Material properties of $UO_2$ and $UB_2$ .....	127
Table A.1	Material Properties of ATF Concept Fuels .....	166
Table A.2	Thermal neutron cross-sections for $^{14}N$ and $^{15}N$ for the $(n,p)$ , $(n, \gamma)$ , and $(n, e)$ reactions [51]. ....	174
Table A.3	Summary of air oxidation UN and UN with additives or composites. ...	180
Table A.4	Summary of water/steam corrosion of UN and UN with additives or composites. ....	188
Table B.1	Summary of air corrosion of $U_3Si_2$ and additives.....	253
Table B.2	Summary of water/steam corrosion of $U_3Si_2$ and additives .....	263
Table C.1	Material properties of ATF concept fuels as compared to the benchmark, $UO_2$ .....	299
Table C.2	Properties of potential dopants into ATF concepts for improved corrosion resistance. References listed in the headers applies to all the materials in the column. ....	302

Table C.3	Summary of oxidation studies on UC samples at various temperatures and partial pressures of oxygen (assumed to be at ~ 1 atm total pressure). Modified from Naito et al. [112].	321
Table C.4	Ignition temperatures and reaction products from ramp tests of UC powders oxidized in synthetic air from DSC and TGA testing. Modified from Berthinier et al. [100].	328
Table C.5	Corrosion rates in steam of unirradiated and irradiated UC at various temperatures. Modified from Dyck and Taylor [137].	334

## LIST OF FIGURES

Figure 1.1	Primary energy consumption for 2019, measured in terawatt-hours, indicating our increase in energy demand remains primarily from industrialized nations [1]......	2
Figure 1.2	United Nations human development index versus annual per capita electricity usage, reflecting that industrialized nations with greater access to electricity, clean water, and other amenities experience a higher quality of life. ....	3
Figure 1.3	Capacity factors for 2020 listed by energy source [11]. ....	4
Figure 1.4	Lifecycle CO <sub>2</sub> emissions of energy sources when accounting for construction, mining, transport, operation, decommissioning, and waste disposal. Modified from IPCC [13]. ....	6
Figure 1.5	Thermal conductivity values at 500 °C versus uranium density for various uranium-bearing fuel forms, color mapped to melting temperature [15]....	8
Figure 1.6	The materials science tetrahedron (or materials paradigm), showing the four interdependent aspects of materials science: structure, properties, processing, and performance, with characterization in the center [16]. ...	15
Figure 2.1	XRD of the two separate batches of UN powders (Batch 1 having a lower starting impurity UO <sub>2</sub> content than that of Batch 2). Powders were synthesized using a hydride-dehydride-nitride route, and as-received UO <sub>2</sub> powder. Left inset shows the morphology of the as synthesized UN powder and right inset is the morphology of the as-received UO <sub>2</sub> powder. ....	23
Figure 2.2	(a) Static autoclave used for hydrothermal oxidation testing showing the location of the heater/hot zone, (b) the custom fabricated containment enclosure for the autoclave bolt assembly, and (c) Side view of sample holder (top image), top view of the custom Autoclave sample holder showing the stainless-steel mesh for positioning up to four pellets in the hot zone of the autoclave (middle image). Once the pellets are inserted, the sample holder is encased with stainless steel (bottom image) to retain corrosion products.....	26

Figure 2.3	XRD patterns of the mixed UN and UN-UO <sub>2</sub> composite powders prior to pressing into pellets. The inset is an SEM micrograph showing the typical morphology of the mixed powders.....	28
Figure 2.4	Images of a typical sintered pellet showing (a) right cylindrical geometry, (b) the grain structure of UN + 5 w% UO <sub>2</sub> pellet surface after polishing and thermal etching, (c) the fracture surface of UN + 10 w% UO <sub>2</sub> pellet, and (d) the typical UO <sub>2</sub> distribution in the UN matrix of a UN + 10 w% UO <sub>2</sub> pellet.....	29
Figure 2.5	Images showing the relative hydrothermal oxidation behavior of pellets fabricated from the two batches of UN powder tested at 250-350 °C. The experiments with pellets fabricated from the Batch 2 powder include UO <sub>2</sub> pellets as a benchmark. In all cases, the right cylindrical pellets were preferentially attacked at the edges and the extent of degradation increased with increasing temperature, with some pellets completely disintegrating. ....	31
Figure 2.6	Comparison of XRD patterns of the as-sintered and corroded UN and UN+UO <sub>2</sub> composite pellets. After autoclave testing the primary phase in the pure UN samples is UN, whereas the 5 and 10 w% samples indicate a UN <sub>2</sub> phase or oxynitride phase (2θ values 29.0, 33.6, 48.3°) and possibly α-U <sub>2</sub> N <sub>3</sub> (2θ values 28.9, 33.6, and 48.4°) as denoted by the chevron markers and droplines, most evident in the 275-325 °C data. ....	33
Figure 2.7	Comparison of XRD patterns from the recovered “sludge” showing the primary phase remains UN. However, as autoclave temperatures increase, phases of UN <sub>2</sub> , possibly an oxynitride, UO <sub>2</sub> , and peaks attributed to α-U <sub>2</sub> N <sub>3</sub> become more prominent. ....	34
Figure 2.8	Backscatter electron micrographs of the corroded UN pellets at 250 °C, 275 °C, and 300 °C. The top images were taken from the less corroded, central, region of the pellet surface and the bottom images were taken from the more heavily corroded outer edges of the pellets (seen in the photograph on the left). Preferential edge and grain boundary attack is evident.....	36
Figure 2.9	Backscatter SEM micrographs of the UN + 5 w% UO <sub>2</sub> and UN + 10 w% UO <sub>2</sub> composite pellets corroded at 250 °C and the UN + 10 w% UO <sub>2</sub> pellet corroded at 275 °C. The top images were taken from the less corroded, central, region of the pellets and the bottom images were taken from the more heavily corroded outer edges of the pellets (seen in the photograph on the left). Preferential edge and grain boundary attack is evident. The pellets corroded at 250 °C also show clear light and dark phases present across the surfaces. The dark phase was identified as an oxide phase via EDS (Figure 2.10). ....	36

Figure 2.10	Chemical analysis via EDS of the UN + 5 w% UO <sub>2</sub> pellet surface corroded at 250 °C (seen in Figure 2.9) showing distinct nitrogen and oxygen-rich regions. ....	37
Figure 2.11	Backscattered electron micrographs of the recovered “sludge” from hydrothermal oxidation experiments from 275-350 °C showing large, distinct grains at 275 °C. However, as the temperature is increased, the grain size of the recovered sludge is reduced, and significant grain degradation is observed at 350 °C. ....	38
Figure 3.1	Ellingham-type diagram constructed using data from FactSage™ 6.4 for select metal-nitride reactions of elements listed in Table B1. No reliable data was available for gadolinium nitride or the U <sub>2</sub> N <sub>3</sub> reaction. ....	56
Figure 3.2	Ellingham-type diagram constructed using data from FactSage™ 6.4 for select metal-oxide reactions of elements listed in Table 3.1. ....	57
Figure 3.3	Yttrium-uranium mononitride phase diagram (generated using FactSage™ 6.4). ....	59
Figure 3.4	Zirconium-uranium mononitride phase diagram (generated using FactSage™ 6.4). ....	59
Figure 3.5	Backscattered electron micrographs of A) As-synthesized UN powder, B) As-received Zr powder, C) As-received Y powder. ....	63
Figure 3.6	Backscattered electron micrographs of A) UN+ 10 w%Zr mixed powder, and B) UN+10 w%Y mixed powder. ....	64
Figure 3.7	XRD patterns for the as-synthesized UN powder, as-received Zr (A), and Y (B) powders, the mixed UN+10 w% metal powders, and the UN+10 w% metal sintered pellets. ....	67
Figure 3.8	BSE micrographs of the UN+10 w%Zr sintered pellet (A-C) and the UN+10 w%Y pellet sintered at 1808K (D-F); A) pellet surface showing phase segregation and increased porosity at the rim (inset). Detailed view of area where liquid U, U-N-Zr, and U-N-Zr-O phases are present. B) Cross-section of the pellet showing the liquid uranium phase was present throughout the bulk of the pellet and that the pellet contained a large amount of porosity. C) Higher magnification view of the cross-section. D) Cross-sectional view showing considerable porosity and inadequate sintering, inset is the full cross-sectional view. E) Higher magnification view of the phase segregation. F) Detailed view of area where liquid U, U-N-Y, and Y-O phases are present. ....	69

Figure 3.9	Local density of states of (a) Zr added to an N site in UN at 1773 K and (b) Y added to an N site in UN at 1808 K. The Fermi level was shifted to 0 eV. ....	72
Figure 3.10	Electron Localization Function of final structures initially configured as (a) Zr at an N site, (b) Y at an N site, (c) Zr at a U site, and (d) Y at a U site. Contour lines show regions of the same energy level. ....	73
Figure 4.1	Compilation of the average grain size (with error bars representing one standard deviation) versus sintering time for all sintered samples used in this study. The %TD for each sample is shown above their respective columns. ....	92
Figure 4.2	XRD patterns for UN feedstock, UN milled powder, and all sintered samples. ....	94
Figure 4.3	Column chart compilation of the average pore size on the left y-axis (with error bars representing one standard deviation) versus sintering time for all sintered samples used in this study. Also shown is the number of pores per 100 $\mu\text{m}^2$ (corresponding to the right y-axis) indicated by the red circles by each sample's average pore size. ....	97
Figure 4.4	Secondary electron micrographs from all sintered samples in this study showing the progression of the pore characteristics as time and temperature are increased. ....	98
Figure 4.5	EBSD inverse pole figure orientation maps from all the sintered samples in this study reflecting the increase in grain size with temperature. The 1950/15 and 1950/25 samples show evidence of abnormal grain growth. ....	99
Figure 4.6	Inverse pole figures for the sintered samples used in this study. It does not appear that there is any significant preferential orientation in the samples. For figure clarity the orientation of the inverse pole figures is only denoted with the 1850/5 sample but is the same for all other samples. ....	100
Figure 4.7	Plot of the best fits (by $R^2$ linear regression values) for various $n$ values for samples sintered from 1850-2000 $^{\circ}\text{C}$ . ....	104
Figure 4.8	Arrhenius plot ( $\ln K$ versus $10^4/T$ ) with the grain growth rate constant, $K$ , values taken from the best fit of the linear regression lines for the 1850-1950 $^{\circ}\text{C}$ sintered samples (i.e., slope of the plots in Figure 7). The data point for the 2000 $^{\circ}\text{C}$ sample fell as an outlier and was excluded from the linear regression fit. Inset shows the data from this work compared to the data from Metroka [11] using the same methodology. ....	106

Figure 4.9	Arrhenius plot for the sintered samples used in this study assuming a consistent dominant grain growth mechanism of grain boundary diffusion (i.e., using a value for the grain growth exponent of $n = 2$ ). A linear regression fit to the data points is shown for the 1850-1950 °C samples. The data point for the 2000 °C sample fell as an outlier and was excluded from the linear regression fit. The inset is the data extracted from Metroka [11] plotted here for comparison using the same methodology. Activation energies are noted next to their respective plots. .... 107
Figure 4.10	Arrhenius plot for the sintered samples used in this study assuming a consistent dominant grain growth mechanism of second phase (porosity) by lattice diffusion or low solubility impurity drag (i.e., using a value for the grain growth exponent of $n = 3$ ). A linear regression fit to the data points is shown for the 1850-1950 °C samples. The data point for the 2000 °C sample fell as an outlier and was excluded from the linear regression fit. The inset is the data extracted from Metroka [11] plotted here for comparison using the same methodology. Activation energies are noted next to their respective plots. .... 108
Figure 5.1	Uranium-boron phase diagram (0-100 at% U, 400-2600 °C). Modified from Okamoto [23]. .... 129
Figure 5.2	XRD patterns of the starting mixed $\text{UO}_2/\text{UB}_2$ powder used for pellet fabrication, the 4 and 8-hour as-sintered samples and 4 and 8-hour samples from the LFA thermal diffusivity measurements. Reference patterns for $\text{UO}_2$ , $\text{UB}_2$ , and $\text{LaB}_6$ (used for line position verification) are indicated by the symbols. Note that the mixed $\text{UO}_2/\text{UB}_2$ powder did not include the $\text{LaB}_6$ NIST SRM; the bottom pattern is of the blank stage used in the analysis for reference and denotes a peak attributed to the silicon disk holder on the XRD stage having a peak at $28.4^\circ 2\theta$ . .... 133
Figure 5.3	a) Backscatter electron (BSE) image of the 4-hour as-sintered microstructure with some of the apparent porosity attributed to pullout of the oxide phase during grinding and polishing, and b) higher magnification BSE image along with EDS elemental mapping of the uranium, oxygen (darker grey), and boron (lighter gray) phases. .... 137
Figure 5.4	a) Backscatter electron (BSE) image of the 8-hour as-sintered microstructure showing less porosity than that of the 4-hour sample. Some of what appears to be porosity has been attributed to pullout of the oxide phase during grinding and polishing. Image b) higher magnification BSE image along with EDS elemental mapping of the uranium, oxygen (darker grey), and boron (lighter gray) phases. .... 137
Figure 5.5	Measured thermal diffusivity as a function of temperature for the 4-hour (blue inverted triangle) and 8-hour (orange triangle) conventionally

	sintered $\text{UO}_2$ -10wt% $\text{UB}_2$ samples, and values from literature for pure $\text{UB}_2$ [21], pure $\text{UO}_2$ from Fink (2000) [40] and Ronchi et al. [50] and for $\text{UO}_2$ -(5,15, and 30 wt%) $\text{UB}_2$ samples sintered via SPS from Kardoulaki et al. [20].....	139
Figure 5.6	Measured heat capacity versus temperature for the 4-hour (blue inverted triangle) and 8-hour (orange triangle) conventionally sintered $\text{UO}_2$ -10wt% $\text{UB}_2$ samples, and values from literature for pure $\text{UO}_2$ from Fink (2000) [40] and pure $\text{UB}_2$ from Fredrickson et al. (1969) [28]. A rule of mixtures (ROM) for a theoretical $\text{UO}_2$ -10wt% $\text{UB}_2$ samples based on values from [28, 40] is denoted by the green triangle plot. ....	141
Figure 5.7	Calculated thermal conductivity versus temperature for the 4-hour (blue inverted triangle) and 8-hour (orange triangle) conventionally sintered $\text{UO}_2$ - 10wt% $\text{UB}_2$ samples, and values from literature for pure $\text{UB}_2$ [21], pure $\text{UO}_2$ from Fink [40], and a calculated ROM plot for a theoretical $\text{UO}_2$ + 10wt% $\text{UB}_2$ composite using the ROM specific heat capacity data from Figure 6.6 and thermal expansion data from Kardoulaki et al. and Fink [21, 40] (green triangle).....	143
Figure A.1	Primary attributes of accident tolerant fuels associated with fuel behavior and cladding at high temperatures. Modified from Carmack [32].....	167
Figure A.2	Thermal conductivity vs. uranium density and color mapped to melting temperature. The four high uranium density candidates discussed throughout these reviews (UN, $\text{U}_3\text{Si}_2$ , and $\text{UB}_2/\text{UC}$ ) are grouped in the center of the plot.....	169
Figure A.3	Uranium-nitrogen phase diagram (35-100 at% U, 400-3200 °C) Modified from Okamoto [48].....	172
Figure A.4	UN dissociation and $\text{U}_2\text{N}_3$ formation as a function of temperature and nitrogen partial pressures, a) From Tennery [46], and b) from Matzke [47]. ....	173
Figure A.5	As-fabricated and SPS sintered UN microspheres (left column) and resulting microstructure (right columns) after oxidation in synthetic air up to 700 °C. Modified from Costa et al. [63].....	177
Figure A.6	Images at 500X magnification of UN single crystal samples, (421) crystal faces, oxidized in flowing oxygen for a) 10 minutes, and b) 30 minutes. From Dell et al. [37]. ....	178
Figure A.7	SEM micrographs of a) degraded microstructure of a UN pellet (98.25% TD) exposed to steam (9 MPa, 300 °C, 30 minutes) and b) higher magnification of the degraded region displaying “sandwich” structure of	

	UO <sub>2</sub> with underlying nitride layer at the grain boundaries. Modified from Lopes et al. [69].	183
Figure A.8	UN degradation under hydrolysis; a) UN pellet following static autoclave testing in DI water at 300 °C/10 MPa for 48 hours (modified from Nelson et al.) [13], b) UN pellet after static auto testing at 300 °C/16 MPa for 30 minutes (modified from Watkins et al.) [14], c) UN after hydrolysis in steam at 340 °C for 105 minutes, d) UN after hydrolysis in steam at 425 °C for 300 minutes (modified from Jolkkonen et al.) [68], and e) UN after static autoclave corrosion at 300 °C, no time duration given (modified from Malkki) [76].	184
Figure A.9	Backscattered electron micrographs of corroded UN pellets submerged in DI water for 30 minutes at 250 °C, 275 °C, and 300 °C and approximately 16 MPa. The top images were taken from the less corroded pellet surface while the bottom images show the preferential degradation from the pellet edges. Grain boundary etching and attack increases with temperature. From Watkins et al. [14].	185
Figure A.10	Optical micrographs of 98.25% TD UN exposed to steam at 9 MPa and 300 °C for 30 minutes. a) UN sample showing section where the matrix was preserved and other degraded regions and b) inset of a) displaying degraded region with grain boundary etching which causes weakening of the matrix. Modified from Lopes et al. [69].	186
Figure A.11	a) SEM micrograph of a UN pellet sintered in UHP-Ar at 1550 °C having an inner region of lower density and an outer rim with higher densification due to UN dissociation forming free elemental uranium resulting in liquid phase sintering, b) higher magnification of Region 1, and c) higher magnification of Region 2. Modified from Jaques et al. [44].	191
Figure A.12	Backscatter electron micrographs of UN+10wt% Zr sintered in argon at 1500 °C. A) As-sintered microstructure showing formation of a liquid uranium phase at the grain boundaries indicating UN dissociation; inset is of the pellet surface showing the “coring” effect due to the UN dissociation, b) as-sintered microstructure highlighting the porous nature of the pellet and the uniformity of the liquid uranium phase, c) slightly higher magnification of the as-sintered microstructure showing the liquid uranium phase, and the phases identified as U-N-Zr and U-N-O-Zr. Modified from Watkins et al. [81].	193
Figure A.13	Ellingham-type diagram showing thermodynamic stability of nitride formation of various metallic elements considered for possible dopants into ATF concepts versus UN. Calculated using HSC Chemistry 9 [62].	194

- Figure A.14 a) Representative optical image of UN+UO<sub>2</sub> pellet conventionally sintered and subjected to static autoclave testing, arrows point to the relevant areas where backscatter electron micrographs were taken of the corroded microstructure. The UN +(5-10 wt%) UO<sub>2</sub> samples corroded at 250 and 275 °C, show preferential edge and grain boundary attack. The pellets corroded at 250 °C also indicate clear light and dark phases present across the surface of the pellets, the dark phase being identified as an oxide phase via EDS (from Watkins et al.) [14]. b) SEM of sintered microstructure of a UN+30at% ZrN composite sintered via SPS and heat treated at 1400 °C for 4 hours in argon displaying U-rich (lighter) and Zr-rich (darker) regions, c) macro image of the sample subjected to autoclave testing in DI water for 4 hours at 150 °C, and d) corroded microstructure of the autoclave tested sample showing degradation and dark regions which were identified as carbon impurities (modified from Malkki) [76].....196
- Figure A.15 Backscatter electron images of the UO<sub>2</sub>-UN samples hot-pressed at 1590 °C, a) 6.9 wt% UN, b) 26.4 wt% UN, and c) 39.3 wt% UN. Modified from Yang et al. [85].....198
- Figure A.16 Backscatter electron micrographs of UN microspheres embedded in a UO<sub>2</sub> matrix. a) showing UN microspheres relatively well dispersed throughout the UO<sub>2</sub> matrix but elongated from their original spherical shape, b) higher magnification of the UN microspheres, c) higher magnification image showing the more porous UN microsphere as compared to the denser UO<sub>2</sub> matrix, and d) highlighting the UO<sub>2</sub>-UN microsphere interface. Modified from Costa et al. [84].....200
- Figure A.17 SEM micrograph compilation of UN-doped microspheres before sintering. a) UN-Cr microsphere after nitridation and b) EDS mapping of surface of the nitrided microsphere showing U and Cr distribution although XRD analysis identified UN, UO<sub>2</sub>, Cr<sub>2</sub>O<sub>3</sub>, and CrN; c) UN-Ni microsphere after nitridation and d) EDS mapping of the UN-Ni nitrided microsphere showing U, Ni, C, and Si distribution, XRD only identified UN; e) UN-Al air-dried microsphere before nitridation and f) EDS mapping of the UN-Al microsphere after nitridation showing U, Al, and Cr distribution, XRD identified UN, AlN, and Al<sub>2</sub>O<sub>3</sub>. Modified from Herman and Ekberg [78]. .....202
- Figure A.18 SEM micrographs of the UN-Cr microsphere microstructure prior to submersion in boiling water and b) UN-Cr microsphere after 5 hours in boiling water. Modified from Herman and Ekberg [78].....204
- Figure A.19 SEM micrographs of the SPS sintered microstructure of UN-U<sub>3</sub>Si<sub>2</sub> composites a) 10 wt% U<sub>3</sub>Si<sub>2</sub>, b) 20 wt% U<sub>3</sub>Si<sub>2</sub>, and c) 25 wt% U<sub>3</sub>Si<sub>2</sub>. Modified from Raftery [86]. .....205

Figure A.20	Backscatter electron image of UN+30 wt% U <sub>3</sub> Si <sub>2</sub> sample sintered at 1700 °C for 3 hours using HDN UN powder and arc-melted U <sub>3</sub> Si <sub>2</sub> exhibiting a fairly continuous U <sub>3</sub> Si <sub>2</sub> phase around the larger UN grains and the accompanying EDS chemical maps showing small areas of silicon-rich regions. Modified from Ortega et al. [8]. .....	206
Figure A.21	Modified from Lopes et al. [69] showing a) the % mass increase during steam corrosion for UN pellets with varying porosity and a UN-10 wt% U <sub>3</sub> Si <sub>2</sub> composite, b) the as-fabricated microstructure of the composite, and c) and d) showing the corroded microstructure with intragranular cracking present. ....	208
Figure A.22	Dependence of thermal conductivity in UN as a function of oxygen content. From Solntceva et al. [96]. .....	211
Figure A.23	High angle annular dark field (HAADF) and bright field (BF) STEM images with EDS chemical maps of a UN-5wt% UO <sub>2</sub> composite after proton irradiation at 710 °C and up to a fluence of 8*10 <sup>18</sup> ions/cm <sup>2</sup> indicating the presence of UN, U <sub>2</sub> N <sub>3</sub> , and UO <sub>2</sub> . The “sandwich structure” of the three phases is denoted by the yellow dashed rectangle in the bottom right image; the proton irradiation beam direction is marked by an arrow in the upper left. Modified from He et al. [103]. ....	214
Figure A.24	Plot of the air oxidation onset temperatures from Table A.3 compared to reference data for air onset oxidation of UO <sub>2</sub> from Wood et al. [106]. ..	218
Figure A.25	Plot of the water/steam onset temperatures from Table A.4. ....	219
Figure B.1	Ellingham-type diagram showing thermodynamic stability of oxide formation of various metallic elements considered for possible dopants into ATF concepts versus UO <sub>2</sub> . Calculated using HSC Chemistry 9 [27]. .....	240
Figure B.2	U-Si Phase diagram modified from ASM Alloy Phase Diagram Database. [36]. .....	241
Figure B.3	From Wood et al. a) cross-sectional micrograph of monolithic U <sub>3</sub> Si <sub>2</sub> during oxidation at 275 °C, and b) backscatter SEM of surface oxide formed at 300 °C [53]; c) ~5.7 μm grain size, and d) 280 nm grain size after ramp testing from room temperature to 1000 °C, modified from Gong et al. [26]. ....	246
Figure B.4	Thermodynamic equilibrium oxidation calculation of 1 mol U <sub>3</sub> Si <sub>2</sub> exposed to 0-2 moles of O <sub>2</sub> at 900 °C using Thermocalc 2020b with TAFID v10 database [59]. .....	248

Figure B.5	a) HR-TEM image of Si-rich and U and O deficient region identified by EDS, showing the 10 nm size crystallites, b) FFT from boxed area of grain 1, and c) grain 2 indexed as crystalline Si, modified from Harrison et al. [9].	250
Figure B.6	Equilibrium phase diagram of 1 mole $U_3Si_2$ in 1 atm of steam in increasing amounts at 400 °C using Thermocalc 2020b with TAFID v10 database [59].	256
Figure B.7	Micrographs taken from cross-sectioned $U_3Si_2$ pellets exposed to steam at a) 350 °C for 6 hours and b) 400 °C for 1.5 hours, modified from Wood et al. [16].	257
Figure B.8	SEM of $U_3Si_2$ after short exposure to steam at a) 465 °C with b) EDS of Si-rich regions and c) EDS of oxygen rich regions d) later stages of steam oxidation at 465 °C, and e) powder morphology following 900 °C steam, modified from Turner et al. [67].	258
Figure B.9	$U_3Si_2$ as-oxidized powder after steam testing a) spherical $U_3Si_2$ particles produced after atomization fabrication. b) $U_3Si_2$ after 400 °C, c) 450 °C, and d) 900 °C steam for 3 hours. Adapted from Yang et al. [14].	259
Figure B.10	Striation formations after steam oxidation. a) 450 °C in steam modified from Yang et al. and b) 400 °C in Ar-6% $H_2$ modified from Wood et al. [16].	260
Figure B.11	SEM images of $U_3Si_2$ sample cross sections following 31 day exposure to 300 °C $H_2O$ at 85 bar under two water chemistry conditions: a) 1 ppm $H_2$ , and b) 5 ppm $H_2$ . White arrows in b) identify needle-like structures that are present following testing, modified from Nelson et al. [15].	261
Figure B.12	Ellingham-type diagram showing thermodynamic stability of silicide formation of various metallic elements considered for possible dopants into ATF concepts versus $U_3Si_2$ . Calculated using HSC Chemistry 9 [27]. Note the databases used in these calculations only included silicates of Al and Y and thus were not included in the plot.	265
Figure B.13	a) Cross-sectional micrograph of the oxidized $U_3Al_2Si_3$ equilibrium composition, and EDS maps of the selected area (b and c) showing $Al_2O_3$ formation along the edges of the sample and along cracks, modified from Wood et al. [58].	267
Figure B.14	SEM of Cr additions to $U_3Si_2$ via a) SPS (modified from Gong et al. who reported 10 wt% Cr additions [68]) and b) arc-melting (modified from Wood et al. who reported 5 vol% (3.3 wt%) Cr additions [65]). c) 10 wt%	

	Cr doped $U_3Si_2$ after a 24 hour isotherm at 360 °C. d) Oxidation patches on the 10 wt% Cr doped $U_3Si_2$ sample after the isotherm hold.....	269
Figure B.15	Modified images from Mohamad et al. [63] of a) 1.8 at% (0.32 wt%) Al addition to nano grain $U_3Si_2$ before and b) after annealing showing migration of the alloying element and c) XRD patterns before and after annealing. ....	270
Figure B.16	Backscatter SEM of the as-melted U-Si-Y composition modified from Wood et al. [65]. ....	271
Figure B.17	Modified images from Mohamad et al. [64]. a) The mechanical properties of the SPS-densified 3Y-TZP incorporated pellets were characterized by indentation b) Micro-cracks are generated through the 3Y-TZP particles. ....	272
Figure B.18	SEM images of $U_3Si_2$ + 25 wt% $UO_2$ composites sintered at a) 1000 °C, and b) 1300 °C. SEM images of $U_3Si_2$ + 50 wt% $UO_2$ composites sintered at c) 1000 °C, and d) 1300 °C. Modified from Gong et al. [62].....	275
Figure B.19	SEM backscatter micrographs of a) $U_3Si_2$ + 10 wt% $UB_2$ , and b) $U_3Si_2$ + 50 wt% $UB_2$ , modified from Turner et al. [72].....	276
Figure B.20	SEM and EDS of $U_3Si_2$ + 50 wt% $UB_2$ composite after steam oxidation at a) 465 °C for 5 min., b) at 565 °C for 5 min., and c) at 900 °C, modified from Turner et al. [67].....	278
Figure B.21	$U_3Si_2$ air onset temperatures taken from Table A1. <sup>a</sup> superscript are samples that have been annealed. mc are micron grain sized and nc are nano grain sized. ....	282
Figure B.22	$U_3Si_2$ steam oxidation onset temperatures from the reviewed literature. <sup>a</sup> superscript are samples that have been annealed.....	284
Figure C.1	Uranium density vs. volume percent non-uranium bearing additive for the ATF fuel concepts as compared to U and $UO_2$ .....	304
Figure C.2	Uranium-boron phase diagram (0-100 at% U, 400-2600 °C) [33]. ....	306
Figure C.3	SEM micrographs of $UB_2$ microstructure from arc-melting synthesis. a) ~95% TD $UB_2$ sample after SPS at 1750 °C and 40 MPa for 5 minutes, modified from Kardoulaki et al. [32]. b) Arc-melted $UB_2$ after conventional sintering in a graphite vacuum furnace for 1 hour at 1800 °C and showing a secondary inter-granular $UO_{0.75}C_{0.25}$ phase. Modified from Turner et al. [85]. ....	307

Figure C.4	Plot of gas absorbed vs. time for $UB_2$ samples tested in $O_2$ (assumed to be at 1atm) at 400 °C, 29 mmHg partial water vapor pressure at 500 °C, and $N_2$ (also assumed to be at 1 atm) at 700 °C, as compared to uranium in $N_2$ at 700 °C. From Tripler et al. [89].....310
Figure C.5	Samples remaining from testing a) $U_3Si_2$ and b) $UB_2$ in steam from 250-900 °C. The $UB_2$ showed less branch cracking than the $U_3Si_2$ sample and a higher onset temperature (629 °C). Modified from Turner et al. [85]. ...311
Figure C.6	a) Backscatter electron image of a $UO_2 + 30wt\% UB_2$ composite sintered via SPS showing the brighter $UB_2$ regions distributed throughout the $UO_2$ matrix, and b) a $UO_2 + 15wt\% UB_2$ composite also sintered via SPS but after thermal property measurements displaying little of the original $UB_2$ phase and formation of $UB_4$ . Modified from Kardoulaki et al. [84].....313
Figure C.7	Ellingham-type diagram showing thermodynamic stability of boride formation of various metallic elements considered for possible dopants into ATF concepts versus $UB_2$ (normalized to 1 mol of B). Calculated using HSC Chemistry 9 [93].....315
Figure C.8	Uranium-carbon phase diagram (25-100 at% U, 700-2700 °C) [95].....318
Figure C.9	In-situ oxidation of a UC fragment at 450 °C and partial pressure of 50 Pa $O_2$ a) just after oxygen insertion, b) 17 minutes after oxygen insertion showing explosive expansion of the sample which occurred during the scanning time frame, and c) 15 seconds after image b) was taken showing the expanded sample surface. Modified from Gasparrini et al. [121]. ....324
Figure C.10	UC fragment oxidized at 575 °C under a partial pressure of 10 Pa $O_2$ , a) just after oxygen introduction, b) 16 min after $O_2$ exposure, c) 16 min + 7 sec after $O_2$ exposure showing crack propagation at top right corner, d-h) secondary electron images starting at 16 min + 8 seconds and taken every 1 second thereafter as the sample ignition progresses, clear volume expansion is evident. Modified from Gasparrini et al. [121].....324
Figure C.11	Mass gain v. time for UC powders isothermally oxidized in 1.1 kPa oxygen partial pressure. Solid and dotted lines denote gas flow rates of 5.7 cm/sec and 0.04 cm/sec, respectively. From Naito et. al. [112]. ....326
Figure C.12	UC powder samples after isothermal testing at 21.3 kPa $O_2$ in synthetic air; a) 121.8 °C for 20 hours, b) 204 °C for 20 hours, and c) 234.6 °C for 5 hours. Modified from Berthinier et al. [96]. ....329
Figure C.13	Ellingham-type diagram showing thermodynamic stability of carbide formation of various metallic elements considered for possible dopants into ATF concepts versus UC (normalized to 1 mol of C). Calculated

using HSC Chemistry 9 [93]. Note: For nickel, the formation of the carbide is not favored and thus was not included in this plot..... 337

Figure C.14	Summary plot of air/O <sub>2</sub> oxidation and steam corrosion onset temperatures for UC, UB <sub>2</sub> , and UB <sub>2</sub> composites. Samples oxidized in air/oxygen are shown in solid blue for UC and solid red for UB <sub>2</sub> . Samples oxidized in steam are denoted by a blue hash pattern for UC, and a red hash pattern for UB <sub>2</sub> .....	340
Figure D.S1	Histograms depicting the grain size distribution of the 1850 °C sintered samples with counts showing on the left y-axis and the cumulative percentage line corresponding to the right y-axis.....	359
Figure D.S2	Histograms depicting the grain size distribution of the 1900 °C sintered samples with counts showing on the left y-axis and the cumulative percentage line corresponding to the right y-axis.....	359
Figure D.S3	Histograms depicting the grain size distribution of the 1950 °C sintered samples with counts showing on the left y-axis and the cumulative percentage line corresponding to the right y-axis.....	360
Figure D.S4	Histograms depicting the grain size distribution of the 2000 °C sintered samples with counts showing on the left y-axis and the cumulative percentage line corresponding to the right y-axis.....	360
Figure D.S5	A) Stitched optical image montage of the cross-sectional area for the 1950/25 sample showing the exaggerated grain growth of the very large (> 1 mm) grains in the middle of the sample surrounded by increasingly smaller grains towards the sample edge, black square inset represents area from where the EBSD mapping occurred; B) EBSD inverse pole map of the inset area from A).....	362
Figure E.S1	a) Backscatter electron (BSE) image of the microstructure for the 4-hour sintered sample after undergoing laser flash analysis to 1273 K, and b) BSE image showing mapped area for EDS along with elemental mapping of the uranium, oxygen (darker grey), and boron (lighter gray) phases. Essentially no difference in the microstructure is observed after thermal property characterization.....	364
Figure E.S2	a) Backscatter electron (BSE) image of the microstructure for the 8-hour sintered sample after undergoing laser flash analysis to 1273 K, and b) higher magnification BSE image along with EDS elemental mapping of the uranium, oxygen (darker grey), and boron (lighter gray) phases. Essentially no difference in the microstructure is observed after thermal property characterization.....	364

Figure E.S3	<p>a) XRD pattern for the 8-hour as-sintered sample as displayed in the HighScore+ software indicating the calculated pattern fit and showing the phase markers for the <math>\text{UO}_2</math> (blue), <math>\text{UB}_2</math> (green), and NIST SRM <math>\text{LaB}_6</math> (gray), and b) the residue and peak list from the calculated fit, the weighted R was 6.1 and the goodness of fit was 18.5.....365</p>
Figure E.S4	<p>a) XRD pattern for the <math>\text{UO}_2</math>-10wt% <math>\text{UB}_2</math> mixed-powder sample as displayed in the HighScore+ software indicating the calculated pattern fit and showing the phase markers for the oxide phases <math>\text{UO}_2</math> (blue) and <math>\text{UB}_2</math> (green), and b) the residue and peak list from the calculated fit, the weighted R was 1.7 and the goodness of fit was 1.8. The calculated phase fraction for the boride phase at almost 13wt% is attributed to sampling of the powder for characterization and an overestimation in the quantitative results from the amorphous nature of the vacuum grease used for sample encapsulation.....366</p>
Figure E.S5	<p>SEM micrograph of the same as-sintered 8-hour <math>\text{UO}_2</math>-10wt% <math>\text{UB}_2</math> sample (seen in Figure 4a in the main manuscript after polishing via focused ion beam. This same cross-sectional surface exhibits a smaller amount of porosity (in line with the 96% TD) than what was achieved through the mechanical polish, confirming much of the porosity seen in the Figure in 4a came from pullout during sample preparation.....367</p>

## LIST OF ABBREVIATIONS

AFC	Advanced Fuels Campaign
AIMD	Ab initio molecular dynamics
AML	Advanced Materials Laboratory
ATF	Advanced Technology Fuel/Accident Tolerant Fuel
BF	Bright field
BSE	Backscattered electron
BSU	Boise State University
CAES	Center for Advanced Energy Studies
CS	Conventionally sintered
CTR-N	Carbothermic reduction and nitridization
DC	Direct current
DFT	Density functional theory
DOE-NE	Department of Energy Office of Nuclear Energy
DSC	Differential scanning calorimetry
EBSD	Electron backscatter diffraction
EDS	Energy dispersive spectroscopy
ELF	Electron localization functions
FAS	Field assisted sintering
FeCrAl	Iron-Chromium-Aluminum alloy
FWHM	Full width half maximum

HAADF	High angle annular dark field
HDN	Hydride-dehydride-nitride
HEBM	High energy ball milling
HIP	Hot isostatic pressing
HR-TEM	High resolution transmission electron microscopy
HT-ESEM	High temperature environmental scanning electron microscopy
HWR	Heavy water reactor
ICSD	Inorganic crystal structure database
IEA	International Energy Agency
INL	Idaho National Laboratory
IPCC	Intergovernmental Panel on Climate Change
IUP	Integrated University Partnership
LDOS	Local density of states
LFA	Laser flash analysis
LOCA	Loss of coolant accident
LPS	Liquid phase sintering
LWR	Light water reactor
MSIPP	Minority Serving Institution Partnership Program
NEUP	Nuclear Energy University Partnership
NIST	National Institute of Standards and Technology
NNSA	National Nuclear Security Administration
NRC	Nuclear Regulatory CommissionPDFPowder diffraction file
PEG	Polyethylene glycol

PVDC	polyvinylidene chloride
RIR	Relative intensity ratio
ROM	Rule of mixtures
SEM	Scanning electron microscopy
SNAP	System Nuclear Auxiliary Power
SPS	Spark plasma sintering
SRM	Standard reference material
STEM	Scanning transmission electron microscopy
TAF-ID	Thermodynamics of Advanced Fuels International Database
TD	Theoretical density
TEM	Transmission electron microscopy
TGA	Thermal gravimetric analysis
TRISO	Tristructural isotropic particle fuel
UB <sub>2</sub>	Uranium diboride
UC	Uranium monocarbide
UHP	Ultra high purity
UN	Uranium mononitride
UO <sub>2</sub>	Uranium dioxide
U <sub>3</sub> Si <sub>2</sub>	Uranium sesquisilicide
VASP	Vienna ab initio simulation package
XRD	X-ray diffraction

## CHAPTER ONE: INTRODUCTION

### 1.1 Motivation

A measure of human well-being and quality of life is directly proportional to energy consumption. A map of the worldwide energy consumption in 2019, measured in terawatt-hours, shows that our industrial nations continue to drive the increase in energy demand (**Figure 1.1**) [1]. An estimation from the United Nations suggests the human population will increase by 2.2 billion by the year 2050 and as of 2019, 10% of the world's population did not have access to electricity, equating to 759 million people [2]. Providing energy to those without and keeping pace with the electricity demands of a growing modern society while safeguarding the environment is a vital need [3].

## Primary energy consumption, 2019

Primary energy consumption is measured in terawatt-hours (TWh).

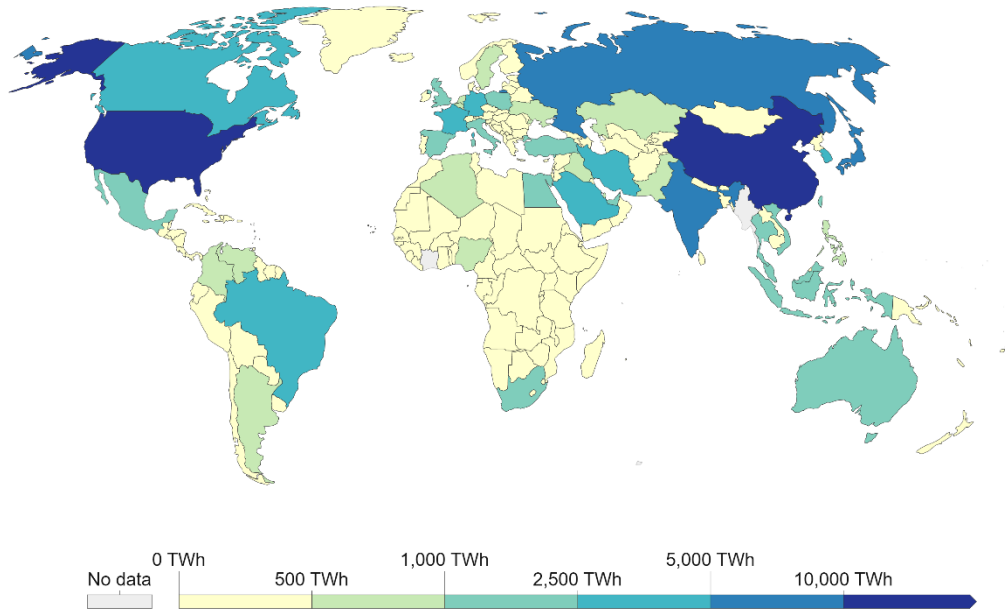


**Figure 1.1 Primary energy consumption for 2019, measured in terawatt-hours, indicating our increase in energy demand remains primarily from industrialized nations [1].**

An overall healthy population and increased quality of life is equated to improved access to electricity, clean water, and other amenities. The United Nation's human development index (a measure of human well-being) versus annual per capita electricity use is seen in **Figure 1.2** [4]. Underdeveloped areas like Asia and Africa are projected to increase access and demand for electricity, which will drive the need for increased energy production. This anticipated increase in energy demand will result in continued greenhouse gas emissions if the energy sector does not focus on usage of clean energy sources.

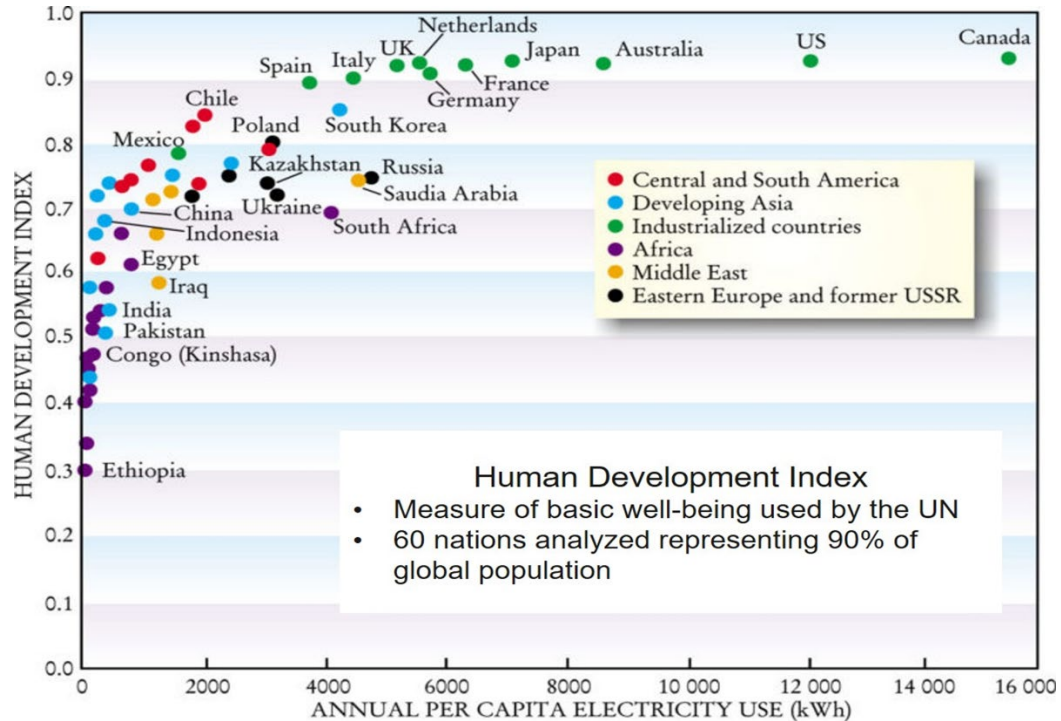


**Figure 1.2 United Nations human development index versus annual per capita electricity usage, reflecting that industrialized nations with greater access to electricity, clean water, and other amenities experience a higher quality of life.**

The reduction in emissions of greenhouse gases that contribute to global warming and climate change is critical to stay on track for keeping the global warming increase to 1.5-2 °C as compared to pre-industrial levels. As of 2021, the global land-ocean temperature increase since 1880 is 1.01 °C [5]. According to the National Oceanic and Atmospheric Administration’s 2020 Global Climate Report, the global annual temperature has increased at a rate of 0.08 °C per decade since 1880, but that rate has increased to 0.18 °C per decade since 1981 [6]. If the current emission rates of carbon continue (just under 10 GtC/year) the upper target limit will be hit in a matter of decades [7]. The energy sector, a chief contributor to greenhouse gas emissions, has been identified as a principal area to focus on for deep decarbonization [8]. According to the International Energy Agency (IEA), nuclear power is the world’s second largest source of

low-carbon electricity, second only to hydroelectric power, and provides one-third of the world's non-emitting clean energy [9].

The energy density and capacity factor (the ratio of the total energy produced to the total rated production of the plant) for nuclear far exceeds that of other power producing forms. One uranium fuel pellet, a roughly 1 cm diameter by 1.5 cm tall cylinder, can produce as much energy as 120 gallons of oil, 1 ton of coal, or 17,000 cubic feet of natural gas [10]. Nuclear energy has the highest capacity factor of any other energy source. As of 2020 nuclear produced maximum power 92.5% of the time (see **Figure 1.3**), with the closest competitor being geothermal at 74.3%, followed by natural gas (56.6%), and coal (40.2%) [11]. When compared to renewables the difference is even more pronounced with hydropower, wind, and solar at capacity factors of 41.5%, 35.4%, and 24.9%, respectively [11].

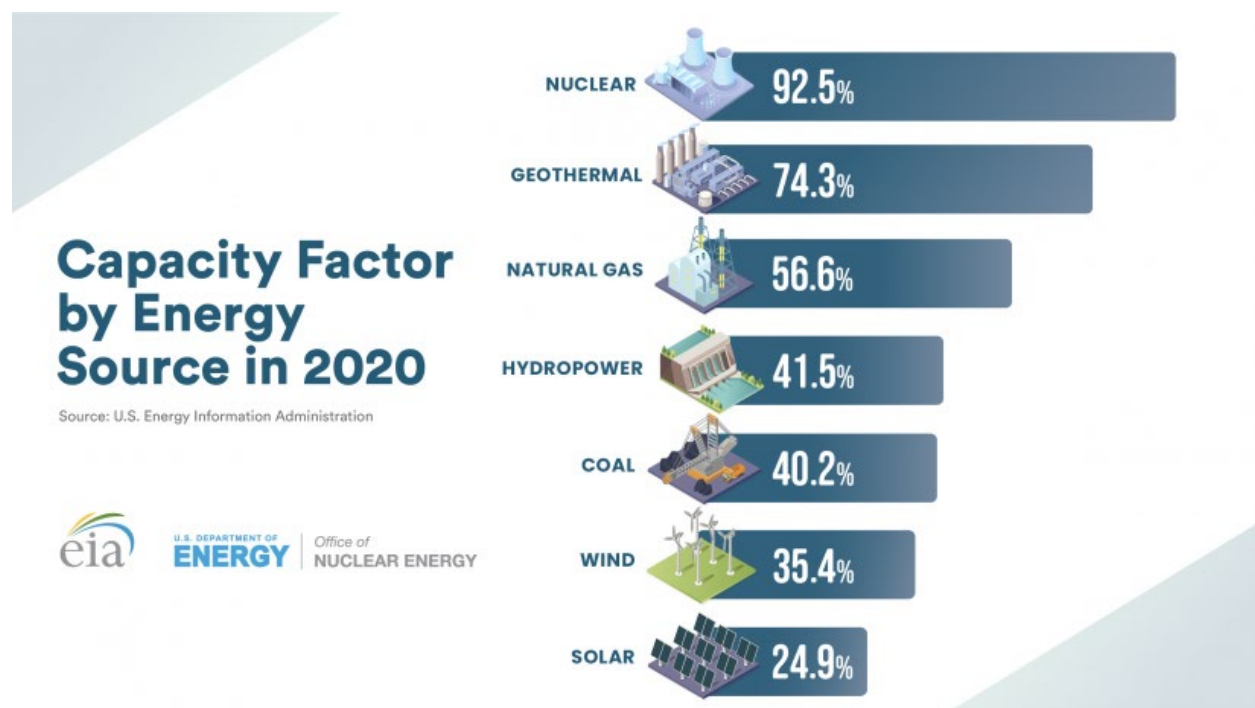


**Figure 1.3** Capacity factors for 2020 listed by energy source [11].

The IEA estimates that global nuclear energy production needs to nearly double within the next 20 years to keep pace with clean energy transition goals worldwide [9]. The global market potential is estimated between \$2.6 to \$4 trillion over the next 20 years if new nuclear reactors are integrated into industrial processes as clean energy sources [12]. Despite overwhelming evidence that nuclear energy is one of the most abundant and scalable carbon-free energy sources, the technology and industry continues to be stigmatized due to historical questions over spent fuel, plant safety, and weapons proliferation [8]. Nuclear also remains undervalued as a clean form of energy production despite reports that show the lifecycle emissions of carbon dioxide from nuclear (when considering construction, mining, transport, operation, decommissioning, and waste disposal) are less than half that of solar and comparable to that of wind (See **Figure 1.4**) [13]. Combining the resistance of the average person (non-scientific and non-technical) to accept nuclear as a clean energy source with the memory of past accident scenarios makes acceptance of new nuclear technologies much more difficult.

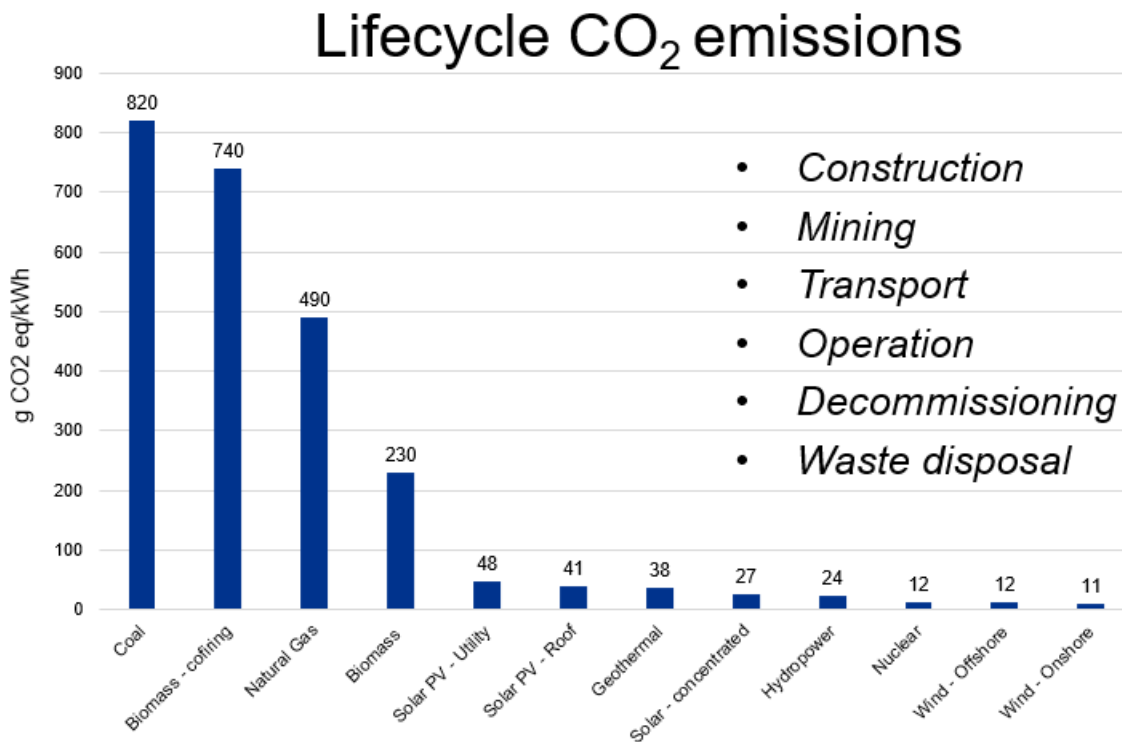


**Figure 1.4 Lifecycle CO<sub>2</sub> emissions of energy sources when accounting for construction, mining, transport, operation, decommissioning, and waste disposal. Modified from IPCC [13].**

After the catastrophic earthquake in 2011, and resulting tsunami that damaged the Fukushima Daiichi Nuclear Power Plant in Japan, the U.S. Congress emphasized funding to the Department of Energy Office of Nuclear Energy (DOE-NE) to develop nuclear fuels and claddings with enhanced accident tolerance [14]. Accident tolerant fuels are defined as those which, when compared to the current UO<sub>2</sub>-Zircaloy system, will provide enhanced tolerance to loss of active core cooling, while maintaining or improving fuel performance during normal operation, transients, design-basis and beyond-design-basis events [14]. Although decades of research have gone into the current commercial reactor benchmark, uranium dioxide fuel/zirconium alloy cladding, continued deployment of advanced technologies to improve economic and safe operation have pushed the existing light water reactor (LWR) fuel technology near its inherent performance limits [14].

Research and development into advanced nuclear fuels that can adapt to extreme conditions while remaining stable under normal operation must be included in investments to the current reactor fleet and new reactor technologies [14].

High uranium-density advanced technology fuels (or accident tolerant fuels, ATF) like uranium mononitride (UN), uranium diboride ( $UB_2$ ), uranium monocarbide (UC), and triuranium disilicide ( $U_3Si_2$ ) can improve nuclear fuel performance by allowing higher burn-up, leading to lower waste volumes and longer cycle lengths. Increased power uprates are possible due to the increased power density ATFs provide due to their increased uranium loading as compared to  $UO_2$ . These fuels can provide better performance in extreme temperatures due to their higher thermal conductivities, which results in reduced fuel failures and more efficient plant operation. A comparison of uranium loading and thermal conductivities as compared to other uranium-bearing fuel forms is shown in **Figure 1.5**.

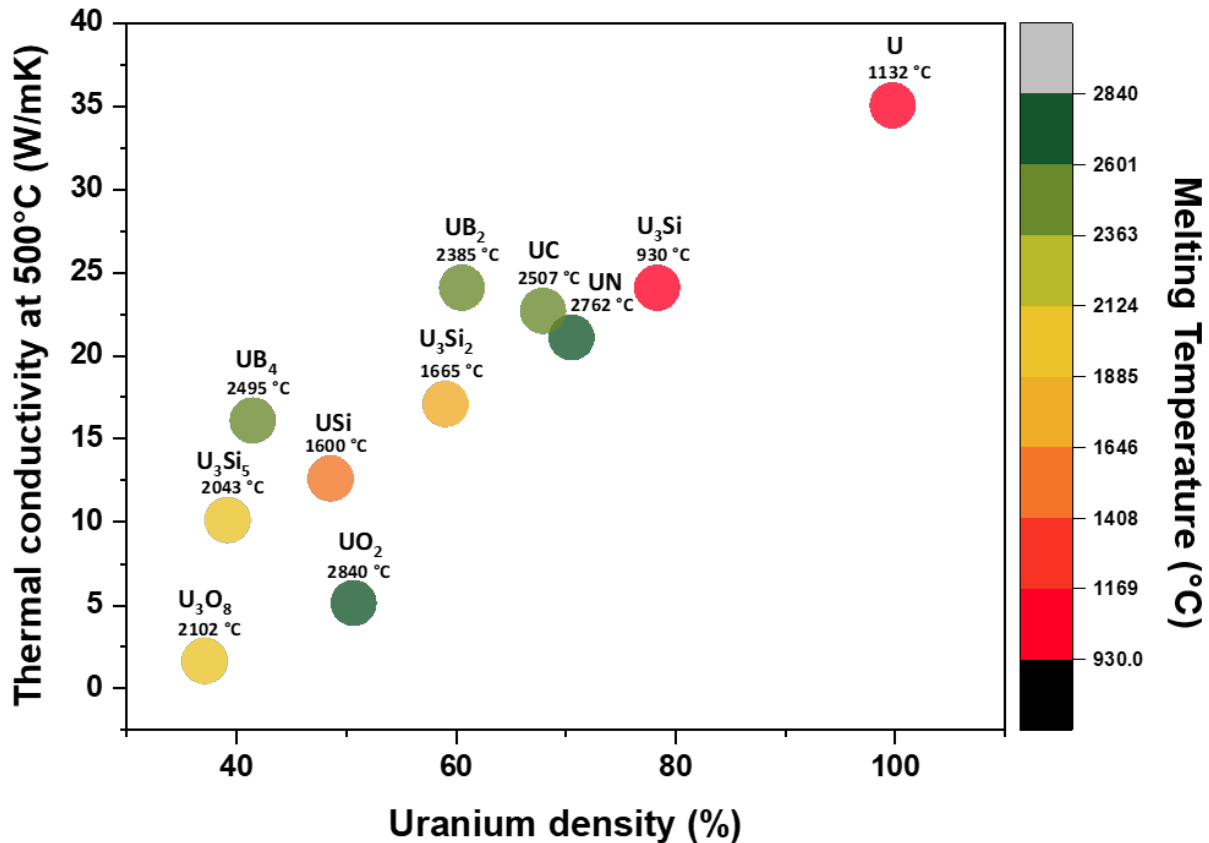


**Figure 1.5** Thermal conductivity values at 500 °C versus uranium density for various uranium-bearing fuel forms, color mapped to melting temperature [15].

These fuels will allow for the use of advanced cladding materials that may have neutronic penalties but provide increased safety margins. However, an obstacle to the use of these fuels in a LWR arises from their susceptibility to degradation in hydrothermal corrosion conditions — like what would be experienced in an accident scenario such as a fuel cladding breach where the fuel would interact directly with the coolant. This obstacle provided the impetus for much of the research presented in this dissertation.

Understanding how and why these fuels suffer from such poor oxidation performance will assist in developing strategies to improve this performance. In addition to improving corrosion resistance, obtaining experimental data on these less well-studied fuels (compared to UO<sub>2</sub>) will help build the database of knowledge for and confidence in these

ATFs, which are necessities required by the rigorous qualification process of new nuclear technology. The objective and scope of the work is outlined in the next sections.

## **1.2 Project Objective and Scope**

The goal of this work is to expand and mature the knowledge base of ATFs to develop fundamental insight to the nature of advanced nuclear fuels. This insight can promote the integration of ATFs with advanced cladding and coolant materials being proposed for use in the existing LWR fleet and next generation reactor designs. The understanding of fuel behavior, synthesis, fabrication, performance under irradiation, and long-term storage of the spent fuel, can be achieved through a combination of experimentation and multiscale modeling. The work included in this dissertation aims to bring insight to the complexities involved with synthesis, fabrication, and sintering of ATF single phase and composite fuel concepts. Understanding performance under corrosion conditions coupled with strategies to mitigate hydrothermal corrosion of ATFs is also a focus. Research involving improvements upon thermophysical characteristics of  $\text{UO}_2$  using  $\text{UB}_2$  will also be presented.

Data from this work will provide inputs to simulation models which will assist in progressing these fuels through the arduous qualification and approval process. The work outlined in this dissertation, while primarily focused on fundamental research towards UN and efforts to mitigate its hydrothermal corrosion behavior, also includes efforts to demonstrate improvements in thermophysical performance of a  $\text{UO}_2$ -composite using an ATF candidate,  $\text{UB}_2$ , as a secondary phase.

The contributions to the literature from this dissertation on improving the properties and advancing acceptance of ATFs have resulted in three journal publications,

one conference proceeding, and one manuscript pending submission for publication. Included in this dissertation is an extensive, 3-part literature review focused on understanding oxidation and corrosion behavior of ATFs, strategies envisioned to improve the resistance to hydrothermal corrosion of ATF candidates, and efforts to test these strategies. This is coupled with experimental work focused on improving the hydrothermal corrosion resistance of UN through the use of secondary phases. Advancing the knowledge base on grain growth in conventionally sintered UN is also important to the fact that grain size affects many important properties in nuclear fuel. It is postulated that if these ATF concepts are to be adopted for use, a fuel with a larger grain size may delay adverse oxidation behavior in a pure or composite system, as well as inhibiting fission product transport and release. Other experimental work provides validation to efforts of improving the thermal conductivity of the benchmark  $\text{UO}_2$  fuel.

### 1.2.1 Objectives

The key theme of this dissertation work was to expand the knowledge base for ATF concepts, in terms of hydrothermal corrosion performance of UN and attempts to improve that performance through the addition of secondary phases, as well as insight into the grain growth behavior of conventionally sintered UN. This theme also included attempts to improve the thermophysical properties of the current benchmark fuel through the use of an ATF additive. The chapter descriptions presented below detail the scope of work presented in the subsequent chapters which allowed for the accomplishment of their related objectives:

Objective 1: Assess the impact of the addition of  $\text{UO}_2$  addition to a UN matrix on the hydrothermal corrosion performance of the bulk monolith and identify the mechanism of degradation.

Chapter 2 presents an experimental study on the corrosion behavior and degradation mechanism of UN and UN-(5-10 wt%)  $\text{UO}_2$  composites subjected hydrothermal corrosion. As a strategy for delaying unfavorable corrosion behavior, it was hypothesized that a desirable composite microstructure could be achieved through conventional sintering methods which would provide protection to the UN base fuel via a preferred pathway for oxidation. The benchmark  $\text{UO}_2$  fuel, a proven and adopted nuclear fuel, has been used and studied for decades in LWRs. It has acceptable hydrothermal corrosion performance under the relevant reactor operating conditions. As such,  $\text{UO}_2$  was chosen as the additive phase for this work to study how its addition to the UN matrix would affect the bulk corrosion behavior. A degradation mechanism for UN and UN- $\text{UO}_2$  composites exposed to water submersion at relevant nuclear reactor operating temperatures was proposed along with insights to experimental parameters that can amplify corrosion behavior.

Objective 2: Investigate the feasibility of adding metallic constituents to a UN matrix for the purpose of improving the corrosion performance of UN.

Chapter 3 furthers the work on strategies to inhibit the unfavorable corrosion behavior of UN and UN-composites. This work documents experimental efforts aimed at inclusion of secondary metallic constituents (namely zirconium and yttrium) to a UN fuel matrix, which would provide a preferential pathway for oxidation to hinder the degradation behavior of the base fuel in corrosive conditions. Microstructural

examination, phase identification, and thermodynamic predictions of the composites are included as part of the study.

Objective 3: Study of the grain growth in conventionally sintered UN to identify the grain growth mechanism, activation energy, and preferential orientation during grain growth.

Chapter 4 focuses on identifying the grain growth mechanism, activation energy and preferential texturing in conventionally sintered UN. The mechanism for the grain growth in conventionally sintered UN has not been well-studied and limited information exists in the literature related to this fundamental behavior. Increasing grain size in nuclear ceramics affects swelling, fission gas release, creep, and thermal conductivity. For UN fuel to be adopted for use, a larger grain size would be more likely for delaying oxidation behavior in a pure or composite system, in addition to inhibiting fission product transport and release. The work is intended to help provide insight to grain growth in UN and inputs for future computational models (which are sensitive to grain size), envisioned for use in decreasing qualification cycles of new fuels. Application of accepted grain growth models to data obtained using electron backscatter diffraction (EBSD) allowed for determination of the most likely value for the grain growth exponent and a proposed activation energy for the UN samples in this study, and the presence of any preferred orientation.

Objective 4: Investigate how the addition of  $UB_2$  to a  $UO_2$  matrix affects the thermal conductivity of the bulk composite.

In addition to expanding the knowledge base for ATF concepts, the nuclear fuels community is interested in improving the accident tolerance of the benchmark  $UO_2$  fuel

through efforts to increase its thermal conductivity. Research has mainly been focused on addition of non-uranium bearing secondary phases, which lowers the fissile density of the composite structure. Chapter 5 describes experimental work on a  $\text{UO}_2$ -(10wt%)  $\text{UB}_2$  composite sintered via conventional methods which resulted in a 36-55% increase in thermal conductivity over pure  $\text{UO}_2$ . By choosing a high-uranium density additive to the  $\text{UO}_2$  matrix, the overall fissile density of the composite is higher than that of  $\text{UO}_2$  alone, which is an ATF characteristic. This work demonstrates that ATF candidates may not only have a future application as stand-alone fuels but can be incorporated as additive phases for improved performance.

As discussed previously, the primary focus of this dissertation is investigating strategies to improve the hydrothermal corrosion behavior of ATFs. While each of the above chapters includes appropriate reviews of existing literature, a more substantial review of the literature related to ATF oxidation and corrosion is provided in the appendices to this dissertation. Appendix A is the first of the three-part review series which provides a comprehensive history on the experimental work on air, oxygen, and water/steam corrosion of UN and includes research needs that remain for advancing this fuel form for future use in LWRs. The second review paper, included as Appendix B, relates to degradation modes, thermodynamics, and oxidation performance of pure  $\text{U}_3\text{Si}_2$  and its reported alloyed and composite architectures. The review also covers the materials and techniques being studied to successfully incorporate additives and dopants to ATF candidates to improve their hydrothermal corrosion behavior. A similar assessment is compiled and examined for  $\text{UB}_2$  and UC in the third part of the literature review series,

included as Appendix C. A summary of the research opportunities that remain for the four ATF candidates is provided at the conclusion of the third paper.

This dissertation, a culminating work from my education and experience — obtained during completion of a Bachelor of Science and a Master of Engineering degree in Materials Science and Engineering at Boise State University, job performance as an undergraduate and graduate research assistant in the Advanced Materials Laboratory at Boise State University, a summer internship at Washington State University focused on nuclear forensics, and a U.S. Department of Energy Nuclear Energy University Partnerships internship and Idaho National Laboratory (INL) graduate fellowship at the Materials and Fuels Complex at INL — presents the significant contributions to the state of the science as it relates to ATF candidates. I have applied my knowledge of materials science and engineering and experience gained during hands-on research to practical applications related the structure, properties, processing, characterization, and performance of advanced technology nuclear fuels. This is the basis of the materials science tetrahedron (or the materials paradigm, **Figure 1.6**).

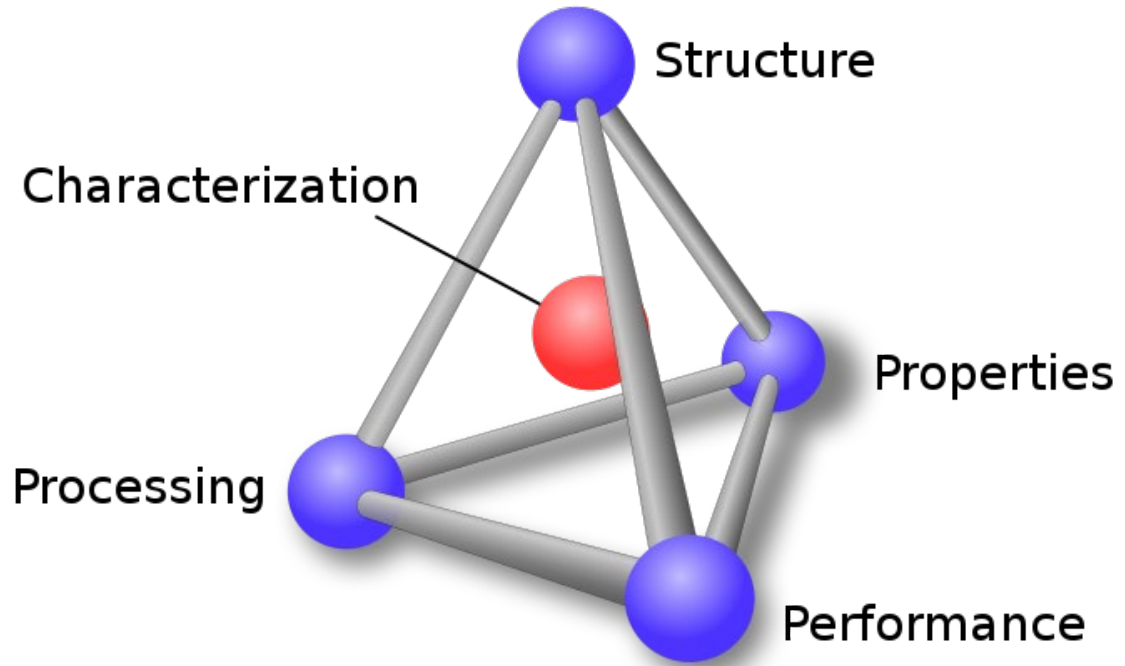


**Figure 1.6** The materials science tetrahedron (or materials paradigm), showing the four interdependent aspects of materials science: structure, properties, processing, and performance, with characterization in the center [16].

## References

- [1] H. Ritchie, M. Roser, Energy, OurWorldInData.org, 2020.
- [2] T.W. Bank, Access to electricity (% of population), 2022.  
<https://data.worldbank.org/indicator/EG.ELC.ACCS.ZS>.
- [3] WNA, World Energy Needs and Nuclear Power, World Nuclear Association, London, UK, 2016-2019.
- [4] S.G. Benka, The Energy Challenge, *Physics Today* 55 (4) (2002) 38-39.
- [5] N.G.I.f.S. Studies, Global Land-Ocean Temperature Index, Goddard Institute for Space Studies 2021.
- [6] NOAA, State of the Climate: Global Climate Report for Annual 2020, 2021.
- [7] USGCRP, Climate Science Special Report: Fourth National Climate Assessment, Volume 1, in: D.J. Wuebbles, D.W. Fahey, K.A. Hibbard, D.J. Dokken, B.C. Stewart, T.K. Maycock (Eds.) Washington, DC, USA, 2017, p. 470.
- [8] MIT, The Future of Nuclear Energy in a Carbon-Constrained World; An Interdisciplinary MIT Study, MIT, Cambridge, MA, 2018.
- [9] IEA, Nuclear Power in a Clean Energy System, International Energy Agency, France, 2019.
- [10] EIA, Energy Explained, 2019.
- [11] U.S. D.O.E., Nuclear power is the most reliable energy source and it's not even close, 2021. <https://www.energy.gov/ne/>.
- [12] S.E. Aumeier, T. Allen, How to reinvigorate US commercial nuclear energy, *Issues in Science and Technology* XXXIV (2) (2018).

- [13] IPCC, Climate Change 2014: Mitigation of Climate Change. Contribution of Working Group III to the Fifth Assessment Report of the Intergovernmental Panel on Climate Change, in: O. Edenhofer, R. Pichs-Madruga, Y. Sokona, E. Farahani, S. Kadner, K. Seyboth, A. Adler, I. Baum, S. Brunner, P. Eickemeier, B. Kriemann, J. Savolainen, S. Schlomer, C. von Stechow, T. Zwickel, J.C. Minx (Eds.) United Kingdom and New York, NY, USA, 2014.
- [14] P. Lyons, B. Crowell, Development of light water reactor fuels with enhanced accident tolerance, Report to Congress, United States Department of Energy, Washington, DC, 2015.
- [15] J.K. Watkins, A. Gonzales, A.R. Wagner, E.S. Sooby, B.J. Jaques, Challenges and opportunities to alloyed and composite fuel architectures to mitigate high uranium density fuel oxidation: Uranium mononitride, *Journal of Nuclear Materials* 553 (2021) 153048.
- [16] W.C. contributors, Materials science tetrahedron; structure, processing, performance, and properties, 2020.  
[https://commons.wikimedia.org/w/index.php?title=File:Materials\\_science\\_tetrahedron;structure,\\_processing,\\_performance,\\_and\\_properties.svg&oldid=476324268](https://commons.wikimedia.org/w/index.php?title=File:Materials_science_tetrahedron;structure,_processing,_performance,_and_properties.svg&oldid=476324268). 2022).

CHAPTER TWO: MICROSTRUCTURAL DEGRADATION OF UN AND UN-UO<sub>2</sub>  
COMPOSITES IN HYDROTHERMAL OXIDATION CONDITIONS

This chapter has been published in the Journal of Nuclear Materials

Reference: J.K. Watkins, D.P. Butt, B.J. Jaques. Microstructural degradation of UN and UN-UO<sub>2</sub> composites in hydrothermal oxidation conditions. Journal of Nuclear Materials 518 (2019): 30-40. <https://doi.org/10.1016/j.jnucmat.2019.02.027>

Microstructural degradation of UN and UN-UO<sub>2</sub> composites in hydrothermal oxidation conditions

Jennifer K. Watkins<sup>a,b</sup>, Darryl P. Butt<sup>c</sup>, and Brian J. Jaques<sup>a,b</sup>

<sup>a</sup> Micron School of Materials Science and Engineering, Boise State University, 1910 University Dr., Boise, ID 83725, USA

<sup>b</sup> Center for Advanced Energy Studies, 995 University Blvd., Idaho Falls, ID 83401, USA

<sup>c</sup> College of Mines and Earth Sciences, University of Utah, Salt Lake City, ID 84112, USA

**Abstract**

The degradation behavior in high pressure water of UN and UN + (5-10 w%) UO<sub>2</sub> monolithic pellets fabricated from UN synthesized via a hydride-dehydride-nitride thermal process was investigated. Sintered pellets (> 90% theoretical density) were subjected to hydrothermal oxidation in a water-filled static autoclave at temperatures ranging from 250-350 °C and pressures to 16.5 MPa. Phase characterization and microstructural and chemical analysis was performed on the resulting corrosion products using X-ray diffraction (XRD), scanning electron microscopy (SEM) coupled with energy dispersive spectroscopy (EDS). The results of this screening study show that grain boundary attack and spallation is the primary degradation mechanism in hydrothermal oxidation conditions. The results also suggest the corrosion rate is higher in UN and UN-UO<sub>2</sub> with higher starting oxygen content.

## 2.1 Introduction

### 2.1.1 Motivation for research

After the earthquake and tsunami which damaged the Fukushima Daiichi nuclear power plant complex in 2011, the Department of Energy's Office of Nuclear Energy (DOE-NE) refocused its mission of developing advanced nuclear fuels with improved performance capabilities and reduced waste generation to include the development of advanced technology fuels (ATFs) for use in light water reactors (LWRs) [1-4]. ATFs are designated as fuels that can tolerate a loss of active cooling in the reactor core for a substantially longer time than the current benchmark, uranium dioxide (UO<sub>2</sub>)-Zircaloy fuel system. In addition, ATFs should maintain or enhance fuel performance under normal and transient operating conditions, and during potential design-basis and beyond-design-basis incidents [3, 4].

Uranium mononitride (UN) and UN composite-based nuclear fuels have been considered for LWR and advanced nuclear reactor applications due to UN's high uranium density, high melting point, high thermal conductivity, and performance under irradiation, as compared to UO<sub>2</sub> [5-9]. These desirable properties contribute to larger power uprates, increased fuel cycle time, and higher burn-up [5, 10, 11]. However, UN has unproven performance in accident scenarios, such as a fuel cladding breach where the fuel pellet would be exposed to water or steam coolant [12-16]. The published literature relating to UN's stability under hydrolysis is limited, contradictory, and does not include the effects of UN submerged in water at elevated temperatures [13-15, 17-19]. It has been proposed that the addition of secondary phases, such as UO<sub>2</sub>, can prevent UN from chemically reacting when exposed to water [5, 10, 16]. The work presented in this

screening study investigates how the addition of  $\text{UO}_2$  affects UN's performance in a simulated accident condition, similar to what would be experienced with a cladding breach under normal operation. Pure UN and UN- $\text{UO}_2$  monolithic pellets (> 90% TD) were subjected to hydrolysis at elevated temperatures (250-350 °C) and pressures (up to 16.5 MPa) relevant to LWR operating conditions for short durations. The evolution of the microstructural degradation as temperature increases is presented. Insight into the degradation mechanism is obtained from examination and comparisons of the corroded microstructures and phase identification in the post-corrosion materials.

## 2.2 Materials and Methods

### 2.2.1 UN powder synthesis

UN powder was synthesized from depleted  $\alpha$ -uranium (99.4% purity, 50 mesh) using a hydride-dehydride-nitride thermal synthesis route [20]. The hydride-dehydride-nitride route was used to limit carbon and oxygen impurities typically resulting from the more industrial carbothermic reduction and nitridation synthesis method of uranium dioxide and carbon (as noted by Muromura *et al.* [21] and Matthews *et al.* [22]). The atomized elemental uranium metal powder was washed in a 50% nitric acid solution and rinsed in methanol to remove oxides. Approximately 15 grams of uranium were loaded into a tungsten-lined alumina crucible inside an inert atmosphere glovebox (< 0.1 ppm  $\text{H}_2\text{O}$  and  $\text{O}_2$ ). The crucible was sealed in a vial, transferred into a high temperature alumina tube furnace, and quickly placed under vacuum to limit exposure to air in preparation for the hydride-dehydride-nitride process. The thermal profile for the hydride-dehydride-nitride method is described in previous work [20]. The oxygen content in the process gas was continually monitored below the detectable limits of the

Neutronics Inc. Model OA1 oxygen analyzer, which was less than parts per billion. Using a glove-bag and in an argon cover gas flow, the synthesized UN powder was removed from the furnace, sealed in a vial, and then immediately transferred back to the inert atmosphere glovebox. Two batches of UN powder, referred to as Batch 1 and Batch 2, prepared for this study were characterized using scanning electron microscopy (SEM) and X-ray diffraction (XRD) (**Figure 2.1**). It is important to note that the Batch 1 UN powder used for pellet fabrication had a lower amount of impurity  $\text{UO}_2$  than the Batch 2 powder; this will be discussed further in succeeding sections. Due to the highly reactive nature, the fine UN powder was mixed into a silicon-based vacuum grease inside an inert atmosphere glovebox prior to XRD characterization in lab air. Combustion analysis was performed using a LECO C230 and RO400 to determine carbon and oxygen content of the starting elemental uranium metal and the synthesized UN powder.

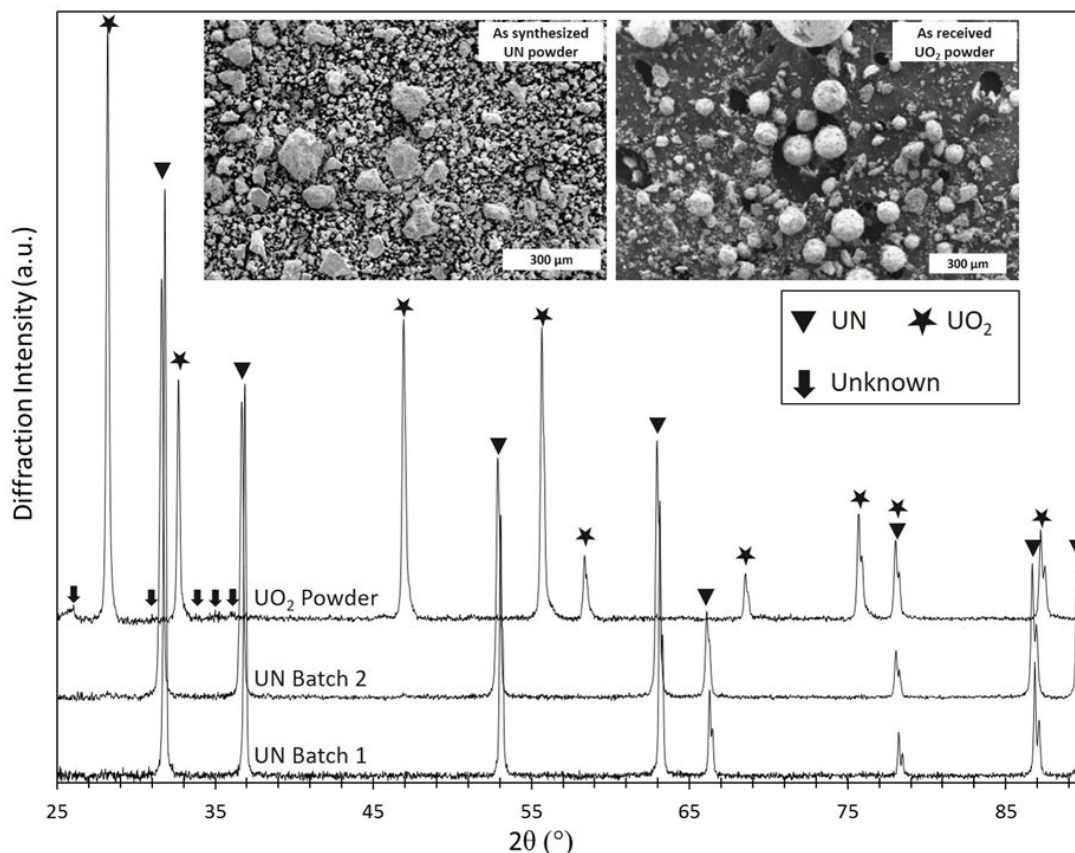


**Figure 2.1** XRD of the two separate batches of UN powders (Batch 1 having a lower starting impurity UO<sub>2</sub> content than that of Batch 2). Powders were synthesized using a hydride-dehydride-nitride route, and as-received UO<sub>2</sub> powder. Left inset shows the morphology of the as synthesized UN powder and right inset is the morphology of the as-received UO<sub>2</sub> powder.

### 2.2.2 Pellet fabrication and sintering

Compacts of UN and UN+ (5-10 w%) UO<sub>2</sub> were fabricated using the synthesized UN powders and UO<sub>2</sub> (99.8% purity, 50 mesh) from Bio-Analytical Industries Incorporated (Boca Raton, FL). The UN and UO<sub>2</sub> powder mixtures were weighed into 5 gram batches, with the proportional amounts of UO<sub>2</sub> for the 5- and 10 w% composites. The powders were hermetically sealed inside polypropylene containers inside an argon-backfilled glovebox (<0.1 ppm O<sub>2</sub>, H<sub>2</sub>O), and mixed in a tabletop mixing mill (MTI 4 Tanks Mixer). Image analysis software was used to estimate particle size. After mixing, the UN and composite powders were cold-pressed at approximately 670 MPa into green

pellets of right cylindrical geometry, with either a 3.175 or 6.35 mm diameter die, to approximately 62 %TD in an inert atmosphere glovebox. A small amount of zinc stearate was used as a lubricant on the die walls and punch faces prior to pressing.

Due to the potential for the green pellets to spontaneously react in air, the pellets were placed on tungsten setter plates and sealed under polyvinylidene chloride (PVDC) film with a small amount of vacuum grease to avoid oxidation during the rapid transfer into the refractory metal sintering furnace. The pellets were sintered for five hours at 1900 °C in an Ar+100 ppm N<sub>2</sub> atmosphere; the complete details for sintering are explained in a previous publication [20]. After sintering, the pellets were immediately transferred to an inert atmosphere glovebox. The sintered samples were prepared for SEM and XRD characterization by grinding with 1200-grit silicon carbide grit paper approximately 1/3 of the way through the pellet to create a cross-sectional surface that was perpendicular to the two parallel faces of the right cylinder. A thermal etch at 1200 °C for 12 minutes was performed in the refractory metal furnace to examine the grain morphology of the sintered pellets. Pellet densities were determined via the Archimedes method in de-ionized water at 21 °C [23].

### 2.2.3 Hydrothermal oxidation

In preparation for radioactive hydrothermal oxidation testing, a custom static autoclave (Parker Autoclave Engineers) was modified with a containment enclosure to house the autoclave bolt assembly seal (**Figure 2.2**) and prevent any external contamination with radioactive material. A stainless-steel sample holder was fabricated to position up to four samples simultaneously within the hot zone of the autoclave, as shown in **Figure 2.2**. Layers of stainless-steel mesh separated the pellets from each other, and

the entire pellet holder was secured by another layer of stainless-steel mesh to ensure the samples would not shift during loading and testing. A pellet of each composition was loaded into the sample holder in lab air; three pellets in the Batch 1 tests, four in the Batch 2 tests, including  $\text{UO}_2$  as a benchmark. After loading the sample holder into the autoclave, 80 mL of 18.2  $\text{M}\Omega\cdot\text{cm}$  de-ionized water was added before the system was sealed and pressurized to approximately 4.1 MPa with UHP helium. This static autoclave configuration, while similar to the static tests performed by Nelson *et al.* [24] on silicide and nitride fuels in deionized water, did not allow for loading of the samples under inert atmosphere. The maximum starting oxygen potential was calculated to be approximately 4700 ppm. It is believed this value was lower as the autoclave enclosure was continuously pressurized with UHP He until it was sealed completely at 200 °C. The temperature was ramped at 1 °C/min to and from the dwell temperature (250 – 350 °C, resulting in a pressure of 4.1-16.5 MPa) where it was held for 30 minutes prior to cooling to room temperature. Density measurements and optical macro images were recorded for the pellets after removal from the autoclave. The pellet surfaces were examined using SEM, energy dispersive spectroscopy (EDS), and XRD.

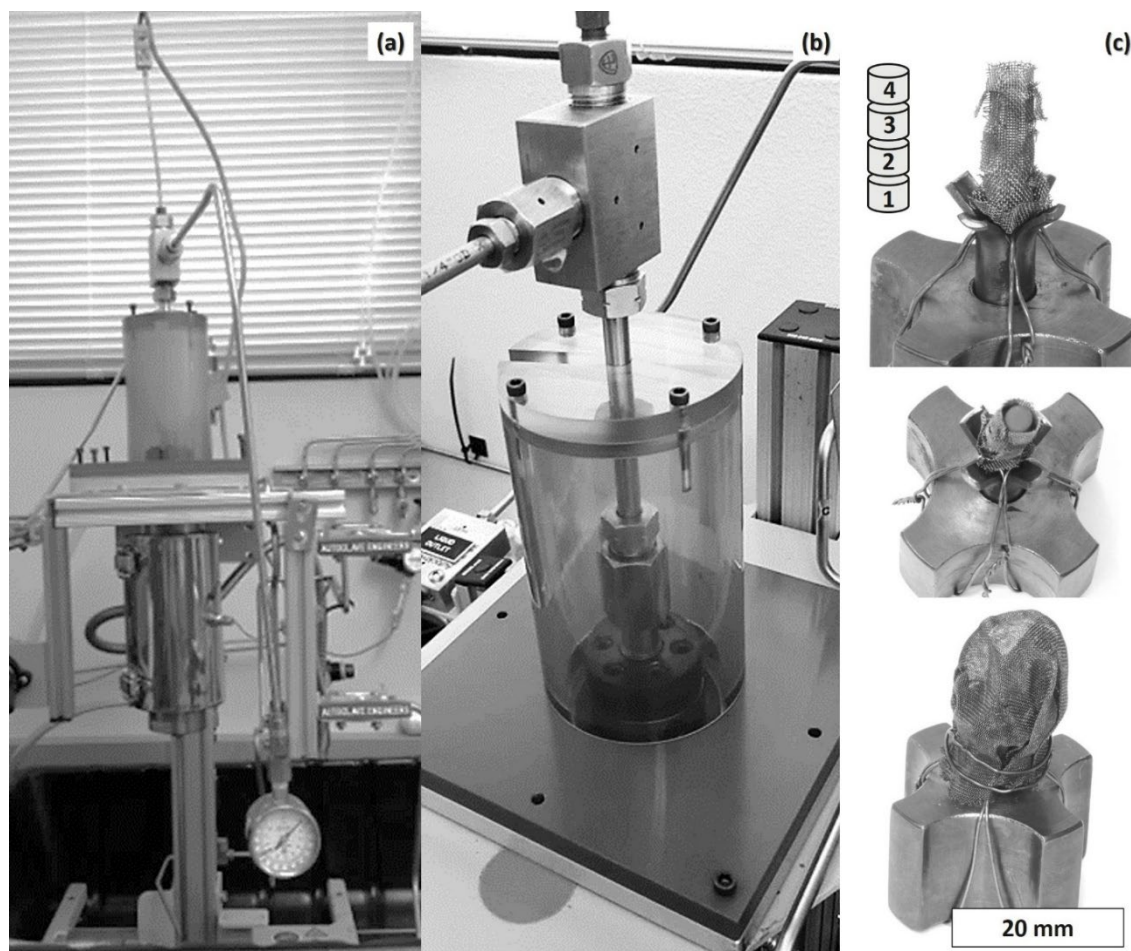


**Figure 2.2** (a) Static autoclave used for hydrothermal oxidation testing showing the location of the heater/hot zone, (b) the custom fabricated containment enclosure for the autoclave bolt assembly, and (c) Side view of sample holder (top image), top view of the custom Autoclave sample holder showing the stainless-steel mesh for positioning up to four pellets in the hot zone of the autoclave (middle image). Once the pellets are inserted, the sample holder is encased with stainless steel (bottom image) to retain corrosion products.

## 2.3 Results

### 2.3.1 UN powder synthesis

The left inset SEM image in **Figure 2.1** shows the as synthesized UN powder exhibiting a bimodal particle size distribution and faceted morphology, as expected from the hydride-dehydride-nitride synthesis route. The larger particles and agglomerates were broken up during the milling process resulting in a powder with an average particle size

of  $1.1 \pm 0.5 \mu\text{m}$  (inset of **Figure 2.3**). XRD of the as-synthesized powders showed the powder as primarily UN (Inorganic Crystal Structure Database powder diffraction file (ICSD PDF) 00-032-1397) with a small fraction of  $\text{UO}_2$ . Comparison of the two synthesized batches indicates increased  $\text{UO}_2$  (ICSD PDF 00-041-1422) content in the Batch 2 powder. A semi-quantitative analysis of the XRD intensities suggests that the  $\text{UO}_2/\text{UN}$  ratio in the Batch 2 powder was twice that of the Batch 1 powder. **Figure 2.1** also includes the pattern for the starting  $\text{UO}_2$  powder which suggests it is primarily  $\text{UO}_2$  but also exhibits additional peaks labeled as unknown after comparing to peaks corresponding to  $\text{U}_3\text{O}_8$  (ICSD 00-014-1493). It is possible a small secondary phase,  $\text{U}_3\text{O}_7$  (ICSD 00-015-0004), may be present. This  $\text{U}_3\text{O}_7$  phase exhibits peak overlap with the indexed  $\text{UO}_2$  pattern but may be contributing to broadening of peaks attributed to  $\text{UO}_2$  [25, 26]. The light element chemical analysis on the starting uranium metal indicated 300 ppm and 170 ppm of carbon and oxygen, respectively, and 275 ppm and 2550 ppm of carbon and oxygen, respectively, in the Batch 1 UN powder.

### 2.3.2 Pellet fabrication and sintering

After mixing and milling the UN with the  $\text{UO}_2$  powders for five hours, SEM characterization shows a bimodal particle size distribution for all compositions (inset of **Figure 2.3**). XRD of the as synthesized UN, the milled UN, and milled compositional powders reflect only UN (ICSD PDF 00-032-1397) denoted by the inverted triangles, and  $\text{UO}_2$  (ICSD PDF 00-041-1422) as indicated by the star shape in **Figure 2.3**. All pellets were  $92 \pm 1.6 \% \text{TD}$ , based on the theoretical density of UN ( $14.33 \text{ g/cm}^3$  [27]), and a typical sintered pellet is seen in **Figure 2.4a**. The typical grain morphology of a cross-sectioned sintered pellet and fracture surface are shown in **Figure 2.4b** and **c**. The

distribution of the  $\text{UO}_2$  phase in the UN matrix for a UN + 10w%  $\text{UO}_2$  pellet is shown in

**Figure 2.4d.**

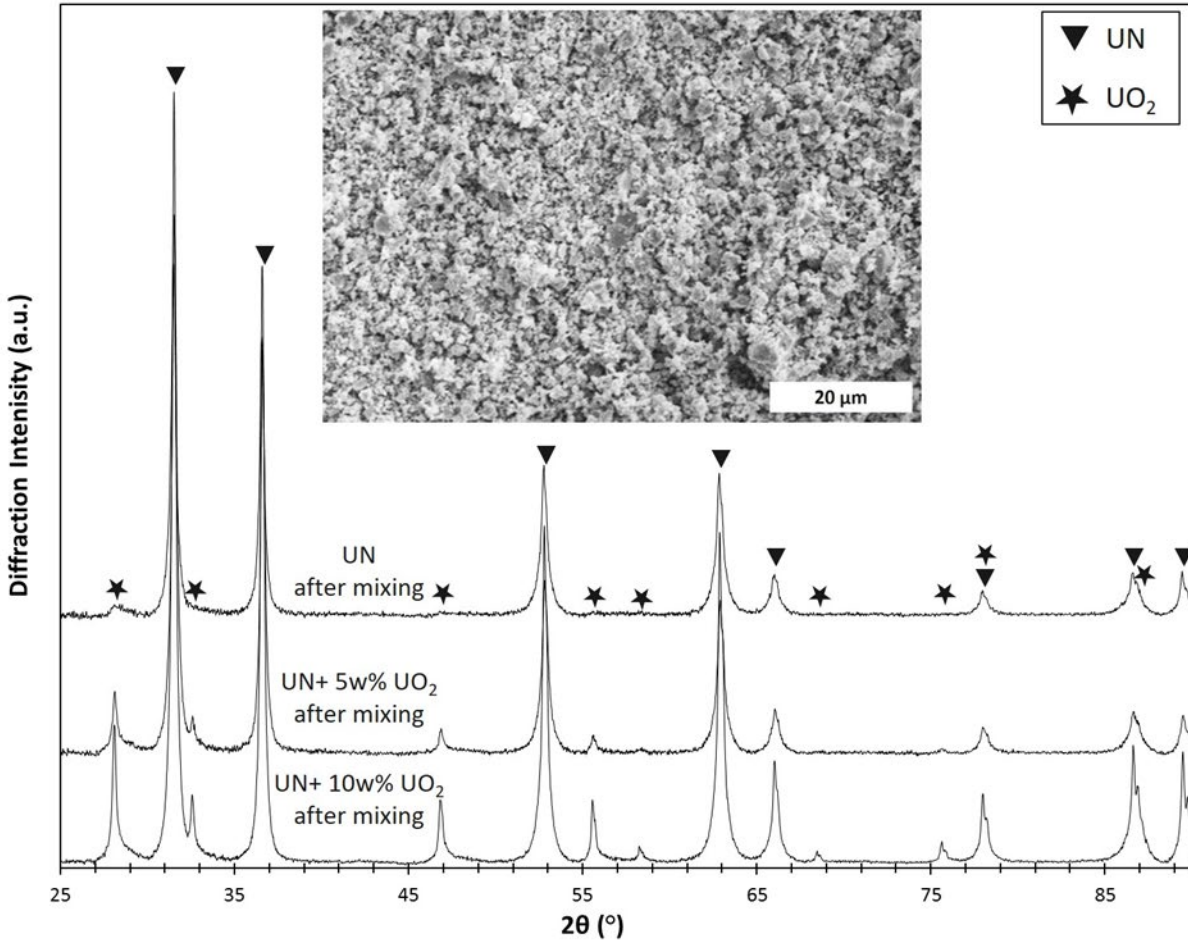


**Figure 2.3** XRD patterns of the mixed UN and UN- $\text{UO}_2$  composite powders prior to pressing into pellets. The inset is an SEM micrograph showing the typical morphology of the mixed powders.

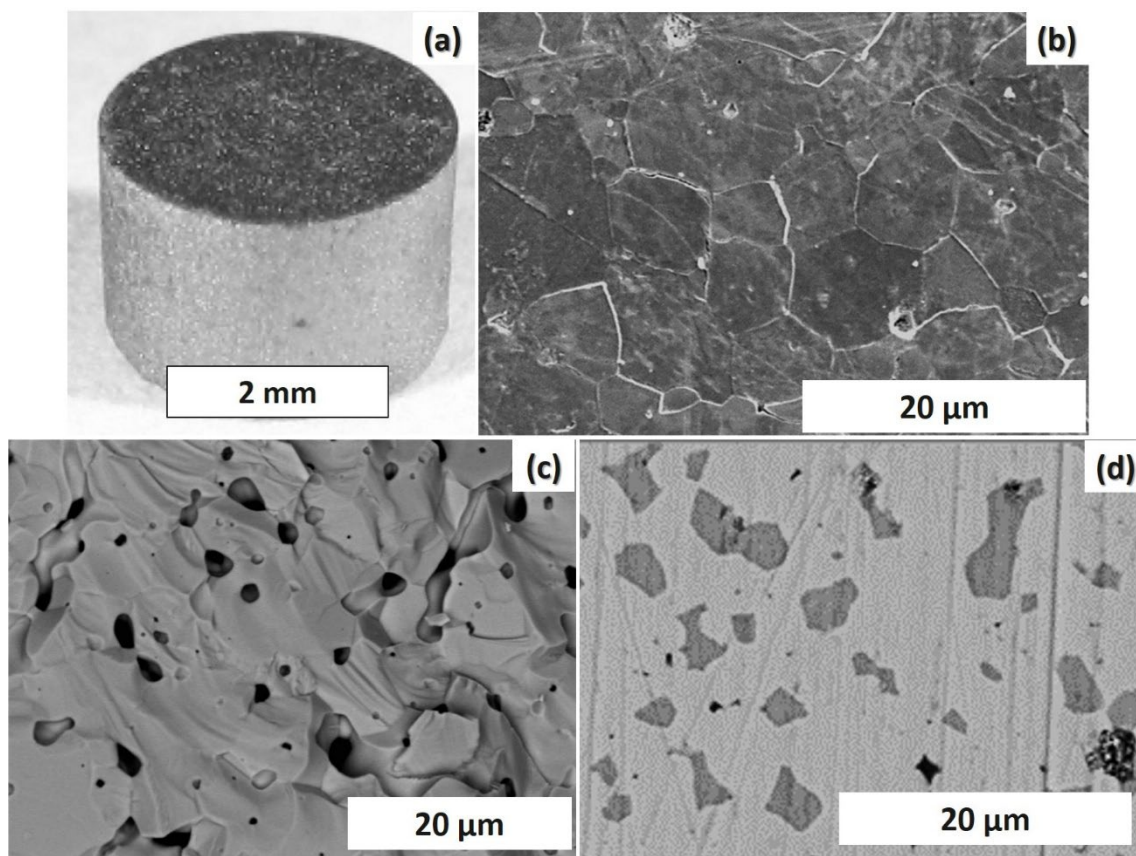


**Figure 2.4** Images of a typical sintered pellet showing (a) right cylindrical geometry, (b) the grain structure of UN + 5 w% UO<sub>2</sub> pellet surface after polishing and thermal etching, (c) the fracture surface of UN + 10 w% UO<sub>2</sub> pellet, and (d) the typical UO<sub>2</sub> distribution in the UN matrix of a UN + 10 w% UO<sub>2</sub> pellet.

### 2.3.3 Pellets post-autoclave

**Figure 2.5** shows the corroded pellets fabricated from both the Batch 1 and Batch 2 powders. Each test, regardless of temperature, resulted in pellets that were considerably darker in color than the un-corroded pellets. The densities of the corroded pellets also remained relatively constant at approximately 90 %TD as determined via Archimedes method.

The pellets fabricated with Batch 1 UN powder (containing less starting impurity UO<sub>2</sub>) were preferentially attacked at the edges and, as expected, the level of degradation increased with increasing temperature. Also, in certain instances, the hydrothermal test

resulted in complete loss of the pellet. For example, the UN + 5 w% UO<sub>2</sub> pellet exposed to 300 °C completely disintegrated (**Figure 2.5**). The tests at 300 and 325 °C were repeated to replicate the results. However, both repeated tests resulted in different outcomes. At 275 °C all Batch 1 pellets were retrieved, but for Batch 2 (having a higher starting impurity UO<sub>2</sub> content) both UN-UO<sub>2</sub> composite pellets were disintegrated. The Batch 1 pellets corroded in the first 300 °C test resulted in complete loss of the 5 w% UO<sub>2</sub> pellet. In the Batch 2 300 °C test both the 5 w% and 10 w% UO<sub>2</sub> composite pellets disintegrated. Similarly, for Batch 1 in the 325 °C test the 10 w% UO<sub>2</sub> pellet was lost and in the 350 °C the 5 w% UO<sub>2</sub> pellet was totally disintegrated, but in Batch 2 tests at 325 °C and 350 °C all pellets except the pure UO<sub>2</sub> pellet were lost. As stated previously, the maximum calculated starting oxygen potential of the pressurized water and volume of air and He balance was roughly 4700 ppm. However, the benchmark UO<sub>2</sub> pellets did not show any significant degradation per visual examination and XRD. The chipping on the UO<sub>2</sub> pellet used in Batch 2 testing at 350 °C occurred in the green state prior to sintering (**Figure 2.5**).

It is believed the starting oxygen potential was much lower since the autoclave was continuously pressurized with UHP He until it fully sealed at 200 °C.

The powder from the disintegrated pellets was retrieved for characterization and will be referred to as “sludge” in the subsequent sections. In the Batch 2 testing, pellets that remained intact showed more significant degradation than Batch 1 pellets (**Figure 2.5**). Apart from the benchmark UO<sub>2</sub> pellets, no discernible UN or UN composite pellets remained above 300 °C testing. As previously stated, the “sludge” was collected and dried for SEM and XRD characterization. The benchmark UO<sub>2</sub> pellets performed as

anticipated, showing little, if any, corrosion behavior, with results similar to those reported by Une *et al.* [28] and Taylor *et al.* [29].

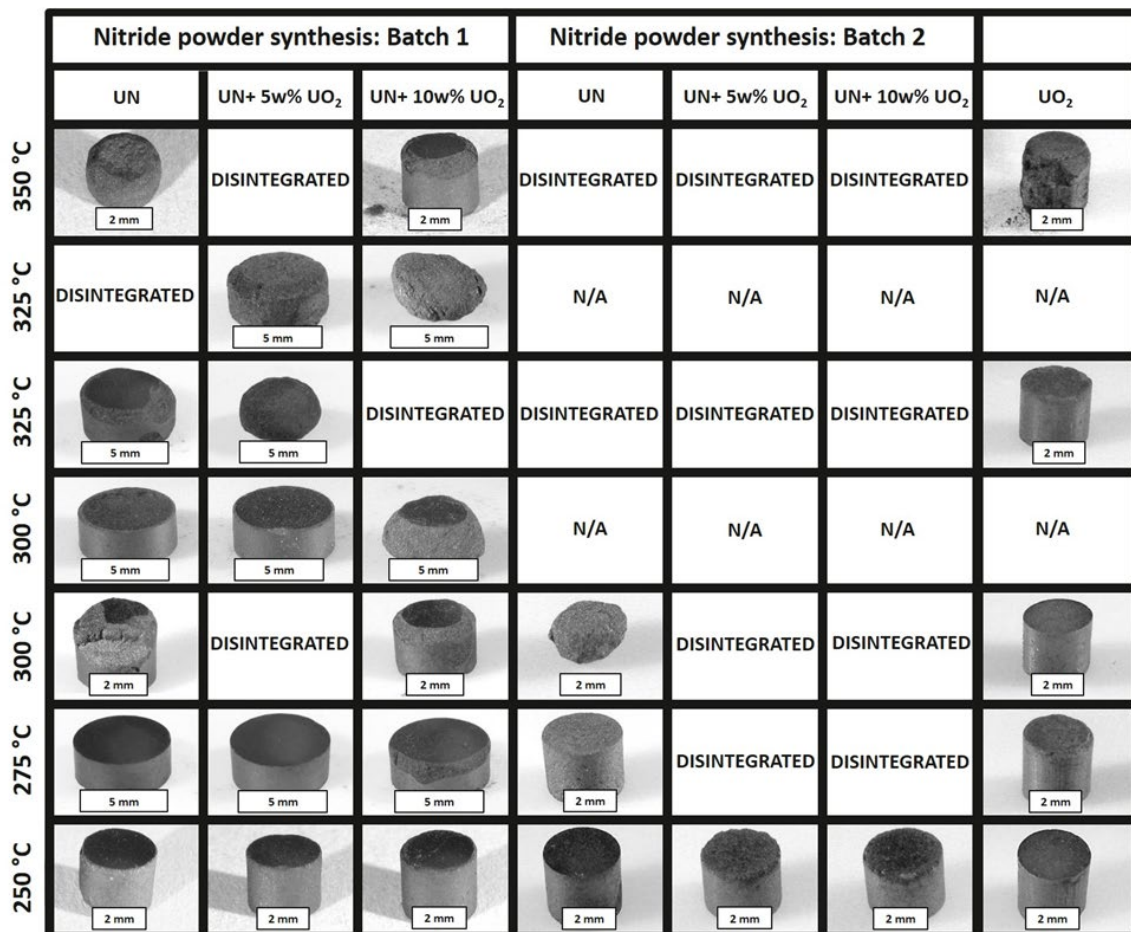


**Figure 2.5** Images showing the relative hydrothermal oxidation behavior of pellets fabricated from the two batches of UN powder tested at 250-350 °C. The experiments with pellets fabricated from the Batch 2 powder include UO<sub>2</sub> pellets as a benchmark. In all cases, the right cylindrical pellets were preferentially attacked at the edges and the extent of degradation increased with increasing temperature, with some pellets completely disintegrating.

#### 2.3.4 Post-autoclave XRD analysis – Pellets

X-ray diffraction of corroded pellet surfaces are shown in **Figure 2.6** with the un-corroded pellet surface patterns included for reference. The XRD patterns show the analysis for the UN, UN + 5 w% UO<sub>2</sub>, and UN + 10 w% UO<sub>2</sub> pellets from left to right. After autoclave testing, the primary phase in the pure UN samples is UN after excluding peaks attributed to the sample holder. However, the corroded composite UN-UO<sub>2</sub> pellets exhibit peaks corresponding to UN<sub>2</sub> (noted by the diamond markers), and what may be  $\alpha$ -U<sub>2</sub>N<sub>3</sub> (ICSD PDF 00-015-0426) as denoted by the chevron markers and droplines. Some overlap in the primary peaks for these two phases exists (29.0, 33.6, and 48.3° 2 $\theta$  values). The XRD patterns show a decrease in the full width half maximum (FWHM) of the first two UO<sub>2</sub> peaks shown in **Figure 2.6**. This observation, most evident in the 275 and 300 °C patterns of the 5 and 10 w% samples, suggests that the UO<sub>2</sub> crystallites increased in size during the hydrothermal oxidation process. An oxynitride layer resulting from dissolved oxygen and/or nitrogen into the UO<sub>2</sub> and UN<sub>2</sub> lattices is most likely contributing to the peak broadening due to distortion of the lattice [30].

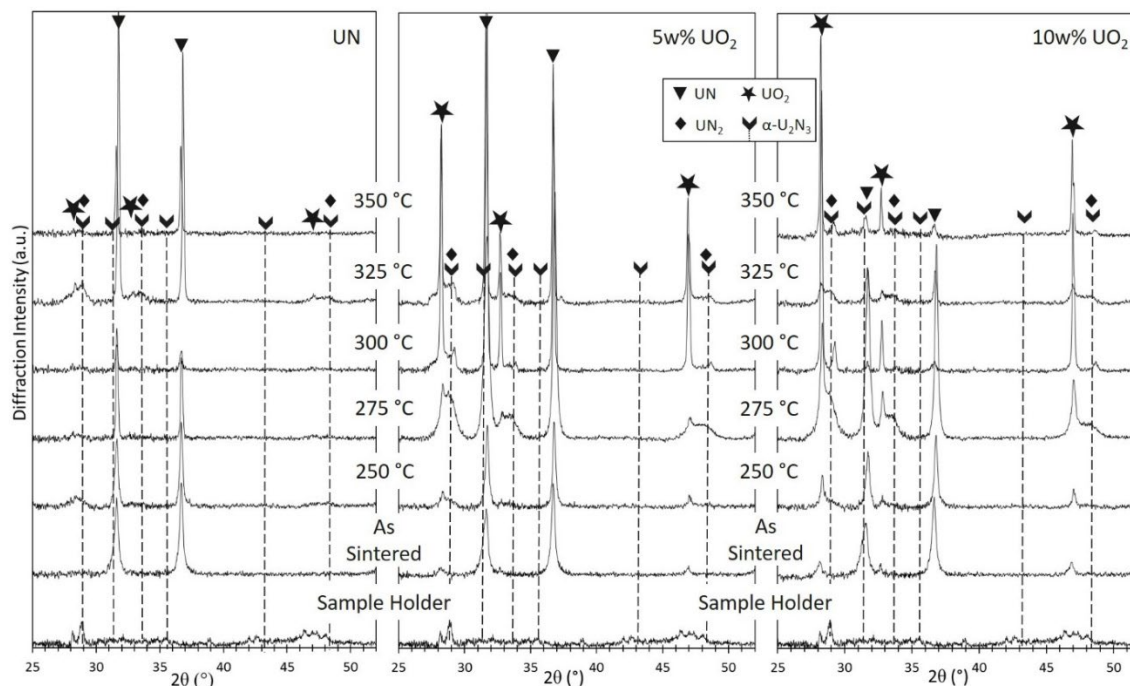


**Figure 2.6 Comparison of XRD patterns of the as-sintered and corroded UN and UN+UO<sub>2</sub> composite pellets. After autoclave testing the primary phase in the pure UN samples is UN, whereas the 5 and 10 w% samples indicate a UN<sub>2</sub> phase or oxynitride phase ( $2\theta$  values 29.0, 33.6, 48.3°) and possibly  $\alpha$ -U<sub>2</sub>N<sub>3</sub> ( $2\theta$  values 28.9, 33.6, and 48.4°) as denoted by the chevron markers and droplines, most evident in the 275-325 °C data.**

### 2.3.5 Post-autoclave XRD analysis – Sludge

As previously mentioned, the material collected from pellets that disintegrated during testing was dried and characterized via SEM and XRD. The XRD patterns in **Figure 2.7** show that the retrieved powder remains primarily UN. However, as autoclave temperatures are increased, peaks attributed to UO<sub>2</sub> and UN<sub>2</sub> phases become more prominent. There is also indication of a slight amount of  $\alpha$ -U<sub>2</sub>N<sub>3</sub> denoted by the chevron marker and seen in the 300 – 350 °C tests, most notably at  $2\theta$  values 28.9, 33.6, 48.4 and 57.2°. The UO<sub>2</sub> phase in the sludge also shows a clear increase in the FWHM (almost an order of magnitude larger) as temperature is increased. This increase in the FWHM can be attributed to peak overlap due to the presence of the other phases as noted above

and/or broadening due to lattice distortion from dissolved oxygen and nitrogen. This is easily seen at  $2\theta$  values 28.3, 32.7, and  $47.0^\circ$ . This increase in the FWHM is most evident in the “sludge” from the  $350^\circ\text{C}$  test (**Figure 2.7**).

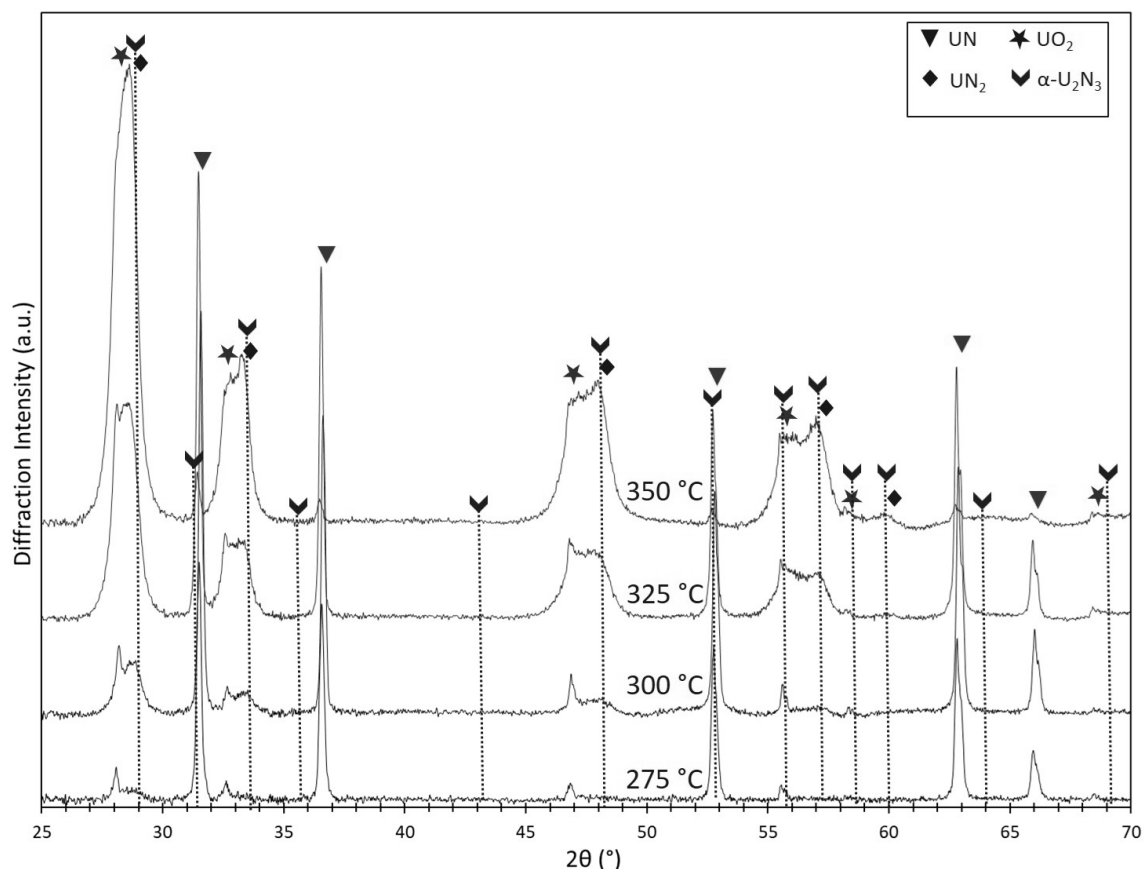


**Figure 2.7** Comparison of XRD patterns from the recovered “sludge” showing the primary phase remains UN. However, as autoclave temperatures increase, phases of UN<sub>2</sub>, possibly an oxynitride, UO<sub>2</sub>, and peaks attributed to  $\alpha$ -U<sub>2</sub>N<sub>3</sub> become more prominent.

### 2.3.6 Post-autoclave morphology – Pellets

Microstructural characterization was performed on the corroded pellets using backscattered electron (BSE) SEM imaging. Each of the pellets that remained intact after exposure showed similar macroscopic features; the edges of the right cylinder were preferentially degraded as seen in **Figure 2.8** and **2.9**. The typical corroded surface

microstructure for pure UN pellets is shown in the top row of **Figure 2.8** for pellets corroded at 250 °C, 275 °C, and 300 °C, respectively. As expected, the level of degradation increases with exposure temperature. **Figure 2.8** also illustrates how the degradation process firstly attacks grain boundaries, providing grain boundary expansion and spallation. The bottom images are from the same pellet but from the corroded edges, showing heavier attack.

The composite UN-UO<sub>2</sub> pellets show similar behavior to the UN, with grain boundary attack and spallation beginning at the corners of the right cylinder. In addition, the attack increases with autoclave temperature. The UN-UO<sub>2</sub> pellets also exhibit an additional noteworthy aspect; **Figure 2.9** shows the top surfaces of the UN + 5 w% UO<sub>2</sub> and UN + 10 w% UO<sub>2</sub> pellets corroded at 250 °C, where light and dark phases are observed. The dark phase was identified as an oxide with EDS, as shown in **Figure 2.10**. These micrographs combined with EDS chemical analysis suggest that the oxide may be nucleating on the grains and propagating across the surface of the grains. The chemical analysis (**Figure 2.10**) of the micrograph of the UN + 5 w% UO<sub>2</sub> pellet surface (**Figure 2.9**) highlights that the lighter phase is distinctly nitrogen-rich, while the darker regions are oxygen-rich.

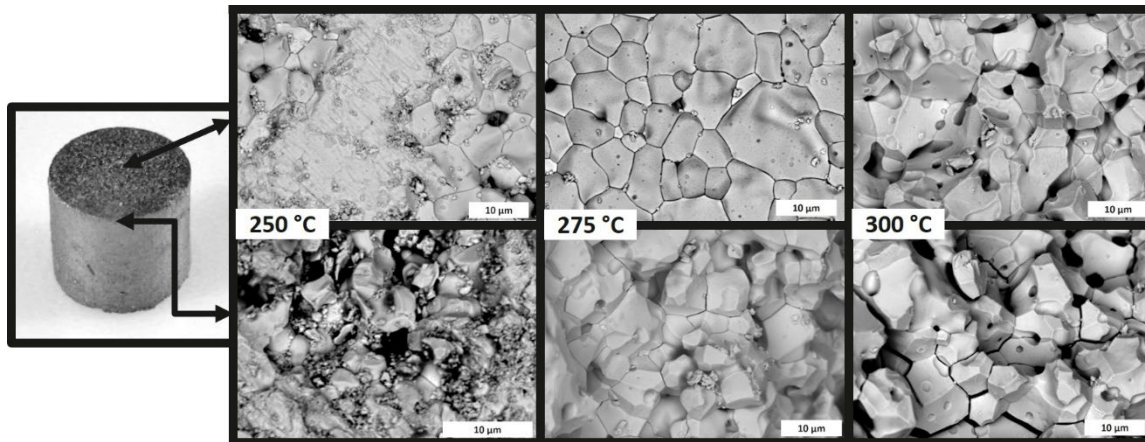


**Figure 2.8** Backscatter electron micrographs of the corroded UN pellets at 250 °C, 275 °C, and 300 °C. The top images were taken from the less corroded, central, region of the pellet surface and the bottom images were taken from the more heavily corroded outer edges of the pellets (seen in the photograph on the left). Preferential edge and grain boundary attack is evident.

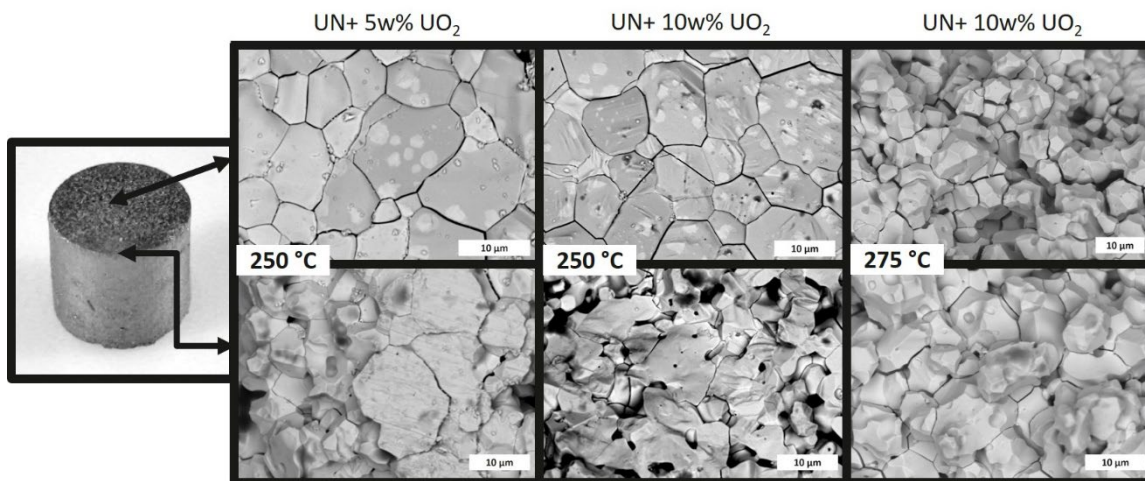


**Figure 2.9** Backscatter SEM micrographs of the UN + 5 w% UO<sub>2</sub> and UN + 10 w% UO<sub>2</sub> composite pellets corroded at 250 °C and the UN + 10 w% UO<sub>2</sub> pellet corroded at 275 °C. The top images were taken from the less corroded, central, region of the pellets and the bottom images were taken from the more heavily corroded outer edges of the pellets (seen in the photograph on the left). Preferential edge and grain boundary attack is evident. The pellets corroded at 250 °C also show clear light and dark phases present across the surfaces. The dark phase was identified as an oxide phase via EDS (Figure 2.10).

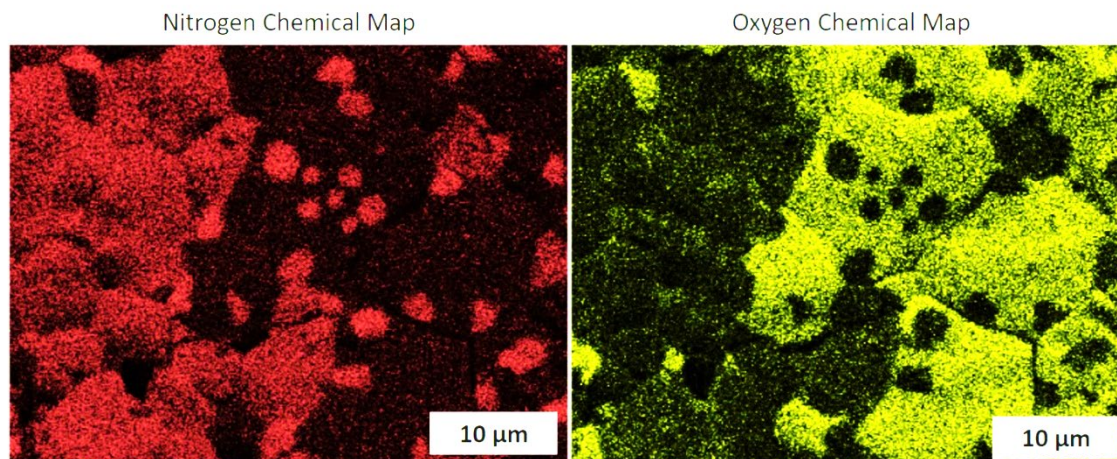


**Figure 2.10** Chemical analysis via EDS of the UN + 5 w% UO<sub>2</sub> pellet surface corroded at 250 °C (seen in Figure 2.9) showing distinct nitrogen and oxygen-rich regions.

### 2.3.7 Post-autoclave morphology – Sludge

Backscattered electron SEM micrographs showing the typical morphology of the spalled material from the autoclave tests at 275 – 350 °C are seen in **Figure 2.11**. The grains are faceted and show clear separation at the grain boundaries. The individual grains in the sludge from the 275 – 300 °C tests show less granular deterioration than those collected at 325 – 350 °C, which show heavier attack.

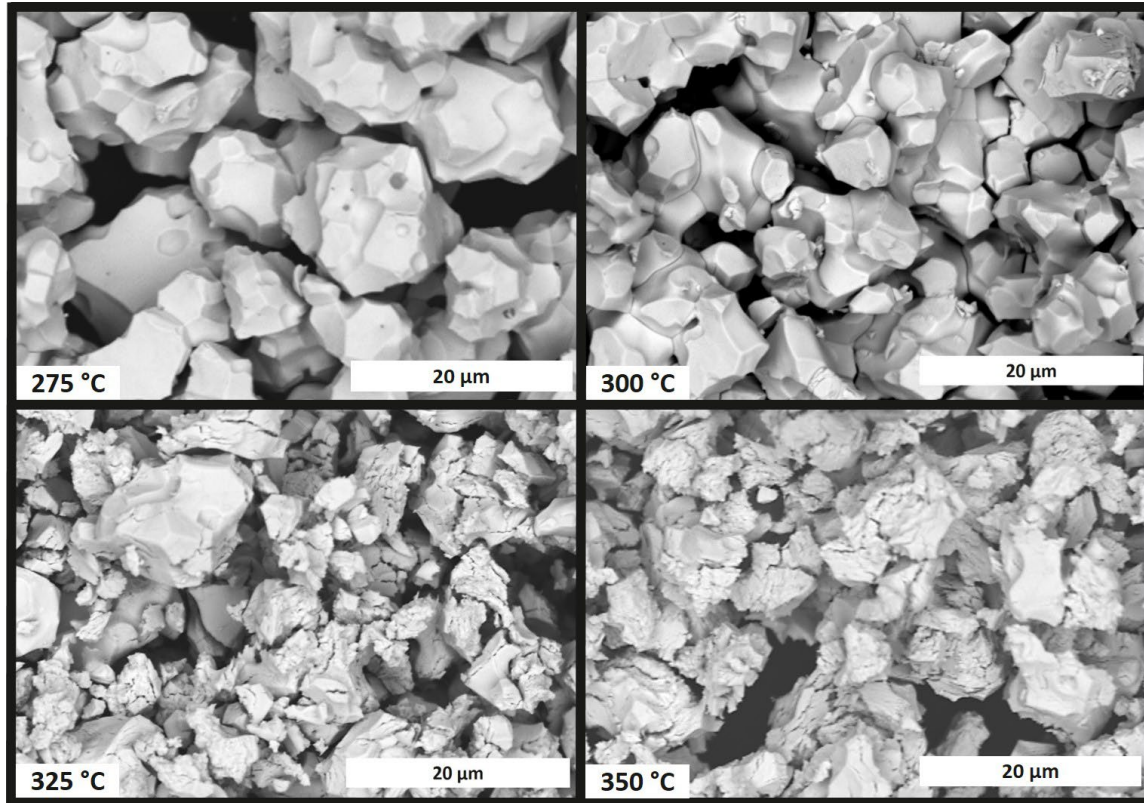


**Figure 2.11** Backscattered electron micrographs of the recovered “sludge” from hydrothermal oxidation experiments from 275-350 °C showing large, distinct grains at 275 °C. However, as the temperature is increased, the grain size of the recovered sludge is reduced, and significant grain degradation is observed at 350 °C.

## 2.4 Discussion

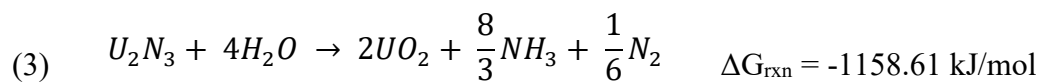
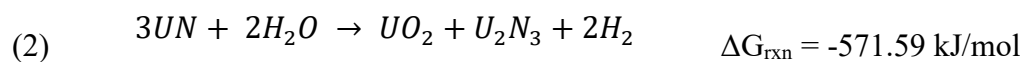
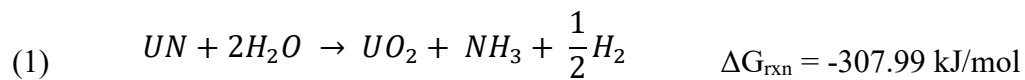
### 2.4.1 Post-autoclave – Pellets

The effect of diameter (2.85 vs. 5.65 mm) was not an intent of this study. It is interesting to note however, tests from the Batch 1 pellets were replicated at 325 °C with pellets fabricated using the larger 6.35 mm die and different results were obtained. The pure UN pellet was lost in one test and the UN + 10 w% UO<sub>2</sub> pellet in the other (**Figure 2.5**). This suggests the hydrothermal oxidation behavior of the tested pellets is stochastic in nature. Further studies are needed to verify that there is no size effect. As stated, the pressure within the autoclave does rise with temperature, reaching a maximum of approximately 16.5 MPa during the 350 °C tests. Although the effects of pressure were

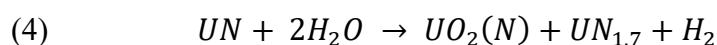
not studied explicitly, it is believed that this pressure change has little effect on the overall hydrothermal oxidation behavior. In the 325 and 350 °C tests for the Batch 1 pellets intact pellets were retrieved, whereas no pellets (with the exception of the benchmark UO<sub>2</sub>) were retrieved from the Batch 2 tests, and both tests experienced similar pressure changes (**Figure 2.5**). Although significant effort was made to reduce exposure of the starting UN powder to atmosphere, subsequent processing and handling of the reactive synthesized UN powder resulted in a pickup of oxygen. The aforementioned light element analysis, indicated 2500 ppm oxygen in the starting Batch 1 powder, which is within previously published specification limits for UN irradiation tests and development of UN fuel for the SNAP-50 program [27, 31]. It is believed that the actual oxygen concentration value is lower than reported, as the external lab which performed the light element chemical analysis indicated the tests were completed in lab air. As previously noted, the pellets fabricated from the Batch 2 powder did not perform as well as those in Batch 1 tests, especially the UN-UO<sub>2</sub> composites. Only the test at 250 °C for the Batch 2 pellets resulted in intact pellets for all three compositions. For Batch 2 pellets, tests above 250 °C resulted in degraded UN pellets and complete loss of the UN-UO<sub>2</sub> pellets, with the UN pellets also completely disintegrating above 300 °C. This is believed to be due to the increased starting oxygen impurity content in the Batch 2 powder.

As previously noted, the primary phase in the pure UN samples post-autoclave is UN (**Figure 2.6**). This result varies from work published by Bugl and Bauer which shows UN<sub>2</sub> as a corrosion product [19]. It is also contrary to results published by Sunder and Miller [17], and Rao *et al.* [14], who indicate that UN quickly converts to UO<sub>2</sub> (the final

phase) upon exposure to water, or  $U_3O_8$  for UN samples which had no starting  $UO_2$  phase in them. Earlier work shows that the addition of  $UO_2$  likely stabilizes a hyper-stoichiometric nitride phase [20]. The presence of this hyper-stoichiometric nitride phase is also in contrast to literature which states only an  $\alpha-U_2N_3$  phase or oxynitride phase would be present [13, 14]. However, work by Jolkkonen *et al.* [15] also indicated UN as the primary phase remaining after hydrolysis of UN in superheated steam along with  $UO_2$  containing dissolved nitrogen and possibly an oxynitride phase. XRD analysis of the corroded pellets suggests that, in addition to  $UN_2$ , some  $\alpha-U_2N_3$  may be present. However, some peak overlap occurs at  $2\theta$  values of  $28.9$  and  $33.6^\circ$  (**Figure 2.6**). A density functional study by Wang *et al.* [30] states that uranium oxynitrides possess similar XRD patterns as compared to  $UN_2$ , and it is likely that the presence of an oxynitride layer is contributing to the intensity of the peaks identified as  $UN_2$ . Studies by Dell *et al.* [13] and Sugihara and Imoto [18] on the hydrolysis of UN, following reactions (1) and (2), suggested that liberated nitrogen that does not form ammonia may dissolve into the  $UO_2$  lattice to form an oxynitride or  $\alpha-U_2N_3$ . As the hydrolysis proceeds,  $U_2N_3$  can form  $UO_2$  according to reaction (3) [13, 18], this was also reported by Jolkkonen *et al.* [15].



It has also been reported that oxygen solubility in pure UN can be as high as 7 at% and results in a slight lattice expansion per XRD [32-34]. This lattice expansion (caused by dissolved oxygen) could explain the slight shift in the UN peaks (near  $2\theta$  values of 31.6 and 36.7°) (**Figure 2.6**). Dell *et al.* [13] suggests that a surface film on UN, either a bcc-nitride or oxynitride, acts as a protective layer during the hydrolysis of UN. However, Dell also mentions that as the reaction propagates along grain boundaries, corresponding to an increase in the available surface area, the particles eventually breakdown along grain boundaries [13]. This mechanism would result in a volume expansion from the differences in the larger lattice parameters of  $UO_2$ ,  $U_2N_3$ , and any oxynitride phase, as compared to UN [30]. This explains the results seen in both the pure UN and UN- $UO_2$  corroded pellets, where spallation of material along grain boundaries is seen (**Figure 2.8 and 2.9**), a result also noted in the work by Jolkkonen *et al.* [15]. Sugihara and Imoto [18] also state that along with an oxynitride phase, a hyper-stoichiometric  $UN_{1.7}$  would be formed during hydrolysis of UN according to reaction (4).



As reported by Jolkkonen *et al.* [15] and according to the above listed reactions (1)-(4), the formation of ammonia and hydrogen would be expected, however the gaseous reaction products, as well as the pH of the waste liquid, was not studied explicitly in this work. The composite UN- $UO_2$  corroded pellets do reflect a hyper-stoichiometric ( $UN_2$ ) phase in the 275-350 °C tests, denoted by the black diamonds on the XRD patterns shown in **Figure 2.6**. Rao *et al.* [14] and Lopes *et al.* [16] noted that a  $U_2N_3$  layer is also

seen between UN and  $\text{UO}_2$  layers during hydrolysis. Work by Matzke [27] on the oxidation of UN suggests that a hyper-stoichiometric  $\text{U}_2\text{N}_{3-x}$  layer forms between the unreacted UN and  $\text{UO}_{2+x}$  surface layer and is dense and resistant to oxygen permeability. Rao *et al.* [14] also notes that samples containing a higher initial amount of  $\text{UO}_2$  result in a higher concentration of reacted  $\text{U}_2\text{N}_3$  and that oxygen has to diffuse through a layer of UN/ $\text{U}_2\text{N}_3$  reacting with UN at the interface. This suggests that strain caused by a change in volume from product formation, leading to breakup of the sample, would be higher in samples having an initial amount of  $\text{UO}_2$ . This result is seen in the corroded UN- $\text{UO}_2$  composite pellets in this work (**Figure 2.5**). Variances between tests replicated for Batch 1 at 300 and 325 °C are indicative of the stochastic nature of the corrosion process. Results from XRD, SEM, and the darkened appearance of the post-exposure pellets also confirm that oxidation is occurring (**Figure 2.5-2.10**). Similar to results by Matzke [27] on the oxidation of UN single crystals, the preferential attack at the grain boundaries from oxygen diffusion and the resulting stresses leading to cleavage would contribute to an increased surface exposure. This leads to propagation of the reactions and ultimately pellet instability. It is possible that the corroded UN samples show less degradation than the corroded UN- $\text{UO}_2$  composite samples because the reactions begin at the surface of the pellet and proceed to the core. In contrast, reactions in the UN- $\text{UO}_2$  samples occur throughout the bulk of the pellet, as described by Rao's oxidation study [14] and Lopes' UN degradation work [16]. It is also possible that the formation of a  $\text{UN}_2$  or oxynitride layer, explained previously based on the work by Dell *et al.* [13], is responsible for the less severe degradation of the pure UN samples as compared to the UN- $\text{UO}_2$  samples.

#### 2.4.2 Post-autoclave – Sludge

As discussed previously, literature indicates a hyper-stoichiometric nitride layer likely exists between the UN and UO<sub>2</sub>. It is likely that a thin layer of this nitride or oxynitride is present in the sludge. While the spalled material is still primarily UN, the other phases present (UO<sub>2</sub>, UN<sub>2</sub>, and possibly  $\alpha$ -U<sub>2</sub>N<sub>3</sub>) support the results in previously published literature of Dell *et al.* [13], Rao *et al.* [14], Sugihara and Imoto [18], Jolkkonen *et al.* [15], Lopes *et al.* [16], and Bugl and Bauer [19]. The resulting lattice strain from the dissolution of nitrogen, or oxygen, into the UO<sub>2</sub> or UN lattices, would contribute to the peak broadening seen in the XRD patterns of **Figure 2.7**. It can be seen from the relative peak intensities that the amount of secondary phases increases in the sludge with increasing autoclave temperature, more so than in the corroded pellets themselves. The increase in the amount of these secondary phases is explained by the fact that the sludge material comes primarily from the full disintegration of the UN-UO<sub>2</sub> composite pellets (**Figure 2.5**) and would consist primarily of spalled matter. According to Rao *et al.* [14], samples with a larger initial amount of UO<sub>2</sub> result in a higher concentration of reacted U<sub>2</sub>N<sub>3</sub>. Following reactions (3) and (4) discussed earlier, a higher concentration of the UO<sub>2</sub> and hyper-stoichiometric UN phases would be expected in the corroded material [18]. This increase in secondary phases, identified by XRD in the sludge (**Figure 2.7**) correlates to the increase in degradation seen in the BSE SEM images of the material from the autoclave tests at 325-350 °C (**Figure 2.11**). The differences between the hydrothermal oxidation test results of Batch 1 and Batch 2 pellets can also be attributed to the increased amount of impurity UO<sub>2</sub> or residual dissolved

oxygen in the starting UN powder used for fabrication. Higher oxygen impurity results in elevated loss of the Batch 2 pellets due to an increased formation of secondary phases.

As seen in **Figures 2.8-2.9** and **2.11**, the principal degradation mechanism is grain boundary attack, leading to subsequent spallation of the pellets into single grains. At temperatures of 275-300 °C, the pellet surfaces show grain boundary relief. As temperatures increase, separation at the grain boundaries is seen (**Figures 2.8-2.9**). As noted above, the hydrolysis reactions propagate along grain boundaries leading to strain from the differences in cell volume of the formation products [13-16, 27]. Differences in the resulting spalled grains from tests performed at a lower temperature versus those at higher temperatures suggest a sequence to the disintegration. As seen in **Figure 2.11**, at 275 °C the spalled material appears to be whole grains, indicating a clear separation at the grain boundaries, whereas in the 350 °C test, the sludge material is significantly more degraded and shows heavier attack. This sequencing to the degradation mechanism and resulting morphology can be explained by the repeated strain caused by changes in cell volume as the reaction products form, as discussed earlier [13, 15-18, 30].

## 2.5 Conclusions

This screening study was performed to test pellets of UN and UN-UO<sub>2</sub> composites under short duration, static hydrothermal oxidation conditions. The effects of the addition of a secondary phase on the microstructural degradation behavior and phase formation were assessed. Examination of the corroded microstructures shows a sequence to the breakdown of the monolithic pellets. At lower temperatures the corroded pellets exhibit clear grain boundary relief and separation. Spallation of single grains is evident as test temperatures increase from 250-350 °C. This spalled material also shows increased

degradation at higher temperatures. It is postulated that as the UN reacts with the water, the propagation of reactants forming secondary phases, starting at the grain boundaries and proceeding through the bulk, increases with temperature. Hyper-stoichiometric UN, uranium oxynitride,  $\alpha$ - $U_2N_3$ , and  $UO_2$  phases along the grain boundaries result in a volume expansion due to increased lattice parameters as compared to UN. In the UN- $UO_2$  composites, an oxide layer appears to nucleate on the grains and propagate across the surface of the grains, presumably  $U_2N_3$  forming  $UO_2$  during the hydrolysis. This propagation behavior was not observed in the pure UN pellets. It is proposed that as the formation of reaction products proceeds (reaction layer and phase segregation at the grain boundaries), the expansion of the intermediate layer ultimately leads to a failure of the pellet structure. It is theorized that an increased oxygen impurity content in the starting powders enhanced the microstructural degradation behavior in samples exposed to elevated temperature and high-pressure conditions for short periods. This introductory study on the degradation mechanism (grain boundary attack) in UN and UN- $UO_2$  composite samples exposed to hydrothermal oxidation conditions can inform on future corrosion studies in UN and other high uranium density fuels. The role of oxygen impurities in increased degradation should be specifically investigated on advanced technology fuels. Further work to more closely match UN test conditions to typical water reactor chemistries must be completed to demonstrate improvements in accident tolerance.

### Acknowledgements

This project was partially supported by the Department of Energy Nuclear Energy University Program (DOE-NEUP) grant #00120690. Additional support was provided by an Integrated University Program Graduate Fellowship.

### References

- [1] S. Bragg-Sitton, Development of advanced accident-tolerant fuels for commercial LWRs, *Nuclear News* 57(3) (2014) 83.
- [2] S.J. Zinkle, K.A. Terrani, J.C. Gehin, L.J. Ott, L.L. Snead, Accident tolerant fuels for LWRs: A perspective, *Journal of Nuclear Materials* 448(1) (2014) 374-379.
- [3] F. Goldner, Development strategy for advanced LWR fuels with enhanced accident tolerance, *Enhanced Accident Tolerant LWR Fuels National Metrics Workshop*, Germantown, MD, 2012.
- [4] D. Wachs, N. Woolstenhulme, Advanced fuel cycle technology: Special session in honor of Dr. Michael Lineberry, *Transactions of the American Nuclear Society* 110(INL/JOU-14-33095) (2014).
- [5] N.R. Brown, A. Aronson, M. Todosow, R. Brito, K.J. McClellan, Neutronic performance of uranium nitride composite fuels in a PWR, *Nuclear Engineering and Design* 275 (2014) 393-407.
- [6] S.L. Hayes, J.K. Thomas, K.L. Peddicord, Material property correlations for uranium mononitride: 1. physical properties, *Journal of Nuclear Materials* 171 (2-3) (1990) 262-270.
- [7] L.H. Ortega, B.J. Blamer, J.A. Evans, S.M. McDeavitt, Development of an accident-tolerant fuel composite from uranium mononitride (UN) and uranium sesquisilicide ( $U_3Si_2$ ) with increased uranium loading, *Journal of Nuclear Materials* 471 (2016) 116-121.
- [8] R.B. Matthews, *Irradiation performance of nitride fuels*, Los Alamos National Lab., NM (United States), 1993.

- [9] H. Zimmermann, Fission gas behavior in oxide fuel elements of fast breeder reactors, *Nuclear Technology* 28(1) (1976) 127-133.
- [10] J. Zakova, J. Wallenius, Fuel residence time in BWRs with nitride fuels, *Annals of Nuclear Energy* 47 (2012) 182-191.
- [11] G.J. Youinou, R.S. Sen, Impact of accident-tolerant fuels and claddings on the overall fuel cycle: A preliminary systems analysis, *Nuclear Technology* 188 (2) (2014) 123-138.
- [12] J. Antill, B. Myatt, Kinetics of the oxidation of UN and U (CO) in carbon dioxide, steam and water at elevated temperatures, *Corrosion Science* 6(1) (1966) 17-23.
- [13] R.M. Dell, V.J. Wheeler, N.J. Bridger, Hydrolysis of uranium mononitride, *Transactions of the Faraday Society* 63 (1967) 1286-1294.
- [14] G.R. Rao, S. Mukerjee, V. Vaidya, V. Venugopal, D. Sood, Oxidation and hydrolysis kinetic studies on UN, *Journal of Nuclear Materials* 185(2) (1991) 231-241.
- [15] M. Jolkkonen, P. Malkki, K. Johnson, J. Wallenius, Uranium nitride fuels in superheated steam, *Journal of Nuclear Science and Technology* 54(5) (2017) 513-519.
- [16] D.A. Lopes, S. Uygur, K. Johnson, Degradation of UN and UN-U<sub>3</sub>Si<sub>2</sub> pellets in steam environment, *Journal of Nuclear Science and Technology* 54(4) (2017) 405-413.
- [17] S. Sunder, N. Miller, XPS and XRD studies of corrosion of uranium nitride by water, *Journal of Alloys and Compounds* 271 (1998) 568-572.
- [18] S. Sugihara, S. Imoto, Hydrolysis of uranium nitrides, *Journal of Nuclear Science and Technology* 6(5) (1969) 237-242.
- [19] J. Bugl, A.A. Bauer, Corrosion and oxidation characteristics of uranium mononitride, Battelle Memorial Institute, Columbus, OH, 1964.

- [20] B.J. Jaques, J. Watkins, J.R. Croteau, G.A. Alanko, B. Tyburska-Püschel, M. Meyer, P. Xu, E.J. Lahoda, D.P. Butt, Synthesis and sintering of UN-UO<sub>2</sub> fuel composites, *Journal of Nuclear Materials* 466 (2015) 745-754.
- [21] T. Muromura, H. Tagawa, Lattice parameter of uranium mononitride, *Journal of Nuclear Materials* 79(1) (1979) 264-266.
- [22] R. Matthews, K. Chidester, C. Hoth, R. Mason, R. Petty, Fabrication and testing of uranium nitride fuel for space power reactors, *Journal of Nuclear Materials* 151 (3) (1988) 345.
- [23] ASTM, Standard Test Methods for Density of Compacted or Sintered Powder Metallurgy (PM) Products Using Archimedes' Principle, B962, ASTM International, West Conshohocken, PA, 2017.
- [24] A.T. Nelson, A. Migdisov, E.S. Wood, C.J. Grote, U<sub>3</sub>Si<sub>2</sub> behavior in H<sub>2</sub>O environments: Part II, pressurized water with controlled redox chemistry, *Journal of Nuclear Materials* 500 (2018) 81-91.
- [25] P.E. Blackburn, J. Weissbart, E.A. Gulbransen, Oxidation of Uranium Dioxide, *The Journal of Physical Chemistry* 62(8) (1958) 902-908.
- [26] L. Desgranges, H. Palancher, M. Gamaléri, J.-S. Micha, V. Optasanu, L. Raceanu, T. Montesin, N. Creton, Influence of the U<sub>3</sub>O<sub>7</sub> domain structure on cracking during the oxidation of UO<sub>2</sub>, *Journal of Nuclear Materials* 402(2-3) (2010) 167-172.
- [27] H. Matzke, Science of advanced LMFBR fuels, North-Holland Physics Publishing, Amsterdam, The Netherlands, 1986.
- [28] K. Une, S. Kashibe, K. Nogita, Corrosion behavior of unirradiated oxide fuel pellets in high temperature water, *Journal of Nuclear Materials* 227(1) (1995) 32-39.
- [29] P. Taylor, D.D. Wood, D.G. Owen, Microstructures of corrosion films on UO<sub>2</sub> fuel oxidized in air-steam mixtures at 225 °C, *Journal of Nuclear Materials* 223(3) (1995) 316-320.

- [30] X. Wang, Z. Long, H. Huang, R. Bin, Y. Hu, L. Luo, K.-Z. Liu, P.-C. Zhang, Insight on the oxidation resistance of  $UO_xN_y$  layers: A density functional study, *Computational Materials Science* 123 (2016) 224-231.
- [31] M. DeCrescente, M. Freed, S. Caplow, Uranium nitride fuel development, SNAP-50, Pratt and Whitney Aircraft, Middletown, Conn.(USA). Connecticut Advanced Nuclear Engineering Lab., 1965.
- [32] Y. Arai, M. Morihira, T. Ohmichi, The effect of oxygen impurity on the characteristics of uranium and uranium-plutonium mixed nitride fuels, *Journal of Nuclear Materials* 202(1-2) (1993) 70-78.
- [33] G. Jain, C. Ganguly, Experimental evaluation of oxygen solubility in UN, PuN and (U, Pu) N, *Journal of Nuclear Materials* 202(3) (1993) 245-251.
- [34] N.A. Javed, Oxygen solubility in uranium mononitride phase, *Journal of the Less Common Metals* 29(2) (1972) 155-159.

CHAPTER THREE: IMPROVED HYDROTHERMAL CORROSION RESISTANCE  
OF UN FUEL FORMS VIA ADDITION OF METALLIC CONSTITUENTS

This chapter was published in the Proceedings for TopFuel 2019

Reference: J.K. Watkins, E. Sikorski, L. Li, B.J. Jaques. Improved hydrothermal corrosion resistance of UN fuel forms via addition of metallic constituents. Proceedings of TopFuel 2019. (2019).

## Abstract

Uranium mononitride (UN) continues to be an attractive alternative fuel form for use in light water and advanced technology nuclear reactors due to its high uranium density, high melting point, high thermal conductivity, and performance under irradiation, as compared to UO<sub>2</sub>. UN's susceptibility to oxidation and pulverization after exposure to water (or steam), similar to conditions experienced during a cladding failure or accident scenario, remains one reason UN has been inhibited from consideration for use as a LWR fuel type. A screening study will be presented that investigates various metallic additions to protect UN from corrosion degradation due to interactions with water or steam. The most desirable candidates will incorporate a material that can provide a barrier to the oxidation of UN and increase water corrosion resistance. The candidate materials were preliminarily screened based on thermophysical properties, neutronic properties that may enhance the fuel performance (e.g. thermal conductivity and irradiation resistance), and thermodynamic considerations. Samples consisting of UN and nominal additions of the candidate materials were synthesized, consolidated, and examined via X-ray diffraction, scanning electron microscopy, and energy dispersive spectroscopy. Ab initio Molecular Dynamics was used to investigate bonding and electronic profiles of candidate metallic additions during the sintering process.

## 3.1 Introduction

### 3.1.1 Motivation for research

The development of advanced technology nuclear fuels (ATFs) — also referred to as accident tolerant fuels — which improve nuclear fuel safety and reliability, and provide economic benefits through increased power uprates, fuel cycle time, and higher

burn-up, remain a focus for the U.S. Department of Energy's (DOE) Office of Nuclear Energy (NE). ATFs are those that maintain or enhance fuel performance under normal and transient operating conditions, during design-basis and beyond-design-basis conditions, and provide additional safety margins in accident scenarios [1].

Among the candidate fuel concepts considered for use in advanced nuclear reactor types and the existing light water reactor (LWR) fleet are uranium mononitride (UN) and UN composite fuels [2]. As compared to the benchmark, uranium dioxide ( $\text{UO}_2$ ) fuel, ATFs have higher uranium densities, improving operational economy, and higher thermal conductivities, which allows for lower peak fuel and cladding temperatures under normal activity and in scenarios such as a loss of coolant accident (LOCA) [3]. A concern with the use of UN in LWR applications is its degradation behavior in water or steam [4, 5]. Studies on UN fuels that include a secondary phase with the intent to protect the UN matrix from reacting when exposed to water or steam, such as  $\text{UO}_2$  and uranium silicides, have been reported with varying results in regards to microstructure, phase evolution, and corrosion resistance [3, 5-9].

The work proposes a UN-based composite fuel with the addition of a metallic constituent that hinders oxidation or corrosion of the UN by preferential formation of an oxide layer in water or steam. The concept of including a secondary constituent in the fuel matrix for preferential oxidation is similar in nature to work proposed in literature for encapsulated  $\text{UO}_2$  and  $\text{U}_3\text{Si}_2$  in which the microstructure created is stable under steam and water exposure [10, 11].

### 3.1.2 Background

In order to create a desirable microstructure, i.e. a corrosion resistant layer surrounding UN grains, a fabrication method proposed by Lessing, utilizing liquid phase sintering (LPS) is investigated [12]. The LPS technique requires a molten phase that will wet and coat the other phase (powder) within a monolith. LPS allows for improved transport rates of dissolved grain material, which increases grain coarsening and densification at lower temperatures than what is required for producing dense solids sintered in the absence of a secondary phase [13]. Lower sintering temperatures provide an additional economic benefit for fabrication of UN-based fuel, which has traditionally required high sintering temperatures ( $\geq 2173$  K) to achieve high-density pellets [7].

The metallic elements considered for the secondary phase were initially screened based on properties suitable for the LPS process, those important for maintaining UN's desirable characteristics as an ATF-type, as well as for neutronic considerations. The properties considered were melting temperature, thermal conductivity, and thermal neutron capture cross-section. An examination of thermodynamic predictions for the nitride and oxide formation of the metallic constituents was considered in parallel with the sintering of the composite pellets. **Table 3.1** summarizes the candidate elements and associated properties.

Thermodynamic considerations for the UN-metal composite systems were included in the screening study to determine suitability from a fabrication and sintering standpoint. Determining which materials could provide protection to the UN matrix in oxidizing or corrosive conditions requires an understanding of thermodynamically favorable phases. Ellingham-type diagrams were created to identify elements that would

preferentially oxidize relative to UN but would not favor nitridation over dissociation of UN.

The effect of the metallic candidates on the overall charge of the composite structure was investigated using *Ab initio* Molecular Dynamics (AIMD). Electronic structure calculations have been previously conducted for UN to investigate the charge effects of additional atoms on the pure system [14, 15]. While such calculations are usually performed using traditional Density Functional Theory (DFT) at 0 °K, the sintering method inherently involves temperature effects, which can be better examined using AIMD.

### 3.2 Materials and Methods

#### 3.2.1 UN powder synthesis

UN powder was synthesized via carbothermic reduction of  $\text{UO}_2 + \text{C}$  followed by nitriding in a  $\text{N}_2 + 6\% \text{H}_2$  gas stream in a high temperature tube furnace. The procedure for the carbothermic reduction was modified from published work of Mathews *et al.* [16] and Muromura *et al.* [17] The starting materials were depleted  $\text{UO}_2$  powder (International Bio Analytical Industries, Inc., Boca Raton, FL, USA) and spherical glassy carbon powder (Alfa Aesar, Ward Hill, MA, USA). Three 12g batches of d- $\text{UO}_2$  and C powder were mixed using a C/ $\text{UO}_2$  molar ratio of 2.5 to maintain a balance of low residual carbon and oxygen content in the resulting UN powder [16, 17]. The mixed  $\text{UO}_2$  and C powders were loaded with yttria-stabilized zirconia milling media into a stainless-steel milling vessel inside an inert atmosphere glovebox ( $<0.1$  ppm  $\text{O}_2$  and  $\text{H}_2\text{O}$ ). The powders were milled for 1 hour at 200 RPM in a high-energy planetary ball mill, with the direction of rotation switching every 15 minutes. The milled powders were loaded into a

tungsten-lined alumina crucible and loaded into the high temperature tube furnace. Three vacuum/purge cycles ( $<10E-3$  torr) were completed prior to starting the furnace profile. Under vacuum, the furnace was ramped to 1773 K. After 5 hours, the atmosphere was switched from vacuum to H<sub>2</sub>/nitrogen and held prior to ramping down to room temperature in argon to prevent sesquinitride formation. At the completion of the furnace profile, the synthesized UN powder was sealed and immediately transferred to the inert atmosphere glovebox to avoid oxidation of the powder in lab air.

**Table 3.1. Properties of the candidate elements screened for use in creation of a UN-metallic composite fuel pellet.**

Element	T <sub>m</sub> [K] <sup>[18]</sup>	Thermal neutron capture cross-section [b] <sup>[18]</sup>	Thermal conductivity at 773 K [W/m·K]
Aluminum	933	0.23	237 <sup>[19]</sup>
Chromium	2180	0.8	75.9 <sup>[20]</sup>
Gadolinium	1586	2-2.4	11 <sup>[21]</sup>
Lanthanum	1191	9	16.2 <sup>[19]</sup>
Manganese	1519	13.3	7.82 (at 573 K) <sup>[19]</sup>
Molybdenum	2896	0.6E-6 - 14	118 <sup>[22]</sup>
Niobium	2750	0.9	58 <sup>[23]</sup>
Titanium	1941	7.9	22.3 <sup>[19]</sup>
Yttrium	1795	0.001	14.1 <sup>[19]</sup>
Zirconium	2128	0.2	19.7 <sup>[24]</sup>

### 3.2.2 Thermodynamic calculations

Ellingham-type diagrams were created to compare the thermodynamic stabilities of the nitrides and oxides of the potential metallic candidates in relation to UN. The calculations to determine the change in the Gibbs free energy of a nitridation or oxidation reaction, normalized to one mole of nitrogen or oxygen, as a function of temperature, were obtained using FactSage™ 6.4 [25]. The plots (**Figure 3.1**, **Figure 3.2**) delineate each reaction (either nitride or oxide) for the candidate elements listed in **Table 3.1**.

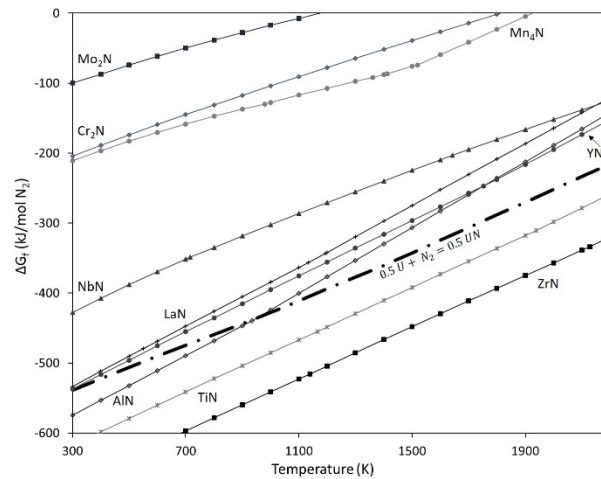


**Figure 3.1** Ellingham-type diagram constructed using data from FactSage™ 6.4 for select metal-nitride reactions of elements listed in Table B1. No reliable data was available for gadolinium nitride or the  $U_2N_3$  reaction.

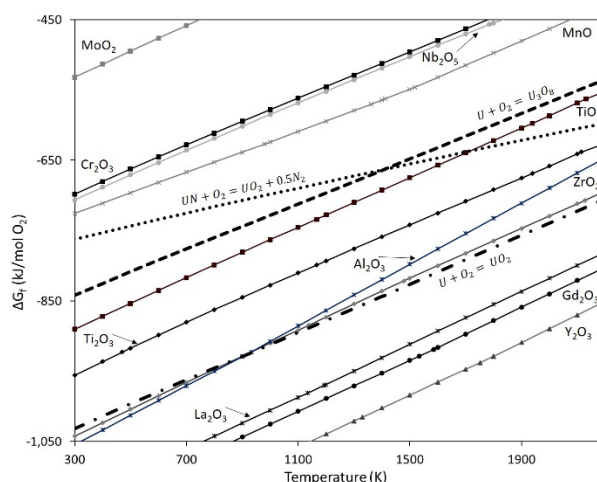


**Figure 3.2 Ellingham-type diagram constructed using data from FactSage™ 6.4 for select metal-oxide reactions of elements listed in Table 3.1.**

### 3.2.3 Powder mixing and characterization

The as-synthesized UN powder and the chosen metallic constituents examined in this work, yttrium (-40 mesh, 99.6%, Alfa Aesar, Tewksbury, MA, USA) and zirconium (-325 mesh, 99.5%, Sigma-Aldrich, St. Louis, MO, USA) were mixed together using a proportional amount of yttrium or zirconium for UN + 10 w% metal composite powders. The powders were loaded and hermetically sealed into polypropylene containers with yttria-stabilized zirconia media. The powders were mixed using a tabletop mixing mill (MTI 4-tank mixer) for 5 hours. The powders, both pre- and post-mixing, were characterized via X-ray diffraction (XRD) (Rigaku Miniflex 600, Japan) for phase identification by encapsulating a small amount of the powder into a silicon-based vacuum grease inside an inert atmosphere glovebox to avoid reaction in air during analysis. A small amount of a standard reference material (NIST SRM 640d Silicon powder, Gaithersburg, MD, USA) was used as line position verification. Characterization of the powder morphology was completed using secondary electron microscopy (SEM) coupled

with energy dispersive spectroscopy (EDS) for qualitative phase identification (Hitachi S-3400-II, Japan).

### 3.2.4 Pellet fabrication, sintering, and characterization

Pellets from the UN + 10 w% metal powders were cold-pressed at approximately 170 MPa into green pellets of right cylindrical geometry, using a 0.25” diameter die inside an inert atmosphere glovebox. A small amount of zinc stearate was used as a lubricant on the die wall punch faces.

All pellets were sintered using a refractory metal furnace. The UN + 10 w% Zr pellet was sintered at 1773 K for 5 hours in an argon atmosphere. The UN + 10 w% Y pellet underwent multiple sintering attempts (in argon) at different temperatures (1483 K – 1808 K) in order to observe the evolution of the liquid phase based on thermodynamic predictions in the phase diagram generated in FactSage™ 6.4 [25] (**Figure 3.3**). Sintering profiles for the UN-Y composite at hold temperatures of 1483, 1533, 1633, 1733, and 1808 K for 12 minutes were ran and the pellet removed from the furnace in between. After grinding the pellet with SiC paper, the microstructure was examined via optical microscopy to ascertain the presence of a potential liquid phase. After the 1808 K run, optical microscopy suggested a liquid phase had formed so the sintering profile was repeated at 1808 K for a 1-hour dwell.

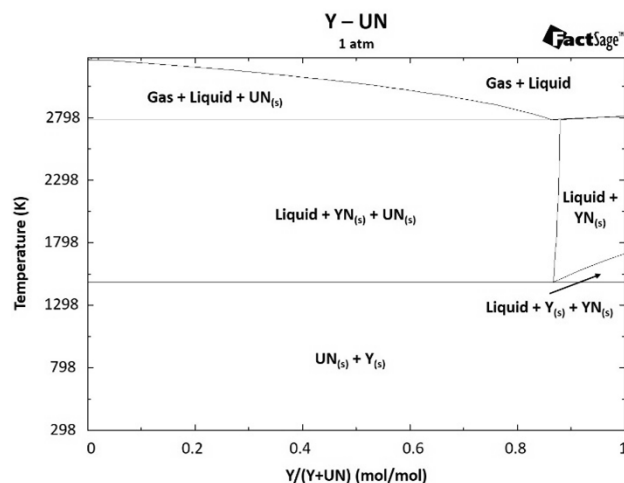


**Figure 3.3 Yttrium-uranium mononitride phase diagram (generated using FactSage™ 6.4).**

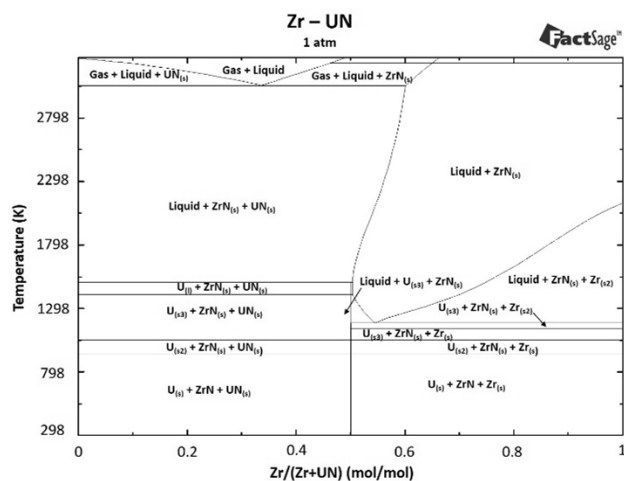


**Figure 3.4 Zirconium-uranium mononitride phase diagram (generated using FactSage™ 6.4).**

The microstructure for the pellets (+10 w%Zr and +10 w%Y) was characterized with SEM. Semi-quantitative data for the phases present in the sintered pellets was obtained through EDS and XRD ( $\text{CuK}\alpha$  radiation source and linear detector). A small amount of the Si standard reference material was used as line position verification in order to correct for sample displacement [26].

### 3.2.5 Electronic calculations

AIMD implemented in the Vienna *ab initio* Simulation Package (VASP) [27] was used to perform structural optimization with respect to temperature. Exchange-correlation energy was treated following the Perdew Burke Ernserhof formalism [28]. An energy cutoff of 320 eV and Brillouin zone sampling at the gamma point was utilized after convergence testing. Fermi smearing was accounted for using 0.2 eV. The highly correlated nature of the U electrons were accounted for using the Hubbard-U term [29] with a Coulomb potential (U) of 2.40 eV and exchange energy (J) of 0.50 eV, as implemented by Bo *et al.* [30]. Type I antiferromagnetic ordering was applied to the U atoms [31, 32].

UN supercells were created with a total of 64 atoms, of which one atom was replaced with either Zr or Y. Each composite structure was heated to its respective sintering temperature (2173 K for Zr and 1808 K for Y) over a span of 5 ps, using 2 fs timesteps. Local density of states (LDOS) and electron localization functions (ELF) [33] were performed the final structures using traditional DFT in VASP with an increased cutoff energy of 500 eV.

## **3.3. Results and Discussion**

### 3.3.1 Metallic element selection

The metallic elements chosen for consideration in this initial screening study for improvement in the corrosion resistance of UN were yttrium and zirconium. One of the properties that makes UN attractive as an accident tolerant fuel is its high melting temperature (2923 K) [34]. The goal was to incorporate a metallic constituent through LPS, with the secondary component having a lower melting temperature than UN.

However, the metallic addition should have a sufficiently high melting temperature to maintain pellet integrity when exposed to high fuel centerline temperatures under normal operating conditions. Another property that makes UN an attractive ATF candidate is its high thermal conductivity, as compared to  $\text{UO}_2$ . The metallic addition should have comparable, or higher, thermal conductivity than that of UN (20.5 W/m·K at 773 K) [34] to avoid negatively affecting the overall thermal performance of the pellet. Another screening parameter considered for potential additions was thermal neutron absorption cross-section. A low thermal neutron absorption cross-section is desirable so overall neutronic performance is not affected.

Yttrium and zirconium met the above listed criteria and were selected for further examination in this screening study. UN's high uranium density (13.5 g/cm<sup>3</sup>) [34] has positive implications for its use as an advanced fuel form. Thus, any non-uranium containing secondary addition should remain well below 30% of the total volume so that the uranium density remains higher than that of the benchmark,  $\text{UO}_2$ . Based on previous work for sintering UN with a secondary phase for improvement in corrosion resistance [5], and to incorporate sufficient amount of the secondary phase to accomplish LPS, the composite pellets consisted of UN + 10 w% of the chosen metallic element. For yttrium this corresponded to 26.3 vol%, and for zirconium to 19.6 vol%.

From the Ellingham-type diagrams, the formation of ZrN was thermodynamically predicted. The calculated phase diagram (**Figure 3.4**) also shows a uranium phase will be present at all temperatures, but at the sintering temperature used the uranium will be in liquid form. The thermodynamic predictions with the use of yttrium indicate UN should be more stable than yttrium nitride but the phase diagram indicated a liquid phase would

form above 1478 K, well below the melting temperature of yttrium (1795 K). This prompted the step-wise sintering profile used for the UN+10 w%Y pellet.

### 3.3.2 Powder and pellet characterization

#### 3.3.2.1 Powder morphology and phase identification

The as-synthesized powders were characterized for morphology and phase identification via SEM coupled with EDS, and XRD. Backscattered electron micrographs show the as synthesized UN powder, the as-received Zr and as-received Y, as well as the UN+10 w% metal powders after mixing for 5 hours (**Figure 3.5**, **Figure 3.6**). The as-synthesized UN contained nodular particle sizes of 1-5  $\mu\text{m}$  and agglomerates of 10-20  $\mu\text{m}$  (as determined using image analysis software) (**Figure 3.5A**). The as-received Zr powder was irregular, with particle sizes of 5-25  $\mu\text{m}$  and agglomerates of 50-100  $\mu\text{m}$  (**Figure 3.5B**), while the as-received yttrium powder consisted of large (>500  $\mu\text{m}$ ) curled flakes (**Figure 3.55C**).

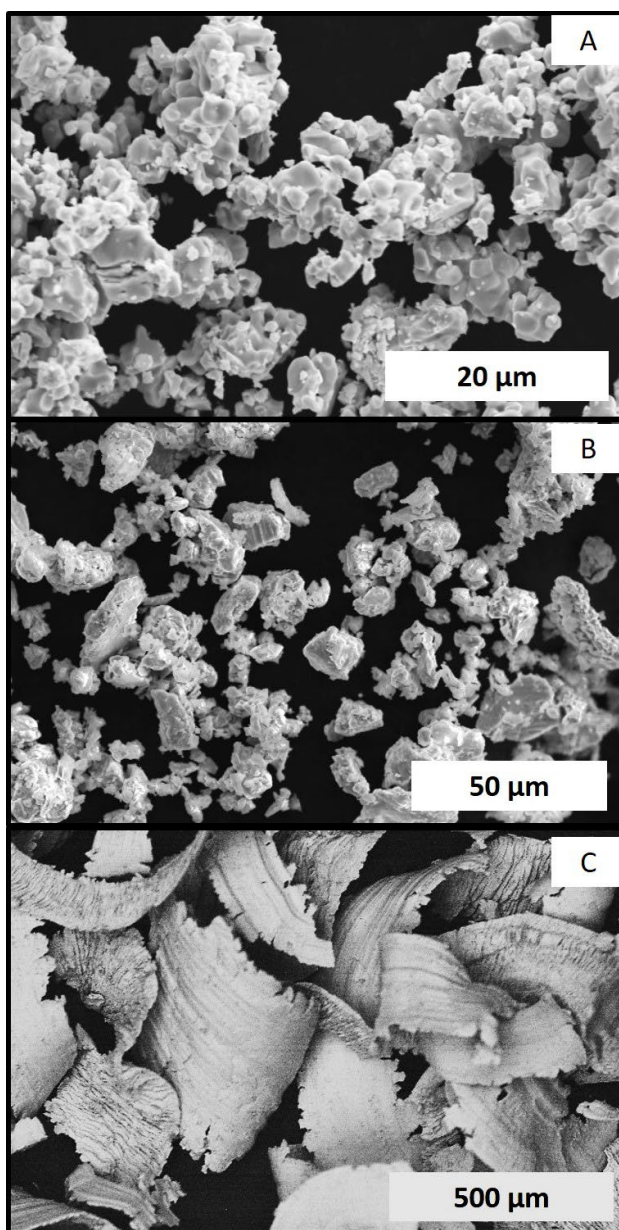


**Figure 3.5** Backscattered electron micrographs of A) As-synthesized UN powder, B) As-received Zr powder, C) As-received Y powder.

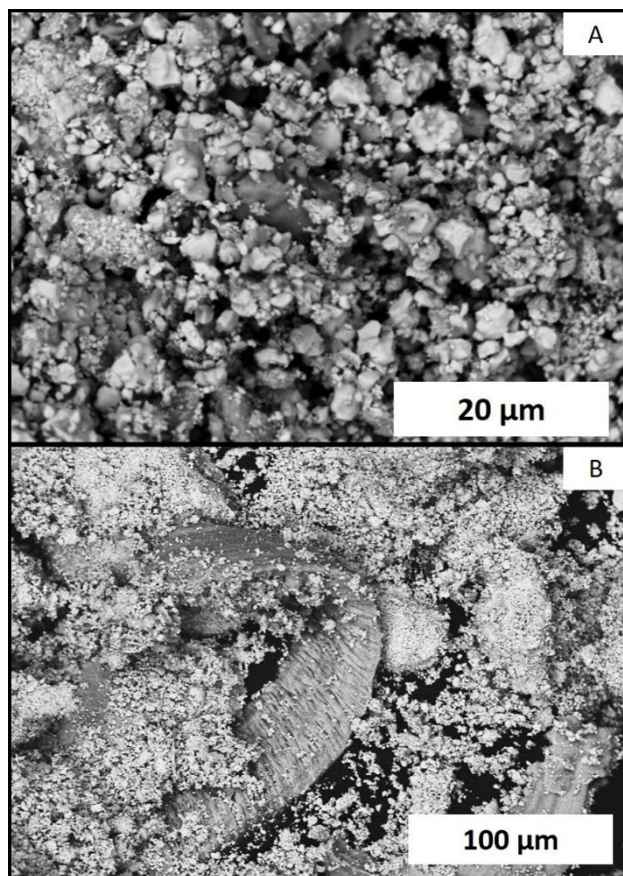


**Figure 3.6** Backscattered electron micrographs of A) UN+ 10 w%Zr mixed powder, and B) UN+10 w%Y mixed powder.

The low energy mixing process did not significantly reduce the size of the metallic particles in the mixed powders. However, the UN powder in the mixtures (**Figure 3.6A-B**) did appear more granular and exhibited a range of particle sizes to include sub-micron particles and large ( $\approx 100 \mu\text{m}$ ) agglomerates.

The XRD patterns relevant to the UN+10 w% metal powders are shown in **Figure 3.7**; the zirconium patterns are shown in the top image (A), the yttrium patterns in the bottom image (B). The as-synthesized UN powder is shown for comparison in both images and indicates the powder is phase pure UN when compared to the Inorganic Crystal Structure Database powder diffraction file (ICSD pdf) #00-032-1397. The as-received zirconium powder is shown as referenced to ICSD pdf #03-065-3366. For

clarity, it is noted that the NIST Si standard reference material was not included in the as-received Zr powder analysis. The as-received Zr powder exhibited peaks at approximately  $32.6$  and  $66.8^\circ 2\theta$  that could not be attributed to an oxide phase or other potential impurity. However, those unidentified peaks were not present in the UN+10 w%Zr mixed powder pattern, in which only peaks attributed to the NIST Si standard (denoted by the arrow marker), UN (inverted triangle marker), and Zr (pattern referenced) were seen.

### 3.3.2.2 Pellet microstructure and phase identification

The XRD pattern for the UN+10 w%Zr sintered pellet (**Figure 3.7A**) was corrected for line position to the silicon reference material (due to sample displacement) and the pattern shows the peaks attributed to UN are shifted slightly left. Peaks corresponding to the ICSD patterns for tetragonal uranium (#00-006-0553, denoted by the dashed droplines),  $\alpha$ - $U_2N_3$  (#00-015-0426, cross markers), and  $ZrO_2$  (#00-034-1084, diamond markers). Although thermodynamics predicts (**Figure 3.1, Figure 3.4**) that ZrN would be the most stable phase under the experimental conditions in this work, the pattern for ZrN (#00-005-0665) did not index well to the analyzed sample.

The sintered microstructure of the UN+10 w%Zr pellet is seen in the backscattered electron micrographs of **Figure 3.8A-C**. The full surface of the sintered pellet (inset of **Figure 3.8**) shows increased porosity around the rim of the pellet. **Figure 3.8A-C** shows the microstructure and porosity is consistent throughout the entirety of the pellet (surface and cross-section). EDS identified the light phase (marked as location 1) as pure uranium, the lighter gray phase (area 2) as U-N-Zr, and the darker gray phase (area 3) as U-N-O-Zr. The relative error for N and O concentrations obtained from EDS

does not allow for precise stoichiometry quantification. However, the EDS data can be related to the results seen in the XRD patterns. The presence of a pure uranium phase in the sintered pellet provides confirmation that it is thermodynamically favorable for the UN to dissociate and the zirconium to replace the uranium, forming a ternary phase of unknown stoichiometry. This left the free uranium to form a liquid metal phase (melting temperature of uranium is 1405 K)[18], also identified in XRD. The incorporation of zirconium into the UN lattice could account for the shift seen in the UN peaks in the XRD results due to lattice contraction, due to the smaller ionic radii of  $Zr^{3+}$  compared to  $U^{3+}$  [35, 36]. Any zirconium metal not incorporated into the unknown ternary phase would have readily oxidized when exposed to atmosphere during removal from the sintering furnace, preparation for and during characterization, which explains the presence of  $ZrO_2$  in XRD. The formation of the sesquinitride ( $U_2N_3$ ) would also be expected when the N/U molar ratio is between 1.05 – 1.54 [16].

The XRD patterns for the as-synthesized UN powder, as-received yttrium powder, the mixed UN+10 w%Y powder, and the UN+10 w%Y sintered pellet are showing in **Figure 3.7B**. The yttrium powder pattern was indexed to ICSD pdf #01-089-2933 for yttrium, the mixed powder only reflected peaks attributed to yttrium and UN (and the NIST Si reference material).

The UN+10 w%Y sintered pellet, despite multiple sintering attempts up to 1808 K, exhibited only partial sintering. Grinding and polishing of the pellet surface was attempted but the surface remained textured and irregular. The NIST Si standard reference material was lightly sprinkled on the surface of the pellet prior to XRD analysis. The pattern for the sintered pellet (**Figure 3.7B**) contained peaks that were

attributed to the Si standard reflecting at different values of  $2\theta$  due to differences in sample height. These additional Si peaks are located at  $27.99^\circ$ ,  $46.99^\circ$ ,  $55.95^\circ$ , and  $68.89^\circ$   $2\theta$ .

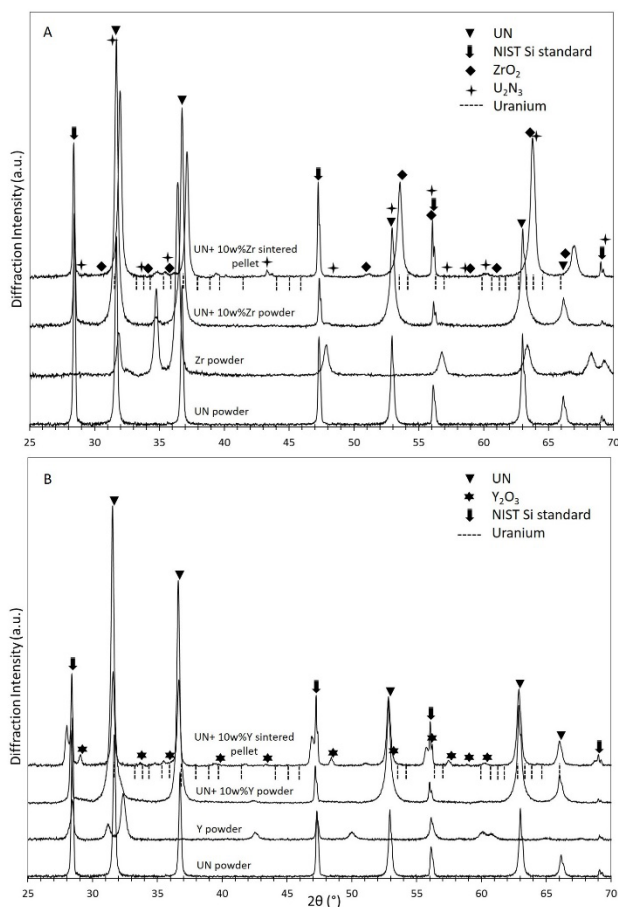


**Figure 3.7** XRD patterns for the as-synthesized UN powder, as-received Zr (A), and Y (B) powders, the mixed UN+10 w% metal powders, and the UN+10 w% metal sintered pellets.

The remaining peaks for the UN+10 w%Y sintered pellet were matched to UN (ICSD #00-032-1397) tetragonal uranium (#00-006-0553, denoted by the dashed droplines), and cubic Y<sub>2</sub>O<sub>3</sub> (#01-041-1105, denoted by the star symbol).

The sintered microstructure of the UN+10 w%Y pellet is shown in the backscattered electron micrographs of **Figure 3.8D-F**. The inset of **Figure 3.8D** is a full

cross-sectional image of the pellet highlighting increased porosity near the edges and surfaces of the pellet and overall inadequate sintering of the monolith. The textured and rough microstructure is apparent in **Figure 3.8D**. The different phases are evident as shown in **Figure 3.8E-F** and were characterized with EDS. The lightest phase (indicated by area 1) was identified as pure uranium, while in area 2 (slightly darker) U-N-Y was detected. The darkest phase (area 3) was identified as a yttrium oxide, all confirmed and corresponding to the data found in the XRD results. Although no shift was seen in the UN peaks for the UN+10 w%Y sintered pellet (unlike the UN+10 w%Zr pellet) the results obtained from the AIMD modeling suggest UN's NaCl crystal structure is maintained even with Y incorporation into the UN lattice. The next section discusses this observation further.

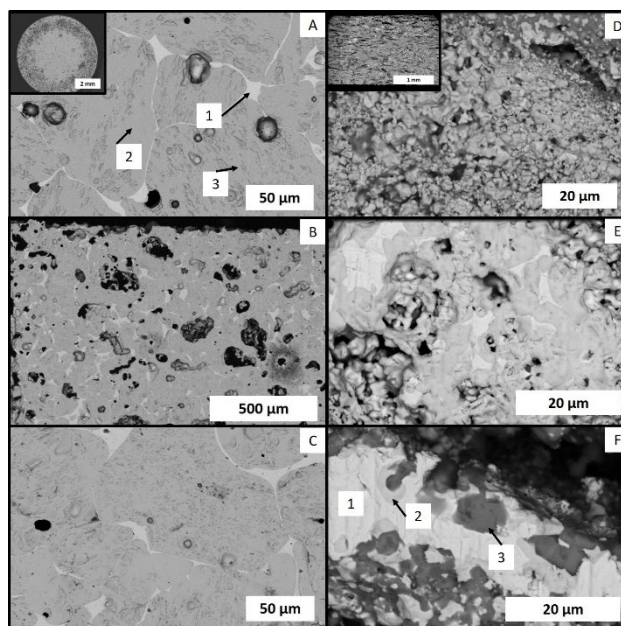


**Figure 3.8** BSE micrographs of the UN+10 w%Zr sintered pellet (A-C) and the UN+10 w%Y pellet sintered at 1808K (D-F); A) pellet surface showing phase segregation and increased porosity at the rim (inset). Detailed view of area where liquid U, U-N-Zr, and U-N-Zr-O phases are present. B) Cross-section of the pellet showing the liquid uranium phase was present throughout the bulk of the pellet and that the pellet contained a large amount of porosity. C) Higher magnification view of the cross-section. D) Cross-sectional view showing considerable porosity and inadequate sintering, inset is the full cross-sectional view. E) Higher magnification view of the phase segregation. F) Detailed view of area where liquid U, U-N-Y, and Y-O phases are present.

Although the oxidation of yttrium did occur, and is favored for a hydrothermal corrosion environment, the presence of a pure uranium phase is undesirable in reactor conditions, as when heated there is the potential for swelling, creep, and interaction with the fuel cladding. Results of sintering of UN composites in nitrogen-free atmospheres has been reported with no indication of free uranium or hyper-stoichiometric nitride phases [3]. However, other work suggests that dissociation of UN will occur unless a certain range of nitrogen partial pressure is maintained [37, 38]. No studies on UN-Y composites and the effect of nitrogen pressures during sintering on the microstructure or stoichiometry exist to the best of the authors' knowledge. It was noted that the

UN+10 w%Y pellet was only partially sintered. The partial sintering was attributed to the short sintering time employed to examine the evolution of the liquid phase, but also due to the large particle size of the yttrium as compared to the UN.

From the thermodynamic predictions of the Ellingham-type diagram (**Figure 3.1**), in the presence of nitrogen during sintering, the zirconium is expected to preferentially form ZrN, which has been proposed as a corrosion resistant coating in other material systems [39]. However, the melting temperature of ZrN is 3225 K [40], which makes it unsuitable for the LPS technique utilized in this work.

### 3.3.2.3 Electronic structure

By examining the LDOS, the resultant bond type between the metal additive and the UN could be determined. For example, overlap between two elements in the LDOS would indicate covalent bonding. While the LDOS can quantitatively show electron sharing, the ELF maps the electrons onto the structure and can qualitatively show the charge profile. In the ELF, 1 represents a high probability of finding an electron while 0 represents low probability.

In **Figure 3.9A**, the Zr bonding to UN was shown to be primarily ionic, as almost no states at the Fermi energy (represented by 0 eV) were localized to Zr. The ionic nature was further evident in **Figure 3.10A** and **C**, where the Zr atom was shown to have a 0 ELF value. These results suggest that the Zr atom donated its valence electrons to the surrounding UN matrix, leading to ionic bonds. As indicated in **Figure 3.10A**, this charge was likely donated to the U atom below the Zr. Structural changes may occur in order to distribute this excess charge. This could explain the shift in the XRD peaks associated with the lattice contraction of UN due to the zirconium addition (**Figure 3.7A**).

Like Zr, Y showed no states around the Fermi level at 0 eV, indicating donated valence electrons. The valence electrons were likely donated to the surrounding atoms rather than one particular atom, as there is no evidence of localized charge build up in **Figure 3.9B** or **C**. Unlike Zr, the Y bonding also showed covalent character, evident by the overlap of Y and U states in **Figure 3.9B**. Furthermore, this overlap occurred at deep electronic levels, as opposed to valence levels closer to the Fermi energy that would be likely to continue reacting. In **Figure 3.10B**, Y had a nonzero ELF value, though less than that of the surrounding U and N atoms, and contour lines indicated it shared electrons with three of the surrounding N atoms.

While both Zr and Y were initially placed at N sites in **Figure 3.10A-B**, both metal additions migrated to maximize bonds with N. With the Zr addition, this resulted in a region where the UN could not replicate its original structure. For Y, regardless of initial placement, the UN was able to return to its characteristic rock salt structure.

It should also be noted that after the addition of Y, bonds are maintained between the surrounding U and N atoms. However, after the addition of Zr at a U site (**Figure 3.10C**), the neighboring U atom to the top left became completely isolated from its neighboring N atoms. Again, this result parallels to the XRD data in that there was no shift associated with the UN peaks (**Figure 3.7**). This suggests there is no lattice contraction or expansion attributed to the incorporation of yttrium, even though the phase associated to UN from EDS suggests there is yttrium present (**Figure 3.8F**).

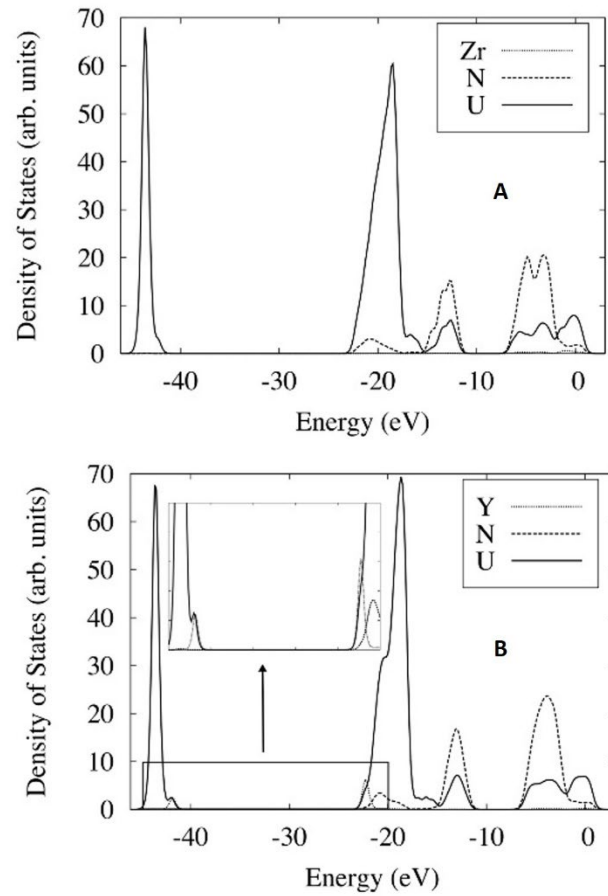


**Figure 3.9** Local density of states of (a) Zr added to an N site in UN at 1773 K and (b) Y added to an N site in UN at 1808 K. The Fermi level was shifted to 0 eV.

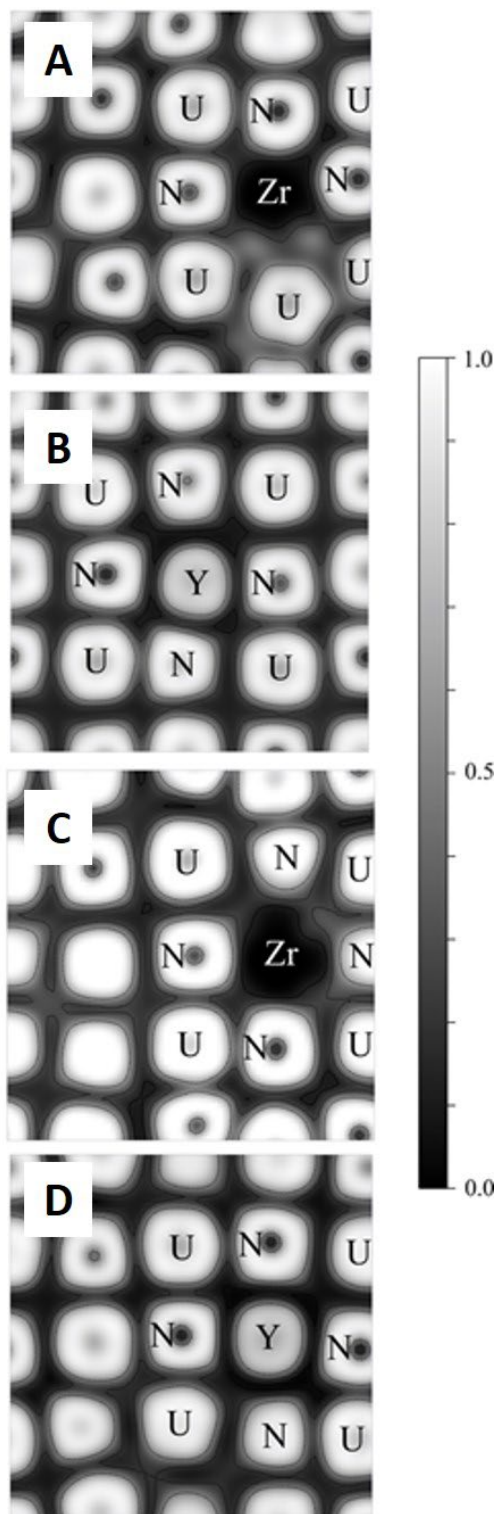


**Figure 3.10** Electron Localization Function of final structures initially configured as (a) Zr at an N site, (b) Y at an N site, (c) Zr at a U site, and (d) Y at a U site. Contour lines show regions of the same energy level.

### 3.4. Conclusions

A screening study to identify metallic elements that can improve the hydrothermal corrosion resistance of UN was undertaken. Candidate elements were evaluated based on melting temperature, thermal conductivity, and thermal neutron absorption cross-section. Zirconium and yttrium were selected for further examination. As part of the screening study, thermodynamic calculations and considerations were assessed to help predict the suitability of the metallic elements for incorporation into monolithic pellets via liquid phase sintering. *Ab initio* molecular dynamics was also employed to investigate the effect of secondary elements on the electronic structure of UN at the sintering temperatures utilized in this work.

Examination of the microstructure and phase evolution in the UN+10 w% metal pellets identified the formation of liquid uranium, ternary U-N-Metal phases and oxide phases. X-ray diffraction results corresponded to the qualitative results found with EDS confirming tetragonal uranium, oxide phases, and shifted UN peaks for the Zr-containing pellets, suggesting a lattice contraction due to the incorporation of Zr in the UN structure. This same shift was not seen in the XRD results for the Y-containing sample despite the indication of a U-N-Y phase from EDS.

The electronic structure calculations also agreed with the thermodynamic predictions of the Ellingham diagram in Figure 1, indicating that Zr is more likely to form a nitride phase than Y. Yttrium showed stable covalent bonding to U, maintained local structure analogous to pure UN, and evenly distributed the change in local charge density due to the metal addition. Conversely, the Zr showed no bonding to U and led either to charge build up around a U atom or to isolation of a U atom from its neighboring N

atoms. This finding correlates to the results seen in XRD that the UN structure is maintained with incorporation of Y, but not Zr. After coupling the modeling results with the thermodynamic predictions, it was deemed unnecessary to pursue further investigation of Zr as an additive for use in improved corrosion resistance of UN. However, further work to optimize the sintering parameters for UN + Y is still ongoing.

The fabrication technique and sintering profile, including the effects of starting powder particle size and sintering atmosphere, needs further investigation to achieve composite pellets having the desired microstructure and those suitable for corrosion testing.

### Acknowledgements

This work is partially supported by a Department of Energy Integrated University Program Graduate Fellowship. This research made use of the High-Performance Computing at Idaho National Laboratory, supported by the Office of Nuclear Energy of the U.S. Department of Energy and the Nuclear Science User Facilities under Contract No. DE-AC07-05ID14517. Further computational resources were provided by the R2 cluster (DOI: 10.18122/B2S41H) provided by Boise State University's Research Computing Department.

### References

- [1] D. Wachs, N. Woolstenhulme, Advanced fuel cycle technology: Special session in honor of Dr. Michael Lineberry, Transactions of the American Nuclear Society 110(INL/JOU-14-33095) (2014).
- [2] N.R. Brown, A. Aronson, M. Todosow, R. Brito, K.J. McClellan, Neutronic performance of uranium nitride composite fuels in a PWR, Nuclear Engineering and Design 275 (2014) 393-407.
- [3] L.H. Ortega, B.J. Blamer, J.A. Evans, S.M. McDeavitt, Development of an accident-tolerant fuel composite from uranium mononitride (UN) and uranium sesquisilicide ( $U_3Si_2$ ) with increased uranium loading, Journal of Nuclear Materials 471 (2016) 116-121.
- [4] M. Jolkkonen, P. Malkki, K. Johnson, J. Wallenius, Uranium nitride fuels in superheated steam, Journal of Nuclear Science and Technology 54(5) (2017) 513-519.
- [5] J.K. Watkins, D.P. Butt, B.J. Jaques, Microstructural degradation of UN and UN- $UO_2$  composites in hydrothermal oxidation conditions, Journal of Nuclear Materials 518 (2019) 30-40.

- [6] J.T. White, A.W. Travis, J.T. Dunwoody, A.T. Nelson, Fabrication and thermophysical property characterization of UN/U<sub>3</sub>Si<sub>2</sub> composite fuel forms, *Journal of Nuclear Materials* 495 (2017) 463-474.
- [7] K.D. Johnson, A.M. Raftery, D.A. Lopes, J. Wallenius, Fabrication and microstructural analysis of UN-U<sub>3</sub>Si<sub>2</sub> composites for accident tolerant fuel applications, *Journal of Nuclear Materials* 477 (2016) 18-23.
- [8] J.H. Yang, D.-J. Kim, K.S. Kim, Y.-H. Koo, UO<sub>2</sub>-UN composites with enhanced uranium density and thermal conductivity, *Journal of Nuclear Materials* 465 (2015) 509-515.
- [9] D.A. Lopes, S. Uygur, K. Johnson, Degradation of UN and UN-U<sub>3</sub>Si<sub>2</sub> pellets in steam environment, *Journal of Nuclear Science and Technology* 54(4) (2017) 405-413.
- [10] H.-G. Kim, J.-H. Yang, W.-J. Kim, Y.-H. Koo, Development Status of Accident-tolerant Fuel for Light Water Reactors in Korea, *Nuclear Engineering and Technology* 48(1) (2016) 1-15.
- [11] E.S. Wood, J. White, A. Nelson, The effect of aluminum additions on the oxidation resistance of U<sub>3</sub>Si<sub>2</sub>, *Journal of Nuclear Materials* 489 (2017) 84-90.
- [12] P.A. Lessing, Oxidation protection of uranium nitride fuel using liquid phase sintering, Idaho National Laboratory (INL), 2012.
- [13] M.N. Rahaman, *Sintering of ceramics*, CRC Press, Boca Raton, FL, 2008.
- [14] D. Bocharov, D. Gryaznov, Y.F. Zhukovskii, E. Kotomin, Ab initio simulations of oxygen interaction with surfaces and interfaces in uranium mononitride, *Journal of Nuclear Materials* 435(1-3) (2013) 102-106.
- [15] Y.-J. Zhang, J.-H. Lan, T. Bo, C.-Z. Wang, Z.-F. Chai, W.-Q. Shi, First-principles study of barium and zirconium stability in uranium mononitride nuclear fuels, *The Journal of Physical Chemistry C* 118(26) (2014) 14579-14585.

- [16] R. Matthews, K. Chidester, C. Hoth, R. Mason, R. Petty, Fabrication and testing of uranium nitride fuel for space power reactors, *Journal of Nuclear Materials* 151 (3) (1988) 345.
- [17] T. Muromura, H. Tagawa, Formation of uranium mononitride by the reaction of uranium dioxide with carbon in ammonia and a mixture of hydrogen and nitrogen—I synthesis of high purity UN, *Journal of Nuclear Materials* 71(1) (1977) 65-72.
- [18] B.M.P.C. KAPL, *Nuclides and Isotopes: Chart of the Nuclides*, (2010).
- [19] Y.S. Touloukian, *Thermal conductivity: metallic elements and alloys*, IFI/Plenum, New York, 1970.
- [20] J. Moore, R. Williams, R. Graves, Thermal conductivity, electrical resistivity, and Seebeck coefficient of high-purity chromium from 280 to 1000 K, *Journal of Applied Physics* 48(2) (1977) 610-617.
- [21] C. Meis, A. Froment, D. Moulinier, Determination of gadolinium thermal conductivity using experimentally measured values of thermal diffusivity, *Journal of Physics D: Applied Physics* 26(4) (1993) 560.
- [22] I. Automation Creations, *MatWeb: Material Property Data*, 2019.  
<http://www.matweb.com/>.
- [23] J. Moore, R. Graves, R. Williams, Thermal transport properties of niobium and some niobium-based alloys from 80 to 1600 K, *High Temperatures-High Pressures* 12(5) (1980) 579-588.
- [24] J. Fink, L. Leibowitz, Thermal conductivity of zirconium, *Journal of Nuclear Materials* 226(1-2) (1995) 44-50.
- [25] C.W. Bale, E. Belisle, P. Chartrand, S.A. Decterov, G. Eriksson, A.E. Gheribi, K. Hack, I.H. Jung, Y.B. Kang, J. Melancon, A.D. Pelton, S. Petersen, C. Robelin, J. Sangster, M.-A. Van Ende, *FactSage Thermochemical Software and Databases*, 2010-2016, *Calphad*, 2016, pp. 35-53.
- [26] S.A. Speakman, *Basics of X-ray powder diffraction*, MIT, 2011.

- [27] G. Kresse, J. Furthmüller, Efficient iterative schemes for ab initio total-energy calculations using a plane-wave basis set, *Physical review B* 54(16) (1996) 11169.
- [28] J.P. Perdew, K. Burke, M. Ernzerhof, Generalized gradient approximation made simple, *Physical review letters* 77(18) (1996) 3865.
- [29] S. Dudarev, G. Botton, S.Y. Savrasov, Z. Szotek, W. Temmerman, A. Sutton, Electronic structure and elastic properties of strongly correlated metal oxides from first principles: LSDA+ U, SIC-LSDA and EELS study of UO<sub>2</sub> and NiO, *Physica status solidi (a)* 166(1) (1998) 429-443.
- [30] T. Bo, J.-H. Lan, Y.-J. Zhang, Y.-L. Zhao, C.-H. He, Z.-F. Chai, W.-Q. Shi, Adsorption and dissociation of H<sub>2</sub>O on the (001) surface of uranium mononitride: energetics and mechanism from first-principles investigation, *Physical Chemistry Chemical Physics* 18(19) (2016) 13255-13266.
- [31] A. Claisse, M. Klipfel, N. Lindbom, M. Freyss, P. Olsson, GGA+ U study of uranium mononitride: A comparison of the U-ramping and occupation matrix schemes and incorporation energies of fission products, *Journal of Nuclear Materials* 478 (2016) 119-124.
- [32] H. Knott, G. Lander, M. Mueller, O. Vogt, Search for lattice distortions in UN, UAs, and USb at low temperatures, *Physical Review B* 21(9) (1980) 4159.
- [33] B. Silvi, A. Savin, Classification of chemical bonds based on topological analysis of electron localization functions, *Nature* 371(6499) (1994) 683.
- [34] S.L. Hayes, J.K. Thomas, K.L. Peddicord, Material property correlations for uranium mononitride: 1. physical properties, *Journal of Nuclear Materials* 171 (2-3) (1990) 262-270.
- [35] U. Schroeder, C.S. Hwang, H. Funakubo, *Ferroelectricity in Doped Hafnium Oxide: Materials, Properties and Devices*, Woodhead Publishing 2019.
- [36] W.-K. Li, G.-D. Zhou, T.C. Mak, T. Mak, *Advanced structural inorganic chemistry*, Oxford University Press 2008.

- [37] B.J. Jaques, J. Watkins, J.R. Croteau, G.A. Alanko, B. Tyburska-Pueschel, M. Meyer, P. Xu, E.J. Lahoda, D.P. Butt, Synthesis and sintering of UN-UO<sub>2</sub> fuel composites, *Journal of Nuclear Materials* 466 (2015) 745-754.
- [38] V. Tennery, T. Godfrey, R. Potter, Sintering of UN as a function of temperature and N<sub>2</sub> pressure, *Journal of the American Ceramic Society* 54 (7) (1971) 327-331.
- [39] I. Dumnernchanvanit, N.Q. Zhang, S. Robertson, A. Delmore, M.B. Carlson, D. Hussey, M.P. Short, Initial experimental evaluation of crud-resistant materials for light water reactors, *Journal of Nuclear Materials* 498 (2018) 1-8.
- [40] A. Lalis, G. Tessier, J. Plain, G. Baffou, Plasmonic efficiencies of nanoparticles made of metal nitrides (TiN, ZrN) compared with gold, *Scientific Reports* 6 (2016) 38647.

CHAPTER FOUR: INVESTIGATING GRAIN GROWTH OF CONVENTIONALLY  
SINTERED URANIUM MONONITRIDE

This manuscript is pending journal submission.

Investigating grain growth of conventionally sintered uranium mononitride

Jennifer K. Watkins<sup>a,b</sup>, Adrian R. Wagner<sup>a</sup>, Fidelma G. Di Lemma<sup>a</sup>, Brian J.

Jaques<sup>b,c</sup>

<sup>a</sup> Idaho National Laboratory, Idaho Falls, ID, USA

<sup>b</sup> Micron School of Materials Science and Engineering, Boise State University, Boise, ID, USA

<sup>c</sup> Center for Advanced Energy Studies, Idaho Falls, ID, USA

#### Author Contributions

Jennifer K. Watkins: Conceptualization, Investigation, Writing – Original Draft, Review and Editing

Adrian R. Wagner: Conceptualization, Investigation, Resources, Supervision, Writing – Review and Editing

Fidelma G. Di Lemma: Investigation, Supervision, Writing – Review and Editing

Brian J. Jaques: Conceptualization, Resources, Supervision, Writing - Review and Editing

## Abstract

This work discusses the mechanism of grain growth and whether any preferential grain orientation is observed in conventionally sintered uranium mononitride (UN). Polycrystalline samples having a range of grain sizes from 4.0-19  $\mu\text{m}$  have been prepared using conventional fabrication and sintering methods. Samples underwent sintering from 1850-2000  $^{\circ}\text{C}$  for 2-25 hours. Samples were characterized using X-ray diffraction (XRD), electron backscatter diffraction (EBSD), and an image analysis software was used to confirm phase purity, grain boundaries, grain orientation, and average grain and pore size. Classic grain growth theory models were employed to elucidate the grain growth mechanism (e.g., grain growth exponent) and to determine activation energies. Finally, factors affecting normal grain growth, and the complexities of comparing results to data mined from existing literature is discussed.

## 4.1 Introduction

Uranium mononitride (UN) continues to be investigated as a potential advanced technology fuel (ATF, also referred to as accident tolerant fuel) due to its favorable thermophysical characteristics such as high thermal conductivity and high melting point as well as its increased metal atom density over the benchmark uranium dioxide ( $\text{UO}_2$ ) fuel [1, 2]. UN fuel has been proposed and researched in the past for use in space power reactors and liquid metal fast breeder reactors due to these desirable properties and its acceptable performance under irradiation [3-7]. However, UN also has some difficult limitations which must be addressed before it can be considered a drop-in replacement for  $\text{UO}_2$ . First, fabrication and handling of air-sensitive UN fuel-forms has proven challenging and requires use of inert atmospheres during synthesis, fabrication, and

handling; second, UN's poor oxidation performance in water and/or oxygen containing atmospheres; third, the use of isotopically enriched nitrogen ( $^{15}\text{N}$ ) is necessary to prevent additional neutron capture via the  $(n,p)$  reaction when using  $^{14}\text{N}$ , resulting in the need for higher  $^{235}\text{U}$  enrichment to compensate for the neutronics penalty and increased production of  $^{14}\text{C}$  [8]. Although the grain size of nuclear fuels can significantly impact its performance in terms of creep, fission gas release, swelling [9], and thermal conductivity [10], little information is available on the mechanism and kinetics of grain growth in conventionally sintered UN. Accordingly, there are limited publications available which specifically discuss UN grain growth and associated mechanisms: Conventional techniques for fabrication and sintering [3, 11-13] as well as spark plasma sintering [14-16]. One of the metrics for proposed ATF concepts is that they must be backwards compatible with existing fuel-handling infrastructure [17]; thus, it is desirable to utilize current conventional commercial frameworks for fuel fabrication scale-up. New approaches to advanced modeling of nuclear materials aim to provide mechanistic models which model fuel behavior that is derived from microstructure instead of burn-up [9]. As such, data on the kinetics of the UN grain growth mechanism is instrumental in advancing simulation and modeling work. Such data will help to decrease qualification times for the use of UN in the existing and proposed advanced reactor fleets. This work aims to identify the grain growth mechanism in conventionally fabricated and sintered UN and identify any preferential grain orientation during sintering. Samples sintered under various time/temperature profiles were examined using electron backscatter diffraction (EBSD) to characterize grain boundaries and grain orientation. Phase characterization was completed using X-ray diffraction (XRD) while image analysis

software was employed to ascertain average grain and pore sizes in the sintered materials. A best fit of the data to accepted values of the grain growth exponent (from the classic grain growth equation [18]) is used to determine the mechanism and activation energy of grain growth. The factors which affect the mechanism and kinetics of grain growth and the implications of experimental parameters on the results is discussed.

## **4.2 Materials and Methods**

### **4.2.2 Pellet fabrication and sintering**

The UN powder feedstock was received from Los Alamos National Laboratory and was synthesized via a carbothermic reduction method. The powder was analyzed for carbon (combustion technique) and oxygen (inert gas fusion technique) impurities prior to shipment to Idaho National Laboratory. The as-received powder was subjected to a high energy ball milling process (300 rpm, 1 hour, Retsch PM 200 planetary ball mill) in a ZrO<sub>2</sub> milling vessel with 5 mm diameter ZrO<sub>2</sub> media in an 8:1 media to powder mass ratio. The milled UN powder was then passed through a 400-mesh (37 μm) sieve prior to pressing into pellets of right cylindrical geometry using an automated Carver hydraulic press at ≈670 MPa with an 8.25 mm WC die. A small amount of dry zinc stearate (Sprayon MR312) was used as a lubricant on the die surface, die punches, and die faces. All milling and pellet fabrication occurred in an inert atmosphere glovebox having under 5 ppm of O<sub>2</sub>. Particle size analysis of the sieved UN powder was completed via X-ray sedimentation analysis using a Micromeritics Sedigraph III 5120.

The UN pellets were sintered in a tungsten metal sintering furnace (Thermal Technology Model 1100). A sintering cover gas of oxygen scrubbed Ar+100ppm N<sub>2</sub> (1 L/min) or scrubbed ultra-high purity (UHP) Ar/N<sub>2</sub> (9.3/0.7 L/min) was used during

sintering. This cover gas was used to maintain a nitrogen partial pressure within the sintering chamber between  $1.1 \times 10^{-5}$  to  $1.2 \times 10^{-2}$  MPa over the temperature ranges used in this study, 1850-2000 °C. The Ar/N<sub>2</sub> mixtures were used to avoid UN dissociation and formation of U<sub>2</sub>N<sub>3</sub> during the sintering ramp (25 °C/min), at the dwell temperatures of interest [19], and during the cool-down phase to 1200 °C. Once the sample reached 1200 °C, the atmosphere was switched to UHP Ar for the final cool-down until room temperature to prevent sesquinitride formation. The sintering runs were not initiated until the starting oxygen levels in the cover gas were below what was considered an acceptable level, which varied between the detectable limit of the O<sub>2</sub> analyzer (< 0.1 ppm) to < 5 ppm of O<sub>2</sub>. Pellets were placed directly on a tungsten sintering plate within the hot zone of the furnace. The samples were run at time/temperature profiles of 1850-2000 °C for 2-25 hours. To simplify the discussion in subsequent sections, samples are denoted as “sintering temperature/sintering time” (e.g., 2000/25). The densities of the sintered samples were determined via the Archimedes measurement method in ethanol [20].

#### 4.2.2 X-ray Diffraction

Phase identification via XRD for the feedstock material, milled powder, and sintered pellets was completed using a Malvern Panalytical Aeris X-ray Diffractometer (Cu K<sub>α</sub>, 40 kV, 15mA, step-size 0.011 2θ). Crystallite size for the milled powder was also determined via XRD, using the Scherrer equation [21]. The as-sintered pellets were ground in a mortar and pestle and the resulting powders (as well as the starting powders) were encapsulated in Dow Corning high vacuum grease inside an inert atmosphere glovebox (<1 ppm O<sub>2</sub>) to avoid oxidation during transfer to the XRD. A LaB<sub>6</sub> powder standard (Standard Reference Material 660c, National Institute of Standards and

Technology, NIST) was added for line position verification. All XRD scans were run using a zero-background silicon disc holder. Initial crystallite size of the starting powder (after milling) and material composition via phase quantification of sintered samples was performed using Rietveld refinement analysis within the Panalytical HighScore+ software [22]. Rietveld refinement was performed using a polynomial fit to the background and a semi-automatic fitting profile. The calculated profile was examined and compared to the experimental, and the residual plot (the portion of the net scan intensity not explained by the scaled reference patterns) was inspected for good agreement. Profile fitting used the Pseudo-Voigt profile function and refinement was completed to generate a minimized weighted residual ( $R_{wp}$ ) profile.

#### 4.2.3 Microstructural analysis

The as-sintered pellets were prepared for microstructural analysis by mounting in epoxy followed by grinding to 1200 grit SiC paper. The pellets were ground approximately to the halfway plane to create a cross-sectional surface that was perpendicular to the two parallel faces of the right cylinder. The cross-sectional surface was polished with a diamond suspension fluid to 1 micron followed by a final polish with colloidal silica (0.25  $\mu\text{m}$ ). To obtain grain size and orientation, the microstructure of the sintered samples was analyzed using a JEOL IT500HR secondary electron microscope (SEM) equipped with an Electron Backscattered Diffraction (EBSD) detector from Oxford Instruments (EBSD symmetry detector, 1.2 megapixel, 3000 pps). All EBSD measurements were performed with the sample tilted at  $70^\circ$  toward the EBSD detector and with the same microscope parameters (20 kV, 75 nA, 1x1 binning, and a 1  $\mu\text{m}$  step size). Patterns were indexed with a crystal structure for UN: FCC with a space group of

Fm-3m [23]. Data was collected with Aztec 4.1 and analyzed with the CHANNEL 5 software. Multiple areas (minimum of 4 sites per sample) were randomly selected for examination from representative areas across the entire cross-sectional surface area on the polished planar surface. The rectangular areas selected for mapping were approximately 260 by 175  $\mu\text{m}$ . The data shown was obtained from results averaging over a mean angular deviation (MAD) value of  $< 0.7$  degrees, which significantly improves results as reported by Nagaya *et.al.* [24]. The MAD is defined as the average value of the angular misfit in degrees between detected and theoretically simulated Kikuchi bands. The data cleanup routine included removal of wild spikes (isolated points that have been indexed incorrectly) and correcting the zero solution via iterative neighboring correlation (NC) with at least 5 neighboring grains. Microstructural characterization to obtain average grain and pore sizes in the sintered samples was performed on the inverse pole figure orientation and grain boundary maps and the electron images obtained during EBSD using the MIPAR<sup>TM</sup> software package [25]. The number of grains analyzed ranged from 280-3600 and the number of pores from 2500-4100, depending on average grain or pore size per area examined.

#### 4.2.4 Calculations for kinetics and grain growth mechanisms

The driving force for grain growth is a reduction in the overall energy associated with a decrease in grain boundary area [18]. The classic work by Burke and Turnbull proposed a parabolic relationship for grain growth kinetics and modeled grain boundary migration as atomic transport across the boundary which is initiated from the pressure gradient across the boundary due to surface curvature [18, 26, 27]. Additionally, grain boundaries are areas of atomic mismatch and have a larger Gibbs free energy than that of

an ideal lattice; thus the driving force for the movement of the grain boundaries in such a way that reduces the area these boundaries occupy is the reduction of the Gibbs free energy [28]. It was proposed that the rate of grain boundary migration is inversely proportional to the boundary radius of curvature [29]. This led to an assumption that the average grain radius is proportional to the radius of curvature and mean migration rate [29]. A general form of the grain growth equation was used to analyze the kinetics of grain growth, the difference in grain size as a function of time is given as following [18, 26, 29-31]:

$$G_t^n - G_0^n = Kt \quad \text{Eqn. (1)}$$

where  $G_0$  is the starting grain size (noted here as the crystallite size as determined by the Scherrer equation via XRD). It should be noted that there are limitations to the application of the Scherrer equation, given that there are other factors that can lead to broadening of the diffraction peak. These factors include experimental resolution of the XRD instrument, the shape and size distributions of the crystallites, and the effects of any microstrain or defects [21]. The Scherrer equation is also limited to applicable grain sizes of 100-200 nm (also dependent on instrumentation, sample variances, and signal-to-noise ratio) [21].  $G_t$  is the grain size after a given sintering time,  $t$ .  $n$  is the grain growth exponent (the value of which is dependent upon the grain growth mechanism) and  $K$  is the grain growth rate constant. Plots of  $G_t^n - G_0^n$  versus  $t$  were generated using values of  $n$  ranging from 1.25 to 4 (see **Table 4.1**). As noted by Brook [18] the various grain growth mechanisms are assigned to different values of  $n$ , ranging from 1-4. In general, for ceramics, the value of  $n$  has typically been noted as being equal to 2 or 3; thus, the values of 1.25-4 used in this study were intended to identify any trend towards those

values. The calculations for the grain growth activation energy were determined by using  $n$  values from the best fit (established from linear trendline  $R^2$ , or the correlation coefficient, values in the plots of  $G_t^n - G_0^n$  versus  $t$ ) but also when using values of  $n$  corresponding to a consistent dominant mechanism. The  $R^2$  value is a statistical indication of the quality of the linear regression, having a value between 0 and 1. The closer the  $R^2$  value is to 1 the better the fit of the line to the data [32]. The grain growth rate constant,  $K$ , is obtained from the slope of the linear regression line in the  $G_t^n - G_0^n$  versus  $t$  plots and the Arrhenius behavior is expressed through [18, 30]:

$$K = K_0 e^{(-Q_G/RT)} \quad \text{Eqn. (2)}$$

where  $K_0$  is the pre-exponential factor,  $R$  is the universal gas constant,  $T$  is the absolute temperature, and  $Q_G$  is the activation energy for grain growth. In order to obtain the activation energy for grain growth, Eqn. 2 can be re-written as:

$$\ln K = \ln K_0 - \frac{Q_G}{RT} \quad \text{Eqn. (3)}$$

Therefore, the grain growth activation energy can be determined from the slope of the line in a plot of  $\ln K$  vs.  $1/T$ , an Arrhenius relationship.

### 4.3 Results and Discussion

#### 4.3.1 Pellet fabrication and sintering

The as-received UN feedstock powder was reported to have carbon and oxygen impurities of 1710 and 336 ppm, respectively, as determined via light element combustion analysis. The mode value for the particle size of the milled UN powder (as determined via sedigraph analysis) was 0.94  $\mu\text{m}$  ( $d_{10} = 0.35 \mu\text{m}$ ,  $d_{50} = 0.93 \mu\text{m}$ ,  $d_{90} = 2.8 \mu\text{m}$ ). The resulting densities for each sample from the Archimedes density analysis (based on the calculated theoretical density (TD) of UN at 14.33  $\text{g/cm}^3$ ) are noted in

**Figure 4.1** above the column for their respective grain sizes in %TD. As anticipated, density increased with increased sintering time; however, the highest density was achieved in the 1850/25 sample (99.1 %TD). It should be noted that a sintered density of this magnitude would not be expected. Comparison of the Archimedes density to a geometric density calculation (95.6%) suggests that there was approximately 3.5% open porosity in this sample, which correlates to what is observed microstructurally for this sample. In contrast, samples sintered at higher sintering temperatures resulted in a maximum density just above 97 %TD. One of the samples resulted in a lower density than what would be expected in this sample set: the 1950/25 sample had a 96.1%TD (not shown in **Figure 4.1**). It was later determined this sample underwent abnormal grain growth, which likely contributed to the lower density value [18]. This anomaly is discussed further in the supplementary file provided online with this manuscript.

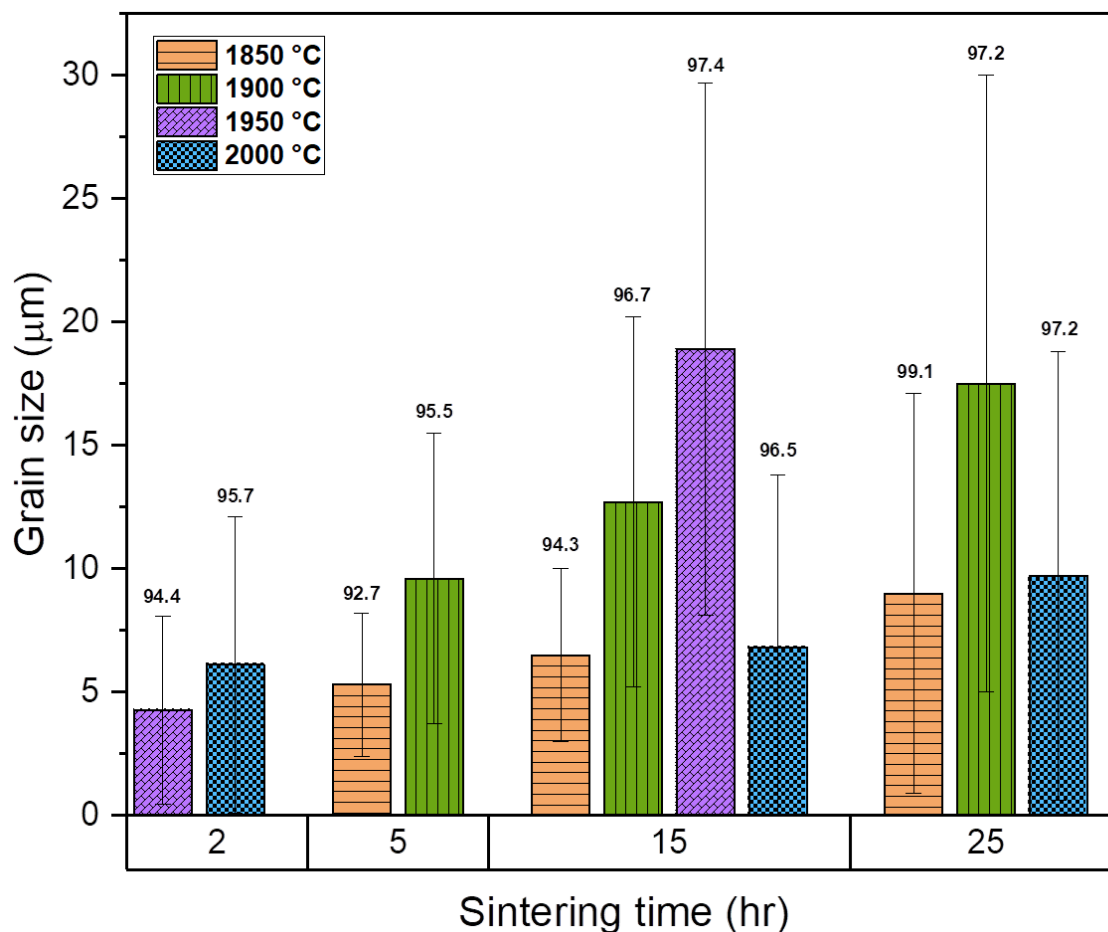


**Figure 4.1** Compilation of the average grain size (with error bars representing one standard deviation) versus sintering time for all sintered samples used in this study. The %TD for each sample is shown above their respective columns.

#### 4.3.2 X-ray Diffraction

The XRD patterns for the UN feedstock powder, the UN powder after ball-milling, and all sintered samples are shown in **Figure 4.2**. The patterns were matched to ICDD powder diffraction files (PDF) for UN (pdf #98-009-0318),  $\text{UO}_2$  (pdf #00-041-1422), and  $\text{U}_2\text{N}_3$  (pdf #03-065-3179). The milled powder exhibited broadened peaks for UN, representative of the reduction in crystallite size from the original feedstock powder. The pattern for the milled powder sample also suggests there may have been some poorly crystallized trace  $\text{U}_2\text{N}_3$  present in the original feedstock as evidenced by the broad peak at

approximately  $28.9^\circ 2\theta$ . The 1850/5 and 2000/25 patterns also suggest a small amount of impurity  $\text{UO}_2$  that may be present, as evidenced by the slight peaks at  $28.4^\circ 2\theta$ . The use of the vacuum grease to encapsulate the samples does contribute an increase in the background as an amorphous phase and can result in overestimation in the quantitative results [33]. The powder batches for each sintering temperature/time profile were freshly prepared from the existing feedstock just prior to pellet fabrication. However, the two samples displaying some trace oxide impurity were prepared from powder batches that combined small amounts of milled powder remaining from previous milling runs, essentially having some “aged” powder. Although the UN powder was kept sealed in glass containers inside the glovebox, it has been shown that UN powder can form an oxide layer ( $\approx 2$  nm) in under 1000 h just from exposure to glovebox atmosphere [34]. The presence of this impurity oxide layer can also negatively affect densification [34].

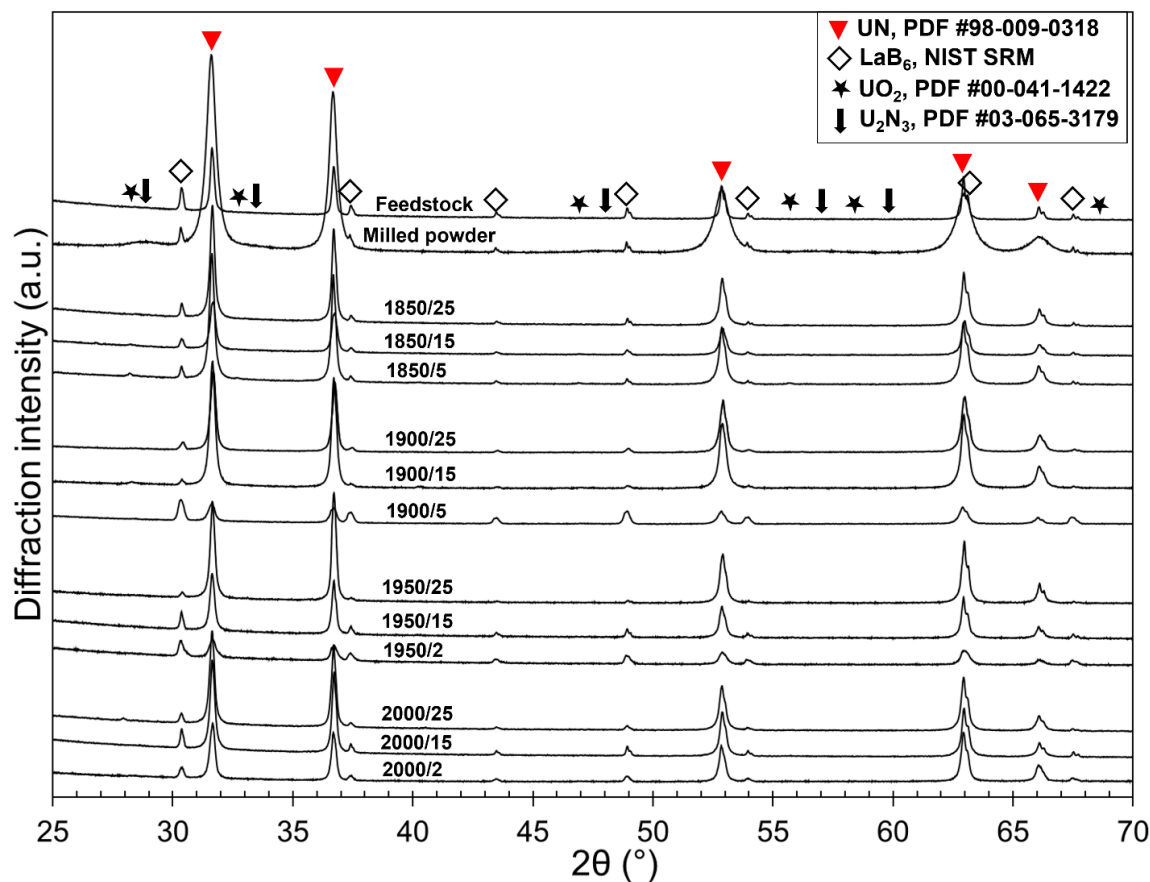


**Figure 4.2** XRD patterns for UN feedstock, UN milled powder, and all sintered samples.

#### 4.3.3 Microstructural analysis

The grain size summary for all the sintered samples is shown in the column chart of **Figure 4.1**. As anticipated, all samples exhibit increased grain size with sintering time. Grain size also increased with sintering temperature, except for the 2000 °C samples. Those samples, sintered at 2000 °C, show a smaller difference in grain size with increased sintering time (a 46% increase from 6.1 to 9.7  $\mu\text{m}$ ) and the average grain sizes are smaller than those in the 1900 °C and 1950 °C samples (9.7  $\mu\text{m}$  for 2000/25 as compared to 17.5  $\mu\text{m}$  and 18.9  $\mu\text{m}$  for the 1900/25 and 1950/15 samples, respectively). This is likely due to a change in the dominant grain growth mechanism at the elevated temperature, which will be discussed further in subsequent sections. The large standard

deviations ( $1\sigma$ ) indicate that, although an average was determined, a wide distribution of grain sizes is present in the samples. A compilation of histograms depicting the grain size distribution for all the samples in this study is shown in the supplementary file submitted online with this manuscript (**Figures D.S1-D.S4**). None of the samples exhibited true Gaussian distribution, with most of them appearing to have a positively skewed multi-modal distribution.

As previously mentioned, the 1950/25 sample exhibited abnormal grain growth during sintering. The analysis revealed very large ( $>1$  mm) grains in the middle of the sample, surrounded by increasingly smaller grains at the outer rim of the pellet (See **Figure D.S5** in the supplementary file). Due to this abnormality in the grain growth for the 1950/25 sample, the grain size values for that sample were excluded from the grain growth mechanism and activation energy calculations. Further discussion regarding this sample is also in the supplementary file.

The average pore sizes of the sintered samples are summarized in **Figure 4.3**. The pore sizes for the 1850 °C and 1900 °C samples decreased with increased sintering time. Also shown in **Figure 4.3** is the number of pores per unit area (pores/ $100 \mu\text{m}^2$ ) denoted next to each sample's average pore size column. According to German, at the onset of the final stage of sintering, a gradual transition occurs where the pores close off, initially decreasing pore diameter, and then increasing with sintering time [35]. Secondary electron micrographs of all the samples showing the characteristics of the pores as sintering temperatures and times increase are shown in **Figure 4.4**. Examination of the pores in the 1850/5 and 1850/15 samples showed they were primarily located at the grain boundaries and triple junctions with small transgranular pores in the 1850/5 sample. The

pores for the 1850/25 and all the 1900 °C samples showed they were largely transgranular. The 2000 °C samples indicate that the pore size remained relatively stable regardless of sintering time and they were also generally transgranular. Interestingly, the 1950 °C samples displayed an increase in pore size as sintering time increased. As previously mentioned, the 1950/25 sample exhibited exaggerated grain growth. This exaggerated grain growth occurs at the expense of neighboring grains undergoing normal grain growth due to grain boundaries breaking away from the pores and halting densification [30, 36]. This reasoning for the AGG provides insight as to why the 1950/25 sample had lower than anticipated density, as mentioned earlier.

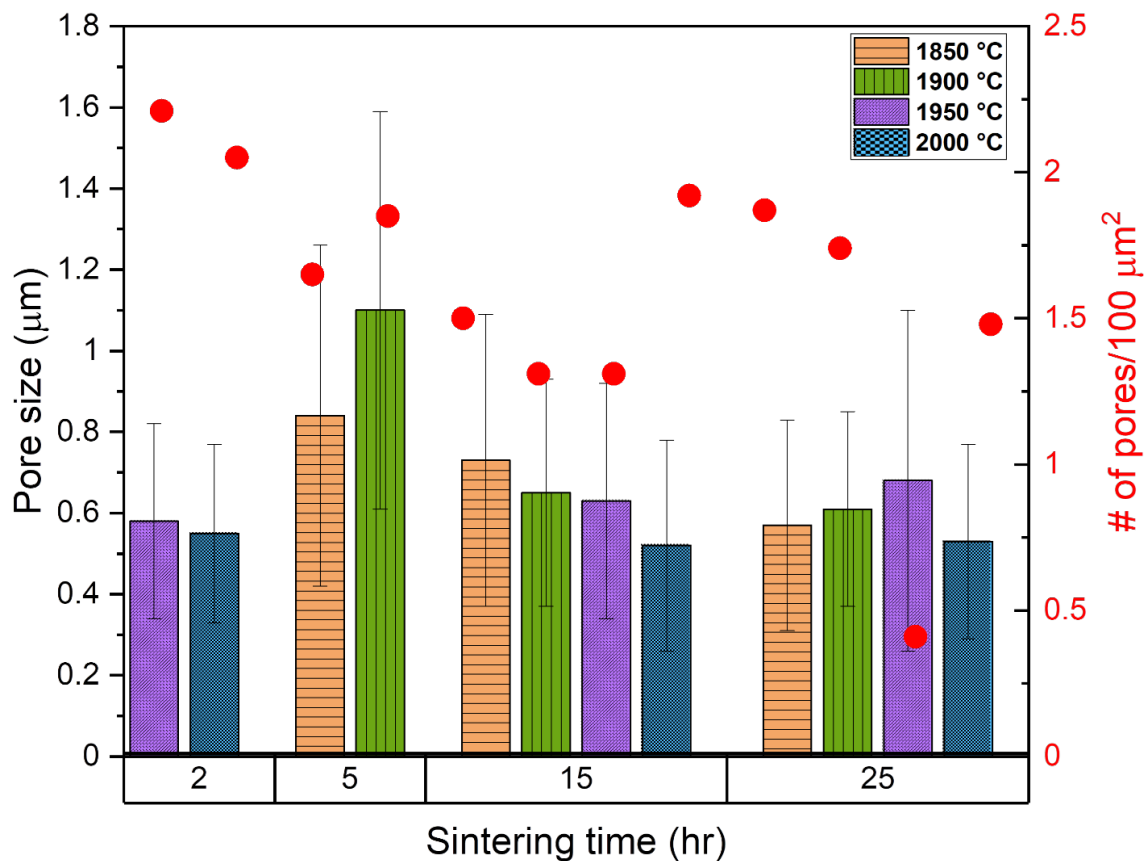


**Figure 4.3** Column chart compilation of the average pore size on the left y-axis (with error bars representing one standard deviation) versus sintering time for all sintered samples used in this study. Also shown is the number of pores per 100 μm<sup>2</sup> (corresponding to the right y-axis) indicated by the red circles by each sample's average pore size.

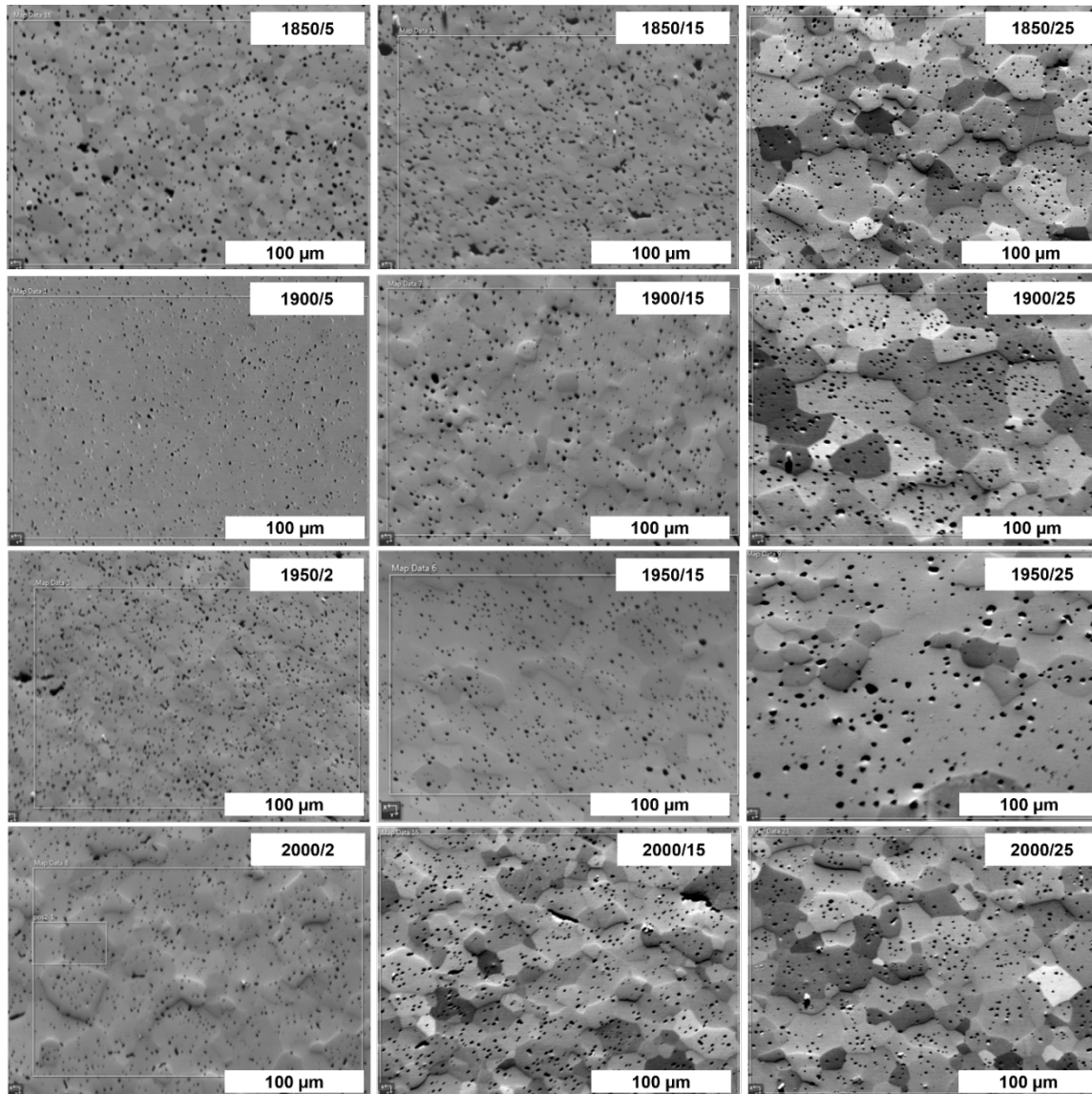


**Figure 4.4** Secondary electron micrographs from all sintered samples in this study showing the progression of the pore characteristics as time and temperature are increased.

**Figure 4.5** is a compilation of the inverse pole figure orientation maps generated through EBSD for the sintered samples, also reflecting the increase in grain size with sintering time. These EBSD maps were used to quantify the grain sizes that are plotted in **Figure 4.1**. The inverse pole figures for sintered samples are seen in **Figure 4.6**. For figure clarity the orientation for all the inverse pole figures is represented on the 1850/5 sample in **Figure 4.6** and applies to all the inverse pole figures in the figure. It is evident

from these inverse pole figure orientation maps and inverse pole figures that no significant preferential orientation is observed in any of the samples. The wide grain size distribution quantified in the grain size analysis can also be observed visually in these inverse pole figure orientation maps (**Figure 4.5**).

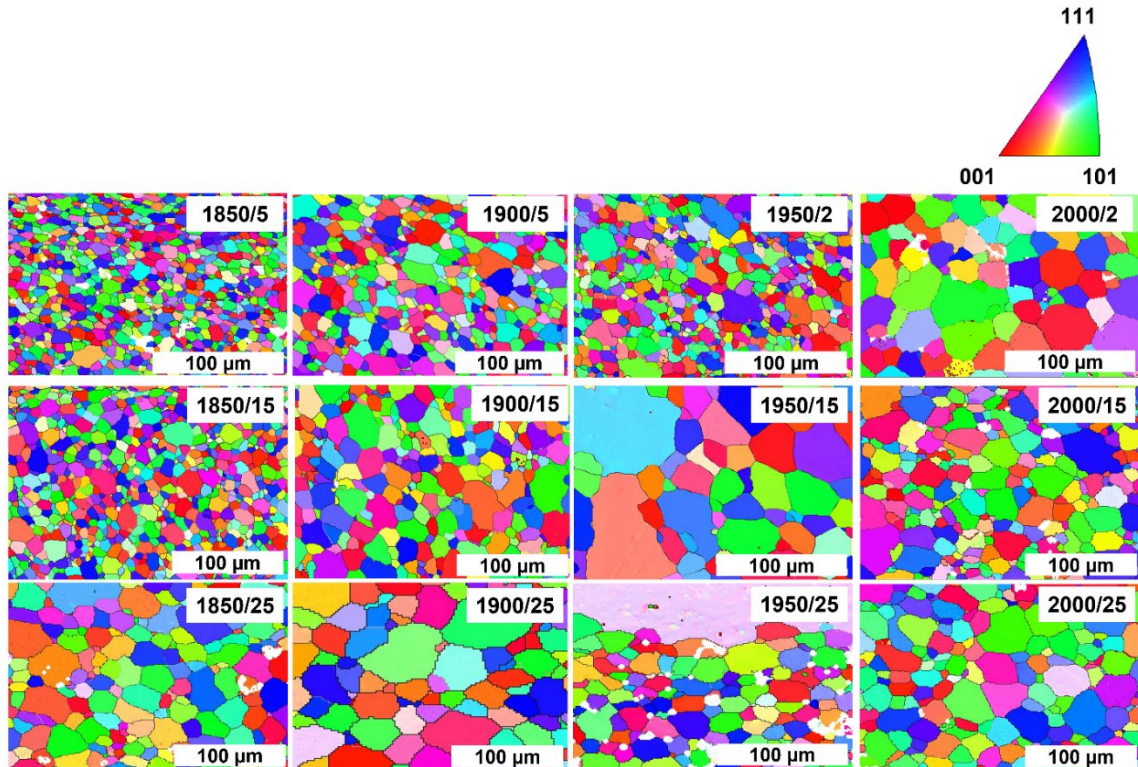


**Figure 4.5** EBSD inverse pole figure orientation maps from all the sintered samples in this study reflecting the increase in grain size with temperature. The 1950/15 and 1950/25 samples show evidence of abnormal grain growth.

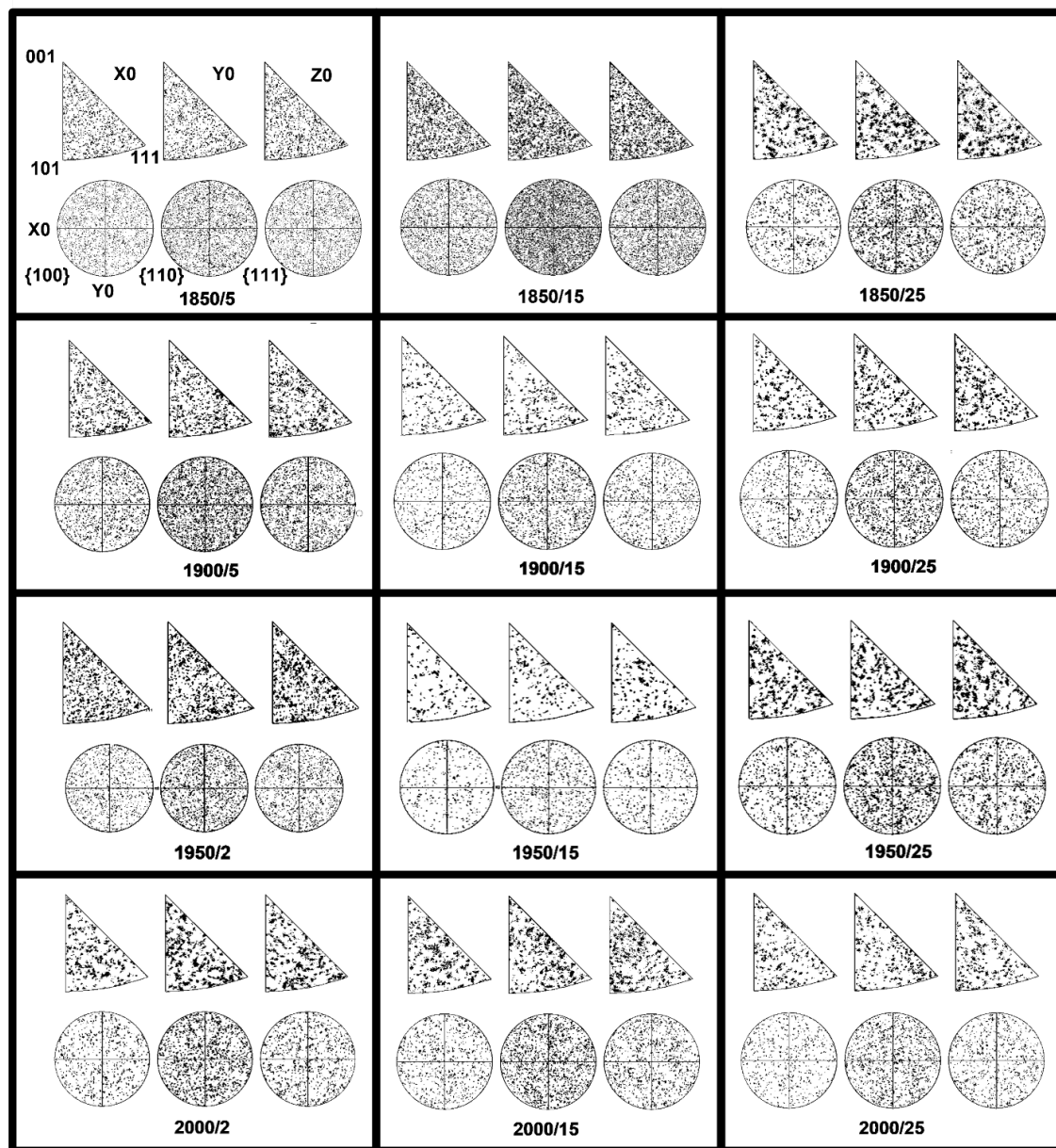


**Figure 4.6** Inverse pole figures for the sintered samples used in this study. It does not appear that there is any significant preferential orientation in the samples. For figure clarity the orientation of the inverse pole figures is only denoted with the 1850/5 sample but is the same for all other samples.

#### 4.3.4 Determination of grain growth exponent and activation energies

Grain growth kinetics and the determination of the grain growth exponent,  $n$ , has commonly been reported in literature for metals and ceramics (albeit limited for nuclear ceramics) according to Eqn. (1). [18, 30, 31]. It is accepted that different grain growth

mechanisms correspond to various values of  $n$ . Early works assumed that the average grain diameter is correlated to the average radius of boundary curvature and that drag at the boundaries is proportional to the boundary mobility [37]. These assumptions led to  $n = 2$  being assigned to the mechanism of grain boundary diffusion; however, it has been noted that for ceramics, in reality, the equation is more reliable when  $n = 3$  [38]. Brook explains that a specific mechanism is not indicated even if a constant value is experimentally observed for a range of temperatures and grain sizes [18]. It is also important to note that this value of the grain growth exponent is only related to the dominant mechanism of grain growth; it is assumed that there exists a combination of mechanisms occurring simultaneously. All these concurrent mechanisms contribute to the effective activation energy. Non-integer values for the grain growth exponent have been noted as a combination of concurrent mechanisms [39-41]. As noted by Fan *et al.* the grain growth exponent can take on any value between 2 and 3 depending on the ratio of lattice diffusion and grain mobility [39]. A set of assigned values for the grain growth exponent was compiled for various grain growth mechanisms and is detailed in **Table 4.1**.

**Table 4.1 Values of the grain growth exponent,  $n$ , for various mechanisms. Taken from Brook [18].**

Kinetics of grain growth for various mechanisms	
	$n$
<i>Pore control</i>	
Surface diffusion	4
Lattice diffusion	3
Vapor transport ( $P = \text{constant}$ )	3
Vapor transport ( $P = 2S/r$ )	2
P: pressure gradient across the boundary, S: grain boundary energy, r: radius of curvature of the boundary surface	
<i>Boundary control</i>	
Pure system	2
Impure system	
Coalescence of 2 <sup>nd</sup> phase by lattice diffusion	3
Coalescence of 2 <sup>nd</sup> phase by grain boundary diffusion	4
Solution of 2 <sup>nd</sup> phase	1
Diffusion through continuous 2 <sup>nd</sup> phase (e.g., liquid phase)	3
Impurity drag (low solubility)	3
Impurity drag (high solubility)	2

Assuming that grain boundary diffusion is the controlling mechanism for conventionally sintered (CS) UN,  $n$  is expected to be equal to, or nearly equal to 2. As stated earlier, very little grain growth kinetics data for UN exists in the open literature, especially for CS materials. As part of this work, the methodology applied to determine the grain growth kinetics and mechanism was applied to literature data to evaluate and contrast the work. Unfortunately, only one report by Metroka [11] on the fabrication of

UN compacts gave sufficient detail on grain sizes, sintering temperatures, and dwell times to directly compare the data. When applying classical grain growth theory to the data in this study, it is assumed that final stage sintering has been achieved and densification has stopped.

Utilizing Eqn. (1) and plotting  $G_t^n - G_0^n$  (in  $\mu\text{m}^n$ ) versus  $t$  (in hours) using various values for  $n$ , the best fit to the data was determined according to the  $R^2$  value. The  $R^2$  values for the linear regression fitting for each sample's grain size differences raised to various  $n$  values versus time at the experimental dwell temperatures are tabulated in **Table 4.2**. The values are close in magnitude over a range of  $n$  values and are generally grouped between 2 and 2.25. The true best fit for the 1950 °C samples corresponded to an  $n$  value of 1.25, but again there is minimal discrepancies in the  $n$  values up to 2.25. This lower  $n$  value for the 1950 °C data is likely biased as only two data points were used since the 1950/25 data was excluded from the calculations. Given that there was no indication of solution of a second phase, using the 1.25 value for  $n$  is unjustified, thus  $n = 2$  was used for the 1950 °C sample. Plots of  $G_t^n - G_0^n$  (in  $\mu\text{m}^n$ ) versus  $t$  (in hours) for the best fits at each sintering temperature is shown in **Figure 4.7**.

**Table 4.2**  $R^2$  values for linear regression fitting from grain growth data raised to various  $n$  values versus time plots for the samples sintered at various dwell temperatures. The best fit to the  $R^2$  values used in obtaining the grain growth rate constant are highlighted in the table for each temperature profile.

Temperature [°C]	$R^2$ from $G_t^n - G_0^n$ vs $t$ plots for various $n$ values											
	1.25	1.5	1.75	2	2.25	2.5	2.75	3	3.25	3.5	3.75	4
1850	0.884	0.922	0.945	0.956	0.959	0.955	0.947	0.936	0.924	0.910	0.897	0.883
1900	0.916	0.950	0.968	0.975	0.974	0.968	0.957	0.945	0.931	0.917	0.903	0.889
1950	1.000	0.999	0.997	0.994	0.992	0.990	0.988	0.987	0.987	0.986	0.986	0.986
2000	0.757	0.802	0.834	0.854	0.865	0.870	0.869	0.864	0.857	0.849	0.840	0.830

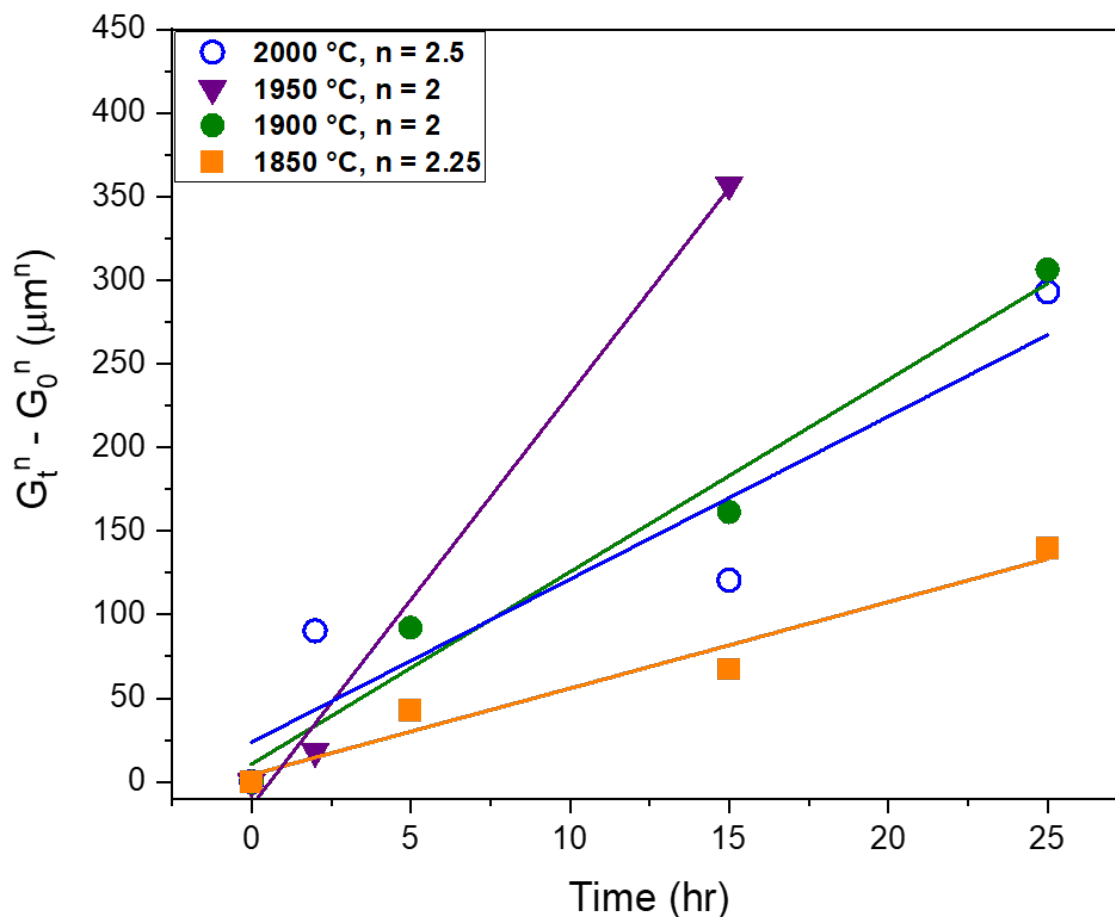


**Figure 4.7** Plot of the best fits (by  $R^2$  linear regression values) for various  $n$  values for samples sintered from 1850-2000 °C.

By taking the values for the determined grain growth rate constant,  $K$ , from the slope of the lines shown in **Figure 4.7** and applying Eqns. (2) and (3), an Arrhenius plot ( $\ln K$  vs.  $10^4/T$ ) for the 1850-1950 °C samples is represented in **Figure 4.8**. It should be noted that the value of the grain growth rate constant for the 2000 °C samples was an outlier in the dataset and was excluded in the linear regression fit. Recall that the  $R^2$  value for the 2000 °C data was lower than those for the other data points in this sample set, indicative of a poorer fit to the data. Another reason for this outlier likely arises from the fact that the average grain size for the 2000 °C data did not follow the trend of increasing grain size with increasing temperature. The 2000 °C outlier also suggests that there may be increased influence from competing mechanisms at the highest sintering temperature used in this study, such as evaporation-condensation, lattice diffusion, or low solubility impurity drag, but there is not enough data here to confirm. The slope of the linear regression line is equal to the grain growth activation energy divided by the universal gas constant ( $Q_G/R$ ); thus, the activation energy for grain growth was determined to be approximately 610 kJ/mol.

Data was extracted from work by Metroka [11] and analyzed using the same methodology as applied to the data in this work. The best fits (by  $R^2$  linear regression) for the Metroka data were also at  $n = 1.25$ ; however all the  $R^2$  values were within  $\pm 0.02$  up to  $n = 2$ , thus the data is plotted using  $n = 2$  and is seen in the inset of **Figure 4.8**, having a grain growth activation energy of 360 kJ/mol.

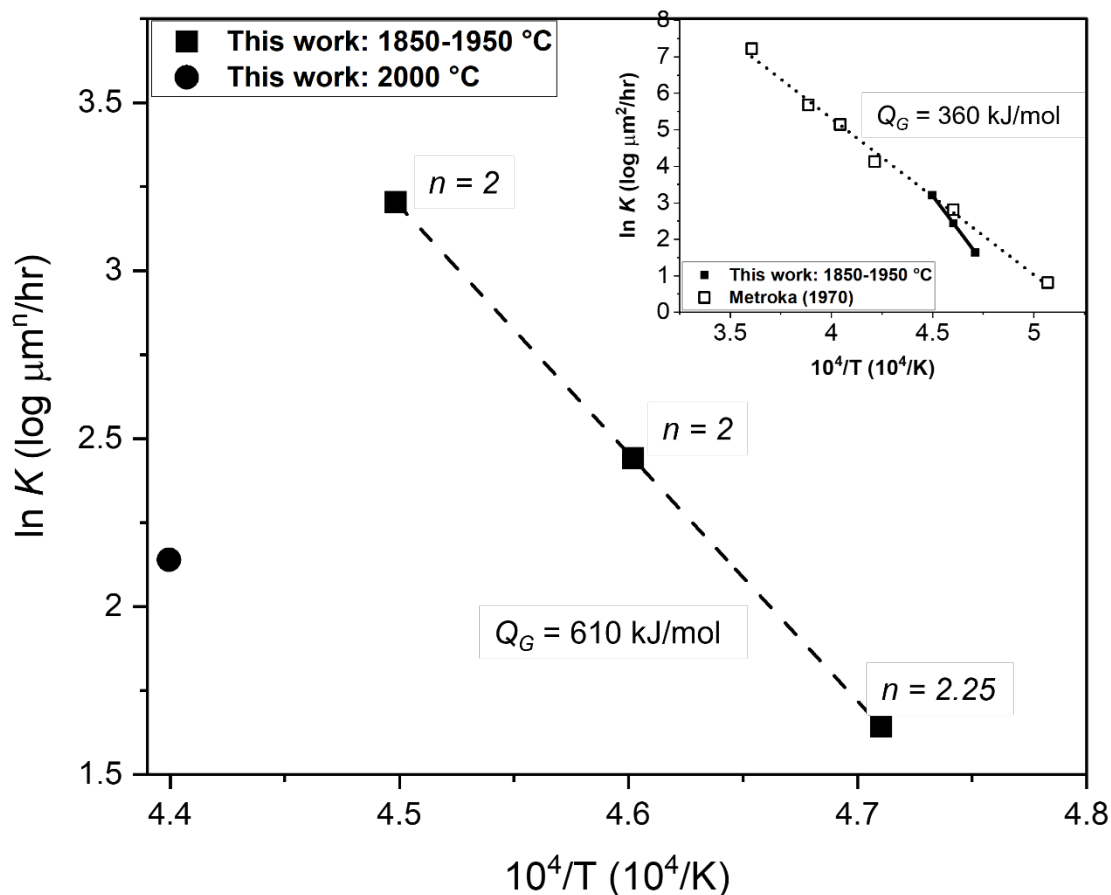


**Figure 4.8** Arrhenius plot ( $\ln K$  versus  $10^4/T$ ) with the grain growth rate constant,  $K$ , values taken from the best fit of the linear regression lines for the 1850-1950 °C sintered samples (i.e., slope of the plots in Figure 7). The data point for the 2000 °C sample fell as an outlier and was excluded from the linear regression fit. Inset shows the data from this work compared to the data from Metroka [11] using the same methodology.

Activation energies were also calculated from an Arrhenius plots assuming a consistent grain growth mechanism, e.g.  $n = 2$  for grain boundary diffusion and  $n = 3$  (likely attributed coalescence of a second phase (porosity) by lattice diffusion or to low solubility impurity drag) [18]. The plots with the affiliated activation energies shown are presented in **Figure 4.9** and **Figure 4.10**. Again, the data point for the 2000 °C samples fell as an outlier and was not included in the linear regression fit. Across the full temperature regime (1850-1950 °C), the values for the grain growth activation energy

increased to 940 kJ/mol and 1100 kJ/mol for  $n = 2$  and  $n = 3$ , respectively. Similar results were seen when applying this approach to the Metroka data, the resulting grain growth activation energy also increased to 540 kJ/mol for  $n = 3$ . **Table 4.3** summarizes these values for easier comparison.

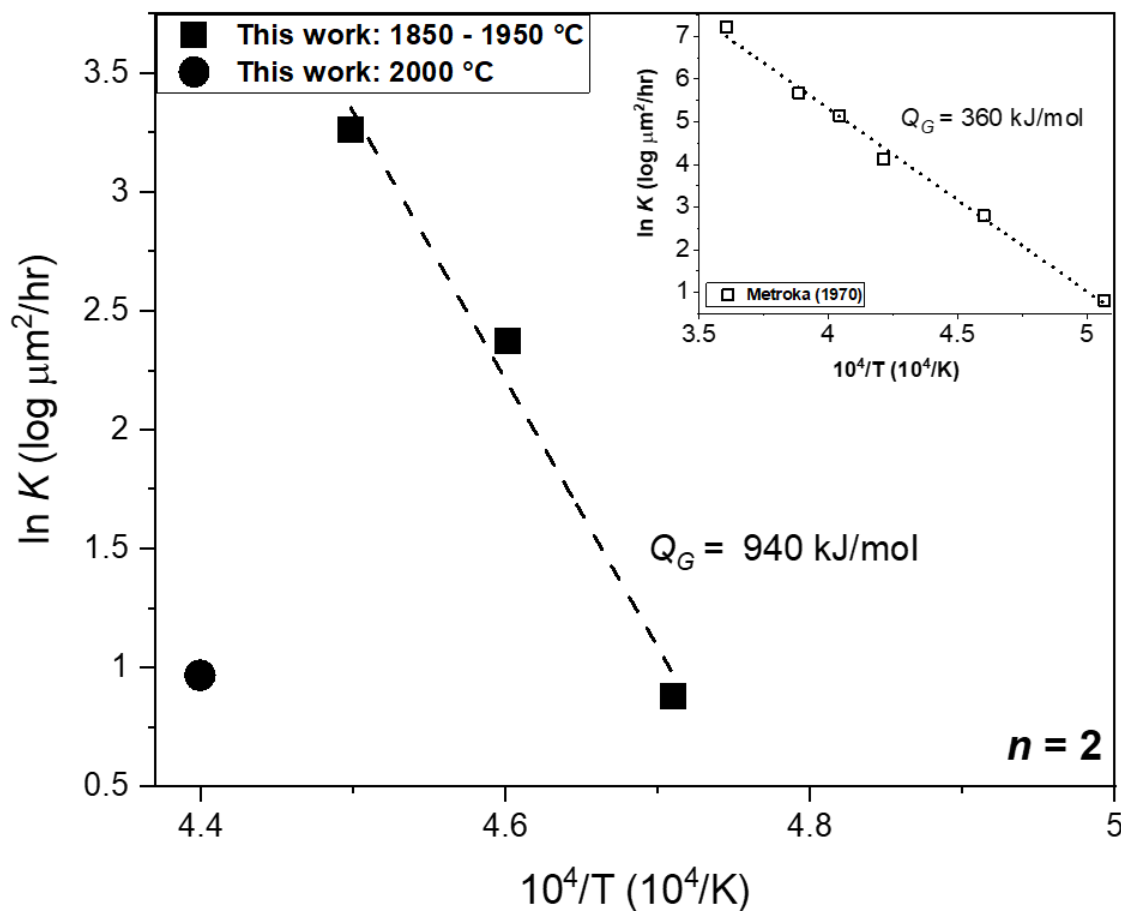


**Figure 4.9** Arrhenius plot for the sintered samples used in this study assuming a consistent dominant grain growth mechanism of grain boundary diffusion (i.e., using a value for the grain growth exponent of  $n = 2$ ). A linear regression fit to the data points is shown for the 1850-1950 °C samples. The data point for the 2000 °C sample fell as an outlier and was excluded from the linear regression fit. The inset is the data extracted from Metroka [11] plotted here for comparison using the same methodology. Activation energies are noted next to their respective plots.

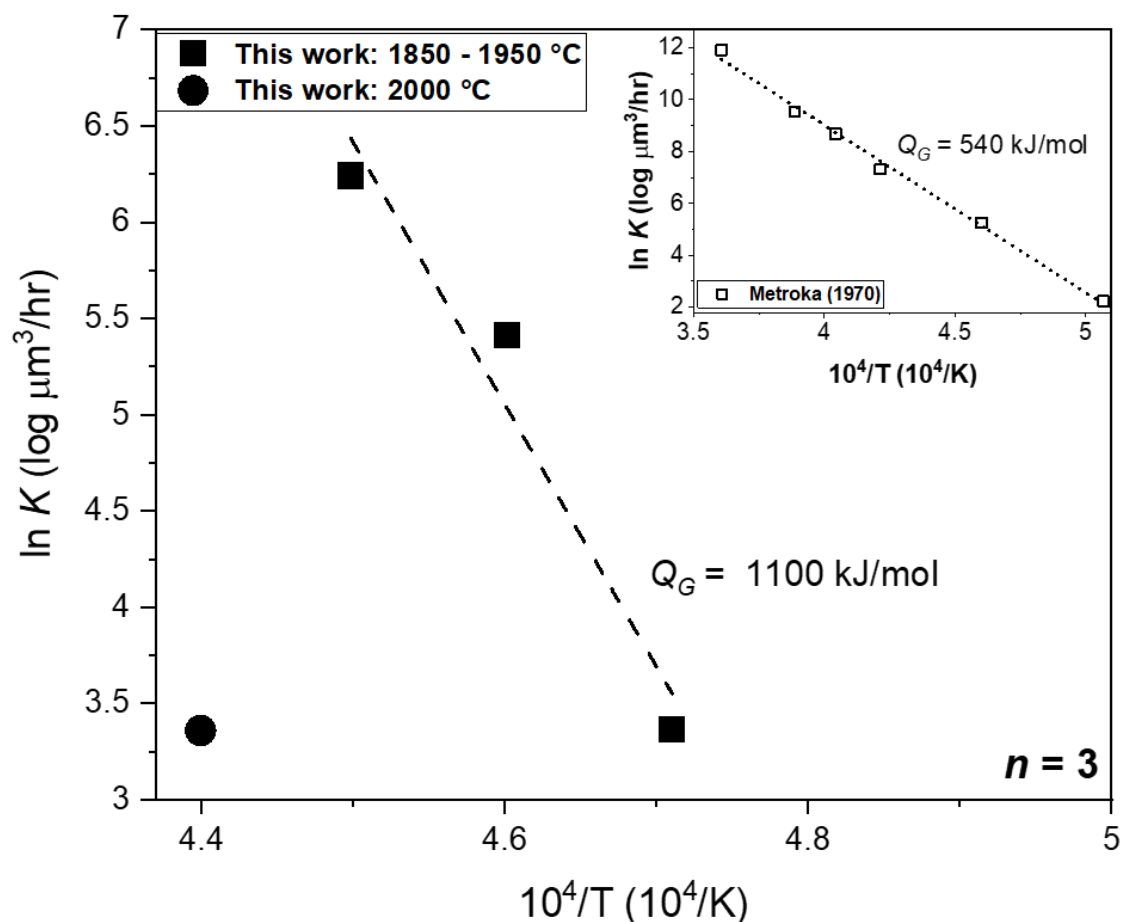


**Figure 4.10** Arrhenius plot for the sintered samples used in this study assuming a consistent dominant grain growth mechanism of second phase (porosity) by lattice diffusion or low solubility impurity drag (i.e., using a value for the grain growth exponent of  $n = 3$ ). A linear regression fit to the data points is shown for the 1850-1950 °C samples. The data point for the 2000 °C sample fell as an outlier and was excluded from the linear regression fit. The inset is the data extracted from Metroka [11] plotted here for comparison using the same methodology. Activation energies are noted next to their respective plots.

**Table 4.3** Calculated grain growth activation energies for the sintered samples used in this study and for data extracted from Metroka [11] when considering a consistent dominant grain growth mechanism ( $n = 2$  and  $n = 3$ ).

Grain growth activation energy, $Q_G$ (kJ/mol)		
	Grain growth exponent, $n = 2$	Grain growth exponent, $n = 3$
This work: 1850 – 1950 °C	940	1100
Metroka [11]: 1700 – 2500 °C	360	540

The results indicated here suggest that, while the likely dominant grain growth mechanism for conventionally sintered UN samples is best correlated to grain boundary diffusion, the large activation energies obtained in this work indicate a significant contribution from error in the collected data. The results do not fit precisely to a specific grain growth exponent and since different mechanisms are attributed to the same  $n$  value, it is likely that competing mechanisms are simultaneously active in the UN system. As noted in **Table 4.1**, a value of 2 for the grain growth exponent could be related to pore control through vapor transport, but also to grain boundary diffusion in a pure system and high solubility impurity drag. Reports on other ceramic systems have shown that higher porosity at lower temperatures likely supports a pore control mechanism like diffusion at the pore surface, but at higher temperatures and lower porosity, lattice diffusion is dominant [42]. Many of the grain growth exponent values for grain boundary diffusion, listed in **Table 4.1**, are related to the presence of a second phase, which includes porosity as the second phase. While the influence of an impurity second phase cannot be completely ruled out for the samples in this study, it is unlikely since the samples appeared to be primarily UN (per XRD), but porosity could be considered the second

phase. As mentioned, a grain growth exponent equal to 3 could also indicate a mechanism of grain growth due to low solubility impurity drag. Although the literature on grain growth in conventionally sintered UN does not specify a grain growth mechanism, the fit of the literature data in this work [11], and work by Accary and Marchal [12] suggests that the grain growth exponent does correspond best to  $n = 2$ , but additional analysis would help further elucidate what is contributing to the spread in the best fit  $n$  values. The study by Accary and Marchal on heat treatments of UN at temperatures of 1200-2200 °C also suggests a wide grain size distribution in the sintered materials (similar to the data in this work) and that their results agree that the grain growth corresponds to  $n = 2$  (a  $\sqrt{t}$  dependence —  $G \approx t^{1/n}$  [18]) [12]. Two distinct stages of grain growth were reported: Initial growth of small grains (activation energy 126 kJ/mol) and initial and second growth of coarse grains (108 and 146 kJ/mol, respectively), considerably lower than what was calculated for the samples in this study [12]. It was noted the heat treatments were performed under vacuum, but it is difficult to evaluate what other factors could be attributed to the differences in activation energies as no details with regards to starting feedstock, initial particle size, or impurity, and phase content were provided [12]. While only the Metroka [11] report had enough specific grain size detail to make a direct comparison to this work, other researchers have reported some details on UN grain growth for conventionally sintered samples. Matthews *et al.* reported on UN fabrication in support of the development of irradiation test assemblies (SP-1) as part of the research on the SP-100 space reactor program [3]. It was reported that relatively low density ( $\approx 87\%$  TD) UN pellets, sintered at 1800 °C for 2 hours had a starting grain size of 17  $\mu\text{m}$ , and that other samples ( $\approx 95\%$  TD, sintering and heat

treatment not specified) had larger grain sizes of 45  $\mu\text{m}$  [3]. A study of grain growth in spark plasma sintered UN suggests that the grain growth mechanism was grain rotation and coalescence — the presence of limited boundaries having a low-angle misorientation implies it is grain rotation that eliminates the low-energy, low angle grain boundaries resulting in coalescence — but no determination of the grain growth exponent or activation energy was explored [15]: It is possibly because classical sintering theory is not believed to be sufficient for explaining the grain growth behavior in the rapid densification processes [43]. Grain boundary mobility has been shown to be affected by grain misorientation [44] and further investigation of the ratio of low-angle/high angle grain boundaries in this UN sample set may provide some insight as to whether or not grain rotation and coalescence was a contributing factor to the grain growth.

As the 2000 °C samples fell outside the dataset when attempts to fit to a grain boundary or volume diffusion mechanism were applied, it is proposed that a change in mechanism at higher temperatures is likely, such as a shift to pore control via a combination of surface or lattice diffusion, and could correspond to even higher values of the grain growth exponent ( $> 4$ ) [45]. It is also likely that the kinetics and mechanism of UN grain growth cannot be accurately determined through application of the simplistic general grain growth Eqn. (1) and that additional influences must be considered. As mentioned previously, the results for the activation energies determined in this work need to be considered in context with the factors that contributed to experimental error. An assumption is made that the material is only exhibiting normal grain growth kinetics when applying Eqn. (1) for determination of grain growth kinetics. This means the material should have a unimodal grain size distribution, and the samples in this work

exhibited a multi-modal grain size distribution (see Figures S1-S4 in Appendix D). Additionally, the grain size distribution indicates that there is evidence that the grain size distribution does not follow a Hillert distribution [46], where the maximum grain radius exceeds the average grain radius by a factor of 2, indicating the grain growth likely did not follow a uniform growth pattern [27]. This deviation from normal grain growth behavior is likely a major factor in the unusually large activation energy values determined in this work. Additionally, the exclusion of the 1950/25 sample in calculation of the grain growth rate factor constant, and exclusion of the 2000 °C data in the linear regression fit for activation energy calculations also gives rise to the assumption that there exists a large error associated with the values of the grain growth activation energies noted in this work. Grain growth activation energies greater than 600-700 kJ/mol for nitride ceramics, specifically conventionally sintered  $\beta$ -Si<sub>3</sub>N<sub>4</sub>, has been reported in literature, but that specific process includes an  $\alpha \rightarrow \beta$  phase transformation and anisotropic grain boundary energies resulting from the  $\beta$ -Si<sub>3</sub>N<sub>4</sub> elongated grains [47]. It would not be expected that the activation energies would be on this order of magnitude for the UN system, but much closer to the values determined for the Metroka work or the Accary and Marchal work. Higher activation energies have been reported for sintering of UO<sub>2</sub> and results similar to what is reported here (i.e. higher activation energies when applying higher values of  $n$  in the grain growth mechanism calculations) were also shown [48]. Bourgeois *et al.* summarized work on the activation energies and reported grain growth exponents for UO<sub>2</sub> for identified mechanisms of pore control through evaporation/condensation but noted that it was difficult to confirm that the mechanism controlling grain boundary migration through the use of the classic grain growth equation

[48]. It was also stated that the relationships identified between the kinetic parameters  $n$ ,  $K$ , and  $Q_G$  simply reflect the choice of better fitting experimental points rather than physical quantities. Bourgeois *et al.* indicated their result of 701 kJ/mol (obtained through the same methodology applied in this work) was considered too high and that activation energies determined using this method should be viewed cautiously [48].

There are other factors that should be considered when determining what may be contributing to the differences in activation energy in this work as compared to literature. As discussed by Matzke [49], the rate controlling species for many high temperature kinetic processes in nuclear ceramics (sintering, grain growth, creep, etc.) is the diffusion of uranium. The difficulties in achieving high densities and large grain sizes in UN can be partially attributed to the low volume diffusion rates of uranium [49, 50]. The uranium diffusion rates in  $UN_{1+x}$  (reported on the order of  $10^{-15}$  to  $10^{-12}$  cm<sup>2</sup>/s from 1600-1860 °C) [50], may be also considered to be artificially high given that grain boundaries, internal surfaces and pores act as fast diffusion paths [49]. . Also, the uranium atom diffusion rate decreases with decreasing nitrogen partial pressure in UN [49], which could also help explain the differences in activation energies between this work and the Metroka data where they used a higher nitrogen partial pressure during sintering ( $6.8 \times 10^{-2}$  MPa). As noted by Matzke,  $U_2N_3$  and  $UO_2$  secondary phases can affect sintering of UN, but the reports listed by Matzke are somewhat contradictory to each other [49]. Negative effects on sintered densities were reported for low  $UO_2$  amounts (1 wt%) but increased densities with a maximum of 5 wt%  $UO_2$  have been seen [49]. Control of oxygen and carbon impurities is an important parameter to consider given that these impurities, when dissolved in the UN lattice, can diffuse quicker to the grain boundaries and result in a

drag effect, pinning the grain boundaries (Zener effect) and effectively retarding grain growth [18]. This impurity drag effect (corresponding to a grain growth exponent equal to 3) could also contribute to the differences seen between this work and the literature data — but is difficult to quantify as the impurity concentrations noted in the literature are not specific to a sample with a corresponding grain size. The feedstock powder used in this study had higher carbon impurity content but lower oxygen impurities than the two feedstock powders used in the Metroka work (93/665 ppm C; 2450/2125 ppm O), all which decreased after sintering to 25-375 ppm C and 418-2500 ppm O [11]. Unfortunately, light element analysis could not be completed on the sintered samples in this study to provide insight as to the potential effects of impurity drag on UN grain growth. It has been reported that preferential orientation and collection of impurities at the grain boundaries will cause a divergence from the parabolic form of Eqn. 1 [28]. No preferential orientation was seen in the samples used in this work and more detailed grain boundary characterization (such as through the use of transmission electron microscopy) to identify and quantify the amount of possible impurity content was not able to be completed. Therefore, the amount of influence that the impurity drag effect may play in the calculation of grain growth activation energies for this work is unknown. A systematic study on the grain growth as a function of carbon and oxygen content is warranted. In addition, the effect of the N/U ratio on diffusion coefficients is needed to fully elucidate the grain growth mechanism, which is known to vary greatly with nitrogen partial pressure during processing [49]. Non-stoichiometry can also influence grain growth. The activation energy for grain growth would likely be lower for a hyperstoichiometric material, like what has been shown for  $\text{UO}_{2+x}$ , where excess O ions

occupy interstitial positions leading to additional uranium ion vacancies (from a Schottky defect equilibrium principle) which will enhance the uranium ion diffusion rate [51], and a similar effect could be assumed for hyperstoichiometry in UN. The N/U ratio for the sintered UN materials in this study was not known so the effect of stoichiometry on the activation energy cannot be determined. More experimentation with very well-characterized materials and stringent regulation of sintering parameters is necessary to provide a like for like comparison of UN grain growth kinetics data.

#### **4.4 Summary**

The mechanism by which grain growth occurs in conventionally sintered UN remains complex and not well-understood. The multi-faceted nature of factors which influence grain growth behavior in ceramics, particularly UN, makes it challenging to identify a specific mechanism. While the results of this study suggest that the most likely mechanism dominating grain growth in conventionally sintered UN is grain boundary diffusion, competing mechanisms of lattice diffusion and low solubility impurity drag are also likely occurring. It is also postulated that a change in mechanism occurs at higher sintering temperatures: Possibly a switch to pore controlled mechanism via surface or lattice diffusion. It was determined that no preferential grain orientation is observed during grain growth. Comparing this work to what exists in the open literature is complex due to differences and unknowns in fabrication methods, starting particle size, sintering atmospheres, sintering temperatures, and starting and ending impurity concentrations, all of which could contribute to the differences seen in the activation energies. Additionally, the high activation energies determined for this work must be considered in terms of the experimental error introduced from the exclusion of data points due to a clear indication

of abnormal grain growth. For additional insight to the factors affecting the grain growth for UN samples in this study, additional research on the impurity concentrations in the sintered materials (namely oxygen and carbon), and a definitive determination of the N/U ratio in the sintered pellets is warranted. This work has provided data which can be utilized in future computational models and will assist efforts in developing fuel qualification for UN's use in the existing and future nuclear reactor fleets. The limited amount of data in the open literature regarding the UN grain growth mechanism(s), kinetics, and activation energies merits additional investigation and is an area of potential research opportunity.

### **Acknowledgements**

This work was supported by the U.S. Department of Energy, Office of Nuclear Energy under DOE Idaho Operations Office Contract DE-AC07-05ID14517, and NASA-DOE Interagency Agreement NNH20OB29A. Accordingly, the U.S. Government retains and the publisher, by accepting the article for publication, acknowledges that the U.S. Government retains a nonexclusive, paid-up, irrevocable, worldwide license to publish or reproduce the published form of this manuscript or allow others to do so, for U.S. Government purposes. **U.S. Department of Energy Disclaimer:** This information was prepared as an account of work sponsored by an agency of the U.S. Government. Neither the U.S. Government nor any agency thereof, nor any of their employees, makes any warranty, express or implied, or assumes any legal liability or responsibility for the accuracy, completeness, or usefulness of any information, apparatus, product, or process disclosed, or represents that its use would not infringe privately owned rights. References herein to any specific commercial product, process, or service by trade name, trademark,

manufacturer, or otherwise, does not necessarily constitute or imply its endorsement, recommendation, or favoring by the U.S. Government or any agency thereof. The views and opinions of authors expressed herein do not necessarily state or reflect those of the U.S. Government or any agency thereof.

### References

- [1] G.J. Youinou, R.S. Sen, Impact of accident-tolerant fuels and claddings on the overall fuel cycle: A preliminary systems analysis, *Nuclear Technology* 188 (2) (2014) 123-138.
- [2] L.H. Ortega, B.J. Blamer, J.A. Evans, S.M. McDeavitt, Development of an accident-tolerant fuel composite from uranium mononitride (UN) and uranium sesquisilicide ( $U_3Si_2$ ) with increased uranium loading, *Journal of Nuclear Materials* 471 (2016) 116-121.
- [3] R. Matthews, K. Chidester, C. Hoth, R. Mason, R. Petty, Fabrication and testing of uranium nitride fuel for space power reactors, *Journal of Nuclear Materials* 151 (3) (1988) 345.
- [4] N.R. Brown, A. Aronson, M. Todosow, R. Brito, K.J. McClellan, Neutronic performance of uranium nitride composite fuels in a PWR, *Nuclear Engineering and Design* 275 (2014) 393-407.
- [5] J. Zakova, J. Wallenius, Fuel residence time in BWRs with nitride fuels, *Annals of Nuclear Energy* 47 (2012) 182-191.
- [6] S.L. Hayes, J.K. Thomas, K.L. Peddicord, Material property correlations for uranium mononitride: 1. physical properties, *Journal of Nuclear Materials* 171 (2-3) (1990) 262-270.
- [7] R.B. Matthews, Irradiation performance of nitride fuels, Los Alamos National Lab., NM (United States), 1993.

- [8] J.K. Watkins, A. Gonzales, A.R. Wagner, E.S. Sooby, B.J. Jaques, Challenges and opportunities to alloyed and composite fuel architectures to mitigate high uranium density fuel oxidation: Uranium mononitride, *Journal of Nuclear Materials* 553 (2021) 153048.
- [9] M.R. Tonks, Y. Zhang, X. Bai, NEAMS FPL M2 Milestone Report: Development of a UO<sub>2</sub> Grain Size Model using Multiscale Modeling and Simulation, Idaho National Lab.(INL), Idaho Falls, ID (United States), 2014.
- [10] K. Shrestha, T. Yao, J. Lian, D. Antonio, M. Sessim, M. Tonks, K. Gofryk, The grain-size effect on thermal conductivity of uranium dioxide, *Journal of Applied Physics* 126 (12) (2019) 125116.
- [11] R.R. Metroka, Fabrication of uranium mononitride compacts, *National Aeronautics and Space Administration* 1970.
- [12] A. Accary, M. Marchal, Behavior of Uranium Mononitride under Heat Treatment, *Mem. Sci. Rev. Met.* 59 (1962).
- [13] B.J. Jaques, J. Watkins, J.R. Croteau, G.A. Alanko, B. Tyburska-Pueschel, M. Meyer, P. Xu, E.J. Lahoda, D.P. Butt, Synthesis and sintering of UN-UO<sub>2</sub> fuel composites, *Journal of Nuclear Materials* 466 (2015) 745-754.
- [14] H. Muta, K. Kurosaki, M. Uno, S. Yamanaka, Thermal and mechanical properties of uranium nitride prepared by SPS technique, *Journal of Materials Science* 43 (19) (2008) 6429-6434.
- [15] K.D. Johnson, D.A. Lopes, Grain growth in uranium nitride prepared by spark plasma sintering, *Journal of Nuclear Materials* 503 (2018) 75-80.
- [16] G. Kim, J. Ahn, S. Ahn, Grain growth and densification of uranium mononitride during spark plasma sintering, *Ceramics International* 47 (5) (2021) 7258-7262.
- [17] S.M. Bragg-Sitton, M. Todosow, R. Montgomery, C.R. Stanek, R. Montgomery, W.J. Carmack, Metrics for the Technical Performance Evaluation of Light Water Reactor Accident-Tolerant Fuel, *Nuclear Technology* 195 (2) (2016) 111-123.

- [18] R. Brook, Controlled grain growth, Treatise on Materials Science & Technology, Elsevier 1976 pp. 331-364.
- [19] V. Tennery, T. Godfrey, R. Potter, Sintering of UN as a function of temperature and N<sub>2</sub> pressure, Journal of the American Ceramic Society 54 (7) (1971) 327-331.
- [20] ASTM, Standard Test Methods for Density of Compacted or Sintered Powder Metallurgy (PM) Products Using Archimedes' Principle, B962, ASTM International, West Conshohocken, PA, 2017.
- [21] U. Holzwarth, N. Gibson, The Scherrer equation versus the 'Debye-Scherrer equation', Nature Nanotech Nature Nanotechnology 6 (9) (2011) 534.
- [22] T. Degen, M. Sadki, E. Bron, U. Konig, G. Nenert, The HighScore suite, Powder Diffraction 29 (2014) S13-S18.
- [23] H. Holleck, E. Smailos, F. Thümmeler, Zur mischphasenbildung der mononitride in den systemen U- (Y, La, Pr)-N, Journal of Nuclear Materials 32 (2) (1969) 281-289.
- [24] T. Nagaya, S.R. Wallis, Y. Seto, A. Miyake, Y. Soda, S. Uehara, M. Matsumoto, Minimizing and quantifying mis-indexing in electron backscatter diffraction (EBSD) determinations of antigorite crystal directions, Journal of Structural Geology 95 (2017) 127-141.
- [25] J.M. Sosa, D.E. Huber, B. Welk, H.L. Fraser, Development and application of MIPAR™: a novel software package for two-and three-dimensional microstructural characterization, Integrating materials and manufacturing innovation 3 (1) (2014) 123-140.
- [26] J. Burke, D. Turnbull, Recrystallization and grain growth, Progress in metal physics 3 (1952) 220-292.
- [27] F. Gil, J. Planell, Behaviour of normal grain growth kinetics in single phase titanium and titanium alloys, Materials Science and Engineering: A 283(1-2) (2000) 17-24.

- [28] A.T. Motta, D.R. Olander, B. Wirth, *Light Water Reactor Materials*, American Nuclear Society 2017.
- [29] T. Maki, Ferrite and Austenite: Grain Growth, in: K.H.J. Buschow, R.W. Cahn, M.C. Flemings, B. Ilshner, E.J. Kramer, S. Mahajan, P. Veysseyre (Eds.), *Encyclopedia of Materials: Science and Technology*, Elsevier, Oxford, 2001, pp. 3012-3015.
- [30] R.M. German, *Sintering theory and practice*, John Wiley & Sons, Inc., New York, 1996.
- [31] M.N. Rahaman, *Sintering of ceramics*, CRC Press, Boca Raton, FL, 2008.
- [32] OriginLab, OriginPro, OriginLab Corporation, Northampton, MA, USA, 2020.
- [33] P. Zhao, X. Liu, A. De La Torre, L. Lu, K. Sobolev, Assessment of the quantitative accuracy of Rietveld/XRD analysis of crystalline and amorphous phases in fly ash, *Analytical Methods* 9 (16) (2017) 2415-2424.
- [34] L.E. Russell, The sintering of pyrophoric powders, *Powder Metallurgy* 10 (20) (1967) 239-263.
- [35] R. German, *Sintering: from empirical observations to scientific principles*, Butterworth-Heinemann 2014.
- [36] J.D. Powers, A.M. Glaeser, Grain boundary migration in ceramics, *Interface Science* 6 (1) (1998) 23-39.
- [37] J. Ainscough, B. Oldfield, J. Ware, Isothermal grain growth kinetics in sintered UO<sub>2</sub> pellets, *Journal of Nuclear Materials* 49 (2) (1973) 117-128.
- [38] W. Kingery, B. Francis, Grain growth in porous compacts, *Journal of the American Ceramic Society* 48 (10) (1965) 546-547.
- [39] D. Fan, S. Chen, L.-Q. Chen, Computer simulation of grain growth kinetics with solute drag, *Journal of materials research* 14(3) (1999) 1113-1123.
- [40] K. Kruska, A. Rohatgi, R.S. Vemuri, L. Kovarik, T.H. Moser, J.E. Evans, N.D. Browning, Grain growth in nanocrystalline Mg-Al thin films, *Metallurgical and Materials Transactions A* 48(12) (2017) 6118-6125.

- [41] R. Dannenberg, E. Stach, J.R. Groza, B.J. Dresser, TEM annealing study of normal grain growth in silver thin films, *Thin Solid Films* 379(1-2) (2000) 133-138.
- [42] G. Kerbart, C. Manière, C. Harnois, S. Marinel, Predicting final stage sintering grain growth affected by porosity, *Applied Materials Today* 20 (2020) 100759.
- [43] J. Hu, Z. Shen, Grain growth by multiple ordered coalescence of nanocrystals during spark plasma sintering of SrTiO<sub>3</sub> nanopowders, *Acta Materialia* 60 (18) (2012) 6405-6412.
- [44] G. Gottstein, D.A. Molodov, L.S. Shvindlerman, D.J. Srolovitz, M. Winning, Grain boundary migration: misorientation dependence, *Current Opinion in Solid State and Materials Science* 5(1) (2001) 9-14.
- [45] N. Daneu, A. Rečnik, S. Bernik, Grain-growth phenomena in ZnO ceramics in the presence of inversion boundaries, *Journal of the American Ceramic Society* 94 (5) (2011) 1619-1626.
- [46] M. Hillert, On the theory of normal and abnormal grain growth, *Acta Metallurgica* 13 (3) (1965) 227-238.
- [47] S.-M. Han, S.-J.L. Kang, Kinetics of Beta-Si<sub>3</sub>N<sub>4</sub> grain growth in Si<sub>3</sub>N<sub>4</sub> ceramics sintered under high nitrogen pressure, *Journal of the American Ceramic Society* 76 (12) (1993) 3178-3179.
- [48] L. Bourgeois, P. Dehaut, C. Lemaignan, J. Fredric, Pore migration in UO<sub>2</sub> and grain growth kinetics, *Journal of nuclear materials* 295(1) (2001) 73-82.
- [49] H. Matzke, Science of advanced LMFBR fuels, North-Holland Physics Publishing, Amsterdam, The Netherlands, 1986.
- [50] D.K. Reimann, D.M. Kroegbr, T.S. Lundy, Cation self-diffusion in UN<sub>1+x</sub>, *Journal of Nuclear Materials* 38 (2) (1971) 191-196.
- [51] T. Yao, K. Mo, D. Yun, S. Nanda, A.M. Yacout, J. Lian, Grain growth and pore coarsening in dense nano-crystalline UO<sub>2+x</sub> fuel pellets, *Journal of the American Ceramic Society* 100(6) (2017) 2651-2658.

CHAPTER FIVE: ENHANCING THERMAL CONDUCTIVITY OF  $\text{UO}_2$  WITH THE  
ADDITION OF  $\text{UB}_2$  VIA CONVENTIONAL SINTERING TECHNIQUES

This paper has been published in the Journal of Nuclear Materials

Reference: J.K. Watkins, A.R. Wagner, S.C. Middlemas, M.C. Marshall, K. Metzger, and  
B.J. Jaques. Enhancing thermal conductivity of  $\text{UO}_2$  with the addition of  $\text{UB}_2$  via  
conventional sintering techniques. (2021). Journal of Nuclear Materials, 153421.

Enhancing thermal conductivity of  $\text{UO}_2$  with the addition of  $\text{UB}_2$  via conventional  
sintering techniques

Jennifer K. Watkins<sup>a,b</sup>, Adrian R. Wagner<sup>a</sup>, Scott C. Middlemas<sup>a</sup>, M. Craig  
Marshall<sup>a</sup>, Kathryn Metzger<sup>c</sup>, Brian J. Jaques<sup>b,d</sup>

<sup>a</sup> Idaho National Laboratory, Idaho Falls, ID, USA

<sup>b</sup> Micron School of Materials Science and Engineering, Boise State University, Boise, ID, USA

<sup>c</sup> Westinghouse Electric Company LLC, Pittsburgh, PA, USA

<sup>d</sup> Center for Advanced Energy Studies, Idaho Falls, ID, USA

Author Contributions

Jennifer K. Watkins: Conceptualization, Investigation, Writing – Original Draft, Review  
and Editing

Adrian R. Wagner: Conceptualization, Investigation, Resources, Supervision, Writing –  
Original Draft, Review and Editing

Scott C. Middlemas: Investigation, Writing – Original Draft, Review and Editing

M. Craig Marshall: Investigation, Writing – Review and Editing

Kathryn Metzger: Resources, Writing – Review and Editing

Brian J. Jaques: Resources, Supervision, Writing - Review and Editing

## Abstract

Uranium dioxide has been the primary fuel type used in light water reactors for more than 40 years and proven to be reliable and robust. However, the Fukushima-Daiichi nuclear accident has motivated new work evaluating fuels with characteristics promoting accident tolerance, including enhanced thermal conductivity. Recently, additives have been investigated to increase thermal conductivity, but research has been largely focused on non-fissile additions. This study investigated the use of fissile additives to not only increase the thermal conductivity but also increase the uranium loading. Uranium diboride was chosen as the additive for this study due to its promising corrosion behavior as well as its significantly higher thermal conductivity at 573 K ( $25 \text{ Wm}^{-1}\text{K}^{-1}$ ) when compared to  $\text{UO}_2$  ( $7 \text{ Wm}^{-1}\text{K}^{-1}$ ). Uranium diboride powder was fabricated via the arc melting technique and a ball milling process prior to mixing with  $\text{UO}_2$  in a 90/10 wt%  $\text{UO}_2/\text{UB}_2$  ratio. Green bodies were made using a uniaxial die and subjected to a traditional pressureless sintering technique at 2073 K in argon. Sintered samples were analyzed via laser flash analysis for thermal diffusivity and differential scanning calorimetry for specific heat capacity in order to calculate thermal conductivity. The samples displayed an increase of 36-55% in thermal conductivity between 323 K and 1273 K when compared to the benchmark samples (pure  $\text{UO}_2$ ) as reported in open literature.

## 5.1 Introduction

Accident tolerant fuel (ATF) types have received renewed emphasis and funding in the wake of the Fukushima-Daiichi accident in 2011. Although a few of the ATF concepts have been based around new fuel types to enhance safety and operational

characteristics, efforts are also being made to improve the performance of the benchmark fuel, uranium dioxide ( $\text{UO}_2$ ).  $\text{UO}_2$  has proven to be a robust fuel type and has been used and studied as a reactor fuel for many years in various applications. Unfortunately, the lower uranium density and thermal conductivity of  $\text{UO}_2$  (paired with Zr alloy cladding), as compared to other high uranium density fuel types being considered as ATF concepts (e.g. uranium mononitride, triuranium disilicide, uranium monocarbide), limits its future use for extended burn-up and longer cycle lengths in light water reactors (LWRs) [1, 2]. A critical challenge for the implementation of new nuclear fuel forms, such as the aforementioned ATF concepts, is the need to utilize existing  $\text{UO}_2$  manufacturing infrastructure for fuel production in order for them to be commercially viable [2]. Therefore, improving the uranium density and thermal conductivity of a  $\text{UO}_2$  based composite fuels would allow the benchmark fuel to be a viable ATF contender. Some of the research efforts in improving  $\text{UO}_2$ 's properties have focused on adding non-nuclear components such as Mo [3-5], BeO [6-8], MgO [9],  $\text{Cr}_2\text{O}_3$  [9],  $\text{Gd}_2\text{O}_3$  [10, 11],  $\text{Al}_2\text{O}_3$  [9],  $\text{TiO}_2$  [12], SiC [13, 14], and some others [15]; however, the use of non-fissile materials further decreases the uranium density of the composite fuel pellet. The use of high uranium bearing compounds, such as the aforementioned ATF concepts or other U compounds, can be utilized to not only increase thermal conductivity, but also increase the uranium density of the composite fuel pellet [16]. An increase in thermal conductivity will lower peak fuel and cladding temperatures under normal operation and in accident scenarios thereby improving the safety margins, while an increase in uranium density will allow for improved operational economy due to ability to achieve higher burnup and longer cycle lengths [17]. This work describes the efforts to improve upon  $\text{UO}_2$ 's thermal

conductivity and uranium density with the addition of nominal amounts of another ATF concept fuel, uranium diboride ( $\text{UB}_2$ ) [18-22], fabricated using conventional sintering methods.

## 5.2 Background

Uranium diboride is known to have high thermal conductivity, high uranium density, and high melting temperature, as shown in **Table 5.1** [19, 21, 23] and is similar to other fuel concepts considered as ATF contenders (i.e. UN,  $\text{U}_3\text{Si}_2$ , and UC). Much of the existing literature for  $\text{UB}_2$  is based on investigations into thermal, electronic, elastic and mechanical properties using theoretical approaches (density function theory) [19, 24-26]. Experimental work on  $\text{UB}_2$ , especially at high temperatures, is limited, and largely focused on thermophysical and mechanical properties [20, 21, 27-35]. As previously stated, an economic driver for commercial implementation of a new fuel is the ability to use existing production infrastructure, however, it has been reported that  $\text{UB}_2$  is difficult to sinter via conventional methods [21]. Fabrication efforts for high density pure  $\text{UB}_2$  and composite pellets ( $\text{U}_3\text{Si}_2$ - $\text{UB}_2$  — for the purposes of improving the corrosion resistance of  $\text{U}_3\text{Si}_2$ ) [21, 34, 36], have been accomplished via pressure assisted or field assisted sintering techniques (unlikely methods for commercial fabrication). Fabrication and determination of thermophysical properties of spark plasma sintered (SPS)  $\text{UO}_2$ - $\text{UB}_2$  composites has been reported [20], however, to the best of the authors' knowledge there is no information on the conventional sintering of  $\text{UO}_2$ - $\text{UB}_2$  composites within the peer-reviewed literature.

Boride compounds have not been extensively explored as candidates for advanced multi-phase nuclear fuels for LWR use mainly due to the large thermal neutron

absorption cross-section of  $^{10}\text{B}$  (3841 b) [37]. However, the use of  $\text{UB}_2$  enriched with  $^{11}\text{B}$ , having a much lower cross-section (0.0055 b), could be implemented using an appropriate isotopic ratio of  $^{10}\text{B}/^{11}\text{B}$ . Tailoring the isotopic ratio will allow the boride phase to act as an integral burnable absorber, like has been done with the use of  $\text{Gd}_2\text{O}_3$  in  $\text{UO}_2$  [38], but also a fissile phase potentially lowering the required  $^{235}\text{U}$  enrichment of the fuel. Naturally occurring boron, which was used in this study, is 80.1%  $^{11}\text{B}$  and 19.9%  $^{10}\text{B}$  [37].

**Table 5.1** Material properties of  $\text{UO}_2$  and  $\text{UB}_2$

Material Properties	$\text{UO}_2$	$\text{UB}_2$
Uranium density ( $\text{g-U}/\text{cm}^3$ ) <sup>[19, 39]</sup>	9.7	11.7
Thermal conductivity ( $\text{W}/\text{m}\cdot\text{K}$ at 573 K) <sup>[21, 40]</sup>	7	~25
Melting temperature (K) <sup>[17, 23]</sup>	3113	2658

### 5.3 Materials and Methods

#### 5.3.1 Powder synthesis, pellet fabrication and sintering

Uranium diboride ( $\text{UB}_2$ ) powder was synthesized via a powder metallurgy and arc-melting technique where elemental uranium and powdered boron was combined to synthesize  $\text{UB}_2$ . As seen in **Figure 5.1**,  $\text{UB}_2$  is a line compound at 33 at% (8.4 wt%) B and 67 at% U (91.6 wt%). Accordingly, the nominal boron addition was adjusted to account for boron volatilization during arc-melting. The final material by mass weight just prior to arc-melting contained 67.11 at% B (8.48 wt%), which places the composition in the  $\text{UB}_2+\text{UB}_4$  phase region, with an estimated composition of 98.9%  $\text{UB}_2$ . These arc-melted materials were comminuted in a method similar to that described by Wagner *et al.* and Harp *et al.* [41, 42]. In addition, 0.2 wt% polyethylene glycol (PEG) was added to aid

in milling of the arc-melted  $\text{UB}_2$  puck. Once the  $\text{UB}_2$  was in acceptable powder form (particles  $<37\mu\text{m}$ ) it was combined with  $\text{UO}_2$  powder (purchased from Areva and held to specifications for sintered  $\text{UO}_2$  pellets for light water reactors, ASTM C-776-00 and passed through -400 mesh sieve) in a 90-10 wt% ratio of  $\text{UO}_2/\text{UB}_2$  (91.2-8.7 vol%). Particle size analysis of the  $\text{UO}_2$  and  $\text{UB}_2$  was completed via X-ray sedimentation analysis using a Micromeritics Sedigraph III 5120. The powders (bi-modal average particle size of 7 and 20  $\mu\text{m}$  and approximately 2  $\mu\text{m}$  for the  $\text{UO}_2$  and  $\text{UB}_2$ , respectively) were blended via a high energy ball milling process (315 rpm, 1 hour, Retsch PM200 planetary ball mill) in a  $\text{ZrO}_2$  milling jar with 5 mm diameter  $\text{ZrO}_2$  media and powder in an 8:1 ratio. The milled powder was then passed through a 400-mesh ( $37\mu\text{m}$ ) sieve prior to pressing into pellets of right cylindrical geometry using an automated Carver hydraulic press, at  $\sim 120\text{MPa}$  with a 9.7 mm WC die. The  $\text{UO}_2/\text{UB}_2$  composite pellets were sintered in a refractory metal sintering furnace (Thermal Technology Model 1100) under flowing ultra-high purity argon cover gas at 2073 K for 4 and 8-hours (20 K/min ramp to dwell temperature, 15 K/min ramp down to room temperature) to examine the effect of dwell time on sintered density and microstructure. The sintering profile also included a 2-hour dwell at 873 K for PEG burnout. Samples were placed directly on a tungsten sintering plate within the hot zone of the furnace. All arc-melting was performed inside an inert atmosphere glovebox having  $\leq 20$  ppm  $\text{O}_2$ . All remaining comminution processes, powder blending, pellet fabrication and sintering occurred within another glovebox at  $\leq 1$  ppm  $\text{O}_2$ . The densities of the sintered samples were determined via the Archimedes measurement method in deionized water. The resulting densities (based on calculated theoretical densities (TD) from the nominal starting composition) were  $10.65 \pm 0.1 \text{ g/cm}^3$

(95.6%TD) and  $10.74 \pm 0.06 \text{ g/cm}^3$  (96.4%TD) for the  $\text{UO}_2/\text{UB}_2$  4 and 8-hour dwell pellets, respectively.

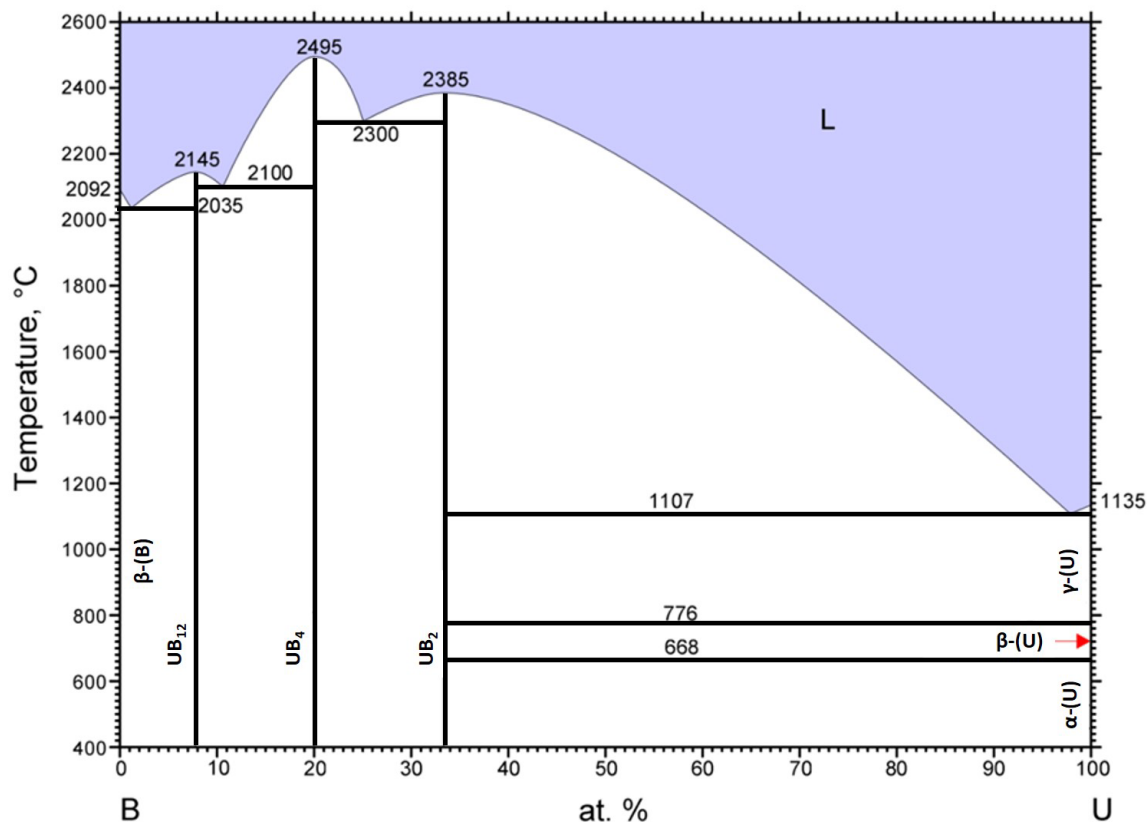


**Figure 5.1** Uranium-boron phase diagram (0-100 at% U, 400-2600 °C). Modified from Okamoto [23].

### 5.3.2 X-ray Diffraction (XRD)

Phase identification via X-ray diffraction (XRD) for the starting materials, synthesized powders, and sintered pellets was completed using a Malvern Panalytical Aeris X-ray Diffractometer (Cu  $K_{\alpha}$ , 40 kV, 15mA, step-size 0.011  $2\theta$ ). The as-sintered pellets and the pellets used for thermal property measurements were ground in a mortar and pestle and the resulting radiological powder samples (as well as the starting powdered materials) were encapsulated in Dow Corning high vacuum grease inside an inert atmosphere glovebox (<1 ppm  $\text{O}_2$ ) to avoid oxidation during transfer to the XRD

equipment and analysis. All XRD scans were run using a zero background silicon disc holder and a pattern of the blank sample holder with only vacuum grease is included in the results (**Figure 5.2**). Final material composition via phase quantification of the sintered samples was carried out using Rietveld refinement analysis within the Panalytical HighScore+ software [43]. Rietveld refinement was performed using a polynomial fit to the background and a semi-automatic fitting profile. The calculated profile was examined and compared to the experimental, and the residual plot (the portion of the net scan intensity not explained by the scaled reference patterns) was inspected for good agreement. Profile fitting used the Pseudo-Voigt profile function and refinement was completed to generate a minimized weighted residual ( $R_{wp}$ ) profile having a value of  $<10$ . The pattern fits generated from the HighScore+ software, along with the residual plots for the 4 and 8-hour as-sintered and LFA samples and the  $UO_2$ - $UB_2$  mixed powder are available in the supplementary data file. The use of the vacuum grease to encapsulate the samples does contribute an increase in the background as an amorphous phase and can result in overestimation in the quantitative results [44].

### 5.3.3 Microstructure and elemental analysis

The as-sintered pellets, as well as the pellets used for thermal property measurements, were prepared for microanalysis by mounting in epoxy followed by grinding to 1200 grit SiC paper. The pellets were ground approximately halfway through to create a cross-sectional surface that was perpendicular to the two parallel faces of the right cylinder. The cross-sectional surface was polished with MetaDi diamond suspension fluid down to 1 micron. The microstructure of the as-sintered and thermal diffusivity samples was examined with backscattered electrons (BSE) using a JEOL IT500HR

secondary electron microscope (SEM) equipped with energy dispersive spectroscopy (EDS) for elemental identification and mapping. Microstructural characterization, including phase quantification and grain size analysis, was performed using the MIPAR™ software package [45]. Images for microstructural image analysis were taken from multiple representative areas across the entire cross-sectional area on one planar surface.

#### 5.3.4 Thermal diffusivity, specific heat, and thermal conductivity

Bulk thermal diffusivity ( $\text{mm}^2/\text{sec}$ ) measurements were performed using a Netzsch laser flash analyzer (LFA 427) adhering to ASTM E1461-13, Standard Test Method for Thermal Diffusivity by the Flash Method [46]. A cover gas of ultra-high purity argon was flowed at 150 mL/min after passing through an Oxy-gon OG-120M  $\text{O}_2$  gettering furnace, resulting in  $< 1$  ppm  $\text{O}_2$  concentrations. A Pyroceram 9606 standard was used to confirm the measurement accuracy within 2%. Five 0.6 ms laser pulse shots (in 3 minute increments) were then taken and averaged at each temperature (323 – 1273 K) in 100 K increments starting at 373 K. The Cape-Lehman model integrated into the Netzsch Proteus 4.8.5 software was used to calculate the thermal diffusivity measured from each shot.

Specific heat capacity ( $C_p$ ) values ( $\text{J/g}\cdot\text{K}$ ) were measured using a Netzsch DSC 404C Differential Scanning Calorimeter (DSC) following the ASTM E1269-95 Standard Test Method for Determining Specific Heat Capacity by Differential Scanning Calorimetry using a sapphire disc as a standard reference material [47]. Measurement accuracy from this standard was  $\leq 2.22\%$ . Samples were placed into a yttria-lined platinum-rhodium crucible during testing. An ultra-high purity argon cover gas was

flowed at 50 mL/min after passing through an Oxy-gon OG-120M O<sub>2</sub> gettering furnace, resulting in a < 1 ppm O<sub>2</sub> concentration. DSC data was collected on two consecutive heating and cooling cycles from 323-1273 K in 25 K increments and the data analyzed with the Netzsch Proteus 4.8.5 thermal analysis software.

Thermal conductivity results were calculated for the UO<sub>2</sub>+10wt% UB<sub>2</sub> composites using Equation 1, the measured thermal diffusivity values, and specific heat values from the rule of mixtures (ROM) calculations for a theoretical UO<sub>2</sub> + 10wt% UB<sub>2</sub> composite taken from literature [28, 40]. In addition, the thermal expansion data was calculated based on the rule of mixtures using data found in the open literature [21, 48]. The standard deviation of the thermal diffusivity measurements is used as the main source of reported experimental error.

$$(1) \quad k = C_p * \rho * \alpha$$

*k*: thermal conductivity (W/m·K)

*C<sub>p</sub>*: heat capacity (J/g·K)

*ρ*: density (g/cm<sup>3</sup>)

*α*: thermal diffusivity (mm<sup>2</sup>/sec)

## 5.4 Results and Discussion

### 5.4.1 X-ray Diffraction

Phase identification of the synthesized powders was performed via XRD. **Figure 5.2** displays the diffraction patterns for the UO<sub>2</sub>-10 wt% UB<sub>2</sub> blended powder as well as both the 4 and 8-hour as-sintered samples and samples analyzed after thermal diffusivity measurements (hereafter referred to as LFA samples). The as-sintered and LFA samples included a LaB<sub>6</sub> National Institute of Standards and Technology standard reference

material (NIST SRM) for line position verification. Only  $\text{UO}_2$ , matching the powder diffraction file (PDF) #00-041-1422, and  $\text{UB}_2$ , PDF #98-008-5413 was identified in all the samples, no  $\text{UB}_4$  phase was identified. Additionally, due to the overlap that peaks for  $\text{U}_4\text{O}_9$  have with  $\text{UO}_2$  it is difficult to determine how much phase fraction, if any, can be attributed to the hyper-stoichiometric oxide phase. The pattern for the blank stage used in analysis is also listed as reference and does reflect a peak at  $28.4^\circ 2\theta$  attributed to the silicon disk holder of the stage.

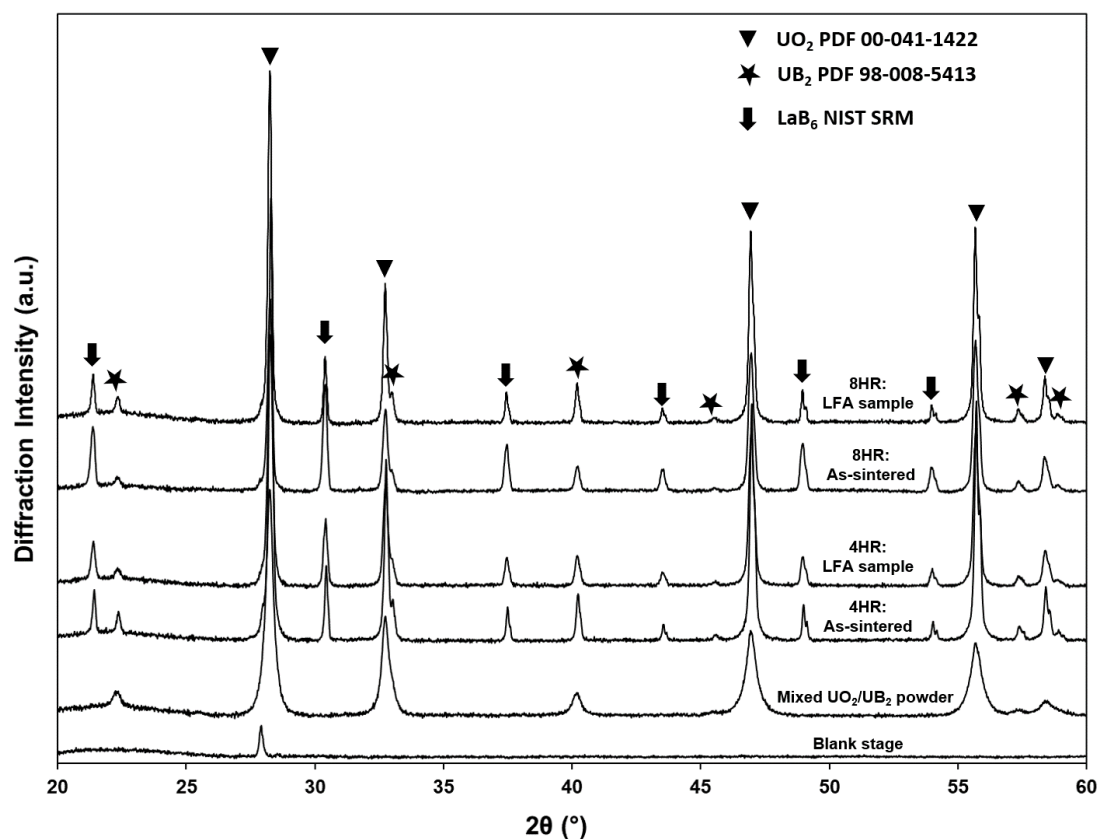


**Figure 5.2** XRD patterns of the starting mixed  $\text{UO}_2/\text{UB}_2$  powder used for pellet fabrication, the 4 and 8-hour as-sintered samples and 4 and 8-hour samples from the LFA thermal diffusivity measurements. Reference patterns for  $\text{UO}_2$ ,  $\text{UB}_2$ , and  $\text{LaB}_6$  (used for line position verification) are indicated by the symbols. Note that the mixed  $\text{UO}_2/\text{UB}_2$  powder did not include the  $\text{LaB}_6$  NIST SRM; the bottom pattern is of the blank stage used in the analysis for reference and denotes a peak attributed to the silicon disk holder on the XRD stage having a peak at  $28.4^\circ 2\theta$ .

The XRD patterns between the as-sintered and LFA samples did not appear to vary significantly either in phase or intensity. However, after Rietveld refinement, comparison of the phase fractions for the boride phase between the as-sintered samples and the LFA samples shows a slight reduction in the LFA 4-hr and 8-hr samples (-1.1 and -0.6%, respectively). Comparing the patterns for the mixed powder sample and the sintered samples shows that the  $\text{UO}_2$  and  $\text{UB}_2$  peaks in the mixed powder are broader than in the sintered samples for both the  $\text{UO}_2$  and  $\text{UB}_2$  phases; indicative of grain growth during sintering, as expected. Comparison of the full width half maximums (FWHM) for the first two peaks for both phases from the mixed powder and the 8-hour sintered sample (approximately 28.2 and 32.7  $2\theta$  for  $\text{UO}_2$  and 22.3 and 32.9  $2\theta$  for  $\text{UB}_2$ ) show the FWHM decreased in the sintered sample. For the  $\text{UO}_2$  phase the FWHM decreased from 0.312 and 0.324 to 0.193 and 0.190, and in the  $\text{UB}_2$  phase the decrease was from 0.295 and 0.326 to 0.182 and 0.174. The increase in crystallite size was calculated using the Scherrer equation [49]. The  $\text{UO}_2$  crystallites in the mixed powder and the 8-hour sintered samples were 22 nm and 45 nm, respectively, while the  $\text{UB}_2$  crystallites in the powder and the 8-hour sintered sample were calculated at 23 nm and 48 nm, respectively. The calculated and residual plots of the  $\text{UO}_2$ - $\text{UB}_2$  mixed powder, 4-hour and 8-hour LFA samples, and 4 and 8-hour as sintered XRD patterns after Rietveld refinement are included in the supplementary data file. Phase quantification after Rietveld refinement was also close to the anticipated 90-10wt%  $\text{UO}_2$ - $\text{UB}_2$  distribution (estimated at ~ 11%  $\text{UB}_2$ ) in the 8-hour as-sintered sample. It has been suggested that given the conditions during sintering and thermal property measurements (i.e. atmosphere and temperature) that  $\text{UB}_4$  could start to form at around 1073 K, or that there could be a loss of boron [20].

However, no  $UB_4$  phase was identified even though the starting composition of the  $UB_2$  prior to arc-melting was approximated at 1.1 wt%  $UB_4$ , according to the phase diagram. This suggests that the additional boron may have volatilized during arc-melting, or any remaining  $UB_4$  is below the resolution of the diffractometer. The XRD patterns for the LFA analyzed samples suggest that there may have been some loss of boron during the thermal property measurements as the boride phase was estimated at  $\sim 9\%$  and  $\sim 10\%$  for the 4-hour and 8-hour samples respectively.

#### 5.4.2 Microstructure and elemental analysis

The microstructure of the 4- and 8-hour sintered samples is seen in **Figure 5.3** and **Figure 5.4**, respectively. In both samples, the  $UB_2$  phase (lighter grey) appears to be uniformly distributed throughout the  $UO_2$  matrix (darker grey). The 4-hour sintered sample (**Figure 5.3a**) exhibits a higher amount of porosity ( $10.0 \pm 0.2\%$  per microstructural image analysis from multiple representative cross-sectional images) than the 8-hour sample ( $6.4 \pm 0.2\%$ , **Figure 5.4a**), even though the measured density of both samples was approximately 96% TD, which could suggest less open and interconnected porosity in the sample sintered for 8-hours. Also, some of the porosity displayed in the micrographs has been attributed to pullout of the oxide phase during the grinding and polishing of the sample in preparation for microscopy, but more so in the 4-hour sintered sample. It appears the pullout is greater at or near the  $UO_2$ - $UB_2$  grain boundary interfaces, as denoted by the red arrows in **Figure 5.3b**. This is likely due to less time in the final sintering stage for the 4-hour sample, resulting in more continuous pore channels throughout the monolithic sample and a lesser degree of bonding between the phases than in the 8-hour sample. Additional confirmation that much of the porosity can be attributed

to pullout during mechanical polishing is seen in an SEM image taken from the same 8-hour as-sintered sample after focused ion beam polishing. That image (included in the supplementary data file published with the online version of this manuscript, Figure 5s) shows a level of porosity that agrees with the measured density. The elemental mapping via EDS for qualitative analysis of uranium (red), oxygen (yellow), and boron (green) is shown for the mapped areas of **Figure 5.3b** and **Figure 5.4b**. However, it is important to note that elemental mapping is only qualitative since EDS cannot accurately quantify light elements such as oxygen and boron. The LFA samples were examined with SEM to confirm that no difference in microstructure was seen after thermal property characterization. Backscatter images and EDS mapping of the 4- and 8-hour LFA thermally characterized samples are included in the supplementary data file for this manuscript. Microstructural analysis using MIPAR™ analysis software [45] was performed on multiple micrographs (> 2000 grains) of the 8-hour and 4-hour sintered samples to verify grain size and phase fraction of the boride phase. The grain size of the UB<sub>2</sub> phase appears relatively stable between the 4-hour and 8-hour sintered samples. The mean and median grain sizes of the UB<sub>2</sub> phase were 1.9 μm and 1.1 μm for the 4-hour samples and 2.7 μm and 1.6 μm for the 8-hour samples, respectively. The UB<sub>2</sub> phase fractions for the 4-hour and 8-hour samples were estimated at 9.5% ±2.0% and 9.9% ±1.6% UB<sub>2</sub>, respectively.

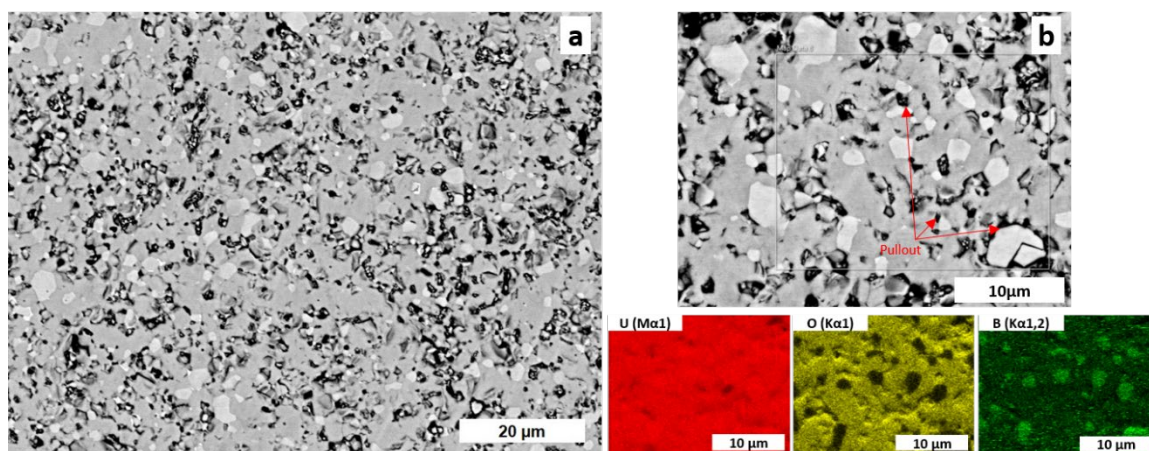


**Figure 5.3** a) Backscatter electron (BSE) image of the 4-hour as-sintered microstructure with some of the apparent porosity attributed to pullout of the oxide phase during grinding and polishing, and b) higher magnification BSE image along with EDS elemental mapping of the uranium, oxygen (darker grey), and boron (lighter grey) phases.

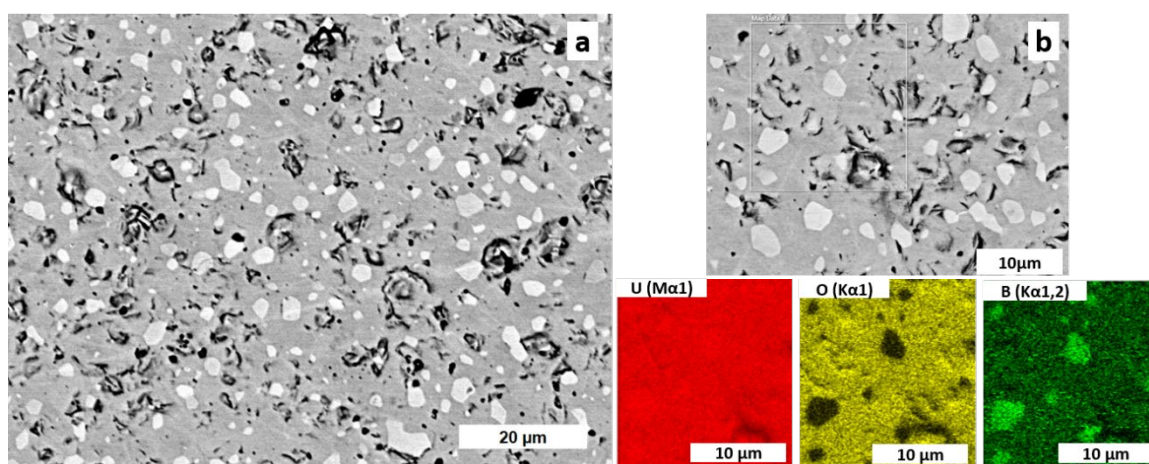


**Figure 5.4** a) Backscatter electron (BSE) image of the 8-hour as-sintered microstructure showing less porosity than that of the 4-hour sample. Some of what appears to be porosity has been attributed to pullout of the oxide phase during grinding and polishing. Image b) higher magnification BSE image along with EDS elemental mapping of the uranium, oxygen (darker grey), and boron (lighter grey) phases.

#### 5.4.3 Thermal diffusivity, specific heat capacity, and thermal conductivity

Results from the thermal diffusivity testing from room temperature to 1273 K for the 4- and 8-hour conventionally sintered (CS) 10wt%  $UB_2$  samples from this work, literature values for  $UO_2$  [40, 50], pure  $UB_2$  [21], and 5, 15, and 30wt%  $UB_2$  spark

plasma sintered (SPS) samples [20] are shown in **Figure 5.5**. Pure  $UB_2$  has a greater thermal conductivity than  $UO_2$  and exhibits an increase in thermal diffusivity above 1073 K, likely due to its metallic nature [21, 24]. Due to the influence and domination of the primary  $UO_2$  phase, the thermal diffusivities of the 4-hr and 8-hr sintered samples decreased with increasing temperature due to the influence of phonon-phonon scattering [21, 40, 50]. However, the  $UB_2$  containing CS samples display an increase in thermal diffusivity (approximately 30-40% over the temperature range measured) when compared to the accepted values for  $UO_2$  [40, 50]. Comparison of the 4-hour and 8-hour sintered 10wt%  $UB_2$  thermal diffusivity data shows the 4-hour sample tracks with the 8-hour sample until approximately 400 K. After 400 K the thermal diffusivity values for the 4-hour sample fall just under the 8-hour sample but the slopes of the data set are similar. Also, when taking the error bars into consideration, the differences between the two samples are negligible. The results for thermal diffusivity for the samples in this work are shown along with values from literature for other  $UO_2$ - $UB_2$  composites (5, 15, and 30 wt%  $UB_2$  samples sintered via SPS [20]). It is seen that the CS samples follow a similar trend as SPS sintered samples. Interestingly, the data for the CS 10wt%  $UB_2$  samples in this work are nearly superimposed with the dataset for the 15wt%  $UB_2$  SPS sample, which falls 5-10% below the CS 10wt% samples. The increase in thermal diffusivity for the CS 10wt%  $UB_2$  samples over the reported SPS 15wt%  $UB_2$  samples is believed to be due to the lack of the  $UB_4$  phase (having a lower overall thermal diffusivity than  $UB_2$  [21]) or other impurity phases in the CS 10wt% samples which was reported in the SPS samples. Another contributing factor to the higher diffusivity values in the CS 10wt%  $UB_2$  sample is that the density was approximately 96% TD versus a reported 92.4% TD

of the SPS 15wt% UB<sub>2</sub> sample. The authors attributed this in part to the hand loading of the graphite die prior to SPS which resulted in sample variability [20]. The samples in this study also had a much smaller grain size of 2.7 μm as compared to the reported 20-30 μm grain size of the SPS samples.

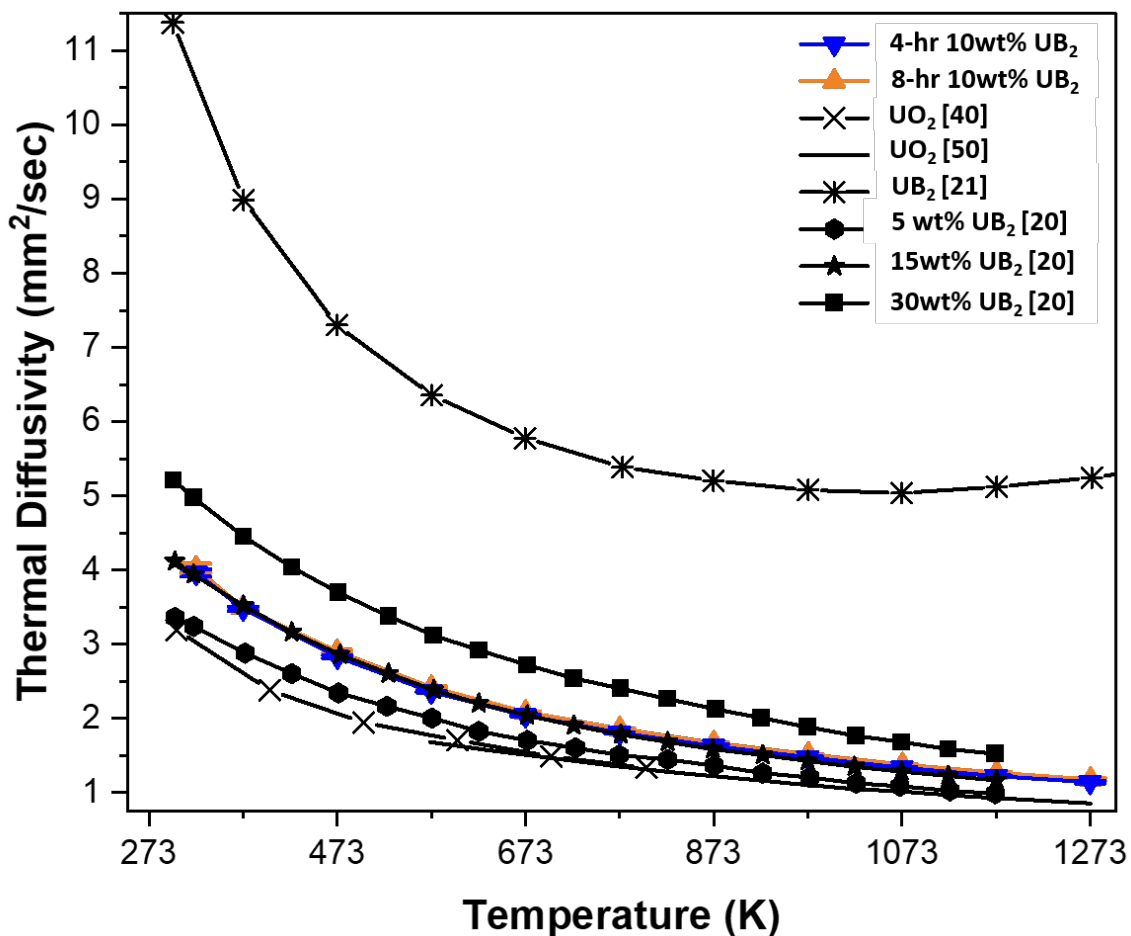


**Figure 5.5** Measured thermal diffusivity as a function of temperature for the 4-hour (blue inverted triangle) and 8-hour (orange triangle) conventionally sintered UO<sub>2</sub>-10wt% UB<sub>2</sub> samples, and values from literature for pure UB<sub>2</sub> [21], pure UO<sub>2</sub> from Fink (2000) [40] and Ronchi et al. [50] and for UO<sub>2</sub>-(5,15, and 30 wt%)UB<sub>2</sub> samples sintered via SPS from Kardoulaki et al. [20].

The measured specific heat capacities (in J/g·K) for the 4-hr and 8-hr sintered samples are shown in **Figure 5.6** along with literature values for pure UB<sub>2</sub> [28] and UO<sub>2</sub> [40]. Up to 848 K, the 4-hr and 8-hr measured heat capacity values are within the

reported error (error bars represent one standard deviation) of each other, at which point the values for the 8-hr sample continue to rise with temperature to  $0.43 \text{ J/g}\cdot\text{K}$ , while the values for the 4-hr sample taper off to an average value of  $0.37 \text{ J/g}\cdot\text{K}$ . The 8-hr sample seems to follow a similar trend of the pure  $\text{UB}_2$  sample, while the 4-hr sample trends more like that of the pure  $\text{UO}_2$ . The differences in the values above  $848 \text{ K}$  may be due to issues with the instrument sensitivity or possibly oxidation of the samples at the elevated temperature. As we were not able to identify the cause of this discrepancy (either through phase identification via XRD or other chemical analysis), a rule of mixtures (ROM) value for a theoretical  $\text{UO}_2 + 10\text{wt}\% \text{UB}_2$  was calculated using the literature values for pure  $\text{UO}_2$  and pure  $\text{UB}_2$  [28, 40] for the purposes of calculating thermal conductivity.

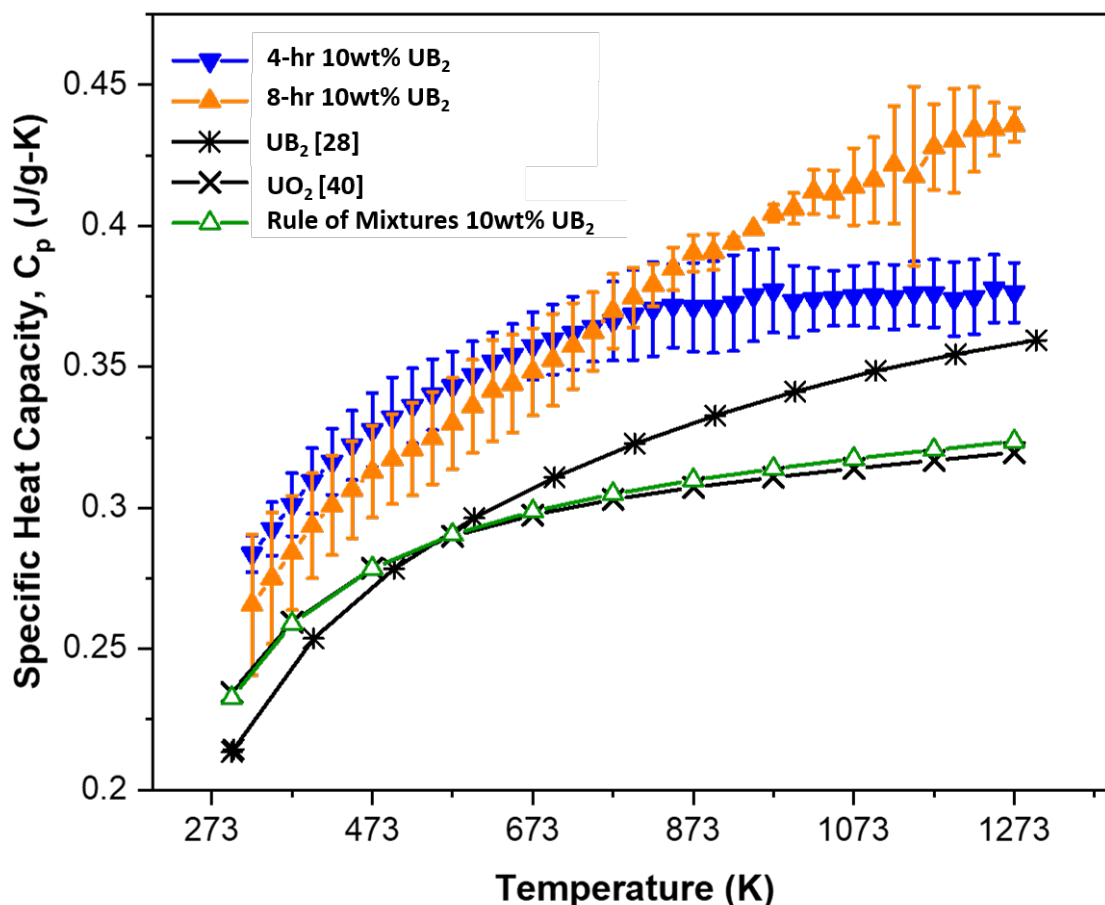


**Figure 5.6** Measured heat capacity versus temperature for the 4-hour (blue inverted triangle) and 8-hour (orange triangle) conventionally sintered  $\text{UO}_2$ -10wt%  $\text{UB}_2$  samples, and values from literature for pure  $\text{UO}_2$  from Fink (2000) [40] and pure  $\text{UB}_2$  from Fredrickson et al. (1969) [28]. A rule of mixtures (ROM) for a theoretical  $\text{UO}_2$ -10wt%  $\text{UB}_2$  samples based on values from [28, 40] is denoted by the green triangle plot.

The calculated thermal conductivity of the CS 4-hr and 8-hr sintered samples (using the calculated ROM values for the specific heat capacity from **Figure 5.6**) is seen in **Figure 5.7** along with pure  $\text{UB}_2$  [21], pure  $\text{UO}_2$  [40], as well as a calculated ROM plot for a theoretical  $\text{UO}_2 + 10\text{wt}\% \text{UB}_2$  composite using thermal expansion data from Kardoulaki *et al.* and Fink [21, 40]. Both CS samples from this study reflect increased thermal conductivity as compared to the benchmark  $\text{UO}_2$ , a 36-55% increase from 323 K to 1273 K. As compared to the theoretical ROM values, the as-sintered samples are 1-

13% higher until 973 K and then drop to 5-16% lower up to 1273 K. We can correct the thermal conductivity values to 100% TD for the CS 4-hr and 8-hr sintered samples by applying the frequently used equation for porosity correction in ceramic fuels [40, 51]. In doing so the thermal conductivity values are 8-10% higher across the temperature range examined. The CS 4-hr sample calculated thermal conductivity values are within 0.5-2% of the CS 8-hr sample across the entire temperature range examined. Based on these results, it is presumed that conventionally sintered samples with increasing boride concentrations would follow the same trends and result in even higher thermal conductivity values over  $\text{UO}_2$ .

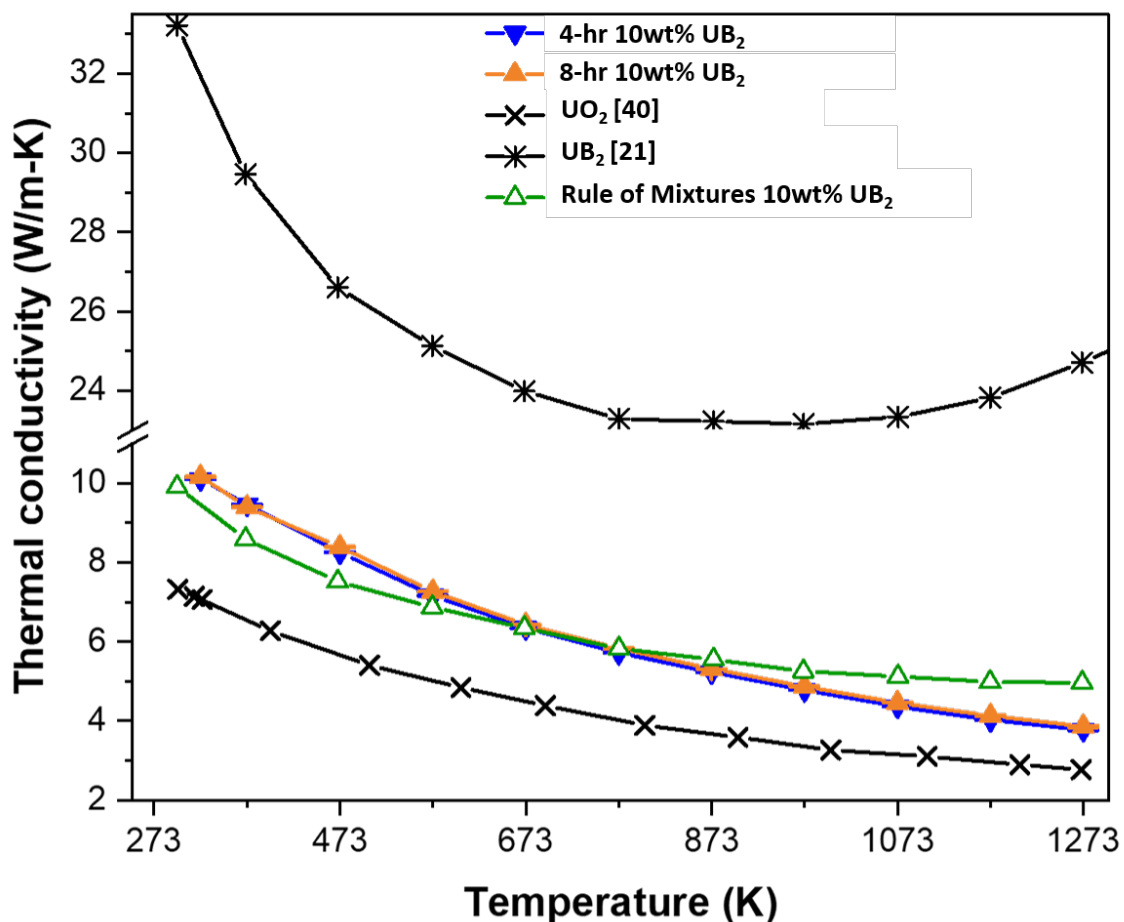


**Figure 5.7** Calculated thermal conductivity versus temperature for the 4-hour (blue inverted triangle) and 8-hour (orange triangle) conventionally sintered UO<sub>2</sub>- 10wt% UB<sub>2</sub> samples, and values from literature for pure UB<sub>2</sub> [21], pure UO<sub>2</sub> from Fink [40], and a calculated ROM plot for a theoretical UO<sub>2</sub> + 10wt% UB<sub>2</sub> composite using the ROM specific heat capacity data from Figure 6.6 and thermal expansion data from Kardoulaki et al. and Fink [21, 40] (green triangle).

### 5.5 Summary

Composite fuel samples of UO<sub>2</sub>-10wt% UB<sub>2</sub> were successfully sintered to high densities using conventional powder metallurgy and pressureless sintering techniques. The sintering conditions employed in this study show that fuel composites containing 10 wt% UB<sub>2</sub> can be effectively sintered at lower temperatures using conventional processes than previously reported for pure UB<sub>2</sub> [21]. Thermal diffusivity and specific heat capacity of the composite samples were measured up to 1273 K. The diffusivities were assessed

and shown along with reference data for pure  $UB_2$ , pure  $UO_2$ , and  $UO_2$ - $UB_2$  composites fabricated using the SPS sintering method (not directly compared to the SPS samples due to differences in fabrication techniques, resultant microstructures, densities, and impurities). The diffusivity values showed a marked increase (30%-40% from 323 K to 1273 K) over the reference  $UO_2$ . Calculated thermal conductivities for the composites were compared to reference data for pure  $UB_2$ , pure  $UO_2$ , and a ROM calculation for a theoretical  $UO_2$ +10wt%  $UB_2$  composite. These findings confirm that the addition of  $UB_2$  (of at least 10wt%) to a  $UO_2$  fuel matrix increases the thermal diffusivity and thermal conductivity compared to reference  $UO_2$  for the studied temperature range. Further investigation is needed to verify that additions greater than 10wt%  $UB_2$  result in appreciable increase in thermal diffusivity. The main advantage of conventional sintering methods over other techniques, such as SPS, is that the infrastructure for CS is already well adapted into the Nuclear Regulatory Commission approved commercial LWR fuel fabrication lines.

Additionally, the  $UB_2$  phase appears to remain stable during post-sintering thermal cycling. However, further investigation aimed at understanding the mechanisms which prevented formation of a secondary phase is warranted and should be pursued. Moreover, advanced imaging and analysis should be performed during future work to quantify boron loss and confirm any phase change which may have occurred during fabrication and post-sintering activities, regardless of consolidation method. Although not specifically seen in this work, the effect of oxidation on the boride phase above 800 K, resulting in formation of  $UB_4$  and hypo-stoichiometric  $UO_2$  needs to be further researched to provide a better indication of in-pile performance of these composite fuels.

The observed (>36%) increase in thermal conductivity in the  $\text{UO}_2\text{-UB}_2$  composite sample over pure  $\text{UO}_2$ , highlights the potential for  $\text{UB}_2$  to be used as an ATF in the current LWR fleet. The use of enriched boron ( $^{11}\text{B}$ ) can allow for tailoring of the thermal neutron adsorption cross-section so that the boride phase can also act as a burnable absorber. Additionally, the capability to fabricate these composites utilizing conventional sintering methods addresses the challenge for ATF production to exploit existing fuel fabrication infrastructure, a considerable economic driver for ATFs in general.

### **Acknowledgements**

This work was supported by the U.S. Department of Energy, Office of Nuclear Energy under DOE Idaho Operations Office Contract DE-AC07-05ID14517, and was part of a collaboration led by Westinghouse Electric Company (DE-NE0008824). Accordingly, the U.S. Government retains and the publisher, by accepting the article for publication, acknowledges that the U.S. Government retains a nonexclusive, paid-up, irrevocable, worldwide license to publish or reproduce the published form of this manuscript or allow others to do so, for U.S. Government purposes.

**U.S. Department of Energy Disclaimer:** This information was prepared as an account of work sponsored by an agency of the U.S. Government. Neither the U.S. Government nor any agency thereof, nor any of their employees, makes any warranty, express or implied, or assumes any legal liability or responsibility for the accuracy, completeness, or usefulness of any information, apparatus, product, or process disclosed, or represents that its use would not infringe privately owned rights. References herein to any specific commercial product, process, or service by trade name, trademark, manufacturer, or otherwise, does not necessarily constitute or imply its endorsement,

recommendation, or favoring by the U.S. Government or any agency thereof. The views and opinions of authors expressed herein do not necessarily state or reflect those of the U.S. Government or any agency thereof.

### References

- [1] S.J. Zinkle, K.A. Terrani, J.C. Gehin, L.J. Ott, L.L. Snead, Accident tolerant fuels for LWRs: A perspective, *Journal of Nuclear Materials* 448(1) (2014) 374-379.
- [2] S.M. Bragg-Sitton, M. Todosow, R. Montgomery, C.R. Stanek, R. Montgomery, W.J. Carmack, Metrics for the Technical Performance Evaluation of Light Water Reactor Accident-Tolerant Fuel, *Nuclear Technology* 195 (2) (2016) 111-123.
- [3] D.J. Kim, Y.W. Rhee, J.H. Kim, K.S. Kim, J.S. Oh, J.H. Yang, Y.H. Koo, K.W. Song, Fabrication of micro-cell  $\text{UO}_2$ -Mo pellet with enhanced thermal conductivity, *Journal of Nuclear Materials* 462 (2015) 289-295.
- [4] J. Buckley, J. Turner, T. Abram, Uranium dioxide-Molybdenum composite fuel pellets with enhanced thermal conductivity manufactured via spark plasma sintering, *Journal of Nuclear Materials* (2019).
- [5] S.C. Finkeldei, J. Kiggans, R.D. Hunt, A.T. Nelson, K.A. Terrani, Fabrication of  $\text{UO}_2$ -Mo composite fuel with enhanced thermal conductivity from sol-gel feedstock, *Journal of Nuclear Materials* 520 (2019) 56-64.
- [6] W. Zhou, R. Liu, S.T. Revankar, Fabrication methods and thermal hydraulics analysis of enhanced thermal conductivity  $\text{UO}_2$ -BeO fuel in light water reactors, *Annals of Nuclear Energy* 81 (2015) 240-248.
- [7] S. Ishimoto, M. Hirai, K. Ito, Y. Korei, Thermal conductivity of  $\text{UO}_2$ -BeO pellet, *Journal of Nuclear Science and Technology* 33(2) (1996) 134-140.
- [8] C.B. Garcia, R.A. Brito, L.H. Ortega, J.P. Malone, S.M. McDeavitt, Manufacture of a  $\text{UO}_2$ -based nuclear fuel with improved thermal conductivity with the addition of BeO, *Metallurgical and Materials Transactions E* 4(2) (2017) 70-76.
- [9] J. Arborelius, K. Backman, L. Hallstadius, M. Limbaeck, J. Nilsson, B. Rebensdorff, G. Zhou, K. Kitano, R. Loeffstroem, G. Roennberg, Advanced doped  $\text{UO}_2$  pellets in LWR applications, *Journal of Nuclear Science and Technology* 43(9) (2006) 967-976.

- [10] M. Amaya, M. Hirai, T. Kubo, Y. Korei, Thermal conductivity measurements on 10 wt% Gd<sub>2</sub>O<sub>3</sub> doped UO<sub>2+x</sub>, *Journal of Nuclear Materials* 231(1) (1996) 29-33.
- [11] K. Iwasaki, T. Matsui, K. Yanai, R. Yuda, Y. Arita, T. Nagasaki, N. Yokoyama, I. Tokura, K. Une, K. Harada, Effect of Gd<sub>2</sub>O<sub>3</sub> dispersion on the thermal conductivity of UO<sub>2</sub>, *Journal of Nuclear Science and Technology* 46(7) (2009) 673-676.
- [12] T. Yao, S.M. Scott, G. Xin, J. Lian, TiO<sub>2</sub> doped UO<sub>2</sub> fuels sintered by spark plasma sintering, *Journal of Nuclear Materials* 469 (2016) 251-261.
- [13] S. Yeo, E. Mckenna, R. Baney, G. Subhash, J. Tulenko, Enhanced thermal conductivity of uranium dioxide–silicon carbide composite fuel pellets prepared by spark plasma sintering (SPS), *Journal of Nuclear Materials* 433(1-3) (2013) 66-73.
- [14] B. Li, Z. Yang, J. Jia, P. Zhang, R. Gao, T. Liu, R. Li, H. Huang, M. Sun, D. Mazhao, High temperature thermal physical performance of SiC/UO<sub>2</sub> composites up to 1600° C, *Ceramics International* 44(9) (2018) 10069-10077.
- [15] W. Zhou, W. Zhou, Enhanced thermal conductivity accident tolerant fuels for improved reactor safety – A comprehensive review, *Annals of Nuclear Energy* 119 (2018) 66-86.
- [16] B. Gong, T. Yao, P. Lei, L. Cai, K.E. Metzger, E.J. Lahoda, F.A. Boylan, A. Mohamad, J. Harp, A.T. Nelson, J. Lian, U<sub>3</sub>Si<sub>2</sub> and UO<sub>2</sub> composites densified by spark plasma sintering for accident-tolerant fuels, *Journal of Nuclear Materials* 534 (2020) 152147.
- [17] G.J. Youinou, R.S. Sen, Impact of accident-tolerant fuels and claddings on the overall fuel cycle: A preliminary systems analysis, *Nuclear Technology* 188 (2) (2014) 123-138.
- [18] K.J. McClellan, FY2015 Ceramic Fuels Development Annual Highlights, Los Alamos National Lab. (LANL), Los Alamos, NM (United States), 2015.
- [19] P. Burr, E. Kardoulaki, R. Holmes, S. Middleburgh, Defect evolution in burnable absorber candidate material: Uranium diboride, UB<sub>2</sub>, *Journal of Nuclear Materials* 513 (2019) 45-55.

- [20] E. Kardoulaki, D.M. Frazer, J.T. White, U. Carvajal, A.T. Nelson, D.D. Byler, T.A. Saleh, B. Gong, T. Yao, J. Lian, K.J. McClellan, Fabrication and thermophysical properties of  $\text{UO}_2\text{-UB}_2$  and  $\text{UO}_2\text{-UB}_4$  composites sintered via spark plasma sintering, *Journal of Nuclear Materials* 544 (2021) 152690.
- [21] E. Kardoulaki, J. White, D. Byler, D. Frazer, A. Shivprasad, T. Saleh, B. Gong, T. Yao, J. Lian, K. McClellan, Thermophysical and mechanical property assessment of  $\text{UB}_2$  and  $\text{UB}_4$  sintered via spark plasma sintering, *Journal of Alloys and Compounds* (2019) 153216.
- [22] J. Turner, F. Martini, J. Buckley, G. Phillips, S.C. Middleburgh, T.J. Abram, Synthesis of candidate advanced technology fuel: Uranium diboride ( $\text{UB}_2$ ) via carbo/borothermic reduction of  $\text{UO}_2$ , *Journal of Nuclear Materials* 540 (2020) 152388.
- [23] H. Okamoto, B-U (Boron-Uranium), *Binary Alloy Phase Diagrams II Edition* 1 (1990) 551-552.
- [24] E. Jossou, L. Malakkal, B. Szpunar, D. Oladimeji, J.A. Szpunar, A first principles study of the electronic structure, elastic and thermal properties of  $\text{UB}_2$ , *Journal of Nuclear Materials* 490 (2017) 41-48.
- [25] E. Jossou, D. Oladimeji, L. Malakkal, S. Middleburgh, B. Szpunar, J. Szpunar, First-principles study of defects and fission product behavior in uranium diboride, *Journal of Nuclear Materials* 494 (2017) 147-156.
- [26] L.J. Evitts, S.C. Middleburgh, E. Kardoulaki, I. Ipatova, M.J. Rushton, W. Lee, Influence of boron isotope ratio on the thermal conductivity of uranium diboride ( $\text{UB}_2$ ) and zirconium diboride ( $\text{ZrB}_2$ ), *Journal of Nuclear Materials* (2019) 151892.
- [27] D. Frazer, B. Maiorov, U. Carvajal-Nuñez, J. Evans, E. Kardoulaki, J. Dunwoody, T.A. Saleh, J.T. White, High temperature mechanical properties of fluorite crystal structured materials ( $\text{CeO}_2$ ,  $\text{ThO}_2$ , and  $\text{UO}_2$ ) and advanced accident tolerant fuels ( $\text{U}_3\text{Si}_2$ ,  $\text{UN}$ , and  $\text{UB}_2$ ), *Journal of Nuclear Materials* (2021) 153035.
- [28] D. Fredrickson, Enthalpy of uranium diboride from 600 to 1500 K by drop calorimetry, *HIGH TEMP SCI* 1(3) (1969) 373-380.

- [29] D. Fredrickson, R. Barnes, M. Chasanov, Enthalpy of uranium diboride from 1300 to 2300 K by drop calorimetry, *High Temperature Science* 2 (1970).
- [30] G. Beckman, R. Kiessling, Thermal Expansion Coefficients for Uranium Boride and  $\beta$ -Uranium Silicide, *Nature* 178(4546) (1956) 1341.
- [31] J.-P. Dancausse, E. Gering, S. Heathman, U. Benedict, L. Gerward, S.S. Olsen, F. Hulliger, Compression study of uranium borides  $UB_2$ ,  $UB_4$  and  $UB_{12}$  by synchrotron X-ray diffraction, *Journal of alloys and compounds* 189(2) (1992) 205-208.
- [32] H. Flotow, D. Osborne, P. O'Hare, J. Settle, F. Mrazek, W. Hubbard, Uranium diboride: Preparation, enthalpy of formation at 298.15 K, heat capacity from 1 to 350 K, and some derived thermodynamic properties, *The Journal of Chemical Physics* 51(2) (1969) 583-592.
- [33] J. Turner, T. Abram, Steam performance of  $UB_2/U_3Si_2$  composite fuel pellets, compared to  $U_3Si_2$  reference behaviour, *Journal of Nuclear Materials* 529 (2020) 151919.
- [34] J. Turner, S. Middleburgh, T. Abram, A high density composite fuel with integrated burnable absorber:  $U_3Si_2-UB_2$ , *Journal of Nuclear Materials* (2019) 151891.
- [35] E. Yamamoto, T. Honma, Y. Haga, Y. Inada, D. Aoki, N. Suzuki, R. Settai, H. Sugawara, H. Sato, Y. Ōnuki, Electrical and Thermal Properties of  $UB_2$ , *Journal of the Physical Society of Japan* 68(3) (1999) 972-975.
- [36] J. Turner, T. Abram, Steam performance of  $UB_2/U_3Si_2$  composite fuel pellets, compared to  $U_3Si_2$  reference behaviour, *Journal of Nuclear Materials* (2019) 151919.
- [37] B.M.P.C. KAPL, Nuclides and Isotopes: Chart of the Nuclides, (2010).
- [38] L. Goldstein, A.A. Strasser, A comparison of gadolinia and boron for burnable poison applications in pressurized water reactors, *Nuclear Technology* 60(3) (1983) 352-361.
- [39] K.J. McClellan, FY2014 Ceramic Fuels Development Annual Highlights, Los Alamos National Lab.(LANL), Los Alamos, NM (United States), 2014.

- [40] J.K. Fink, Thermophysical properties of uranium dioxide, *Journal of Nuclear Materials* 279(1) (2000) 1-18.
- [41] A.R. Wagner, J.M. Harp, K.E. Archibald, S.C. Ashby, J.K. Watkins, K.R. Tolman, Fabrication of Stoichiometric  $U_3Si_2$  Fuel Pellets, *MethodsX* (2019).
- [42] J.M. Harp, P.A. Lessing, R.E. Hoggan, Uranium silicide pellet fabrication by powder metallurgy for accident tolerant fuel evaluation and irradiation, *Journal of Nuclear Materials* 466(Supplement C) (2015) 728-738.
- [43] T. Degen, M. Sadki, E. Bron, U. Konig, G. Nenert, The HighScore suite, *Powder Diffraction* 29 (2014) S13-S18.
- [44] P. Zhao, X. Liu, A. De La Torre, L. Lu, K. Sobolev, Assessment of the quantitative accuracy of Rietveld/XRD analysis of crystalline and amorphous phases in fly ash, *Analytical Methods* 9(16) (2017) 2415-2424.
- [45] J.M. Sosa, D.E. Huber, B. Welk, H.L. Fraser, Development and application of MIPAR™: a novel software package for two- and three-dimensional microstructural characterization, *Integrating Materials and Manufacturing Innovation* 3(1) (2014) 123-140.
- [46] A. Standard, E1461 (2013) Standard test method for thermal diffusivity by the flash method, ASTM International, West Conshohocken, PA, doi 10 (2013).
- [47] A. E-95., Standard Test Method for Determining Specific Heat Capacity by Differential Scanning Calorimetry, American Society for Testing and Materials, 1995.
- [48] S. Popov, J.J. Carbajo, G. Yoder, Thermophysical properties of MOX and  $UO_2$  fuels including the effects of irradiation, Oak Ridge, TN, 2000.
- [49] F.T.L. Muniz, M.A.R. Miranda, C. Morilla dos Santos, J.M. Sasaki, The Scherrer equation and the dynamical theory of X-ray diffraction, *Acta Crystallographica Section A: Foundations and Advances* 72(3) (2016) 385-390.
- [50] C. Ronchi, M. Sheindlin, M. Musella, G. Hyland, Thermal conductivity of uranium dioxide up to 2900 K from simultaneous measurement of the heat capacity and thermal diffusivity, *Journal of Applied Physics* 85(2) (1999) 776-789.

- [51] R. Brandt, G. Neuer, Thermal Conductivity and Thermal Radiation Properties of  $\text{UO}_2$ , *Journal of Non-Equilibrium Thermodynamics* 1(1) (1976) 3-23.

## CHAPTER SIX: SUMMARY AND FUTURE WORK

### 6.1 Summary

If we, as a society, do not support efforts to diminish global greenhouse gas concentrations, the temperature increase that will occur by the end of this century will exceed the Paris Agreement limit of 1.5-2 °C. Critical requirements of a viable climate change mitigation plan include investments to research and development of advanced nuclear technologies. Just as I was able to build on the work from my predecessors within the materials science and nuclear fuels community, the work presented in this dissertation provides a basis upon which current and future researchers can develop their contributions to advanced nuclear fuel research. The contributions to literature from this dissertation have advanced the state of the science on ATFs and highlighted many opportunities for future work.

Materials are at the hub around which the growth, well-being, and safety of our world as we know it has been built. Without advances in materials science and engineering, even when it was not strictly defined as a discipline, we would not enjoy the innumerable conveniences of modern-day life. I have applied theoretical and practical materials science and engineering concepts and the use of sophisticated characterization tools to develop an understanding of nuclear fuel behavior. The presented work covers all points of the materials science tetrahedron: Structure, processing, properties, performance, and characterization. For every new material that has been developed, the way the material performs or the properties that it exhibits have been of utmost interest.

The relation between how the structure of a material informs on its processing (and vice versa), and how this structure/processing dependence affects the properties — which leads to an impact on the material performance — this is the basis that defines what materials science and engineering is. This intricate and intertwining relationship between understanding a material at its atomistic level, how it ultimately performs in service, and how we characterize all levels of these associations, is why materials science will always be at the forefront of multi-disciplinary discoveries and advancements. No advanced degree in materials science would be considered complete without addressing how the work demonstrates this use of the materials science tetrahedron. The subsequent sections below summarize how this body of work has achieved this objective.

#### 6.1.1 Uranium mononitride

The manuscripts presented in this dissertation related to UN (Chapters 2, 3, and 4) have contributed the following original work:

Chapter 2: Short exposures of UN and UN-(5-10wt%)UO<sub>2</sub> pellets to water submersion in static autoclave conditions over a temperature range of 250- 350 °C resulted in microstructural degradation of the monolithic samples. At lower temperatures, grain boundary relief and separation was observed, while spallation of single grains and increased degradation was evident as testing temperatures increased. Evidence of the propagation of an oxide layer across the surface of the UN-UO<sub>2</sub> composites was seen, proposed to be U<sub>2</sub>N<sub>3</sub> leading to formation of UO<sub>2</sub> during hydrolysis. The formation of this intermediate U<sub>2</sub>N<sub>3</sub> phase during UN steam corrosion has been confirmed by others in more recent research efforts. It was determined that formation of these corrosion products at the grain boundaries leads to segregation and volume expansion at the grain boundaries

leading to failure of the pellet structure. It was also postulated that an increased impurity oxygen content in the starting materials contributed to increased degradation behavior.

Chapter 3: A screening study was completed that included thermodynamic predictions and experimental results for fabrication of UN-Zr and UN-Y composite materials for the purposes of improving hydrothermal corrosion of UN. Microstructural examination of UN+(10wt%) Zr/Y composites identified formation of liquid uranium, ternary U-N-Metal and oxide phases in the sintered materials. XRD confirmed the qualitative results and a shift in the UN peaks for the Zr containing samples suggests a lattice contraction due to incorporation of Zr in the UN structure but not in the Y containing samples. The thermodynamic predictions and electronic structure calculations agreed with the experimental results. It was concluded that incorporation of Zr into the UN structure is more likely to form a nitride phase and change the UN structure, while addition of Y does not.

Chapter 4: The mechanism and activation energy for grain growth in conventionally sintered UN was experimentally determined through a sintering study over the temperature range 1850-2000 °C and dwell times of 2-25 hours. Application of classic theoretical grain growth models were used to identify the most likely value of the grain growth exponent, corresponding to grain boundary diffusion, but contribution from a competing mechanisms (most likely volume diffusion and low solubility impurity drag) is likely. An approximated activation energy of 610 kJ/mol was identified over the temperature range 1850-1950 °C. It was proposed that a change in the dominant grain growth mechanism, from grain boundary diffusion to pore control via surface or lattice diffusion, as sintering temperature increases to 2000 °C. No preferential grain orientation

was observed in the sintered samples. Included is a discussion of the experimental parameters and error/deviation in the results which influenced the determination of the grain growth mechanism and the activation energy calculations.

### 6.1.2 Uranium diboride as a secondary phase in UO<sub>2</sub>

The original work presented in Chapter 6 is related to UB<sub>2</sub> as an additive phase in a UO<sub>2</sub> matrix which resulted in the following pioneering results:

Chapter 5: Composite structures of UO<sub>2</sub>-(10wt%) UB<sub>2</sub> samples were successfully sintered via conventional powder metallurgy and pressureless sintering techniques at lower temperatures than in previously reported studies for sintering of pure UB<sub>2</sub>, without loss of boron. The thermal diffusivities of the composite showed a 30-40% increase over referenced literature values of pure UO<sub>2</sub>. The calculated thermal conductivities for the composite suggest an increase of 36-55% over referenced pure UO<sub>2</sub>.

## **6.2 Future Work**

### 6.2.1 Research opportunities for ATFs

The literature reviews and experimental research presented in this dissertation has highlighted several opportunities for future work related to ATFs. Opportunities which could result in significant economic benefits include the development of scalable and cost-effective synthesis and sintering methods that are backwards compatible with existing fuel manufacturing infrastructure. These methods should be optimized for the following parameters:

- Achieving high densification.
- Allowing inclusion of a dopant without the formation of undesirable secondary phases.

- Allowing for strain engineering as a method for improvement to corrosion behavior.

In addition to corrosion experiments with water or steam, the increased interest in the use of molten salts as a coolant or as part of a fuel mixture in advanced reactor concepts warrants studies on the interaction of ATFs with various molten salts.

Furthermore, valuable information could be obtained from experimentation on how oxidation and corrosion behavior of ATFs is affected by irradiation, given that irradiated fuel is more likely to be exposed to coolant during a leaker rod scenario than fresh fuel. Also, the addition of traditionally used burnable absorbers in ATF concepts may affect their corrosion behavior, thus research in this area would be beneficial. Since the desirable thermophysical properties are a driving factor for ATF implementation, an understanding of how these thermophysical properties are affected by parameters such as grain size, impurity content, and processing conditions would be useful — especially as inputs for computational modeling.

## 6.2.2 Research opportunities for individual fuel forms

### 6.2.2.1 UN

In addition to the above-mentioned research, other prospects specific to UN exist. A recurring question and concern in the experimental studies of UN is how light elements, namely carbon and oxygen, affect various fuel performance metrics. Investigations on the best methods to limit and control carbon and oxygen impurities in feedstock and sintered materials would be of particular interest. The research should also include systematic and detailed investigations on the effects of oxygen and carbon impurities and N/U ratios on densification and grain size during conventional and novel

sintering methods. The corrosion study on UN-UO<sub>2</sub> composites in this work suggested that an increased oxygen impurity in the Batch 2 powder enhanced the corrosion behavior. An expansion of this work could include a study of sintered UN pellets with deliberate addition of varying amounts of oxygen impurity, which could then be examined using more advanced characterization tools, like TEM, to identify where the oxygen impurities reside (e.g. interstitially, segregated at grain boundaries, or in secondary phase). This would be followed by exposure to hydrothermal corrosion conditions to study how the amount of oxygen impurity and affects the corrosion behavior. And additional parameter to look at in such a study would be to include an investigation on how the stoichiometry of the matrix or any additive affects air or water corrosion performance. It was noted that the degradation behavior in the hydrothermal corrosion studies in this work was stochastic in nature, but this was complicated by the fact that different diameter samples were employed within the same study, thus a study to investigate the influence of sample size on could be something to consider. Additionally, post-sintering machining treatments have been known to introduce surface defects and a study of the corrosion behavior between machined pellets and polished pellets. Studies to investigate the ideal amount of various secondary phases for the purposes of either improving corrosion performance, enhancing densification, or controlling grain growth in UN would also be beneficial. The various empirical inputs that would need to be provided to modeling and simulation work for grain growth mechanisms include starting grain size distribution, grain boundary energies (which could be identified through analysis of boundary locations, triple junctions and grain boundary dihedral angles); for corrosion modeling knowledge of grain boundary diffusivities and elemental mass loss

(for validation purposes) as well as temperatures, corrosive medium activities and concentrations, or any applied electrochemical potentials used during corrosion experiments are warranted. Advanced modeling efforts related to dopant additions could provide direction to future experimental work as well. While  $\text{UO}_2$  additions for corrosion improvement in this work were shown not to improve corrosion behavior, the effect on grain growth was not examined. For grain growth enhancement in UN, it is important to consider the implication of any oxide addition on the corrosion behavior. Other elemental additions during that would preferentially form an oxide either during sintering or under corrosion is still an opportunity for research. Like shown for dopant additions to  $\text{UO}_2$ , the effects of the change in nitrogen potential during sintering which can affect the uranium vacancy concentration and thus the self-diffusion of uranium, as well as thermodynamic stability predictions, material interactions (e.g. eutectics), and solubility limits should all be taken into consideration. Any use of UN will have to address the need to isotopically enrich UN with  $^{15}\text{N}$  to avoid formation of  $^{14}\text{C}$  and to limit neutron absorption during irradiation. As such, research that seeks to provide a scalable and economic method to accomplish this enrichment will be helpful. Systematic oxidation and corrosion experiments that more closely mirror LWR coolant conditions under normal operation and LOCA conditions will also provide a more comprehensive understanding of fuel behavior in reducing conditions.

#### 6.2.2.2 Grain growth in UN

I would make specific recommendations for a future grain growth study in UN to expand on the work detailed in Chapter 4. The sintering profiles should include a range of temperatures to cover 1800-2200 °C to identify a switch to pore control with an

evaporation/condensation mechanism and should include at least one more time step for additional sampling points. Additionally, consistent sintering times across the entire dataset should be used. The insight that could have been provided by carbon and oxygen impurities as well as N/U ratio differences in the samples would have been very valuable in identifying a trend towards a specific mechanism (like low solubility impurity drag) so any future study needs to include this characterization. A consistent sintering atmosphere should also be used, as it may be likely that the grain growth behavior in some of the samples was influenced by the increased heat dissipation from the higher flow rate, which could have retarded grain growth. Additional characterization to study the misorientation of the grain boundary angles, such as the ratio of low angle/high angle grain boundaries and any differences between the samples could help determine if there is contribution from a grain rotation and coalescence mechanism. The use of more advanced deep learning automated image analysis when evaluating grain size could eliminate some of the error which was introduced via some of the manual evaluation of the grain boundaries and thus the grain size determination. Additionally, the use of TEM to characterize the grain boundaries and atomic arrangements at the interfaces to see how the misorientation angle between the grains is allowing for diffusion of defects or impurity atoms, as grain boundary diffusion would be increased with an increased mismatch due to a larger grain boundary area. Identifying if there is solute segregation at the grain boundaries could also provide insight as to whether grain boundary pinning is occurring.

#### 6.2.2.3 $UB_2$ as an additive component in $UO_2$

Questions remain on the stability of the  $UB_2$  phase during traditional and novel processing methods. A systematic study on boron retention during sintering in pure and

composite samples would address this gap in the literature. Although this work discussed  $UB_2$  as an additive to  $UO_2$ , and other recent work has investigated composites with both UN and  $U_3Si_2$ , the use of  $UB_2$  additions to other fuel forms would be of interest. The behavior in corrosion studies and investigations on thermophysical behavior as a function of different parameters (similar to those discussed in Section 6.2.1) of these composites will also provide beneficial data.

### 6.2.3 Conclusions

The work presented in this dissertation has provided scientific benefit and a basis from which the nuclear fuels research community can build and expand upon. The studies related to the incorporation of secondary phases to a UN matrix provided valuable insight to the degradation mechanism in UN and highlighted the importance of identifying suitable secondary additions, not only from a synthesis and fabrication perspective, but also the need to account for the thermodynamic implications on the material behavior. The grain growth study underscored the need for detailed and expanded experimental work to elucidate how the different processing and sintering parameters affect the mechanism of grain growth in conventionally sintered UN. The experimental data is necessary for the extensive computational modeling which will help accelerate the timeline to adopt new nuclear fuel technologies. Additionally, the work on efforts to improve the thermal conductivity of  $UO_2$  with the ATF candidate,  $UB_2$ , emphasized that conventional sintering techniques can be employed with the less-well studied ATF fuel concept. The work suggests that  $UB_2$  may not only hold promise as an additive, but may still be considered a potential stand-alone fuel.

Clearly, additional research and development into ATF candidates is necessary before they will be able to be considered as drop-in replacements for the benchmark UO<sub>2</sub> fuel. However, the work presented here, as well as the recommendations for future research opportunities, can help accelerate the timeline for approval of ATFs for use in LWRs and advanced nuclear technologies. These advancements of ATF technology can help accelerate the nuclear sector as a major player in the goal of decarbonizing our energy sources and ultimately help in meeting climate change objectives.

APPENDIX A: CHALLENGES AND OPPORTUNITIES TO ALLOYED AND  
COMPOSITE FUEL ARCHITECTURES TO MITIGATE HIGH URANIUM DENSITY  
FUEL OXIDATION: URANIUM MONONITRIDE

This chapter has been published in the Journal of Nuclear Materials.

Reference: J.K. Watkins, A. Gonzales, A.R. Wagner, E.S. Sooby, B.J. Jaques, Challenges and opportunities to alloyed and composite fuel architectures to mitigate high uranium density fuel oxidation: Uranium mononitride, Journal of Nuclear Materials (2021) <https://doi.org/10.1016/j.jnucmat.2021.153048>.

Challenges and Opportunities to Alloyed and Composite Fuel Architectures to Mitigate  
High Uranium Density Fuel Oxidation: Uranium Mononitride

Jennifer K. Watkins<sup>a,b</sup>, Adrian Gonzales<sup>c</sup>, Adrian R. Wagner<sup>a</sup>, Elizabeth S. Sooby<sup>c</sup>, Brian J. Jaques<sup>b,d</sup>

<sup>a</sup> Idaho National Laboratory, Idaho Falls, ID, USA

<sup>b</sup> Micron School of Materials Science and Engineering, Boise State University, Boise, ID, USA

<sup>c</sup> Department of Physics and Astronomy, The University of Texas at San Antonio, San Antonio, TX, USA

<sup>d</sup> Center for Advanced Energy Studies, Idaho Falls, ID, USA

Author Contributions

Jennifer K. Watkins: Conceptualization, Investigation, Writing – Original Draft, Review and Editing

Adrian Gonzales: Investigation, Writing – Original Draft, Review and Editing

Adrian R. Wagner: Investigation, Resources, Supervision, Writing – Original Draft, Review and Editing

Elizabeth S. Sooby: Conceptualization, Resources, Supervision, Writing - Review and Editing

Brian J. Jaques: Conceptualization, Resources, Supervision, Writing - Review and Editing

**Abstract**

The challenges and opportunities to alloyed and composite fuel architectures designed and intended to mitigate oxidation of the fuel during a cladding breach of a water-cooled reactor are discussed in three review manuscripts developed in parallel, with the presented article focused on the oxidation performance of uranium mononitride. Several high uranium density fuels are under consideration for deployment as accident tolerant and/or advanced technology nuclear reactor fuels, including one on each: UN, U<sub>3</sub>Si<sub>2</sub>, UC and UB<sub>2</sub>. Presented here is the research motivation for the incorporation of additives, dopants, or composite fuel architectures to improve the oxidation/corrosion behavior of high uranium density nuclear fuels for use in LWRs. Furthermore, this review covers the literature on the degradation modes, thermodynamics, and oxidation

performance of pure UN and UN-compounds as well as reported alloyed and composite architectures.

### **A.1 Introduction**

The 2011 earthquake and resulting tsunami that damaged the Fukushima Daiichi Nuclear Power Plant in Japan, prompted an increase in the development of fuels and claddings with enhanced accident tolerance [1]. Although decades of research have gone into the current benchmark uranium dioxide fuel/zirconium alloy cladding, continued deployment of advanced technologies to improve economic and safe operation have pushed the existing light water reactor (LWR) fuel technology near its inherent performance limits [1]. Investments in the current reactor fleet and new reactor technologies must include research and development into advanced nuclear fuels that can adapt to extreme conditions while remaining thermodynamically and mechanically stable. These advanced fuels need to maintain or improve fuel performance during normal operations, operational transients, as well as design-basis, and beyond design-basis events [1-5].

This review, presented in multiple related publications, focuses on the review of available literature on high uranium density nuclear fuels and their composites: Uranium mononitride (UN), triuranium disilicide ( $U_3Si_2$ ), and other high density fuels including uranium monocarbide (UC) and uranium diboride ( $UB_2$ ). Each of which are investigated in the United States (U.S.), and internationally, as alternatives to the benchmark uranium dioxide ( $UO_2$ ) fuel. Industry and utility partners are motivated to advance high uranium density fuel technology, as the increase in fuel economy, in addition to the added safety margins enabled by the high thermal conductivity of these fuels, is attractive. However,

for each of these fuel forms, there are two known challenges that must be addressed: First is fabrication as each of these are air sensitive fuel forms, and second is oxidation in water containing atmospheres. As fundamental research on these fuel forms has progressed over the last decade, it has been shown experimentally that these advanced technology fuels exhibit superior thermophysical properties compared to  $\text{UO}_2$  [6-9]. Both  $\text{U}_3\text{Si}_2$  and UN have also exhibited favorable irradiation performance, albeit at low temperatures ( $<250\text{ }^\circ\text{C}$ ) and low burnup for  $\text{U}_3\text{Si}_2$  [6], while data on UN is limited to fast reactor applications [10, 11]. Accordingly, research interest has significantly increased for a drop-in replacement for  $\text{UO}_2$ . However, hand-in-hand with thermophysical and irradiation performance data, accident testing of these ATF (accident tolerant fuel) concepts has proven them, particularly UN and  $\text{U}_3\text{Si}_2$  with less data available for UC and  $\text{UB}_2$ , to be highly susceptible to degradation and pulverization in simulated LWR off-normal conditions; namely, exposure to pressurized water and high temperature steam environments characteristic of a cladding breach during normal operation or loss of coolant accident [12-15].

This review will cover the research motivation (in this uranium mononitride review publication), and materials and techniques (in the uranium silicide review publication) for the incorporation of additives, dopants, or composite fuel architectures to improve the oxidation/corrosion behavior of high uranium density nuclear fuels for use in LWRs. It should be noted that while this review is intended to highlight the seminal literature on high uranium density nuclear fuels, it may not be fully exhaustive and it also does not specifically focus on synthesis and fabrication methods; although, they are briefly discussed due to their influence on fuel behavior and performance, particularly

with respect to the impact of microstructure and presence of contaminant phases. The various methods for advanced fuel fabrication have been detailed in other recent publications [16, 17]. This review article also does not include literature discussing the use of these fuel compounds, particularly UN and UC, in tristructural-isotropic particle (TRISO) fuels as direct exposure of the fuel to coolant and impurities is not an issue due to the inherent protection provided by fuel encapsulation.

### A.2 Motivation for the implementation of high uranium density fuels

Compared to the benchmark,  $\text{UO}_2$ , each of the ATF candidates reviewed here, UN, UC,  $\text{UB}_2$ , and  $\text{U}_3\text{Si}_2$  have higher uranium densities and higher thermal conductivities, as well as maintaining relatively high melting temperatures (see **Table A.1**). In addition, the nitride and silicide fuels have shown acceptable performance under irradiation [7-9, 18-20]. The screening process for high density LWR fuel candidates includes those in which the uranium density exceeds that of  $\text{UO}_2$  and includes a sufficiently high melting temperature which exceed the melting point of other core components [21].

**Table A.1 Material Properties of ATF Concept Fuels**

Material Properties	$\text{UO}_2$	$\text{U}_3\text{Si}_2$	$\text{UB}_2$	UC	UN
Uranium density ( $\text{g-U}/\text{cm}^3$ ) <sup>[7, 22, 23]</sup>	9.7	11.3	11.7	13	13.5
Thermal conductivity ( $\text{W}/\text{m}\cdot\text{K}$ at $300\text{ }^\circ\text{C}$ ) <sup>[24-28]</sup>	6.5 (95% TD)	14.7 (98% TD)	16.6 (80% TD)	20.4 (570 $^\circ\text{C}$ , 99% TD)	16.6 (95% TD)
Melting temperature ( $^\circ\text{C}$ ) <sup>[7, 29-31]</sup>	2840	1665	2385	2525	2847

The United States Department of Energy defined accident tolerant fuels as those that can tolerate loss of active cooling in the reactor core for a considerably longer time period (increased coping time) than the benchmark  $\text{UO}_2$ -Zircaloy system [4]. The

important considerations that need to be addressed for ATFs are highlighted in green and summarized in **Figure A.1**. The ATF concepts discussed in this review do address the required improved fuel properties such as lower fuel center-line temperatures (due to their higher thermal conductivity) and an increased power to melt safety margin. The metrics for improved reaction kinetics with steam still need to be addressed and demonstrated by the ATF concepts discussed in this review; however, their use allows for the incorporation of advanced cladding structures which can provide additional safety margins with regards to steam reaction kinetics. Other considerations for these ATF concepts with regards to minimizing fuel-cladding interactions and retention of fission products also needs to be addressed.

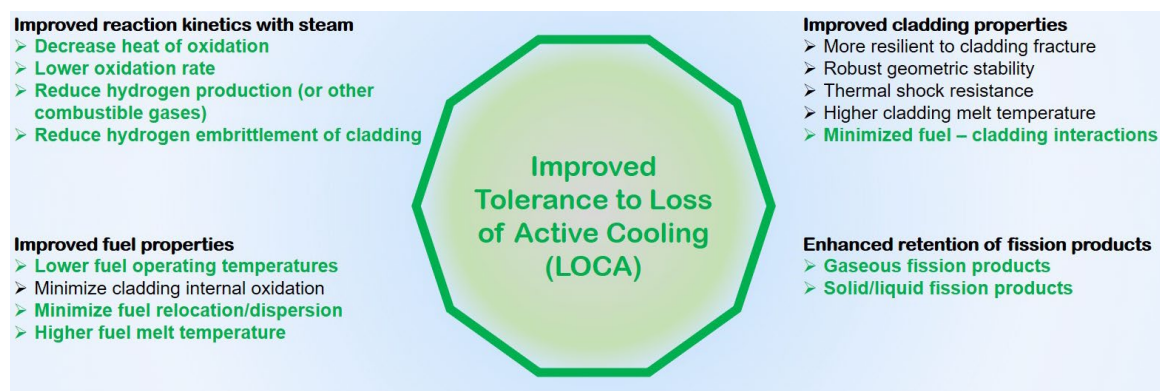


**Figure A.1 Primary attributes of accident tolerant fuels associated with fuel behavior and cladding at high temperatures. Modified from Carmack [32].**

Implementation of UN,  $U_3Si_2$ , UC, or  $UB_2$  will improve nuclear fuel performance by enabling higher burn-up, leading to lower waste volumes and longer cycle lengths [7, 15, 33]. Increased power up-rates are possible due to the increased power density these ATFs provide because of the increased uranium loading. These ATF materials can provide better performance in extreme temperatures due to their higher thermal conductivities, which reduce the stored energy in the core, mitigate high thermal

gradients across fuel pellets, and increase the rate of heat transfer to the cladding during temperature transients. These thermal transport benefits result in reduced fuel failures and more efficient plant operation [7, 15, 33]. The four high uranium density candidates discussed in this review are grouped in the middle of **Figure A.2** as meeting these initial selection criteria.

The uranium mononitride part of this review (this publication) presents the background and motivation for the investigation of alloyed or composite high density fuel architectures. In addition, this review focuses on the performance of UN and UN-composites in oxygen and water containing atmospheres, whereas the uranium silicide part of the review introduces the various approaches to mitigating the water reaction and presents the current understanding of the performance of  $U_3Si_2$  and the alloys and composites investigated to date. Lastly, the part of the review on  $UB_2$  and UC will summarize the state of knowledge on alloyed and composite architectures and present the current literature on lesser studied fuels, UC and  $UB_2$ .

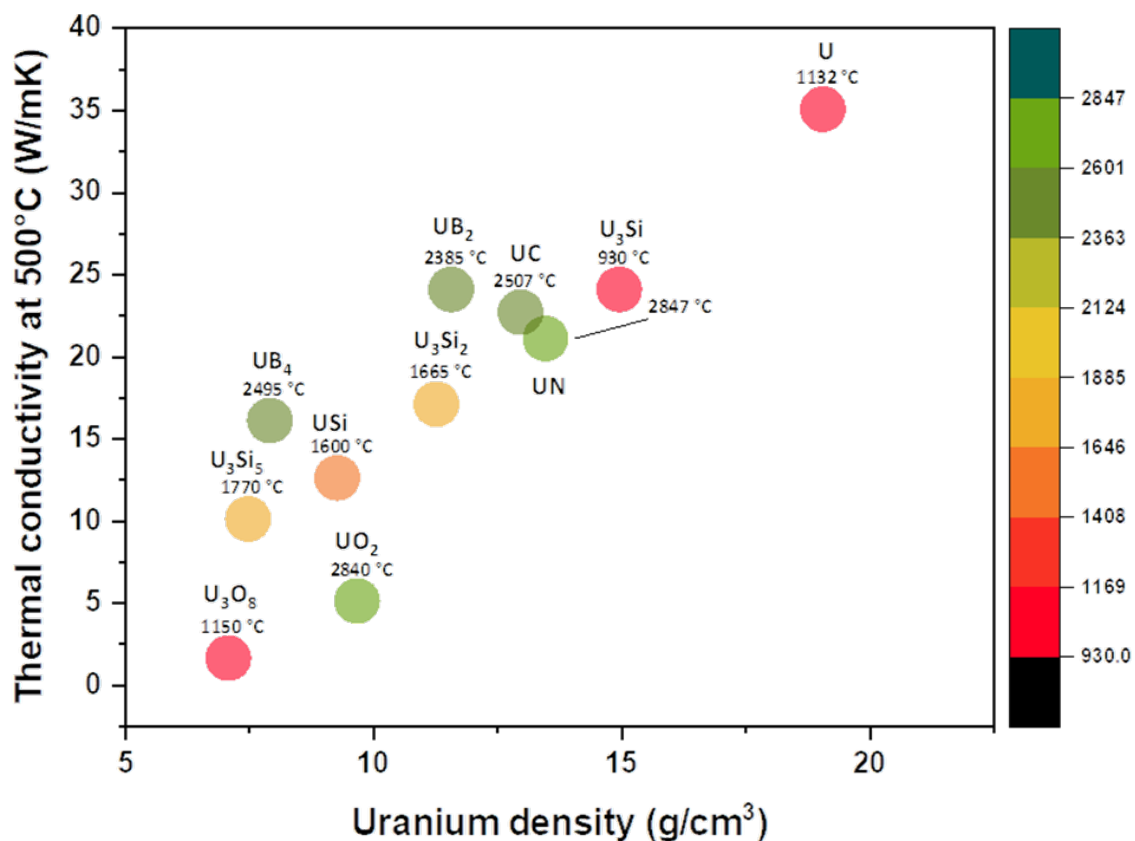


**Figure A.2 Thermal conductivity vs. uranium density and color mapped to melting temperature. The four high uranium density candidates discussed throughout these reviews (UN, U<sub>3</sub>Si<sub>2</sub>, and UB<sub>2</sub>/UC) are grouped in the center of the plot.**

### A.3 Uranium Mononitride (UN)

Uranium mononitride fuels have been proposed, researched, and demonstrated for space power reactors and liquid metal fast breeder reactors because of their previously mentioned desirable properties [34, 35]. The following sections of the report present a review of publicly available literature on the current status of UN research; specifically related to the performance of UN and UN-composites in oxygen and water containing atmospheres. The low oxidation and corrosion resistance of the nitride fuel is a major concern for deployment into existing and advanced LWRs [36, 37]. The literature on UN's stability under oxidation and hydrothermal corrosion conditions is limited;

moreover, it is evident that UN corrodes when exposed to oxygen, water, and steam environments. Accordingly, the succeeding sections present a review of literature, which is organized into the common bulk UN synthesis methods, oxidation and corrosion testing of pure UN, reports on the introduction of additives and dopants into the UN matrix in attempts to mitigate corrosion behavior, and the effects of impurities and secondary phases in UN. It should be noted that in an attempt to include the applicable data on publicly available literature for UN, the following sections do include references to issued patents and graduate theses, which should be viewed in light of the fact that they may not have undergone the same extensive peer-review processes as journal publications.

#### A.3.1 Synthesis Methods

Typically, UN feedstock is synthesized via two primary methods: metal hydride-dehydride-nitride (HDN) or carbothermic reduction and nitridization (CTR-N) [38]. The CTR-N method holds benefits over the HDN method in that it is easier to obtain, handle, and transport the  $\text{UO}_2$  feedstock (starting materials) than that of the powdered elemental uranium feedstock necessary for HDN. In addition to safety and economic concerns associated with handling the finely divided UN powder achieved through the HDN route, CTR-N is the favored synthesis route due to the fact that it can utilize the existing conversion processes and infrastructure for current oxide fuel fabrication [38]. Bragg-Sitton *et al.* noted in design constraints for ATF concepts, that a new fuel concept must be backwards compatible with existing fuel handling equipment, fuel rod or assembly geometry, and coresident fuel in existing LWRs [39]. This constraint, along with the fact that CTR-N has been used and optimized for decades, makes the CTR-N

method the most likely to be implemented for commercial scale-up production [16]. Although favored, the CTR-N method typically results in higher carbon and oxygen impurity levels in the starting powder, which must also be addressed prior to implementation. It is worth noting that the sol-gel method has also been successfully demonstrated for UN production, typically related to UN microspheres for fabrication of TRISO fuel [40], but it has not been commonly used for fabricating bulk UN and UN composites. To produce nuclear fuel relevant geometries, compact fabrication has been achieved by traditional cold pressing and sintering, hot isostatic pressing (HIP), and field assisted sintering, e.g. spark plasma sintering (SPS) methods. All these methods for synthesis and fabrication have been demonstrated in the literature [15, 16, 18, 34, 41-45].

The incorporation of dopants or secondary phases can be achieved through traditional powder metallurgy processes followed by any of the previously mentioned sintering methods; however, the sintering method and parameters must be tailored to each additive to avoid formation of unwanted phases or precipitates [14, 44]. Secondary phases and dissociation can be detrimental to fuel performance due to liquid phase formation and swelling, leading to fuel failure. Accordingly, it is important to understand that the activity of uranium is a function of partial pressure of nitrogen and oxygen as well as the presence of any alloying agent(s). As seen in the uranium-nitrogen binary phase diagram (**Figure A.3**), stoichiometric UN has a narrow phase field and is known to be relatively unstable, either dissociating to form a liquid uranium phase or forming hyper-stoichiometric UN<sub>2</sub> and U<sub>2</sub>N<sub>3</sub>. Additionally, both Tennery and Matzke reported that UN is sensitive to decomposition at higher temperatures and low nitrogen partial pressures, and forms U<sub>2</sub>N<sub>3</sub> at lower temperatures and higher N<sub>2</sub> partial pressures (see

**Figure A.4)** [46, 47]. This thermodynamic instability presents challenges for both synthesis and fabrication of UN and UN-composites. The phase field for stoichiometric UN can be widened above approximately 1200 °C if a sufficient nitrogen partial pressure is maintained, but at lower temperatures, only very low N<sub>2</sub> partial pressures will prevent formation of the U<sub>2</sub>N<sub>3</sub> phase.

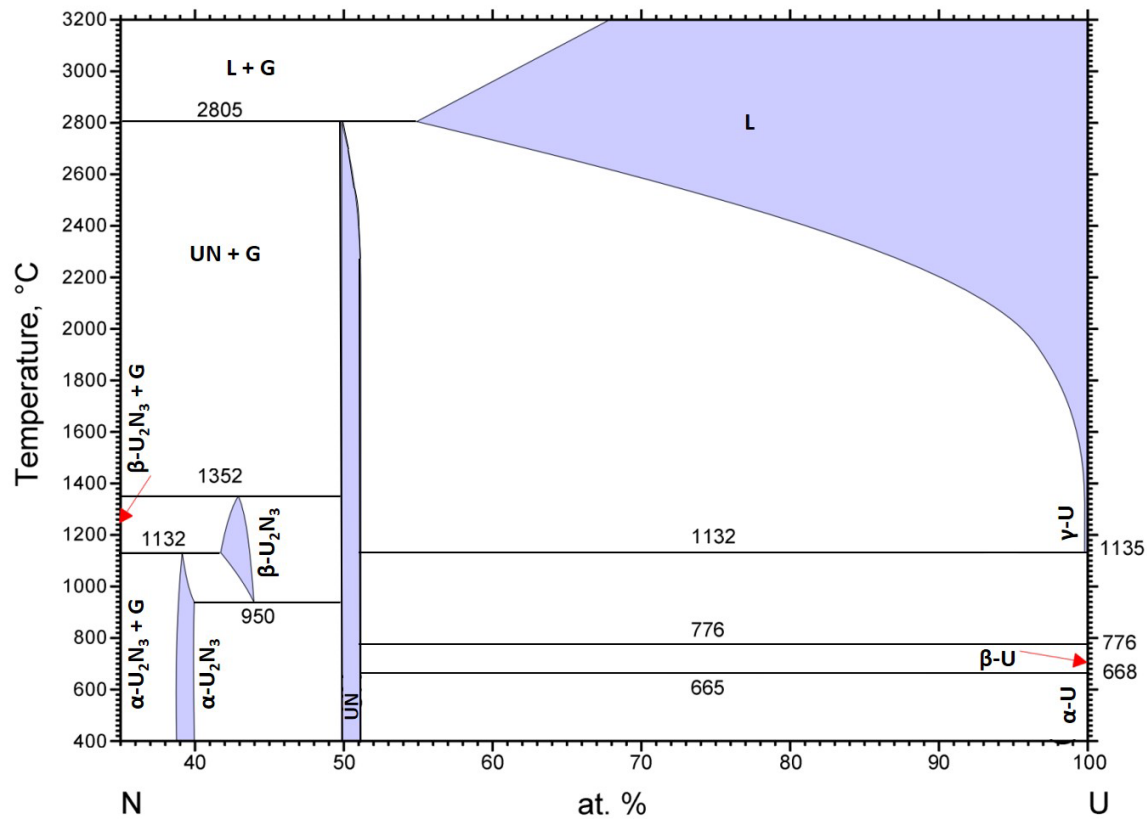


**Figure A.3** Uranium-nitrogen phase diagram (35-100 at% U, 400-3200 °C)  
Modified from Okamoto [48].

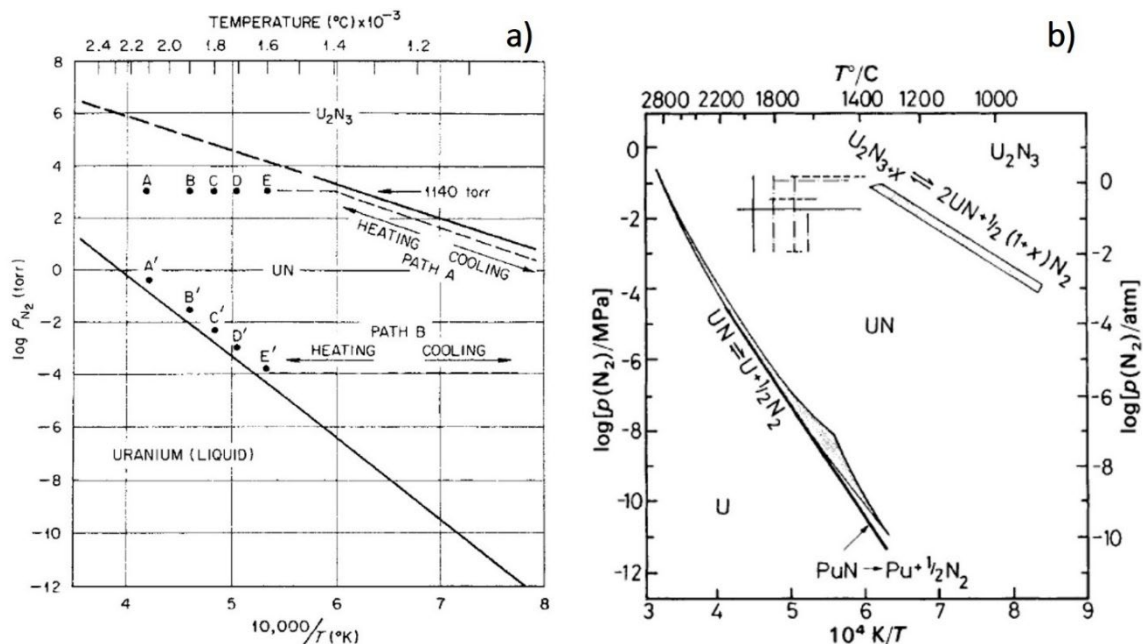


**Figure A.4 UN dissociation and U<sub>2</sub>N<sub>3</sub> formation as a function of temperature and nitrogen partial pressures, a) From Tennery [46], and b) from Matzke [47].**

It is important to note, however, that regardless of synthesis method or additives into the nuclear fuel forms, a fundamental challenge is presented when considering nitrogen in a nuclear reactor. It is understood that nitrogen in any fuel concept would need to be isotopically enriched from <sup>14</sup>N to <sup>15</sup>N to avoid significant <sup>14</sup>C production through the <sup>14</sup>N(*n,p*)<sup>14</sup>C reaction (enrichment will lead to a 2 order of magnitude decrease in <sup>14</sup>C production [7]). Accordingly, Wallenius *et al.* investigated the influence of nitrogen enrichment on neutronics, cost, and <sup>14</sup>C production for different closed fuel cycle scenarios for fast reactors and accelerator driven systems [49]. It was determined a <sup>15</sup>N enrichment level of 99% was necessary to achieve the same amount of <sup>14</sup>C as with an oxide loaded core. The increased fuel fabrication cost was estimated at > 25%, albeit that increase dropped to 5-10% if reprocessing and a closed gas cycle was utilized [49]. As previously stated, nitrogen enrichment concerns must be considered regardless of the proposed UN synthesis method. However, some of the challenges are mitigated through

the use of a closed gas cycle (e.g. when using CTR-N or HDN synthesis techniques) and recovery during UN synthesis, sintering, and reprocessing [49, 50]. Although not a specific focus of this review, the complications arising from the need for nitrogen enrichment in UN highlights an additional area of research in UN synthesis and reprocessing that must be pursued prior to deployment. An additional advantage to enriching the nitrogen in UN is the decrease in the thermal neutron cross section, as shown in **Table A.2**.

**Table A.2** Thermal neutron cross-sections for  $^{14}\text{N}$  and  $^{15}\text{N}$  for the  $(n,p)$ ,  $(n,\gamma)$ , and  $(n,e)$  reactions [51].

Isotope	$(n,p)$ [b]	$(n,\gamma)$ [b]	$(n,e)$ [b]
$^{14}\text{N}$	$1.86 \pm 0.03$	$80.1\text{E-}3 \pm 0.6\text{E-}3$	$10.02 \pm 0.12$
$^{15}\text{N}$	-	$2.4\text{E-}5 \pm 8\text{E-}6$	4.590.05

### A.3.2 Oxidation/corrosion testing of UN

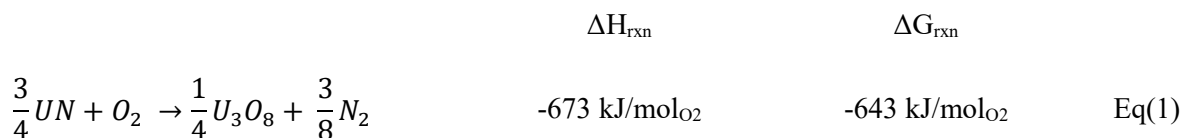
#### A.3.2.1 Air oxidation of UN

Much of the literature that exists on the oxidation and corrosion behavior of UN was published in between the 1960's and 1990's as the fuel was being investigated for space power applications, radioisotope thermoelectric generators, LWRs, and HWRs. A summary of UN oxidation studies is presented in **Table A.3** and provides information (if provided within the reference) on synthesis and sintering methods, the type of sample oxidized (e.g. powder, compact, etc.), temperature testing range, test conditions, onset temperature, sample phase composition, grain size, and reaction products. Studies of the oxidation behavior of UN, including single crystal, polycrystalline, powder, and monolithic samples have been investigated in air, oxygen,  $\text{CO}_2$ , and  $\text{NO}_x$  atmospheres

with varying results [36, 37, 52-59]. The onset of breakaway oxidation for UN has been reported from 200-340 °C with powder samples underperforming monolithic samples, which typically result in severe degradation or pulverization above 300 °C. Also, it has been observed that denser samples exhibit increased oxidation resistance, which is likely due to a lower surface area to volume ratio in higher density samples. Only general conclusions can be drawn as testing parameters for air oxidation of UN vary in the literature with regards to fabrication methods, sample configuration, partial pressures of oxygen (if reported) and temperatures. Results in the literature vary for the oxidation products identified under the various testing parameters, but generally included  $\text{UO}_2$ ,  $\text{U}_2\text{N}_3$ ,  $\text{UO}_3$ , and  $\text{U}_3\text{O}_8$ . In many cases, it was noted that either a  $\text{U}_2\text{N}_3$  phase or an intermediate phase was “sandwiched” between the bulk UN and a surface  $\text{UO}_2$  [36, 37, 52-61]. This was validated in a fundamental study by Sole *et al.* who observed oxidation products of  $\text{U}_2\text{N}_{3+x}$  and  $\text{UO}_2$  via TEM diffraction patterns of UN foils heated for 2 minutes at 600 °C ( $\text{O}_2$  partial pressure not given) [53]. The bulk of the publications on oxidation behavior of pure UN describe the oxidation behavior and provide kinetics data which indicate, as expected, increased reaction rate constants and mass gains with increased temperatures and durations.

The presence of images and micrographs of the evolution of UN oxidized in air or  $\text{O}_2$  is limited in literature. However, a recent study has provided microstructural images of as-fabricated UN microspheres and SPS sintered UN microsphere samples oxidized in synthetic air up to 700 °C (**Figure A.5**). The researchers stated the general behavior followed a successive oxidation path as denoted by Equations 1-2 ( $\Delta H_{\text{rxn}}$  and  $\Delta G_{\text{rxn}}$  values calculated using HSC Chemistry 9 [62]), resulting in a final oxidation product of

U<sub>3</sub>O<sub>8</sub>. The  $\Delta G_{\text{rxn}}$  is indicative of the thermodynamic likelihood the reaction will occur, but the  $\Delta H_{\text{rxn}}$  is important to consider as the heat generated during the reaction can have a large impact on the reaction behavior, especially during an accident scenario. Adsorption of oxygen on the external surface, inside the open porosity as well as an external interface reaction allowed oxide diffusion towards the UN. Oxidation along grain boundaries also produced stresses causing intergranular cracking and spallation [63]. The intermediate step for formation of U<sub>2</sub>N<sub>3</sub> and UO<sub>2</sub> is shown in Equation 3. Different results were reported by Dell *et al.* for UN powders oxidized in 0.07 MPa oxygen, stating that the powders ignited at 290 °C and that the final product was UO<sub>3</sub>, not UO<sub>2</sub> or U<sub>3</sub>O<sub>8</sub> [37, 64]. Dell further studied these UN powders under oxidation at 260 °C, finding that after 1-2 days, both UO<sub>2</sub> and  $\alpha$ -U<sub>2</sub>N<sub>3</sub> were identified via X-ray diffraction. Another study oxidized UN microspheres at 6.6 kPa O<sub>2</sub> resulting in an oxidation onset of 217 °C and U<sub>3</sub>O<sub>8</sub> containing dissolved nitrogen as the reaction product [56].



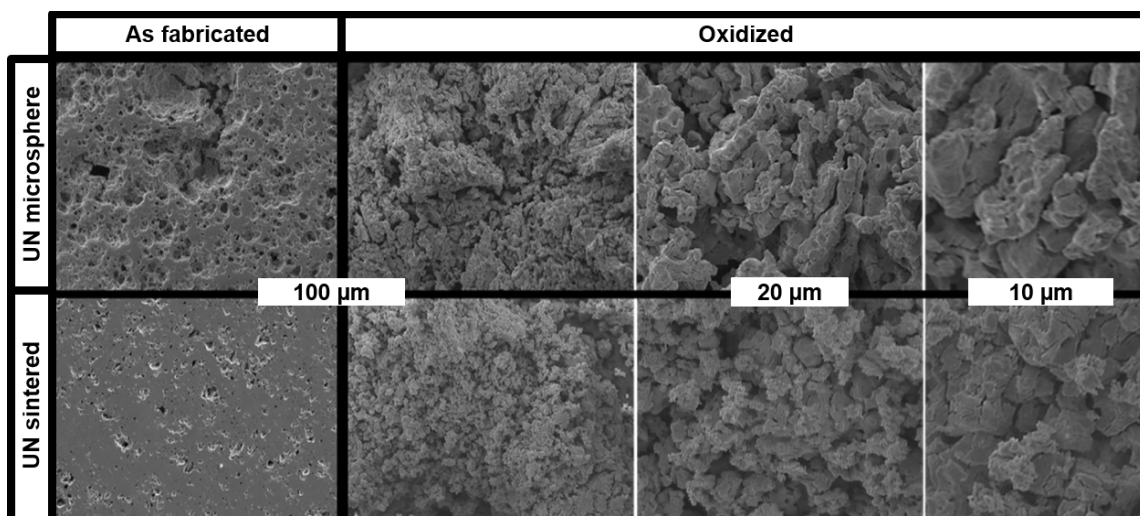


**Figure A.5** As-fabricated and SPS sintered UN microspheres (left column) and resulting microstructure (right columns) after oxidation in synthetic air up to 700 °C. Modified from Costa et al. [63].

In an attempt to better understand the mechanism of the oxidation of a UN surface, Dell *et al.* studied the oxidation of single crystal UN [37]. Accordingly, the (421) face of a UN crystal was oxidized in flowing oxygen at 400 °C for 10 and 30 minutes. The authors describe “track” formation in the early stages of oxidation and a general surface roughening; however, as the surface oxide thickened, a “blistering” was observed (**Figure A.6**). This blistering effect can be attributed to nitrogen bubbles forming beneath the film. As the oxide thickened the surface detail was still retained leading the authors to postulate that the mechanism was oxygen diffusion inward rather than outward diffusion of uranium. Nitrogen atoms are released as gas through the oxide layer, while other nitrogen atoms partially dissolve into the lattice at the nitride interface, resulting in the aforementioned “sandwich” structure [37].

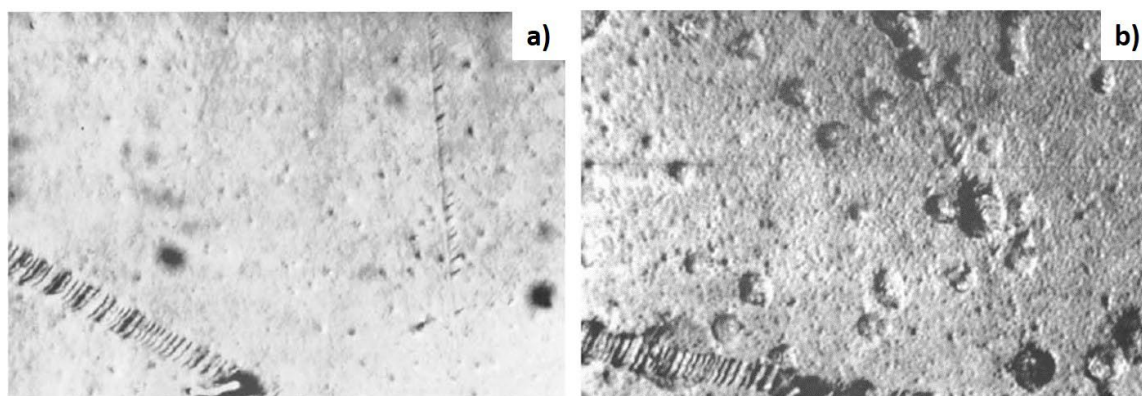


**Figure A.6** Images at 500X magnification of UN single crystal samples, (421) crystal faces, oxidized in flowing oxygen for a) 10 minutes, and b) 30 minutes. From Dell et al. [37].

While the above results for UN powders, microspheres, and single crystals do provide insight to the oxidation behavior of UN, oxidation studies on monolithic, polycrystalline samples are more relevant to samples in a LWR condition. Oxidation kinetics of UN polycrystalline samples (hypo-, stoichiometric, and hyper-), fabricated by powder metallurgy followed by hot isostatic pressing and by arc-melting were analyzed during oxidation in air and  $O_2$  at 1 atm and 300-700 °C [36]. These oxidized samples ultimately formed  $U_3O_8$  as the corrosion product and displayed linear reaction kinetics with the rate constant increasing with temperature, similar to other work by Ohmichi where the oxidation reaction activation energy of 124 kJ/mol was identified [36, 65]. Similar work oxidizing UN compacts (via HDN and conventionally sintered in 2.5 atm  $N_2$ ) showed oxidation begins at 200 °C forming both  $U_2N_3$  and an oxynitride. Rapid oxidation starts at 250 °C along with  $N_2$  release and  $UO_3$  is formed, ultimately forming  $U_3O_8$  at 400 °C [52]. Other oxidation experiments on UN compacts (via HDN) in air and oxygen indicated the rate of oxidation in  $O_2$  (onset 320 °C) was approximately 5x that in air (onset 348 °C) [55].

Despite the limited amount of literature available, UN powder synthesized via the HDN process and then subsequently arc-melted or conventionally sintered, or samples fabricated through arc-melting and SPS appear to provide an increased oxidation onset temperature [36, 37, 52, 53, 55, 58]. The increased resistance in these samples is attributed to a higher sintered density and reduced open porosity that is more easily achievable using SPS and arc melting. Samples fabricated through the sol-gel method (both microspheres and sintered compacts) reported the lowest onset temperatures in the available literature [56, 57]. The majority of samples tested in air were for pure UN, suggesting that air oxidation studies on UN-composites may be an area of research interest.

**Table A.3 Summary of air oxidation UN and UN with additives or composites.**

	Ref.	Synthesis method	Sintering method	Type	Temp. test range [°C]	Test conditions	Onset temp. [°C]	Composition	Grain Size [μm]	Reaction products
Air/Oxygen	[36]	HDN/arc-melting	HIP	Single crystal, polycrystalline compacts	300-700	Isothermal	-	UN	n/a	U <sub>3</sub> O <sub>8</sub>
	[37, 64]	HDN	n/a	Powder	230-290	Isothermal	250 (powder ignited at 290)	UN	n/a	UO <sub>3</sub> with intermediates of UO <sub>2</sub> , U <sub>2</sub> N <sub>3</sub> , and UO <sub>3</sub> N <sub>x</sub>
	[37]	Arc-melting	n/a	Single crystal	280-500	Isothermal	n/a	UN	n/a	U <sub>2</sub> N <sub>3</sub> , UO <sub>2</sub>
	[52]	HDN	Conventional	Powder, compact	Up to 900	Ramped, 0.85 °C/min and 0.4 °C/min	250 (powder), 340 (compact)	UN	n/a	U <sub>3</sub> O <sub>8</sub> with intermediates of U <sub>2</sub> N <sub>3</sub> , UO <sub>2</sub> , and UO <sub>3</sub>
	[53]	Arc-melting	n/a	Single crystal foil	Up to 800	Ramped	-	<sup>a</sup> UN	n/a	U <sub>2</sub> N <sub>3+x</sub> , UO <sub>2</sub>
	[55]	HDN	n/a	Compact	325-450	Ramped, 2.5 °C/min	320-348	UN	n/a	U <sub>3</sub> O <sub>8</sub>
	[56]	Sol-gel	n/a	Microspheres	Up to 927	Ramped, 4 °C/min	217	UN	n/a	U <sub>3</sub> O <sub>8</sub> with intermediates of U <sub>2</sub> N <sub>3</sub> , UO <sub>2</sub>
	[56]	Sol-gel	n/a	Microspheres	Up to 927	Ramped, 4 °C/min	212 (15mol%), <sup>b</sup> 172 (30 mol%)	(U,Ce)N (15 and 30 mol% Ce)	n/a	U <sub>2</sub> N <sub>3</sub> and MO <sub>2+x</sub> (15 mol%); M <sub>3</sub> O <sub>8</sub> and MO <sub>2+x</sub> (30 mol%)
	[57]	Sol-gel	Conventional	Compact	25-767	Ramped, 3 °C/min	202 (air), 232 (8% O <sub>2</sub> ), 257 (20% O <sub>2</sub> )	UN	n/a	U <sub>3</sub> O <sub>8</sub> with intermediates of U <sub>2</sub> N <sub>3</sub> , and UO <sub>2</sub>
	[58]	HDN (UN), Arc-melting (U <sub>3</sub> Si <sub>2</sub> )	SPS	Compact fragments	Up to 800	Ramped, 5 °C/min	320 (UN), 450 (UN+U <sub>3</sub> Si <sub>2</sub> )	UN, UN+10v% U <sub>3</sub> Si <sub>2</sub>	6-9.1 (UN), 80 (UN+10v% U <sub>3</sub> Si <sub>2</sub> )	U <sub>3</sub> O <sub>8</sub> (UN)
	[59]	n/a	n/a	Pellet	Up to 452	Ramped, 10 °C/min	307	<sup>c</sup> UN	n/a	U <sub>3</sub> O <sub>8</sub> with intermediates of U <sub>2</sub> N <sub>3</sub> , and UO <sub>2</sub>
	[63]	Sol-gel	SPS	UN microspheres and Pellet fragments	Up to 700	Ramped, 5 °C/min	260 (UN microspheres), 283-320 (UO <sub>2</sub> +UN)	UN microsphere, <sup>d</sup> UO <sub>2</sub> +(10,30,50)UN	3.1-9.5	U <sub>3</sub> O <sub>8</sub>

	Ref.	Synthesis method	Sintering method	Type	Temp. test range [°C]	Test conditions	Onset temp. [°C]	Composition	Grain Size [μm]	Reaction products
	[65]	n/a	n/a	Crushed sintered pellet	Up to 315	Ramped (1,3, and 5 °C/min, and Isothermal	Below 300 °C	UN	n/a	U <sub>3</sub> O <sub>8</sub>
<p><sup>a</sup> Starting material had adherent U<sub>2</sub>N<sub>3+x</sub> layer at beginning of testing and heating parameters were not listed, sample had oxidized after diffraction pattern taken at 600 °C; <sup>b</sup> Ignited; <sup>c</sup> Samples had “detectable” amounts of UO<sub>2</sub> in starting material; <sup>d</sup> Composite samples had U<sub>2</sub>N<sub>3</sub> phase present in varying amounts (3.7-16.3 wt%) and sample with highest oxidation onset temperature was calculated to be 95 wt% UO<sub>2</sub>/1.3 wt% UN/3.7 wt% U<sub>2</sub>N<sub>3</sub>.</p>										

### A.2.2 Water corrosion of UN

Results like that from the oxidation testing have been found with UN corroded in water-saturated air, steam, nitric acid,  $\text{H}_2\text{O}_2$ , and for samples submerged in water. Various reaction products identified under an assortment of testing parameters generally included  $\text{UO}_2$ ,  $\text{UO}_3$ ,  $\text{U}_3\text{O}_7$ ,  $\text{U}_3\text{O}_8$ ,  $\text{U}_2\text{N}_3$ ,  $\text{UN}_{1.7}$ ,  $\text{UN}_2$ , as well as oxynitride phases (see **Table A.4**) [13, 14, 36, 54, 57, 60, 61, 66-69]. In most cases, like seen in the air oxidation studies, it was noted that the  $\text{U}_2\text{N}_3$  phase was “sandwiched” between the bulk UN and surface  $\text{UO}_2$  or identified as an intermediate. An example of this “sandwich-like” structure of a non-protective surface layer of  $\text{UO}_2$  followed by  $\text{U}_2\text{N}_3$ , which covers the UN grain is shown in **Figure A.7** [69]. **Figure A.7a** shows an area of degradation for the UN steam exposure sample (9 MPa, 300 °C, 30 minutes). The chemical analysis of the higher magnification area (**Figure A.7b**) shows region 1 as only UN, but regions 2 and 3 (at the grain boundary triple junctions) were identified as lower density with increased oxygen content. This oxide formation was correlated to the separation of the grains from the matrix due to the stress caused by the secondary phase formation at the grain boundaries [69].

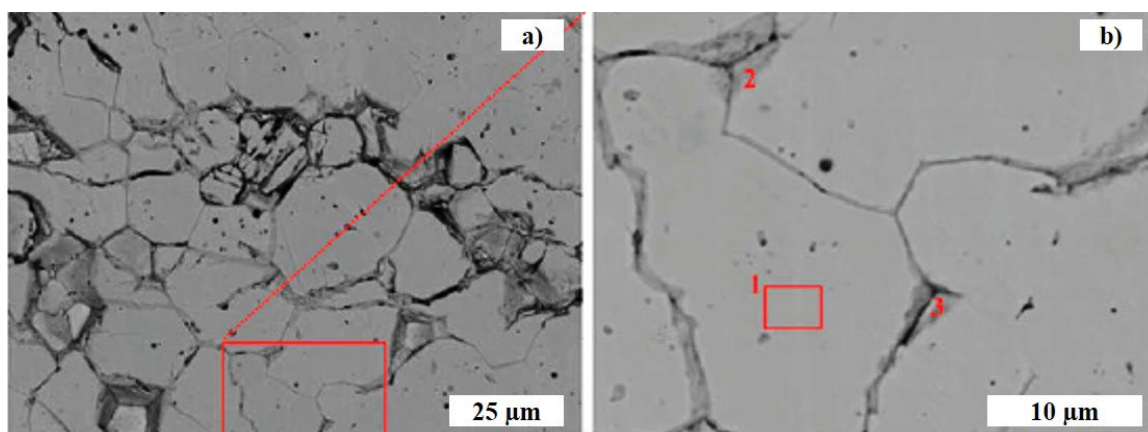
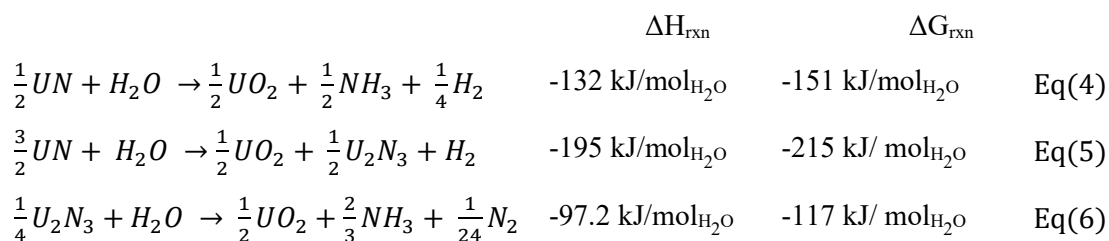


**Figure A.7** SEM micrographs of a) degraded microstructure of a UN pellet (98.25% TD) exposed to steam (9 MPa, 300 °C, 30 minutes) and b) higher magnification of the degraded region displaying “sandwich” structure of  $UO_2$  with underlying nitride layer at the grain boundaries. Modified from Lopes et al. [69].

It is important to note that the formation of these intermediate phases creates a volume expansion and results in pulverization of monolithic samples. It is generally agreed that hydrolysis of UN occurs according to the following reactions [54, 61]:



The final oxidation product of UN under hydrolysis is  $UO_2$ , not the  $U_3O_8$  seen during oxidation of UN. This is similar to the hydrothermal corrosion behavior of  $U_3Si_2$  [70],  $UO_2$  [71-74], and uranium metal [75].

The documentation of the microstructural evolution of UN in hydrothermal corrosion conditions is sparse in the open literature. **Figure A.8** is a compilation of available macro images for UN degradation under various hydrothermal corrosion conditions. **Figure A.8a** (from UN feedstock via CTR-N) and **b** (from UN feedstock via

HDN) show the degradation of conventionally sintered UN pellets in static autoclave conditions at 300 °C for 48 hours and 30 minutes, respectively [13, 14]. **Figure A.8c** and **d** show UN pellets sintered via SPS from HDN UN feedstock under steam corrosion at 340 °C for 105 minutes and 425 °C for 300 minutes [68]. Another high density UN sample (99.0% TD) sintered via SPS and subjected to static autoclave testing (time duration not listed) at 300 °C is shown in **Figure A.8e** [76]. All samples show either complete pulverization to powder or fragments or cracking, spallation, and overall degradation of the monolithic samples.

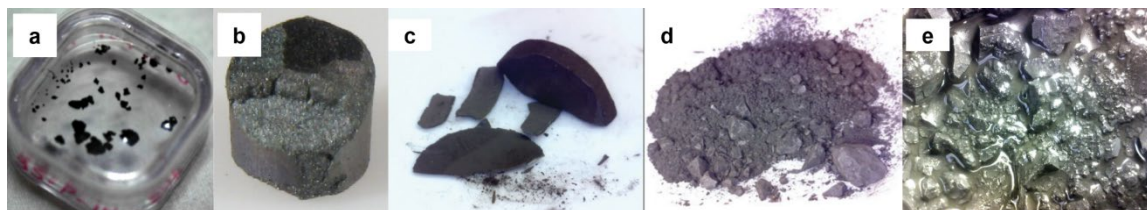


**Figure A.8 UN degradation under hydrolysis; a) UN pellet following static autoclave testing in DI water at 300 °C/10 MPa for 48 hours (modified from Nelson et al.) [13], b) UN pellet after static auto testing at 300 °C/16 MPa for 30 minutes (modified from Watkins et al.) [14], c) UN after hydrolysis in steam at 340 °C for 105 minutes, d) UN after hydrolysis in steam at 425 °C for 300 minutes (modified from Jolkkonen et al.) [68], and e) UN after static autoclave corrosion at 300 °C, no time duration given (modified from Malkki) [76].**

Examining the microstructural evolution of UN under corrosion conditions can help identify the reaction progression over various times and temperatures but to date, as previously stated, this information has been limited in literature. **Figure A.9** shows UN samples of approximately 92% TD (fabricated using HDN powder and conventional sintering) submerged in DI water for 30 minutes at ~16 MPa and temperatures of 250 °C, 275 °C, and 300 °C. UN sample degradation is noticeable at 250 °C with the edges of the right cylinders showing preferential attack. Grain boundary etching and eventual spallation increases with increasing time and temperature. While the post-corrosion

results indicated the corroded samples were still primarily UN, the degradation behavior was attributed to the formation of secondary phases including hyper-stoichiometric UN,  $\text{UO}_2$ , and possibly an oxynitride phase. These results from Watkins *et al.* [14] correspond to the results reported by Jolkkonen *et al.* for UN samples of 96.6 and 97.7% TD fabricated via SPS with HDN powder [68].

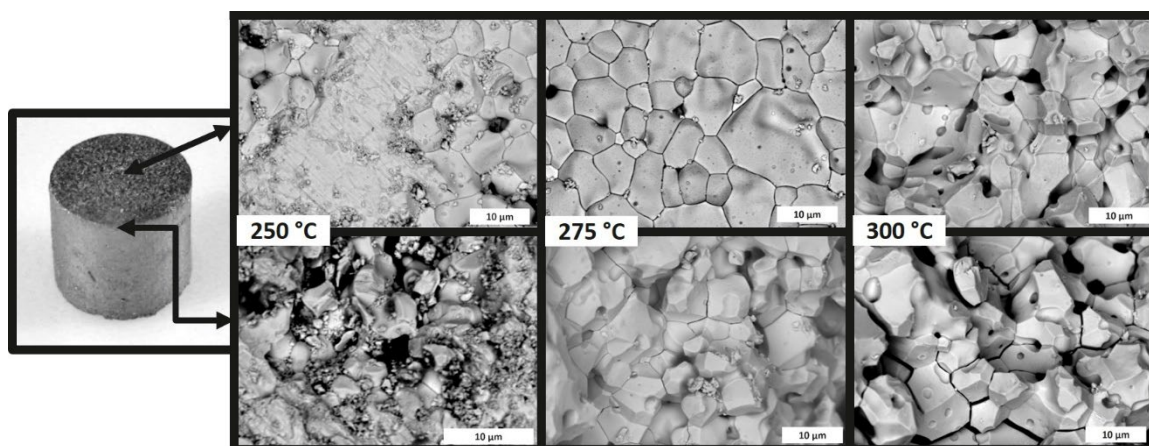


**Figure A.9** Backscattered electron micrographs of corroded UN pellets submerged in DI water for 30 minutes at 250 °C, 275 °C, and 300 °C and approximately 16 MPa. The top images were taken from the less corroded pellet surface while the bottom images show the preferential degradation from the pellet edges. Grain boundary etching and attack increases with temperature. From Watkins *et al.* [14].

Micrographs of UN microstructural degradation for 98.25% TD samples (fabricated with HDN powder and sintered via SPS) exposed to steam for 90 minutes at 300 °C and 9 MPa are seen in **Figure A.10** [69]. Similar to the above work seen in **Figure A.8b** and **Figure A.9**, some areas of the matrix are preserved but degraded regions display grain boundary etching causing weakening of the matrix.

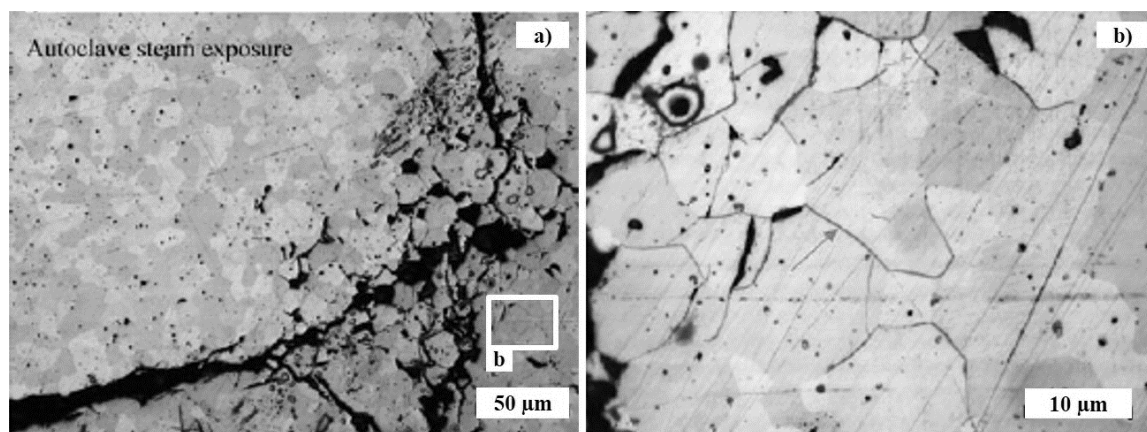


**Figure A.10** Optical micrographs of 98.25% TD UN exposed to steam at 9 MPa and 300 °C for 30 minutes. a) UN sample showing section where the matrix was preserved and other degraded regions and b) inset of a) displaying degraded region with grain boundary etching which causes weakening of the matrix. Modified from Lopes et al. [69].

No literature was found for monolithic UN samples subjected to corrosion in radiolysis conditions, such as would be expected for fuel exposed in a leaker/failed rod during reactor operation or during spent fuel storage. However, one study looked at the interaction of UN thin films exposed to 0.1 M  $\text{H}_2\text{O}_2$  (a product of water radiolysis) at room temperature [77]. The results showed that a UN specimen (prepared via DC magnetron sputtering of a uranium target and containing a small amount of  $\text{U}_2\text{N}_3$  contamination) exposed to  $\text{H}_2\text{O}_2$  for 50, 250, 1250, and 6000 seconds did oxidize to  $\text{UO}_2$  and  $\text{UO}_{2+x}$ . The results also suggested UN had a lower corrosion rate in  $\text{H}_2\text{O}_2$  as compared to a  $\text{UO}_2$  sample tested under the same conditions [77]. These findings could suggest that UN may be more corrosion resistant in an accident scenario than previously believed and underscores the necessity for additional research for UN in radiolytic conditions.

While the differences in synthesis and sintering methods and variations in testing parameters make it difficult to provide definitive conclusions about UN in hydrolysis conditions, general observations can be made. **Table A.4** summarizes the available

literature on UN and UN-composites under corrosion via water or steam. The summary includes (if available) the synthesis method for UN feedstock, sintering method, the physical form exposed to corrosion (i.e., powder, pellet, etc.), the temperature test range, test conditions, onset temperature, sample composition, grain size, and the resulting reaction products. Onset temperatures for UN and UN-composites tested in steam and water were generally  $< 200$  °C for powder samples, between 200-300 °C for monolithic samples, and again, dense, high purity samples performed the best. Most of the available data is for pure UN samples, thus presenting a research opportunity for hydrothermal corrosion testing of UN-composites. Grain size was included in the table, even though most of the investigations did not report it. However, one of the studies which provided grain size data indicated samples having smaller grain size performed better due to increased mechanical stability and less susceptibility to intergranular cracking [69], highlighting that this is an important parameter to consider.

**Table A.4 Summary of water/steam corrosion of UN and UN with additives or composites.**

	Ref.	Synthesis method	Sintering method	Type	Temp. test range [°C]	Test conditions	Onset temp. [°C]	Composition	Grain Size [μm]	Reaction products
Water/steam	[13]	CTR-N	Conventional	Pellet	300 (48 hr)	Static autoclave, ramped*	n/a	UN	15-25	UO <sub>2</sub>
	[14]	HDN	Conventional	Pellet	250-350	Static autoclave, ramped, 1 °C/min	250 (UN), 275-300 (UN-UO <sub>2</sub> composites)	UN, UN+5w% UO <sub>2</sub> , UN+10w% UO <sub>2</sub>	n/a	Hyper-stoichiometric UN, U-oxynitride, U <sub>2</sub> N <sub>3</sub> , and UO <sub>2</sub>
	[36]	HDN/arc-melting	HIP	Single crystal, polycrystalline compacts	300-700	Isothermal	-	UN	n/a	U <sub>3</sub> O <sub>8</sub> (H <sub>2</sub> O sat. air), UO <sub>2</sub> (H <sub>2</sub> O)
	[54]	n/a	n/a	Powder	100-400	Ramped, 5 °C/min	250	UN	n/a	NH <sub>3</sub> , H <sub>2</sub> , U <sub>2</sub> N <sub>3+x</sub> , and UO <sub>2+y</sub>
	[57]	Sol-gel	Conventional	Compact	25-767	Ramped, 3 °C/min	~ 347	UN	n/a	UO <sub>2</sub> with U <sub>2</sub> N <sub>3+x</sub>
	[59]	n/a	n/a	Pellet	Up to 452, 30 min 13% water vapor	Ramped, 40 °C/min	n/a	*UN	n/a	U <sub>3</sub> O <sub>8</sub> with intermediates of U <sub>2</sub> N <sub>3</sub> , and UO <sub>2</sub>
	[60]	n/a	Conventional	Compact	200-1000 (steam); 80-300 (water)	Ramped*	250	UN	n/a	UO <sub>2</sub> , U <sub>2</sub> N <sub>3</sub> , NH <sub>3</sub>
	[61]	Direct nitride of U metal	n/a	Powder	340-420	Isothermal	~ 300	UN	n/a	UO <sub>2</sub> , U <sub>2</sub> N <sub>3</sub> , NH <sub>3</sub> , H <sub>2</sub>
	[61]	Direct nitride of U metal	Arc-melting	Single crystal	Up to 750	Ramped*	~ 400	UN	n/a	UO <sub>2</sub> , U <sub>2</sub> N <sub>3</sub>
	[61]	Direct nitride of U metal	Arc-melting, Conventional	Powder, single crystal, pellet	210-300 (in high pressure, 80 atm)	Isothermal	180 (powder), 200 (pellet), 230 (single crystal)	UN	n/a	UO <sub>2</sub> , U <sub>2</sub> N <sub>3</sub>
[67]	n/a	n/a	Pellet	23 and 92	Static chamber, Ramped (for 92 °C test*)	n/a	UN	n/a	UO <sub>2</sub> and NH <sub>3</sub>	

Ref.	Synthesis method	Sintering method	Type	Temp. test range [°C]	Test conditions	Onset temp. [°C]	Composition	Grain Size [μm]	Reaction products
[68]	HDN	SPS	Pellet	400-500	Isothermal	400	UN	n/a	UO <sub>2</sub> , NH <sub>3</sub> , H <sub>2</sub> , U <sub>2</sub> N <sub>3</sub> , oxynitride
[69]	HDN (UN), Arc-melting (U <sub>3</sub> Si <sub>2</sub> )	SPS	Pellet	300 (30-90 min)	Static autoclave, Ramped, 15 °C/min	n/a	UN, UN+10w% U <sub>3</sub> Si <sub>2</sub>	6-24 (UN), 9 (UN+10w% U <sub>3</sub> Si <sub>2</sub> )	Oxide phase
[76]	HDN	SPS	Pellet	150	Static autoclave, Ramped*	≤150	UN+30at%ZrN	n/a	n/a
[78]	Sol-gel, CTR-N	Conventional	Pellet	Boiling water	n/a	<sup>b</sup> Intact after 5hr (UN-Cr), pulverized 10 min (UN-Ni), pulverized 5 min (UN-Al)	<sup>b</sup> UN+2.7w%Cr, UN+2.8w%Ni, UN+1.5w%Al	n/a	CrO <sub>2</sub> , Cr <sub>2</sub> O <sub>3</sub> (UN-Cr sample)
[77]	DC magnetron sputtering	n/a	Thin film	0.1 M H <sub>2</sub> O <sub>2</sub> at room temp	50, 250, 1250, 6000 seconds	n/a	<sup>c</sup> UN	10 nm	UO <sub>2</sub> and UO <sub>2+x</sub>
<sup>a</sup> no rate listed; <sup>a</sup> Samples had “detectable” amounts of UO <sub>2</sub> in starting material; <sup>b</sup> Material referred to as the UN-Cr sample noted as surviving 5 hours in boiling water was characterized prior to testing and identified as UO <sub>2.11</sub> , with UC <sub>0.18</sub> N <sub>0.82</sub> and CrO <sub>2</sub> , material referred to as UN-Al sample was characterized prior to testing and identified as UC <sub>0.5</sub> N <sub>0.5</sub> , <sup>c</sup> Sample contained some U <sub>2</sub> N <sub>3</sub> contamination									

#### A.4 Additives/dopants to UN to mitigate oxidation behavior

A primary screening for suitable compounds or elements as a secondary addition to a UN fuel matrix includes oxidation resistance to LWR-relevant environments and temperatures. While many compounds could meet this challenge, the inclusion of a non-uranium bearing component to the UN fuel in excess of 28 vol% nullifies the advantages of UN over the benchmark UO<sub>2</sub> in terms of uranium density; this point is elaborated upon in the U<sub>3</sub>Si<sub>2</sub> publication of this review series. Incorporation of a uranium-bearing compound to a UN matrix would ensure that the uranium density of the compound would always exceed that of UO<sub>2</sub>. Research on combining UN with uranium silicide compounds, such as U<sub>3</sub>Si<sub>2</sub>, has been investigated, as until recently it was reported that

$U_3Si_2$  was more resilient to oxidizing atmospheres [35, 79]. However, as reported by Wood *et al.* [12],  $U_3Si_2$  is also susceptible to hydrothermal corrosion conditions resulting in an increase in research focusing on the addition of other compounds and alloying elements to UN that can hinder its corrosion behavior. The relevant literature related to UN alloys and composites is discussed, along with a thermodynamic assessment of the various systems. As previously mentioned, this review is not specifically focused on fabrication methods. The fabrication methods are discussed in terms of how synthesis and fabrication affect the additive/dopant additions, resulting microstructures, subsequent phase compositions, and oxidation/corrosion performance. Few, if any of the studies discussed are fully optimized to explore the effects of time, temperature, and atmosphere on either fabrication or oxidation/corrosion conditions. This is a non-trivial issue and highlights the need for more robust, controlled experimentation conditions in both fabrication and corrosion testing.

As mentioned in **Section A3.1** and shown in **Figure A3**, UN has a narrow phase field and is thermodynamically sensitive to decomposition, especially at higher temperatures and low partial pressures of nitrogen. To provide a better empirical observation of this phenomenon, the effect of sintering atmosphere on phase formation and microstructure was investigated by Jaques *et al.* with synthesis and sintering of UN-(5-10 wt%) $UO_2$  composites [44]. Pellets fabricated using UN feedstock (synthesized via the HDN method) were sintered in ultra-high purity Ar, Ar+1wt% $N_2$ , and Ar+100 ppm  $N_2$  to better understand how the nitrogen concentration affected secondary phase formation. Accordingly, sintering in pure argon at 1550 °C resulted in a “coring” effect, where UN dissociated, leading to an elemental liquid phase uranium along grain

boundaries and an outer rim with enhanced densification (seen in **Figure A.11**). The composites had  $\text{UO}_2$  homogeneously distributed throughout, but with increased phase fractions of  $\text{UO}_2$  and higher sintering temperatures, the structure coarsened and lowered the overall pellet density. This behavior is believed to be due to the favorable formation of oxygen stabilized nitrides or uranium oxynitrides [44].

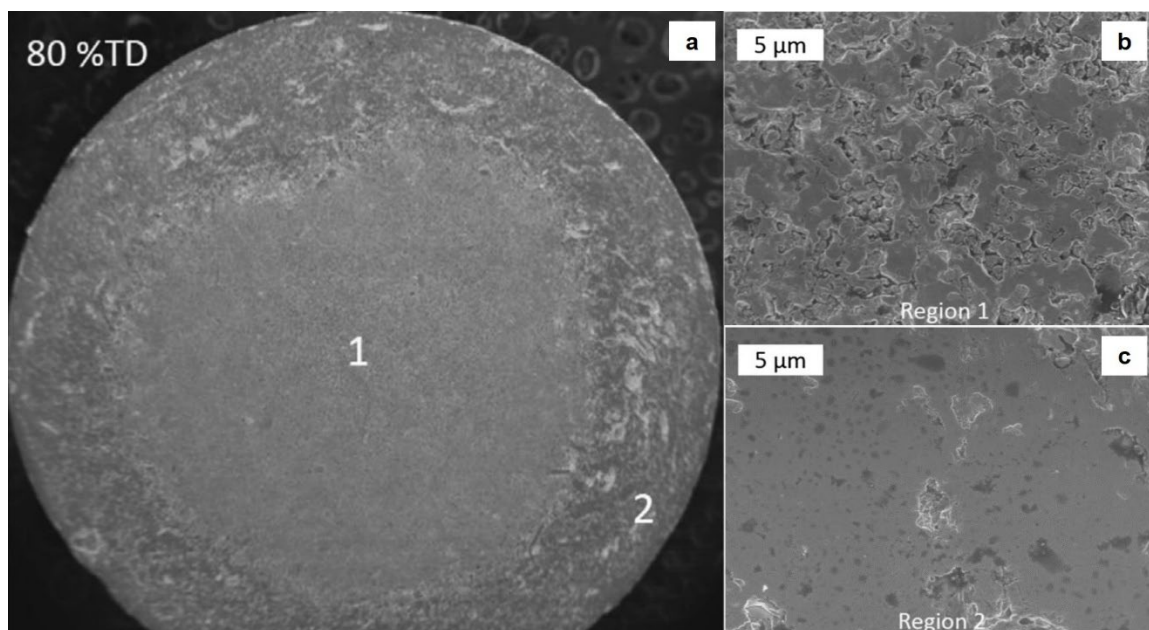


**Figure A.11** a) SEM micrograph of a UN pellet sintered in UHP-Ar at 1550 °C having an inner region of lower density and an outer rim with higher densification due to UN dissociation forming free elemental uranium resulting in liquid phase sintering, b) higher magnification of Region 1, and c) higher magnification of Region 2. Modified from Jaques et al. [44].

Work on another UN composite type to hinder UN dissociation was presented by Potter and Scott under a patent for a (U,Zr)N alloy consisting of single-phase UN containing dissolved Zr (as ZrN) [80]. The invention describes nitriding uranium and < 10 wt% Zr to achieve a single-phase material, with 3-5 wt% being ideal for UN stabilization in preventing formation of higher uranium nitride phases, sintered in 1 atm of  $\text{N}_2$  above 2200 °C. Potter and Scott compared the sintered pure UN samples and

(U,Zr)N samples heated at 1600 °C under vacuum for 8 hours, followed by a 1700 °C dwell for an additional 8 hours. The results indicate UN dissociated and sintered to the tungsten plate used for sintering after only 1 hour at 1600 °C [80], a result which would be expected according to the above mentioned work of Tennery and Matzke (**Figure A.4**) [46, 47]. The UN sample also showed extensive formation of free uranium, while the mass loss of the (U,Zr)N sample was 50% and 75% of the UN sample at 1600 °C and 1700 °C, respectively, and only had trace surface amounts of free uranium present [80]. These findings are similar to those of Watkins *et al.* who conventionally sintered UN (from CTR-N) composites of 10 wt% Zr in pure argon at 1500 °C [81]. In **Figure A.12**, UN dissociation is evident in the highly porous structure having a phase identified as liquid uranium (region 1) and areas having U-N-Zr (region 2) and U-N-O-Zr (region 3). The inset in **Figure A.12a** highlights a similar “coring” effect that was noted by Jaques *et al.* [44] due to UN dissociation, while **Figure A.12b** and **c** show the extent and uniformity of the porosity and liquid uranium phase present in the monolithic pellet [81]. These results were confirmed in their XRD analysis showing shifted UN peaks (attributed to Zr incorporation in the UN lattice to form a ternary phase of unknown stoichiometry) and ZrO<sub>2</sub>, as well as a small amount of U<sub>2</sub>N<sub>3</sub>. A similar result was seen in their fabrication of UN+10wt% Y samples sintered in argon [81].

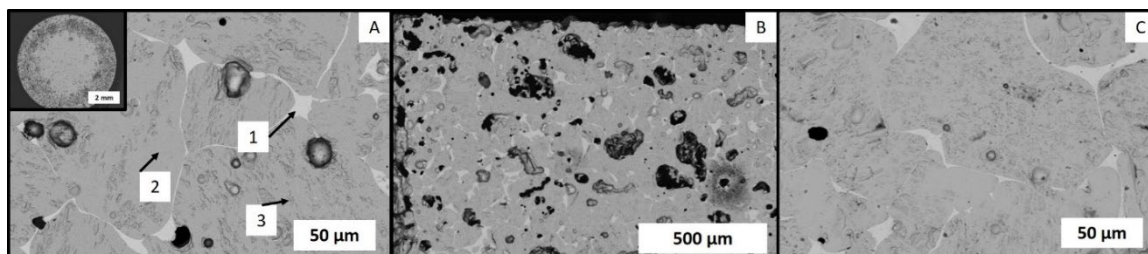


**Figure A.12** Backscatter electron micrographs of UN+10wt% Zr sintered in argon at 1500 °C. A) As-sintered microstructure showing formation of a liquid uranium phase at the grain boundaries indicating UN dissociation; inset is of the pellet surface showing the “coring” effect due to the UN dissociation, b) as-sintered microstructure highlighting the porous nature of the pellet and the uniformity of the liquid uranium phase, c) slightly higher magnification of the as-sintered microstructure showing the liquid uranium phase, and the phases identified as U-N-Zr and U-N-O-Zr. Modified from Watkins et al. [81].

This UN dissociation can be predicted through the use of an Ellingham diagram, which shows the relative thermodynamic stability of UN as compared to the nitride formation for potential additives (**Figure A.13**) [82]. The importance of a diagram like this is that it provides a thermodynamic prediction of the most stable phases in relation to UN. Accordingly, if at any time during the processing of a fuel the free energy of formation ( $\Delta G$ ) of an additive nitride is lower than that of UN, it is thermodynamically favorable for the UN to dissociate (leaving elemental uranium) and form the nitride of the additive. Two examples of nitrides that are more favorable than UN are AlN below 600 °C and Si<sub>3</sub>N<sub>4</sub> under approximately 800 °C (**Figure A.13**). This predicted thermodynamic stability of ZrN and TiN relative to UN was empirically validated by Potter and Watkins *et al.* [80, 81]

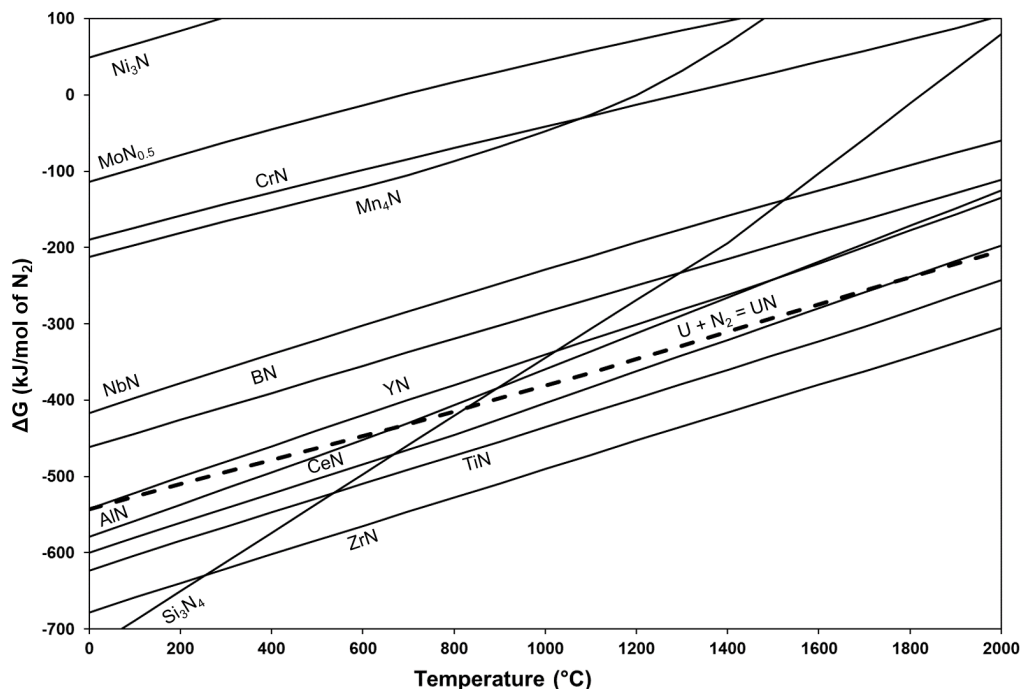


**Figure A.13** Ellingham-type diagram showing thermodynamic stability of nitride formation of various metallic elements considered for possible dopants into ATF concepts versus UN. Calculated using HSC Chemistry 9 [62].

In a follow-on study from that of Jaques *et al.* [44], UN-(5-10 wt%)UO<sub>2</sub> composites were examined for microstructural degradation under hydrothermal conditions [14]. Monolithic samples of approximately 92% TD were prepared using UN powder from a HDN method and commercially available UO<sub>2</sub>. Green pellets were conventionally sintered in an Ar+100 ppm N<sub>2</sub> atmosphere. The sintered monoliths, along with pure UN and pure UO<sub>2</sub> samples as benchmarks, were submerged in DI water and heated to 250-350 °C and up to 16 MPa for 30 minutes [14]. As depicted in **Figure A.14a**, the corrosion morphology of the pellets shows that reactions begin at the grain boundaries, resulting in grain boundary expansion and spallation. As the corrosion process advances with temperature, pellet degradation increases (as anticipated). The top surfaces of the composite pellets (top row of **Figure A.14**) also exhibited an interesting phenomenon where an oxygen-rich phase (as identified with EDS) consumes the surface

of the UN grains, suggesting that the oxide may be nucleating on the grains and propagating across the surface. This was not observed in the pure UN benchmark samples (**Figure A.9**) [14]. The authors postulated that the UN reaction with water proceeds as a reaction layer and phase segregation occurs at the grain boundaries. The phase segregation results in the expansion of the intermediate layer leading to mechanical breakdown of the pellet. The researchers also noted in their batch study that the pellets fabricated with a higher starting oxygen impurity enhanced the degradation behavior [14]. Similar attempts at a solid solution of UN + (15,30at%) ZrN (~ 6.9,15.2 wt% ZrN) pellets was attempted through SPS, but found both U-rich and Zr-rich regions post-sintering [76]. **Figure A.14b** shows the fabricated microstructure of a UN+30at%ZrN pellet (approximately 91.3% TD) which had been heat treated in argon at 1400 °C for 4 hours after SPS. The brighter areas identified as the U-rich regions and the darker areas being Zr-rich. The sample was also subjected to autoclave testing in 3mL of DI water at 150 °C for 4 hours, and was already showing significant degradation as seen in **Figure A.14c**. The authors postulated this degradation at 150 °C could have been enhanced by impurities introduced during the pre-corrosion heat treatment to improve the solid solution between the UN and ZrN. The corroded microstructure is shown in **Figure A.14d** and the authors indicated there was possibly increased degradation due to carbon

impurities (dark, pitted regions) that were introduced either from their uranium feedstock or through the SPS process from the graphite foil [76].

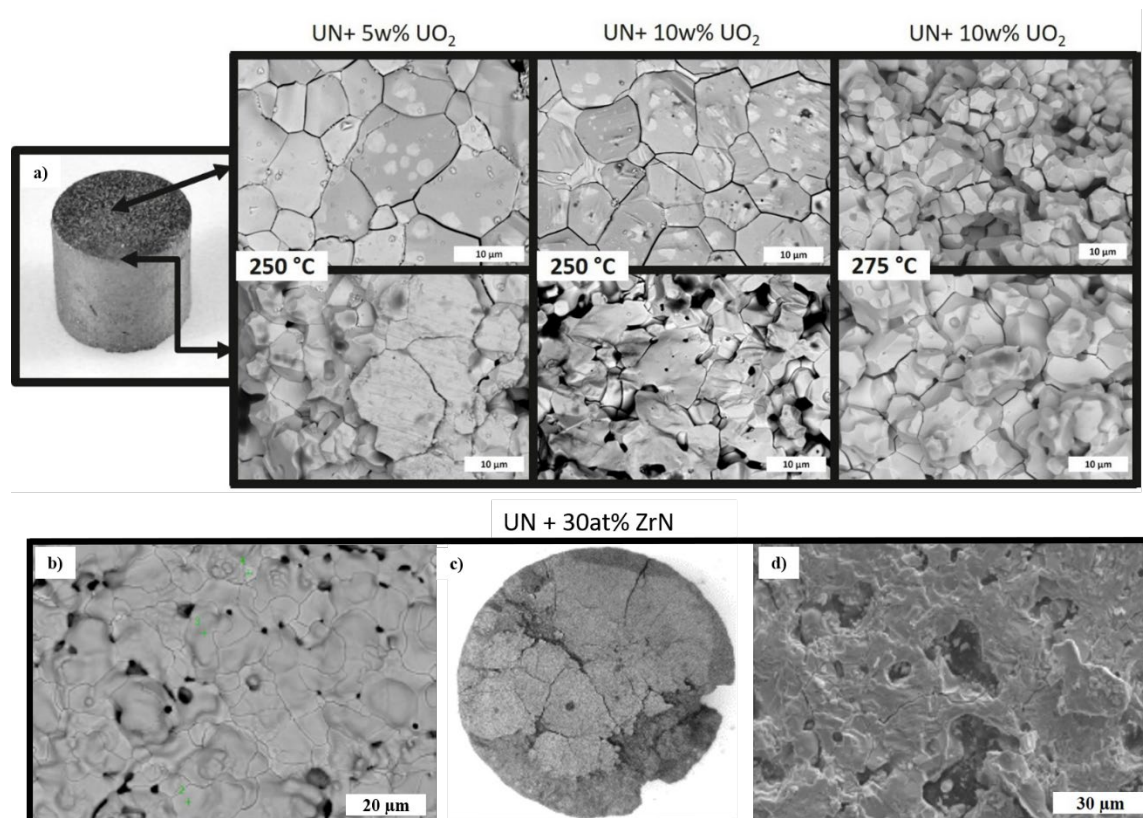


**Figure A.14** a) Representative optical image of UN+UO<sub>2</sub> pellet conventionally sintered and subjected to static autoclave testing, arrows point to the relevant areas where backscatter electron micrographs were taken of the corroded microstructure. The UN +(5-10 wt%) UO<sub>2</sub> samples corroded at 250 and 275 °C, show preferential edge and grain boundary attack. The pellets corroded at 250 °C also indicate clear light and dark phases present across the surface of the pellets, the dark phase being identified as an oxide phase via EDS (from Watkins et al.) [14]. b) SEM of sintered microstructure of a UN+30at% ZrN composite sintered via SPS and heat treated at 1400 °C for 4 hours in argon displaying U-rich (lighter) and Zr-rich (darker) regions, c) macro image of the sample subjected to autoclave testing in DI water for 4 hours at 150 °C, and d) corroded microstructure of the autoclave tested sample showing degradation and dark regions which were identified as carbon impurities (modified from Malkki) [76].

Discussed in more detail in the U<sub>3</sub>Si<sub>2</sub> review publication, several methods and strategies for corrosion protection have been considered; one such strategy is to incorporate an additive or dopant which will preferentially oxidize, forming a

protective/passivating barrier (oxide, nitride, or silicide) on the surface of the fuel element to protect it from corrosion [78, 81]. An Ellingham-type diagram, similar to **Figure A.13**, for the thermodynamic stability of oxide formation for various proposed elemental additions to high uranium density fuels, is reported in the  $U_3Si_2$  focused part of this review series. Using a similar strategy, Lahoda *et al.* have recently submitted a U.S. patent application on grain boundary enhanced UN and  $U_3Si_2$  pellets for improved oxidation resistance [83]. The invention describes mixing UN or  $U_3Si_2$  powders with an additive of selected passivating materials (<20 wt%) including Mo, Ti, Al, Cr, Th, Cu, Ni, Mn, W, Nb, Zr, Y, Ce, or Mg, or alloys containing at least 50 at% of the metal, MgN,  $ZrSi_2$ ,  $ZrSiO_4$ ,  $CrSi_2$ , BeO,  $UO_2$ , or glassy materials [83].

As previously stated, limited publications are available in the open literature that investigate the effects of adding dopants or components to the corrosion behavior of UN; however, there is more data on the addition of UN to other host matrices, including  $UO_2$  and  $U_3Si_2$ . Accordingly, Yang *et al.* and Costa *et al.* investigated the oxidation resistance of  $UO_2$ /UN composite fuel compacts with up to 50 wt% UN [84, 85]. However, the synthesis techniques and observed behavior were significantly different. In the study by Yang *et al.*, hot-pressed composites of nearly 100%TD  $UO_2$  along with (6-39 wt%)UN (synthesized from the HDN method) were fabricated for the purposes of improving the uranium density and thermal conductivity of  $UO_2$ . The authors indicated that approximately 7 wt%  $UO_2$  impurity existed in the starting HDN UN powder along with approximately 3 wt%  $U_2N_3$  (as determined by XRD via a relative intensity ratio, RIR, analysis). Although starting weight fractions for UN were listed as 19.4, 37.4, and 51.2, it was reported that the sintered composites had a marked decrease in the UN weight

fraction (6-39 wt%), which was attributed to decomposition or the oxidation of the UN phase during sintering under vacuum. However, precise control of the sintering atmosphere was not detailed, and no elemental uranium phase was detected and so oxidation is probable and decomposition is unlikely. Backscatter electron images of the hot-pressed samples are shown in **Figure A.15** and show the UN (light phase) and  $\text{UO}_2$  phase (dark contrast) comprising the microstructure. The authors suggest that the formation of a hypo-stoichiometric  $\text{UO}_2$  is likely, which may be due to the low oxygen potential during hot-pressing in vacuum, resulting in the oxidation of UN. If the UN is oxidized, it is postulated that nitrogen dissolution into the  $\text{UO}_2$  is possible, forming an oxynitride that decomposed upon cooling to  $\text{UO}_2$  and  $\text{U}_2\text{N}_3$ . The authors also acknowledged that the RIR method for determining the final sintered compositions did not reflect the actual composition as the pattern was obtained from the sample surface and likely varied from the bulk [85].

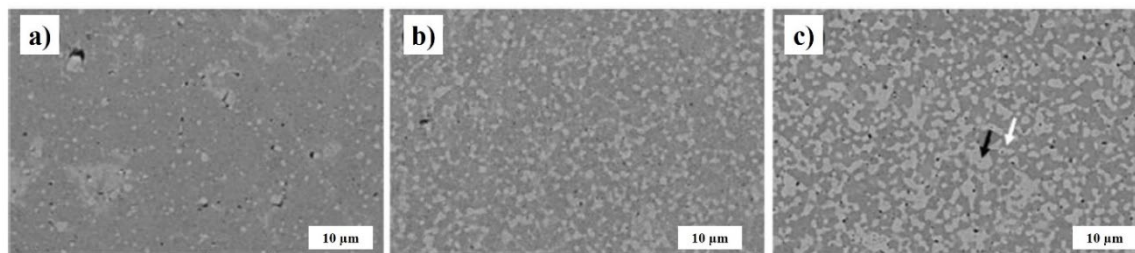


**Figure A.15** Backscatter electron images of the  $\text{UO}_2$ -UN samples hot-pressed at 1590 °C, a) 6.9 wt% UN, b) 26.4 wt% UN, and c) 39.3 wt% UN. Modified from Yang et al. [85].

More recently, Costa *et al.* also looked at composites of  $\text{UO}_2$  with (10, 30, and 50wt%) UN (microspheres from the sol-gel process) sintered via SPS in vacuum. The following general behaviors were observed: Higher sintering temperatures and pressures resulted in a lower concentration of UN and a higher concentration of  $\alpha$ - $\text{U}_2\text{N}_3$ , and the

cooling rate impacts the amount, size, and morphology of the  $U_2N_3$  precipitates. Faster cooling resulted in less of the sesquinitride phase with a coarse grain structure and slow cooling rates produced a long range lamellar-type structure [84]. The sintered microstructure of the UN- $UO_2$  composites are shown in **Figure A.16a-d**. The highly porous UN microspheres are well distributed throughout the  $UO_2$  matrix but deviate from their original spherical shape to a more elongated oval, which is attributed to the induced compressive stresses applied during the SPS process. EDS chemical mapping was also used to identify  $\alpha-U_2N_3$  precipitates throughout the  $UO_2$  matrix (identified by P3 in **Figure A.16d**) [84]. As a follow-on study to this work, the authors oxidized their as fabricated UN microspheres, sintered UN microspheres,  $UO_2$ , and  $UO_2$ -(10,30, and 50 wt%) UN in a TGA in synthetic air up to 700 °C. The degradation of the as-fabricated and sintered UN microspheres oxidized in air was shown previously in **Figure A.5**. The authors reported the highest oxidation onset temperature of 320 °C for their  $UO_2$ /10wt% UN sample, outperforming even the benchmark  $UO_2$  sample. It should be noted that the authors indicated the actual phase composition of their  $UO_2$ /10wt% UN sample after sintering was 95 wt%  $UO_2$ /1.7 wt% UN/3.7 wt%  $U_2N_3$  via XRD RIR method. This composite also had a higher maximum reaction temperature and lower oxidation rate at its maximum than their benchmark  $UO_2$  sample. The as fabricated UN microspheres (52% TD) and sintered UN microspheres (83.8% TD) had the lowest oxidation onset temperatures (276 and 260 °C, respectively).

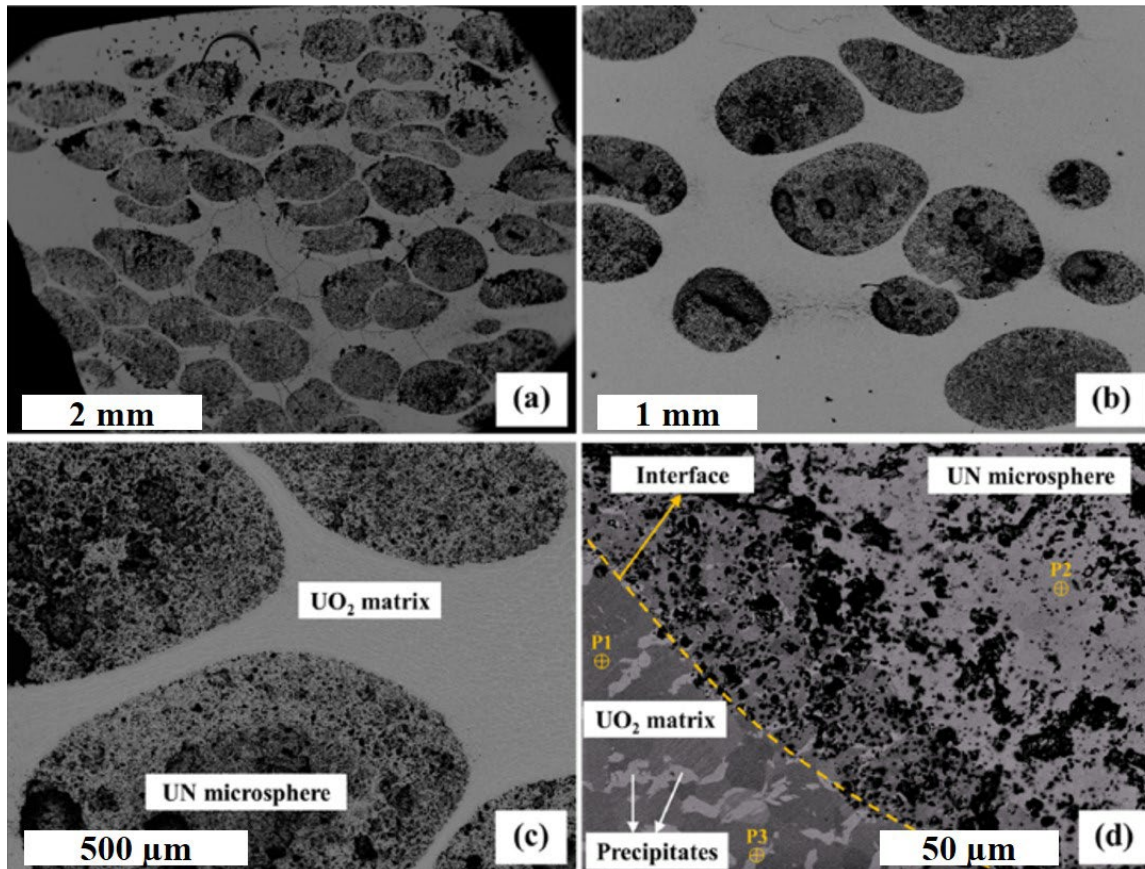


**Figure A.16** Backscatter electron micrographs of UN microspheres embedded in a  $\text{UO}_2$  matrix. a) showing UN microspheres relatively well dispersed throughout the  $\text{UO}_2$  matrix but elongated from their original spherical shape, b) higher magnification of the UN microspheres, c) higher magnification image showing the more porous UN microsphere as compared to the denser  $\text{UO}_2$  matrix, and d) highlighting the  $\text{UO}_2$ -UN microsphere interface. Modified from Costa et al. [84].

Other work using UN microspheres investigated dopants of Cr, Ni, or Al (2.7, 2.8, and 1.5 wt% respectively) to achieve a passivation via preferentially formed oxide layers of the metallic additives during water exposure [78]. The desired additives were dissolved into the feed solution to make spheres which then underwent carbothermic reduction. The authors indicate as-fabricated microspheres were all highly porous (< 80% TD for their proposed compositions). Due to the use of carbon nano-powder during the internal sol-gel process, significant washout of carbon into the solution occurred making control of carbon contaminants in the final product difficult. Considerable contamination

of the microsphere's surfaces with silicon oil was found which likely affected the sintering process. X-ray diffraction of the nitride microspheres indicated the UN/Cr samples contained UN,  $\text{UO}_2$ ,  $\text{Cr}_2\text{O}_3$ , and CrN, the UN/Ni samples only indicated UN, while the UN/Al samples corresponded to UN, AlN, and  $\text{Al}_2\text{O}_3$  [78]. **Figure A.17a** and **c** show SEM micrographs of the UN-Cr and UN-Ni doped microspheres after nitridation and prior to sintering, **Figure A.17e** is the air-dried UN-Al microsphere prior to nitridation, while **b**, **d**, and **f** are the SEM micrographs and chemical maps showing elemental distribution on the sphere surfaces.

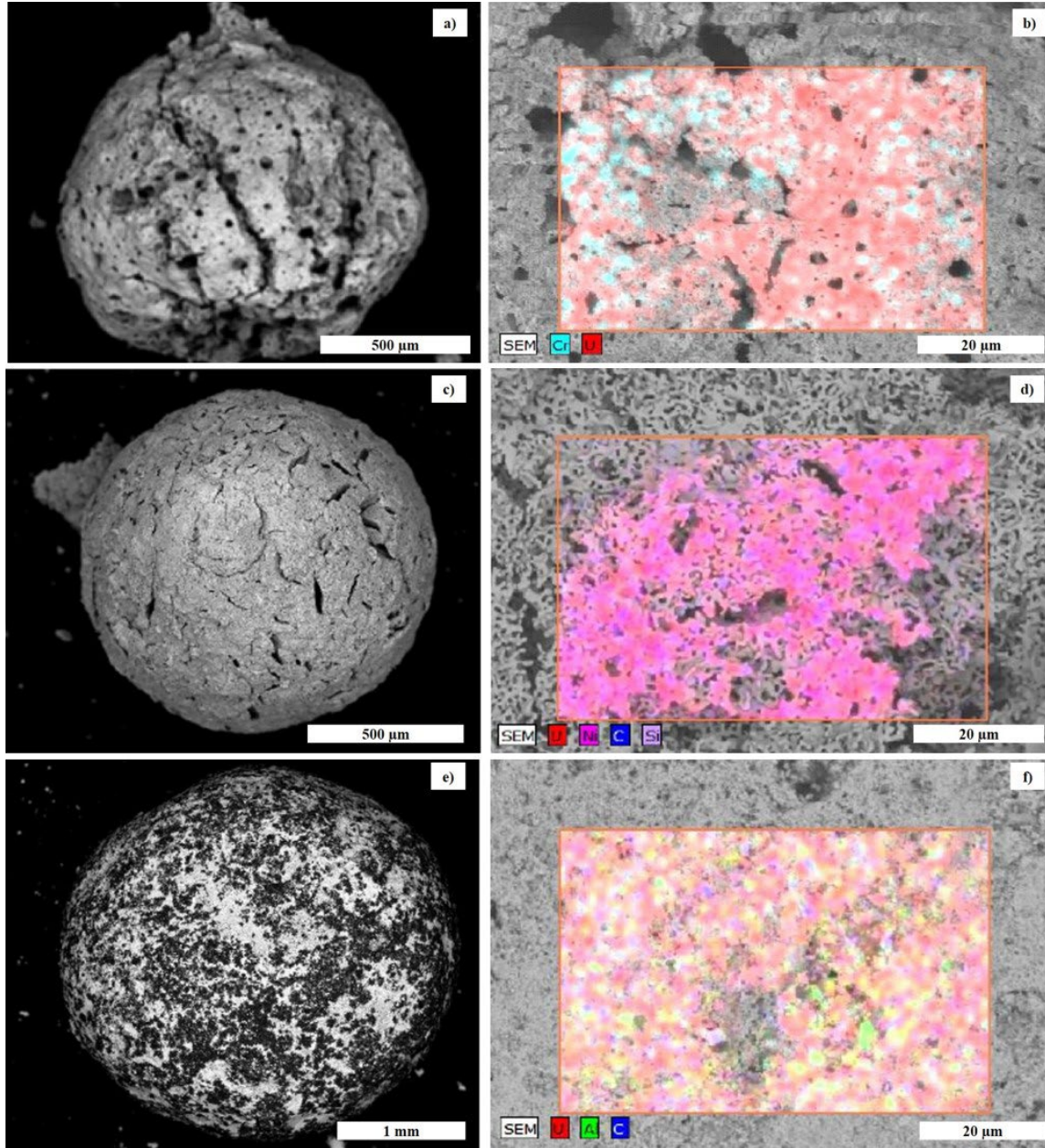


**Figure A.17** SEM micrograph compilation of UN-doped microspheres before sintering. a) UN-Cr microsphere after nitridation and b) EDS mapping of surface of the nitrided microsphere showing U and Cr distribution although XRD analysis identified UN,  $\text{UO}_2$ ,  $\text{Cr}_2\text{O}_3$ , and CrN; c) UN-Ni microsphere after nitridation and d) EDS mapping of the UN-Ni nitrided microsphere showing U, Ni, C, and Si distribution, XRD only identified UN; e) UN-Al air-dried microsphere before nitridation and f) EDS mapping of the UN-Al microsphere after nitridation showing U, Al, and Cr distribution, XRD identified UN, AlN, and  $\text{Al}_2\text{O}_3$ . Modified from Herman and Ekberg [78].

The microspheres were compacted and conventionally sintered inside a graphite element furnace. The UN/Cr pellet had varying porosity across the pellet (calculated to be 40% TD of UN) and showed indication of chromium migration away from the surface and an interaction between the W-setter plate using during sintering and the pellet bottom. XRD patterns from the surface identified  $\text{UO}_2$ ,  $\text{CrO}_2$  and a uranium carbonitride. The UN/Ni samples showed nickel segregation to the grain boundaries and formation of what the authors identified as  $\text{UNi}_5$  (calculated 57% TD of UN). The UN/Al samples showed Al segregated to the edge of the pellet and the surface was cracked and extremely porous, while XRD only identified a uranium carbonitride phase (calculated 50% TD of UN). All the as-sintered samples were subsequently placed into boiling DI water, with the authors stating the UN/Cr sample survived 5 hours without disintegrating. Although the pH of the final solution containing the UN-Cr sample was neutral, bubble formation was seen at the pellet surface. These bubbles were postulated to be from ammonia formation which could be correlated back to the UN corrosion Eqn. 4. [78]. As seen in **Figure A.18a-b**, the microstructure appeared unchanged (per SEM) after the corrosion experiment. The authors indicated the peak intensity of the XRD analysis of the nitride phase was smaller after corrosion, while the intensity of the detected oxide phases ( $\text{CrO}_2$  and  $\text{Cr}_2\text{O}_3$ ) were larger. The UN/Ni pellet disintegrated after 10 minutes in the boiling water and the UN/Al pellet was lost after 5 minutes and both solutions measured pH were neutral [78]. Another reference to UN composite formation using a sol-gel method was part of the oxidation study performed by Dehadraya *et al.* which included samples of (U,Ce)N microspheres having 15 and 30 mol% cerium [56]. The final oxidation product of the composites containing 15 mol% Ce were  $\text{MO}_{2+x}$  (M = metal) with a sesquinitride

as an intermediate. The authors reported the 30 mol% Ce sample ignited during the reaction forming a mix of  $M_3O_8$  and  $MO_{2+x}$  [56].

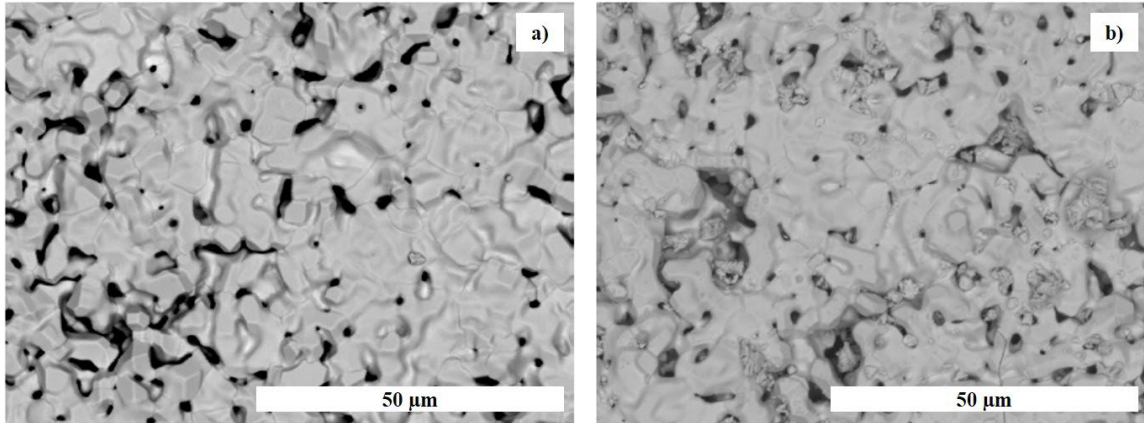


**Figure A.18** SEM micrographs of the UN-Cr microspheres microstructure prior to submersion in boiling water and b) UN-Cr microspheres after 5 hours in boiling water. Modified from Herman and Ekberg [78].

Several researchers have investigated the use of another ATF concept,  $U_3Si_2$ , as a secondary phase in UN for increased accident tolerance. The microstructure of UN- $U_3Si_2$  compacts of various compositions (10, 20, and 25 wt% silicide) fabricated via SPS using HDN UN powder and arc-melted  $U_3Si_2$  are seen in **Figure A.19a-c** [86]. The formation of a ternary U-N-Si phase was identified as the dark phase in the figures. In **Figure A.19a-c** the lighter phase inside the large silicon-rich inclusion (seen in all the compositions due to the UN and silicide powders being manually mixed) was said to most closely match the original  $U_3Si_2$  phase. In the 20 wt% and 25 wt% silicide samples (**Figure A.19b-c**) this phase was seen primarily at the grain boundaries. The authors proposed that this intergranular phase led to liquid phase sintering during the SPS process as they also found evidence of a liquid phase melt on their graphite dies [86]. This same work was also documented by Johnson *et al.* who stated that the resulting pellets had high

homogeneity with well dispersed  $U_3Si_2$  confined to the grain boundaries, although complete saturation of the UN grain boundaries was not achieved [87].

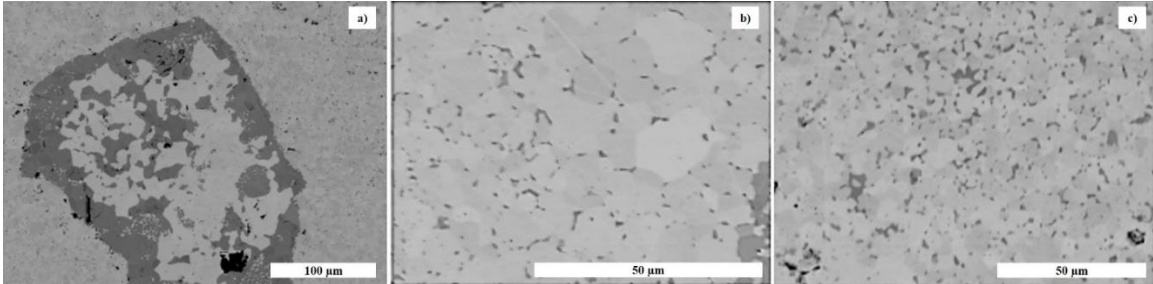


**Figure A.19** SEM micrographs of the SPS sintered microstructure of UN- $U_3Si_2$  composites a) 10 wt%  $U_3Si_2$ , b) 20 wt%  $U_3Si_2$ , and c) 25 wt%  $U_3Si_2$ . Modified from Raftery [86].

A separate study using UN powder from CTR-N and UN microspheres prepared from a sol-gel process combined with (25-35 wt%) arc-melted  $U_3Si_2$  powder and then conventionally sintered resulted in different behavior [8]. Higher temperature sintering resulted in increased interactions with the crucible material, pellet slumping, and evidence of a separate silicide phase formation. The phase morphology of the samples fabricated with conventional sintering methods (<95% TD) indicated a relatively continuous  $U_3Si_2$  phase with UN existing as separate regions within it (see **Figure A.20**) [8].

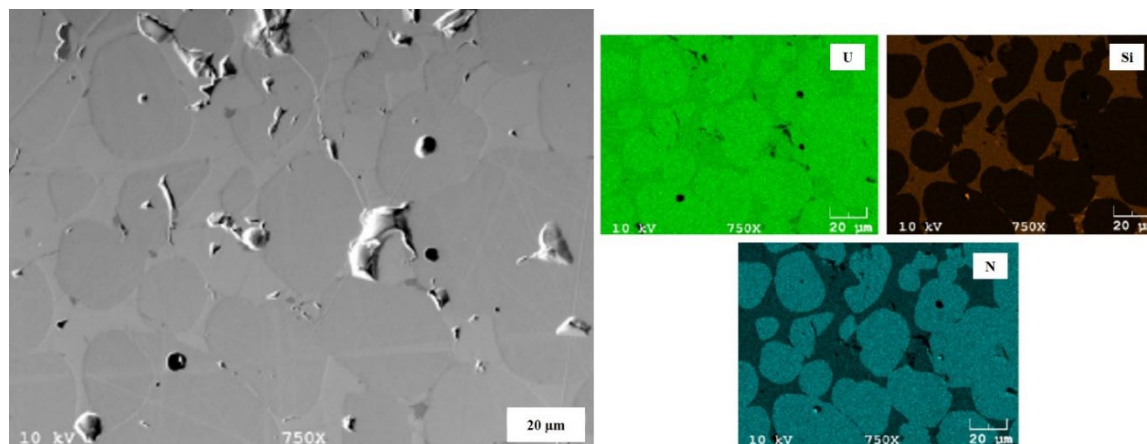


**Figure A.20** Backscatter electron image of UN+30 wt%  $U_3Si_2$  sample sintered at 1700 °C for 3 hours using HDN UN powder and arc-melted  $U_3Si_2$  exhibiting a fairly continuous  $U_3Si_2$  phase around the larger UN grains and the accompanying EDS chemical maps showing small areas of silicon-rich regions. Modified from Ortega *et al.* [8].

Only a couple of studies have examined the oxidation and corrosion behavior of UN/ $U_3Si_2$  composites. A UN-10 wt%  $U_3Si_2$  crushed powder sample oxidized in air up to 800 °C (along with pure UN as noted earlier, see **Table A.3**) generally followed the same reaction behavior of UN [58]. Although the oxidation onset was slightly delayed, given the more rapid kinetics like they observed with pure  $U_3Si_2$  the oxidation reaction completed at the same point as the typically more poor performing UN [58]. A follow-on study examined the degradation behavior of a UN-10wt% $U_3Si_2$  composite in a steam environment (along with pure UN samples as noted previously) using pellets sintered as outlined in Johnson *et al.* [87]. A UN-10wt% $U_3Si_2$  sample was subjected to steam exposure at 300 °C and 9 MPa for 90 minutes [69, 88]. The corrosion mechanism in the composite was identified as intragranular cracking, as opposed to the intergranular cracking (seen in their pure UN samples resulting in matrix degradation and pesting). The exposure of less fresh surfaces to oxidation in the composite delayed the attack on the UN grains resulting in a 5x lower mass increase during steam exposure as compared to

the pure UN sample of the same porosity [69]. **Figure A.21a** shows the mass increase for UN as a function of porosity as well as for the UN-U<sub>3</sub>Si<sub>2</sub> sample, b) the as-fabricated microstructure of the composite, and c) and d) exhibiting the corroded microstructure and intragranular cracking of the composite pellet [69]. The UN matrix appeared to have no chemical variation at the cracks, but the U<sub>3</sub>Si<sub>2</sub> exhibited regions having increased oxygen content. This suggests that it is not the silicide which has an increased resistance to corrosion but that the presence of the silicide provides mechanical stability by reducing or eliminating intergranular cracking and grain relief in the UN matrix [69].

Although noted above with regards to the specific experiments, the differences in synthesis and fabrication methods, along with the inclusion of the various additive components many times result in samples that are not of the nominal composition as intended and reported by the researchers. While this review has attempted to bring to light those experimental conditions and the actual phase compositions of the samples tested, readers are cautioned to examine the literature carefully for specific experimental details regarding fabrication.

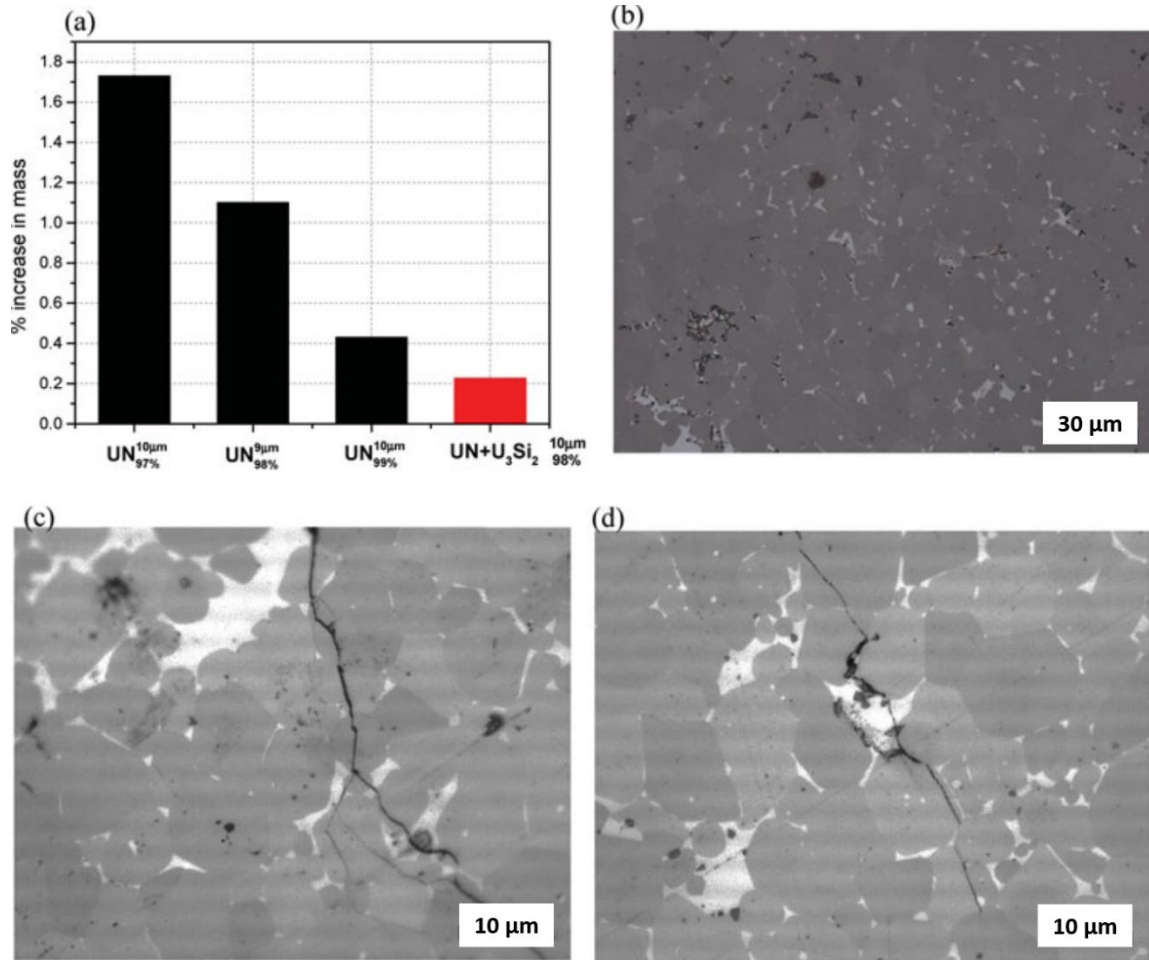


**Figure A.21** Modified from Lopes et al. [69] showing a) the % mass increase during steam corrosion for UN pellets with varying porosity and a UN-10 wt% U<sub>3</sub>Si<sub>2</sub> composite, b) the as-fabricated microstructure of the composite, and c) and d) showing the corroded microstructure with intragranular cracking present.

## A.5 Effects of impurities and secondary phases in UN

### A.5.1 Impurities in UN

This section briefly discusses the role impurities have on the performance of UN under corrosion. More information has been published about how impurities affect UN's in-pile behavior. The role that impurities play in the degradation behavior of UN in oxidation and corrosion conditions has not been well studied. Only a couple of the previously mentioned corrosion studies postulated that increased oxygen content in the UN resulted in more severe oxidation and corrosion behavior [14, 57]. Incorporation of C

and O impurities on the N, U, and interstitial lattice sites of UN via DFT theory found that C and O are energetically favorable in the N site and that O is stable in the interstitial position [89]. Carbon and oxygen strongly interact with vacancies and cluster at grain boundaries, dislocations, or surfaces. Oxygen also has a lower energy barrier for diffusion as compared to N or C and O will form a pseudo  $\text{UO}_2$  coordination, while C has very directional and inflexible bonding with U, requiring much more energy [89]. Carbon direct interstitial diffusion was found to have a low energy barrier and can rapidly diffuse to a N vacancy position, while O has a 0.15 eV lower energy barrier than N self-diffusion, all of which can be significant in UN fuel [89]. Concentration of residual carbon in UN should also be held to a minimum as formation of UC can result in even less desirable corrosion behavior, which is elaborated upon in the  $\text{UB}_2/\text{UC}$  publication of this review series [90].

The effects of carbon and oxygen impurities in UN are also important to note due to the effects their presence can have on formation and separation of phases within the fuel (with fission products and uranium) during the course of irradiation [91]. Experimental results show the maximum oxygen solubility in UN is 3-7 mol% (1.5-3.5 at% O) in the temperature range 1527-1900 °C and an increase in oxygen concentration likely leads to formation of separate phases of  $\text{UO}_2$ , U, and  $\text{U}_2\text{N}_3$  [91]. Oxygen and carbon content within the mononitride fuel can affect creep, radiation swelling, emission of gaseous fission products, and thermal conductivity [92]. UN fuel with mass fractions of 0.4-0.5% oxygen and 0.35-0.45% carbon were tested in two zones in a BR-10 reactor. Gaseous emissions from the fuel was approximately 25% of the total amount of gaseous fission products formed. Fuel having mass fractions of 0.1% for oxygen and carbon had

gaseous emissions of 20-22% of the total gaseous fission products formed [92]. UN's compatibility with E1847 steel cladding in the BR-10 was affected by increased oxygen and carbon content in the fuel [92]. Carbonization of the cladding inner surface was three times greater in fuel that had O and C mass fractions of 0.3-0.45% versus fuel having mass fractions below 0.15% [92]. The importance of oxygen and carbon impurities on in-pile performance is still not well understood, likely due to other parameters which prevent absolute determination of impurity effects on irradiation behavior [93]. It has been observed that carbon and oxygen content does have a strong correlation to fission product behavior due to the stability of the carbide, nitride and oxide phases of the major fission products [93]. Irradiation tests on UN with various cladding materials (Nb-1% Zr and Nb-1%Zr-0.1% C) were conducted as part of the SNAP-50 reactor development program [10, 94, 95]. Overall irradiation performance was deemed satisfactory, but the data on the swelling results exhibited substantial scatter for fuel burnup <1.12 at% [10]. Testing parameters varied — from 10-93% <sup>235</sup>U enrichment, burnups from 0.3-4.58 (at%) and centerline temperatures from 912-1565 °C — however tests for both cladding materials indicated carbon impurities of 300-600 ppm C, and 1000-2000 ppm O. It was proposed that the oxide was present as a fine precipitate and was considered an advantageous nucleating field for fission gases, suspected to have aided in the superior irradiation performance of UN as compared to UC [94]. As part of the SP-100 research, other irradiation tests on UN with cladding materials of W-26% Re showed significant scatter in the swelling data as well cladding failures which did not allow for definitive analysis, while cladding of Ta-111 was similar to that of the Nb-1% Zr and Nb-1%Zr-0.1% C [10].

The effects of C and O impurities on the thermal conductivity of UN fuel has also been studied [96]. Carbon impurities up to 0.5 wt% resulted in a slight increase in thermal conductivity, but above that concentration the thermal conductivity showed a marked decrease. The effects on UN thermal conductivity as a function of oxygen concentration in argon and helium atmospheres from 293-1273 K was also studied [96]. The thermal conductivity of UN for O<sub>2</sub> concentrations of 0.2-2.25 wt% was decreased by approximately 41% at 600 °C and by almost 53% at 100 °C (see **Figure A.22**). UN samples having 0.13 wt% oxygen content (and 12.4% porosity) had the highest thermal conductivity values [96].

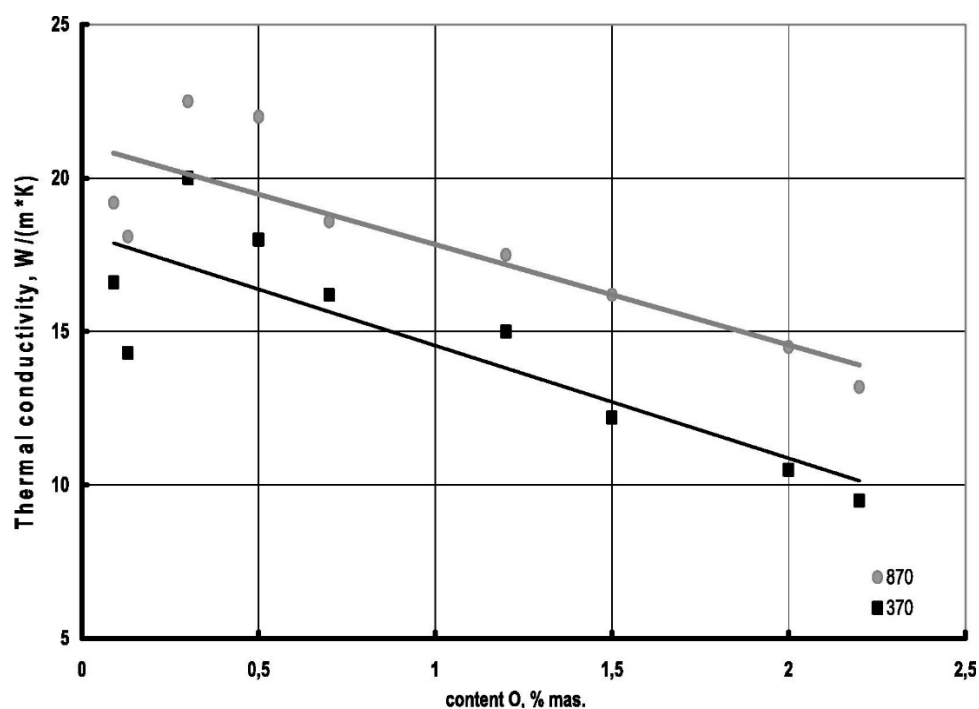


**Figure A.22** Dependence of thermal conductivity in UN as a function of oxygen content. From Solntceva et al. [96].

### A.5.2 Secondary phases in UN

In addition to the role secondary phases play on oxidation and corrosion behavior, the impact these phases can have on other properties (e.g. thermophysical and neutronic) and irradiation effects needs to be considered. Early work, from the 1960's to the 1980's, on additives to a UN fuel matrix included additions of other nitrides and elements such as AlN, ThN, ZrN, O, C, Mo, Th, Ti, and Y. One of the earlier investigations reported on the addition of refractory AlN to UN via cold compacting and sintering and hot isostatic pressing [97]. The results suggest that the thermal conductivity is slightly decreased with the addition of 10-30 vol% AlN over pure UN (even though AlN has a higher thermal conductivity than UN under  $\sim 600$  °C). The authors attributed these lower thermal conductivity values to intra- and inter-granular cracking due to differences in the thermal expansion of the two materials [97]. These UN/AlN compacts (having 75-85% TDs) were oxidized at 500 °C in dry CO<sub>2</sub> and results showed initial mass gain was very rapid but that a protective oxide formed after about 1 hour. Significant mass gain was seen after  $\sim 14$  hours (although no samples disintegrated) and UO<sub>2</sub> was identified as the final oxidation product [97]. Other work for UN/metal nitride composites was proposed in a patent referencing a solid solution of (U,Th,Pu)N and a metal nitride, with the preferred fuel comprised of UN and TiN or YN [98]. It is stated that both TiN and YN will result in a loss of thermal conductivity of the composite fuel but are not dissimilar to that of a (U,Pu)N fuel. Addition of Gd<sub>2</sub>O<sub>3</sub> and GdN as a burnable absorber to a UN matrix has also been reported to lower the thermal conductivity of UN [99]. The impact of UN addition to a UO<sub>2</sub> matrix (39 wt% UN) has been shown to provide a 2x increase in thermal conductivity as compared to reference UO<sub>2</sub> [85]. A UN-Mo cermet was also

fabricated from binder-jet printed Mo and UN microspheres sintered via SPS showing an increase in thermal conductivity when compared to pure UN [100]. Alexander addresses an important challenge with fabrication of UN and UN-composites, indicating that additives, such as TiN or YN (5-10-20 mol%) can stabilize the UN, decreasing the thermodynamic activity of the uranium, and preventing the formation of a molten uranium phase [98].

Other efforts related to in-pile performance investigated incorporating additions of O, C, Mo, and Th to the UN structure based on findings that fine precipitates in uranium metal reduce fission-induced swelling [101]. The authors state Mo is slightly soluble at approximately 0.10 wt% at 2600 °C, precipitating as submicroscopic particles upon rapid cooling. Thorium, dissolved as ThN into UN, can be oxidized to UO<sub>2</sub> forming (U,Th)O<sub>2</sub> precipitates within UN grains [101]. It has also been reported that ThN is more reactive towards water than UN [102]. Potter *et al.* indicate that oxygen quantities can be controlled by adding carbon to samples [101], although as previously mentioned, carbon and oxygen impurities in UN can be detrimental to fuel performance. More recently, a UN-5 wt% UO<sub>2</sub> composite system (via HDN and conventionally sintered) under proton irradiation (2 MeV up to 4\*10<sup>18</sup> and 8\*10<sup>18</sup> ions/cm<sup>2</sup> at 400 °C and 700 °C and <10<sup>-6</sup> torr) was studied for phase and defect evolution [103]. High angle annular dark field (HAADF) and bright field (BF) scanning transmission electron microscopy images of the UN-5wt%UO<sub>2</sub> composite irradiated at 710 °C and up to 8\*10<sup>18</sup> ions/cm<sup>2</sup> along with EDS chemical maps show the aforementioned sandwich structure of UN/U<sub>2</sub>N<sub>3</sub>/UO<sub>2</sub> as previously mentioned in the oxidation literature (see **Figure A.23**). The authors concluded that the irradiation accelerated the oxidation and phase transformation in the

composite sample. The study also found that in the nitride phases the dislocation loops grew (3x that of  $\text{UO}_2$ ) and with increasing temperature and dose the number density of the loops also increased [103].

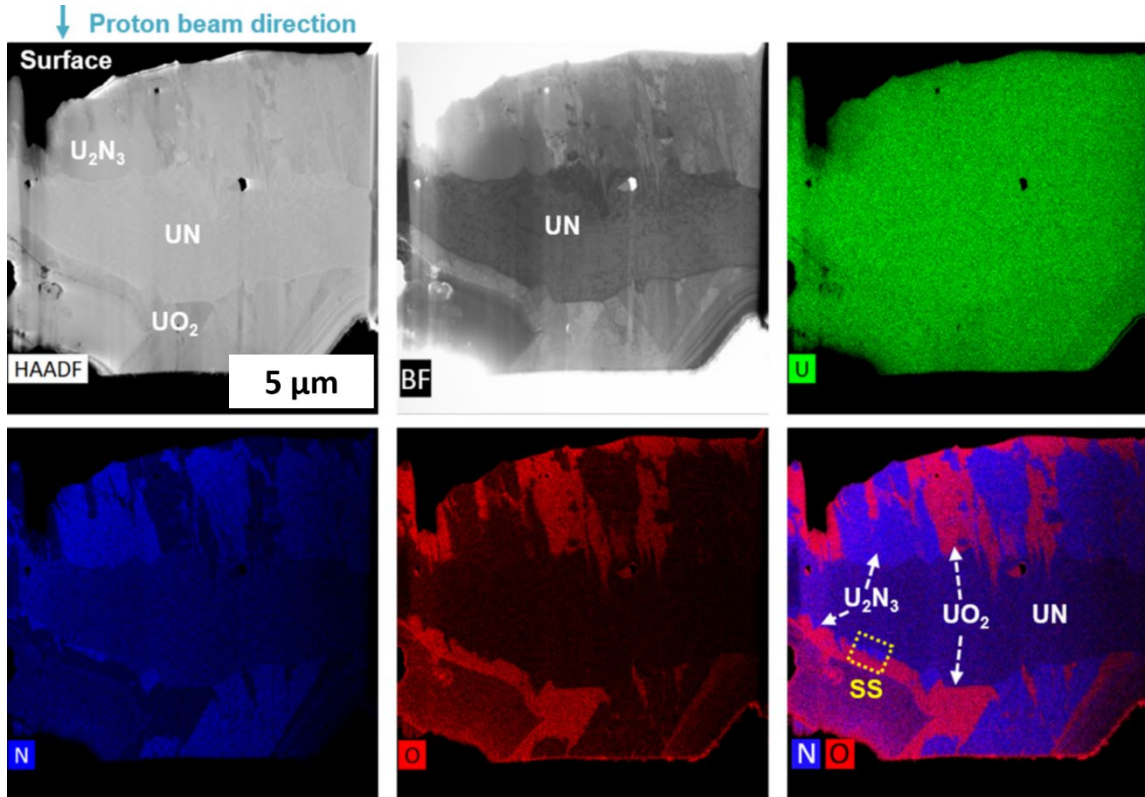


**Figure A.23** High angle annular dark field (HAADF) and bright field (BF) STEM images with EDS chemical maps of a UN-5wt%  $\text{UO}_2$  composite after proton irradiation at 710 °C and up to a fluence of  $8 \cdot 10^{18}$  ions/cm<sup>2</sup> indicating the presence of UN,  $\text{U}_2\text{N}_3$ , and  $\text{UO}_2$ . The “sandwich structure” of the three phases is denoted by the yellow dashed rectangle in the bottom right image; the proton irradiation beam direction is marked by an arrow in the upper left. Modified from He et al. [103].

The effects of secondary constituents in UN on neutronic performance of UN fuel has also been studied through modeling [19, 104]. A neutronics simulation was performed on UN and UN-(Al, Cr, Nb, Ni) metal composites with Zr-clad fuel pins [104]. The cycle length on undoped UN increased by 25% compared to  $\text{UO}_2$ , while dopant addition to the UN lattice only slightly affected the increased cycle length. The changes to the increased cycle length were smallest in the following order: Al > Cr > Ni

> Nb [104]. Another neutronic assessment was performed for UN with secondary candidate materials of  $U_3Si_5$ ,  $U_3Si_2$ ,  $UB_4$ , and  $ZrO_2$  in nominal conditions in a reference pressurized water reactor with Zr cladding [19]. Small volume fractions (<10%) have a relatively small influence on the neutronic behavior of these UN-based composite fuels [19]. A further study examined a UN- $U_3Si_5$  composite fuel concept with advanced cladding materials (FeCrAl alloys) finding that the reactor physics and fuel performance were similar to that of the benchmark  $UO_2$ -Zr cladding [105].

Given the impact impurities have on UN's performance, it is essential that the synthesis and sintering conditions are controlled to limit impurity concentrations, especially oxygen and carbon. The impact that these impurities play on corrosion behavior is also clearly not well-studied, leaving open the opportunity for research in this area. The authors postulate that delaying the onset of reaction of UN in oxidizing atmospheres can be achieved by enhancing the purity and density of UN, though mitigation strategies are necessary to facilitate oxidation performance similar to benchmark  $UO_2$ . Examining the results presented in the above literature synthesis of UN via the HDN method may be the best choice for achieving high-purity UN feedstock with limited C and O impurities, followed by CTR-N. The sol-gel method for UN microspheres used to make monolithic pellets appears to result in much higher carbon impurities and unwanted secondary phase formation during sintering than the other two more traditional synthesis routes. The SPS method provides for obtaining high-density samples at lower temperatures and shorter sintering times. However, the opportunity for introduction of impurities (from the dies or barrier materials used during sintering) is much greater, as is the potential for metastable phases which can impact the

microstructure and fuel performance. The influence that secondary additions have not only to oxidation and corrosion behavior, but to thermophysical, neutronic, and fission product interaction/behavior must also be considered. As mentioned above, specific research into how oxygen and carbon impurities affect UN's performance in hydrothermal corrosion conditions is warranted. Additionally, the effects that irradiation may have on the corrosion behavior of UN must also be considered. Moreover, little data exists on the effects that microstructural evolution and the presence of fission products may have on oxidation and corrosion of UN, which is important not only for in-pile performance but for storage and transportation of spent fuel. As future work is explored on UN, including irradiation, opportunities exist for research in this area.

#### **A.6 Summary**

If UN is to be considered as a replacement for  $\text{UO}_2$  for use in existing and future LWRs, a modification of the fuel matrix to mitigate its undesirable corrosion behavior is required. The literature on UN corrosion, while somewhat varied due to differences in synthesis, fabrication, and testing parameters, agrees that the onset of oxidation occurs at temperatures too low for use in LWRs. Research suggests that samples with high densities and low oxygen and carbon impurities perform better, therefore benchmarking leaker-rod tests of high purity, high density UN would indicate the extent to which hydrothermal corrosion will limit deployment. As the literature is limited and varied for synthesis and fabrication, it would be presumptive to conclude that one method is superior over another; however, it has been shown that the hydride-dehydride-nitride method for UN synthesis generally results in less C and O impurities and SPS or HIP can provide higher density samples. Fewer impurities and higher density can contribute to

higher onset oxidation temperatures and improved performance. However, the CTR-N method is backwards compatible with current  $\text{UO}_2$  fabrication facilities and has been demonstrated in the fabrication of large quantities of fuel quality UN. The issue of isotopically enriching UN with  $^{15}\text{N}$  to avoid formation of  $^{14}\text{C}$  and limit neutron absorption, remains an opportunity for research, whether through implementation of a closed gas cycle during synthesis, or recovery of nitrogen during synthesis, sintering, and reprocessing.

Oxidation experiments of UN in air, although not relevant to LWR conditions, can provide a comparison to the oxidation behavior of other fuel forms. This behavior in air is also applicable to off-normal transportation and storage scenarios. A summary of the onset temperatures from the UN air oxidation experiments in **Table A.3** is shown in **Figure A.24** compared to the reported ramp testing air onset oxidation of 455 °C for  $\text{UO}_2$  from Wood *et al.* [106]. The values range from 202 °C to 450 °C, with this range due to a variety of factors related to UN synthesis and sintering methods, as well as the addition of a secondary phase. The lowest onset temperature was for UN compacts fabricated from the sol-gel method, and the highest onset temperature was for a UN+10vol%  $\text{U}_3\text{Si}_2$  compact fabricated from HDN powder and sintered via SPS, close to that of  $\text{UO}_2$ .  $\text{U}_3\text{Si}_2$  is further reviewed in the  $\text{U}_3\text{Si}_2$  publication of this review series. The highest onset for a pure UN sample (fabricated from HDN powder and conventionally sintered) was 340 °C.

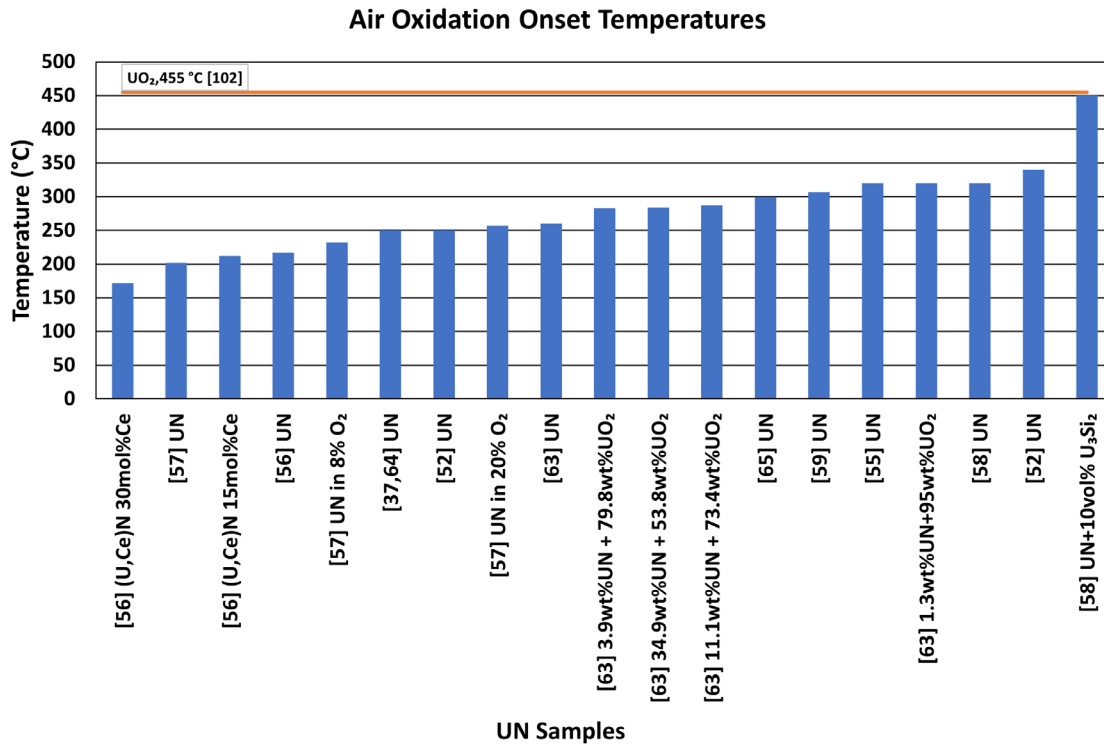


**Figure A.24** Plot of the air oxidation onset temperatures from Table A.3 compared to reference data for air onset oxidation of UO<sub>2</sub> from Wood et al. [106].

Data from water and/or steam corrosion experiments is considered here to be the most relevant for screening conditions when evaluating possible ATF fuel forms. Onset temperatures for UN or UN-composite samples tested in water or steam are summarized in **Figure A.25**. The lowest reported onset temperature in water/steam (~150 °C) was for a UN+30at%ZrN sample (via HDN and SPS) and 180 °C for UN powder. The highest onset was at 400 °C for a pure UN pellet fabricated via HDN and SPS. Only one reported study looked at UN thin film corrosion in radiolytic conditions at room temperature. While the results suggested improved corrosion resistance in conditions similar to what would be seen in a leaker/failure rod scenario, more extensive research is required in this area.

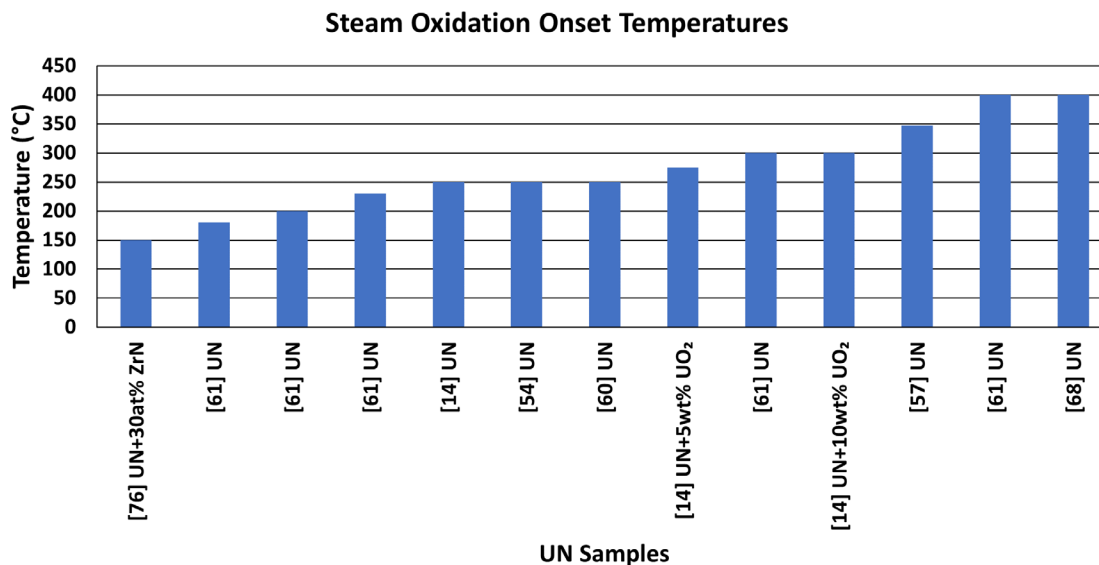


**Figure A.25** Plot of the water/steam onset temperatures from Table A.4.

Regardless of synthesis technique, UN pulverization during corrosion is due to the formation of a reaction product at grain boundaries. The reaction product is generally a progressive formation of sesquinitride and oxynitride phases (with an associated volume expansion) leading to instability in monolithic samples. The U<sub>3</sub>Si<sub>2</sub> focused publication of this review series will explore protection strategies in more depth. However, current research on UN protection is primarily directed at the addition of a suitable additive that will act as a protective barrier. This is envisaged to be through either the preferential oxidation of the dopant over UN and subsequent formation of another corrosion resistant phase during oxidation/corrosion or microstructural refinement in which the UN grains are protected by the additive; some combination of these degradation mitigating phenomena could also be expected. The literature that includes incorporation of an additive or secondary phase to UN favors more traditional synthesis techniques, such as HDN and CTR-N for UN synthesis followed by conventional powder metallurgy and sintering. The challenges remain in identifying a scalable process for synthesis and

fabrication which limits impurities (namely O and C), and one in which additives can be easily incorporated without formation of unwanted secondary phases, or dissociation of the UN. Research opportunities also remain in identifying the specific effects that O and C impurities play in hydrothermal corrosion of monolithic UN.

While still limited and somewhat varied, the available literature on oxidation and corrosion of UN and UN with various additions demonstrates the continued need to identify a pathway for improving UN's corrosion resistance. To date, none of the literature has successfully demonstrated significant improvements to the corrosion resistance of pure UN or UN with an additive/secondary phase. Additionally, a proven method to fabricate and sinter high density UN with an additive that can improve corrosion performance, which is scalable, economical, and does not result in unwanted phases or undesirable impurity levels remains elusive. Further investigation into suitable additives for UN as well as more relevant water and steam testing for such systems remains an opportunity in fuels research.

### Acknowledgements

Work at the collaborating institutions, including Westinghouse Electric Company, was supported by the U.S. Department of Energy, Office of Nuclear Energy under DOE Idaho Operations Office Contract DE-NE0008824 funding opportunity. Accordingly, the U.S. Government retains and the publisher, by accepting the article for publication, acknowledges that the U.S. Government retains a nonexclusive, paid-up, irrevocable, worldwide license to publish or reproduce the published form of this manuscript or allow others to do so, for U.S. Government purposes.

### References

- [1] P. Lyons, B. Crowell, Development of light water reactor fuels with enhanced accident tolerance, Report to Congress, United States Department of Energy, Washington, DC, 2015.
- [2] S. Bragg-Sitton, Development of advanced accident-tolerant fuels for commercial LWRs, Nuclear News 57(3) (2014) 83.
- [3] S.J. Zinkle, K.A. Terrani, J.C. Gehin, L.J. Ott, L.L. Snead, Accident tolerant fuels for LWRs: A perspective, Journal of Nuclear Materials 448(1) (2014) 374-379.
- [4] F. Goldner, Development strategy for advanced LWR fuels with enhanced accident tolerance, Enhanced Accident Tolerant LWR Fuels National Metrics Workshop, Germantown, MD, 2012.
- [5] D. Wachs, N. Woolstenhulme, Advanced fuel cycle technology: Special session in honor of Dr. Michael Lineberry, Transactions of the American Nuclear Society 110(INL/JOU-14-33095) (2014).
- [6] F. Cappia, J.M. Harp, Postirradiation examinations of low burnup  $U_3Si_2$  fuel for light water reactor applications, Journal of Nuclear Materials 518 (2019) 62-79.

- [7] G.J. Youinou, R.S. Sen, Impact of accident-tolerant fuels and claddings on the overall fuel cycle: A preliminary systems analysis, *Nuclear Technology* 188 (2) (2014) 123-138.
- [8] L.H. Ortega, B.J. Blamer, J.A. Evans, S.M. McDevitt, Development of an accident-tolerant fuel composite from uranium mononitride (UN) and uranium sesquisilicide ( $U_3Si_2$ ) with increased uranium loading, *Journal of Nuclear Materials* 471 (2016) 116-121.
- [9] R.B. Matthews, Irradiation performance of nitride fuels, Los Alamos National Lab., NM (United States), 1993.
- [10] S.B. Ross, M.S. El-Genk, R.B. Matthews, Uranium nitride fuel swelling correlation, *Journal of Nuclear Materials* 170(2) (1990) 169-177.
- [11] S.S. Voss, Space Fission Power: Historical Review, Reference Module in Earth Systems and Environmental Sciences, Elsevier 2021.
- [12] E.S. Wood, J.T. White, C.J. Grote, A.T. Nelson,  $U_3Si_2$  behavior in  $H_2O$ : Part I, flowing steam and the effect of hydrogen, *Journal of Nuclear Materials* 501 (2018) 404-412.
- [13] A.T. Nelson, A. Migdisov, E.S. Wood, C.J. Grote,  $U_3Si_2$  behavior in  $H_2O$  environments: Part II, pressurized water with controlled redox chemistry, *Journal of Nuclear Materials* 500 (2018) 81-91.
- [14] J.K. Watkins, D.P. Butt, B.J. Jaques, Microstructural degradation of UN and UN- $UO_2$  composites in hydrothermal oxidation conditions, *Journal of Nuclear Materials* 518 (2019) 30-40.
- [15] H. Matzke, Science of advanced LMFBR fuels, North-Holland Physics Publishing, Amsterdam, The Netherlands, 1986.
- [16] E.S. Wood, J.T. White, B. Jaques, D. Burkes, P. Demkowicz, Advances in fuel fabrication, *Advances in Nuclear Fuel Chemistry*, Elsevier 2020, pp. 371-418.
- [17] M. Kato, Fuel Design and Fabrication: Pellet-Type Fuel, Reference Module in Earth Systems and Environmental Sciences, Elsevier 2021.

- [18] S.L. Hayes, J.K. Thomas, K.L. Peddicord, Material property correlations for uranium mononitride: 1. physical properties, *Journal of Nuclear Materials* 171 (2-3) (1990) 262-270.
- [19] N.R. Brown, A. Aronson, M. Todosow, R. Brito, K.J. McClellan, Neutronic performance of uranium nitride composite fuels in a PWR, *Nuclear Engineering and Design* 275 (2014) 393-407.
- [20] J. Zakova, J. Wallenius, Fuel residence time in BWRs with nitride fuels, *Annals of Nuclear Energy* 47 (2012) 182-191.
- [21] A.T. Nelson, Property and performance assessment to support candidacy of  $U_3Si_2$  as LWR fuel, Los Alamos National Lab, Los Alamos, NM, 2018.
- [22] K.J. McClellan, FY2014 Ceramic Fuels Development Annual Highlights, Los Alamos National Lab.(LANL), Los Alamos, NM (United States), 2014.
- [23] Y.S. Kim, 3.14 - Uranium Intermetallic Fuels (U–Al, U–Si, U–Mo), in: R.J.M. Konings (Ed.), *Comprehensive Nuclear Materials*, Elsevier, Oxford, 2012, pp. 391-422.
- [24] J.T. White, D.D. Byler, Report on the basic chemistry, microstructure and physical properties of high uranium density boride compounds, Los Alamos National Laboratory, Los Alamos, NM, 2015.
- [25] J.K. Fink, Thermophysical properties of uranium dioxide, *Journal of Nuclear Materials* 279(1) (2000) 1-18.
- [26] S.L. Hayes, J.K. Thomas, K.L. Peddicord, Material property correlations for uranium mononitride: III. Transport properties, *Journal of Nuclear Materials* 171(2) (1990) 289-299.
- [27] R. De Coninck, W. Van Lierde, A. Gijs, Uranium carbide: Thermal diffusivity, thermal conductivity and spectral emissivity at high temperatures, *Journal of Nuclear Materials* 57(1) (1975) 69-76.

- [28] J.T. White, A.T. Nelson, J.T. Dunwoody, D.D. Byler, D.J. Safarik, K.J. McClellan, Thermophysical properties of  $U_3Si_2$  to 1773K, *Journal of Nuclear materials* 464 (2015) 275-280.
- [29] H. Okamoto, B-U (Boron-Uranium), *Binary Alloy Phase Diagrams II Edition 1* (1990) 551-552.
- [30] D. Burns, S. Johnson, *Nuclear Thermal Propulsion Reactor Materials*, Nuclear Materials, IntechOpen2020.
- [31] U.C. Nunez, D. Prieur, R. Bohler, D. Manara, Melting point determination of uranium nitride and uranium plutonium nitride: A laser heating study, *Journal of Nuclear Materials* 449(1-3) (2014) 1-8.
- [32] J. Carmack, Update on U.S. Accident Tolerant Fuel Program Nuclear Regulatory Commission Briefing, 2016.
- [33] G. Pastore, A. Toptan, *Fresh Fuel Properties: Ceramic Compounds*, Reference Module in Earth Systems and Environmental Sciences, Elsevier2021.
- [34] R. Matthews, K. Chidester, C. Hoth, R. Mason, R. Petty, Fabrication and testing of uranium nitride fuel for space power reactors, *Journal of Nuclear Materials* 151 (3) (1988) 345.
- [35] P.A. Lessing, Oxidation protection of uranium nitride fuel using liquid phase sintering, Idaho National Laboratory (INL), 2012.
- [36] J. Bugl, A.A. Bauer, *Corrosion and oxidation characteristics of uranium mononitride*, Battelle Memorial Institute, Columbus, OH, 1964.
- [37] R. Dell, V. Wheeler, E. McIver, Oxidation of uranium mononitride and uranium monocarbide, *Transactions of the Faraday Society* 62 (1966) 3591-3606.
- [38] S. Voit, K. McClellan, R. Margevicius, C. Stanek, H. Hawkins, The design and production of actinide nitride fuels at the Los Alamos National Laboratory for the Advanced Fuel Cycle Initiative program, LANL, 2006.

- [39] S.M. Bragg-Sitton, M. Todosow, R. Montgomery, C.R. Stanek, R. Montgomery, W.J. Carmack, Metrics for the Technical Performance Evaluation of Light Water Reactor Accident-Tolerant Fuel, *Nuclear Technology* 195 (2) (2016) 111-123.
- [40] K.A. Terrani, B.C. Jolly, J.M. Harp, Uranium nitride tristructural-isotropic fuel particle, *Journal of Nuclear Materials* 531 (2020) 152034.
- [41] R.R. Metroka, Fabrication of uranium mononitride compacts, National Aeronautics and Space Administration 1970.
- [42] H. Muta, K. Kurosaki, M. Uno, S. Yamanaka, Thermal and mechanical properties of uranium nitride prepared by SPS technique, *Journal of Materials Science* 43 (19) (2008) 6429-6434.
- [43] K.D. Johnson, J. Wallenius, M. Jolkkonen, A. Claisse, Spark plasma sintering and porosity studies of uranium nitride, *Journal of Nuclear Materials* 473 (2016) 13-17.
- [44] B.J. Jaques, J. Watkins, J.R. Croteau, G.A. Alanko, B. Tyburska-Pueschel, M. Meyer, P. Xu, E.J. Lahoda, D.P. Butt, Synthesis and sintering of UN-UO<sub>2</sub> fuel composites, *Journal of Nuclear Materials* 466 (2015) 745-754.
- [45] G. Kim, J. Ahn, S. Ahn, Grain growth and densification of uranium mononitride during spark plasma sintering, *Ceramics International* 47 (5) (2021) 7258-7262.
- [46] V. Tennery, T. Godfrey, R. Potter, Sintering of UN as a function of temperature and N<sub>2</sub> pressure, *Journal of the American Ceramic Society* 54 (7) (1971) 327-331.
- [47] H. Matzke, Atomic mechanisms of mass transport in ceramic nuclear fuel materials, *Journal of the Chemical Society, Faraday Transactions* 86(8) (1990) 1243-1256.
- [48] H. Okamoto, NU (nitrogen-uranium), *Journal of Phase Equilibria* 18(1) (1997).
- [49] J. Wallenius, Y. Arai, K. Minato, Influence of N-15 enrichment on neutronics, costs and C-14 production in nitride fuel cycle scenarios, 2004.

- [50] K. Johnson, D.A. Lopes, Fabrication of High Density UN with Enriched N-15 for Test Irradiation, 2017 Water Reactor Fuel Performance Meeting, Jeju Island, Korea, 2017.
- [51] I.A.E.A.N.D. Section, LiveChart of Nuclides, Vienna, Austria.
- [52] M. Paljević, Z. Despotović, Oxidation of uranium mononitride, *Journal of Nuclear Materials* 57(3) (1975) 253-257.
- [53] M.J. Sole, C. Van der Walt, Oxidation and deformation studies of uranium nitride by electron microscopy, *Acta Metallurgica* 16(4) (1968) 501-510.
- [54] S. Sugihara, S. Imoto, Hydrolysis of uranium nitrides, *Journal of Nuclear Science and Technology* 6(5) (1969) 237-242.
- [55] G. Novoselov, V. Kushnikov, V. Baronov, V. Serebryakov, N. Stepenova, Oxidation of uranium and plutonium mononitride and monocarbide briquettes, *Soviet Atomic Energy* 53(2) (1982) 528-532.
- [56] J. Dehadraya, S. Mukerjee, G.R. Rao, V. Vaidya, V. Venugopal, D. Sood, The oxidation of uranium-cerium mononitride microspheres, *Journal of Alloys and Compounds* 257(1-2) (1997) 313-321.
- [57] G.R. Rao, S. Mukerjee, V. Vaidya, V. Venugopal, D. Sood, Oxidation and hydrolysis kinetic studies on UN, *Journal of Nuclear Materials* 185(2) (1991) 231-241.
- [58] K. Johnson, V. Ström, J. Wallenius, D.A. Lopes, Oxidation of accident tolerant fuel candidates, *Journal of Nuclear Science and Technology* 54(3) (2017) 280-286.
- [59] S.A. Kulyukhin, Y.M. Nevolin, A.V. Gordeev, A.A. Bessonov, Gas-phase volume oxidation of uranium mononitride, *Radiochemistry* 61(2) (2019) 146-155.
- [60] J. Antill, B. Myatt, Kinetics of the oxidation of UN and U(CO) in carbon dioxide, steam and water at elevated temperatures, *Corrosion Science* 6(1) (1966) 17-23.
- [61] R.M. Dell, V.J. Wheeler, N.J. Bridger, Hydrolysis of uranium mononitride, *Transactions of the Faraday Society* 63 (1967) 1286-1294.

- [62] A. Roine, HSC Chemistry, Outotec, Pori, 2019.
- [63] D.R. Costa, M. Hedberg, S.C. Middleburgh, J. Wallenius, P. Olsson, D.A. Lopes, Oxidation of UN/U<sub>2</sub>N<sub>3</sub>-UO<sub>2</sub> composites: an evaluation of UO<sub>2</sub> as an oxidation barrier for the nitride phases, *Journal of Nuclear Materials* 544 (2020) 152700.
- [64] R. Dell, V. Wheeler, The ignition of uranium mononitride and uranium monocarbide in oxygen, *Journal of Nuclear Materials* 21(3) (1967) 328-336.
- [65] T. OHMACHI, T. HONDA, The oxidation of UC and UN powder in air, *Journal of Nuclear Science and Technology* 5(11) (1968) 600-602.
- [66] L.M. Ferris, Reactions of uranium mononitride thorium monocarbide and uranium monocarbide with nitric acid and other aqueous reagents, *Journal of Inorganic & Nuclear Chemistry* 30(10) (1968) 2661-&.
- [67] S. Sunder, N. Miller, XPS and XRD studies of corrosion of uranium nitride by water, *Journal of Alloys and Compounds* 271 (1998) 568-572.
- [68] M. Jolkkonen, P. Malkki, K. Johnson, J. Wallenius, Uranium nitride fuels in superheated steam, *Journal of Nuclear Science and Technology* 54(5) (2017) 513-519.
- [69] D.A. Lopes, S. Uygur, K. Johnson, Degradation of UN and UN-U<sub>3</sub>Si<sub>2</sub> pellets in steam environment, *Journal of Nuclear Science and Technology* 54(4) (2017) 405-413.
- [70] E.S. Wood, C. Moczygema, G. Robles, Z. Acosta, B.A. Brigham, C.J. Grote, K.E. Metzger, L. Cai, High temperature steam oxidation dynamics of U<sub>3</sub>Si<sub>2</sub> with alloying additions: Al, Cr, and Y, *Journal of Nuclear Materials* 533 (2020) 11.
- [71] J. Abrefah, A.d. Aguiar Braid, W. Wang, Y. Khalil, D.R. Olander, High temperature oxidation of UO<sub>2</sub> in steam-hydrogen mixtures, *Journal of Nuclear Materials* 208(1) (1994) 98-110.
- [72] D.R. Olander, Oxidation of UO<sub>2</sub> by High-Pressure Steam, *Nuclear Technology* 74(2) (1986) 215-217.

- [73] D. Olander, Mechanistic interpretations of  $\text{UO}_2$  oxidation, *Journal of nuclear materials* 252(1-2) (1998) 121-130.
- [74] B. Dobrov, V. Likhanskii, V. Ozrin, A. Solodov, M. Kissane, H. Manenc, Kinetics of  $\text{UO}_2$  oxidation in steam atmosphere, *Journal of nuclear materials* 255(1) (1998) 59-66.
- [75] J.M. Haschke, Corrosion of uranium in air and water vapor: consequences for environmental dispersal, *Journal of Alloys and Compounds* 278(1) (1998) 149-160.
- [76] P. Malkki, The manufacturing of uranium nitride for possible use in light water reactors, KTH Royal Institute of Technology, 2015.
- [77] E.L. Bright, S. Rennie, A. Siberry, K. Samani, K. Clarke, D. Goddard, R. Springell, Comparing the corrosion of uranium nitride and uranium dioxide surfaces with  $\text{H}_2\text{O}_2$ , *Journal of Nuclear Materials* (2019).
- [78] A. Herman, C. Ekberg, A Uranium Nitride Doped with Chromium, Nickel or Aluminum as an Accident Tolerant Fuel, *Res. Rev. J. Mater. Sci* 5(4) (2017) 83.
- [79] J.T. White, A.W. Travis, J.T. Dunwoody, A.T. Nelson, Fabrication and thermophysical property characterization of UN/ $\text{U}_3\text{Si}_2$  composite fuel forms, *Journal of Nuclear Materials* 495 (2017) 463-474.
- [80] R.A. Potter, J.L. Scott, (U, Zr) N alloy having enhanced thermal stability, Google Patents, 1977.
- [81] J.K. Watkins, E. Sikorski, L. Li, B.J. Jaques, Improved hydrothermal corrosion resistance of UN fuel forms via addition of metallic constituents, TopFuel 2019, Seattle, WA, 2019.
- [82] H.J.T. Ellingham, Reducibility of oxides and sulfides in metallurgical processes, *Journal of the Society of Chemical Industry Transactions and Communications* 63 (1944).

- [83] E.J. Lahoda, P. Xu, R.L. Oelrich, H. Shah, J. Wright, C. Lu, Grain boundary enhanced UN and  $U_3Si_2$  pellets with improved oxidation resistance, Google Patents, 2019.
- [84] D.R. Costa, M. Hedberg, S.C. Middleburgh, J. Wallenius, P. Olsson, D.A. Lopes, UN microspheres embedded in  $UO_2$  matrix: An innovative accident tolerant fuel, *Journal of Nuclear Materials* (2020) 152355.
- [85] J.H. Yang, D.-J. Kim, K.S. Kim, Y.-H. Koo,  $UO_2$ -UN composites with enhanced uranium density and thermal conductivity, *Journal of Nuclear Materials* 465 (2015) 509-515.
- [86] A.M. Raftery, Fabrication and characterization of UN- $USi_x$  nuclear fuel, 2015.
- [87] K.D. Johnson, A.M. Raftery, D.A. Lopes, J. Wallenius, Fabrication and microstructural analysis of UN- $U_3Si_2$  composites for accident tolerant fuel applications, *Journal of Nuclear Materials* 477 (2016) 18-23.
- [88] S. Uygur, Degradation mechanisms of UN and UN- $10U_3Si_2$  pellets of varying microstructure by comparative steam oxidation experiments, TRITA-FYS, 2016, p. 48.
- [89] D.A. Lopes, A. Claisse, P. Olsson, Ab-initio study of C and O impurities in uranium nitride, *Journal of Nuclear Materials* 478 (2016) 112-118.
- [90] P. Xu, J. Yan, E. Lahoda, S. Ray, Uranium mononitride as a potential commercial LWR fuel, *Proceedings of the 2012 International Congress on Advances in Nuclear Power Plants-ICAPP'12*, 2012.
- [91] D.Y. Lyubimov, A. Androsov, G. Bulatov, K. Gedgovd, Thermodynamic modeling of oxygen dissolution in uranium mononitride at 900–1400 K, *Radiochemistry* 56(5) (2014) 496-500.
- [92] B. Rogozkin, N. Stepenova, A. Proshkin, Mononitride fuel for fast reactors, *Atomic Energy* 95(3) (2003) 624-636.
- [93] A.T. Nelson, P. Demkowicz, Other power reactor fuels, *Advances in Nuclear Fuel Chemistry*, Elsevier 2020, pp. 215-247.

- [94] M. DeCrescente, M. Freed, S. Caplow, Uranium nitride fuel development, SNAP-50, Pratt and Whitney Aircraft, Middletown, Conn.(USA). Connecticut Advanced Nuclear Engineering Lab., 1965.
- [95] S. Weaver, J. Scott, R. Senn, B. Montgomery, Effects of irradiation on uranium nitride under space-reactor conditions, 1969.
- [96] E.S. Solntceva, M.L. Taubin, V.I. Vybyvanets, I.E. Galyov, V.G. Baranov, O.V. Homyakov, A.V. Tenishev, Thermal conductivity of perspective fuel based on uranium nitride, *Ann. Nucl. Energy* 87, Part 2 (2016) 799-802.
- [97] T. Davies, P. Evans, The preparation and examination of mixtures of aluminium nitride (AlN) and uranium mononitride (UN), *Journal of Nuclear Materials* 13(2) (1964) 152-168.
- [98] C.A. Alexander, Metal-actinide nitride nuclear fuel, Google Patents, 1986.
- [99] G. Kim, S. Ahn, Thermal conductivity of gadolinium added uranium mononitride fuel pellets sintered by spark plasma sintering, *Journal of Nuclear Materials* 546 (2021).
- [100] A. Raftery, R. Seibert, D. Brown, M. Trammell, A. Nelson, K. Terrani, Fabrication of UN-Mo CERMET nuclear fuel using advanced manufacturing techniques, Oak Ridge National Lab.(ORNL), Oak Ridge, TN (United States), 2020.
- [101] R. Potter, T. Godfrey, J. Leitnake, Precipitates in Uranium Nitride, *American Ceramic Society Bulletin*, Amer Ceramic Soc 735 Ceramic Place, P.O. Box 6136, Westerville, OH 43081-6136, 1966, pp. 822-823.
- [102] S. Peterson, R. Adams, D. Douglas Jr, Properties of thorium, its alloys, and its compounds, Oak Ridge National Lab., Tenn., 1965.
- [103] L. He, M. Khafizov, C. Jiang, B. Tyburska-Püschel, B.J. Jaques, P. Xiu, P. Xu, M.K. Meyer, K. Sridharan, D.P. Butt, J. Gan, Phase and defect evolution in uranium-nitrogen-oxygen system under irradiation, *Acta Materialia* 208 (2021) 116778.

- [104] K. Insulander Björk, A. Herman, M. Hedberg, C. Ekberg, Scoping Studies of Dopants for Stabilization of Uranium Nitride Fuel, *Nuclear Science and Engineering* 193(11) (2019) 1255-1264.
- [105] N.R. Brown, M. Todosow, A. Cuadra, Screening of advanced cladding materials and UN–U<sub>3</sub>Si<sub>5</sub> fuel, *Journal of Nuclear Materials* 462 (2015) 26-42.
- [106] E.S. Wood, J. White, A. Nelson, Oxidation behavior of U-Si compounds in air from 25 to 1000 C, *Journal of Nuclear Materials* 484 (2017) 245-257.

APPENDIX B: CHALLENGES AND OPPORTUNITIES TO ALLOYED AND  
COMPOSITE FUEL ARCHITECTURES TO MITIGATE HIGH URANIUM DENSITY  
FUEL OXIDATION: URANIUM SILICIDE

This chapter has been published in the Journal of Nuclear Materials

Reference: A.R. Gonzales, J.K. Watkins, A.R. Wagner, B.J. Jaques, E.S. Sooby. Challenges and Opportunities to Alloyed and Composite Fuel Architectures to Mitigate High Uranium Density Fuel Oxidation: Uranium Silicide. Journal of Nuclear Materials. (2021). DOI: 10.1016/j.jnucmat.2021.153026.

## Abstract

The challenges and opportunities to alloyed and composite fuel architectures designed and intended to mitigate oxidation of the fuel during a cladding breach of a water-cooled reactor are discussed in three review manuscripts developed in parallel, with the presented article focused on the oxidation performance of uranium silicide. Several high uranium density fuels are under consideration for deployment as accident tolerant and/or advanced technology nuclear reactor fuels, including UN,  $U_3Si_2$ , UC and  $UB_2$ . Presented here are the literature for the  $U_3Si_2$  degradation modes, thermodynamics, and oxidation performance of the pure compound and its reported alloyed and composite architectures. Furthermore, this review covers the materials and techniques for the incorporation of additives, dopants, or composite fuel architectures to improve the oxidation/corrosion behavior for high uranium density fuels for use in LWRs.

### B.1 Introduction

Following the accident at the Fukushima Daiichi power plant in March 2011, a decade before the publishing of this manuscript, researchers across the globe accelerated efforts to develop fuel forms that could better withstand a loss of coolant accident (LOCA) [1, 2]. Fuel geometries that could be readily exchanged with the conventional  $UO_2$ -Zircaloy fuel form were prioritized, so fuel-clad pairs were designed to be ‘drop-in’ replacements, posing both an accelerated path to licensing and a design constraint for novel fuels [3, 4]. Improvements to both the cladding and the uranium bearing fuel form have been proposed and a number of concepts are currently undergoing lead test rod and lead test assembly irradiations in commercial reactors. Cladding candidates that could withstand high temperature,  $T > 1200$  °C, steam exposure were prioritized and uranium-

bearing fuel compounds with enhanced thermal conductivity and fuel economy were considered [5-8]. These high uranium density fuels include UN and  $U_3Si_2$ , the topics of two of the manuscripts prepared in this three-part review series on the opportunities and challenges to the implementation of high uranium density fuels in water cooled reactors. Though significantly less studied than UN and  $U_3Si_2$ , UC and  $UB_2$  are covered in the third manuscript in this series. A challenge to each of these high uranium density fuel compounds is their exothermic reaction when exposed to water, whether pressurized at  $T > 250$  °C or as steam at  $T > 350$  °C [8-12].

In the current manuscript, the authors present a background on the variety of strategies that are envisioned to delay or mitigate the response of high uranium density fuels to coolant exposure, and exemplifying this topic are the oxidation performance and degradation of pure and alloyed  $U_3Si_2$  through an extensive review of the available literature [9, 13-17]. When fuel rods perform as designed, the uranium-bearing fuel compound does not encounter the coolant. However, during normal operation the mechanical integrity and hermetic seal of cladding degrade due to environmental (electrolysis and hydrothermal corrosion), mechanical (fretting), and irradiation effects [13, 18]. The data collected between 2009 and 2015 found PWR fuel assembly failure rates occurred at 2 per 1000 discharged [19]. Between 2009 and 2015, boiling water reactors reported less than 2 leaking assemblies for every 1000 that were discharged [19]. In addition to fuel rod failures there are other opportunities for the nuclear fuel to contact water, for example wet storage of used fuel following discharge as well as possible long-term repository storage. Sweet *et al.* investigated the performance of  $U_3Si_2$  in a LWR cladding breach using the BISON code [13], reporting that during normal operation to a

burnup of 20 MWd/kgU, the peak cladding stress is about 20 MPa, but then rapidly increases as the fuel expands due to coolant exposure [13]. The cladding stress reaches the yield stress of approximately 670 MPa after about 20% of the fuel mass has reacted to form  $U_3Si_2H_2$  and  $UO_2$  [13]. Once ~60% of the fuel volume has reacted, the cladding hoop strain exceeds 1%, which is currently the regulatory limit on acceptable fuel behavior. The maximum cladding strain of ~2.3% was reached during complete fuel reaction to  $U_3Si_2H_2$  and  $UO_2$ , resulting in the ‘unzipping’ of the breached rod and exemplifying the motivation to mitigate the water reaction for this high uranium density, accident tolerant fuel candidate.

Beyond normal operation, reactor designers, fuel vendors, and the regulatory bodies must consider the behavior of the fuel form during design basis, and even some beyond design basis, accidents. Though motivated here, the review article on the performance of uranium nitride oxidation, also published in this series, further discusses the need to address oxidation resistance of high uranium density fuels in the event of a LOCA. Also it is a conclusion of the present review that significant investigation is still needed to identify a suitable additive or dopant to high uranium density fuels to protect the fuel matrix from degradation in oxidative or corrosive conditions. Each fuel compound degrades via unique thermochemical mechanisms, therefore varied methodologies are necessary to mitigate the water reaction for each fuel form— a single approach will not sufficiently protect all high uranium density fuels to water exposure. The following sections review and present a background in the materials science and engineering approaches to mitigate water-side corrosion.

## B.2 Methods to Improve Oxidation Resistance

Research has shown that high uranium density fuels rapidly degrade under hydrothermal oxidation/corrosion conditions, such as in the event of a cladding breach, whether pinhole (leaker) or tube rupture, [15, 16, 20-22].

Potential techniques for providing effective protection and improving the fuel reaction kinetics with steam and pressurized water are proposed and correlate to oxidation and corrosion protection technologies used in non-nuclear systems:

- Surface coatings
- Mechanical or chemical surface treatments
- Microstructural engineering
- Addition of an alloying or impurity element that
  - is proven to be oxidation/corrosion resistant
  - creates or acts as a second phase which improves the overall corrosion resistance, or
  - results in a reaction product that offers protection from oxidation and corrosion

The application of an oxidation resistant coating to a monolithic fuel pellet is similar to coated-cladding approaches to accident tolerance. The coatings are envisaged to adhere to the fuel pellet, hermetically sealing the uranium bearing compound to prevent interaction with the coolant or steam in the event of a cladding breach. Typical coating or surface modifications in non-nuclear systems have been achieved via anodization, gas-phase deposition processes (chemical vapor deposition, physical vapor deposition, atomic layer deposition), electrochemical plating, laser surface alloying/cladding, and organic coatings [23]. The likely method for achieving such coatings on nuclear fuel pellets would be a gas-phase deposition process that can coat the exterior of the monolith after it has been sintered. Although this technique has been proven successful in other applications, utilization of a coating for nuclear fuel is

particularly challenging. Engineered coating systems which reduce mismatch in thermal expansion coefficients, are graded to minimize thermal stresses, and/or have a diffusion bonded region are most effective in extreme environment applications. Further, any coating technology would need to demonstrate robustness within the extreme irradiation environment, in addition to high temperature stability, as any protection provided is only sufficient as long as the coating's integrity is not compromised. Additionally, the chemical, thermodynamic, and mechanical stability, as well as the kinetics of a system incorporating a coating needs to be considered.

Grain boundary engineering or refinement has also been reported to improve corrosion resistance in non-nuclear materials [24]. Although this could potentially be an area of research to explore further, due to the extreme thermodynamic instability of these fuel forms,  $U_3Si_2$  in particular, to water and oxygen containing atmospheres, it is conjectured that any attempts at grain boundary refinement is anticipated to provide only marginal increases in oxidation resistance. However, recent work suggests microstructural engineering via spark plasma sintering, including the addition of a dopant, could prove to be a practical way to improve oxidation resistance as well as thermo-mechanical properties [25, 26].

Lastly, a common approach to increasing oxidation resistance in alloys is to incorporate additives or dopants which either stabilize the bulk structure under corrosive exposure or form a protective diffusion barrier or passivation layer which slows or mitigates corrosion entirely. As with the coatings, it is important to note that any dopant or secondary phase, proposed to either preferentially oxidize over the fuel matrix or provide protection to granular corrosion of the fuel, also needs to be compatible with fuel

and cladding and not contribute to the degradation of the fuel's desirable thermophysical and neutronic properties. When determining the likelihood of a material to provide protection to the fuel matrix in an oxidizing or corrosive environment, an understanding of thermodynamically favorable phases is required. In **Figure B.1**, an Ellingham-type diagram was created using calculations from HSC Chemistry 9 [27] to compare the thermodynamic stabilities of the oxides for various elements (considered as potential dopants to high-U density fuels) to that of  $\text{UO}_2$ , normalized to 1 mol of  $\text{O}_2$ . Although Ellingham diagrams [28] are calculated based on equilibrium conditions, they are a useful tool for predicting whether or not a reaction is spontaneous, which is determined by the enthalpy (H) and entropy (S) values as a function of temperature and is based on the change in the Gibbs ( $\Delta G$ ) free energy equation:

$$\Delta G = \Delta H - T\Delta S \quad \text{Eq (1)}$$

A reaction is considered spontaneous if the value for the change in the Gibbs free energy is negative. The lower the line on the plot, or the more negative the  $\Delta G$  value is, the more favorable the reaction. The dashed line indicates the change in the Gibbs free energy for the oxidation of U to  $\text{UO}_2$ . Thermodynamically, an oxide with a lower  $\Delta G$  is preferred, and while these plots provide a starting basis to predict the thermodynamic favorability of a reaction, they do not take into account reaction kinetics, or provide complete information about complex reactions that may occur (i.e. other oxides, hydroxides, etc.).

Several investigations have been published in recent years on dopants and alloying additions to high uranium density fuels, each of which are guided by either thermodynamics or historical/known performance of potential alloying addition, e.g.

passive oxide formers like Cr. The focus of this review is to investigate the literature related to  $U_3Si_2$  and additives/dopants to  $U_3Si_2$ . To guide this discussion from the perspective of thermodynamic stability, **Figure B.1** presents the  $\Delta G$  normalized per mole of  $O_2$  for several oxide forming elements, each of which are commonly considered oxidation resistant dopants or additives. Several of the elements/oxides plotted have been explored experimentally in the U-Si system. The dopant oxides are compared to the  $\Delta G$  of  $UO_2$  to thermodynamically assess if a protective oxide is expected to form preferentially.

Additionally, the review will cover fuel composite microstructures that have been engineered to both increase uranium density compared to  $UO_2$  and mitigate water-side corrosion of the fuel form. Thereby, the authors present a few of the important properties to consider when screening candidates for consideration, in addition to the thermodynamic stability of the formed oxide:

- The melting temperature of the resulting alloy/alloy phases should be sufficient for use in LWR conditions, although additives with melting temperatures above the base fuel matrix may pose challenges during fabrication.
- The thermal neutron capture cross-section should also be examined to avoid unwanted neutronic penalties.
- The limit to the amount of dopants/additives that can be incorporated in the fuel form before detrimentally effecting the uranium density must be considered.

- Materials with a large mismatch in their coefficient of thermal expansion as compared to the fuel could introduce undesirable stresses in a composite architecture.
- It is also important to understand how the additive/dopant crystal structure and solubility impacts the stability of a composite microstructure.

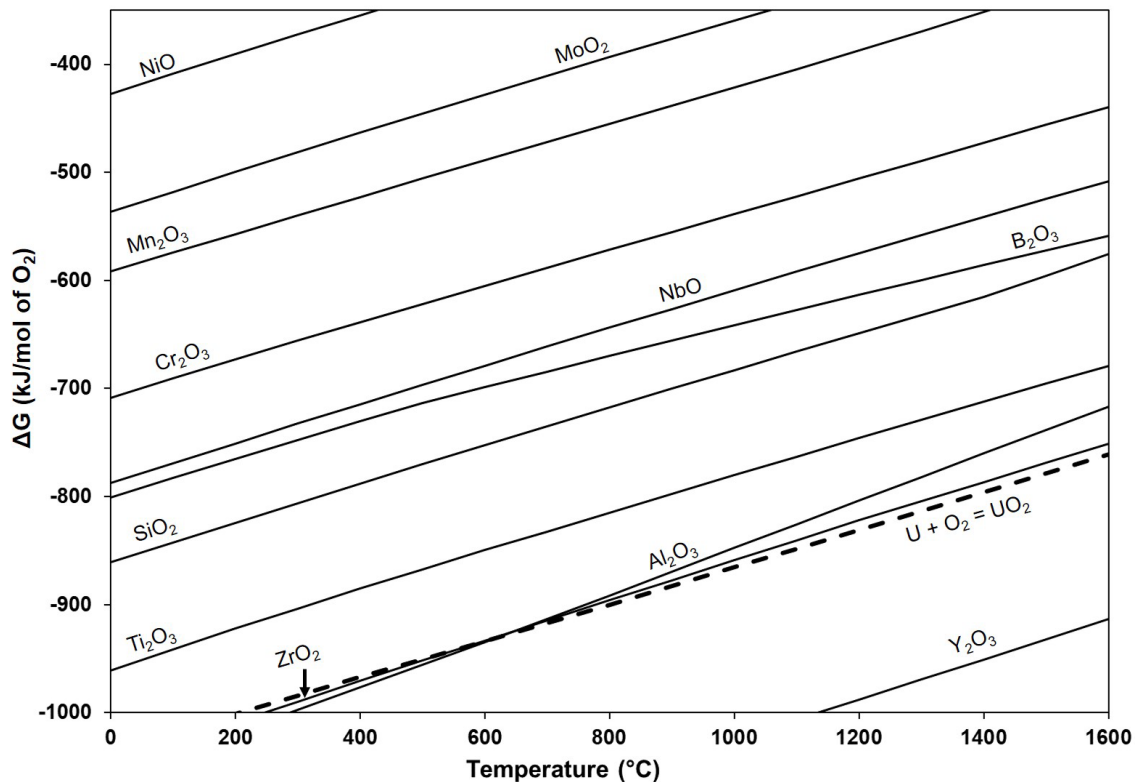


**Figure B.1** Ellingham-type diagram showing thermodynamic stability of oxide formation of various metallic elements considered for possible dopants into ATF concepts versus  $\text{UO}_2$ . Calculated using HSC Chemistry 9 [27].

### B.3 Triuranium Disilicide ( $\text{U}_3\text{Si}_2$ )

Uranium and silicon can form many stoichiometric compounds that include  $\text{USi}$ ,  $\text{USi}_2$ ,  $\text{U}_3\text{Si}$ ,  $\text{U}_3\text{Si}_2$ , and  $\text{U}_3\text{Si}_5$  as seen in the phase diagram of **Figure B.2**. The uranium density and thermophysical properties of high uranium containing uranium silicides (i.e.  $\text{U}_3\text{Si}_2$  and  $\text{U}_3\text{Si}$ ) make them attractive materials for replacement of  $\text{UO}_2$  [29]. However,

$U_3Si$  has been shown to swell appreciably under irradiation in research reactor investigations [30-32] while  $U_3Si_2$  has shown an encouraging record under irradiation in research reactor fuels and maintains several advantageous properties over  $UO_2$  [31-35]. The lower melting temperature of  $U_3Si_2$  compared to  $UO_2$  is off-set by its much higher thermal conductivity that significantly reduces the anticipated centerline temperature in the fuel pin compared to  $UO_2$  [29].  $U_3Si_2$ , however, has an unfavorable oxidation history when compared to  $UO_2$ .

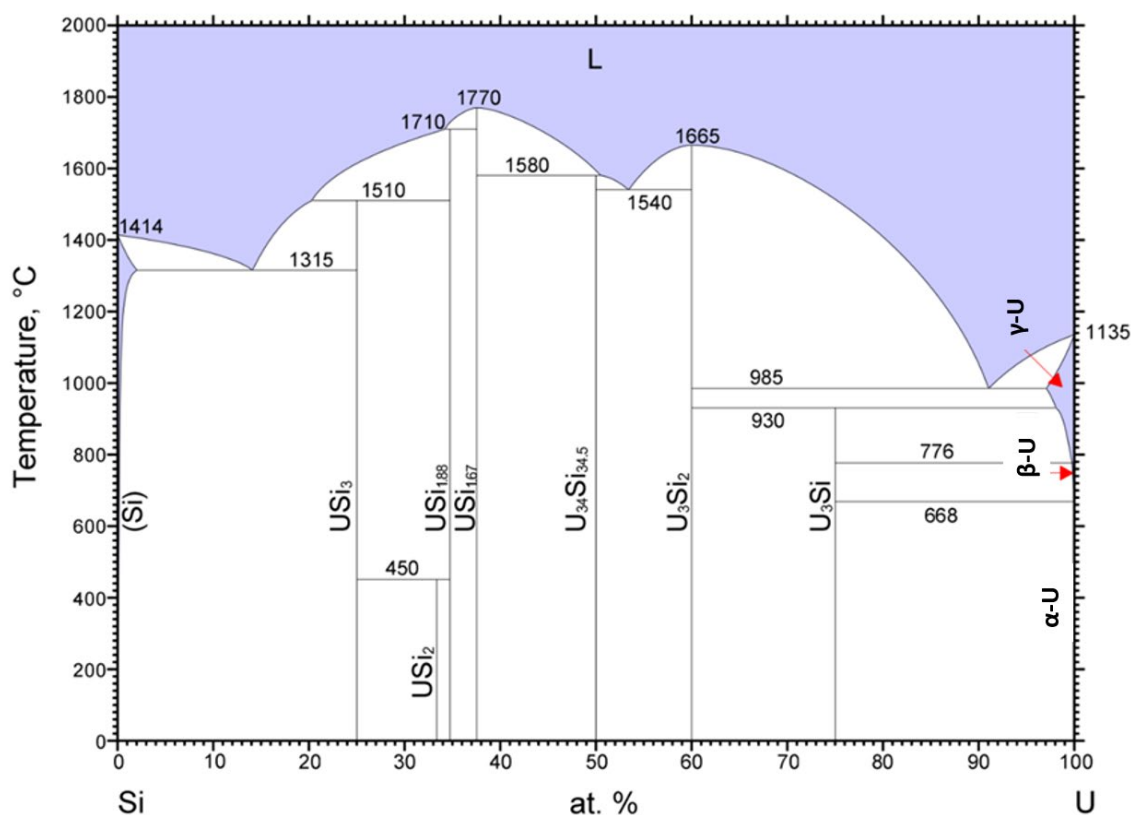


**Figure B.2 U-Si Phase diagram modified from ASM Alloy Phase Diagram Database. [36].**

### B.3.1 Synthesis Methods

The conventional synthesis route for  $U_3Si_2$ , from Harp *et al.*, is through arc melting non-stoichiometric amounts of U and Si, 92.5 wt% U and 7.5 wt % Si (59.27 at%)

U, 40.73 at% Si). The increased Si in the mixture accounts for suspected silicon volatilization during arc-melting. Following the alloying step is the use of traditional powder metallurgical methods for pellet fabrication [29, 37-39]. The route produced pellets which were 84–88%  $U_3Si_2$ , 8–13%  $USi$ , and 2–4%  $UO_2$  [29]. In 2019, Wagner *et al.* improved upon this fabrication process using stoichiometric amounts, 92.7 wt% U and 7.3 wt% Si (60 at% U, 40 at% Si), to produce pellets with greater than 94%  $U_3Si_2$ , while also containing secondary phases:  $UO_2$  (~1–2%) and  $USi$  (~4-5%) [40]. Most investigations on  $U_3Si_2$  performance used the non-stoichiometric composition and conventional sintering techniques that employ high temperatures (above 1400 °C) with hold times up to 12 hours [41]. Recently, field assisted sintering (FAS), also referred to as spark plasma sintering (SPS), has become a popular technique to densify nuclear fuels and has been shown to be scalable for industrial applications [42-48]. Specific to  $U_3Si_2$ , Mohamad *et al.* [49] and Lopes *et al.* [46] manufactured  $U_3Si_2$  pellets and both authors obtained more than 95% theoretical density using SPS with short hold times (~10 min). Additives to  $U_3Si_2$  have also been deployed using the above synthesis techniques. All  $U_3Si_2$  fabrication routes start by using elemental uranium and silicon, which is suitable for research laboratories; however it should be noted that another challenge to the implementation of silicide fuels is scaled-up production for industrial use, if starting from pure metal precursors, brings about proliferation and criticality concerns arise [50, 51].

### B.3.2 Oxidation/Corrosion testing

#### B.3.2.1 Air Oxidation of $U_3Si_2$

Predicting the susceptibility of candidate fuels, such as  $U_3Si_2$ , to degradation under coolant exposure is a challenging and a multifaceted problem. Often, screening

experiments in air are performed to provide comparative analysis to the oxidation response of fuel forms. The available oxidation literature dates to the 1950's and is presented in this subsection along with comparative results for the air oxidation of both arc-melted  $U_3Si_2$  samples and those fabricated using SPS. The authors will also argue here that air oxidation of uranium bearing compounds is not relevant to their behavior under reactor accident conditions, though it is an applicable assessment when considering an off-normal fuel transportation or storage event. Nevertheless, presented below is a review of the air oxidation behavior of  $U_3Si_2$  for both completeness and to highlight discrepancies in the data where varied fabrication methods have produced structures with different onsets of breakaway oxidation.

An initial assessment of  $U_3Si_2$  oxidation in 1956 by Loch *et al.* found  $U_3Si_2$  disintegrated in air at 400 °C in over 7.5 hr [52]. The 2017 investigation by Wood *et al.*, showed that the onset of breakaway oxidation for  $U_3Si_2$  in a synthetic air (20%  $O_2$ , balance argon) thermal ramp occurs at 384 °C, below that of  $UO_2$  (455 °C) [53] and the initial results reported in 1956. Johnson *et al.* reported an onset of an as-melted sample at 470 °C [8] while Gong *et al.* (2020) reported onsets of 520 °C and 510 °C prior to annealing [26]. The fabrication of each of these samples differs from one another. Wood *et al.* arc-melted metallic U and Si then used conventional powder metallurgy and sintering to form pellets. Johnson *et al.* reported using arc-melted material but did not specify the feedstock form; the sample was neither powderized nor sintered after arc-melting. Gong *et al.* used high energy ball milling (HEBM) to reduce the particle size of  $U_3Si_2$  arc melted samples prior to SPS for densification/pelletization.

The reported grains sizes of the samples used in the experiments also differ from study to study. Accordingly, the initial oxidation study by Wood *et al.* did not report a grain size for their sample. Johnson *et al.* reported a greater than 80  $\mu\text{m}$  grain size. Gong *et al.* used HEBM prior to SPS to control the grain size of their samples which were 5.7  $\mu\text{m}$  (onset of 520  $^{\circ}\text{C}$ ) and 280 nm (onset of 510  $^{\circ}\text{C}$ ). The 5.7  $\mu\text{m}$  grain size had a slightly higher onset temperature but the 280 nm sample took 42 minutes to fully oxidize while the 5.7  $\mu\text{m}$  took only 12 minutes. The study by Wood *et al.* reported a time of 6 minutes to full oxidation and Johnson *et al.* did not report an oxidation rate. The results indicated that the nanocrystalline-specimen displays an improved oxidation behavior compared to its micron-grain-size counterparts in extending the time to full oxidation.

Gong *et al.* is the only study to report the effects of annealing samples. After annealing at 300  $^{\circ}\text{C}$  for 2 hours, the onset for a 280 nm grain size sample decreased to 500  $^{\circ}\text{C}$  from 510  $^{\circ}\text{C}$  and fully oxidized in 17 minutes. The onset temperature for the 5.7  $\mu\text{m}$  sample increased to 560  $^{\circ}\text{C}$  from 520  $^{\circ}\text{C}$  and fully oxidized in 9 minutes. It was believed that residual strain induced from SPS played a significant role in improving the oxidation resistance of  $\text{U}_3\text{Si}_2$ . Annealing caused relaxation of the tensile strain in micron-grain-sized silicide reducing the oxidation rate, while the relaxation of the compressive strain in nano-sized  $\text{U}_3\text{Si}_2$  pellet resulted in the degradation of the oxidation performance. The result is consistent with Gokce *et al.* [54] who found that tensile strain increases the oxidation kinetics while compressive strain decreases it.

A collection of SEM images for  $\text{U}_3\text{Si}_2$  after air oxidation can be seen in **Figure B.3a** and **b** (Wood *et al.*) and **Figure B.3c** and **d** (Gong *et al.*) [26, 53]. Using EDS, Wood *et al.* and Gong *et al.* both reported the formation of  $\text{U}_3\text{O}_8$  after air oxidation. The

uniform phase (light gray area) in **Figure B.3a** was hypothesized to be  $\text{UO}_2$ , while the dark gray area was an adherent  $\text{UO}_2$  layer and spalling  $\text{U}_3\text{O}_8$  powder. **Figure B.3b** shows the surface of the oxidized  $\text{U}_3\text{Si}_2$  sample with a relatively uniform oxide of varying textures. During isothermal exposures, Wood *et al.* found that  $\text{USi}_3$  formed at 25 °C above the calculated onset temperature of breakaway oxidation and the transformation of  $\text{UO}_2$  to  $\text{U}_3\text{O}_8$  was observed as the temperatures increased, as determined by X-ray diffraction (XRD). The results of the experiments demonstrated that preferential oxidation of uranium will dominate the response of the U-Si compounds investigated and oxidation of Si will not occur before the formation of  $\text{UO}_2$  [9, 53]. Yan *et al.* used X-ray photoelectron microscopy (XPS), a more surface sensitive method, to study the very initial oxidation of  $\text{U}_3\text{Si}_2$  and confirmed these results [55]. No Si or  $\text{SiO}_2$  was identified in the reaction products [55].

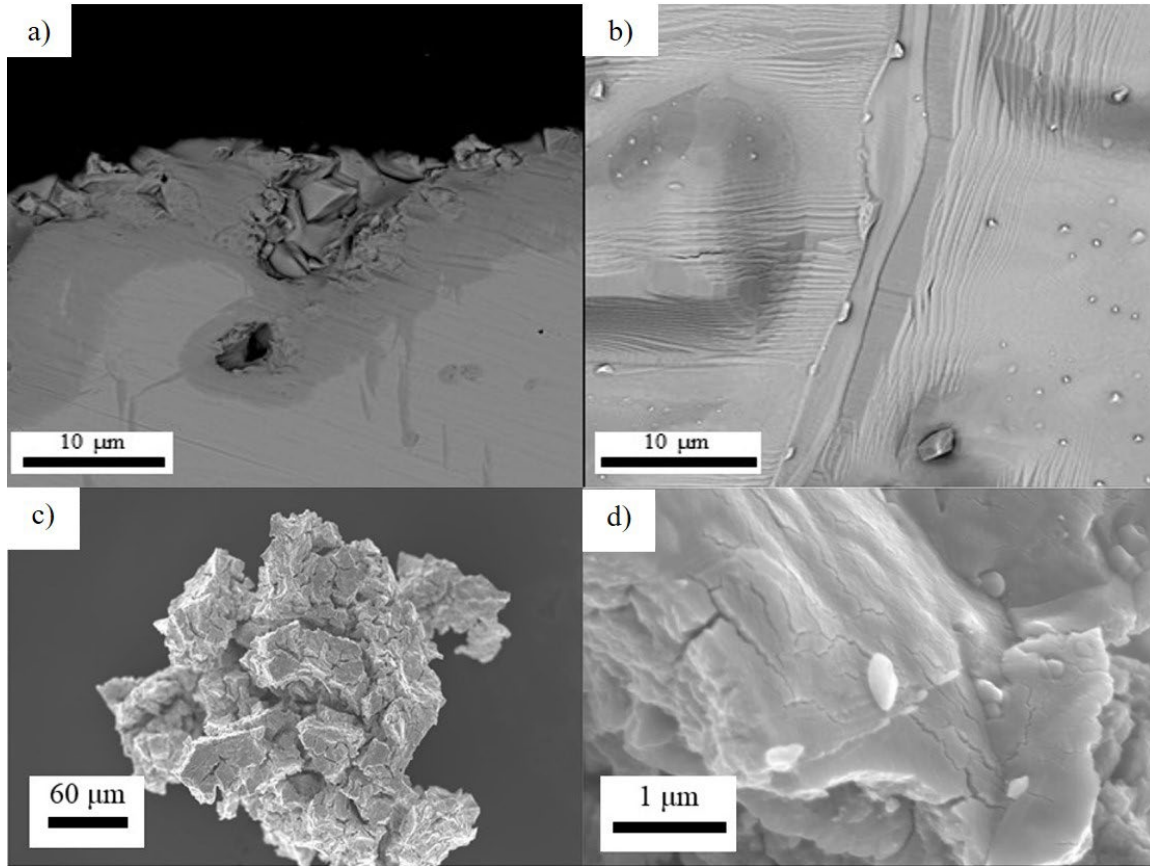
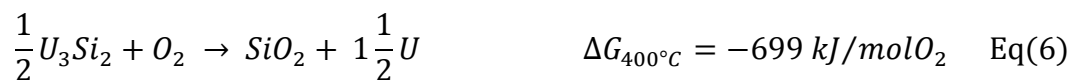


**Figure B.3** From Wood *et al.* a) cross-sectional micrograph of monolithic  $U_3Si_2$  during oxidation at 275 °C, and b) backscatter SEM of surface oxide formed at 300 °C [53]; c)  $\sim 5.7 \mu m$  grain size, and d) 280 nm grain size after ramp testing from room temperature to 1000 °C, modified from Gong *et al.* [26].

In 2017 Wood *et al.* also conducted an initial thermodynamic assessment of the oxidation of  $U_3Si_2$  [53]. When comparing Equations 2-6, U preferentially oxidizes over Si (Equation 5) and  $U_3Si_2$  oxidizing to any other compounds (Equations 3,4, and 6), as shown by having a lower  $\Delta G$  at 400 °C per mol of  $O_2$ .





UO<sub>2</sub> then will further oxidize in air above 400 °C in a two-step process that terminates at U<sub>3</sub>O<sub>8</sub>. [56, 57].



**Figure B.4** shows a computational calculation of the equilibrium phases and the compositional variation for 1 mole of U<sub>3</sub>Si<sub>2</sub> reacting with O<sub>2</sub> maintained at 1 atm at 900 °C using Thermocalc 2020b TAFID v10. The diagram was created by calculating the equilibrium conditions for one mole of U<sub>3</sub>Si<sub>2</sub> in the presence of 0-2 moles of O<sub>2</sub> at increasing increments of 0.1 moles of O<sub>2</sub>. Equilibrium calculations of this type provide insight into the oxidation behavior of U<sub>3</sub>Si<sub>2</sub> where excess amounts of O<sub>2</sub> is supplied. The diagram illustrates U preferentially oxidizing to UO<sub>2</sub> first, in agreement with the initial assessment of Wood *et al.* As oxidation progresses and additional O<sub>2</sub> is supplied, UO<sub>2</sub> continues to be produced linearly as a function of O<sub>2</sub> content as Si-rich U-Si compounds begin to form. Thermocalc predicts USi forming early in the oxidation stages then dissociates to U<sub>3</sub>Si<sub>5</sub>, USi<sub>2</sub>, and finally USi<sub>3</sub> forming last as U continues to form UO<sub>2</sub> leaving Si rich phases. Wood *et al.* detected USi<sub>3</sub> experimentally [53] and USi, U<sub>3</sub>Si<sub>5</sub>, and USi<sub>2</sub> have not been seen as a product experimentally in air. This is mostly likely due to their early formation and subsequent formation of higher Si containing phases during oxidation. However, elemental silicon begins to form after the U-Si rich phases react and the remaining uranium oxidizes. Silicon then begins to oxidize to SiO<sub>2</sub> only after all the uranium oxidizes. SiO<sub>2</sub> amounts increase linearly until it reaches completion then UO<sub>2</sub>

begins to further oxidize to  $U_4O_9$  which finally oxidizes to  $U_3O_8$  in a two-step process as shown in equation 7 and agree with literature findings [56, 57]. Thermocalc predicts the final oxidation products for  $U_3Si_2$  in synthetic air as  $U_3O_8$  and  $SiO_2$ . The prediction aligns well with thermal ramp testing up to 1000 °C as  $U_3O_8$  has been detected in multiple experiments [9, 26, 53, 58]; however no  $SiO_2$  has been detected experimentally. No experiment has demonstrated that the reaction reaches terminal oxidation which could be why  $SiO_2$  has not been observed.

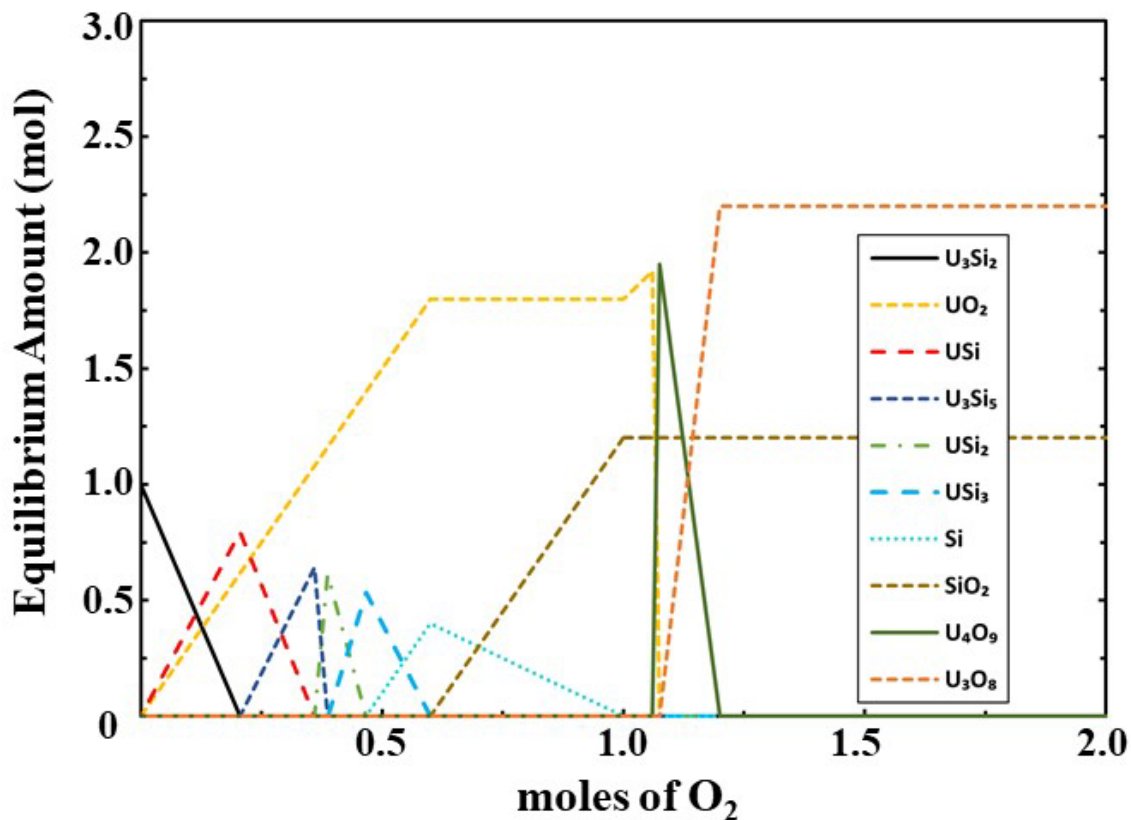


**Figure B.4** Thermodynamic equilibrium oxidation calculation of 1 mol  $U_3Si_2$  exposed to 0-2 moles of  $O_2$  at 900 °C using Thermocalc 2020b with TAFID v10 database [59].

$U_3Si_2$  mass weight gains in air oxidation were reported by Wood *et al.*, Johnson *et al.*, and Gong *et al.* at 21, 19.9, and 21.2 and 22.4%, respectively. This is notably lower than the expected mass gain (~25%) for complete oxidation assuming  $U_3O_8$  and  $SiO_2$  as

the final oxidation product. Johnson *et al.* assumed the final oxidation products of  $U_3O_8$  and SiO based off their mass gains; however, SiO has been shown to oxidize to  $SiO_2$  under oxidizing atmospheres and non-ambient temperatures [60]. Accordingly, SiO would not be anticipated to be the final oxidation product of Si. The mass discrepancies found in these research efforts was addressed by Harrison *et al* [9]. Since x-ray diffraction, used in each of the previous studies for phase identification, only probes crystalline material and the Si products could be amorphous and/or in quantities below XRD detection limits, scanning transmission electron microscopy (STEM) with EDS (or the like) is necessary to detect any chemical segregation at the micrometer scale [9]. The researchers therefore used STEM with EDS to characterize  $U_3Si_2$  oxidized in air with a mass gain of ~21%, and an onset between 350-450 °C, in-line the previous studies. Only  $U_3O_8$  was found with XRD, while the STEM/EDS mapping revealed the presence of U- and O-rich regions along with some Si-rich regions that were deficient in both U and O. High resolution transmission electron microscopy (HR-TEM) images (**Figure B.5a**) of this same region analyzed by STEM-EDS were indexed as Si nano-crystallites of about 10 nm in size (**Figure B.5b and c**). Other regions showed nano crystallites of  $U_3O_8$  confirming the XRD findings.

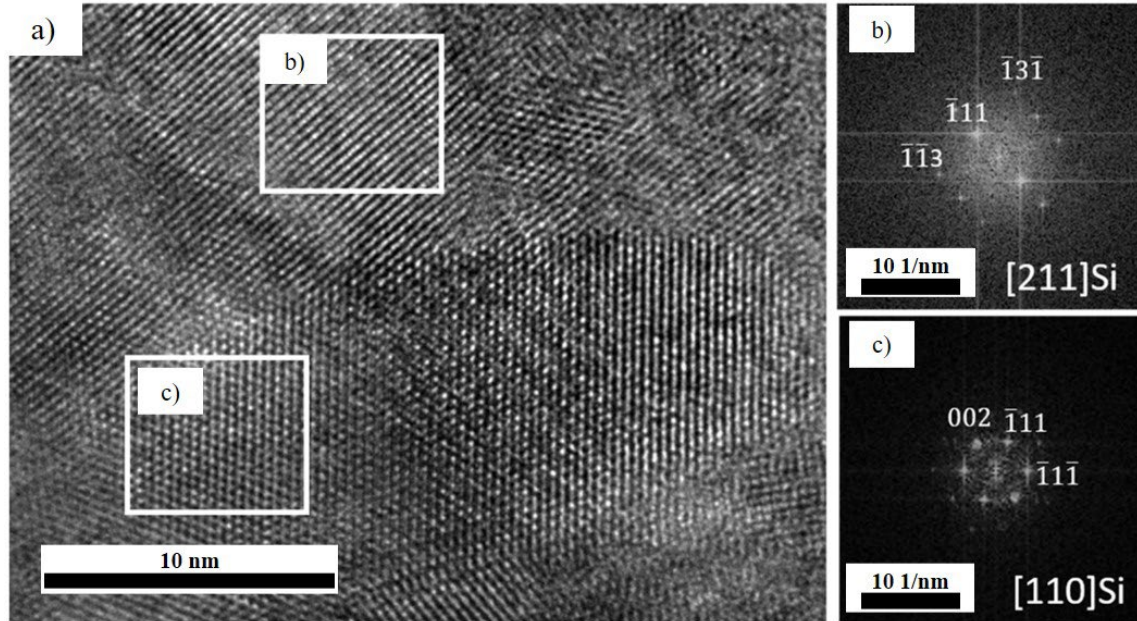


**Figure B.5** a) HR-TEM image of Si-rich and U and O deficient region identified by EDS, showing the 10 nm size crystallites, b) FFT from boxed area of grain 1, and c) grain 2 indexed as crystalline Si, modified from Harrison *et al.* [9].

It was concluded from Harrison *et al.* that the oxidation of Si to SiO<sub>2</sub> must occur as the total mass gain observed was 21.1 wt.%, which is well above the ~ 16.6 wt% mass gain had the sample oxidized to U<sub>3</sub>O<sub>8</sub> and free Si. The Si observed in the work is remnant from unreacted Si, not from production of SiO, suggesting the incomplete mass gains can be attributed to a mixture of oxidation of Si to SiO<sub>2</sub> and unreacted Si [9]. The thermodynamic reaction pathway was stated as the U in U<sub>3</sub>Si<sub>2</sub> was found to preferentially oxidize over the Si to form UO<sub>2</sub> leading to Si-rich USi<sub>3</sub> phases, experimentally shown by Wood *et al.* [53]. The majority of Si then oxidizes to SiO<sub>2</sub> and some nanoscale (<100 nm) regions of free Si, that are protected by the UO<sub>2</sub> formed in the previous reaction, shown by Harrison *et al.* [9]. Finally, UO<sub>2</sub> further oxidizes to U<sub>3</sub>O<sub>8</sub> in a two-step process, resulting in volumetric expansion in the fuel leading to pulverization of U<sub>3</sub>Si<sub>2</sub> [26, 53].

The volumetric expansion during air oxidation due to the formation of  $\text{UO}_2$  from  $\text{U}_3\text{Si}_2$  causes pulverization [9, 26, 53]. Harrison *et al.* reported a ~17 vol.% expansion and subsequent oxidation of  $\text{UO}_2$  to  $\text{U}_3\text{O}_8$  leads to a further 36 vol.% expansion. Coupled with the volumetric expansion of the formation of  $\text{SiO}_2$  (assuming a density of  $2.2 \text{ g/cm}^3$  for amorphous silica) and free Si, this leads to a total change of 133 vol.% during oxidation [9]. The strain arising from the large volumetric change and associated nano-grain formation leads to the pulverization of the material from a solid form into powder.

In summary, air oxidation testing of undoped  $\text{U}_3\text{Si}_2$  has shown that fabrication methods can impact oxidation performance, likely due to variations in microstructure, residual stresses, and impurity phase distribution resulting from different techniques. Although composition variations, e.g., the incorporation of excess Si or contaminant  $\text{UO}_2$  phase concentration, were not extensively investigated in the reviewed literature. Additionally, it is determined that Si remains largely unreacted under these exposures. **Table B.1** summarizes the air oxidation parameters of  $\text{U}_3\text{Si}_2$  for the reviewed literature. Criticism of the presentation of air oxidation of  $\text{U}_3\text{Si}_2$  samples argue that oxidation in  $\text{O}_2$  atmospheres is of little relevance when considering the accident tolerance of a fuel, as it does not represent off-normal, water-cooled reactor accident conditions. At temperatures relevant to LWR operations, the oxygen activity in  $\text{H}_2\text{O}$  is vanishingly small compared to air. At  $400 \text{ }^\circ\text{C}$  the oxygen activity of 1 atmosphere of  $\text{H}_2\text{O}$  is equivalent to  $10^{-5}$  parts per million (ppm)  $\text{O}_2$  [61]. It should be noted that none of the reviewed experiments, in either this section or the following, accurately represent a leaker condition; however, a flowing, chemistry-controlled, pressurized water test is an expensive and most often inaccessible experimental atmosphere. The authors argue here that a relevant and more accessible

screening atmosphere for assessing a potential ATF candidate's performance during coolant exposure is a water-based corrosion atmosphere, including exposure to flowing steam.

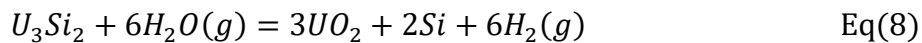
**Table B.1 Summary of air corrosion of U<sub>3</sub>Si<sub>2</sub> and additives.**

	Ref.	Synthesis method	Sintering method	Composition	Terminal Mass Gain (%)	Temp. testing (°C)	Onset temp. (°C)	Time to full oxidation	Grain size	Reaction Product(s)
Air	[52]	Electric Arc Furnace	Conventional	U <sub>3</sub> Si <sub>2</sub>	18.5	400	N/A	7.5hr	N/A	N/A
	[53]	Arc-Melting + excess Si	Conventional	U <sub>3</sub> Si <sub>2</sub>	21	25-1000	384	N/A	N/A	U <sub>3</sub> O <sub>8</sub> , UO <sub>2</sub>
	[53]	Arc-Melting + excess Si	Conventional	U <sub>3</sub> Si <sub>2</sub>	18	425	N/A	6 min	N/A	U <sub>3</sub> O <sub>8</sub> , USi <sub>3</sub> , UO <sub>2</sub>
	[8]	Arc-Melting	As-cast	U <sub>3</sub> Si <sub>2</sub>	19.9	25-800	470	N/A	>80μm	N/A
	[26]	Arc-Melting Metallurgy HEBM Powder	SPS	U <sub>3</sub> Si <sub>2</sub>	21.2 - 22.4	25 -1000	520, 510 (prior to anneal) 560, 500 (after anneal)	12- 42 min (prior to anneal) 9 - 17 min (after to anneal)	~5.7μm ~280nm	U <sub>3</sub> O <sub>8</sub>
	[58]	Arc-Melting + excess Si	As-cast	U <sub>3</sub> Si <sub>1.91</sub> Al <sub>0.09</sub> U <sub>3</sub> Si <sub>2</sub> Al <sub>0.75</sub> U <sub>3</sub> Si <sub>2</sub> Al <sub>1.25</sub> U <sub>3</sub> Al <sub>2</sub> Si <sub>2</sub>	21 21 23 25	25-1100	415 466 523 670	N/A	N/A	U <sub>3</sub> O <sub>8</sub> , UO <sub>2</sub>
	[62]	Arc-Melting Powder Metallurgy HEBM	SPS	5 wt% UO <sub>2</sub> 25 wt% UO <sub>2</sub> 50 wt% UO <sub>2</sub> 75 wt% UO <sub>2</sub> 25wt% UO <sub>2</sub> * 50wt% UO <sub>2</sub> *	N/A	25-1000	480 390 300 260 500 420	12 min 15 min 18 min 20 min N/A N/A	N/A	N/A
	[63]	Arc-Melting Powder Metallurgy HEBM	SPS	1.8 at% (0.32 wt%) Al 7.2 at% (1.34 wt%) Al 25 at% (5.5 wt%) Al	17.8-21.7	25-1000	501-610	N/A	6μm-600nm	N/A

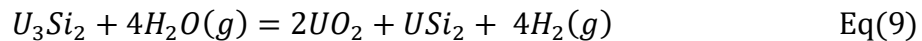
	Ref.	Synthesis method	Sintering method	Composition	Terminal Mass Gain (%)	Temp. testing (°C)	Onset temp. (°C)	Time to full oxidation	Grain size	Reaction Product(s)
	[64]	Arc-Melting Powder Metallurgy HEBM	SPS	1 vol% 3Y-TZP 3 vol% 3Y-TZP 5 vol% 3Y-TZP	20.8-20.9	25-1000	565.1-574.5 (prior to anneal) 592.7-617 (after anneal)	N/A	U <sub>3</sub> Si <sub>2</sub> (2µm) 3Y-TZP (200 nm)	α-U <sub>3</sub> O <sub>8</sub> , UO <sub>2</sub> , ZrSiO <sub>4</sub> , mono-clinic ZrO <sub>2</sub>
*sintered higher temperature										

### B.3.2.2 Water Corrosion of U<sub>3</sub>Si<sub>2</sub>

U<sub>3</sub>Si<sub>2</sub> has been proven experimentally to be susceptible to degradation modes that are governed by both reactions with oxygen, resulting in the formation of a non-passivating UO<sub>2</sub> scale and hydrogen which forms a stable U<sub>3</sub>Si<sub>2</sub>H<sub>2</sub> structure resulting in a 10% volumetric expansion [16, 17, 65, 66]. A U<sub>3</sub>Si<sub>2</sub> thermodynamic assessment of steam oxidation showed the primary reaction as equation 8 due to it having a lower Gibbs free energy per mole of H<sub>2</sub>O(g) than the other equations tested. Equations (9) and (10) were found to be secondary reactions [65]:



with two secondary reactions identified as [65]:



These results are in agreement with a density functional theory (DFT) calculation performed by Jossou *et al.* that indicated the oxygen molecule interacts strongly with the U<sub>3</sub>Si<sub>2</sub> surfaces and results in the formation of a peroxo-like (O<sub>2</sub><sup>-2</sup>) species [10]. It was concluded that the U<sub>3</sub>Si<sub>2</sub> surfaces are easily oxidized by dissociated oxygen molecules

which implies that dissociation of the water molecule is a necessary step before the oxidation of  $U_3Si_2$  [10].

**Figure B.6** shows a phase equilibrium calculation of 1 mole of  $U_3Si_2$  reacting with up to 10 moles of  $H_2O(g)$  at 400 °C using Thermocalc 2020b with TAFID v10 database [59]. The oxidation process shown here is similar to the air oxidation discussed in the previous section (**Figure B.4**) with the exception of  $UO_2$  being the final oxidation state not  $U_3O_8$ , agreeing with experimental results [14, 16, 65, 67, 68]. Steam oxidation testing expose  $U_3Si_2$  to excess amounts of steam and display products in the latter stages of oxidation.  $USi_3$  is the most detected U-Si phase experimentally following steam oxidation [14, 16, 65, 67, 68] which aligns well with the Thermocalc model prediction, as  $USi_3$  is the final U-Si phase predicted to form in an abundance of steam. To the author's knowledge, Yang *et al.* are the only authors to report  $U_3Si_5$  and  $USi_2$  phases experimentally [14]. It should be noted that the stable U-Si-H ternary phase is not available in TAFID, and therefore it is left out of this analysis. A more accurate thermodynamic assessment would include ternary phases.

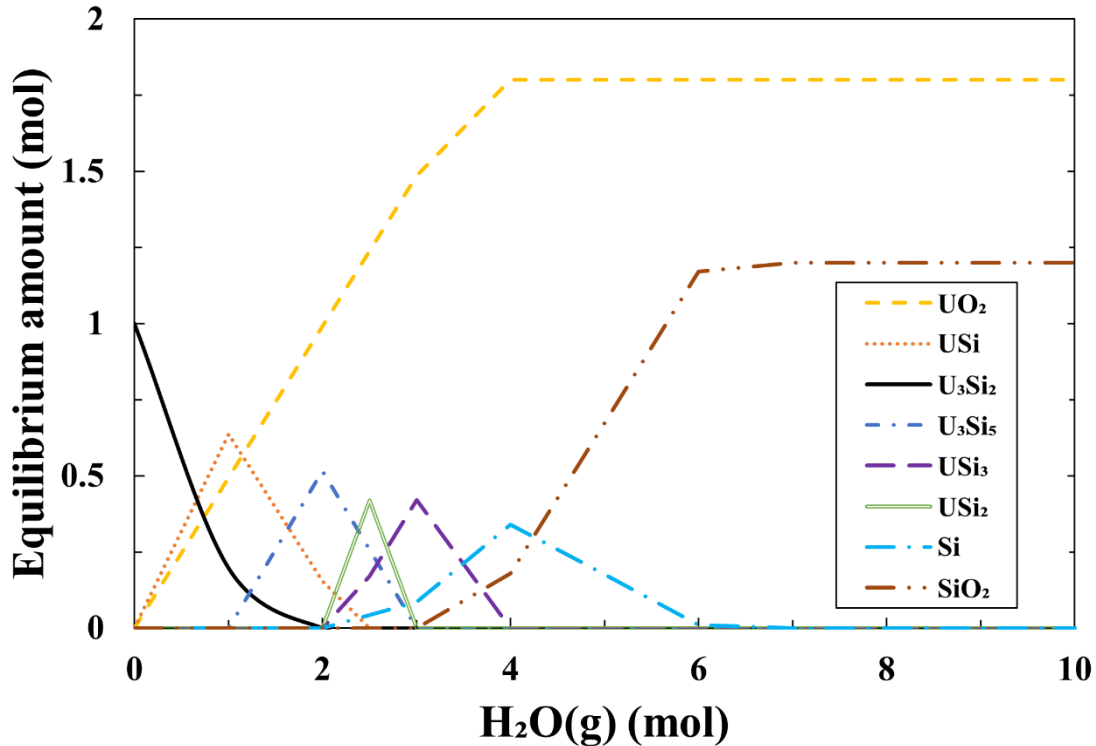
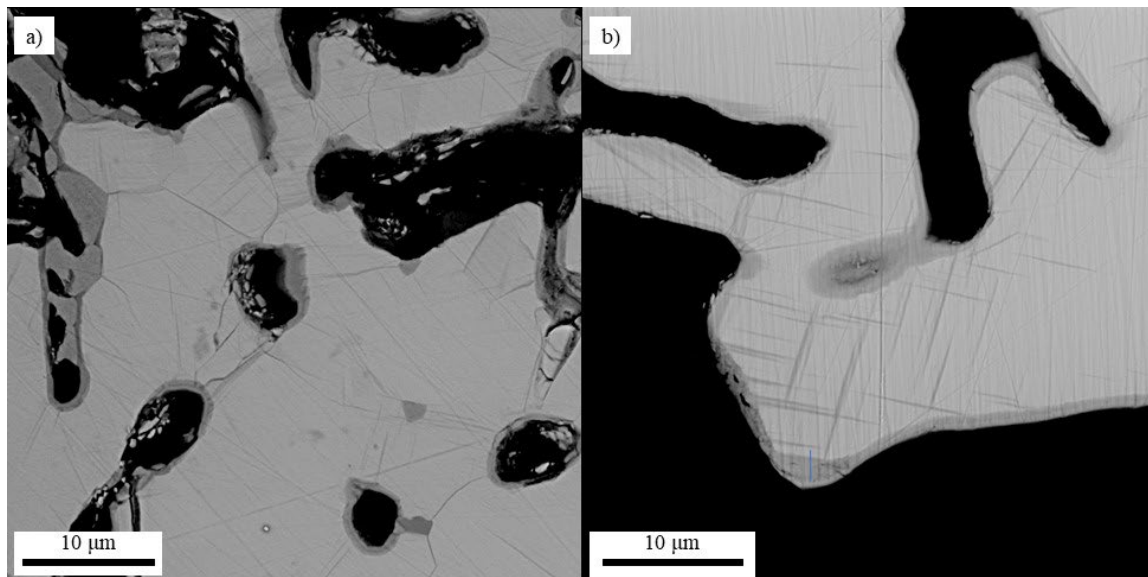


**Figure B.6** Equilibrium phase diagram of 1 mole U<sub>3</sub>Si<sub>2</sub> in 1 atm of steam in increasing amounts at 400 °C using Thermocalc 2020b with TAFID v10 database [59].

With LWR accident conditions and relevant oxidant levels in mind, Wood, Turner, and Yang *et al.* measured the response of U<sub>3</sub>Si<sub>2</sub> to flowing steam [14, 16, 67]. All authors reported an onset of breakaway oxidation for U<sub>3</sub>Si<sub>2</sub> between 406-480 °C. The range for the onset temperature arises from the differences in sample properties/geometry, testing conditions, and fabrication; all of which are summarized in **Table B.2**.

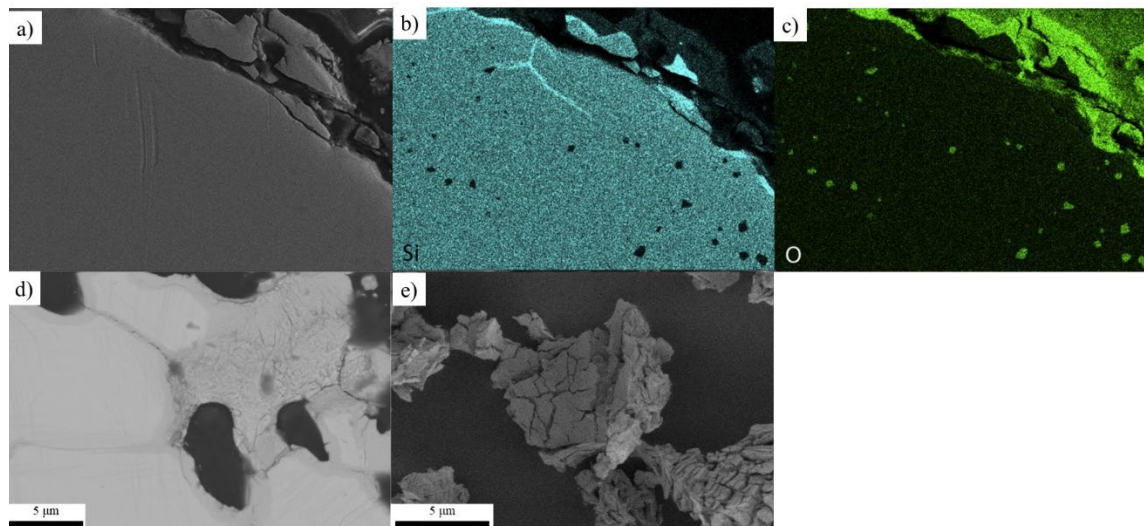
In a study where U<sub>3</sub>Si<sub>2</sub> was shown to pulverize within minutes over 400 °C, **Figure B.7** displays microstructural degradation following hours of exposure at (a) 350 °C and (b) 400 °C in steam from Wood *et al.* No significant gravimetric event was observed during a 6 hour hold at 350 °C but was observed to undergo significant structural degradation within 1 hour of exposure at 350 °C. The two images (**Figure B.7**)

exhibit the typical elongated pores and hash marks (needle like microstructure) identified in all the  $U_3Si_2$  samples exposed to flowing steam.



**Figure B.7** Micrographs taken from cross-sectioned  $U_3Si_2$  pellets exposed to steam at a) 350 °C for 6 hours and b) 400 °C for 1.5 hours, modified from Wood *et al.* [16]

In 2020, Turner *et al.* [67] compared the effects of  $U_3Si_2/UB_2$  fuel composite pellets (see section A4) to a reference  $U_3Si_2$  pellet during steam oxidation. **Figure B.8a**, **b**, and **c** show an SEM with EDS of  $U_3Si_2$  after a short exposure to steam. **Figure B.8b** shows the Si-rich regions that formed at a sharp edge to the existing oxide layer (**Figure B.8c**) and are similar in size and morphology to the cracks which appear to develop at later stages of the reaction, (**Figure B.8d**). **Figure B.8a** and **d** are short exposures (5 min) at 465 °C of  $U_3Si_2$  to steam. The Si is surrounded by oxide which appears to progress from the cracks inwards, further displacing Si. In the same study,  $U_3Si_2$  was exposed at 900 °C and was reduced to powder (**Figure B.8e**) identified as  $UO_2$  per XRD and having many branching cracks on the surface.



**Figure B.8** SEM of  $U_3Si_2$  after short exposure to steam at a) 465 °C with b) EDS of Si-rich regions and c) EDS of oxygen rich regions d) later stages of steam oxidation at 465 °C, and e) powder morphology following 900 °C steam, modified from Turner *et al.* [67]

Both Wood and Turner samples were pellet geometries (right cylinders), as opposed to spherical particles or fragmented ingots, and showed elongated pores and cracking following high temperature steam exposures. In another study, Yang *et al.* tested spherical  $U_3Si_2$  particles produced via centrifugal atomization, as shown in **Figure B.9a**. As previously mentioned,  $U_3Si_2$  samples with pellet geometries showed degradation as low as 350 °C while **Figure B.9b** shows very little structural difference when compared to its non-oxidized counter-part (**Figure B.9a**). Elongated pores were not present in the particles, but cracks formed and worsened with increasing temperature (**Figure B.9c** and **d**). Both Turner (**Figure B.8e**) and Yang (**Figure B.9d**) show severe cracking at 900 °C and samples readily pulverized.

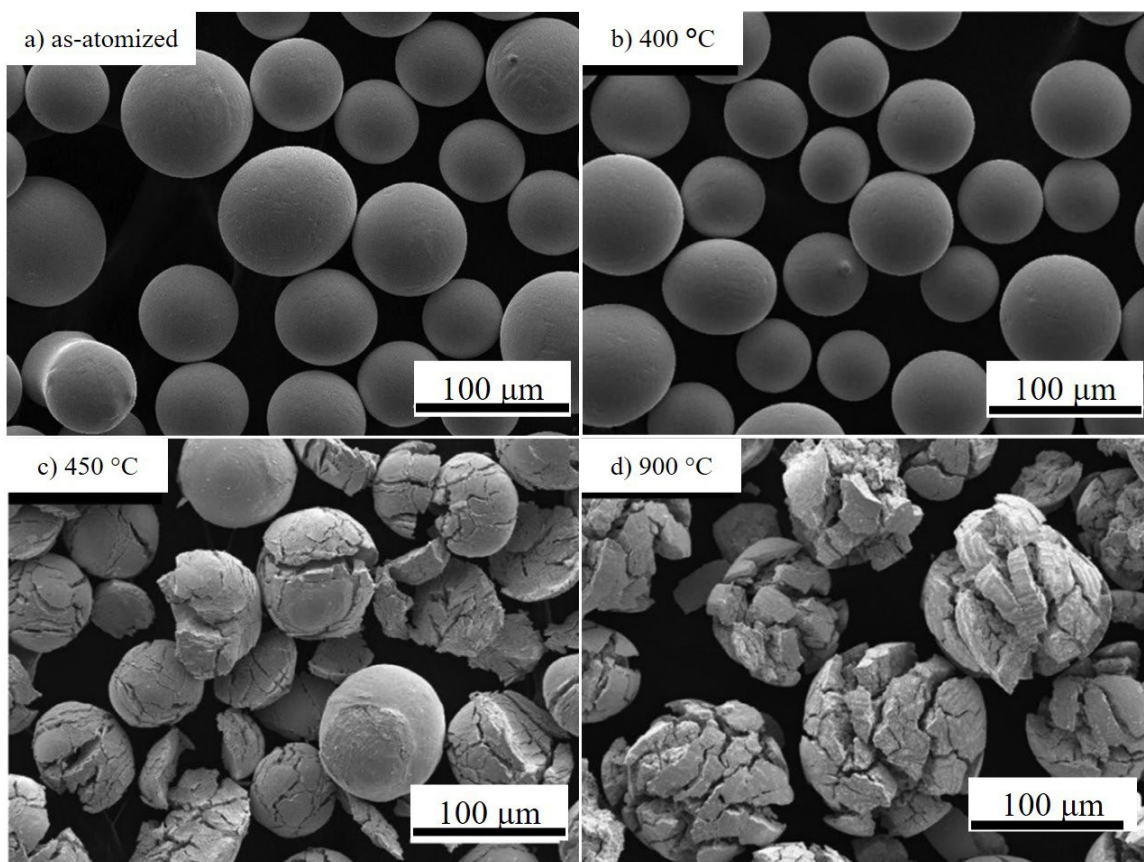


**Figure B.9**  $U_3Si_2$  as-oxidized powder after steam testing a) spherical  $U_3Si_2$  particles produced after atomization fabrication. b)  $U_3Si_2$  after 400 °C, c) 450 °C, and d) 900 °C steam for 3 hours. Adapted from Yang *et al.* [14].

Oxidation that occurs in  $H_2O$  environments will also produce hydrogen as a reaction product. Hydrogen produced in this manner will reduce the oxidation potential of the system. There is debate in the literature as to whether hydrogen will additionally participate in other degrading reactions. Yang *et al.* reported striations that occurred after steam oxidation for the atomized particles were a U-Si compound (**Figure B.10a**). Wood *et al.* used Ar-6% $H_2$  to probe the effect of hydrogen on the degradation of  $U_3Si_2$  in the reaction with steam (**Figure B.10b**). Under these conditions, XRD analysis indicated the formation of a  $U_3Si_2H_{1.8}$  hydride that is also supported by other experiments [15, 65-67, 69]. The onsets of pulverization and ejection of material occurred in up to  $\approx 1$  hour less time under Ar-6% $H_2$  conditions than steam, implying an enhanced sensitivity of  $U_3Si_2$  to

H<sub>2</sub> containing atmospheres in the temperature range tested (350 - 400 °C). The potential H<sub>2</sub> reaction has also been linked to the unique response of U<sub>3</sub>Si<sub>2</sub> to steam, proving detrimental to its exposure to a reducing water chemistry.

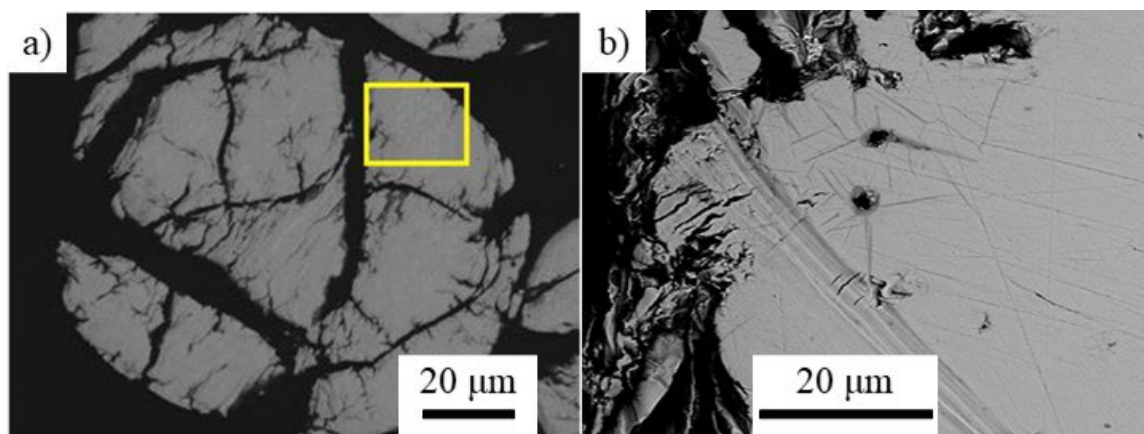


**Figure B.10** Striation formations after steam oxidation. a) 450 °C in steam modified from Yang *et al.* and b) 400 °C in Ar-6%H<sub>2</sub> modified from Wood *et al.* [16].

The exposures of U<sub>3</sub>Si<sub>2</sub>, U<sub>3</sub>Si<sub>5</sub>, UN, and UO<sub>2</sub> to pressurized water, by Nelson *et al.*, were performed to assess their general response to conditions relevant to LWR fuel service [15]. All U-Si samples tested using the methodology of the study exhibited behavior less favorable than UO<sub>2</sub>. Testing in a 1 ppm H<sub>2</sub> water chemistry at 300 °C resulted in continuous weight loss/dissolution for the bulk sample leading to pulverization in roughly 30 days. Increasing the H<sub>2</sub> content of the water reduced weight loss as measured during short time intervals when compared to 1 ppm studies, which is somewhat contradictory to the hydrogen testing performed in a flowing atmosphere. However, exposures beyond 31 days caused severe loss of mechanical integrity and pulverization. There is minimal difference in the microstructure of the U<sub>3</sub>Si<sub>2</sub> pellets exposed to 1 ppm and 5 ppm H<sub>2</sub> at 300 °C (**Figure B.11**). The 1 ppm exposure image (**Figure B.11a**) identified a UO<sub>2</sub> region on the pellet surface that is thought to also be in

the 5 ppm H<sub>2</sub> sample (**Figure B.11b**) but could not be conclusively identified. A Si-rich region was also identified in the 1 ppm sample similar to air oxidized samples while the 5 ppm sample exhibited needle like structures (white arrows in **Figure B.11b**) beneath its surface, typical of hydride formation. The data presented in this study exemplifies the concerns of the stability of U<sub>3</sub>Si<sub>2</sub> during a “leaker” scenario, where the fuel pin has been breached yet a major loss of coolant or cladding rupture has not occurred.

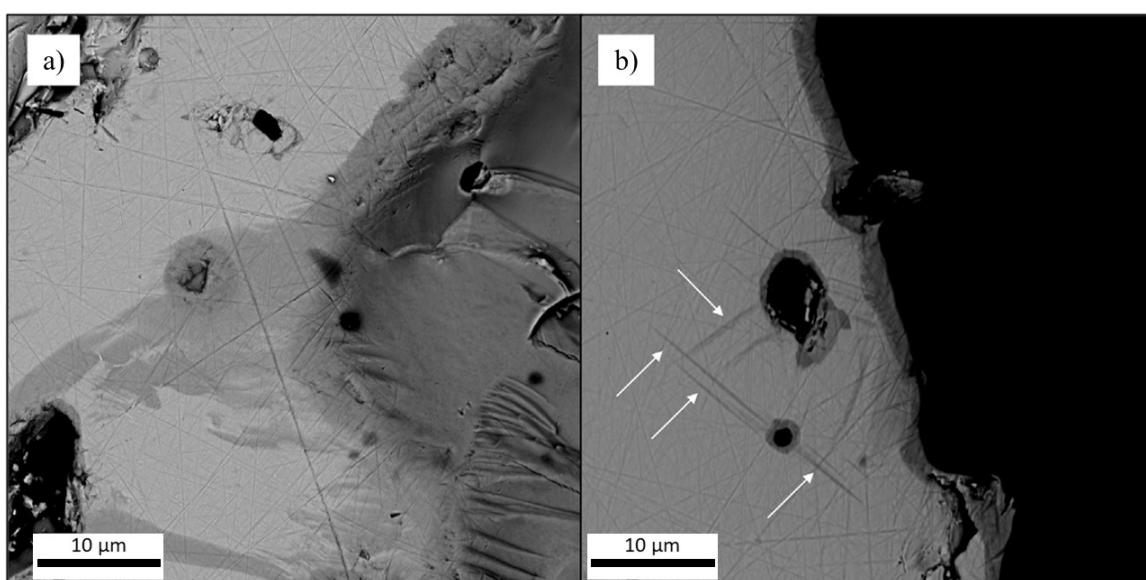


**Figure B.11** SEM images of U<sub>3</sub>Si<sub>2</sub> sample cross sections following 31 day exposure to 300 °C H<sub>2</sub>O at 85 bar under two water chemistry conditions: a) 1 ppm H<sub>2</sub>, and b) 5 ppm H<sub>2</sub>. White arrows in b) identify needle-like structures that are present following testing, modified from Nelson et al. [15].

On the mechanism of pulverization, when U<sub>3</sub>Si<sub>2</sub> is exposed to the 1 ppm H<sub>2</sub> hydrothermal treatment [15], pulverization was dominated by slow oxidation of the pellet surface to form UO<sub>2</sub>; continued growth of the surface oxide resulted in spallation, seen in cross-sectional SEM images in **Figure B.11a**. However, testing under the 5 ppm H<sub>2</sub> conditions [15] showed a sudden loss of integrity after 31 days, rather than continuous mass loss leading to pulverization. These results suggest a different corrosion mechanism than the 1 ppm H<sub>2</sub> test. In the 5 ppm test, UO<sub>2</sub> could not be conclusively identified and

had a thinner layer on the surface sample versus the 1 ppm test. The residual powder after the 5 ppm test was primarily  $U_3Si_2$  suggesting a non-oxidizing mechanism, likely the formation of a hydride due to the similar needle-like structures (**Figure B.11b**) as compared to the steam tested sample (**Figure B.7b**). Hydride formation will induce strain in the bulk  $U_3Si_2$  due to the volume expansion of the hydride phase. The only reported U-Si-H compound,  $U_3Si_2H_2$ , possesses the same structure as  $U_3Si_2$  and is difficult to resolve using XRD [66]. An onset of pulverization attributed to hydriding was also observed during atmospheric steam testing at elevated temperatures although no additional hydrogen beyond the  $H_2O$  was present in that system [16]. It is postulated that the hydrogen liberated from  $H_2O$  during oxidation can form hydrides within the bulk  $U_3Si_2$ . This hydride could also be present in the 1 ppm  $H_2$  study but is hidden by the pulverization due to the formation of  $UO_2$ .

In summary of the water/steam oxidation of pure  $U_3Si_2$ , oxidation testing of  $U_3Si_2$  in  $H_2O$  atmospheres revealed sample cracking and pulverizing regardless of how the samples were fabricated or the  $H_2O$  atmosphere (steam or pressurized) it was tested in [14-16, 67]. **Table B.2** summarizes the oxidation parameters of  $U_3Si_2$  for the reviewed literature. To address the performance of  $U_3Si_2$  in air and  $H_2O$  atmospheres, researchers have looked towards the use of additives/dopants. The use of alloying or dopant additions can stabilize the bulk structure under corrosive exposure and/or form protective diffusion/passivation layers which slow or mitigate corrosion entirely.

**Table B.2 Summary of water/steam corrosion of U<sub>3</sub>Si<sub>2</sub> and additives**

	Ref.	Synthesis method	Sintering method	Composition	Terminal Mass Gain (%)	Temp. testing (°C)	Onset temp. (°C)	Time to full oxidation	Grain size	Reaction Product(s)	
Steam	[16]	Arc-Melting + excess Si	Conventional	U <sub>3</sub> Si <sub>2</sub> in 6% H <sub>2</sub> atm	N/A	290-500	460-480	Structural degradation after 1hr	N/A	UO <sub>2</sub> , USi <sub>3</sub> , U <sub>3</sub> Si <sub>2</sub> H <sub>1.8</sub>	
	[15]	Arc-melting	Conventional	U <sub>3</sub> Si <sub>2</sub> in 1 ppm H <sub>2</sub>	N/A	Autoclave: 300	N/A	Pulverization prior 30 days	30-35 μm	N/A	
	[15]	Arc-melting	Conventional	U <sub>3</sub> Si <sub>2</sub> in 5 ppm H <sub>2</sub>	N/A	Autoclave: 300	N/A	Pulverization after 30 days	30-35 μm	N/A	
	[67]	Arc-melting Powder Metallurgy	Conventional	U <sub>3</sub> Si <sub>2</sub> 10wt% UB <sub>2</sub> 50wt% UB <sub>2</sub>	N/A	250-900	453 553 575	N/A	N/A	N/A	UO <sub>2</sub> , Hydride
	[65]	Arc-Melting + excess Si	As-melted	2 vol% (1.2 wt%) Cr 5.5 vol% (3.3 wt%) Cr 7 vol% (4.2 wt%) Cr 10.3 vol% (6.3 wt%) Cr 6.1 vol% (2.3 wt%) Y 13.5 vol% (5.4 wt%) Y U <sub>3</sub> Al <sub>2</sub> Si <sub>2</sub> UAlSi	N/A	250-1000	451 456 439 426 427 400 >800 >800	Yttrium - rapid pulverization	N/A	USi <sub>3</sub> , UO <sub>2</sub> , Al <sub>2</sub> O <sub>3</sub>	
	[14]	Centrifugal atomization	As-fabricated	U <sub>3</sub> Si <sub>2</sub>	16-17	400-900	406-480	N/A	Particle diameter - 90μm	UO <sub>2</sub> , USi <sub>3</sub> , U <sub>3</sub> Si <sub>5</sub> , USi <sub>2</sub>	
	[68]	Arc-Melting Powder Metallurgy HEBM	SPS	3 wt% Cr 5 wt% Cr 10 wt% Cr	19-23	25-1000	520-570	13-23 min	Micron-nano	UO <sub>2</sub> , UCr <sub>1.375</sub> Si <sub>10.625</sub> , SiO <sub>2</sub> , Cr <sub>2</sub> O <sub>3</sub> , USi <sub>3</sub> , U <sub>3</sub> O <sub>8</sub>	

## B.4. Additives/Dopants to $U_3Si_2$ and Fuel Composite Architectures to Mitigate Oxidation Behavior

### B.4.1 Alloying Additions and Dopants

Several investigations have been performed to assess the effectiveness of alloying and doping  $U_3Si_2$  to enhance its oxidation resistance. Most of the existing studies on alloying/doping have focused on additions to  $U_3Si_2$ , denoted here as  $U_3Si_2+X$ , rather than lattice substitutions. **Figure B.12** shows an Ellingham-type diagram (similar to **Figure B.1**) indicating the relative thermodynamic stability for silicide formation of potential additives as compared to  $U_3Si_2$ . During high temperature synthesis (arc melting) and traditional sintering, the addition of an additive which will preferentially form a silicide, causing the dissociation of  $U_3Si_2$ , is undesirable as it will result in free uranium in the fuel form. According to **Figure B.12**, molybdenum, chromium, magnesium, nickel, titanium, and zirconium will all form a silicide preferentially to  $U_3Si_2$ .

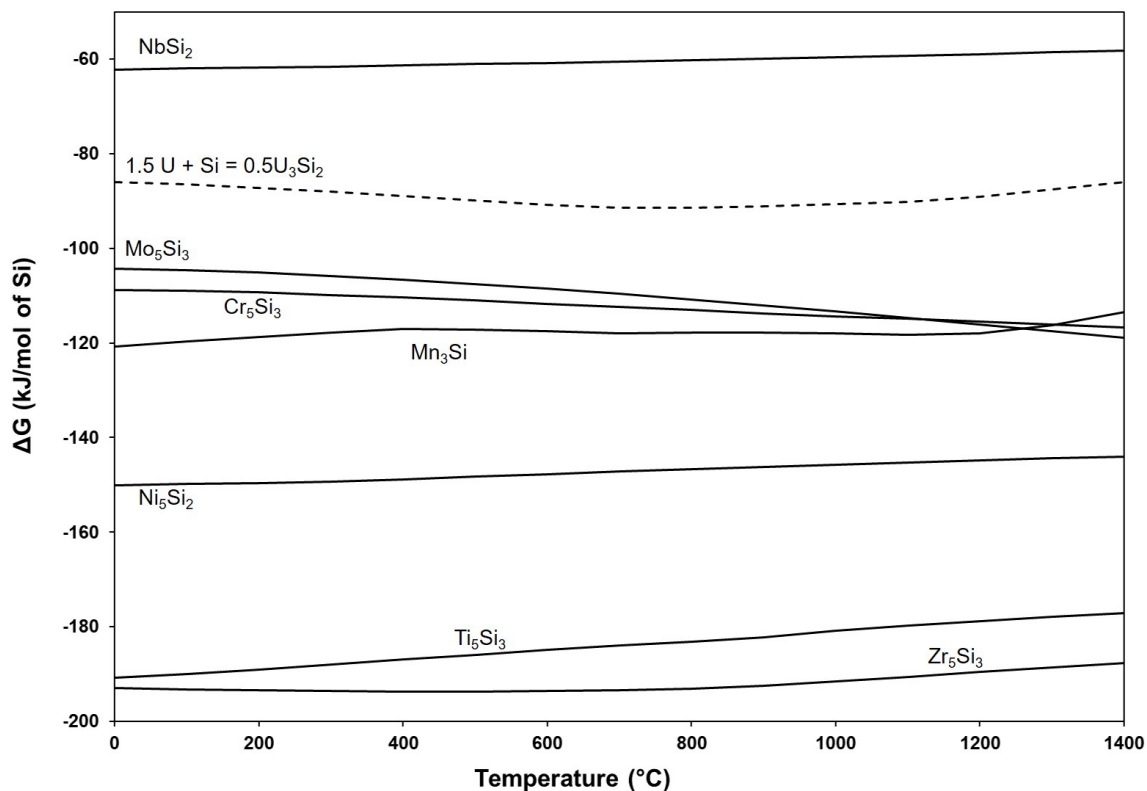


**Figure B.12** Ellingham-type diagram showing thermodynamic stability of silicide formation of various metallic elements considered for possible dopants into ATF concepts versus  $U_3Si_2$ . Calculated using HSC Chemistry 9 [27]. Note the databases used in these calculations only included silicates of Al and Y and thus were not included in the plot.

There are other potential additions, Al for example, which also occupy U ( $UAl_x$ ), and there are a host of ternary systems that have been observed to form as well. Wood *et al.* began investigating the introduction of additives to  $U_3Si_2$  with the incorporation of aluminum [58]. Aluminum was chosen due to the formation of  $Al_2O_3$  being more thermodynamically favorable than  $UO_2$  below 600 °C [58] (**Figure B.1**).

By arc-melting elemental uranium, silicon, and aluminum, Wood *et al.* fabricated  $U_3Al_2Si_3$ , as the upper bound for Al additions, and 1.8 at% (0.32 wt%) Al addition to form  $U_3Si_{1.91}Al_{0.09}$  as the lower bound, along with two intermediate compositions,  $U_3Si_2Al_{1.25}$  and  $U_3Si_2Al_{0.75}$ . Mohamad *et al.* fabricated a 1.8 at%(0.32 wt%), 7.2 at%(1.34

wt%), and 25 at% (5.5 wt%) Al additions to stoichiometric  $U_3Si_2$ , 60 at% U and 40 at% Si (92.7 wt% U and 7.3 wt% Si); created through arc-melting and atomization prior to SPS. It is the first experiment to report oxidation testing of stoichiometric  $U_3Si_2$  fabricated using SPS [63]. Results from TGA testing indicated that increased amounts of Al in  $U_3Si_2$  further delayed the onset of breakaway oxidation in synthetic air (80% Ar, 20%  $O_2$ ) [58, 63]. The reported onset temperatures from both experiments ranged from 415 - 670 °C and are collected in **Table B.1**. The  $U_3Al_2Si_3$  and 25 at% (5.5 wt%) Al additions had the highest report onset temperatures, 670 and 601 °C respectively but they reduced the fissile element density below that of  $UO_2$ , defying the purpose of Al-doped  $U_3Si_2$  as a high density ATF candidate fuel form. However, the minimal amount of additive used, 1.8at% (0.32 wt%) Al, by Mohamad et al. also reached an onset above 600 °C after annealing.

Both authors reported little phase segregation at low dopant percentages, even though they used different fabrication routes. Scanning electron microscopy paired with EDS revealed that an  $Al_2O_3$  layer forms during oxidation at 500 °C of  $U_3Al_2Si_3$ , (**Figure B.13**). A cross-sectional micrograph of the oxidized  $U_3Al_2Si_3$  (**Figure B.13a**) and EDS maps of the selected area (**Figure B.13b** and **c**) show  $Al_2O_3$  formation along the edges of the sample and along cracks [58]. The presence of Al along the cracks of the button fragment demonstrates that  $Al_2O_3$  has indeed formed preferentially to  $UO_2$  and is likely the cause for the delayed onset. Though this layer was not found to be passivating as the sample pulverized during exposure, it demonstrated the potential for aluminum to increase the oxidation resistance of  $U_3Si_2$  [58].

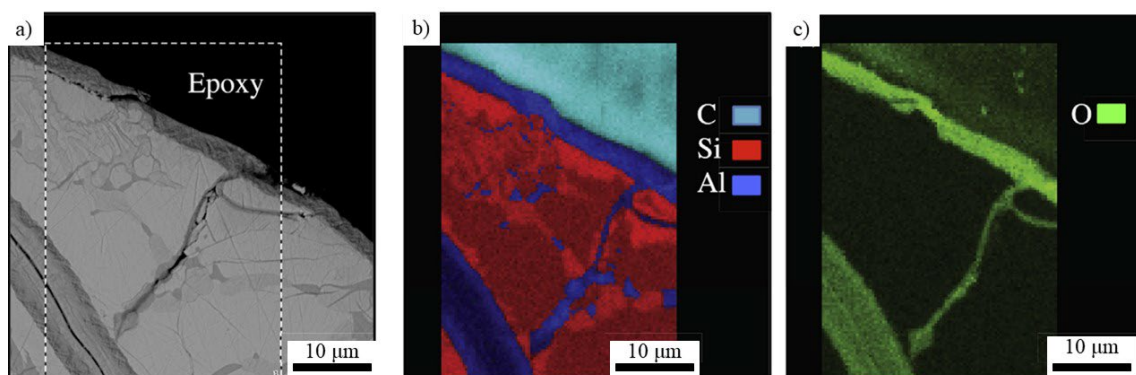


**Figure B.13** a) Cross-sectional micrograph of the oxidized  $U_3Al_2Si_3$  equilibrium composition, and EDS maps of the selected area (b and c) showing  $Al_2O_3$  formation along the edges of the sample and along cracks, modified from Wood et al. [58].

Steam testing of the U-Si-Al samples fabricated by Wood *et al.* was presented in an investigation published in 2020 [65]. The U-Si-Al compositions ( $UAl_2$ ,  $USiAl$  and  $U_3Si_2Al_3$ ) showed promising oxidation kinetics behavior demonstrating gradual and minimal mass gain in flowing steam, however the samples are at a lower U-atom density than  $UO_2$  and therefore would likely only be considered as a composite constituent; a summary of the results is listed in **Table B.2**. Further investigation is necessary to determine the impact of lower addition percentages.

Experimental analysis of the steam oxidation behavior of  $U_3Si_2$  alloyed with chromium (Cr) was conducted by Wood and Gong *et al.* [65, 68]. The tested samples were 2 vol% (1.2 wt%), 5.5 vol% (3.3 wt%), 7 vol% (4.2 wt%), and 10.3 vol% (6.3 wt%) Cr by Wood *et al.* and 3, 5, and 10 wt% Cr by Gong *et al.* The onset of breakaway oxidation for Cr additions were reported between 426-570 °C [65, 68]. The range for the onset temperatures can be attributed to the differences in fabrication, Cr addition percentages used, and annealing. Gong *et al.* used HEBM to distribute the Cr additions throughout the samples followed by SPS, resulting in a microstructure shown in **Figure B.14a** while Wood *et al.* used as-cast arc-melted samples with resulting microstructures

shown in **Figure B.14b**. Both authors report the formation of a ternary phase,  $\text{UCr}_{1.375}\text{Si}_{0.625}$ , in addition to  $\text{UO}_2$  formation after oxidation. All of the Wood *et al.* Cr samples displayed an improvement to the onset temperature when compared to their reference  $\text{U}_3\text{Si}_2$ , 409 °C. It is difficult to see the effect Cr additions had on  $\text{U}_3\text{Si}_2$  for Gong *et al.* samples as there are no reference steam tested  $\text{U}_3\text{Si}_2$  pellet that has been SPS sintered to compare to. However, the Cr samples by Gong *et al.* had an onset temperature of up to 570 °C prior to annealing. The 10 wt% Cr- $\text{U}_3\text{Si}_2$  sample was also tested in an isotherm at 360 °C under steam for 24 hours and maintained its structural integrity with small changes to its mass (**Figure B.14c**) [68]. No visible fractures were seen, and only isolated areas of oxide growth were detected (**Figure B.14d**). Wood *et al.* reported isotherm holds at 350 °C for 6 hours on the Cr additions which all pulverized [65]. The impact that fabrication and the methods for incorporation of alloying phases can have on the oxidation performance of the fuel form is exemplified in the comparison of the results of these studies.

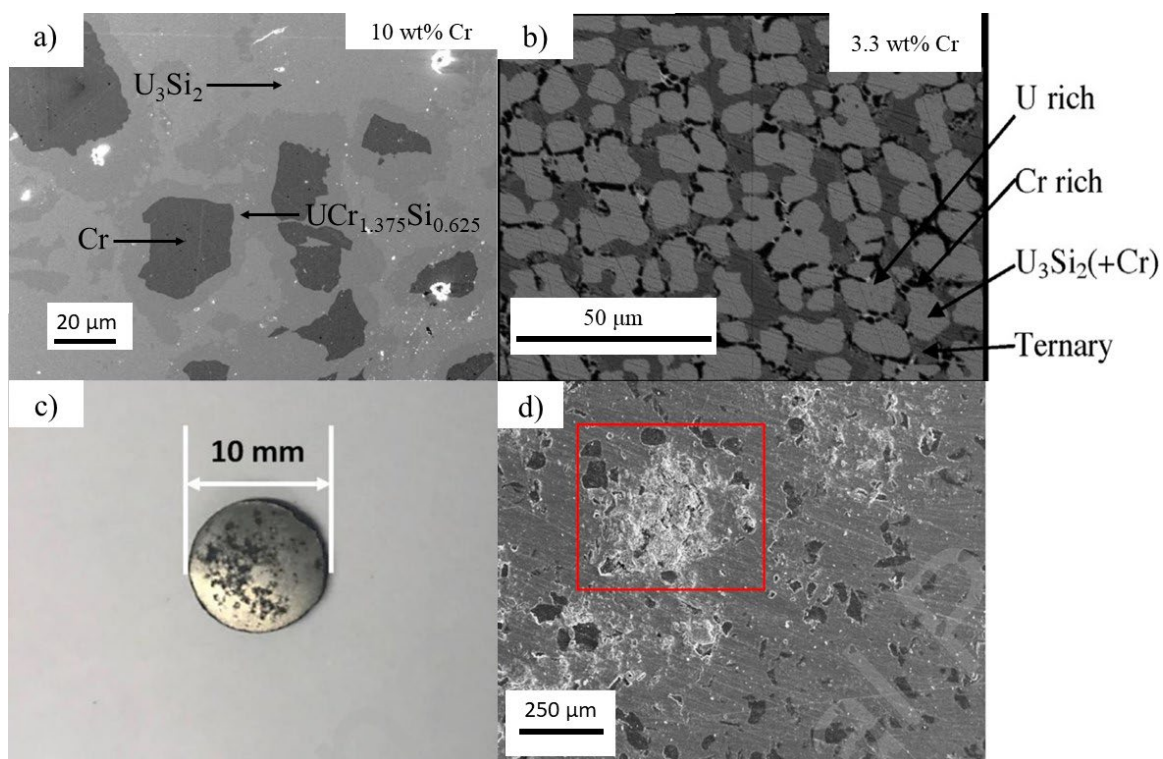


**Figure B.14** SEM of Cr additions to  $U_3Si_2$  via a) SPS (modified from Gong *et al.* who reported 10 wt% Cr additions [68]) and b) arc-melting (modified from Wood *et al.* who reported 5 vol% (3.3 wt%) Cr additions [65]). c) 10 wt% Cr doped  $U_3Si_2$  after a 24 hour isotherm at 360 °C. d) Oxidation patches on the 10 wt% Cr doped  $U_3Si_2$  sample after the isotherm hold.

To further improve the oxidation resistance of the Al and Cr-doped pellets, Mohamad and Gong *et al.* used isothermal annealing in air performed at 300 °C for 2 hours, below the onset oxidation temperature for  $U_3Si_2$ , and thus no significant oxidation was expected for silicide fuel matrix [68]. The goal of the air anneal was to deliberately oxidize Al and Cr first to form  $Al_2O_3$  and  $Cr_2O_3$  protective scales. After annealing, the onset temperatures for every sample increased relative to the as-fabricated state, with the exception of the 1.8 at% (0.31 wt%) Al addition. However, no evidence of the  $Al_2O_3$  or  $Cr_2O_3$  scales forming after annealing was performed.

After annealing, Mohamad *et al.* presented SEM images of the migration of Al from the Al-enriched grains towards grain boundaries (**Figure B.15a** and **b**). The Al

mobility reduced the extent of the oxidation response due to the rapid formation of  $\text{Al}_2\text{O}_3$  [63]. Lattice strain from SPS in the 1.8 at% (0.32 wt%) and 7.2 at% (1.34 wt%) doped samples, as seen by an observed shift of the XRD peaks toward higher diffraction angles, suggests possible strain relaxation after annealing, (**Figure B.15c**) [63]. Mohamad *et al.* determined a synergistic effect of strain, alloy migration, and oxide scales were used to promote an improvement to  $\text{U}_3\text{Si}_2$  oxidation [63]. The migration of the alloying Al was the only additive to show this type mobility from the reviewed literature.

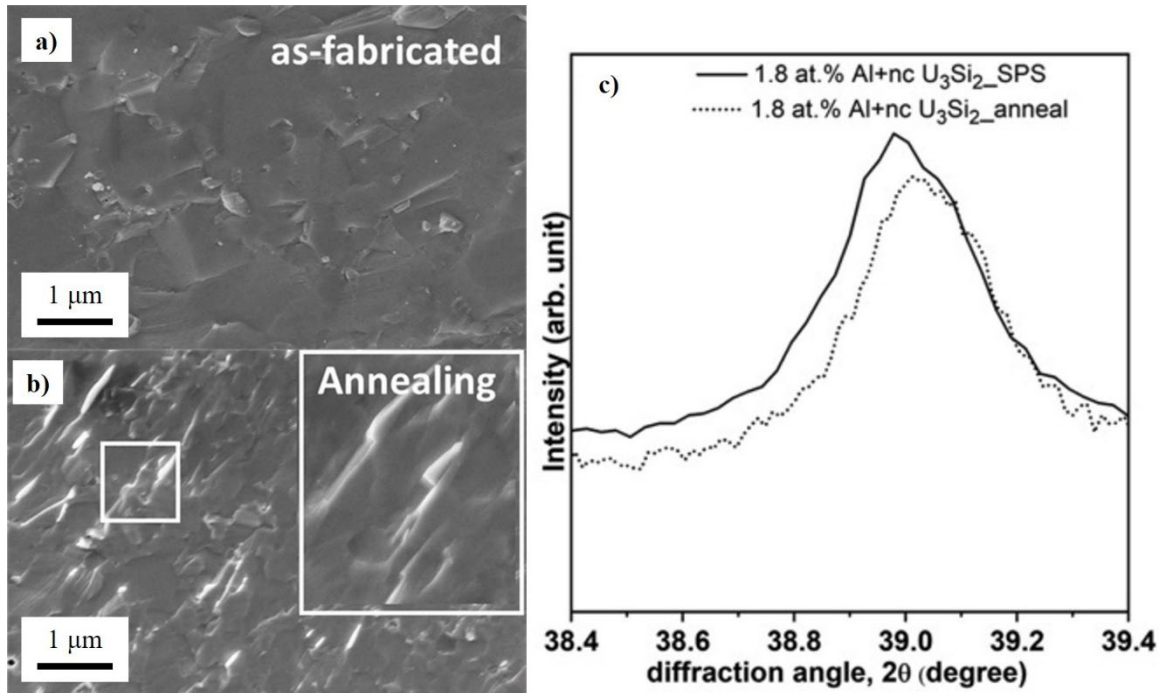


**Figure B.15** Modified images from Mohamad *et al.* [63] of a) 1.8 at% (0.32 wt%) Al addition to nano grain  $\text{U}_3\text{Si}_2$  before and b) after annealing showing migration of the alloying element and c) XRD patterns before and after annealing.

Experimental analysis of the steam oxidation behavior of  $\text{U}_3\text{Si}_2$  alloyed with yttrium alongside pure  $\text{U}_3\text{Si}_2$  was also reported by Wood *et al.* in 2020 [65]. Even though  $\text{Y}_2\text{O}_3$  is thermodynamically favorable (**Figure B.1**) versus the formation of  $\text{UO}_2$ , it was not detected under the experimental conditions presented. It was suggested to introduce Y

additions through powder milling due to the phase segregations seen in the arc-melted samples (**Figure B.16**). U-Si-Y compositions displayed varied oxidation dynamics in flowing steam and did not exhibit significant improvement to the response of pure  $U_3Si_2$  in flowing steam to consider further. It is important to note that both Wood *et al.* investigations resulted in phase segregated microstructures at addition concentrations greater than 2 vol% (0.74 wt%).

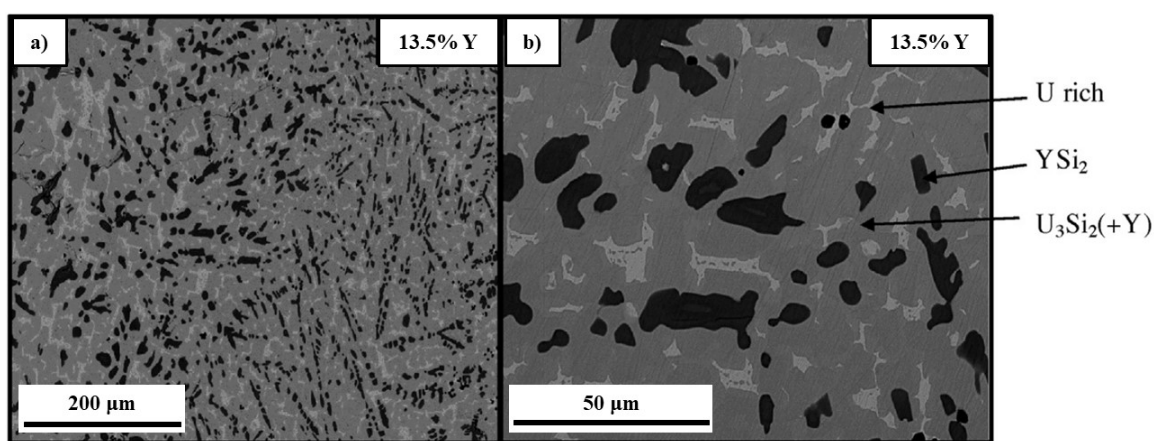


**Figure B.16** Backscatter SEM of the as-melted U-Si-Y composition modified from Wood *et al.* [65].

Zirconia containing 3 mol% yttria ( $Y_2O_3$ ) as a stabilizer (3Y-TZP) was used to mechanically toughen  $U_3Si_2$  along with microstructural control and oxide protection to improve the air oxidation performance [64]. Micron grain  $U_3Si_2$  was synthesized via arc-melting and the use of HEBM followed by SPS was used to incorporate 3Y-TZP nanoparticles homogeneously to form 1, 3 and 5 vol% additive samples. Micro-cracks (**Figure B.17a** and **b**) in the 3Y-TZP particles were generated during micro-hardness testing and are responsible for the stress induced monoclinic to tetragonal phase transformation toughening. Increased amounts of 3Y-TZP additive caused an increase in fracture toughness while causing a decrease in hardness. The 1, 3, and 5 vol% 3Y-TZP toughened

$U_3Si_2$  had air oxidation onset temperatures of 574.5, 566.4, and 565.1 °C, respectively, and displayed improved air oxidation performance over  $UO_2$  (455 °C) and any non-doped/alloyed  $U_3Si_2$  samples tested to date. After thermal annealing, the 3 vol% 3Y-TZP- $U_3Si_2$  sample has the highest onset to be reported (617 °C) for any air oxidation studies of the silicide fuel forms that maintain a higher uranium density over  $UO_2$ . 3Y-TZP displayed its potential to simultaneously increase the fracture toughness and oxidation resistance of  $U_3Si_2$ .

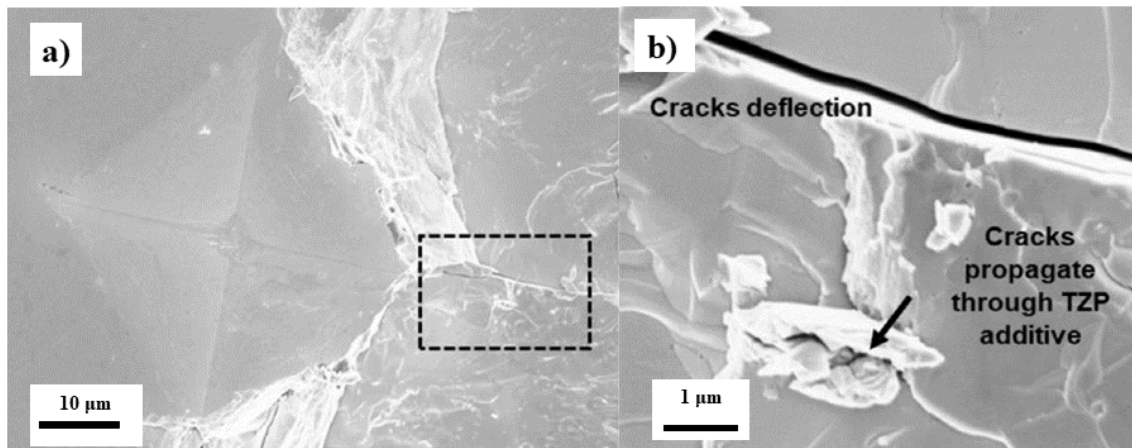


**Figure B.17** Modified images from Mohamad et al. [64]. a) The mechanical properties of the SPS-densified 3Y-TZP incorporated pellets were characterized by indentation b) Micro-cracks are generated through the 3Y-TZP particles.

As indicated by the recent study on 3Y-TZP doping of  $U_3Si_2$ , mechanical properties such as fracture toughness can correlate to oxidation/corrosion performance. Crack propagation during oxidation leads to an increase in exposed surface area, resulting in further sample fragmentation. An increase in fracture toughness can lead to an alloy which is more resistant to cracking during oxidation. Arc-melted  $U_3Si_2$  with micron size grains conventionally sintered between 1400-1500 °C (87-97% TD) displayed a fracture toughness from 0.82 – 1.23  $MPa \cdot m^{1/2}$ , comparable to that of  $UO_2$  [70]. Recall, the air oxidation of  $U_3Si_2$  fabricated and sintered in a similar manner had an onset of 384 °C

[53]. Arc-melt fabricated micron sized  $U_3Si_2$  that was milled and sintered via SPS had a fracture toughness of  $3.25 \text{ MPa}\cdot\text{m}^{1/2}$  with a theoretical density above 96% [49]. Fuel pellets fabricated in this manner displayed an air oxidation onset of  $520 \text{ }^\circ\text{C}$  prior to annealing [71]. Nano-grained  $U_3Si_2$  doped with 7.2 at% Al sintered via SPS reported the highest fracture toughness of the SPS samples reviewed; however, it exhibited a lower oxidation onset temperature than the micro-grained  $U_3Si_2$  doped with 7.2 at% Al. The 10 wt% Cr sample, 5 vol% 3Y-TZP, and 75 wt%  $UO_2$  all reported the highest fracture toughness for each additive type, which does not correspond to the highest oxidation onset for each additive type as previously discussed. Accordingly, an increased fracture toughness in doped- $U_3Si_2$  does not necessarily correlate to an improved oxidation performance whereas it appears to have a direct correlation in the un-doped  $U_3Si_2$  monoliths.

#### B.4.2 Composite Fuel Forms of $U_3Si_2$ to Mitigate Oxidation

Gong *et al.* synthesized and characterized different  $U_3Si_2$ - $UO_2$  composites sintered via SPS; the microstructures were controlled to examine the effect on  $U_3Si_2$  air oxidation [62]. The as-received  $U_3Si_2$  powders were HEBM to reduce grain size and increase sinterability, while nano-sized  $UO_2$  powders were achieved with repeated ball milling.  $U_3Si_2$  powders were mixed with various weight ratios (25, 50, and 75 wt%) of  $UO_2$  before SPS of the composites. When sintered at relatively low temperatures, an increase in the  $UO_2$  content decreased the sintered density and TGA results showed that the higher wt%  $UO_2$  lowered the mass gain onset temperatures. However, when sintered at higher temperatures, the density of the sintered composites increased, thus an increase in onset temperatures, **Table B.1**. Accordingly, density has a direct impact on exposed

surface area; thus, a correlation between onset temperature and exposed surface area can be identified. Sintering temperature was also found to have a significant impact on the microstructure of the composite fuels, which, in turn, significantly impacted oxidation resistance of the composites [62]. **Figure B.18a** and **b** show SEM images of  $U_3Si_2 + 25 \text{ wt\% } UO_2$  composites sintered at 1000 °C and 1300 °C, respectively. Also shown are SEM images of  $U_3Si_2 + 50 \text{ wt\% } UO_2$  composites sintered at 1000 °C and 1300 °C (**Figure B.18c** and **d**). The two pellets sintered at 1300 °C (**Figure B.18b** and **d**), as expected, show that the pores are fewer and smaller than those of the 1000 °C sintered pellets (**Figure B.18a** and **c**) [62].

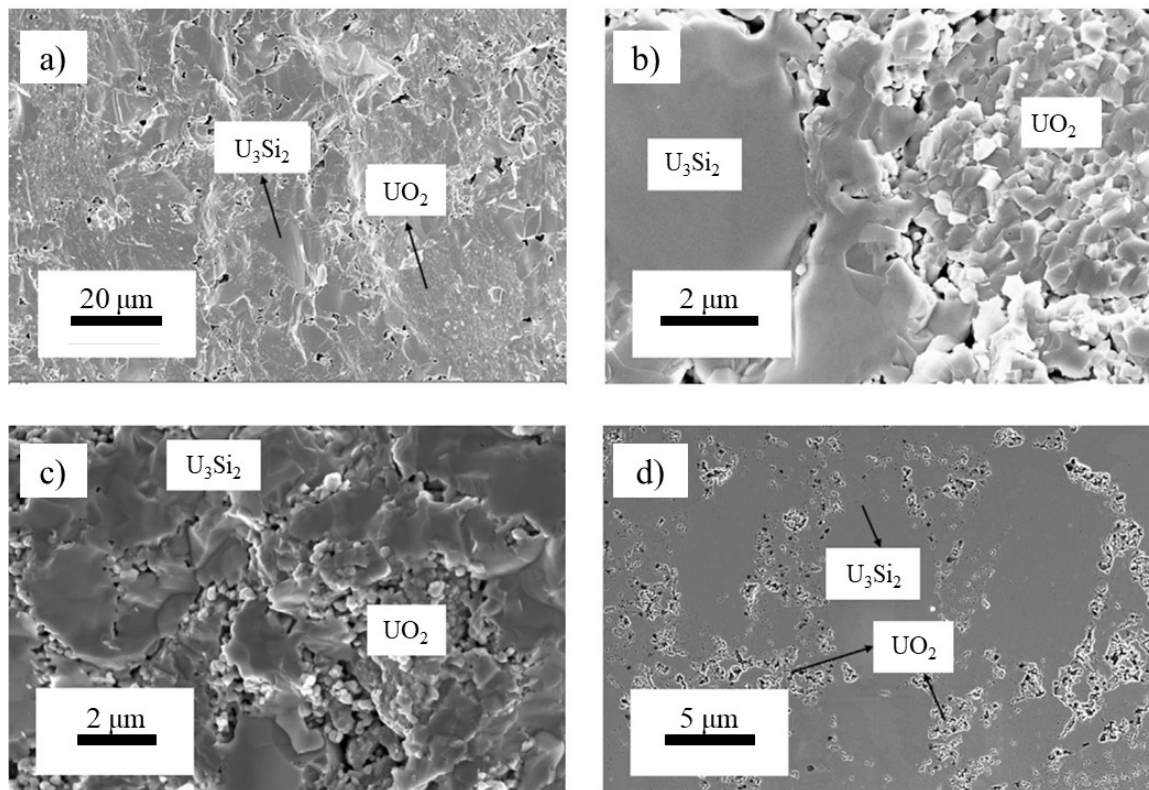


**Figure B.18** SEM images of  $U_3Si_2 + 25 \text{ wt}\% UO_2$  composites sintered at a) 1000 °C, and b) 1300 °C. SEM images of  $U_3Si_2 + 50 \text{ wt}\% UO_2$  composites sintered at c) 1000 °C, and d) 1300 °C. Modified from Gong *et al.* [62].

$UB_2$ , though considered as a composite phase in this manuscript, has also been researched as a high-density fuel compound. The authors discuss the literature available on  $UB_2$  in more detail in the third manuscript in this review series. Turner *et al.* investigated  $UB_2$  as a burnable absorber in  $U_3Si_2$  to improve its behavior during steam oxidation [67, 72]. The research team introduced the  $UB_2$  to  $U_3Si_2$  through HEBM in a tungsten carbide vessel, which also inadvertently introduced a  $UC_{0.75}O_{0.25}$  phase throughout the sample from the uranium reacting with the carbide walls. **Figure B.19** shows SEM micrographs of a 90/10wt% (a) and a 50/50wt%  $U_3Si_2$ - $UB_2$  composite indicating  $UB_2$  regions are well dispersed within a  $U_3Si_2$  matrix, along with small inclusions of  $UO_2$  and  $UC_{0.75}O_{0.25}$  identified with XRD. The researchers also performed atomic-scale modeling of hydrogen solubility within  $UB_2$  and demonstrated that the

reaction is endothermic with a predicted volume change of less than 10% of that expected for  $U_3Si_2$  [72]. Therefore, the volume change in the absorption of  $H_2$  is not expected to be a factor in the degradation of  $UB_2$ , in contrast to its detrimental impact to the  $U_3Si_2$  structure, when exposed to aqueous environments. The inclusion of a  $UB_2$  phase may therefore offer some improvements to the steam performance of  $U_3Si_2$  fuel without compromising the improved thermal performance or uranium density, which are key drivers of  $U_3Si_2$  development. The onset temperature of 553 °C for the 10 wt%  $UB_2$  composites was determined manually instead of using the automated software routine. Two 50 wt%  $UB_2$  composites had an onset of 548 and 575 °C. The variation in onset temperature was thought to be from the surface area to volume ratio, as the fragments varied in shape and size, similar to alloyed samples tested by Wood et al [65, 72].

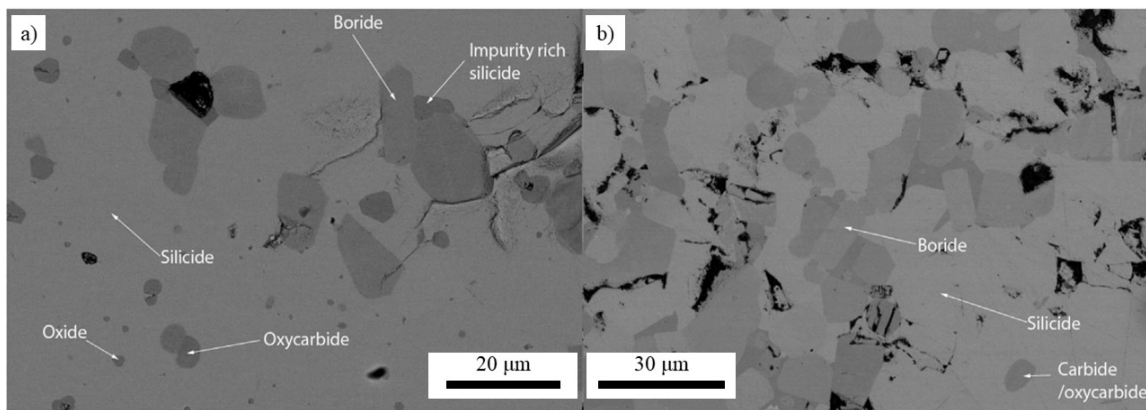


**Figure B.19** SEM backscatter micrographs of a)  $U_3Si_2$  + 10 wt%  $UB_2$ , and b)  $U_3Si_2$  + 50 wt%  $UB_2$ , modified from Turner et al. [72].

**Figure B.20** shows SEM micrographs with paired EDS analysis for the  $U_3Si_2$  + 50wt%  $UB_2$  composite after steam oxidation at a) 465 °C for 5 minutes, b) 565 °C for 5 minutes, and c) 900 °C. **Figure B.20a** shows an open crack on the surface, where silicon rich regions appear to form in bands across the  $U_3Si_2$  grain towards nearby  $UB_2$  grains. The existing crack has a layer of  $UO_2$  directly adjacent to it, similar to those

which have formed adjacent to cracks on  $U_3Si_2$  (**Figure B.20b**). Following exposure to 565 °C steam for 5 minutes, only small solid fragments of the composite remained; the edge of the cross section of a solid fragment is shown in **Figure B.20b**. Also, a large proportion of the sample had formed  $UO_2$  powder and appears to form as striations across the silicide material, possibly due to the distortions caused by the formation of the  $U_3Si_2H_2$  phase [67]. **Figure B.20c** shows the powder produced after 900 °C in steam which displays a limited number of branching cracks, although some are present on exposed surfaces. XRD analysis after oxidation showed all samples exhibited only  $UO_2$ ; no boron or silicon compounds were observed (within the detectable limits of the XRD) which aligns well with the thermodynamic assessment of  $SiO_2$  and  $B_2O_3$  being less favorable to form over  $UO_2$  (**Figure B.1**).

Lastly, attempts to add gadolinium as a burnable absorber into  $U_3Si_2$  were also made by Turner *et al.* via arc-melting and powder blending [73]. Both fabrication methods resulted in inhomogeneous distribution and agglomeration of Gd in the samples [73]. The increased reactivity of the  $U_3Si_2$  due to the Gd inclusion makes it less desirable from an oxidation standpoint.

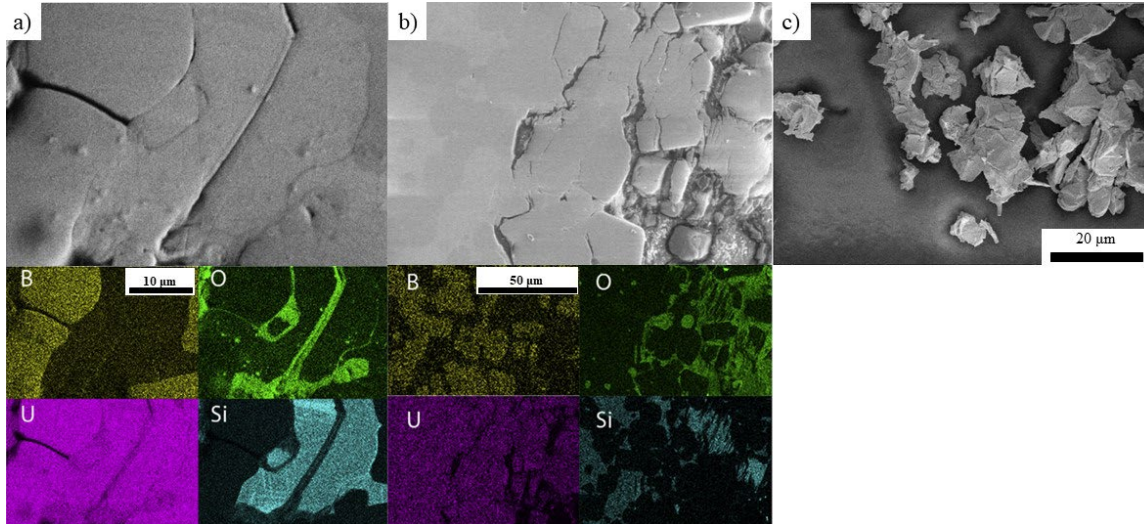


**Figure B.20** SEM and EDS of  $U_3Si_2 + 50 \text{ wt}\% UB_2$  composite after steam oxidation at a) 465 °C for 5 min., b) at 565 °C for 5 min., and c) at 900 °C, modified from Turner *et al.* [67].

To mitigate oxidation, the use of additives to  $U_3Si_2$  are reviewed above, while no surface coatings or chemical surface treatments have been reported in the available literature. There have been two additives, aluminum and  $UO_2$ , tested for improving  $U_3Si_2$  air oxidation which resulted in a reaction onset range of 260-670 °C compared to the air onset for monolithic  $U_3Si_2$  of 384-560 °C. Chromium, yttrium, and  $UB_2$  are  $U_3Si_2$  additives that have been investigated for steam oxidation and resulted in an onset range of 400-575 °C, compared to the steam onset of monolithic  $U_3Si_2$  at 406-480 °C. The oxidation parameters for the reviewed literature are summarized in **Table B.2**. The authors note that the range of onset temperatures come from not only the addition incorporation but also the different fabrication methods, amount of additive used, surface area of the sample, and any impurities in the samples. One sample from the reviewed literature reported carbon impurities by Turner *et al.* [67] and the effects of impurities are discussed in the following section.

#### B.4.3 Effect of Impurities in $U_3Si_2$

To the author's knowledge, there is no data available on the impact of impurities on the corrosion behavior of  $U_3Si_2$ , however there have been a number of studies which observed the impact of impurities on phase segregation in bulk samples and on the mechanical properties of fuel pellets.  $UO_2$  inclusions are a typical impurity phase present in  $U_3Si_2$  as fabricated from arc melting and powder metallurgy given the rapid oxidation of  $U_3Si_2$  powders even when stored under inert, controlled environments [29]. The majority of the reviewed literature used the non-stoichiometric powder metallurgy synthesis method reported by Harp *et al.* [29], which had a major  $U_3Si_2$  phase (84-88%) as well as minor  $USi$  (8-13 %) and  $UO_2$  (2-4%) phases. Using stoichiometric amounts of U and Si during fabrication, the phase purity was observed to be greater than 94%  $U_3Si_2$  with minor  $UO_2$  (~1–2%) and  $USi$  (~4-5%) phases and other minor phases that were significantly less than 1% [40]. With this in mind, Carvajal-Nunez *et al.* made two sets of samples containing different amounts of  $UO_2$  to explore the potential effect the impurity phases will have on the mechanical properties of  $U_3Si_2$  [74]. The samples were prepared through arc-melting using different feedstocks to create different  $UO_2$  impurities. SEM and EDS confirmed the  $UO_2$  phase in each sample set, set A had < 1vol%  $UO_2$  while set B had  $1.4 \pm 0.4$  vol%  $UO_2$ . Assessment of the measured and calculated elastic properties (Young's, bulk, and shear modulus, as well as Poisson's ratio) all showed values were not increased by the presence of  $UO_2$ . The result would only be expected to hold for relatively low volume contents of impurity phases as studied here [74].

Carbon impurities in  $U_3Si_2$  are not typically reported from the synthesis and fabrication methods presented in the reviewed literature; unlike UN, where carbon

impurities are introduced by the carbothermic reduction synthesis route, and therefore it is more common to report carbon content. However, one instance of reported carbon impurity in  $U_3Si_2$  was found in Turner *et al.* [67]. During synthesis through HEBM in a tungsten carbide vessel, a  $UC_{0.75}O_{0.25}$  phase was identified throughout the 50-50 wt%  $U_3Si_2$ - $UB_2$  sample; assumed to originate from the uranium reacting with the carbide walls of the milling vessel. Carbide phases are known to be highly reactive with water even at low temperatures and as a result, the material containing this phase was considered to form a lower bound of steam performance (i.e. it was detrimental to the performance) [67]. Another 50-50 wt%  $U_3Si_2$ - $UB_2$  sample was made that did not contain this carbon impurity. The two samples had onset temperatures of 548 and 575 °C. The researchers attributed the disparity to differences in surface area to volume ratio, as the fragments varied in shape and size but did not mention which of the two samples contained the carbon impurity [67].

### **B.5. Summary of $U_3Si_2$ Oxidation/Corrosion**

**Table B.1** and **Table B.2** provide a summary of the samples in the reviewed literature which were tested in various atmospheres with different experimental parameters. Although none of the reviewed experiments represent an actual leaker rod scenario, which are expensive and mostly inaccessible, the experiments do represent relative atmospheres in assessing potential ATF candidates. Synthesis methods varied from arc-melting pure metals or using a powder metallurgy method for mixing U and Si followed by arc-melting. Also, the fabrication methods for the various samples ranged from using conventional sintering, SPS, and as-melted samples.

Screening experiments in air are performed to provide comparative analysis to the oxidation response of fuel forms, while it is not relevant to their behavior under reactor accident conditions, it is an applicable assessment when considering an off-normal fuel transportation or storage event. Under air oxidation, the theoretical terminal mass gain is 24.9%, if fully oxidized  $U_3Si_2$  terminates at  $U_3O_8$  and  $SiO_2$ . However, from **Table B.1**, the terminal mass gain varied between ~18-22% amongst experiments. Nanometer-sized Si was identified using SEM and EDS by Harrison *et al.* and attributed to the missing mass discrepancy. **Figure B.21** is a collection of onsets of breakaway oxidation in air for  $U_3Si_2$  samples reviewed. The onset ranged from 250-670 °C based on the type and amounts of additive used, surface area of the sample, fabrication routes, testing environment, sintering method, and annealing of sample. HEBM and arc-melted  $U_3Si_2$  samples that have been SPS sintered or as-cast have shown improvements over  $UO_2$  while conventional sintered  $U_3Si_2$  proved to have a lower onset temperature than  $UO_2$  in air. The use of SPS provided the highest onset of breakaway oxidation temperatures at 520 °C, prior to annealing, for pure  $U_3Si_2$  in air testing [26] and also after annealing with an onset temperature at 570 °C. The authors identified the strain effects in the dense silicide matrix during the SPS sintering as the cause for the improved oxidation behavior [26, 63]. The relaxation of tensile strain in micron-sized silicide reduces the oxidation rate; while the relaxation of the compressive strain in nano-sized  $U_3Si_2$  results in the degradation of the oxidation performance [26]. Various amounts of aluminum and  $UO_2$  additives to  $U_3Si_2$  have shown improvement over  $UO_2$  that were fabricated using arc-melting or HEBM and sintered using SPS or were tested in the as-cast state. The  $U_3Al_2Si_2$  sample displays the highest onset temperature to be reported (670 °C) but contains a

lower uranium density than  $\text{UO}_2$ . However, a minimal amount Al used, 0.33 wt%, also has an onset temperature above 600 °C at 610 °C. After annealing, the mechanically toughened 3 vol% 3Y-TZP- $\text{U}_3\text{Si}_2$  displayed the highest reported air onset temperature at 617 °C that contained a higher uranium density than  $\text{UO}_2$ . Conventionally sintered  $\text{U}_3\text{Si}_2$  samples with additives were not found in this literature review.

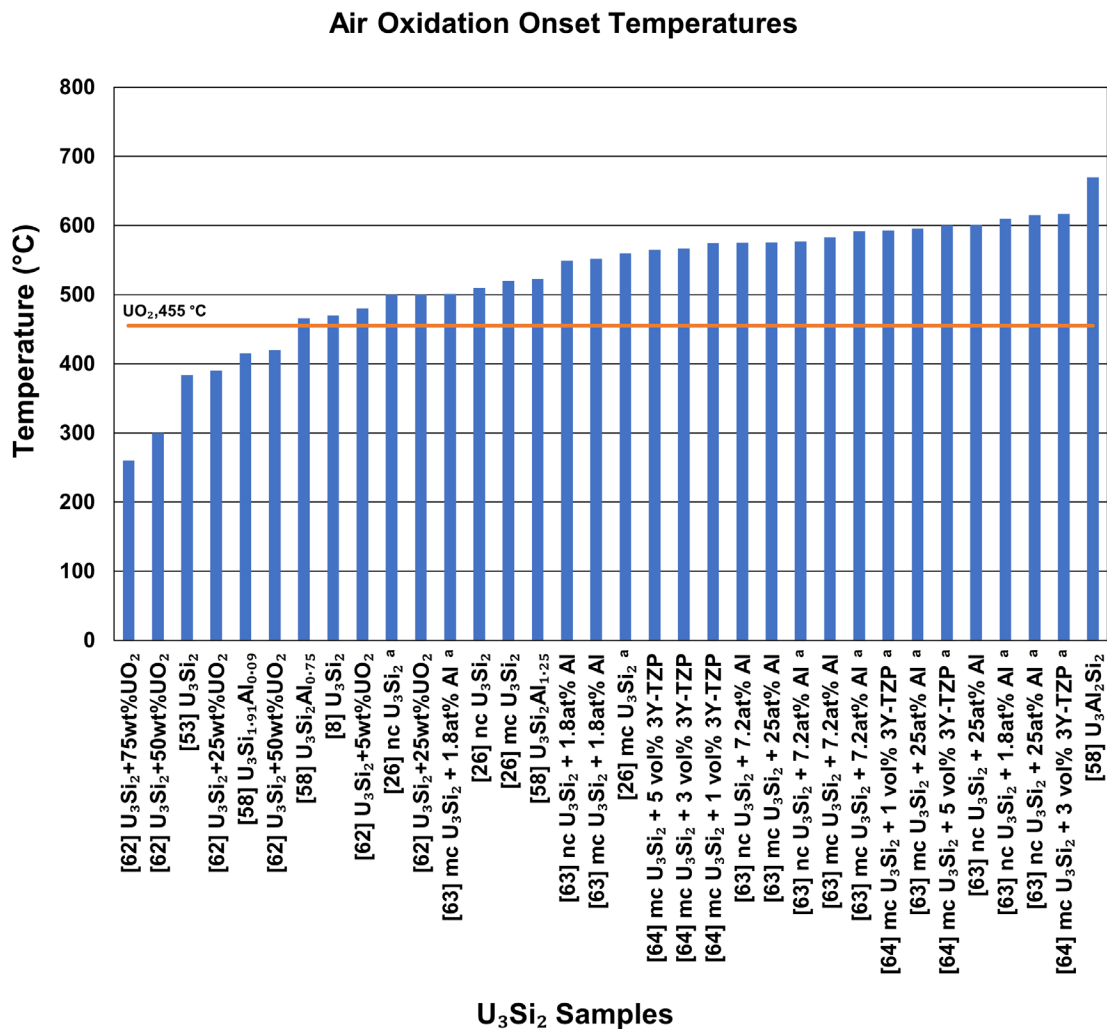


**Figure B.21**  $\text{U}_3\text{Si}_2$  air onset temperatures taken from Table A1. <sup>a</sup> superscript are samples that have been annealed. mc are micron grain sized and nc are nano grain sized.

Water corrosion, whether pressurized water or steam, is argued here to be the most relevant screening atmosphere for assessment of potential ATF candidate materials. The current thermochemical behavior of pure  $U_3Si_2$  fuel under steam/ $H_2$  atmospheres results in a significant underperformance when compared to  $UO_2$  steam oxidation.  $UO_2$  was shown to have a mass gain of  $< 0.1\%$  in a thermal ramp up to  $1000\text{ }^\circ\text{C}$  in flowing steam. **Figure B.22** displays the onset temperatures of  $U_3Si_2$  samples tested in water/steam, showing onsets far below  $1000\text{ }^\circ\text{C}$ , ranging from  $400\text{-}575\text{ }^\circ\text{C}$ . The onset range of temperature comes from the different fabrication routes, type of additive, amount of additive,  $H_2O$  testing environment used, sintering technique, and annealing of sample. Steam oxidation testing with  $U_3Si_2$  was found to be an energetic reaction as some experiments reported samples being ejected from the testing crucibles [16, 65, 67]. There is no appreciable oxygen potential in the steam to promote oxidation to  $U_3O_8$ , but rather  $UO_2$  becomes hyperstoichiometric during prolonged exposures to high temperature steam; [75]; hence an onset is not plotted in **Figure B.22** for  $UO_2$ . Alloying additions of Cr and Y provided some delay in the onset of breakaway oxidation for  $U_3Si_2$  in steam, however no amount of addition has been identified that both protects the bulk fuel structure at  $T > 800\text{ }^\circ\text{C}$  and retains a uranium density higher than that of  $UO_2$ . The highest reported onset temperature came from the  $U_3Si_2\text{-}50\%$   $UB_2$  composite at  $575\text{ }^\circ\text{C}$  for steam oxidation testing; an improvement to the pure  $U_3Si_2$  onset of  $480\text{ }^\circ\text{C}$  [67].  $UB_2$  is also a high density fuel and when paired with  $U_3Si_2$  it provides a better oxidation performance than pure  $U_3Si_2$  while maintaining a high uranium density.

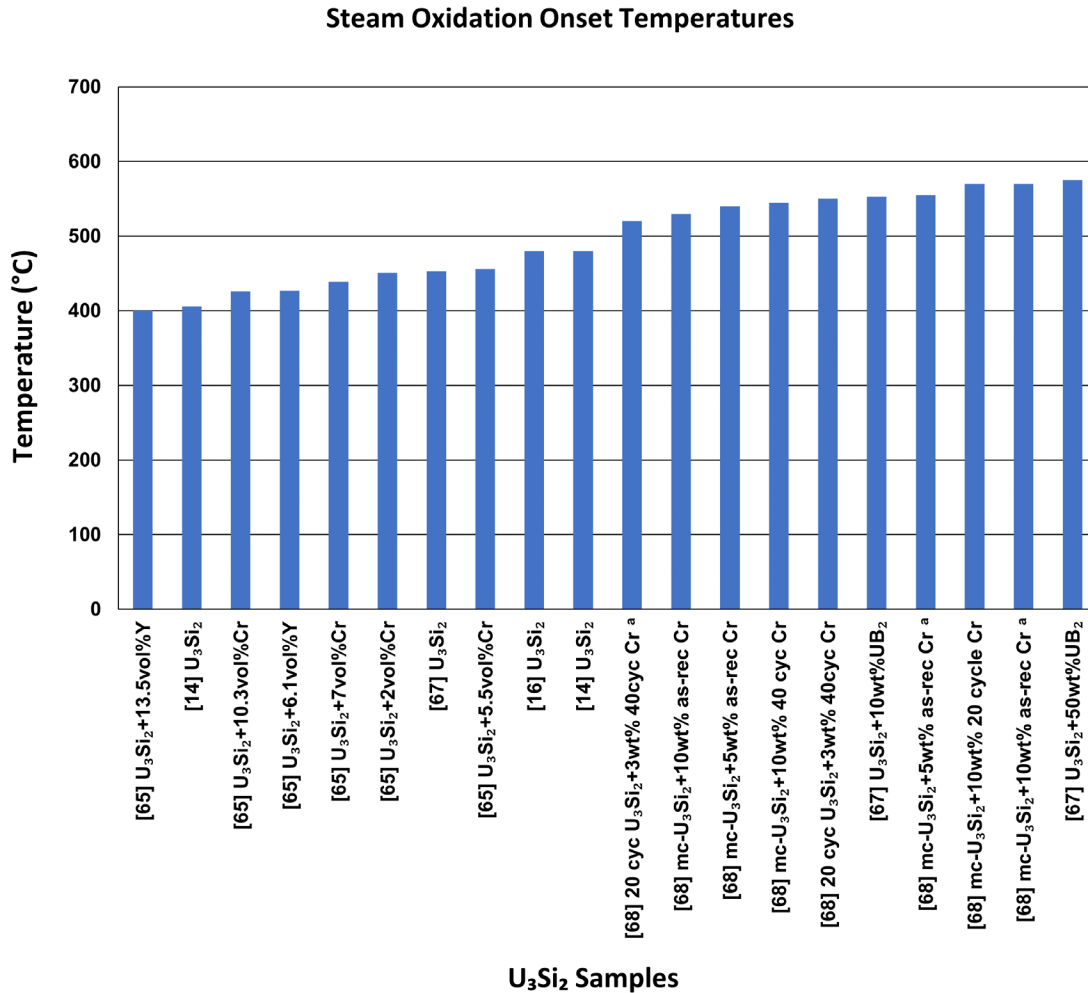


**Figure B.22** U<sub>3</sub>Si<sub>2</sub> steam oxidation onset temperatures from the reviewed literature. <sup>a</sup>superscript are samples that have been annealed.

Oxidation that occurs in H<sub>2</sub>O environments will also produce hydrogen as a reaction product. The solubility of H<sub>2</sub> in U<sub>3</sub>Si<sub>2</sub> has been predicted through DFT + U calculations [17] which showed hydrogen incorporation is exothermic up to a stoichiometry of U<sub>3</sub>Si<sub>2</sub>H<sub>2</sub>, agreeing with experimental results. The volume expansion of U<sub>3</sub>Si<sub>2</sub>H<sub>2</sub> cannot be accommodated, and pulverization results.

It is a conclusion of this review that additional research and fuel development is needed before U<sub>3</sub>Si<sub>2</sub> can be considered as a drop-in replacement for UO<sub>2</sub>. In addition to concerns about coolant exposure, all U<sub>3</sub>Si<sub>2</sub> fabrication routes start by using elemental

uranium and silicon which is suitable for research laboratories but scaled up production for industrial use brings about proliferation and criticality concerns. With respect to the current status of oxidation performance of this candidate fuel form improvements to  $U_3Si_2$  during air oxidation have been made using additives or composites and sintering techniques inducing residual strain. Additional research into the use of additives or composite structures in steam environments is needed as the reported additives and composites have shown improvements to pure  $U_3Si_2$  oxidation performance, however pulverization and volumetric expansion of these fuels at operationally relevant temperatures,  $<600\text{ }^\circ\text{C}$ , continues to prove detrimental. There were no reported attempts of other oxidation mitigation techniques such as surface coatings, mechanical or chemical surface treatments in the reviewed literature. The induced strain from SPS showed improvements to  $U_3Si_2$  in air but has not been tested in steam environments for monolithic  $U_3Si_2$ , however Cr doped  $U_3Si_2$  has been tested in steam and displayed an improvement to air tested Cr doped  $U_3Si_2$ . Further investigation into strain engineering for improvement to  $U_3Si_2$  steam oxidation behavior is an area of potential research.

Although many challenges in oxidation performance still need to be overcome,  $U_3Si_2$  as a high-density fuel and an ATF material can improve nuclear fuel performance and safety if these challenges are met. The higher uranium density and thermal conductivity when compared to  $UO_2$  can lead to increased power up-rates, reduced fuel centerline temperatures, increased power to melt safety margins, and an increase to the rate of heat transfer to the cladding during high temperature transients. These thermal transport benefits result in reduced fuel failures and more efficient plant operations. Furthermore, high uranium density fuels can better accommodate the use of advanced

cladding structures which can provide additional safety margins with regards to steam reaction kinetics.

### **Acknowledgements**

This work was supported by the U.S. Department of Energy, Office of Nuclear Energy. This work is also part of a collaboration led by Westinghouse Electric Company comprising several national laboratories, vendors, and universities awarded in response to the DE-NE0008824 funding opportunity. Accordingly, the U.S. Government retains and the publisher, by accepting the article for publication, acknowledges that the U.S. Government retains a nonexclusive, paid-up, irrevocable, worldwide license to publish or reproduce the published form of this manuscript or allow others to do so, for U.S. Government purposes. Additional funding for student and faculty support was provided by the U.S. NRC Grant number 31310018M0046 and NNSA MSIPP CONNECT program, Grant Number DE-NA0003948.

### **References**

- [1] P. Lyons, B. Crowell, Development of light water reactor fuels with enhanced accident tolerance, Report to Congress, United States Department of Energy, Washington, DC, 2015.
- [2] S. Bragg-Sitton, Development of advanced accident-tolerant fuels for commercial LWRs, *Nuclear News* 57(3) (2014) 83.
- [3] S.J. Zinkle, K.A. Terrani, J.C. Gehin, L.J. Ott, L.L. Snead, Accident tolerant fuels for LWRs: A perspective, *Journal of Nuclear Materials* 448(1) (2014) 374-379.
- [4] S.M. Bragg-Sitton, M. Todosow, R. Montgomery, C.R. Stanek, R. Montgomery, W.J. Carmack, Metrics for the Technical Performance Evaluation of Light Water Reactor Accident-Tolerant Fuel, *Nuclear Technology* 195 (2) (2016) 111-123.

- [5] F. Goldner, Development strategy for advanced LWR fuels with enhanced accident tolerance, Enhanced Accident Tolerant LWR Fuels National Metrics Workshop, Germantown, MD, 2012.
- [6] G.J. Youinou, R.S. Sen, Impact of accident-tolerant fuels and claddings on the overall fuel cycle: A preliminary systems analysis, *Nuclear Technology* 188 (2) (2014) 123-138.
- [7] J. Carmack, Update on U.S. Accident Tolerant Fuel Program Nuclear Regulatory Commission Briefing, 2016.
- [8] K. Johnson, V. Ström, J. Wallenius, D.A. Lopes, Oxidation of accident tolerant fuel candidates, *Journal of Nuclear Science and Technology* 54(3) (2017) 280-286.
- [9] R.W. Harrison, C. Gasparrini, R.N. Worth, J. Buckley, M.R. Wenman, T. Abram, On the Oxidation Mechanism of  $U_3Si_2$  Accident Tolerant Nuclear Fuel, *Corrosion Science* (2020) 108822.
- [10] E. Jossou, U. Eduok, N.Y. Dzade, B. Szpunar, J.A. Szpunar, Oxidation behaviour of  $U_3Si_2$ : an experimental and first principles investigation, *Physical Chemistry Chemical Physics* 20(7) (2018) 4708-4720.
- [11] S.A. Kulyukhin, Y.M. Nevolin, A.V. Gordeev, A.A. Bessonov, Gas-phase volume oxidation of uranium mononitride, *Radiochemistry* 61(2) (2019) 146-155.
- [12] D.R. Costa, M. Hedberg, S.C. Middleburgh, J. Wallenius, P. Olsson, D.A. Lopes, Oxidation of UN/ $U_2N_3$ - $UO_2$  composites: an evaluation of  $UO_2$  as an oxidation barrier for the nitride phases, *Journal of Nuclear Materials* 544 (2020) 152700.
- [13] R.T. Sweet, Y. Yang, K.A. Terrani, B.D. Wirth, A.T. Nelson, Performance of  $U_3Si_2$  in an LWR following a cladding breach during normal operation, *Journal of Nuclear Materials* 539 (2020) 152263.
- [14] J.H. Yang, D.S. Kim, D.-J. Kim, S. Kim, J.-H. Yoon, H.S. Lee, Y.-H. Koo, K.W. Song, Oxidation and Phase Separation of  $U_3Si_2$  Nuclear Fuel in High-temperature Steam Environments, *Journal of Nuclear Materials* (2020) 152517.

- [15] A.T. Nelson, A. Migdisov, E.S. Wood, C.J. Grote,  $U_3Si_2$  behavior in  $H_2O$  environments: Part II, pressurized water with controlled redox chemistry, *Journal of Nuclear Materials* 500 (2018) 81-91.
- [16] E.S. Wood, J.T. White, C.J. Grote, A.T. Nelson,  $U_3Si_2$  behavior in  $H_2O$ : Part I, flowing steam and the effect of hydrogen, *Journal of Nuclear Materials* 501 (2018) 404-412.
- [17] S. Middleburgh, A. Claisse, D. Andersson, R. Grimes, P. Olsson, S. Mašková, Solution of hydrogen in accident tolerant fuel candidate material:  $U_3Si_2$ , *Journal of Nuclear Materials* 501 (2018) 234-237.
- [18] R.J. Baker, Uranium minerals and their relevance to long term storage of nuclear fuels, *Coordination Chemistry Reviews* 266 (2014) 123-136.
- [19] K.A. Gamble, G. Pastore, D. Andersson, M. Cooper, ATF material model development and validation for priority fuel concepts, Idaho National Lab.(INL), Idaho Falls, ID (United States), 2019.
- [20] J.K. Watkins, D.P. Butt, B.J. Jaques, Microstructural degradation of UN and UN- $UO_2$  composites in hydrothermal oxidation conditions, *Journal of Nuclear Materials* 518 (2019) 30-40.
- [21] J. Antill, B. Myatt, Kinetics of the oxidation of UN and U(CO) in carbon dioxide, steam and water at elevated temperatures, *Corrosion Science* 6(1) (1966) 17-23.
- [22] R.M. Dell, V.J. Wheeler, N.J. Bridger, Hydrolysis of uranium mononitride, *Transactions of the Faraday Society* 63 (1967) 1286-1294.
- [23] J.E. Gray, B. Luan, Protective coatings on magnesium and its alloys — a critical review, *Journal of Alloys and Compounds* 336(1) (2002) 88-113.
- [24] C.L. Hu, S. Xi, H. Li, T.G. Liu, B.X. Zhou, W.J. Chen, N. Wang, Improving the intergranular corrosion resistance of 304 stainless steel by grain boundary network control, *Corrosion Science* 53(5) (2011) 1880-1886.

- [25] A. Cheniour, M.R. Tonks, B. Gong, T. Yao, L. He, J.M. Harp, B. Beeler, Y. Zhang, J. Lian, Development of a grain growth model for  $U_3Si_2$  using experimental data, phase field simulation and molecular dynamics, *Journal of Nuclear Materials* 532 (2020) 152069.
- [26] B. Gong, T. Yao, P. Lei, J. Harp, A.T. Nelson, J. Lian, Spark plasma sintering (SPS) densified  $U_3Si_2$  pellets: Microstructure control and enhanced mechanical and oxidation properties, *Journal of Alloys and Compounds* (2020) 154022.
- [27] A. Roine, HSC Chemistry, Outotec, Pori, 2019.
- [28] H.J.T. Ellingham, Reducibility of oxides and sulfides in metallurgical processes, *Journal of the Society of Chemical Industry Transactions and Communications* 63 (1944).
- [29] J.M. Harp, P.A. Lessing, R.E. Hoggan, Uranium Silicide pellet fabrication by powder metallurgy for accident tolerant fuel evaluation and irradiation, *Journal of Nuclear Materials* 466 (2015) 728-738.
- [30] G.L. Hofman, Crystal structure stability and fission gas swelling in intermetallic uranium compounds, *Journal of Nuclear Materials* 140(3) (1986) 256-263.
- [31] R. Birtcher, J. Richardson, M. Mueller, Amorphization of  $U_3Si_2$  by ion or neutron irradiation, *Journal of nuclear materials* 230(2) (1996) 158-163.
- [32] M. Finlay, G. Hofman, J. Snelgrove, Irradiation behaviour of uranium silicide compounds, *Journal of Nuclear Materials* 325(2-3) (2004) 118-128.
- [33] H. Shimizu, The properties and irradiation behavior of  $U_3Si_2$ , *Atomics International* 1965.
- [34] G. Copeland, R. Hobbs, G. Hofman, J. Snelgrove, Performance of low-enriched  $U_3Si_2$ -aluminum dispersion fuel elements in the Oak Ridge Research Reactor, Oak Ridge National Lab., 1987.
- [35] F. Cappia, J.M. Harp, Postirradiation examinations of low burnup  $U_3Si_2$  fuel for light water reactor applications, *Journal of Nuclear Materials* 518 (2019) 62-79.

- [36] H. Okamoto, Si-U (Silicon-Uranium), *Journal of phase equilibria and diffusion* 34(2) (2013) 167-168.
- [37] V.P. Sinha, G.P. Mishra, S. Pal, K.B. Khan, P.V. Hegde, G.J. Prasad, Development of powder metallurgy technique for synthesis of  $U_3Si_2$  dispersoid, *Journal of Nuclear Materials* 383(1-2) (2008) 196-200.
- [38] G.A. Alanko, D.P. Butt, Mechanochemical synthesis of uranium sesquisilicide, *Journal of Nuclear Materials* 451(1–3) (2014) 243-248.
- [39] E.S. Wood, J.T. White, B. Jaques, D. Burkes, P. Demkowicz, Advances in fuel fabrication, *Advances in Nuclear Fuel Chemistry*, Elsevier 2020, pp. 371-418.
- [40] A.R. Wagner, J.M. Harp, K.E. Archibald, S.C. Ashby, J.K. Watkins, K.R. Tolman, Fabrication of Stoichiometric  $U_3Si_2$  Fuel Pellets, *MethodsX* (2019).
- [41] J.T. White, A.T. Nelson, J.T. Dunwoody, D.D. Byler, D.J. Safarik, K.J. McClellan, Thermophysical properties of  $U_3Si_2$  to 1773 K, *Journal of Nuclear Materials* 464 (2015) 275-280.
- [42] H. Muta, K. Kurosaki, M. Uno, S. Yamanaka, Thermal and mechanical properties of uranium nitride prepared by SPS technique, *Journal of Materials Science* 43 (19) (2008) 6429-6434.
- [43] E.A. Olevsky, W.L. Bradbury, C.D. Haines, D.G. Martin, D. Kapoor, Fundamental aspects of spark plasma sintering: I. Experimental analysis of scalability, *Journal of the American Ceramic Society* 95(8) (2012) 2406-2413.
- [44] S. Yeo, E. Mckenna, R. Baney, G. Subhash, J. Tulenko, Enhanced thermal conductivity of uranium dioxide–silicon carbide composite fuel pellets prepared by spark plasma sintering (SPS), *Journal of Nuclear Materials* 433(1-3) (2013) 66-73.
- [45] K.D. Johnson, A.M. Raftery, D.A. Lopes, J. Wallenius, Fabrication and microstructural analysis of UN- $U_3Si_2$  composites for accident tolerant fuel applications, *Journal of Nuclear Materials* 477 (2016) 18-23.

- [46] D.A. Lopes, A. Benarosch, S. Middleburgh, K.D. Johnson, Spark plasma sintering and microstructural analysis of pure and Mo doped  $U_3Si_2$  pellets, *Journal of Nuclear Materials* 496 (2017) 234-241.
- [47] B. Gong, T. Yao, C. Lu, P. Xu, E. Lahoda, J. Lian, Consolidation of commercial-size  $UO_2$  fuel pellets using spark plasma sintering and microstructure/microchemical analysis, *MRS Communications* 8(3) (2018) 979-987.
- [48] T. Yao, S.M. Scott, G. Xin, B. Gong, J. Lian, Dense nanocrystalline  $UO_{2+x}$  fuel pellets synthesized by high pressure spark plasma sintering, *Journal of the American Ceramic Society* 101(3) (2018) 1105-1115.
- [49] A. Mohamad, Y. Ohishi, H. Muta, K. Kurosaki, S. Yamanaka, Thermal and mechanical properties of polycrystalline  $U_3Si_2$  synthesized by spark plasma sintering, *Journal of Nuclear Science and Technology* (2018) 1-10.
- [50] D.T. Goddard, J.I. Paul, R. Logsdon, E.P. Vernon, J. Buckley, T. Abram, S. Rennie, E. Lawrence-Bright, L. Harding, R. Springell, Progress in the development of high density fuels for enhanced accident tolerance, *TOPFUEL REACTOR FUEL PERFORMANCE* (2018).
- [51] A. Gonzales, E.S. Wood, K. Coulter, An Alternative Synthesis Route to  $U_3Si_2$ , *Transactions of the American Nuclear Society* 122 (2020) 196-198.
- [52] L.D. Loch, G.B. Engle, M.J. Snyder, W.H. Duckworth, Survey of refractory uranium compounds, Battelle Memorial Inst., Columbus, Ohio, 1956.
- [53] E. Sooby Wood, J.T. White, A.T. Nelson, Oxidation behavior of U-Si compounds in air from 25 to 1000 C, *Journal of Nuclear Materials* 484 (2017) 245-257.
- [54] B. Gokce, D.E. Aspnes, K. Gundogdu, Effect of strain on bond-specific reaction kinetics during the oxidation of H-terminated (111) Si, *Applied Physics Letters* 98(12) (2011) 121912.
- [55] T. Yan, D. Xie, Z. Chen, R. Yang, K. Zhu, C. Jiang, C. Ma, J. Liu, X. Wang, K. Liu, L. Luo, Q. Pan, Y. Hu, Initial oxidation of  $U_3Si_2$  studied by in-situ XPS analysis, *Journal of Nuclear Materials* 520 (2019) 1-5.

- [56] R.J. McEachern, P. Taylor, A review of the oxidation of uranium dioxide at temperatures below 400 C, *Journal of Nuclear Materials* 254(2-3) (1998) 87-121.
- [57] J. Belle, Uranium dioxide: properties and nuclear applications, Naval Reactors, Division of Reactor Development, US Atomic Energy Commission 1961.
- [58] E.S. Wood, J. White, A. Nelson, The effect of aluminum additions on the oxidation resistance of  $U_3Si_2$ , *Journal of Nuclear Materials* 489 (2017) 84-90.
- [59] J.O. Andersson, T. Helander, L. Hoglund, P.F. Shi, B. Sundman, Thermo-Calc 2020b, Computational tools for materials science, Calphad, 2020.
- [60] L. Brewer, R.K. Edwards, The stability of SiO solid and gas, *The Journal of Physical Chemistry* 58(4) (1954) 351-358.
- [61] E.S. Wood, K. Terrani, A. Nelson, Sensitivity of measured steam oxidation kinetics to atmospheric control and impurities, *Journal of Nuclear Materials* 477 (2016) 228-233.
- [62] B. Gong, T. Yao, P. Lei, L. Cai, K.E. Metzger, E.J. Lahoda, F.A. Boylan, A. Mohamad, J. Harp, A.T. Nelson, J. Lian,  $U_3Si_2$  and  $UO_2$  composites densified by spark plasma sintering for accident-tolerant fuels, *Journal of Nuclear Materials* 534 (2020) 152147.
- [63] A. Mohamad, T. Yao, B. Gong, J. Harp, A.R. Wagner, A.T. Nelson, J. Lian, Aluminum-doped  $U_3Si_2$  composite fuels with enhanced oxidation resistance, *Journal of Alloys and Compounds* (2020) 157319.
- [64] A. Mohamad, B. Gong, T. Yao, A.R. Wagner, M.T. Benson, J. Lian, 3Y-TZP Toughened and Oxidation-resistant  $U_3Si_2$  Composites for Accident Tolerant Fuels, *Journal of Nuclear Materials* 544 (2021) 152691.
- [65] E.S. Wood, C. Moczygamba, G. Robles, Z. Acosta, B.A. Brigham, C.J. Grote, K.E. Metzger, L. Cai, High temperature steam oxidation dynamics of  $U_3Si_2$  with alloying additions: Al, Cr, and Y, *Journal of Nuclear Materials* 533 (2020) 11.
- [66] S. Mašková, K. Miliyanchuk, L. Havela, Hydrogen absorption in  $U_3Si_2$  and its impact on electronic properties, *Journal of Nuclear Materials* 487 (2017) 418-423.

- [67] J. Turner, T. Abram, Steam performance of  $UB_2/U_3Si_2$  composite fuel pellets, compared to  $U_3Si_2$  reference behaviour, *Journal of Nuclear Materials* 529 (2020) 151919.
- [68] B. Gong, L. Cai, P. Lei, K.E. Metzger, E.J. Lahoda, F.A. Boylan, K. Yang, J. Fay, J. Harp, J. Lian, Cr Doped  $U_3Si_2$  Composite Fuels under Steam Corrosion, *Corrosion Science* (2020) 109001.
- [69] E. Jossou, L. Malakkal, N.Y. Dzade, A. Claisse, B. Szpunar, J. Szpunar, DFT+ U Study of the Adsorption and Dissociation of Water on Clean, Defective, and Oxygen-Covered  $U_3Si_2$  {001}, {110}, and {111} Surfaces, *The Journal of Physical Chemistry C* 123(32) (2019) 19453-19467.
- [70] K.E. Metzger, T.W. Knight, E. Roberts, X. Huang, Determination of mechanical behavior of  $U_3Si_2$  nuclear fuel by microindentation method, *Progress in Nuclear Energy* 99 (2017) 147-154.
- [71] B. Gong, T. Yao, P. Lei, J. Harp, A.T. Nelson, J. Lian, Spark plasma sintering (SPS) densified  $U_3Si_2$  pellets: Microstructure control and enhanced mechanical and oxidation properties, *Journal of Alloys and Compounds* 825 (2020) 154022.
- [72] J. Turner, S. Middleburgh, T. Abram, A high density composite fuel with integrated burnable absorber:  $U_3Si_2-UB_2$ , *Journal of Nuclear Materials* 529 (2020) 151891.
- [73] J. Turner, J. Buckley, G. Phillips, T. Abram, The use of gadolinium as a burnable poison within  $U_3Si_2$  fuel pellets, *Journal of Nuclear Materials* 509 (2018) 204-211.
- [74] U. Carvajal-Nunez, T.A. Saleh, J.T. White, B. Maiorov, A.T. Nelson, Determination of elastic properties of polycrystalline  $U_3Si_2$  using resonant ultrasound spectroscopy, *Journal of Nuclear Materials* 498 (2018) 438-444.
- [75] D. Olander, Oxidation of  $UO_2$  by High-Pressure Steam, *Nucl. Technol.* 74(2) (1986) 215-217.

APPENDIX C: CHALLENGES AND OPPORTUNITIES TO ALLOYED AND  
COMPOSITE FUEL ARCHITECTURES TO MITIGATE HIGH URANIUM DENSITY  
FUEL OXIDATION: URANIUM DIBORIDE AND URANIUM CARBIDE

This paper has been submitted to the Journal of Nuclear Materials

Reference: J.K. Watkins, A. Gonzales, A.R. Wagner, E. S. Sooby, and B. J. Jaques.

"Challenges and opportunities to alloyed and composite fuel architectures to mitigate high uranium density fuel oxidation: Uranium diboride and uranium carbide." Journal of Nuclear Materials (2021): 153502.

Challenges and Opportunities to Alloyed and Composite Fuel Architectures to Mitigate High Uranium Density Fuel Oxidation: Uranium Diboride and Uranium Carbide

Jennifer K. Watkins <sup>a,b</sup>, Adrian R. Wagner <sup>a</sup>, Adrian Gonzales<sup>c</sup>, Brian J. Jaques<sup>b,d</sup>,

Elizabeth S. Sooby<sup>c</sup>

<sup>a</sup> Idaho National Laboratory, Idaho Falls, ID, USA

<sup>b</sup> Micron School of Materials Science and Engineering, Boise State University, Boise, ID, USA

<sup>c</sup> Department of Physics and Astronomy, The University of Texas at San Antonio, San Antonio, TX, USA

<sup>d</sup> Center for Advanced Energy Studies, Idaho Falls, ID, USA

Author Contributions

Jennifer K. Watkins: Conceptualization, Investigation, Writing – Original Draft, Review and Editing

Adrian R. Wagner: Investigation, Resources, Supervision, Writing – Original Draft, Review and Editing

Adrian Gonzales: Investigation, Writing – Original Draft, Review and Editing

Brian J. Jaques: Conceptualization, Resources, Supervision, Writing - Review and Editing

Elizabeth S. Sooby: Conceptualization, Resources, Supervision, Writing - Review and Editing

**Abstract**

The challenges and opportunities to alloyed and composite fuel architectures designed and intended to mitigate oxidation of the fuel during a cladding breach of a water-cooled reactor are discussed in this manuscript focused on the oxidation performance of uranium diboride and uranium monocarbide. Several high uranium

density fuels are under consideration for deployment as accident tolerant and/or advanced technology nuclear reactor fuels, including UN,  $U_3Si_2$ ,  $UB_2$ , and UC. Presented here is the literature for  $UB_2$  and UC degradation modes, thermodynamics, and oxidation performance of the pure compounds and reported alloyed and composite architectures. Furthermore, this review covers the materials and techniques for the incorporation of additives, dopants, or composite fuel architectures to improve the oxidation behavior for high uranium density fuels for use in LWRs.

### C.1 Introduction

The authors present a review on the challenges and opportunities to alloyed and composite fuel architectures of high uranium density fuels. The current review focuses on the response of uranium diboride ( $UB_2$ ) and uranium monocarbide (UC) to air, oxygen, and water containing atmospheres. Though not commonly investigated as drop-in replacements for  $UO_2$ , they have been proposed as additive phases ( $UB_2$ ) or are known contaminant phases (UC), for commonly proposed, long-term advanced technology fuels (ATF), also referred to as accident tolerant fuel, candidates. Generally speaking, the increase in uranium density coupled with the higher thermal conductivity of proposed ATFs such as  $UB_2$ , UC, uranium mononitride (UN), and triuranium disilicide ( $U_3Si_2$ ), can lead to increased power up-rates, longer cycle lengths, improved performance due to lowered thermal gradients across the fuel pellet, reduced stored energy in the core, and allow for increased coping time during accident scenarios [1-6]. For use in light water reactors (LWRs), the fuel performance during design basis, beyond design basis, and accident conditions must also be considered.

Coolant ingress can occur through a cladding breach typical of a pin-hole in the cladding or a more catastrophic, less common, event like a tube rupture during a loss of coolant accident (LOCA). The presented review is intended to summarize the state of the literature for air, oxygen, and water exposure of  $UB_2$  and UC as well as the strategies envisioned for delaying or mitigating the degradation of these high uranium density fuels under oxidative and hydrothermal corrosion conditions. This review article also discusses specific challenges with regards to synthesis, fabrication, thermodynamics, and degradation modes of  $UB_2$  and UC which would be most relevant for their use in current and advanced reactor concepts. UC was of particular interest in the 1950s and 1960's for liquid metal fast breeder reactors [7], organic-cooled, heavy water reactors [8], high temperature advanced reactors [9], and in nuclear thermal propulsion systems [10], but not necessarily for LWR considerations. Accordingly, the authors did not find literature specifically related to UC for use in water-cooled reactors and much of the literature presented is focused on air/oxygen exposure. The concept of an organic-cooled reactor dates back to the Manhattan project and incorporated a hydrocarbon fluid with a low vapor pressure to be used as a coolant with heavy water as the moderator. The reaction of UC with water would have been of importance as the fuel performance in a loss-of-coolant accident or fuel cladding breach could expose the fuel to the heavy water moderator. Legacy UC fuels are already converted to an oxide form for safe storage and transportation [11], therefore the oxidation and corrosion behavior of UC is an important consideration, even if it is only further pursued as an advanced reactor option and not a LWR fuel. It is important to note that this review does not cover the literature relating to UC in tristructural isotropic (TRISO) fuel applications. At present, there is no peer-

reviewed literature (to the best of the authors' knowledge) regarding attempts to improve the oxidation or hydrothermal corrosion resistance of monolithic UC. Although coating UC particles or monolithic UC could alleviate issues associated with hydrothermal corrosion, a more practical approach should be taken since any protection afforded by a coating is compromised if the coating is breached (i.e. if the coating were to be penetrated, the fuel would be subject to the same oxidation or corrosion behavior as discussed in previous publications [12, 13]). Despite the fact that UC's uranium density and melting temperature falls just below that of UN, it has not received the same interest in terms of research into improving its oxidation resistance. The literature suggests that UC's propensity for oxidation is higher than that of UN which may be why UC has not been pursued as a LWR fuel, but there is not enough data to provide a good comparison. A couple of broad reviews of the historical property data for uranium carbides ( $U_xC_y$ ) is available and include brief sections on the chemical reactivity of uranium carbides [14, 15] and a wide-ranging overview of uranium carbides. However, neither of these publications specifically focus on oxidation and hydrolysis studies or incorporation of additives, dopants, and secondary phases for the purposes of improving oxidation performance of uranium carbides [14, 15]. Much of the research involving sintering aids and dopants are aimed at easing the sintering of UC by achieving high sintered densities at lower temperatures, rather than being discussed for improving UC's degradation behavior.

Both  $UB_2$  and UC can be considered ATF's of their own accord as both possess higher uranium density and thermal conductivity when compared to  $UO_2$  (**Table C.1**). They also both exhibit relatively high melting temperatures. However, these ATF

concepts are highly susceptible to oxidation and are potentially pyrophoric, even under ambient conditions. The next sections will examine the available literature on synthesis methods, thermodynamic considerations, oxidation and corrosion behavior, and relevant information related to dopants or additives to  $UB_2$  and UC. While this review is not specifically focused on synthesis and fabrication, it is discussed in terms of the differences seen in as-fabricated samples and their oxidation and corrosion behavior. The methods for fabrication of these advanced fuels have been detailed in other recent publications [14, 16, 17] but will be discussed briefly here. This review is focused on experimental results regarding oxidation and corrosion behavior. However, modeling efforts (which will assist in providing predictions on fuel behavior necessary for future licensing of these ATF concepts) related to thermal conductivity, electronic and elastic properties, and defect evolution have been performed on both  $UB_2$  [18-21] and UC [22-24].

**Table C.1 Material properties of ATF concept fuels as compared to the benchmark,  $UO_2$ .**

<b>Material Properties</b>	<b><math>UO_2</math></b>	<b><math>U_3Si_2</math></b>	<b><math>UB_2</math></b>	<b>UC</b>	<b>UN</b>
Uranium density (g-U/cm <sup>3</sup> ) <sup>[25-27]</sup>	9.6	11.3	11.7	12.7	13.5
Thermal conductivity (W/m·K at 300 °C) <sup>[28-32]</sup>	6.5 (95% TD)	14.7 (98% TD)	25 (100% TD)	20.4 (570 °C, 99%TD)	16.6 (95% TD)
Melting temperature (°C) <sup>[10, 25, 33, 34]</sup>	2840	1665	2385	2525	2847

Although this review only covers the advanced fuels themselves, a parallel motivation for the development of these fuels stems from the implementation of ATF cladding technologies and materials that may have neutronic penalties. These penalties

arise from an increased cladding thickness (SiC) or larger neutron absorption cross-sections (FeCrAl). These claddings can provide increased safety margins with respect to oxidation performance and, when used in conjunction with the advanced fuels, offer similar or improved neutronics relative to the traditional  $\text{UO}_2$ -Zr alloy system [35-37].

### **C.2 Additives or secondary phases in ATFs**

Potential techniques for providing protection from and improving fuel reaction kinetics with steam and pressurized water could include oxidation and corrosion mitigation technologies typically seen with non-nuclear systems. These techniques include surface coatings, mechanical or surface treatments, microstructural engineering, and the addition of an alloying or secondary phase/element. The bulk of the literature with regard to ATF concepts focuses on the latter proposal and is discussed in this review for  $\text{UB}_2$  and UC.

The objective for the inclusion of an additive or secondary phase to the primary fuel matrix is to stabilize the bulk monolith under corrosive conditions or form a passivation layer which will hinder or fully prevent degradation. The proposed additive should also be compatible with the fuel and cladding while maintaining the fuel's desired thermophysical and neutronic properties. **Table C.2** lists many of the elements and compounds that have been proposed or considered as additives for corrosion mitigation, mostly for UN and  $\text{U}_3\text{Si}_2$  but could be extended to  $\text{UB}_2$  and UC. Other important properties that should be considered (e.g., neutron capture cross-section, thermal conductivity, etc.) are also listed in **Table C.2**. The additive phase or resulting alloy should also have a melting temperature that can withstand typical LWR conditions, although use of an additive with a melting temperature exceeding that of the fuel matrix

could create additional challenges during fabrication. In addition, unwanted stresses in a composite microstructure could be introduced due to an additive with (1) a large coefficient of thermal expansion mismatch (compared to the base fuel) or (2) a significant (>15%) lattice mismatch from coherent precipitates and substitutional defects. Lattice mismatches can be due to differences in crystal structure, lattice parameters, and solubility limits. The additive's functionality will be affected by its solubility within the fuel matrix and must be taken into consideration. Also, not all additives will be thermodynamically or otherwise compatible with different ATF concepts. This is discussed in more detail in Sections 5.3.3 and 5.3.4. As previously stated, the high thermal conductivity of these ATF concepts is a primary driving factor for their implementation; thus, using an additive or secondary phase which does not lower the overall thermal conductivity is desirable. Additionally, avoidance of neutronic penalties, which could arise from additives having a high thermal neutron capture cross-section, is important for maintaining fuel economy.

**Table C.2 Properties of potential dopants into ATF concepts for improved corrosion resistance. References listed in the headers applies to all the materials in the column.**

Additive	Melting temp. (°C)	Coefficient of thermal expansion at 500 °C ( $10^{-6} \text{C}^{-1}$ )	Thermal conductivity at 500 °C (W/m·K)	Thermal neutron capture cross-section (b) <sup>[38]</sup>	Crystal structure <sup>[39]</sup>	Space Group <sup>[39]</sup>
Aluminum	660 <sup>[40]</sup>	32.5 <sup>[41]</sup>	237 <sup>[42]</sup>	0.23	FCC	Fm-3m
AlN	3000 <sup>[40]</sup>	4.3 (400 °C) <sup>[43]</sup>	~100 <sup>[44]</sup>	Al: 0.23 <sup>14</sup> N: 1.91 <sup>15</sup> N: 0.00002	Wurtzite	P63mc
Chromium	1907 <sup>[40]</sup>	11.2 <sup>[45]</sup>	75.9 <sup>[42]</sup>	0.8	BCC	Im-3m
CrN	1080 <sup>[40]</sup> decomposes	9.7 <sup>[46]</sup>	2 (300 °C) <sup>[47]</sup>	Cr: 0.8 <sup>14</sup> N: 0.080 <sup>15</sup> N: 0.00002	NaCl	Fm-3m
Cr <sub>2</sub> O <sub>3</sub>	2432 <sup>[40]</sup>	8.4 <sup>[48]</sup>	2.94 <sup>[49]</sup>	Cr: 0.8	Al <sub>2</sub> O <sub>3</sub>	R-3cH
Manganese	1246 <sup>[40]</sup>	~31 <sup>[50]</sup>	7.82 (300 °C) <sup>[42]</sup>	13.3	BCC	I-43m
Molybdenum	2622 <sup>[40]</sup>	~5.6 <sup>[50]</sup>	118 <sup>[42]</sup>	6E-7 to 14	BCC	Im-3m
Nickel	1455 <sup>[40]</sup>	16 <sup>[51]</sup>	~55 <sup>[52]</sup>	4.6	FCC	Fm-3m
Niobium	2477 <sup>[40]</sup>	7.47 <sup>[53]</sup>	4.3 <sup>[53]</sup>	0.9	BCC	Im-3m
Thorium	1750 <sup>[40]</sup>	~13.9 <sup>[50]</sup>	43.1 <sup>[54]</sup>	<sup>232</sup> Th: 7.34	FCC	Fm-3m
ThN	2820 <sup>[40]</sup>	6.4 <sup>[55]</sup>	47.6 (127 °C) <sup>[56]</sup>	<sup>232</sup> Th: 7.34	NaCl	Fm-3m
Titanium	1670 <sup>[40]</sup>	9.7 <sup>[57]</sup>	22.3 <sup>[42]</sup>	7.9	HCP	P63/mmc
Yttrium	1522 <sup>[40]</sup>	9.4 ( <i>a</i> -axis) 21.8 ( <i>c</i> -axis) <sup>[50]</sup>	14.1 <sup>[42]</sup>	0.001	HCP	P63/mmc
Y <sub>2</sub> O <sub>3</sub>	2439 <sup>[40]</sup>	~5 (25°C) <sup>[58]</sup>	35 (25 °C) <sup>[58]</sup>	0.001	Bixbyite	Ia-3
Zirconium	1854 <sup>[40]</sup>	7.2 <sup>[50]</sup>	19.7 <sup>[42]</sup>	<sup>90</sup> Zr: 0.2	HCP	P63/mmc
ZrN	2952 <sup>[40]</sup>	7.0 <sup>[59]</sup>	26 <sup>[60]</sup>	<sup>90</sup> Zr: 0.2 <sup>14</sup> N: 0.080 <sup>15</sup> N: 0.00002	NaCl	Fm-3m
UAl <sub>2</sub>	1620 <sup>[61]</sup>	14.8 <sup>[62]</sup>	9.3 <sup>[63]</sup>	Al: 0.23	MgCu <sub>2</sub>	Fd-3m

Additive	Melting temp. (°C)	Coefficient of thermal expansion at 500 °C ( $10^{-6} \text{ C}^{-1}$ )	Thermal conductivity at 500 °C (W/m·K)	Thermal neutron capture cross-section (b) <sup>[38]</sup>	Crystal structure <sup>[39]</sup>	Space Group <sup>[39]</sup>
UAl <sub>3</sub>	1350 <sup>[59]</sup>	15.2 <sup>[62]</sup>	15.2 <sup>[63]</sup>	Al: 0.23	Cu <sub>3</sub> Au	Pm-3m
UAl <sub>4</sub>	646 <sup>[59]</sup>	19.1 <sup>[62]</sup>	5.2 <sup>[63]</sup>	Al: 0.23	UAl <sub>4</sub>	Imma
UB <sub>2</sub>	2385 <sup>[33]</sup>	9 ( <i>a</i> -axis); 8 ( <i>c</i> -axis); 6 ( <i>U-B</i> bond direction) (205 °C) <sup>[64]</sup>	~25 (300 °C) <sup>[32]</sup>	<sup>10</sup> B: 3841 <sup>11</sup> B: 0.0055	AlB <sub>2</sub>	P6/mmm
UB <sub>4</sub>	2530 <sup>[40]</sup>	7.1 <sup>[65]</sup>	~16 <sup>[32]</sup>	<sup>10</sup> B: 3841 <sup>11</sup> B: 0.0055	UB <sub>4</sub>	P4/mbm
UC	2525 <sup>[10]</sup>	10.9 <sup>[66]</sup>	20.4 (300 °C) <sup>[29]</sup>	<sup>12</sup> C: 0.00387	NaCl	Fm-3m
UC <sub>2</sub>	2350 <sup>[40]</sup>	14.6 (avg.) <sup>[67]</sup>	13 <sup>[68]</sup>	<sup>12</sup> C: 0.00387	CaC <sub>2</sub>	I4/mmm
UN	2847 <sup>[34]</sup>	8.9 <sup>[69]</sup>	16.6 (300 °C) <sup>[30]</sup>	<sup>14</sup> N: 0.080 <sup>15</sup> N: 0.00002	NaCl	Fm-3m
U <sub>2</sub> N <sub>3</sub>	950 <sup>[40]</sup> *decomposes to UN	n/a	n/a	<sup>14</sup> N: 0.080 <sup>15</sup> N: 0.00002	La <sub>2</sub> N <sub>3</sub>	P-3m1
UO <sub>2</sub>	2840 <sup>[25]</sup>	9.8 <sup>[70]</sup>	5 <sup>[28]</sup>	<sup>235</sup> U: 681 <sup>238</sup> U: 2.7	Fluorite	Fm-3m
USi	1580 <sup>[71]</sup>	20 <sup>[72]</sup>	12.5 <sup>[72]</sup>	<sup>28</sup> Si: 0.169	FeB	Pnma
U <sub>3</sub> Si <sub>2</sub>	1665 <sup>[25]</sup>	17 <sup>[31]</sup>	17.9 <sup>[31]</sup>	<sup>28</sup> Si: 0.169	Tetragonal	P4/mbm
U <sub>3</sub> Si <sub>5</sub>	1750 <sup>[71]</sup>	11 <sup>[73]</sup>	10 <sup>[73]</sup>	<sup>28</sup> Si: 0.169	AlB <sub>2</sub>	P6/mmm

In addition to the considerations arising from the use of the potential additives listed in **Table C.2**, the amount of the additive needed must also be addressed. There exists a limit to the amount of additive or secondary phase that these high uranium density fuels can accommodate before their uranium density is below that of the benchmark UO<sub>2</sub> fuel (9.7 g/cm<sup>3</sup>). As seen in **Figure C.1**, UN allows for the largest amount of non-uranium bearing additive, 28.2 vol%, followed by UC at 25.4 vol%, and

then  $UB_2$  and  $U_3Si_2$  at 17 and 14.2 vol%, respectively. The use of a uranium-bearing compound into one of the high uranium density fuels increases these limits even further.

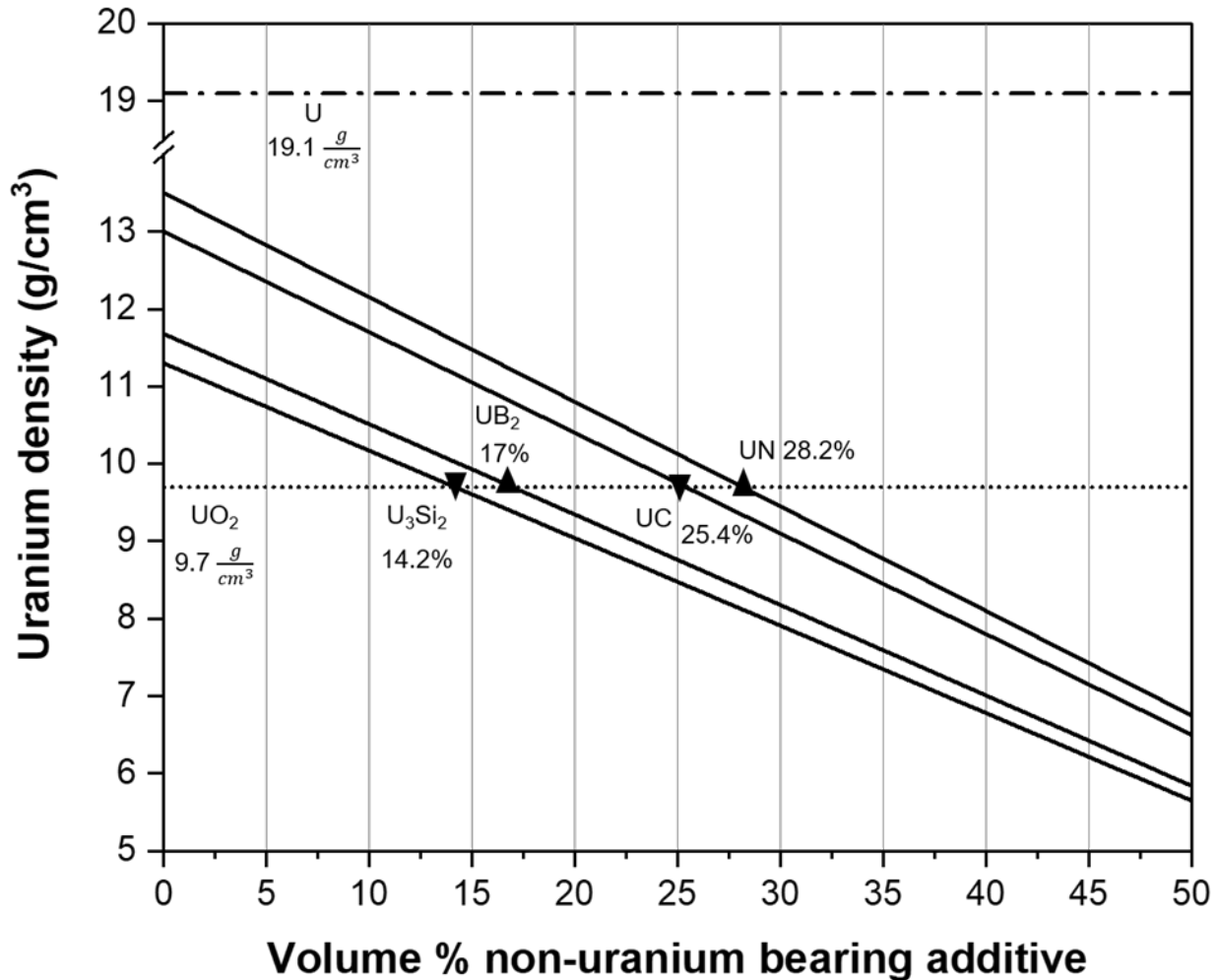


**Figure C.1** Uranium density vs. volume percent non-uranium bearing additive for the ATF fuel concepts as compared to U and  $UO_2$ .

### C.3 Uranium diboride ( $UB_2$ )

Uranium diboride ( $UB_2$ ) has received interest as an ATF concept despite the fact that  $^{10}B$  has a high neutron absorption cross-section and has historically been used for nuclear core control rods. Enriched  $UB_2$  (with a tailored isotopic  $^{10}B/^{11}B$  ratio) could serve as an integrated burnable absorber within the fuel pellet itself [32, 74]. The ability

to use a burnable absorber material as part of the fuel matrix, while increasing the fissile content, helps to moderate fuel reactivity at beginning-of-life and extend cycle lengths which improves the overall reactor economics [26]. Much of the literature on  $UB_2$  relates to thermal, mechanical, electronic, or magnetic properties [19, 32, 75-82] and not on the oxidation or corrosion performance or methods to improve this behavior. While these other properties (thermal, mechanical, etc.) are important for overall nuclear fuel performance, the following sections will examine the available literature on  $UB_2$  with regards to synthesis methods, oxidation and corrosion behavior, and composite fuels containing the diboride.

### C.3.1 Synthesis and fabrication methods

There are only three known U-B compounds ( $UB_2$ ,  $UB_4$ , and  $UB_{12}$ ), all with melting temperatures above 2000 °C, but all are considered line compounds with  $UB_2$  having a lower eutectic melt point if not stoichiometric (see the binary phase diagram for the U-B system in **Figure C.2**) [33]. However, some limited deviations in stoichiometry have been suggested by density functional theory simulations at high temperatures [21].

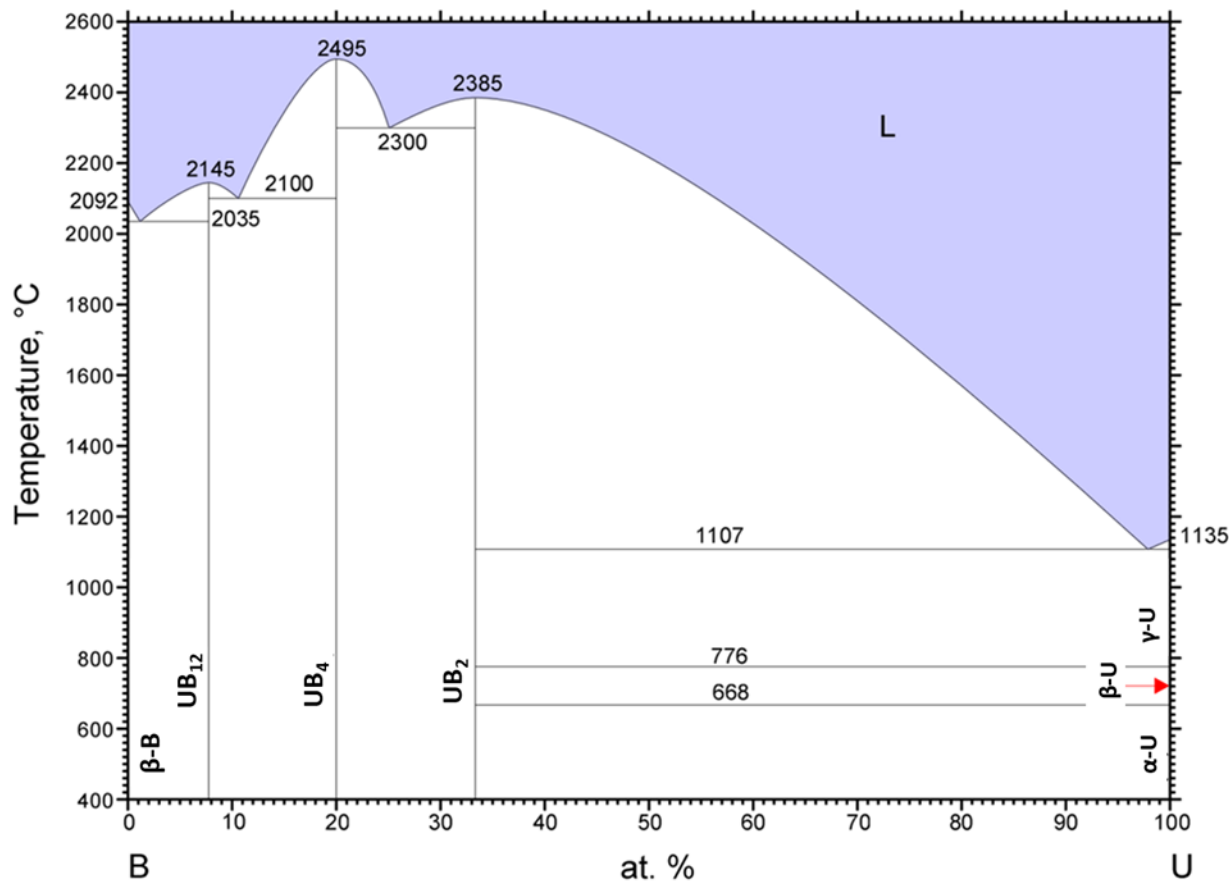


**Figure C.2 Uranium-boron phase diagram (0-100 at% U, 400-2600 °C) [33].**

The primary method for obtaining UB<sub>2</sub> powder which can be formed into compacts is through arc-melting uranium metal and elemental boron and using traditional powder metallurgy techniques to achieve the desired particle size [32, 74, 76, 78, 83-85]. Reaction of the pure elements or hydrides in an inert atmosphere and borothermic reduction of UO<sub>2</sub> and B<sub>2</sub>O<sub>3</sub> with a reactive element such as C, Al, or Mg has also been reported but both of these methods have indicated that some volatilization of the boron occurs resulting in non-stoichiometry although it has not been quantified [65, 83]. Arc-melting of the pure metals followed by spark plasma sintering (SPS) has been shown to result in UB<sub>2</sub> samples having high density (~95% TD) and a microstructure which appears phase pure (see **Figure C.3a**) [32]. However, x-ray diffraction (XRD) did

identify small secondary phases of  $\text{UO}_2$  (also present in the U feedstock powder),  $\text{UB}_4$  (likely from the reaction with the  $\text{UO}_2$  impurities in the feedstock, impurities in the UHP argon during SPS, or oxygen pickup during powder loading), and  $\text{UBC}$  (due to carbon from the graphite dies and paper used in the SPS process) [32]. Additionally, these processes can cause undesirable impurity phases which can be identified in the sintered microstructure [85]. From Turner *et al.*, the microstructure of  $\text{UB}_2$  synthesized using the arc-melting of elemental U and B and vacuum sintered at 1800 °C for 1 hour (%TD of this sample was unclear in the paper) reflects an inter-granular  $\text{UO}_{0.75}\text{C}_{0.75}$  phase, as shown in **Figure C.3b** [85]. The authors attributed this secondary phase formation to excess elemental uranium left in the arc-melted  $\text{UB}_2$  ingot that reacted with the WC milling vessel used their powder metallurgy processes [85].

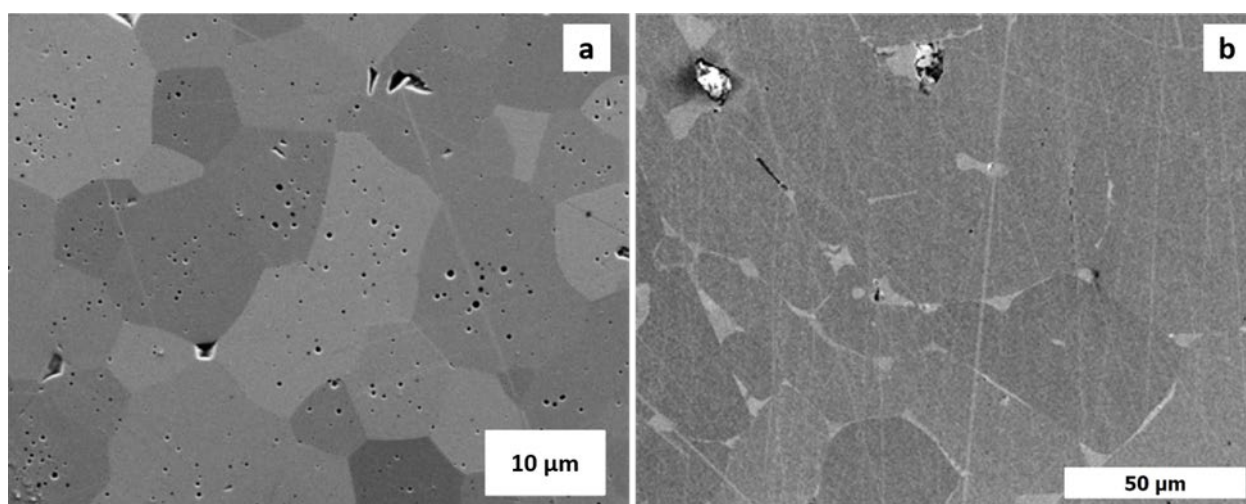


**Figure C.3** SEM micrographs of  $\text{UB}_2$  microstructure from arc-melting synthesis. a) ~95% TD  $\text{UB}_2$  sample after SPS at 1750 °C and 40 MPa for 5 minutes, modified from Kardoulaki *et al.* [32]. b) Arc-melted  $\text{UB}_2$  after conventional sintering in a graphite vacuum furnace for 1 hour at 1800 °C and showing a secondary inter-granular  $\text{UO}_{0.75}\text{C}_{0.25}$  phase. Modified from Turner *et al.* [85].

It has been recently reported that the conversion of  $\text{UO}_2$  to  $\text{UB}_2$  during carbo/borothermic reduction will not occur unless a low carbon monoxide (CO) partial

pressure ( $\leq 0.1$  kPa at 1800 °C) is maintained, resulting in the thermodynamically favorable formation of  $UB_4$  (which has a lower uranium density than that of  $UO_2$ , 7.94 g/cm<sup>3</sup>) [26]. There exists a challenge of maintaining that low partial pressure of CO during the high temperature reaction as CO is continually released [26].

Additional synthesis methods for borides that are mentioned in the literature are electrolysis using molten fluoride or chloride salts [86], reaction of diborane with the metal hydride [87], and thermal decomposition of borohydrides [88]. However, these latter processes involve specialty setups to accommodate the reactants and high temperatures [65].

Compacting and sintering using conventional methods as well as hot-pressing and SPS for densification has also been reported [32, 74, 89]. Accordingly, SPS methods have been shown to achieve higher densities ( $> 90\%$  TD) at temperatures under 1800 °C [32], whereas temperatures above 2000 °C are required for conventional methods to reach  $> 90\%$  TD [32].

### C.3.2 Oxidation and corrosion of $UB_2$

Only two studies on the oxidation of  $UB_2$  in pure oxygen, water vapor, and steam have been identified in the open literature [85, 89]. As seen in **Figure C.4**,  $UB_2$  demonstrates linear reaction kinetics (i.e. a linear mass gain vs. time) for arc-melted  $UB_2$  (96.5% TD) under isothermal holds in  $O_2$  at 400 °C (assumed to be at 1 atm although the authors did not specifically state those conditions for these tests) and 29 mmHg partial water vapor pressure at 500 °C, versus a parabolic trend for the reaction in  $N_2$  at 700 °C (also assumed to be at 1 atm) [89]. This suggests that the reaction in nitrogen forms a passivating layer, whereas the reactions with oxygen and water vapor do not. The

reaction products were noted as  $U_3O_8$ ,  $UO_2$ , and  $UN_x$  (with  $x$  between 1.5-2) for the  $O_2$ , water vapor, and nitrogen reactions, respectively. It was noted that the as-fabricated sample contained a uranium-rich solid solution as a grain boundary phase with  $UB_2$  (likely metallic uranium) which would have had a negative effect on the oxidation behavior [89].

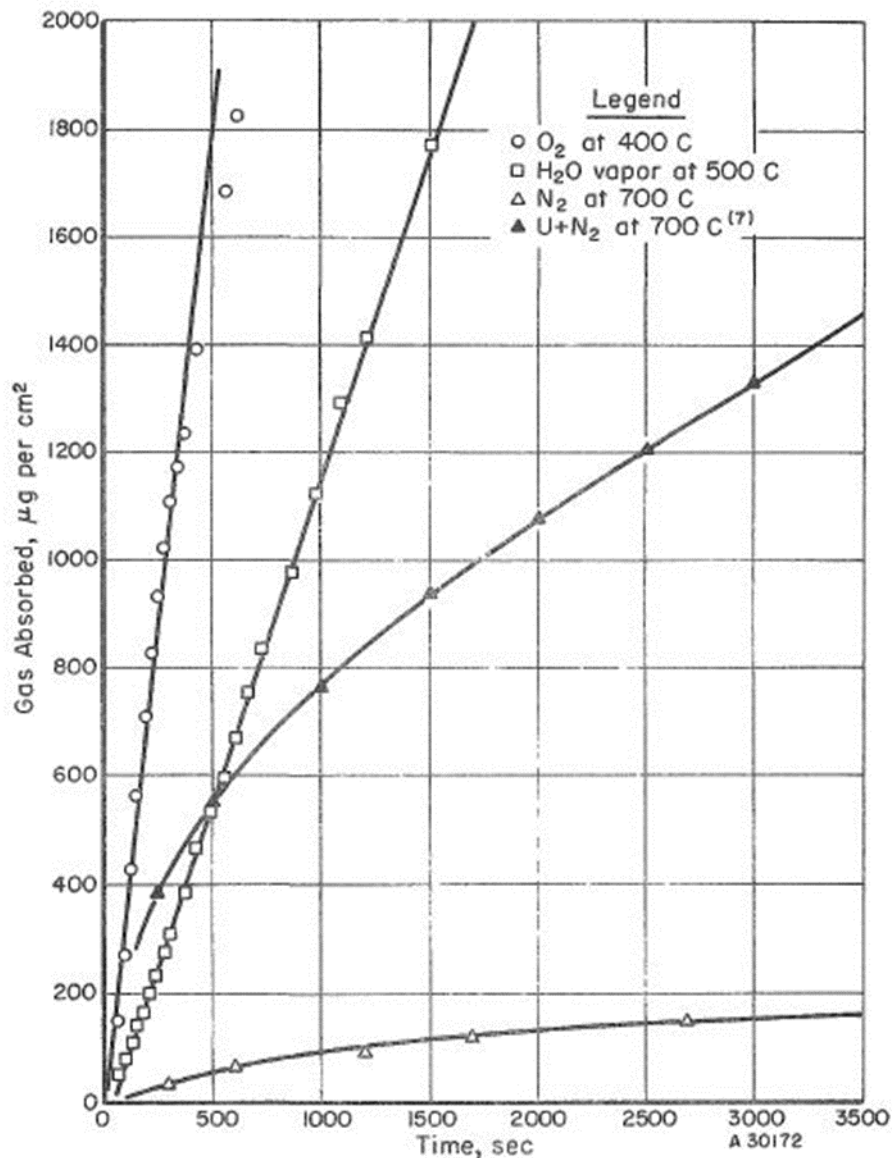


**Figure C.4** Plot of gas absorbed vs. time for  $UB_2$  samples tested in  $O_2$  (assumed to be at 1 atm) at 400 °C, 29 mmHg partial water vapor pressure at 500 °C, and  $N_2$  (also assumed to be at 1 atm) at 700 °C, as compared to uranium in  $N_2$  at 700 °C. From Tripler et al. [89].

A pure  $UB_2$  sample (as previously shown in Figure C.3b) was also investigated as a reference in  $U_3Si_2/UB_2$  composite work and was found to have an oxidation onset temperature of 629 °C in flowing steam (tested from 250-900 °C), versus 453 °C for a pure  $U_3Si_2$  sample (noted to be above 90 % TD per [74]) [85]. Figure C.5 shows the

powdered samples remaining after the 900 °C testing for  $U_3Si_2$  and  $UB_2$ , although the researchers confirmed that the material was identified as  $UO_2$  upon the completion of testing. The powder morphology shows less branch cracking across the particle surfaces for the  $UB_2$  sample as compared to the  $U_3Si_2$  sample [85]. They suggest that while the number of branch cracks in their composite materials were not fully eliminated, they were reduced significantly which likely prevented the rapid increase in surface area. The reported higher oxidation onset temperature for  $UB_2$  versus  $U_3Si_2$  suggests that  $UB_2$  may be considered as a viable contender for LWR use. Further systematic corrosion testing is required, including investigations with conditions more closely matched to LWR reactor chemistry.

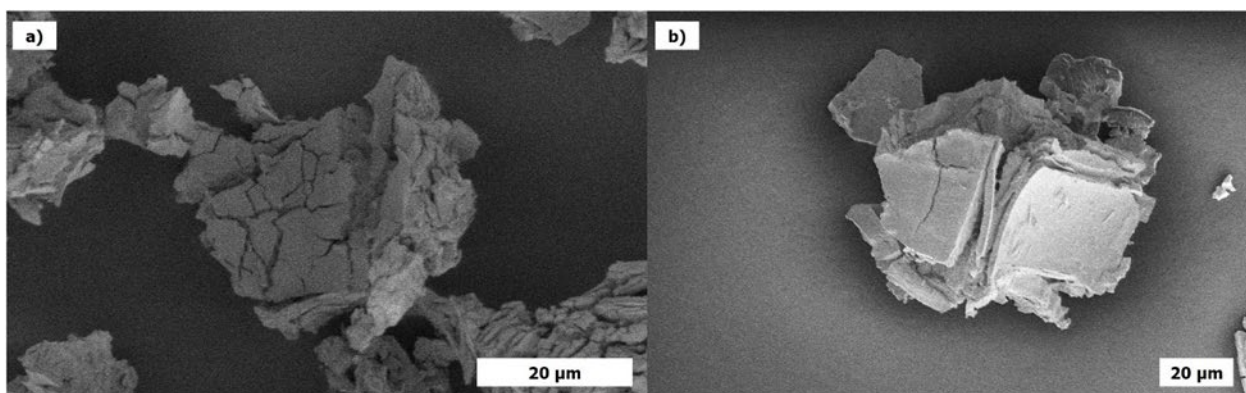


**Figure C.5** Samples remaining from testing a)  $U_3Si_2$  and b)  $UB_2$  in steam from 250-900 °C. The  $UB_2$  showed less branch cracking than the  $U_3Si_2$  sample and a higher onset temperature (629 °C). Modified from Turner et al. [85].

### C.3.3 Composites with $UB_2$

Similar to the oxidation/corrosion of pure  $UB_2$ , the literature is sparse on composites containing  $UB_2$  as a secondary phase and, to the best of the author's knowledge, it does not exist for composites where  $UB_2$  is the primary phase. However, research at Los Alamos National Laboratory demonstrated the use of  $UB_2$  within a  $UO_2$

matrix for the purposes of increasing the thermal conductivity of  $\text{UO}_2$  while providing a burnable poison [84]. It was reported that SPS of the composites ( $\text{UO}_2 + (5,15,30 \text{ wt}\%)\text{UB}_2$ ) were sintered to high densities ( $> 95\% \text{ TD}$ ) and that thermal conductivity calculations increased as the weight fraction of  $\text{UB}_2$  increased, with the 30wt%  $\text{UB}_2$  pellet having a 57% increase over a pure  $\text{UO}_2$  sample [84]. **Figure C.6a** is a backscatter electron image of an as fabricated via SPS  $\text{UO}_2 + 30\text{wt}\% \text{UB}_2$  sample showing the brighter  $\text{UB}_2$  phase distributed throughout the  $\text{UO}_2$  matrix. A  $\text{UO}_2 + 15\text{wt}\% \text{UB}_2$  sample had similar morphology to the 30wt%  $\text{UB}_2$  sample and is shown in **Figure C.6b** after thermal property measurements up to 1000 °C. The thermally cycled sample exhibited a distinct spinodal microstructural change with only a small fraction of the original  $\text{UB}_2$  phase remaining; however, it was shown that  $\text{UB}_4$  was formed within a  $\text{UO}_2$  matrix. The authors suggested both the  $\text{UB}_4$  and  $\text{UO}_2$  formed simultaneously based on previously reported thermodynamic calculations of an 80/20 mol%  $\text{UO}_2/\text{UB}_2$  system that predict  $\text{UB}_4$  and  $\text{UO}_{2-x}$  formation from  $\text{UB}_2$  above 800 °C [84].

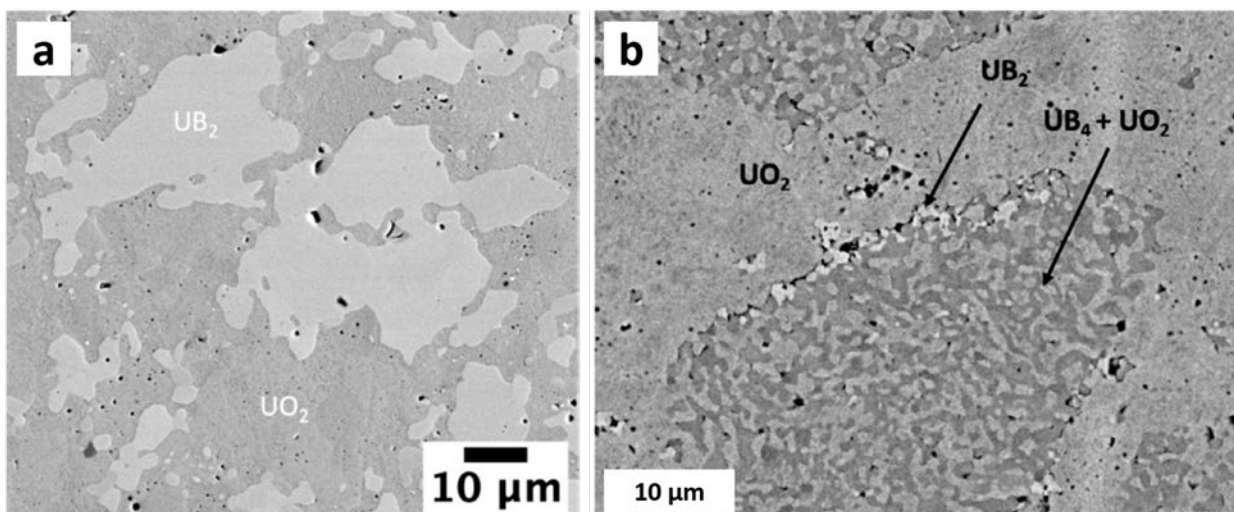


**Figure C.6** a) Backscatter electron image of a  $\text{UO}_2 + 30\text{wt}\% \text{UB}_2$  composite sintered via SPS showing the brighter  $\text{UB}_2$  regions distributed throughout the  $\text{UO}_2$  matrix, and b) a  $\text{UO}_2 + 15\text{wt}\% \text{UB}_2$  composite also sintered via SPS but after thermal property measurements displaying little of the original  $\text{UB}_2$  phase and formation of  $\text{UB}_4$ . Modified from Kardoulaki et al. [84].

The only reported corrosion behavior for a  $\text{UB}_2$  containing composite is that by Turner *et al.*, who investigated the addition of 10wt% and 50wt%  $\text{UB}_2$  to  $\text{U}_3\text{Si}_2$  for improving the corrosion resistance of the silicide phase [85]. These composite samples were examined along with pure  $\text{U}_3\text{Si}_2$  and  $\text{UB}_2$  samples in flowing steam atmosphere from 250 – 1000 °C. It was reported that the composite samples had onset temperatures roughly 100 °C greater than pure  $\text{U}_3\text{Si}_2$  and approximately 80 °C lower than a pure  $\text{UB}_2$  sample [85]. In addition, it was found that only  $\text{UO}_2$  remained after exposing the samples to 900 °C steam, although a small amount of  $\text{UB}_2$  remained in the 50wt%  $\text{UB}_2$  composite, which suggests that any silicon or boron compounds volatilized during testing or were amorphous and would not have been detected via XRD analysis. In an effort to better understand the response to steam oxidation, a  $\text{U}_3\text{Si}_2$ -50wt%  $\text{UB}_2$  composite sample was exposed to steam for 5 minutes at 465 °C and showed  $\text{UO}_2$  formed as striations across the silicide, reported as likely due to distortions caused by formation of the  $\text{U}_3\text{Si}_2\text{H}_2$  phase —

this ternary phase has been referenced in both modeling and experimental work by other researchers [90-92]. The researchers acknowledged the complexity of the silicide-steam reaction and conceded that a better understanding of the mechanism by which  $U_3Si_2$  degrades under steam exposure is required. They also state the mechanism by which  $UB_2$  improves upon the corrosion resistance of  $U_3Si_2$  is also complex and not well understood. They postulate the mechanism which provides enhanced protection to steam degradation is not likely from interruption of the hydride phase formation as the hydride striations were observed in the composite samples. However, they suggest that surface formation of a thin protective borosilicate glass layer (which would be resistant up to its melting point of 500-600 °C) as a possible alternate mechanism [85].

An Ellingham-type plot showing the relative thermodynamic stability for the boride phases of the previously mentioned potential additives is shown in **Figure C.7**. Note that no data existed in the HSC database [93] for yttrium borides and the silicon boride compounds listed were not favorable (e.g. had a positive Gibb's free energy of formation); therefore, neither are included. From this diagram, it is important to point out that Gibb's free energy of formation for the  $UB_2$  reaction is relatively high, suggesting that it may be difficult to find an appropriate elemental addition that will not preferentially form its boride phase and cause dissociation of the  $UB_2$ . For example, reactions for compounds such as  $SiB_{14}$  and  $AlB_{12}$  lie above the  $UB_2$  reaction (having a higher Gibb's free energy of formation) and thus are unlikely to form in a composite architecture with  $UB_2$ . Conversely,  $UB_2$  dissociation is more likely in the presence of elemental cations of Ti, Zr, or Mo, where the formation of their respective boride phases is more thermodynamically favorable than  $UB_2$  at all temperatures.

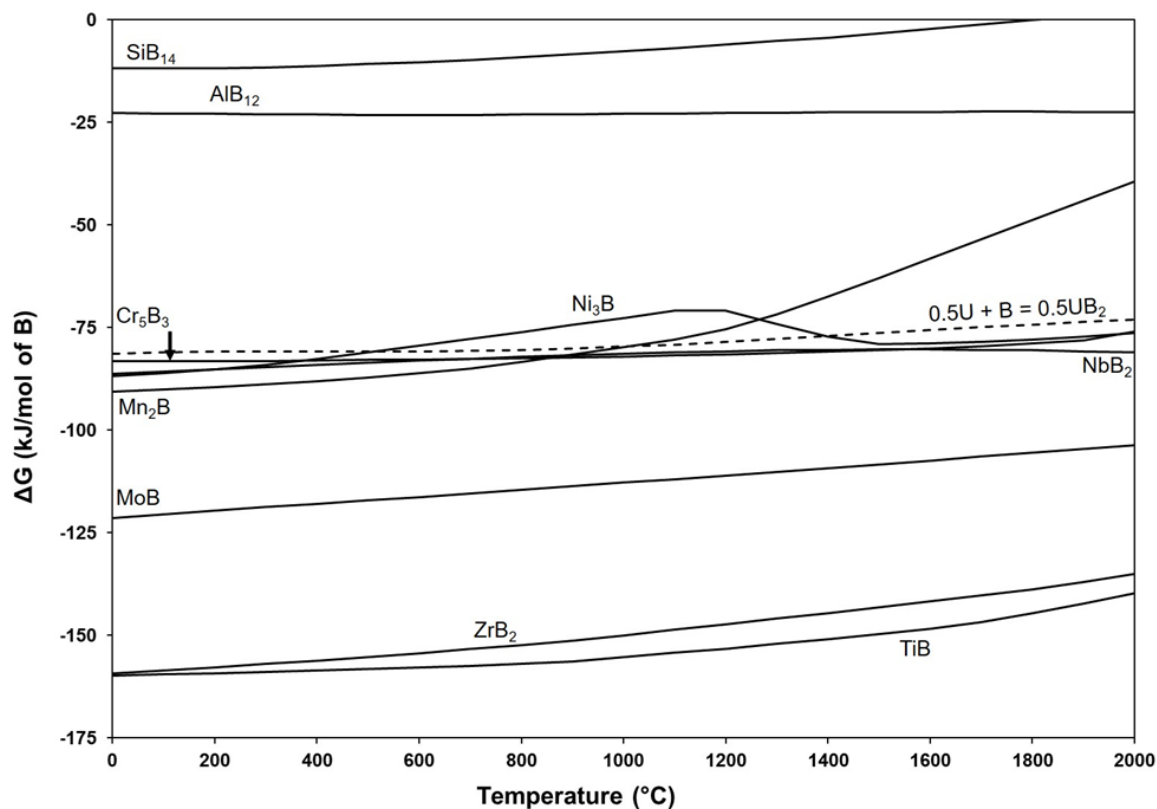


**Figure C.7** Ellingham-type diagram showing thermodynamic stability of boride formation of various metallic elements considered for possible dopants into ATF concepts versus  $UB_2$  (normalized to 1 mol of B). Calculated using HSC Chemistry 9 [93].

#### C.3.4 Summary of previous $UB_2$ research

This limited work highlights an area of research opportunity regarding  $UB_2$  as a potential long-term (low technical readiness) ATF candidate and replacement for  $UO_2$ . The initial results from corrosion testing for  $UB_2$  (showing a higher onset temperature as compared to pure  $U_3Si_2$ ), pure  $UB_2$  samples and  $U_3Si_2$ - $UB_2$  composite samples are promising. Although further oxidation and corrosion studies are necessary, even for pure  $UB_2$ , a similar approach to adding a secondary constituent (dopant) to  $UB_2$  or additional work with  $UB_2$  in other composite systems for improved corrosion resistance would fill a gap in the existing literature. As seen in **Figure C.1**,  $UB_2$  can accommodate up to 17 vol% additive before the uranium density is below that of  $UO_2$ . Additional

opportunities exist for pure  $UB_2$  and its composite systems in terms of optimization of fabrication and sintering methods which can be economically scaled up. Further studies should also be considered which investigate the use of  $UB_2$  as a dopant with an appropriately tailored isotopic ratio of  $^{10}B/^{11}B$ .

#### C.4 Uranium monocarbide (UC)

Along with its high thermal conductivity and melting temperature, the decomposition temperature of UC is relatively high in comparison to other ATF fuels like UN (1200 °C in a nitrogen deficient atmosphere). It has been observed that UC remains relatively stable up to 2000 °C (vacuum atmosphere) with primary weight loss from elemental U [94]; therefore making it an ideal candidate for advanced high temperature reactor concepts. The binary uranium-carbon phase diagram is shown in **Figure C.8** to highlight that the UC phase field increases as temperature increases from 1100 °C — although it is difficult to maintain at lower temperatures since it is a line compound. This causes challenges in stoichiometric UC fabrication due to the ease of secondary phase formation (i.e  $UC_2$ ,  $U_2C_3$ ) [95] and, similar to other ATF concepts, UC is unstable in oxidizing and corrosive conditions. It has been reported that UC is pyrophoric in oxygen containing environments, even at relatively low temperatures (< 230 °C) [96] and gaseous products of methane and hydrogen result when UC reacts with water [97-99]. As previously mentioned, a broad overview of the historical data for uranium carbides including physical, thermal, thermodynamic, transport, electrical, magnetic, electronic, optical, and mechanical properties, as well as general chemical behavior with other elements and compounds has been reported [14, 15]. These previous publications are not directed towards the investigating the reactions of UC with air, water, or steam for the

purposes of improving corrosion resistance. As such, the following sections are presented to compare and contrast the specifics in the available literature on UC oxidized in air, water, and steam. Section 5.4.1 discusses UC synthesis methods which is important in terms of the opportunities for creating composite architectures for the purposes of mitigating UC degradation under hydrothermal corrosion conditions. In Section 5.4.2 the available literature including the experimental specifics on oxidation and hydrothermal corrosion of UC is presented, including corroded microstructures, kinetics data, proposed oxidation and corrosion mechanisms, and oxidation onset temperatures. The use of additives or dopants in UC is briefly presented in Section 5.4.3, addressing the challenges these potential additives present in terms of thermodynamic considerations, secondary phase formation, and uranium mobility.

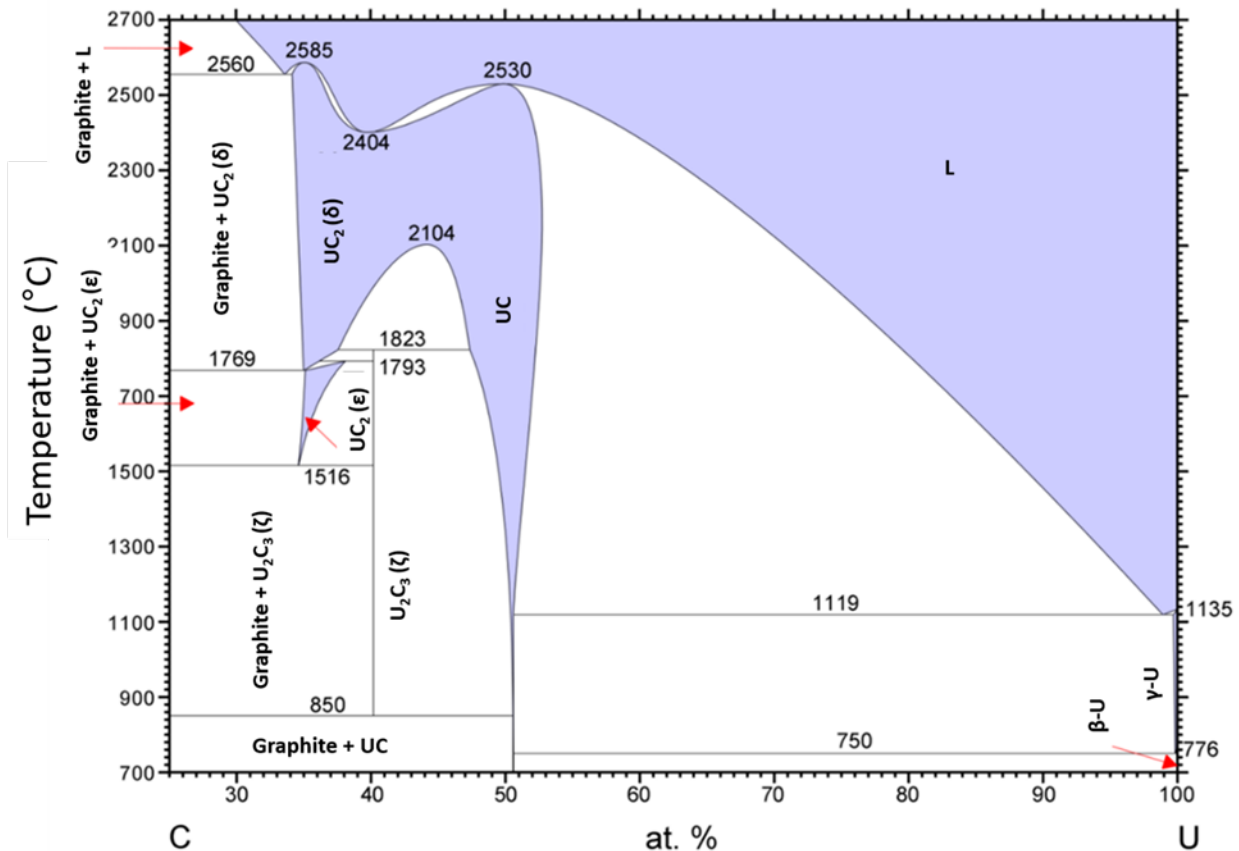


**Figure C.8 Uranium-carbon phase diagram (25-100 at% U, 700-2700 °C) [95].**

#### C.4.1 Synthesis methods

Like some of the other non-oxide fuels, fabrication of high purity and stoichiometric UC feedstock is challenging as inert atmospheres are required during handling and processing due to its affinity for oxygen and its pyrophoricity [9, 100]. When exposed to water or steam UC is also highly susceptible to corrosion [7, 89, 97, 101]. Synthesis techniques have mainly included the carbothermic reduction method (reaction of  $\text{UO}_2$  with C, which is a precursor to UN formation via CTR-N [12]), which requires the use of furnaces capable of the high reaction/sintering temperatures necessary. The process then requires grinding and pelletization of the reactive carbide powders [16, 102]. Successful synthesis has been achieved through arc-melting [103] or solid-state

reactions of metallic uranium or  $\text{UH}_3$  with carbon powder or graphite [104]; although, additional processing and powder metallurgy techniques are required to fabricate appropriate fuel geometries [16, 102]. Another synthesis route, although not common for production of monolithic UC samples, is the internal gelation technique which has been demonstrated to synthesize carbon containing uranium oxide microspheres (allowing control of carbon stoichiometry), which can then be subjected to traditional carbothermic reduction [105, 106]. It is uncertain which synthesis method, if any, is preferable for incorporation of a dopant or additive for the purposes of improving UC's corrosion resistance. It may be more likely that any secondary constituent would be integrated into the fuel matrix during post-synthesis processes.

#### C.4.2 Oxidation/corrosion testing

##### C.4.2.1 Air oxidation of UC

The literature on the oxidation of UC in air varies in terms of testing parameters (i.e., temperature, sample configuration, and oxygen partial pressures). Many of the reviewed papers state that UC is known to readily oxidize or hydrolyze in air due to the moisture content in ambient conditions [107-109]. The work described below compares the results of UC samples in various physical configurations (single crystal, block, and powder) and under varying experimental conditions.

Testing to investigate reprocessing methods for arc-melted and cast reactive UC (with the term "reactive" to indicate aged material) showed that UC ignites in the presence of pure oxygen at approximately 275 °C and in air at approximately 350 °C. The reaction products were  $\text{UO}_{2+x}$  during heating but complete oxidation results in  $\text{U}_3\text{O}_8$  (above 375 °C), and it was reported that the reaction was difficult to control once

ignition had occurred as the heat of the reaction was sufficient to drive the reaction to completion [110]. The researchers noted that “fresh” UC oxidized more slowly, even at 500 °C [110]. Single crystal fragments of UC oxidized for 10 minutes in oxygen at 400 °C were found to have only UO<sub>2</sub> as a reaction product with no evidence of U, U<sub>3</sub>O<sub>8</sub>, U<sub>2</sub>C<sub>3</sub> or UC<sub>2</sub> [107]. Results similar to [110] were also seen on “aged” arc-melted and sintered UC ingots oxidized at 7\*10<sup>-2</sup> MPa oxygen partial pressure, igniting at 340 °C and 320 °C, respectively [111]. Other work describes UC single crystals exposed to relative humidity of 0%, 30%, 60%, and 95% at room temperature [109]. An initial linear fast oxidation occurred within a few hours, followed by further oxidation having a square root of exposure time dependence, which suggested a volume diffusion process [109]. Naito *et al.* [112] compared their work to previous oxidation studies on UC which were performed on block, powder, and single crystal UC samples at various temperatures and various oxygen partial pressures, including the aforementioned publication by Murbach [110]. A summary of the results from various studies (see **Table C.3**) found linear reaction rates (if the rate is listed) for all but one sample which was tested at a lower temperature range [112]. The differences in the mechanisms of oxidation, which must be considered in context of the kinetics data, were attributed to discrepancies in oxygen partial pressures and sample variances [112].

**Table C.3 Summary of oxidation studies on UC samples at various temperatures and partial pressures of oxygen (assumed to be at ~ 1 atm total pressure). Modified from Naito et al. [112].**

Reference	Reaction rate	Sample Type	Temperature range (°C)	Oxygen partial pressure (MPa)
[107]	n/a	Crushed block	260-330	$6.66 \cdot 10^{-3}$ to 0.1
[111]	n/a	Crushed ingot	240-500	$6.8 \cdot 10^{-2}$ and $6.6 \cdot 10^{-3}$
[110]	n/a	Block	325-600	$6.66 \cdot 10^{-4}$ to 0.09
[113]	Linear	Block	350-1000	0.1
[114]	Linear	Block	550-800	$1.33 \cdot 10^{-3}$ to 0.1
[115]	Parabolic	Block	60-160	$3.99 \cdot 10^{-3}$
[116]	Linear	Block	500-800	$1.33 \cdot 10^{-2}$ to 0.1
[111]	n/a	“aged” Arc-melted and sintered ingot	250-400	$7 \cdot 10^{-2}$
[117]	Linear	Single crystal	700-2025	$1.33 \cdot 10^{-7}$ to $1.33 \cdot 10^{-9}$
[118]	Linear	Single crystal	900-1000	$1.33 \cdot 10^{-8}$
[107]	n/a	Single crystal	400	n/a
[119]	n/a	Powder	140-230	n/a
[120]	Linear	Powder	300-700	$6.66 \cdot 10^{-4}$ to $1.33 \cdot 10^{-3}$

A lightly crushed arc-melted sample — tested between 260-330 °C under various oxygen partial pressures — was also reported to react slowly even at 330 °C, finding only traces of UC remaining along with a uranium oxycarbide ( $\text{UO}_{3.57}\text{C}_{0.29}$ ) [107]. Another UC oxidation study on crushed ingots performed at  $6.8 \cdot 10^{-2}$  and  $6.6 \cdot 10^{-3}$  MPa partial pressures of oxygen resulted in reaction products of  $\text{U}_3\text{O}_8$  [111]. It was noted that ignition did not occur until the oxidation had proceeded to 20% completion and the temperature reached 365 °C, although this was also noted to be likely due to a particle size effect [111]. More recently, two studies investigated the mechanism of UC oxidation in air or

oxygen for sintered UC fragments [99, 121]. No synthesis or fabrication method is listed but it is noted that the UC samples came from Commissariat à l’Energie Atomique (manufactured in 2013) and from Dounreay legacy fuel (approximately 50 years old). Samples oxidized to  $UO_2$  then to  $U_3O_8$  at 450-575 °C in 10-100 Pa  $O_2$ . At 450 °C in  $\leq 25$  Pa  $O_2$  the product was  $UO_{2+x}$ , detailing a three-step oxidation pathway, similar to pure U oxidation, which is summarized by equations 1-3 listed below. The initial step includes oxidation of the surface of UC particles, followed by an expansion which includes crack formation and propagation which then stabilizes, suggesting the propagation has concluded [121].



The authors noted that reactions 1 and 2 are simultaneous, but reaction 3 is believed to happen only when all of the available carbon has oxidized to  $CO_2$ . They also investigated how the ignition temperature of UC (proposed reaction given in equation 4) is strongly correlated to temperature and oxygen partial pressure. The other oxidation pathway proposed was based on UC fragment samples which show the nature of the ignition reaction — namely area expansion as soon as oxygen is introduced where crack propagation and crack length correspond to an exponential law. Crack propagation then proceeds in a network fashion and fragments the oxide layer which is followed by an “explosive” reaction. A sample isothermally oxidized at 450 °C and partial pressure of 50 Pa  $O_2$  (**Figure C.9**) results in the ignition of UC, which occurred within the 17 minute +

15 second scanning time frame after oxygen insertion. Another sample isothermally oxidized at 575 °C and partial pressure of 10 Pa O<sub>2</sub> is seen in **Figure C.10a-h**. These images follow the ignition progression which began within 16 minutes of oxygen insertion. There was a highly energetic oxidation pathway after the initial sample expansion and crack formation the authors attributed to UO<sub>2</sub> oxidizing to U<sub>3</sub>O<sub>8</sub> [121]. Further oxidation work of UC at higher temperatures by Gasparrini *et al.* reported on the characterization of the cracking and spalled oxide; it was noted that the oxidation reaction for UC is also influenced by the nature of the adherent oxide layer (whether it is UO<sub>2</sub> or U<sub>3</sub>O<sub>8</sub> and its thickness) which can affect the reaction rate [99]. Examinations were made via high temperature environmental scanning electron microscopy (HT-ESEM) during 10 Pa O<sub>2</sub> and 50 Pa of air exposure from 600-900 °C and compared to samples oxidized in air at the same temperatures in a muffle furnace [99]. Oxidation was found to occur more rapidly at 600 °C, with samples pulverizing homogeneously and forming an oxide powder. The samples oxidized at 700 °C or 800 °C only pulverized around the edges and freshly cracked surfaces due to the denser nature of the resulting oxide layer, slowing the oxidation reaction. The authors reported that the final reaction product for the furnace samples was U<sub>3</sub>O<sub>8</sub>, while for the HT-SEM samples it was UO<sub>2</sub> or UO<sub>2+x</sub> which they attributed to the lower oxygen partial pressure [99].

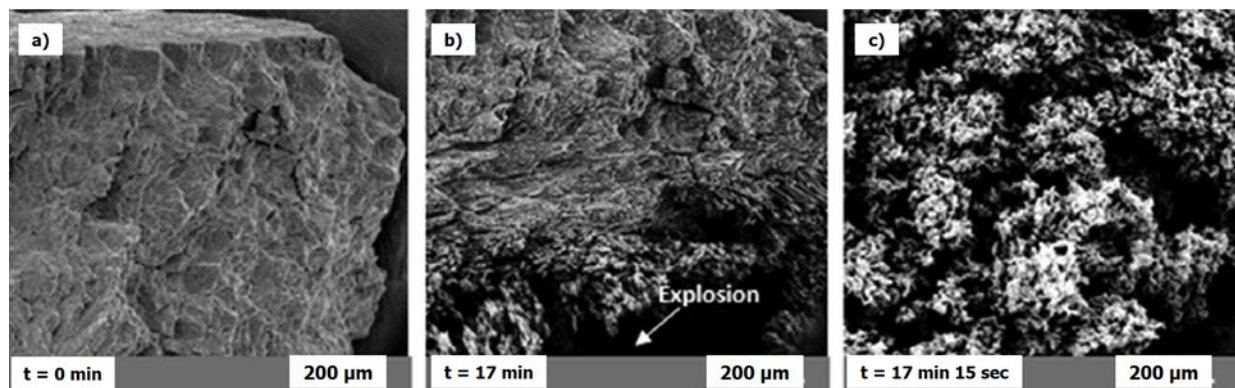


**Figure C.9** In-situ oxidation of a UC fragment at 450 °C and partial pressure of 50 Pa O<sub>2</sub> a) just after oxygen insertion, b) 17 minutes after oxygen insertion showing explosive expansion of the sample which occurred during the scanning time frame, and c) 15 seconds after image b) was taken showing the expanded sample surface.

Modified from Gasparrini et al. [121].

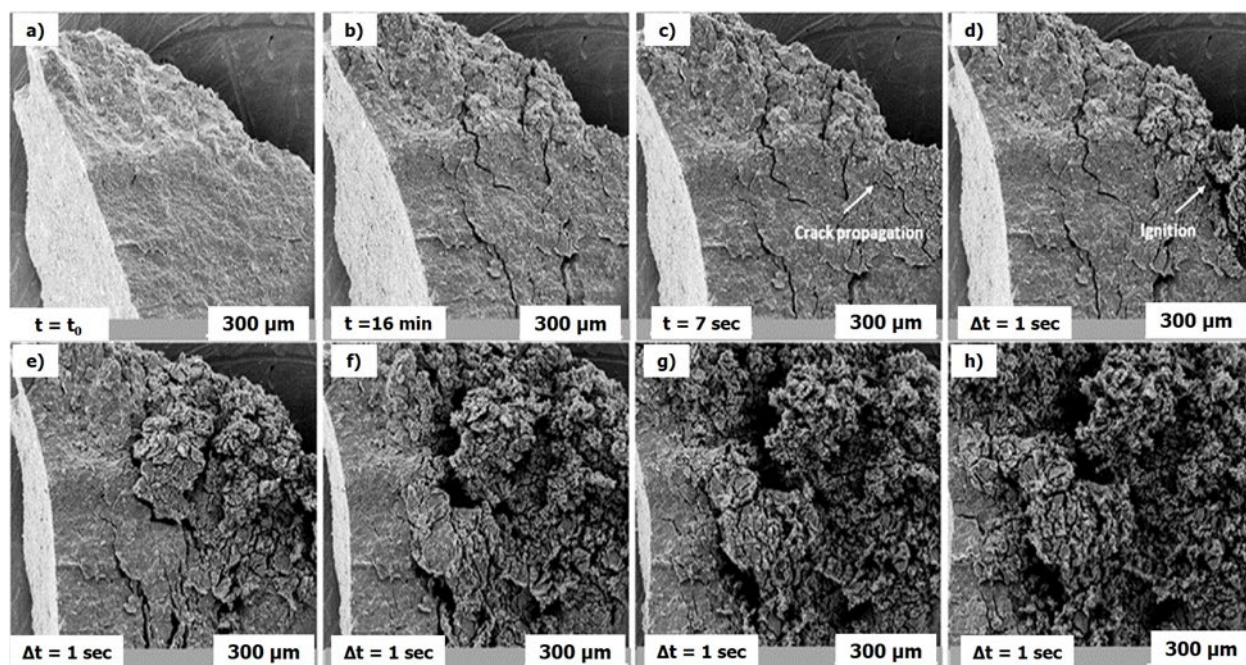


**Figure C.10** UC fragment oxidized at 575 °C under a partial pressure of 10 Pa O<sub>2</sub>, a) just after oxygen introduction, b) 16 min after O<sub>2</sub> exposure, c) 16 min + 7 sec after O<sub>2</sub> exposure showing crack propagation at top right corner, d-h) secondary electron images starting at 16 min + 8 seconds and taken every 1 second thereafter as the sample ignition progresses, clear volume expansion is evident. Modified from Gasparrini et al. [121].

Thermogravimetric analysis of UC powders (produced by arc-melting of elemental uranium and carbon) in a dry air flow rate of 2 L/hr showed an initial onset of

oxidation at 140 °C, with another exothermic reaction at approximately 175 °C, and a major exothermic reaction peak occurring at 202.3 °C corresponding to an ignition event [122]. It was noted that there remained some unreacted UC (up to 275 °C), while reaction products were an oxygen saturated oxycarbide solid solution,  $\text{UO}_2$ , and  $\text{U}_3\text{O}_8$  was the final oxidation product. Ignition only occurred after the initial  $\text{UO}_2$  layer reached a critical thickness and cracked allowing fresh surfaces for rapid oxygen ingress [122].

UC powders obtained from carbothermic reduction were examined in isothermal conditions ranging from 400-1400 °C in various oxygen partial pressures, also resulting in oxidation products of sub-stoichiometric UC,  $\text{UO}_2$ ,  $\text{U}_3\text{O}_8$ , as well as uranium oxycarbides [112]. Reported oxidation rates were linear for all cases in the initial stages of oxidation up to 800 °C (up to approximately 10% mass gain). The authors suggest that the surface reaction should be proportional to the surface area, and as the reaction is linear in this initial regime (~ 10%), the reaction is likely controlled by surface processes. The formation of  $\text{UO}_2$  (weight increase of 8.0%) results in free carbon which reacts simultaneously with oxygen to form carbon monoxide, which is thought to be the rate limiting mechanism. The results (shown for UC powder in 1.1 kPa oxygen partial pressure in **Figure C.11**) show that after this initial stage, the reaction rates transition to parabolic behavior until the final reaction product,  $\text{U}_3\text{O}_8$ , is formed, resulting in a plateau in the mass gain (at 12.3% mass increase), which does not occur until all the free carbon is consumed [112]. These reaction products are similar to those reported UC powder oxidation at 140-230 °C in oxygen (partial pressure not listed) [119].

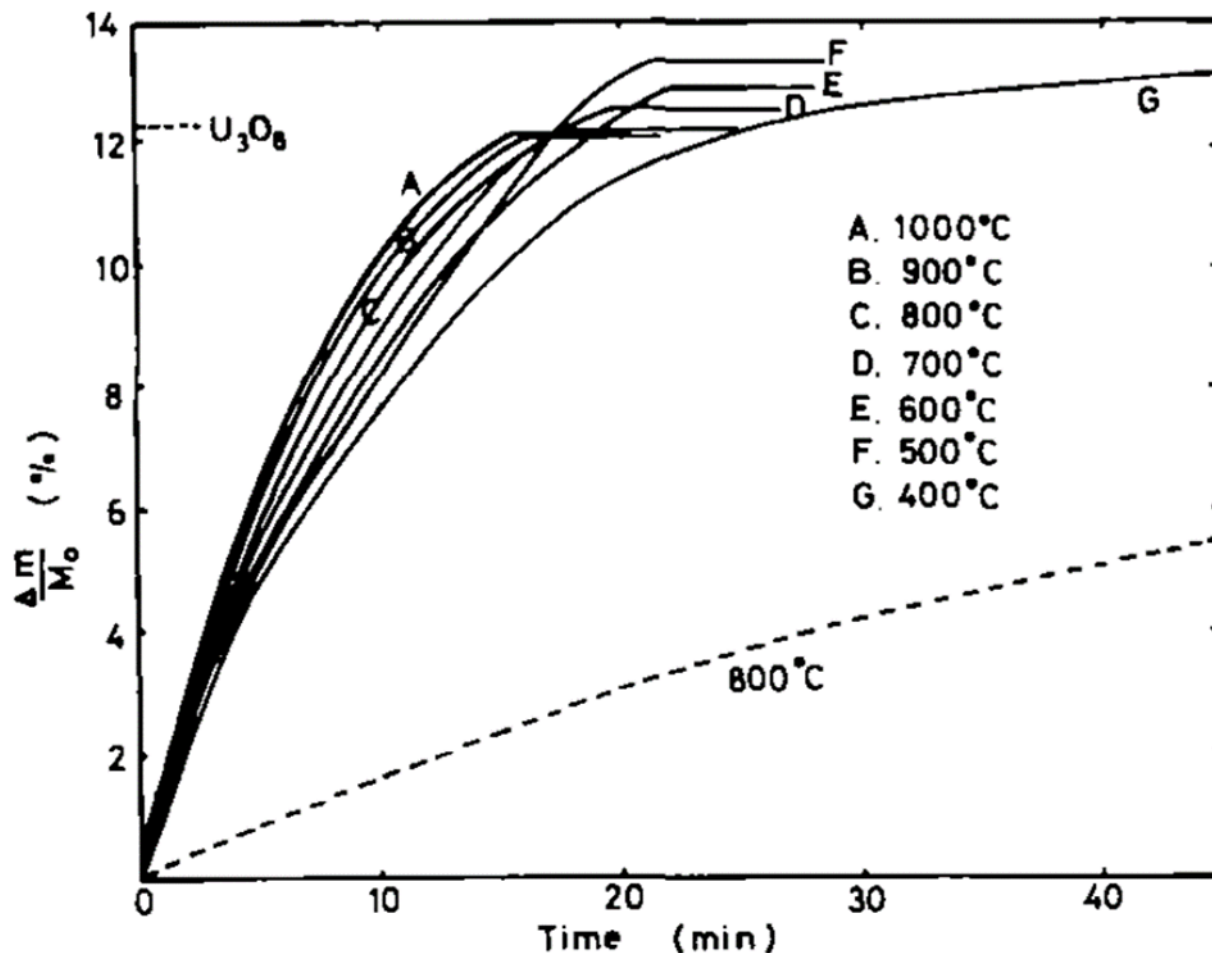


Figure C.11 Mass gain v. time for UC powders isothermally oxidized in 1.1 kPa oxygen partial pressure. Solid and dotted lines denote gas flow rates of 5.7 cm/sec and 0.04 cm/sec, respectively. From Naito et. al. [112].

In addition to the previously discussed work, the oxidation reaction of UC microspheres (prepared by an internal gelation process) has been reported. Oxidation of UC under various partial pressures of oxygen (1-30 kPa), different heating rates (1-10 °C/min), and various sample weights (12-200 mg) influenced the oxidation of bulk UC microspheres [106]. The authors found that the onset of oxidation occurred at 261 °C in 1 kPa O<sub>2</sub> partial pressure, 200 °C in 20 kPa O<sub>2</sub> partial pressure, and 217 °C in 30 kPa O<sub>2</sub> partial pressure. The reaction completion temperature increased as heating rates and sample sizes increased [106]. Similar to the above studies, reaction products were an

intermediate  $\text{UO}_2$  with the final product being  $\text{U}_3\text{O}_8$ . They also noted all the oxide products contained free carbon but the amount of carbon decreased with increasing oxygen partial pressures [106]. Pyrophoricity of UC powders (fabricated through arc-melting of uranium metal with graphite) in dry synthetic air was examined during DSC and TGA ramp testing from 170-500 °C. The ignition temperatures and reaction products are summarized in **Table C.4** [100]. Tests were interrupted at various temperatures (denoted as the “shut down temperature” in **Table C.4**) in order to identify any intermediate phases via XRD analysis. The authors attributed the difference in ignition temperatures of the samples to the differences in the crucible geometries between the DSC (low-walled and wide opening) and TGA (high-wall and narrow opening) instruments used in testing with the DSC crucible configuration being more favorable for oxygen introduction [100].

**Table C.4 Ignition temperatures and reaction products from ramp tests of UC powders oxidized in synthetic air from DSC and TGA testing. Modified from Berthinier et al. [100].**

Shut down temperature [°C]	Ignition temperature [°C]	Phases identified via XRD
DSC		
170	n/a	UC
200	195	UC, U <sub>3</sub> O <sub>8</sub> , UO <sub>2+x</sub> , and U <sub>3</sub> O <sub>7</sub>
250	187	U <sub>3</sub> O <sub>8</sub> , UO <sub>2+x</sub> , U <sub>3</sub> O <sub>7</sub> , and possibly residual UC at the core
390	203	U <sub>3</sub> O <sub>8</sub> , UO <sub>2+x</sub> , and U <sub>3</sub> O <sub>7</sub>
430	170	U <sub>3</sub> O <sub>8</sub>
500	223	U <sub>3</sub> O <sub>8</sub>
TGA		
200	n/a	UC
300	240	UC, UO <sub>2+x</sub> , and U <sub>3</sub> O <sub>7</sub>
380	237	UO <sub>2+x</sub> , U <sub>3</sub> O <sub>7</sub> , and U <sub>3</sub> O <sub>8</sub>
420	240	U <sub>3</sub> O <sub>8</sub>
500	252	U <sub>3</sub> O <sub>8</sub>

Isothermal TGA studies were also performed on crushed arc-melted UC at oxygen partial pressures of 3 kPa in a 97% N<sub>2</sub>-3%O<sub>2</sub> gas mixture and 21.3 kPa O<sub>2</sub> partial pressure in synthetic air at 100-235 °C finding only UC and UO<sub>2</sub> as an oxidation products per XRD analysis [96]. The authors noted that additional intermediate phases (C, U<sub>3</sub>O<sub>7</sub>, U<sub>4</sub>O<sub>9</sub>, U<sub>3</sub>O<sub>8</sub>) would be expected as was observed in previous investigations [100, 112, 119, 122]). The absence of these intermediate phases was attributed to the oxygen partial pressures used in this study being higher than the equilibrium thermodynamic oxygen partial pressures imposed by those phases, they were amorphous, or they were below the detection limit of the XRD system used [100]. Electron micrographs of the powders

oxidized in 21.3 kPa O<sub>2</sub> in synthetic air are shown in **Figure C.11a-c**. The morphology of the grains in the sample oxidized at 121.8 °C for 20 hours retained a similar appearance to that of the freshly milled UC powders (**Figure C.11a**) and the conversion to UO<sub>2</sub> + C was only 13%. The sample tested at 204 °C (**Figure C.11b**) was noted to be at nearly 94% conversion and resulted in grain fracturing and crack formation in the oxide layers (denoted by the black arrow in **Figure C.11b** and **c**). The sample tested at 234.6 °C (**Figure C.11c**) was reported to be at 97% conversion with all particles being fractured. This fracturing and fragmentation is caused by the stress induced from the oxide growth and the volumetric expansion occurring during conversion to UO<sub>2</sub> containing C [96].

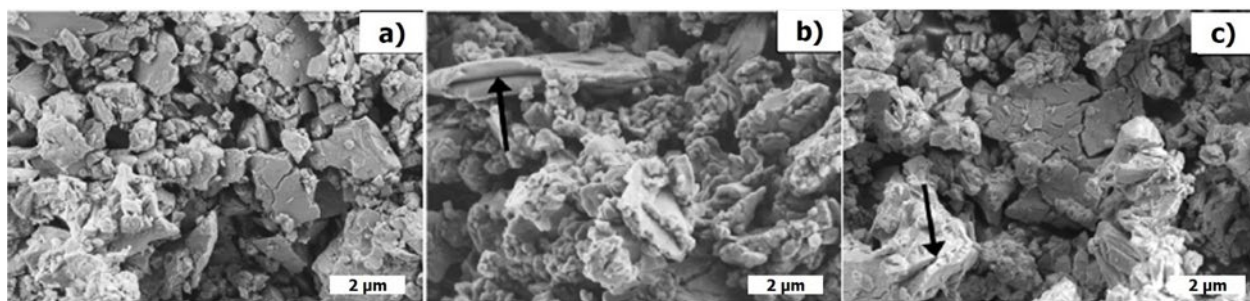
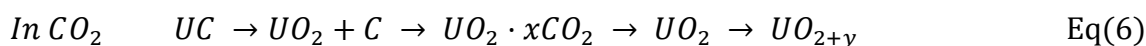
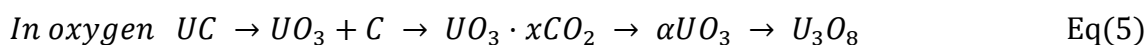


**Figure C.12** UC powder samples after isothermal testing at 21.3 kPa O<sub>2</sub> in synthetic air; a) 121.8 °C for 20 hours, b) 204 °C for 20 hours, and c) 234.6 °C for 5 hours. Modified from Berthinier et al. [96].

An additional publication on the oxidation of “fine” UC powder in dry oxygen and CO<sub>2</sub> offers an alternate proposed reaction pathway [108]. Accordingly, the authors suggest that the following product formations occur during the oxidation of UC in oxygen and CO<sub>2</sub> during a non-isothermal test up to 750 °C [108]:



Here, the oxidation in CO<sub>2</sub> more closely matches the other reported results for UC in air/oxygen, while the oxidation reaction by Van Tets [108] suggests formation of non-

stoichiometric carbonates ( $\text{UO}_3 \cdot x\text{CO}_2$ ), not  $\text{UO}_2$ ; likely due to the higher temperatures investigated. However, it should be noted that the previous studies for UC powder show that  $\text{U}_3\text{O}_8$  should be the terminal reaction product at  $750\text{ }^\circ\text{C}$  [96, 100, 112, 119, 122]. The author indicated that the O/U ratios were determined via a TGA reduction method and reaction products were identified using examination of infrared absorption spectrum. No information was provided on the synthesis or fabrication of the UC powder used in these experiments and it was noted that very small powder sample sizes (0.05 mg) were heated in cyclohexane and benzene slurries prior to the introduction of oxygen or  $\text{CO}_2$  to avoid any oxidation of the powders during experimental loading. Therefore, it is difficult to directly compare the oxidation results of this literature with those previously discussed. The consensus from the literature on UC oxidation, despite variations in fabrication methods, sample configuration, and testing parameters, is that the UC oxidation reaction shown in equations 1-4 are generally observed (except for the Van Tets study [108]). There is also a general agreement that the oxidation onset temperature is between  $200\text{-}250\text{ }^\circ\text{C}$  and reaction products include  $\text{UC}_{1-x}\text{O}_x$ ,  $\text{UO}_2$ ,  $\text{U}_3\text{O}_7$ ,  $\text{U}_4\text{O}_9$ , and  $\text{U}_3\text{O}_8$ .

#### C.4.2.2 Water corrosion of UC

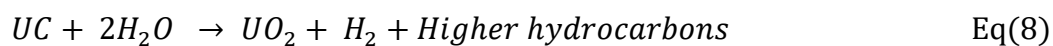
The uranium carbide compositions investigated in the open literature have ranged from hypo-/hyperstoichiometric UC [101],  $\text{U}_2\text{C}_3$  [123], to  $\text{UC}_2$  [123, 124]. The gas cooled/graphite moderated and water cooled/water moderated reactor types were proved viable in the early 1950's and pursued over the previously mentioned organic-cooled concepts. Most of the data that exists on water/steam corrosion for UC dates back to the 1950's through the 1970's. It may be that interest in UC for reactors at the time was not investigated further due to the abandonment of the organic-cooled reactor concept and the

successes of  $\text{UO}_2$ . It also is likely that due to UC's reported poor oxidation and hydrothermal corrosion behavior, extensive and more recent investigations on the hydrothermal corrosion of UC does not exist in the open literature. A thorough review of the hydrolysis of lanthanide and actinide carbides was performed in 1974 which summarized the state of the literature at the time; some of which are discussed in further detail below [125]. The consensus was that the early studies (prior to 1950) [126-128] of the reaction of uranium carbides with water was that the samples used, as well as the reaction products, were not well characterized and thus little consideration was given to them [125].

The investigations that have studied the effects hydrothermal corrosion of UC report similar results [89, 97, 101, 110, 123, 124, 129-134]. UC and  $\text{UC}_2$  monoliths (fabricated from arc-melted powder which was subsequently vacuum sintered) were tested in boiling water at atmospheric pressure for 1 hour [89]. It was noted that the disintegration of both samples was so rapid that it was not possible to determine which sample was more stable. The disintegrated material from both samples also oxidized rapidly after testing [89]. In another study while also investigating air oxidation, the degradation of UC in 20 mmHg water vapor was reported. Accordingly, the authors reported a mass gain rate of 0.05 mg/min-g at 400 °C, which rose to 0.44 mg/min-g at 460 °C [110]. Another sample heated to 600 °C initially gained mass quickly at 1.81 mg/min-g but then slowed to 0.17 mg/min-g, which was attributed to the second sample having approximately half the amount of initial material (as compared to the first sample) available for oxidation [110]. Gaseous products of the hydrolysis of arc-melted UC in 25-99 °C water were analyzed to find primarily  $\text{CH}_4$  and  $\text{H}_2$ ; which follows the UC-water

reactions in equations 7-10 listed below and is in good agreement with other studies examining gaseous reaction products from UC reaction with water [98, 101, 123, 132-135]. Others looked at hydrothermal corrosion of UC in water vapor from 53-164 °C and at 80 °C in H<sub>2</sub>SO<sub>4</sub>, and similar results to those found in the hydrolysis experiments were observed [97].

The UC-water reaction primarily proceeds as follows [97]:



In general, the investigators found that methane (CH<sub>4</sub>) was the primary byproduct during testing and hydrogen (H<sub>2</sub>) was the secondary while all the UC converted to UO<sub>2</sub> [136]. Both unirradiated and irradiated UC were examined in steam from 150-2500 °C and similarly reported that fresh UC fuel was more reactive at lower temperatures, while the irradiated fuel was less reactive up to 700 °C [137]. This corresponds to other work on neutron irradiated UC [138]. This is an important result due to the implications this could have on the behavior of fresh UC fuel that may be exposed to reactor coolant. The authors noted that at temperatures of 1400-2500 °C, the hydrolysis was much faster than at lower temperatures. This was explained by the change in the rate-limiting process, where at temperatures below 150 °C the reaction is limited by the steam decomposition on the sample surface into OH<sup>-</sup> and H<sup>+</sup> ions, whereas the higher temperature reactions are controlled by diffusion of the steam through the adherent oxide [137]. The authors

exposed the surface of a UC sample to steam at atmospheric pressure (flowed at the equivalent of 1-2 cm<sup>3</sup> of H<sub>2</sub>O/minute for an unspecified amount of time) at 2500 °C. The authors describe the corroded microstructure as a multi-layered reaction product where the outer layer (formed in later stages of the hydrolysis in steam) as UO<sub>2</sub>, an inner layer of UO<sub>2</sub> + C, and an inner region characterized as the unreacted molten interior [137]. The differences in reaction rates between the fresh and irradiated UC at lower temperatures was attributed to the formation of waxy, high molecular weight hydrocarbons. At higher temperatures these hydrocarbons oxidize to CO and CO<sub>2</sub> [137]. A compilation of the corrosion rates for the samples used in the above study are listed in **Table C.5**. It was noted these values were of limited quantitative validity due to the uncertainty in the actual surface area which changed rapidly [137]. These authors also noted another relevant study which found a parabolic reaction rate (no quantitative value for the rate was listed) of this secondary inner layer during UC corrosion in steam at 1000-1200 °C on a block sample at a partial pressure of oxygen of 3.13 kPa [129].

**Table C.5 Corrosion rates in steam of unirradiated and irradiated UC at various temperatures. Modified from Dyck and Taylor [137].**

Temperature (°C)	Corrosion Rates (mg/cm <sup>2</sup> h)		
	UC (unirradiated)	UC (irradiated - 81 MWh/kg)	UC (irradiated 400 MWh/kg)
150	550-1200	0.4-8	0.5
300	130-210	~2	~1
400	~12	2-8	~2
700	40-100	40-90	140-210
900	270-440	55-150	1900-5800
1400	~7000	-	-
1500	~9500	-	-
1600	13,000-15,000	-	11,000-15,000
1800	23,000-27,000	-	-
1900	40,000	-	-
2000	-	-	30,000-42,000
2100	~57,000	-	-
2500	53,000-63,000	-	-

The lack of extensive oxidation and hydrothermal corrosion testing on UC remains a gap in the open literature and an area of opportunity for research if UC is to be considered for use in water-cooled or advanced reactor concepts with a steam secondary cycle. Even if UC is not furthered as a candidate for future water-cooled use, its oxidation and corrosion behavior is important in terms of transportation and storage conditions should it remain an option for advanced reactor use.

### C.4.3 Additives or dopants to UC

To the best of the authors knowledge, investigations associated with the addition of additives or dopants to UC for the purposes of improving corrosion behavior are extremely limited. A published patent discusses improving the hydrolysis of UC by the addition of a uranium silicide ( $U_3Si_2$  or  $USi_2$ ), which the inventors state not only acts as a sintering aid, but precipitates upon cooling forming an adherent silicide layer completely enveloping the carbide [139]. They report that a compact of UC + (9.1-18.25wt%) $U_3Si_2$  compact survived a 4-hour immersion in boiling water, which is better than previously reported for pure UC in boiling water [89]. It is difficult to compare these results to the behavior of pure  $U_3Si_2$  as this test was shorter and at a lower temperature than reported  $U_3Si_2$  water/steam corrosion experiments [13]. It should be noted that the specifics on the composition and sintering parameters for the sample that survived this corrosion testing is unclear [140]. Other studies have been conducted on coatings, sintering aids, and dopant additions to UC for purposes other than hindering corrosion behavior. Advanced high temperature reactor concepts have considered both ZrC and SiC coatings [141-143] as fission product diffusion barriers for TRISO fuel, but not for monolithic UC, as well as for the purposes of gettering oxygen or as an inert matrix material. Other uranium bearing alloys ( $UAl_2$ ,  $UBe_{13}$ ), as well as the aforementioned  $U_3Si_2$ , have been investigated as sintering aids to UC consolidation; all of which could be eliminated from the matrix with further processing during fabrication so as to not affect fuel performance [139, 140]. Other sintering aids for UC reported in literature include Fe, Cu [144], and Ni [144-146], where the studies involving nickel reported secondary phase formations. Similarly, additions of Mo, Nb, Rh, W, Y, [147] and Zr [148, 149] were used to investigate ternary

phase relationships with UC. Interest in mixed carbides for fast breeder reactors prompted a thermodynamic assessment of ternary systems for uranium carbides, plutonium carbides, and mixed carbide systems ( $U_{1-x}Pu_x$ )C ( $0 < x < 0.2$ ) which included alkali and alkaline earth metals, transition metals including the lanthanides and actinides, and metals and non-metals of the B groups [150]. Dopants to UC have also been used to observe the effect they have on U self-diffusion in UC [151-154] as uranium mobility can affect creep, grain growth, fuel restructuring and actinide redistribution, important factors for any nuclear fuel, not just ATFs [151].

Interestingly, an assumption of impurity dopants in UC forming their respective metal monocarbide is assumed. This is thermodynamically predicted for many potential additives in UC. As seen in the Ellingham-type plot for carbide formation, several of the potential dopants or additives into UC would preferentially form their respective carbide phase over the UC reaction, which may result in UC dissociation and the subsequent formation of an undesirable liquid uranium phase at higher temperatures (**Figure C.13**). Nickel carbide was not included in the figure as it is not thermodynamically predicted as a spontaneous reaction (having a positive change in the Gibbs free energy).

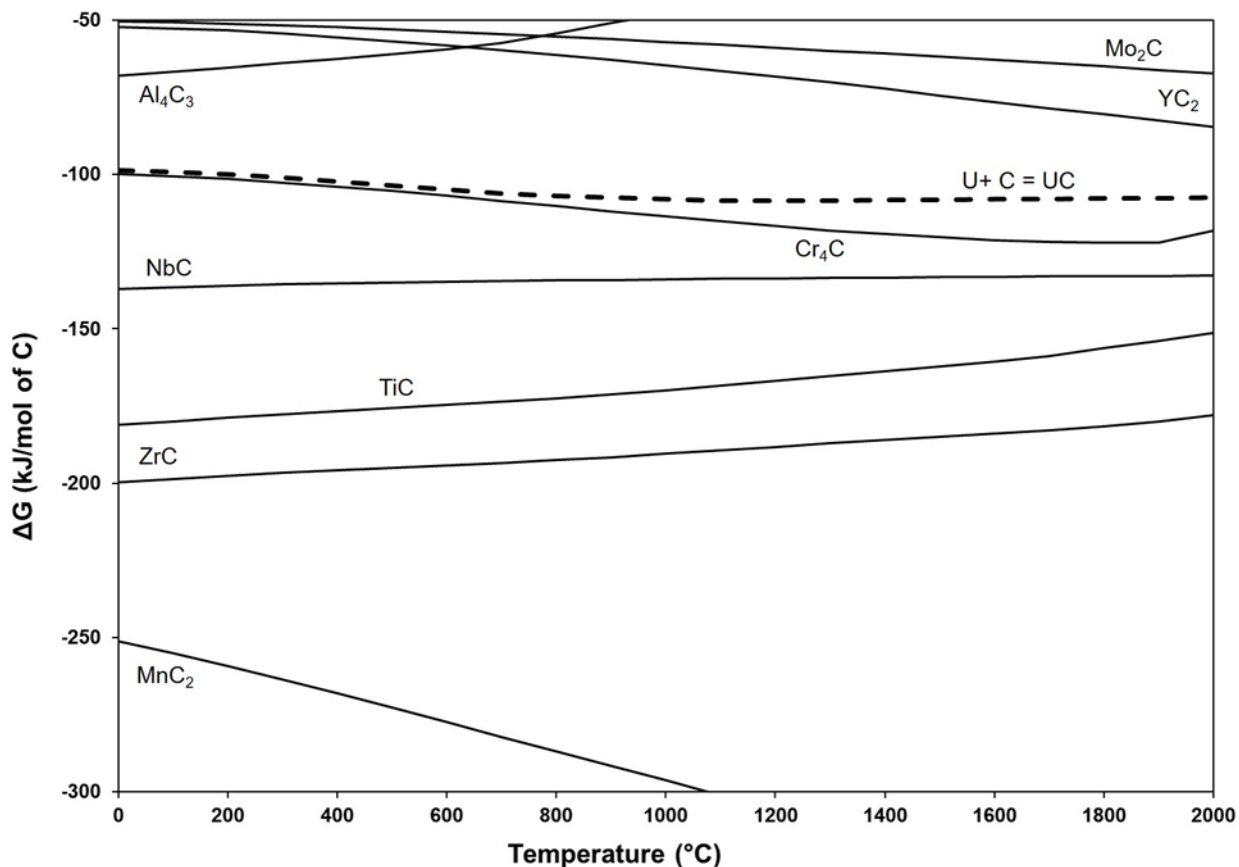


**Figure C.13** Ellingham-type diagram showing thermodynamic stability of carbide formation of various metallic elements considered for possible dopants into ATF concepts versus UC (normalized to 1 mol of C). Calculated using HSC Chemistry 9 [93]. Note: For nickel, the formation of the carbide is not favored and thus was not included in this plot.

#### C.4.4 Summary of UC

Although the literature suggests that UC has a higher propensity for oxidation and corrosion than other high uranium density fuels examined in previous publications [12, 13], a systematic investigation using modern techniques and equipment to provide an accurate comparison is warranted. Further screening experiments, either with pressurized water or steam, which correlate to the most relevant atmospheric conditions for assessing the oxidation/hydrolysis of potential ATF candidates remain an area of exploration for UC. Fabrication and corrosion testing of UC composites would fill a gap in the literature

as the ability to create UC composites that do not contain unwanted secondary phases remains elusive — and no peer-reviewed literature has been presented which addresses UC composites for improved hydrothermal corrosion resistance.

### **C.5 Summary of the review of high density fuels for water cooled reactors**

The challenges to ready any of the high uranium density fuels reviewed for replacements to the benchmark  $\text{UO}_2$  fuel for use in LWRs include fabrication and oxidation performance. Significant and continued research on materials development to improve corrosion resistance is necessary to move these fuels forward for performance to match or exceed that of  $\text{UO}_2$ . As a summary of available literature, **Figure C.14** shows a collection of the onsets of oxidation in air, oxygen, and steam for the  $\text{UB}_2$  and UC high density fuel samples from the reviewed literature. The air/oxygen tested samples are shown in solid blue (UC) and solid red ( $\text{UB}_2$ ). The references for the onset of UC oxidation [106, 122] show that UC has a lower onset than  $\text{UO}_2$ . Only one  $\text{UB}_2$  sample has been tested for air oxidation also exhibiting a lower onset temperature than  $\text{UO}_2$  [89].  $\text{UO}_2$  was shown to sustain in the steam environment at 1000 °C with a mass gain of less than 0.1% [155] and therefore the onset would be over 1000 °C. Onset temperatures of the high density fuel samples tested in water/steam are denoted by the blue and red hash pattern for UC and  $\text{UB}_2$  samples, respectively (**Figure C.14**), showing onsets far below 1000 °C. Only two onset temperatures for  $\text{UB}_2$  in steam were reported: The pure  $\text{UB}_2$  sample at 629 °C is currently the highest onset temperature for all steam tested high density samples [85]. The reviewed literature for UC mainly discusses the reaction rates, products formed, and reaction mechanisms in water vapor which contained various stoichiometry but very little data exists on the oxidation (or ignition) onset temperatures.

However, during air oxidation studies, Murbach also investigated the oxidation of UC in water vapor indicating a mass gain at 460 °C [110]. UC is still likely to find promise as a high temperature reactor fuel, notably for proposed small modular reactor types or fast breeder reactors [14]; however, its known pyrophoricity and production of flammable gases under low temperature oxidation and hydrolysis mean that issues with safety and security still exist in terms of synthesis, reprocessing, transport, and storage. The experiments vary in several ways: differences in testing environments (i.e. different O<sub>2</sub> partial pressures used during oxidation), sample fabrication methods, and different additives and amounts of additive. Due to the limited dataset, a determination cannot be made as to whether or not these fuels could outperform UO<sub>2</sub> in hydrothermal corrosion conditions. Another important consideration is the influence of irradiation effects on corrosion behavior, and testing exposure to radiolytic conditions for ATF concepts remains a gap in the open literature.

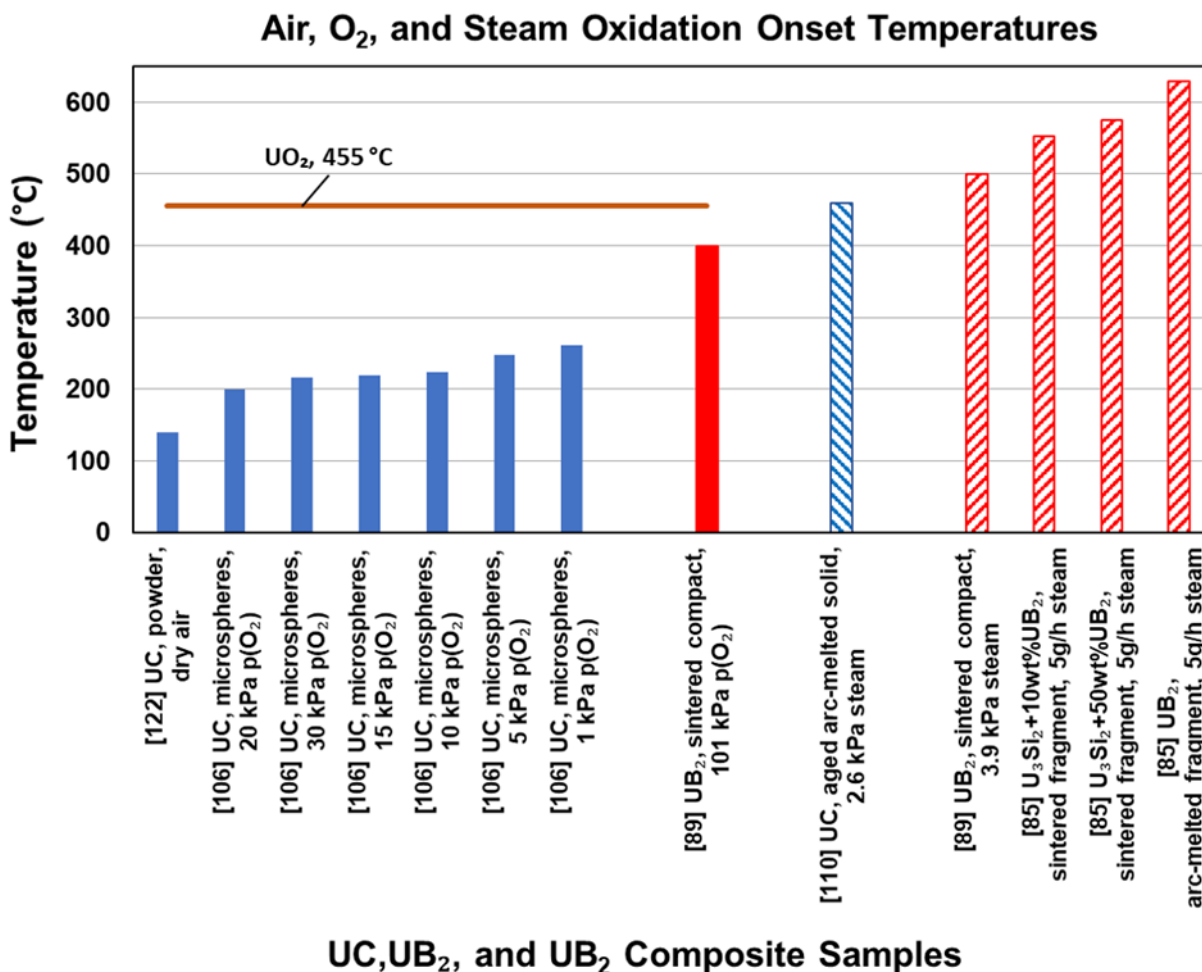


**Figure C.14** Summary plot of air/O<sub>2</sub> oxidation and steam corrosion onset temperatures for UC, UB<sub>2</sub>, and UB<sub>2</sub> composites. Samples oxidized in air/oxygen are shown in solid blue for UC and solid red for UB<sub>2</sub>. Samples oxidized in steam are denoted by a blue hash pattern for UC, and a red hash pattern for UB<sub>2</sub>.

### C.6 Research Needs

As outlined from the above literature, further work is needed to identify a suitable additive, dopant, or composite architecture to high uranium density fuels which will protect the fuel matrix from degradation in oxidative or corrosive conditions typical of coolant ingress. Additional work to investigate water or steam corrosion of the fuels in conditions that more closely mirrors LWR coolant chemistry should be completed. Identifying a synthesis and fabrication route that is not only scalable and economical, but

that achieves high densification, and can incorporate possible dopants without unwanted secondary phases, is also an area which needs further exploration. How these high uranium density fuels oxidation and corrosion behavior is affected by irradiation and fission product formation is also an area for further exploration as fresh fuel is less likely to be exposed to reactor coolant. As noted above, irradiated UC exhibited superior oxidation performance over fresh fuel whereas many of the experiments discussed used as-sintered/as-cast/as-fabricated samples for corrosion testing. The behavior of as-processed fuel is also important to note, and processes that fresh fuel pellets typically undergo (grinding, annealing, etc.) may also affect their corrosion behavior.

The literature also suggests that due to the higher reactivity of UC (as compared to the other high-uranium density fuels) it may be unlikely that it will be pursued as a LWR fuel. Given the extremely limited literature on  $UB_2$ , many research opportunities remain for it not only as a stand-alone high uranium density fuel, but also for incorporation as an additive for various purposes (i.e. higher thermal conductivity and corrosion resistance). Another area for research is to investigate how other traditionally used burnable absorbers ( $Gd_2O_3$ ,  $Er_2O_3$ , and  $B_4C$ ) [156] affect the corrosion behavior of any of the aforementioned high uranium density fuels (UN,  $U_3Si_2$ , and UC).

The benefits gained from resolving this complex research problem remains high when viewed from a safety, economical, and non-proliferation standpoint. The ability to achieve extended burn-up of LWR fuel due to the increased metal atom loading of these high uranium density fuels provides many benefits [1-6]. Economic advantages come through fewer refueling outages and fuel cycle costs, as well as a decrease in the amount of discharged spent fuel, which has implications for safety and non-proliferation [6]. The

additional safety margins provided with the use of these ATF candidates, as compared to  $\text{UO}_2$ , by their increased thermal conductivity is another driving factor to solve the challenges these fuels present in regard to oxidation performance. The thermal transport benefits of these fuels such as reduced fuel centerline temperatures, increased power to melt margins, and improved rate of heat transfer to advanced cladding materials should result in less fuel failures and provide more efficient reactor operations, both of which impact plant economics and safety.

### **Acknowledgements**

Work at the collaborating institutions, including Westinghouse Electric Company, was supported by the U.S. Department of Energy, Office of Nuclear Energy under DOE Idaho Operations Office Contract DE-NE0008824 funding opportunity. Accordingly, the U.S. Government retains and the publisher, by accepting the article for publication, acknowledges that the U.S. Government retains a nonexclusive, paid-up, irrevocable, worldwide license to publish or reproduce the published form of this manuscript or allow others to do so, for U.S. Government purposes. Additional funding for student and faculty support was provided by the U.S. NRC Grant number 31310018M0046 and NNSA MSIPP CONNECT program, Grant Number DE-NA0003948. All work performed at Idaho National Laboratory was conducted under the prime contract: DE-AC07-05ID14517.

This information was prepared as an account of work sponsored by an agency of the U.S. Government. Neither the U.S. Government nor any agency thereof, nor any of their employees, makes any warranty, express or implied, or assumes any legal liability or responsibility for the accuracy, completeness, or usefulness of any information,

apparatus, product, or process disclosed, or represents that its use would not infringe privately owned rights. References herein to any specific commercial product, process, or service by trade name, trademark, manufacturer, or otherwise, does not necessarily constitute or imply its endorsement, recommendation, or favoring by the U.S. Government or any agency thereof. The views and opinions of authors expressed herein do not necessarily state or reflect those of the U.S. Government or any agency thereof.

### References

- [1] P. Lyons, B. Crowell, Development of light water reactor fuels with enhanced accident tolerance, Report to Congress, United States Department of Energy, Washington, DC, 2015.
- [2] S. Bragg-Sitton, Development of advanced accident-tolerant fuels for commercial LWRs, *Nuclear News* 57(3) (2014) 83.
- [3] S.J. Zinkle, K.A. Terrani, J.C. Gehin, L.J. Ott, L.L. Snead, Accident tolerant fuels for LWRs: A perspective, *Journal of Nuclear Materials* 448(1) (2014) 374-379.
- [4] F. Goldner, Development strategy for advanced LWR fuels with enhanced accident tolerance, Enhanced Accident Tolerant LWR Fuels National Metrics Workshop, Germantown, MD, 2012.
- [5] D. Wachs, N. Woolstenhulme, Advanced fuel cycle technology: Special session in honor of Dr. Michael Lineberry, *Transactions of the American Nuclear Society* 110(INL/JOU-14-33095) (2014).
- [6] T. Wiss, V.V. Rondinella, R.J.M. Konings, D. Staicu, D. Papaioannou, S. Bremier, P. Pöml, O. Benes, J.-Y. Colle, P.V. Uffelen, A. Schubert, F. Cappia, M. Marchetti, D. Pizzocri, F. Jatuff, W. Goll, T. Sonoda, A. Sasahara, S. Kitajima, M. Kinoshita, Properties of the high burnup structure in nuclear light water reactor fuel, *Radiochimica Acta* 105(11) (2017) 893-906.
- [7] H. Matzke, Science of advanced LMFBR fuels, North-Holland Physics Publishing, Amsterdam, The Netherlands, 1986.

- [8] A. Tachis, W. Mathers, J. May, In-reactor thermal conductivity of uranium carbide, Atomic Energy of Canada Ltd., Pinawa (Manitoba). Whiteshell Nuclear Research ..., 1966.
- [9] A.T. Nelson, P. Demkowicz, Other power reactor fuels, *Advances in Nuclear Fuel Chemistry*, Elsevier2020, pp. 215-247.
- [10] D. Burns, S. Johnson, Nuclear Thermal Propulsion Reactor Materials, *Nuclear Materials*, IntechOpen2020.
- [11] N.D. Authority, Uranics: Credible Options Summary (Gate A), Ref: SMS/TS/B2-UR/002/A, NDA, Moor Row, 2014.
- [12] J.K. Watkins, A. Gonzales, A.R. Wagner, E.S. Sooby, B.J. Jaques, Challenges and opportunities to alloyed and composite fuel architectures to mitigate high uranium density fuel oxidation: Uranium mononitride, *Journal of Nuclear Materials* (2021) 153048.
- [13] A. Gonzales, J.K. Watkins, A.R. Wagner, B.J. Jaques, E.S. Sooby, Challenges and opportunities to alloyed and composite fuel architectures to mitigate high uranium density fuel oxidation: uranium silicide, *Journal of Nuclear Materials* (2021) 153026.
- [14] G. Vasudevamurthy, A.T. Nelson, Uranium Carbide Properties for Advanced Fuel Modeling – A Review, *Journal of Nuclear Materials* (2021) 153145.
- [15] H. Holleck, H. Kleykamp, *U Uranium: Uranium Carbides*, Springer Science & Business Media2013.
- [16] E.S. Wood, J.T. White, B. Jaques, D. Burkes, P. Demkowicz, Advances in fuel fabrication, *Advances in Nuclear Fuel Chemistry*, Elsevier2020, pp. 371-418.
- [17] M. Kato, Fuel Design and Fabrication: Pellet-Type Fuel, Reference Module in Earth Systems and Environmental Sciences, Elsevier2021.

- [18] L.J. Evitts, S.C. Middleburgh, E. Kardoulaki, I. Ipatova, M.J. Rushton, W. Lee, Influence of boron isotope ratio on the thermal conductivity of uranium diboride ( $UB_2$ ) and zirconium diboride ( $ZrB_2$ ), *Journal of Nuclear Materials* (2019) 151892.
- [19] E. Jossou, L. Malakkal, B. Szpunar, D. Oladimeji, J.A. Szpunar, A first principles study of the electronic structure, elastic and thermal properties of  $UB_2$ , *Journal of Nuclear Materials* 490 (2017) 41-48.
- [20] E. Jossou, D. Oladimeji, L. Malakkal, S. Middleburgh, B. Szpunar, J. Szpunar, First-principles study of defects and fission product behavior in uranium diboride, *Journal of Nuclear Materials* 494 (2017) 147-156.
- [21] P. Burr, E. Kardoulaki, R. Holmes, S. Middleburgh, Defect evolution in burnable absorber candidate material: Uranium diboride,  $UB_2$ , *Journal of Nuclear Materials* 513 (2019) 45-55.
- [22] V.H. Mankad, P.K. Jha, Thermodynamic properties of nuclear material uranium carbide using density functional theory, *Journal of Thermal Analysis and Calorimetry* 124(1) (2016) 11-20.
- [23] B. Szpunar, J. Szpunar, Thermal conductivity of uranium nitride and carbide, *International Journal of Nuclear Energy* 2014 (2014).
- [24] M. Freyss, Ab initio Study of the Behavior of Point Defects and Volatile Elements in Uranium Carbide, (2008).
- [25] G.J. Youinou, R.S. Sen, Impact of accident-tolerant fuels and claddings on the overall fuel cycle: A preliminary systems analysis, *Nuclear Technology* 188 (2) (2014) 123-138.
- [26] J. Turner, F. Martini, J. Buckley, G. Phillips, S.C. Middleburgh, T.J. Abram, Synthesis of candidate advanced technology fuel: Uranium diboride ( $UB_2$ ) via carbo/borothermic reduction of  $UO_2$ , *Journal of Nuclear Materials* 540 (2020) 152388.

- [27] J.H. Kittel, B.R.T. Frost, J.P. Mustelier, K.Q. Bagley, G.C. Crittenden, J. Van Dievoet, History of fast reactor fuel development, *Journal of Nuclear Materials* 204 (1993) 1-13.
- [28] J.K. Fink, Thermophysical properties of uranium dioxide, *Journal of Nuclear Materials* 279(1) (2000) 1-18.
- [29] R. De Coninck, W. Van Lierde, A. Gijs, Uranium carbide: Thermal diffusivity, thermal conductivity and spectral emissivity at high temperatures, *Journal of Nuclear Materials* 57(1) (1975) 69-76.
- [30] S.L. Hayes, J.K. Thomas, K.L. Peddicord, Material property correlations for uranium mononitride: 1. physical properties, *Journal of Nuclear Materials* 171 (2-3) (1990) 262-270.
- [31] J.T. White, A.T. Nelson, J.T. Dunwoody, D.D. Byler, D.J. Safarik, K.J. McClellan, Thermophysical properties of  $U_3Si_2$  to 1773K, *Journal of Nuclear materials* 464 (2015) 275-280.
- [32] E. Kardoulaki, J. White, D. Byler, D. Frazer, A. Shivprasad, T. Saleh, B. Gong, T. Yao, J. Lian, K. McClellan, Thermophysical and mechanical property assessment of  $UB_2$  and  $UB_4$  sintered via spark plasma sintering, *Journal of Alloys and Compounds* (2019) 153216.
- [33] H. Okamoto, B-U (Boron-Uranium), *Binary Alloy Phase Diagrams II Edition* 1 (1990) 551-552.
- [34] U.C. Nunez, D. Prieur, R. Bohler, D. Manara, Melting point determination of uranium nitride and uranium plutonium nitride: A laser heating study, *Journal of Nuclear Materials* 449(1-3) (2014) 1-8.
- [35] N.R. Brown, M. Todosow, A. Cuadra, Screening of advanced cladding materials and UN- $U_3Si_5$  fuel, *Journal of Nuclear Materials* 462 (2015) 26-42.
- [36] Y. Yamamoto, B.A. Pint, K.A. Terrani, K.G. Field, Y. Yang, L.L. Snead, Development and property evaluation of nuclear grade wrought FeCrAl fuel cladding for light water reactors, *Journal of Nuclear Materials* 467 (2015) 703-716.

- [37] K.A. Terrani, Accident tolerant fuel cladding development: Promise, status, and challenges, *Journal of Nuclear Materials* 501 (2018) 13-30.
- [38] B.M.P.C. KAPL, *Nuclides and Isotopes: Chart of the Nuclides*, (2010).
- [39] F. Karlsruhe, *Inorganic Crystal Structure Database (ICSD)*, FIZ Karlsruhe, Germany.
- [40] *CRC Handbook of Chemistry and Physics*, in: J.R. Rumble (Ed.) CRC Press/Taylor & Francis, 2020.
- [41] A. Wilson, The thermal expansion of aluminium from 0 to 650 C, *Proceedings of the Physical Society* 53(3) (1941) 235.
- [42] Y.S. Touloukian, *Thermal conductivity: metallic elements and alloys*, IFI/Plenum, New York, 1970.
- [43] Y. Kurokawa, K. Utsumi, H. Takamizawa, T. Kamata, S. Noguchi, AlN Substrates with High Thermal Conductivity, *IEEE Transactions on Components, Hybrids, and Manufacturing Technology* 8(2) (1985) 247-252.
- [44] G.A. Slack, R.A. Tanzilli, R. Pohl, J. Vandersande, The intrinsic thermal conductivity of AlN, *Journal of Physics and Chemistry of Solids* 48(7) (1987) 641-647.
- [45] P. Hidnert, Thermal expansion of case and of swaged chromium, *Journal of Research of the National Bureau of Standards* (1941).
- [46] K. Yamamoto, T. Sato, E. Iwamura, Temperature dependence of thermal expansion coefficient and bi-axial modulus of arc-ion plated Tin, CrN, Cr<sub>2</sub>N and AlTiN coatings, *Journal of the Surface Finishing Society of Japan* 50(1) (1999) 52-57.
- [47] O. Jankovský, D. Sedmidubský, Š. Huber, P. Šimek, Z. Sofer, Synthesis, magnetic and transport properties of oxygen-free CrN ceramics, *Journal of the European Ceramic Society* 34(16) (2014) 4131-4136.

- [48] D.F. Susan, N.R. Sorensen, J.R. Michael, B.B. McKenzie, J. Christensen, C.A. Walker, S.L. Monroe, V. Den Avyle, Effects of austenitic stainless steel composition on pre-oxidation behavior and glass/metal bonding, Sandia National Lab.(SNL-NM), Albuquerque, NM (United States), 2008.
- [49] Y. Liao, Practical electron microscopy and database, Table 1828: Properties of Cr<sub>2</sub>O<sub>3</sub>, GlobalSino, 2006.
- [50] R.K. Kirby, T.A. Hahn, B.D. Rothrock, Thermal Expansion, American Institute of Physics Handbook 1972, pp. 119-142.
- [51] F. Nix, D. MacNair, The thermal expansion of pure metals: copper, gold, aluminum, nickel, and iron, Physical Review 60(8) (1941) 597.
- [52] C.Y. Ho, R. Powell, P. Liley, Thermal Conductivity of Selected Materials. Part II, National Standard Reference Data System, 1968.
- [53] F. Schmidt, H.R. Ogden, The engineering properties of columbium and columbium alloys, Defense Metals Information Center, Battelle Memorial Institute 1963.
- [54] O. Carlson, P. Chiotti, G. Murphy, D. Peterson, B. Rogers, J. Smith, M. Smutz, M. Voss, H. Wilhelm, The metallurgy of thorium and its alloys, Proceedings of the International Conference on the Peaceful Uses of Atomic Energy, 1956.
- [55] S.S. Parker, J.T. White, P. Hosemann, A.T. Nelson, Thermophysical properties of thorium mononitride from 298 to 1700 K, Journal of Nuclear Materials 526 (2019) 151760.
- [56] S.C. Weaver, An investigation of the thermal conductivity, electrical resistivity, and thermoelectric power of thorium nitride-uranium nitride alloys, (1972).
- [57] C.-H. Hsueh, C.R. Luttrell, T. Cui, Thermal stress analyses of multilayered films on substrates and cantilever beams for micro sensors and actuators, Journal of Micromechanics and Microengineering 16(11) (2006) 2509.

- [58] P.H. Klein, W.J. Croft, Thermal conductivity, diffusivity, and expansion of  $Y_2O_3$ ,  $Y_3Al_5O_{12}$ , and  $LaF_3$  in the range 77–300 K, *Journal of Applied Physics* 38(4) (1967) 1603-1607.
- [59] T. Baker, The coefficient of thermal expansion of zirconium nitride, *Acta Crystallographica* 11(4) (1958) 300-300.
- [60] J. Adachi, K. Kurosaki, M. Uno, S. Yamanaka, Thermal and electrical properties of zirconium nitride, *Journal of Alloys and Compounds* 399(1) (2005) 242-244.
- [61] H. Okamoto, Al-U (Aluminum-Uranium), *Journal of Phase Equilibria and Diffusion* 33(6) (2012) 489-490.
- [62] Z.-G. Mei, A.M. Yacout, First-principles study of structural, elastic, electronic, vibrational and thermodynamic properties of uranium aluminides, *Computational Materials Science* 158 (2019) 26-31.
- [63] Z.-G. Mei, Y.S. Kim, A.M. Yacout, J. Yang, X. Li, Y. Cao, First-principles study of thermal conductivities of uranium aluminides, *Materialia* 4 (2018) 449-456.
- [64] G. Beckman, R. Kiessling, Thermal Expansion Coefficients for Uranium Boride and  $\beta$ -Uranium Silicide, *Nature* 178(4546) (1956) 1341.
- [65] K. Matterson, H. Jones, A study of the tetraborides of uranium and thorium, *Trans. Brit. Ceram. Soc.* 60 (1961).
- [66] C. LLC, CINDAS LLC Thermophysical Properties of Matter Database (TPMD) Version 12, West Lafayette, IN, 2020.
- [67] W. Martienssen, H. Warlimont, *Springer handbook of condensed matter and materials data*, Springer Science & Business Media 2006.
- [68] L. Grande, B. Villamere, L. Allison, S. Mikhael, A. Rodriguez-Prado, I. Pioro, Thermal aspects of uranium carbide and uranium dicarbide fuels in supercritical water-cooled nuclear reactors, *Journal of Engineering for Gas Turbines and Power* 133(2) (2010).

- [69] K. Taylor, C. McMurtry, Synthesis and fabrication of refractory uranium compounds. Summary report for May 1959 through December 1960, Carborundum Co. Research and Development Div., Niagara Falls, NY, 1961.
- [70] S. Popov, J.J. Carbajo, G. Yoder, Thermophysical properties of MOX and UO<sub>2</sub> fuels including the effects of irradiation, Oak Ridge, TN, 2000.
- [71] H. Vaugoyeau, L. Lombard, J. Morlevat, A Contribution to the study of the Uranium-Silicon equilibrium diagram, Atomic Energy of Canada Ltd., 1972.
- [72] J. White, A. Nelson, J. Dunwoody, D. Byler, K. McClellan, Thermophysical properties of USi to 1673 K, *Journal of Nuclear Materials* 471 (2016) 129-135.
- [73] J. White, A. Nelson, D. Byler, D. Safarik, J. Dunwoody, K. McClellan, Thermophysical properties of U<sub>3</sub>Si<sub>5</sub> to 1773 K, *Journal of Nuclear Materials* 456 (2015) 442-448.
- [74] J. Turner, S. Middleburgh, T. Abram, A high density composite fuel with integrated burnable absorber: U<sub>3</sub>Si<sub>2</sub>-UB<sub>2</sub>, *Journal of Nuclear Materials* 529 (2020) 151891.
- [75] P.-Y. Chevalier, E. Fischer, Thermodynamic modelling of the C-U and B-U binary systems, *Journal of nuclear materials* 288(2-3) (2001) 100-129.
- [76] J.-P. Dancausse, E. Gering, S. Heathman, U. Benedict, L. Gerward, S.S. Olsen, F. Hulliger, Compression study of uranium borides UB<sub>2</sub>, UB<sub>4</sub> and UB<sub>12</sub> by synchrotron X-ray diffraction, *Journal of alloys and compounds* 189(2) (1992) 205-208.
- [77] G.A. Haas, J.T. Jensen Jr, Thermionic Studies of Various Uranium Compounds, *Journal of Applied Physics* 34(12) (1963) 3451-3457.
- [78] H. Flotow, D. Osborne, P. O'Hare, J. Settle, F. Mrazek, W. Hubbard, Uranium diboride: Preparation, enthalpy of formation at 298.15 K, heat capacity from 1 to 350 K, and some derived thermodynamic properties, *The Journal of Chemical Physics* 51(2) (1969) 583-592.

- [79] E. Yamamoto, T. Honma, Y. Haga, Y. Inada, D. Aoki, N. Suzuki, R. Settai, H. Sugawara, H. Sato, Y. Ōnuki, Electrical and Thermal Properties of  $UB_2$ , *Journal of the Physical Society of Japan* 68(3) (1999) 972-975.
- [80] D. Fredrickson, Enthalpy of uranium diboride from 600 to 1500 K by drop calorimetry, *HIGH TEMP SCI* 1(3) (1969) 373-380.
- [81] D. Fredrickson, R. Barnes, M. Chasanov, Enthalpy of uranium diboride from 1300 to 2300 K by drop calorimetry, *High Temperature Science* 2 (1970).
- [82] D. Frazer, B. Maiorov, U. Carvajal-Nuñez, J. Evans, E. Kardoulaki, J. Dunwoody, T.A. Saleh, J.T. White, High temperature mechanical properties of fluorite crystal structured materials ( $CeO_2$ ,  $ThO_2$ , and  $UO_2$ ) and advanced accident tolerant fuels ( $U_3Si_2$ , UN, and  $UB_2$ ), *Journal of Nuclear Materials* (2021) 153035.
- [83] L. Brewer, D.L. Sawyer, D. Templeton, C.H. Dauben, A study of the refractory borides, *Journal of the American Ceramic Society* 34(6) (1951) 173-179.
- [84] E. Kardoulaki, D.M. Frazer, J.T. White, U. Carvajal, A.T. Nelson, D.D. Byler, T.A. Saleh, B. Gong, T. Yao, J. Lian, K.J. McClellan, Fabrication and thermophysical properties of  $UO_2$ - $UB_2$  and  $UO_2$ - $UB_4$  composites sintered via spark plasma sintering, *Journal of Nuclear Materials* 544 (2021) 152690.
- [85] J. Turner, T. Abram, Steam performance of  $UB_2/U_3Si_2$  composite fuel pellets, compared to  $U_3Si_2$  reference behaviour, *Journal of Nuclear Materials* 529 (2020) 151919.
- [86] J. Andrieux, P. Blum, On the electrolytic preparation and properties of uranium borides, *Compt. rend.* 229 (1949).
- [87] A.S. Newton, J. Oliver, Preparation of compounds of uranium and nonmetals, Google Patents, 1950.
- [88] H. Hoekstra, J.J. Katz, The preparation and properties of the group IV-B metal borohydrides, *Journal of the American Chemical Society* 71(7) (1949) 2488-2492.
- [89] A.B. Tripler Jr, M.J. Snyder, W.H. Duckworth, Further Studies of Sintered Refractory Uranium Compounds, Battelle Memorial Inst., Columbus, Ohio, 1959.

- [90] S. Mašková, K. Miliyanchuk, L. Havela, Hydrogen absorption in  $U_3Si_2$  and its impact on electronic properties, *Journal of Nuclear Materials* 487 (2017) 418-423.
- [91] S. Middleburgh, A. Claisse, D. Andersson, R. Grimes, P. Olsson, S. Mašková, Solution of hydrogen in accident tolerant fuel candidate material:  $U_3Si_2$ , *Journal of Nuclear Materials* 501 (2018) 234-237.
- [92] A.P. Shivprasad, V. Kocevski, T.L. Ulrich, J.R. Wermer, D. Andersson, J.T. White, The  $U_3Si_2$ -H system, *Journal of Nuclear Materials* 558 (2022) 153278.
- [93] A. Roine, HSC Chemistry, Outotec, Pori, 2019.
- [94] P. Vozzella, A. Miller, M. DeCrescente, Dissociation Behavior of Uranium Monocarbide, *The Journal of Chemical Physics* 49(2) (1968) 876-881.
- [95] H. Okamoto, C-U (Carbon-Uranium, Binary Alloy Phase Diagrams II Edition 1 (1990) 892-893.
- [96] C. Berthinier, C. Rado, O. Dugne, M. Cabie, C. Chatillon, R. Boichot, E. Blanquet, Experimental kinetic study of oxidation of uranium monocarbide powders under controlled oxygen partial pressures below 230° C, *Journal of nuclear materials* 432(1-3) (2013) 505-519.
- [97] Y. Hori, T. Mukaibo, Kinetic study of the reaction between uranium monocarbide and water vapor, *Bulletin of the Chemical Society of Japan* 40(8) (1967) 1878-1883.
- [98] A. Schürenkämper, Kinetic studies of the hydrolysis of uranium monocarbide in the temperature range 30° C–90° C, *Journal of Inorganic and Nuclear Chemistry* 32(2) (1970) 417-429.
- [99] C. Gasparini, R. Podor, O. Fiquet, D. Horlait, S. May, M.R. Wenman, W.E. Lee, Uranium carbide oxidation from 873 K to 1173 K, *Corrosion Science* 151 (2019) 44-56.
- [100] C. Berthinier, S. Coullomb, C. Rado, E. Blanquet, R. Boichot, C. Chatillon, Experimental study of uranium carbide pyrophoricity, *Powder technology* 208(2) (2011) 312-317.

- [101] M.J. Bradley, L.M. Ferris, Hydrolysis of uranium carbides between 25 and 100°. I. Uranium monocarbide, *Inorganic Chemistry* 1(3) (1962) 683-687.
- [102] A.K. Sengupta, R. Agarwal, H.S. Kamath, 3.03 - Carbide Fuel, in: R.J.M. Konings (Ed.), *Comprehensive Nuclear Materials*, Elsevier, Oxford, 2012, pp. 55-86.
- [103] W.M. Phillips, W. Chubb, E.L. Foster, Direct casting of uranium monocarbide reactor fuel elements, *Journal of the Less Common Metals* 2(6) (1960) 451-457.
- [104] J. Williams, R.A.J. Sambell, The uranium monocarbide-uranium mononitride system, *Journal of the Less Common Metals* 1(3) (1959) 217-226.
- [105] S.K. Mukerjee, J.V. Dehadraya, V.N. Vaidya, D.D. Sood, Kinetic study of the carbothermic synthesis of uranium monocarbide microspheres, *Journal of Nuclear Materials* 172(1) (1990) 37-46.
- [106] S.K. Mukerjee, G.A.R. Rao, J.V. Dehadraya, V.N. Vaidya, V. Venugopal, D.D. Sood, The oxidation of uranium monocarbide microspheres, *Journal of Nuclear Materials* 210(1) (1994) 97-106.
- [107] R. Dell, V. Wheeler, E. McIver, Oxidation of uranium mononitride and uranium monocarbide, *Transactions of the Faraday Society* 62 (1966) 3591-3606.
- [108] A. Van Tets, Reaction of uranium monocarbide powder in oxidizing atmospheres, *Thermochimica Acta* 6(2) (1973) 195-203.
- [109] H. Matzke, Effect of humidity on the surface oxidation of UC single crystals at room temperature, *Journal of Applied Physics* 40(9) (1969) 3819-3824.
- [110] E. Murbach, The oxidation of "reactive" uranium carbide, *Atomics International* 1961.
- [111] R. Dell, V. Wheeler, The ignition of uranium mononitride and uranium monocarbide in oxygen, *Journal of Nuclear Materials* 21(3) (1967) 328-336.
- [112] K. Naito, N. Kamegashira, T. Kondo, S. Takeda, Isothermal oxidation of uranium monocarbide powder under controlled oxygen partial pressures, *Journal of Nuclear Science and Technology* 13(5) (1976) 260-267.

- [113] K. Peakall, J. Antill, Oxidation of uranium monocarbide, *Journal of the less common metals* 4(5) (1962) 426-435.
- [114] J. Besson, C. Moreau, J. Philippot, La reaction de loxygene pur sur le monocarbure duranium massif, *Comptes Rendus Hebdomadaires des Seances de L Academie Des Sciences* 258(16) (1964) 4079.
- [115] P. Camagni, A. Manara, E. Landais, Growth of oxide films onto cleavage faces of crystalline UC, *Surface Science* 10(3) (1968) 332-348.
- [116] B. Herrmann, F.-J. Herrmann, Oxidation of uranium monocarbide in dry or moist oxygen, CEA Grenoble, 1968.
- [117] G. Ervin Jr, *High Temperature Technology*, (1969).
- [118] G. Ervin, k.T. Miller, Oriented growth of oxidation products on single crystals of uranium monocarbide, *Acta Metallurgica* 14(2) (1966) 222-228.
- [119] R.G. Sowden, N. Hodge, M.J. Moreton-Smith, Gold as a heat dispersant in exothermic solid-gas reactions. Application to the oxidation of uranium monocarbide powder, *Transactions of the Faraday Society* 60(0) (1964) 759-762.
- [120] K. Sudo, M. Osawa, Behavior of uranium carbides at high temperatures. I. The oxidation of uranium monocarbide, Tohoku Univ., Sendai, 1967.
- [121] C. Gasparri, R. Podor, D. Horlait, M.J. Rushton, O. Fiquet, W.E. Lee, Oxidation of UC: an in situ high temperature environmental scanning electron microscopy study, *Journal of Nuclear Materials* 494 (2017) 127-137.
- [122] F. Le Guyadec, C. Rado, S. Joffre, S. Coullomb, C. Chatillon, E. Blanquet, Thermodynamic and experimental study of UC powders ignition, *Journal of Nuclear Materials* 393(2) (2009) 333-342.
- [123] C. Kempter, Hydrolysis properties of uranium monocarbide and dicarbide, *Journal of the Less Common Metals* 4(5) (1962) 419-425.
- [124] M.J. Bradley, L.M. Ferris, Hydrolysis of uranium carbides between 25 and 100°. II. Uranium dicarbide, uranium metal-monocarbide mixtures, and uranium monocarbide-dicarbide mixtures, *Inorganic Chemistry* 3(2) (1964) 189-195.

- [125] J. Griess Jr, Hydrolysis of lanthanide and actinide carbides: a survey of recent literature, Oak Ridge National Lab., Tenn.(USA), 1974.
- [126] H. Moissan, Etude du carbure d'uranium, *Compt. rend* 122 (1896) 274.
- [127] P. Lebeau, A. Damiens, Sur la composition des mélanges gazeux résultant de l'action de l'eau sur les carbures d'uranium et de thorium, *Comptes rendus de l'Académie des Sciences de Paris* 156 (1913) 1987.
- [128] L.M. Litz, Uranium carbides: their preparation, structure, and hydrolysis, Ohio State University, 1948.
- [129] C. Moreau, J. Philippot, Kinetics of the reaction of steam with uranium monocarbide at high temperature, *Compt. Rend.* 259 (1964).
- [130] Y. Hori, T. Mukaibo, Study on the Rate and the Products of the Reaction between Uranium Monocarbide and Water, *Journal of Nuclear Science and Technology* 4(9) (1967) 477-481.
- [131] Y. Hori, T. Mukaibo, Hydrolysis of Uranium Monocarbide and Oxidation Potentials, *Bulletin of the Chemical Society of Japan* 41(9) (1968) 1983-1989.
- [132] F.H. Pollard, G. Nickless, S. Evered, Chromatographic studies on hydrolysis of carbides Part 2. Hydrolysis of uranium carbides, *Journal of Chromatography* 15(2) (1964) 223-27.
- [133] G. Baudin, P. Blum, J. Spitz, J. Besson, L'Hydrolyse du Monocarbure d'uranium, *Comptes Rendus Hebdomadaires Des Seances De L Academie Des Sciences* 254(24) (1962) 4179-81.
- [134] L. Colby Jr, Kinetics of the reaction of uranium monocarbide with water, *Journal of the Less Common Metals* 10(6) (1966) 425-431.
- [135] A. Benadik, Benadiko.H, Reaction of uranium monocarbide and uranium carbonitrides with water, *Collect. Czech. Chem. Commun.* 35(3) (1970) 915-22.

- [136] R. Dyck, D. Boase, A. Gerwing, A Study of the Hydrolysis of Uranium Monocarbide: Part III, Radioiodine Species Formed During the Hydrolysis of Irradiated Uranium Carbide with Water, Whiteshell Nuclear Research Establishment 1975.
- [137] R. Dyck, R. Taylor, D. Boase, A study of the hydrolysis of uranium monocarbide Pt. 1: reactions in steam in the temperature range 150 degrees C to 2500 degrees C, Atomic Energy of Canada Ltd., 1975.
- [138] S. Evered, Moretons.Mj, R.G. Sowden, Hydrolysis of neutron-irradiated uranium and uranium-plutonium monocarbides, *Journal of Inorganic & Nuclear Chemistry* 27(8) (1965) 1867-68.
- [139] J.P. Hammond, G.M. Adamson, Activated sintering of uranium monocarbide, in: H.H. Hausner (Ed.), *Modern Developments in Powder Metallurgy*, Springer, Boston, MA, 1966.
- [140] J.P. Hammond, J.D. Sease, Method for improving hydrolysis resistance of uranium carbide containing composition, Google Patents, 1964.
- [141] P. Wagner, High-temperature fuel technology for nuclear process heat: ZrC-containing coated particle fuels and high-density graphite fuel matrices, Los Alamos Scientific Lab., N. Mex.(USA), 1977.
- [142] L.L. Snead, T. Nozawa, Y. Katoh, T.S. Byun, S. Kondo, D.A. Petti, Handbook of SiC properties for fuel performance modeling, *Journal of Nuclear Materials* 371(1-3) (2007) 329-377.
- [143] Y. Katoh, G. Vasudevamurthy, T. Nozawa, L.L. Snead, Properties of zirconium carbide for nuclear fuel applications, *Journal of Nuclear Materials* 441(1-3) (2013) 718-742.
- [144] M. Korchynsky, *Powder Metallurgy of Uranium Monocarbide*, TID (1960) 66.
- [145] S. Pickles, G. Yates, J. Bramman, M.B. Finlayson, The sintering of uranium carbide and of uranium-plutonium carbide, and the role of nickel as a sintering additive, *Journal of Nuclear Materials* 89(2-3) (1980) 296-315.

- [146] B. Eyre, A. Bartlett, Effects of nickel on the structure of sintered uranium carbide, Atomic Energy Research Establishment, Harwell, England (United Kingdom), 1967.
- [147] W. Chubb, D.L. Keller, Constitution of the systems of uranium and carbon with molybdenum, niobium, rhenium, tungsten, and yttrium, Battelle Memorial Inst., Columbus, Ohio, 1964.
- [148] D.P. Butt, T.C. Wallace Sr, The U–Zr–C Ternary Phase Diagram above 2473 K, *Journal of the American Ceramic Society* 76(6) (1993) 1409-1419.
- [149] D.P. Butt, T.C. Wallace, W.A. Stark Jr, E. Storms, F. Hampel, M. Williamson, P. Kleinschmidt, Experimental and numerical optimization of the U-Zr-C ternary phase diagram, Los Alamos National Lab., NM (United States), 1992.
- [150] H. Holleck, H. Kleykamp, Thermodynamics of multi-component systems containing UC and PuC A review, *Journal of Nuclear Materials* 32(1) (1969) 1-19.
- [151] J. Routbort, H. Matzke, Uranium self-diffusion in impurity-doped uranium carbide, *Journal of Nuclear Materials* 54(1) (1974) 1-8.
- [152] T. Inoue, H. Matzke, Uranium self-diffusion in UC doped with Y, Zr, La or Ce, *Journal of Nuclear Materials* 91(1) (1980) 1-12.
- [153] H. Hirsch, H. Scherff, Actinide diffusion in uranium monocarbide, *Journal of Nuclear Materials* 45(2) (1972) 123-130.
- [154] H. Matzke, The effect of Fe, Ni and W impurities on uranium diffusion in uranium monocarbide, *Journal of Nuclear Materials* 52(1) (1974) 85-88.
- [155] E.S. Wood, J.T. White, C.J. Grote, A.T. Nelson, U<sub>3</sub>Si<sub>2</sub> behavior in H<sub>2</sub>O: Part I, flowing steam and the effect of hydrogen, *Journal of Nuclear Materials* 501 (2018) 404-412.
- [156] C. Sanders, J. Wagner, Study of the effect of integral burnable absorbers for PWR burnup credit, ORNL/TM-2000/321 (2002).

APPENDIX D: SUPPLEMENTARY FILE FOR CHAPTER FOUR: INVESTIGATING  
GRAIN GROWTH OF CONVENTIONALLY SINTERED URANIUM  
MONONITRIDE

This document is pending journal submission along with the original manuscript.

## D.1 Grain size statistics

A compilation of histograms grouped by sintering temperature for the samples in this study (1850-2000 °C) is shown in **Figure D.S1 – Figure D.S4**. None of the sample sets exhibit true Gaussian distribution, the closest being those for the 1850/5, 1850/15, 1900/5, 1900/15, and 1950/15 samples. The remainder are all positively skewed with the largest number of occurrences in the lower values. The average grain size and the number of grains analyzed are also noted on each plot with the exception of the 1950/25 sample. The 1950/25 sample underwent abnormal grain growth so the grains analyzed were only those around the perimeter of the sample.

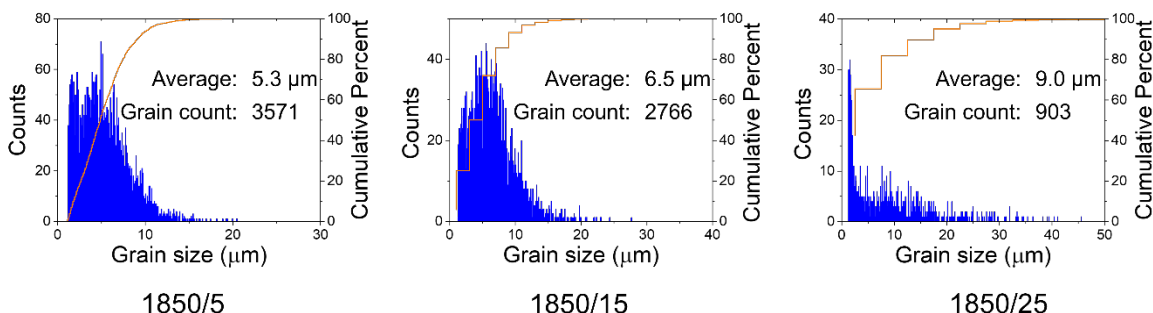


**Figure D.S1** Histograms depicting the grain size distribution of the 1850 °C sintered samples with counts showing on the left y-axis and the cumulative percentage line corresponding to the right y-axis.

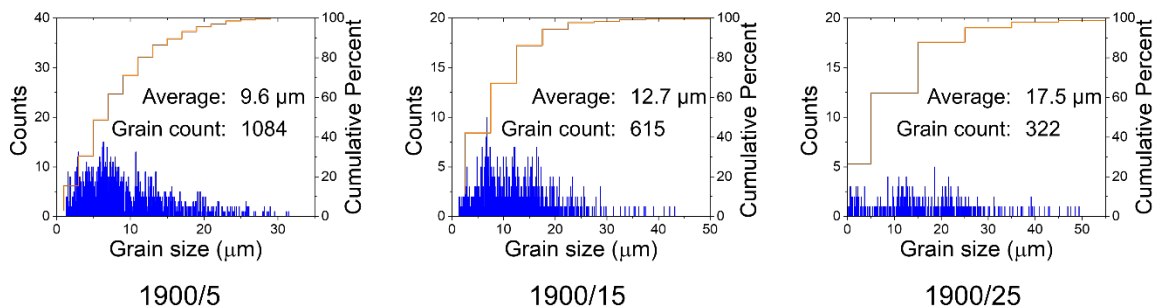


**Figure D.S2** Histograms depicting the grain size distribution of the 1900 °C sintered samples with counts showing on the left y-axis and the cumulative percentage line corresponding to the right y-axis.

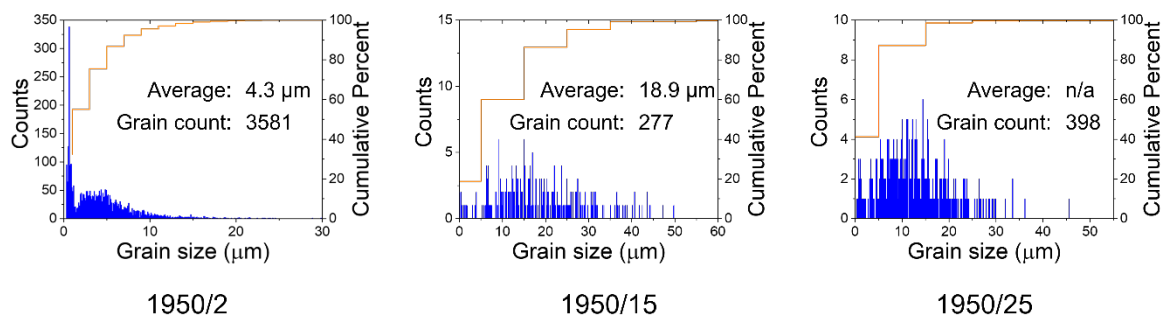


**Figure D.S3** Histograms depicting the grain size distribution of the 1950 °C sintered samples with counts showing on the left y-axis and the cumulative percentage line corresponding to the right y-axis.

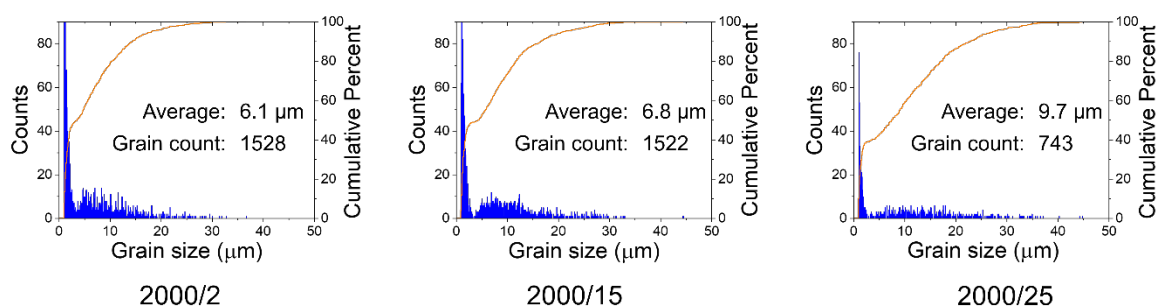


**Figure D.S4** Histograms depicting the grain size distribution of the 2000 °C sintered samples with counts showing on the left y-axis and the cumulative percentage line corresponding to the right y-axis.

## D.2 Abnormal grain growth in 1950/25

As previously mentioned, sample 1950/25 was found to have undergone abnormal grain growth during the sintering process. The fabrication and sintering process used for this sample was the same as employed for all other samples and none of the other samples exhibited this exaggerated grain growth behavior. A stitched montage optical image of the cross-section of the 1950/25 sample is seen in **Figure D.S5A**. The AGG is apparent from the existence of three large grains in the middle of the pellet surrounded by increasingly smaller grains near the pellet perimeter. The inset is to identify the location where the EBSD inverse pole figure map, (**Figure D.S5B**) was taken from. No preferential orientation appears to be present in the larger grains. Literature on the factors

leading to exaggerated grain growth (also referred to as secondary recrystallization) state that a wide distribution of grain sizes in the starting material can prompt abnormal grain growth since it is more likely that at least one grain is much larger than the average [1-3]. Another condition leading to AGG is when a mobile secondary phase (being either an impurity or porosity) is present that inhibits continuous grain growth in the matrix [2]. As grain growth occurs, pores can become isolated from the grain boundaries, which not only diminishes densification, but can increase the grain boundary mobility allowing growth at the expense of neighboring grains [3-5]. As mentioned in section 3.3, the pore size increased with sintering time for the 1950 °C sintered samples. As one grain is consumed, pores that were isolated from the grain boundaries can coarsen during extended sintering [6]. Exaggerated grain growth (also > 1 mm diameter) has been reported for UN under specific conditions [7]. The sintering parameters were only noted as 1900 °C for 24 hours under a partial pressure of nitrogen equal to  $1.2 \cdot 10^{-8}$  MPa, but also stated that the results were not reproducible and no other specifics were available as the original reference could not be obtained [7]. It may be that a combination of the wide grain size distribution in the starting materials coupled with the possibility of an unintended agglomeration of particles (due to an unknown anomaly during pellet fabrication) leading to inhomogeneity in the starting pore distribution could have led to the AGG seen in this sample. It is also possible that because the milled powder used for this pellet fabrication was not used within a few days of milling, that contamination from the glovebox atmosphere after “aging” resulted in unwanted oxygen impurities. A more detailed investigation into the cause of this AGG is warranted but outside the scope of this study.

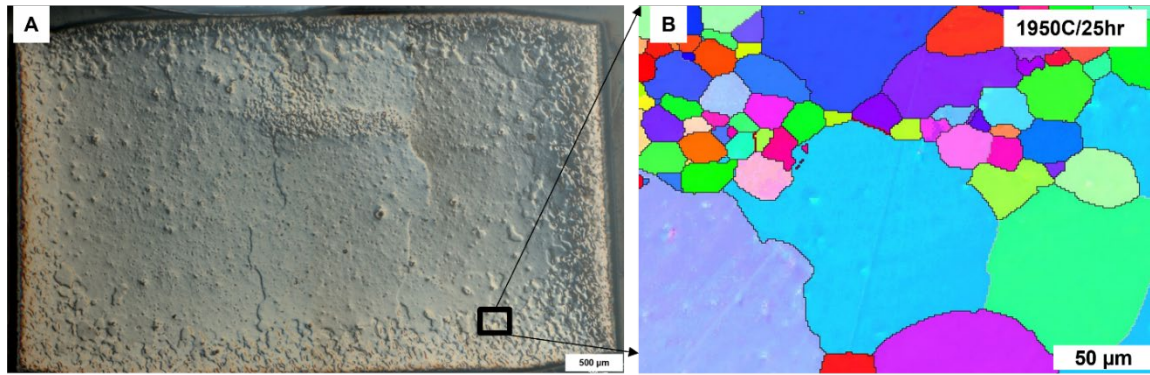


**Figure D.S5** A) Stitched optical image montage of the cross-sectional area for the 1950/25 sample showing the exaggerated grain growth of the very large (> 1 mm) grains in the middle of the sample surrounded by increasingly smaller grains towards the sample edge, black square inset represents area from where the EBSD mapping occurred; B) EBSD inverse pole map of the inset area from A).

### References

- [1] M. Hillert, On the theory of normal and abnormal grain growth, *Acta Metallurgica* 13 (3) (1965) 227-238.
- [2] R. Brook, Controlled grain growth, *Treatise on Materials Science & Technology*, Elsevier 1976 pp. 331-364.
- [3] W.D. Kingery, H.K. Bowen, D.R. Uhlmann, *Introduction to ceramics*, John Wiley & Sons, New York, 1976.
- [4] R.M. German, *Sintering theory and practice*, John Wiley & Sons, Inc., New York, 1996.
- [5] J.D. Powers, A.M. Glaeser, Grain boundary migration in ceramics, *Interface Science* 6 (1) (1998) 23-39.
- [6] R. German, *Sintering: from empirical observations to scientific principles*, Butterworth-Heinemann 2014.
- [7] H. Matzke, *Science of advanced LMFBR fuels*, North-Holland Physics Publishing, Amsterdam, The Netherlands, 1986.

APPENDIX E: SUPPLEMENTARY FILE FOR CHAPTER FIVE: ENHANCING  
THERMAL CONDUCTIVITY OF  $\text{UO}_2$  WITH THE ADDITION OF  $\text{UB}_2$  VIA  
CONVENTIONAL SINTERING TECHNIQUES

This document has been published online with the Journal of Nuclear Materials along with the original manuscript.

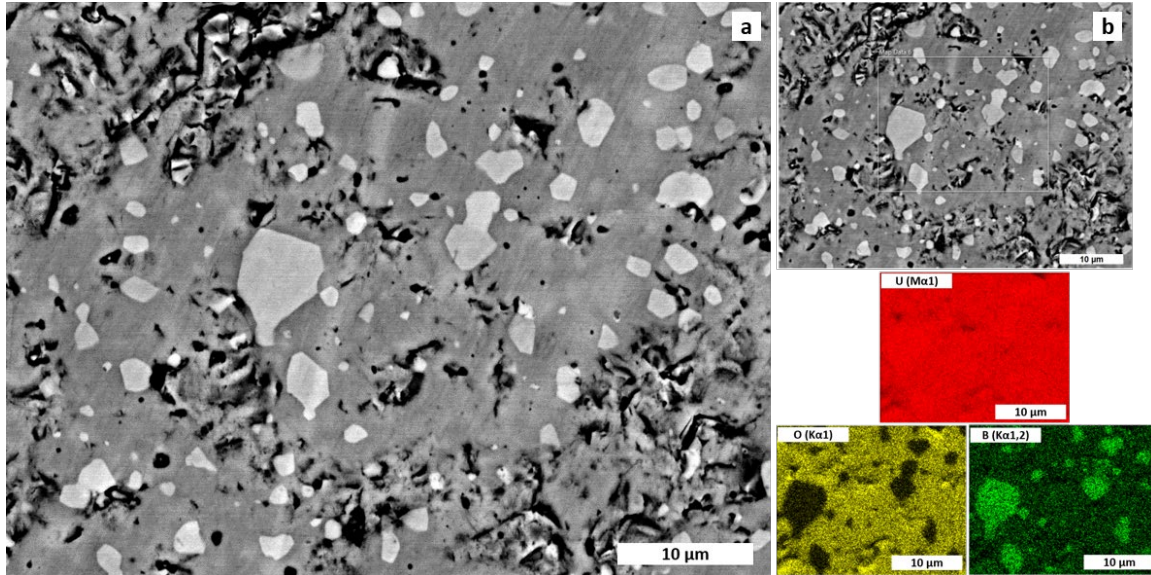


**Figure E.S1** a) Backscatter electron (BSE) image of the microstructure for the 4-hour sintered sample after undergoing laser flash analysis to 1273 K, and b) BSE image showing mapped area for EDS along with elemental mapping of the uranium, oxygen (darker grey), and boron (lighter gray) phases. Essentially no difference in the microstructure is observed after thermal property characterization.

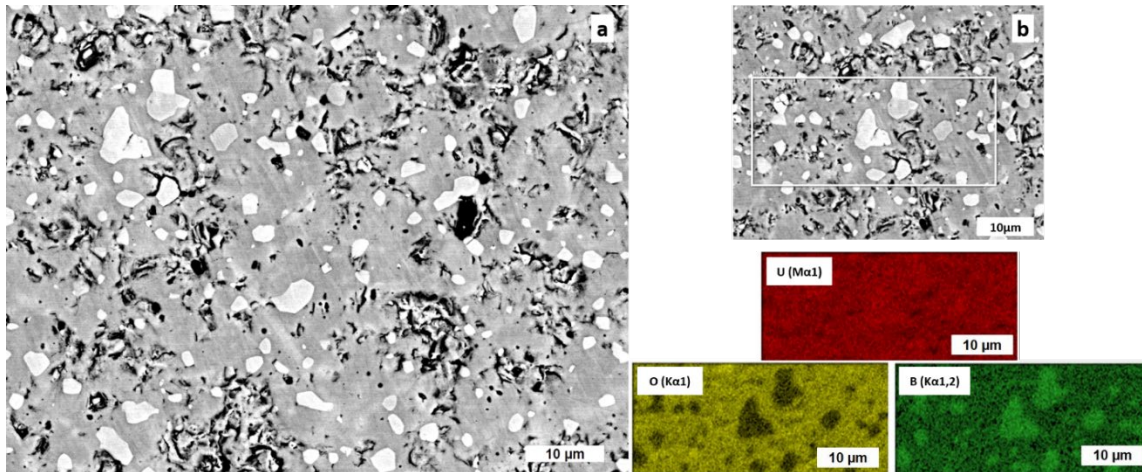


**Figure E.S2** a) Backscatter electron (BSE) image of the microstructure for the 8-hour sintered sample after undergoing laser flash analysis to 1273 K, and b) higher magnification BSE image along with EDS elemental mapping of the uranium, oxygen (darker grey), and boron (lighter gray) phases. Essentially no difference in the microstructure is observed after thermal property characterization.

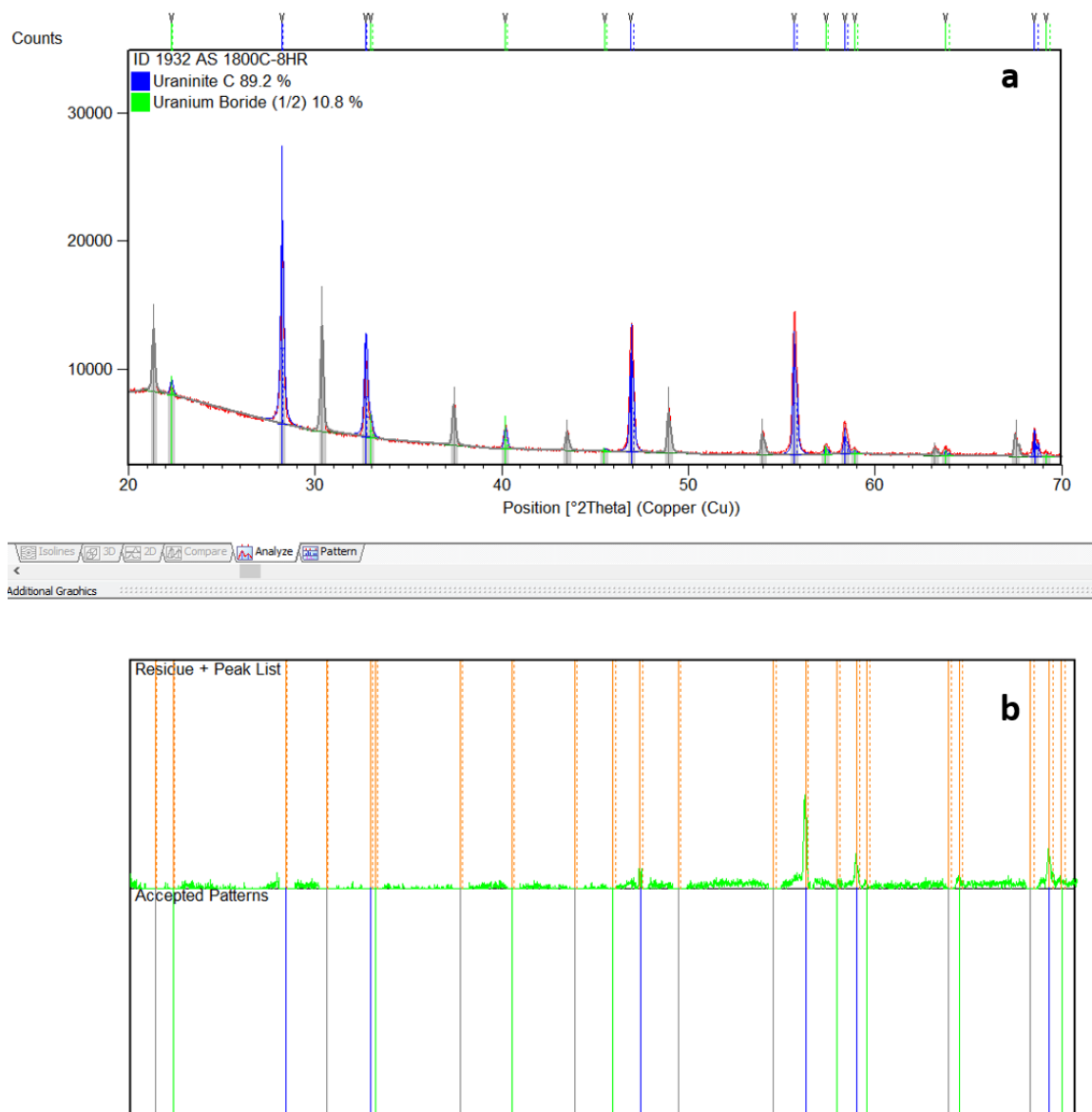


**Figure E.S3** a) XRD pattern for the 8-hour as-sintered sample as displayed in the HighScore+ software indicating the calculated pattern fit and showing the phase markers for the  $\text{UO}_2$  (blue),  $\text{UB}_2$  (green), and NIST SRM  $\text{LaB}_6$  (gray), and b) the residue and peak list from the calculated fit, the weighted R was 6.1 and the goodness of fit was 18.5.

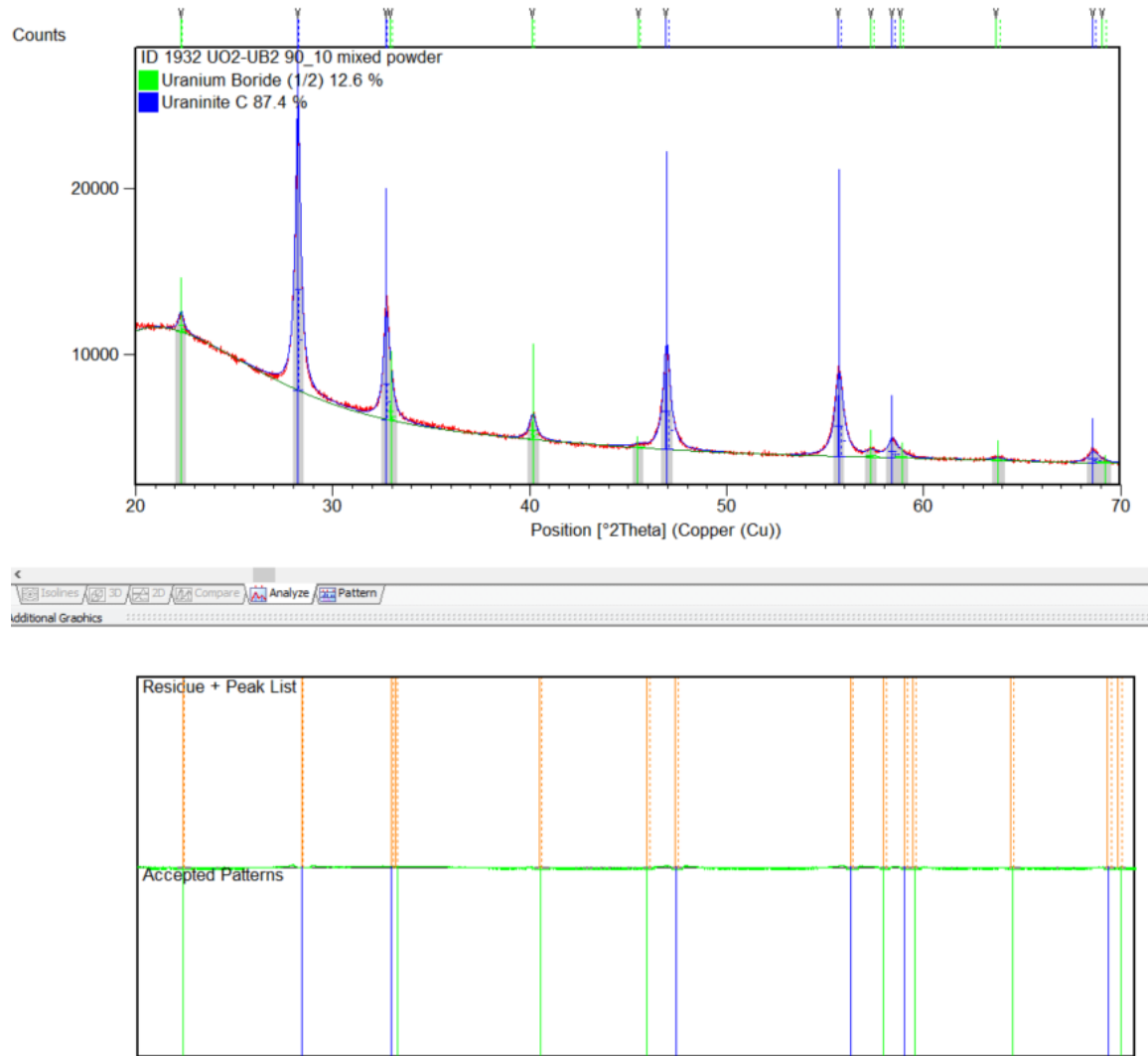


**Figure E.S4** a) XRD pattern for the  $\text{UO}_2$ -10wt%  $\text{UB}_2$  mixed-powder sample as displayed in the HighScore+ software indicating the calculated pattern fit and showing the phase markers for the oxide phases  $\text{UO}_2$  (blue) and  $\text{UB}_2$  (green), and b) the residue and peak list from the calculated fit, the weighted R was 1.7 and the goodness of fit was 1.8. The calculated phase fraction for the boride phase at almost 13wt% is attributed to sampling of the powder for characterization and an overestimation in the quantitative results from the amorphous nature of the vacuum grease used for sample encapsulation.

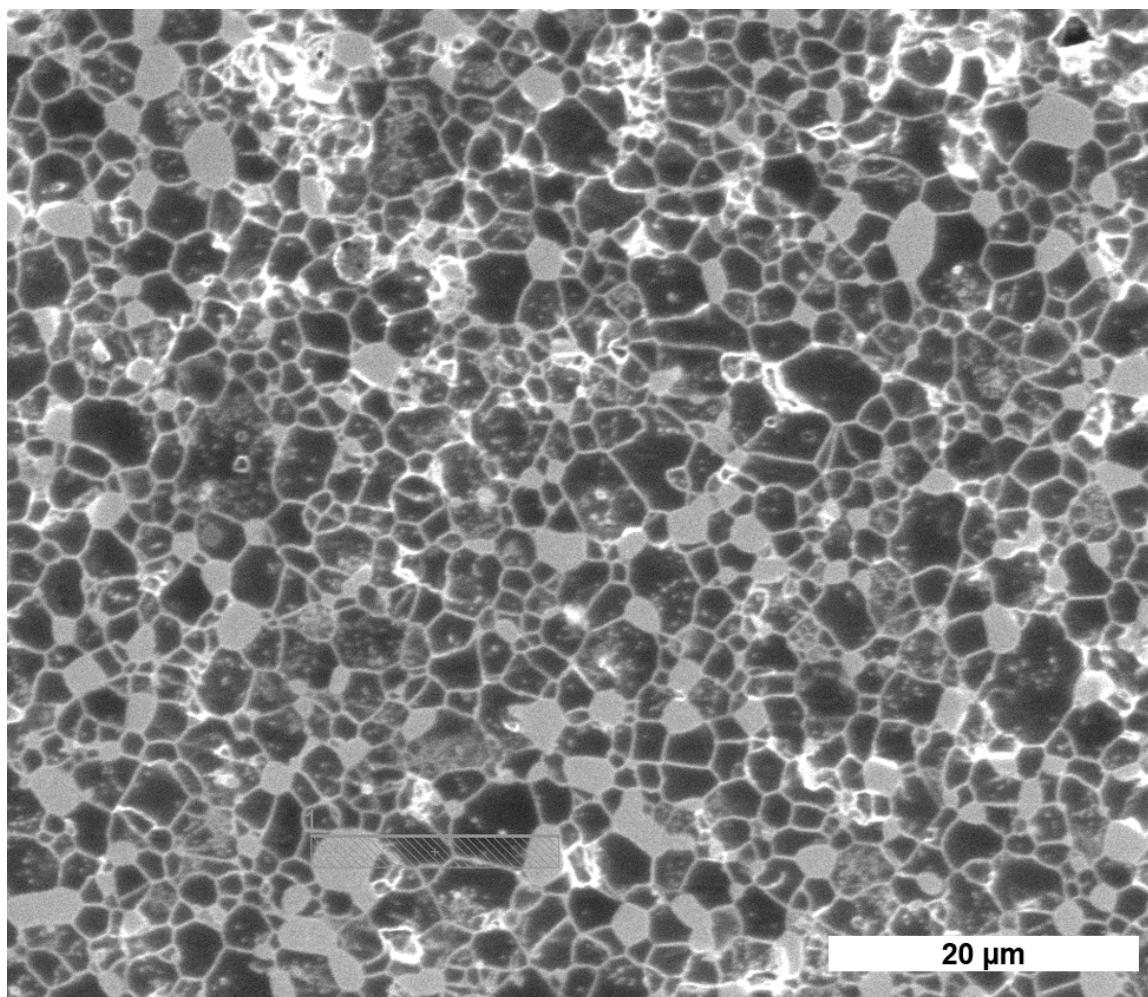


**Figure E.S5** SEM micrograph of the same as-sintered 8-hour  $\text{UO}_2$ -10wt%  $\text{UB}_2$  sample (seen in Figure 4a in the main manuscript after polishing via focused ion beam). This same cross-sectional surface exhibits a smaller amount of porosity (in line with the 96% TD) than what was achieved through the mechanical polish, confirming much of the porosity seen in the Figure in 4a came from pullout during sample preparation.